MICROCOPY RESOLUTION TEST CHART

NATIONAL BUREAU OF STANDARDS-1963-A

AFML-TR-78-68

LEVEL

ADA063404

INFLUENCE OF METALLURGICAL FACTORS ON THE FATIGUE CRACK GROWTH RATE IN ALPHA-BETA TITANIUM ALLOYS.

J. C. CHESNUTT,
A. W. THOMPSON
J. C. WILLIAMS

ROCKWELL INTERNATIONAL, SCIENCE CENTER
1049 CAMINO DOS RIOS
THOUSAND OAKS, CALIFORNIA 91360

MAY 1978

4 23 P.

SC584. 42 TR

2418

Φ2

Approved for public release; distribution unlimited.

F 33615-74-C-5Φ67

AIR FORCE MATERIALS LABORATORY
AIR FORCE WRIGHT AERONAUTICAL LABORATORIES
AIR FORCE SYSTEMS COMMAND
WRIGHT-PATTERSON AIR FORCE BASE, OHIO 45433

389 949

79 01 15 073

NOTICE

When Government drawings, specifications, or other data are used for any purpose other than in connection with a definitely related Government procurement operation, the United States Government thereby incurs no responsibility nor any obligation whatsoever; and the fact that the Government may have formulated, furnished, or in any way supplied the said drawings, specifications, or other data, is not to be regarded by implication or otherwise as in any manner licensing the holder or any other person or corporation, or conveying any rights of permission to manufacture, use, or sell any patented invention that may in any way be related thereto.

This report has been reviewed by the Information Office (OI) and is releasable to the National Technical Information Service (NTIS). At NTIS, it will be available to the general public, including foreign nations.

This technical report has been reviewed and is approved for publication.

LRBidwell

Lawrence R. Bidwell
Project Engineer
Structural Metals Branch
Metals and Ceramics Division

FOR THE COMMANDER

NG Tupper

Nathan G. Tupper
Chief
Structural Metals Branch
Metals and Ceramics Division

"If your address has changed, if you wish to be removed from our mailing list, or if the addressee is no longer employed by your organization please notify AFML/LLS, W-PAFB, OH 45433 to help us maintain a current mailing list."

Copies of this report should not be returned unless return is required by security considerations, contractual obligations, or notice on specific document.

AIR FORCE/56780/8 January 1979— 250

REPORT DOCUMENTATION PAGE		READ INSTRUCTIONS BEFORE COMPLETING FORM
1. REPORT NUMBER AFML-TR-78-68	2. GOVT ACCESSION NO.	3. RECIPIENT'S CATALOG NUMBER
4. TITLE (and Subtitle) INFLUENCE OF METALLURGICAL FACTORS ON THE FATIGUE CRACK GROWTH RATE IN ALPHA-BETA TITANIUM ALLOYS		5. TYPE OF REPORT & PERIOD COVERED Final Technical Report 1 APR 74 - 21 NOV 77
		6. PERFORMING ORG. REPORT NUMBER SC584.42TR
7. AUTHOR(s) J. C. Chesnutt A. W. Thompson J. C. Williams		8. CONTRACT OR GRANT NUMBER(s) F33615-74-C-5067 new
9. PERFORMING ORGANIZATION NAME AND ADDRESS Rockwell International Science Center Thousand Oaks, CA 91360		10. PROGRAM ELEMENT, PROJECT, TASK AREA & WORK UNIT NUMBERS Project No. 2418
11. CONTROLLING OFFICE NAME AND ADDRESS Air Force Materials Laboratory Air Force Systems Command Wright-Patterson Air Force Base, Ohio 45433		12. REPORT DATE May 1978
		13. NUMBER OF PAGES 420
14. MONITORING AGENCY NAME & ADDRESS(if different from Controlling Office) Same as Block 11		15. SECURITY CLASS. (of this report) Unclassified
		15a. DECLASSIFICATION/DOWNGRADING SCHEDULE NA

16. DISTRIBUTION STATEMENT (of this Report)

Approved for public release; distribution unlimited.

17. DISTRIBUTION STATEMENT (of the abstract entered in Block 20, if different from Report)

18. SUPPLEMENTARY NOTES

19. KEY WORDS (Continue on reverse side if necessary and identify by block number)

Ti Alloys, Ti-6Al-4V, Ti-6Al-2Sn-4Zr-6Mo, thermomechanical processing, microstructure, mechanical properties, cyclic hardening, fatigue life, fatigue crack propagation, fracture toughness, fractography

20. ABSTRACT (Continue on reverse side if necessary and identify by block number)

Research was conducted on two alpha-beta titanium alloys, Ti-6Al-4V and Ti-6Al-2Sn 4Zr-6Mo, as a function of alloy composition microstructure and strength level, environment, and fatigue loading conditions. A wide range of microstructural conditions, seven for Ti-6Al-4V and three for Ti-6Al-2Sn-4Zr-6Mo, was chosen to provide a full range of constituent types and morphologies and a range of mechanical properties. All the material for the program was obtained in the form of pancake forgings which were uniformly and weakly textured.   (continued)

DD FORM 1473 1 JAN 73   EDITION OF 1 NOV 65 IS OBSOLETE

79 01 15 023

The initial portion of the program consisted of material characterization and base line fatigue crack propagation (FCP) testing. Characterization included a full description of microstructures, as well as mechanical property testing, fracture toughness tests, S-N curve determination and measurement of other properties such as modulus and texture. Base line FCP testing in dry air at two stress ratios (R) of 0.1 and 0.3; and in a 3.5% NaCl solution at 1 and 20 Hz was conducted in this portion of the program.

The following portion of the program involved selection of six of the original ten microstructures for more detailed FCP testing which included differences in environment (100% RH air, dry argon), stress ratio (R = 0.5, 0.7), and hold time and spike overload experiments.

Additional testing was done to study the effect of temperature on FCP rates for three microstructural conditions of Ti-6Al-4V and the effect interstitial content on FCP rates for two microstructures of Ti-6Al-4V.

Results of this study included the determination that transformed beta microstructures generally exhibit the greatest fatigue crack propagation resistance and that increasing the load ration, R, can lead to significant increases in crack growth rate; the behavior in both cases was rationalized in terms of crack tip interaction with microstructural constituents. Aggressive environments with the exception of 3.5% NaCl at 1 Hz, were found to have little effect on this weakly textured material. Increases in temperature produced significant increases in crack growth rates while only the beta quenched microstructure of Ti-6Al-4V proved sensitive to interstitial content from a fatigue crack propagation standpoint.

ACCESSION for

NTIS
DDC
UNANNOUNCED
JUSTIFICATION

BY
DISTRIBUTION
D

A

FOREWORD

This report describes the results of a program performed by the Rockwell International Science Center during the period 1 April 1974 through 21 November 1977 under USAF Contract No. F33615-74-C-5067. The contract was administered by the Air Force Materials Laboratory, Air Force Systems Command, Wright-Patterson AFB, Ohio, under Task 241802, with Dr. L. R. Bidwell as Program Monitor.

Dr. J. C. Williams, Dr. A. W. Thompson, and Mr. J. C. Chesnutt served as Program Managers successively. This report has been assigned Science Center No. SC584.42TR for internal control purposes.

The authors wish to acknowledge the following members of the Science Center for technical assistance:

Mr. J. D. Frandsen*	Mr. P. Q. Sauers
Dr. M. R. Mitchell	Mr. D. M. Sellman
Mr. L. F. Nevarez	Mr. R. A. Spurling
Ms. R. J. Richards	Mr. E. H. Wright

and Dr. M. R. Mitchell, Mr. M. W. Mahoney, Dr. N. E. Paton and Mr. C. G. Rhodes for helpful technical discussions. Additionally, we wish to thank Mr. H. S. Brenner of Almay Research and Testing for making the S-N measurements, Mr. A. L. Wiengert and Mr. R. H. Olsen of The Boeing Company for

---

*Now with Failure Analysis Associates, Los Angeles, California

iii

TABLE OF CONTENTS

TABLE OF CONTENTS
(continued)

LIST OF TABLES

LIST OF ILLUSTRATIONS

Page

LIST OF ILLUSTRATIONS
(continued)

LIST OF ILLUSTRATIONS
(continued)

LIST OF ILLUSTRATIONS
(continued)

xvii

LIST OF ILLUSTRATIONS
(continued)

INTRODUCTION

Program Background

The fatigue crack propagation behavior of titanium and its alloys represents an area of major technological importance. Current airframe design philosophies assume the existence of a flaw which can subsequently grow during service. When this philosophy is applied, the design of efficient structures requires accurate knowledge of the crack growth behavior. The parameter of interest is thus the fatigue crack propagation (FCP) rate, which must be known for reliable and efficient design. This requirement is complicated, for example, by the significant variations in crack growth rate which have been observed between various heats of Ti-6Al-4V. It is clearly desirable to design to the lowest growth rates observed, provided that material which exhibits these rates can be reproducibly obtained in the required quantities. Thus, an improved understanding of the factors which control fatigue crack growth rate can result in weight reductions of future generations of hardware.

In spite of the importance of fatigue cracking behavior, however, relatively few systematic studies have been made. As a result, there are several aspects of the subject which are currently unresolved. For instance, it is important to know whether FCP can be either retarded or accelerated by metallurgical variables, both to ensure reproducibility of results, and to design improved materials. Yet the extensive literature on FCP testing and

1

evaluation has been only marginally concerned with microstructure,

composition, texture, strength level, and other metallurgical variables, and

only a part of what does exist relates to titanium alloys. The program was

planned, therefore, to examine certain metallurgical variables in two

alpha-beta alloys, particularly microstructure, while holding other variables,

particularly texture, constant. The alloys studied were Ti-6Al-4V, chosen

because of its extensive usage and broad background of understanding, and

Ti-6Al-2Sn-4Zr-6Mo, chosen as an alloy with rather greater beta stabilization

and because of its increasing popularity as a higher strength alloy. A series

of microstructures described below were produced in each alloy to enable the

separation of fatigue crack propagation (FCP) effects due to both

microstructural variables and strength level. Details of the program outline

are given in the following section.

Program Outline

The program was conducted on two alpha-beta titanium alloys,

Ti-6Al-4V and Ti-6Al-2Sn-4Zr-6Mo, as a function of alloy microstructure and

strength level, environment, and fatigue loading conditions. A wide range of

microstructural conditions, seven for Ti-6Al-4V and three for

Ti-6Al-2Sn-4Zr-6Mo, was chosen to provide a full range of constituent types

and morphologies and a range of mechanical properties. All the material for

the program was obtained in the form of pancake forgings.

2

Phase I of the program consisted of two parts, material characterization and baseline fatigue crack propagation (FCP) testing. Characterization included a full description of microstructures, as well as mechanical property testing, fracture toughness tests, S-N curve determination and measurement of other properties such as modulus and texture. Baseline FCP testing in dry air at two stress ratios (R) of 0.1 and 0.3, and in a 3.5% NaCl solution at 1 and 20 Hz was included in this phase of the program.

Phase II of the program involved selection of six of the original ten microstructures for more detailed FCP testing which included differences in environment (100% RH air, dry argon), stress ratio (R = 0.5, 0.7), and hold time and spike overload experiments. For Phase II, four microstructural conditions of Ti-6Al-4V and two of Ti-6Al-2Sn-4Zr-6Mo were chosen on the basis of the Phase I results.

Phase III of the program extended the program to the study of the effect of temperature on FCP rates for three microstructural conditions of Ti-6Al-4V and to study the effect interstitial content on FCP rates for two microstructures of Ti-6Al-4V. Pancake forgings of two additional oxygen contents were obtained for this phase.

In order to present the results in a more readable form, this report will be organized into a format differing from the Program Outline.

Report Outline

The report is organized into four major sections, each representing a logical grouping of technical information. The four sections are preceded by

3

an introduction and followed by a general discussion and conclusions. The four major sections, designated Parts I through IV, deal with the following topics:

Part I Material Characterization

Part II Crack Propagation in Ti-6Al-4V and Ti-6Al-2Sn-4Zr-6Mo

Part III Environmental Effects of Fatigue Crack Propagation

Part IV Temperature and Interstitial Effects on

Fatigue Crack Propagation

Individual parts have been organized to be self-contained and will include introduction, experimental procedures, results and discussion sections and a bibliography. A complete set of fatigue crack propagation curves generated during the program are presented in Appendix A; additional data not directly applicable to the four major parts is contained in Appendix B. Appendix C contains a list of papers and technical talks resulting from this program.

PART I: MATERIALS CHARACTERIZATION

INTRODUCTION

This section describes the materials characterization studies
conducted on the seven microstructural conditions of Ti-6Al-4V and the three
conditions of Ti-6Al-2Sn-4Zr-6Mo. This characterization includes
microstructure studies using both light and thin foil electron microscopy (LM
and TEM); texture determinations; and determination of a range of mechanical
properties including yield and ultimate strengths, fracture toughness, smooth
and notched fatigue properties and cyclic work hardening characteristics. All
of these types of information are prerequisities to any detailed
interpretation of the interrelation between fatigue crack growth rate and
metallurgical variables such as microstructure.

EXPERIMENTAL PROCEDURE

The material used for this part was press forged into 5.08 cm (2 in.)
thick pancakes from 22.9 cm (9 in.) round billet. The forging was
accomplished in two stages. The details of forging temperatures and
reductions are shown in Table I-I. The chemical compositions of the starting
materials are shown in Table I-II.

Light metallography specimens were prepared by electropolishing using a Buehler recirculating pump cell. Specimens were etched in Kroll's etchant (95% H_2O, 3% HNO_3, 2% HF) or an etchant composed of equal parts of 10% aqueous oxalic acid and 1% aqueous HF solutions. Photomicrographs were taken with a Zeiss Ultraphot Metallograph.

Thin foils were prepared by the window method using an electrolyte consisting of 5% H_2SO_4 in methanol. Polishing was conducted at ~18 volt open circuit. The electrolyte temperature was ~-30°C. Thin foils were examined in a Philips EM300 equipped with a goniometer tilting stage and high resolution dark field coils.

Tensile tests were performed in an Instron machine at a strain rate of 1.67×10^{-4} s^{-1} using an extensometer. Fatigue tests were conducted on an Amsler Vibraphone resonant machine. Notched bars had a stress concentration factor of $K_t = 3.4$. Smooth bars ($K_t = 1$) were electropolished prior to testing. Low cycle fatigue tests were run in strain control using an hourglass specimen and a diametral strain measuring device.

Fracture toughness tests were conducted in accordance with ASTM E399 using compact tension specimens. Electron fractrography was performed on the fractured K_{Ic} specimens using an ETEC scanning electron microscope. Crack path studies were conducted using the technique described elsewhere by Chesnutt and Spurling.[1]

Texture determinations were performed by The Boeing Company using a reflection technique on a specimen which was machined from the original stock

6

in a way which exposes a plane whose normal lies at the center of the first quadrant of the stereographic projection. This technique permits measurement of the entire quadrant by the reflection method.

RESULTS

Forging and Heat Treatment

The forging history and detailed heat treatment schedules for the two alloys are summarized in Table I-III. Examination of the various as-forged conditions showed that the forging practice defined by Table I-I had been accomplished. The pancakes were then cut up for specimen fabrication and given the final heat treatments shown in Table I-III. Light metallography examination of three mutually perpendicular planes was conducted. These planes are normal to the radial, circumferential and longitudinal directions in the pancake forging as shown schematically in Fig. I-1. The microstructures after heat treatment are displayed as three-dimensional cubes in Fig. I-2 through I-11. Comparison of these microstructures with the forging and heat treatment summary in Table I-III confirms that the seven microstructures of Ti-6Al-4V and the three in Ti-6Al-2Sn-4Zr-6Mo were successfully produced. It can be noted from Fig. I-2 through I-11 that essentially no directionality exists in the microstructures after final heat treatment.

7

Systematic point counting was performed on micrographs of all the alloys of this study to determine the volume fraction of primary α and retained β. These measurements were made on light micrographs or bright and dark field electron micrographs, as appropriate. Results are shown in Table I-IV. The fine scale of the microstructures in Ti-6Al-2Sn-4Zr-6Mo has not permitted detailed volume fraction determinations. It is interesting that the amounts of retained β differ relatively little among the Ti-6Al-4V microstructures.

Microstructure Characterization

After completion of the light metallography, each microstructural condition was examined by transmission electron microscopy. These results are described separately below for each microstructural condition.

Condition 1 (Ti-6Al-4V) - This is the recrystallization anneal (RA) condition and is characterized by an equiaxed $\alpha+\beta$ microstructure, Fig. I-2. The α-phase is fully recrystallized and has a low dislocation density; those dislocations which are observed are frequently contained in sub-boundaries. These boundaries frequently contain ledges as shown in Fig. I-12(a). The presence of ledges is most easily detected by examining the offsets in the fringe patterns at the point where the boundary intersects the foil surface. The presence of such ledges lowers the total boundary energy by permitting most of the boundary to lie in a low energy orientation.

8

The β-phase regions in this condition lie principally at α-grain triple points. These regions consist on only β-phase when they are narrow, Fig. I-12(b), but contain α-phase precipitates when they are larger, Fig. I-12(c). The equilibrium β-phase volume fraction decreases on cooling from 1700°F; this can be accomplished through lateral contraction by outward diffusion of titanium or by nucleation and growth of the titanium-rich α-phase within the β-phase regions. The determining factor is the diffusion path length.

The regions near the α/β interphase boundaries have a complex structure as shown in Figs. I-12(b) and (c). These regions have been shown to consist of fine particles of α-phase which nucleate at the interface and grow into the primary α. These particles of α-phase are shown in the dark field micrograph, Fig. I-12(d). This reaction product has been termed "interface phase" and we will adhere to this terminology. The presence of interface phase no doubt influences the ease of slip transfer across the interphase boundaries and its presence is, therefore, considered to be important. As will be seen in the following, this interface phase is very common in the microstructures of this study.

<u>Condition 2 (Ti-6Al-4V)</u> - This condition consists of 10-20 vol% equiaxed primary α and a Widmanstätten $\alpha+\beta$ matrix, Fig. I-3. The primary α is fully recrystallized as seen in Fig. I-13(a). The primary α also has a continuous layer of interface phase along its perimeter as shown in

9

Fig. I-13(b) and (c). The Widmanstätten $\alpha+\beta$ structure seen in Fig. I-13(a) and (b) also has interface phase along the α/β boundaries as shown in the dark field micrograph, Fig. I-13(d).

Condition 3 (Ti-6Al-4V) - This condition is similar to Condition 2 except that the amount of the equiaxed primary α is higher, 40-50 vol%, as Fig. I-4 shows. The scale of the Widmanstätten $\alpha+\beta$ structure is somewhat finer and less regular, owing to the temperature used to establish the primary α volume fraction. The primary α particles in this condition are outlined with interface phase, as can be seen in Fig. I-14(a) and (b). The Widmanstätten α plates also have a layer of interface phase. Figure I-14(b) through (d) sequentially show the structure in bright field, then show the β-phase and interface phase in dark field. This series is taken of the same area and the arrows mark the same area on the photos.

Condition 4 (Ti-6Al-4V) - This condition is called β processed, and consists entirely of Widmanstätten $\alpha+\beta$, as Fig. I-5 shows. Electron microscopy of the same structure reveals the strips of β between the α-phase plates, Fig. I-15(a) and (b). Figure I-15(b) also clearly shows the presence of interface phase, which is verified by the dark-field micrographs of the interface (Fig. I-15(c)) and β (Fig. I-15(d)) phases.

10

Condition 5 (Ti-6Al-4V) - This condition is quenched from above the β transus after which the material should be fully martensitic. Examination of the microstructure of the compact tension specimens used for FCP tests shows that they contain a mixture of martensitic α' and Widmanstätten $\alpha+\beta$ as seen in Fig. I-6. The existence of substantial amounts of Widmanstätten $\alpha+\beta$, which is a nucleation and growth transformation product, suggests that the nose of the C-curve for the $\beta \rightarrow \alpha+\beta$ transformation is situated at times too short to permit formation of fully martensitic structures in the section sizes 1.27 cm (0.5 in.) used in the compact tension specimens. Figure I-16(a) through (d) is a series of micrographs which shows (a) the $\alpha+\beta$ structure in bright field; (b) the α plates; (c) the β plates; and (d) the interface phase. Figure I-17(a) and (b) show a region which has transformed to α' during quenching and decomposed to form β-phase during the stabilization treatment at 1300°F (see Table I-III).

Condition 6 (Ti-6Al-4V) - This condition ideally consists of equiaxed primary α particles in a matrix of tempered α' martensite. In practice the matrix of the compact tension specimens exhibited a mixed α' and Widmanstätten $\alpha+\beta$ structure (Fig. I-7), similar to that described above for Condition 5. An example of the Widmanstätten structure is shown in Fig. I-18(a). The presence of interface phase both at the Widmanstätten α plane boundaries and at the primary α boundaries can be seen in Fig. I-18(a) and (b). In those regions where α' has been formed, β-phase precipitates within the α' plates have

11

formed during aging, as seen in Fig. I-18(c) and (d). Note that the β-phase in (c) is platelet shaped and has a complex interfacial structure. This occurs when the β-phase nucleates along a martensite sub-boundary. In (d) the β-phase has a more equiaxed morphology with a smooth interface; this is typical of β which has nucleated at an individual dislocation.

Condition 7 (Ti-6Al-4V) - This condition is very similar to Condition 6. It also can be seen to contain both tempered α' and Widmanstätten $\alpha + \beta$. Fig. I-19(a) shows the $\alpha + \beta$ structure while Fig. I-19(b) shows the complex nature of the α plate boundaries due to the presence of interface phase. Figure 19(c) and (d) show the β precipitates which form in a martensitic region during aging. The primary α is fully recrystallized as can be seen in (a).

It was noted above for Conditions 5, 6, and 7 that the structures obtained in the 1.27 cm compact tension specimens was not martensitic, although such a structure would be expected to result from water quenching specimens from the solution temperature. The observation of nucleation and growth, Widmanstätten α-phase instead of martensite is simply an expression of the limited hardenability of Ti-6Al-4V. To illustrate this point, a thin slice ~0.5 mm (0.02 in.) of Condition 7 was water quenched from 1750°F (see Table I-III) and examined by electron microscopy. Figure I-20(a) shows the resulting fine α' martensite surrounding a primary α particle. Figure I-20(b) depicts the high dislocation density which is produced within the α' plates

12

during transformation. Compare Fig. I-20(b) to Fig. I-16(a), I-17(a) and (b), I-18(a), and I-19(a); the differences in structure are evident.

Condition 8 (Ti-6Al-2Sn-4Zr-6Mo) - This condition consists of equiaxed primary α particles in an $\alpha+\beta$ matrix (Fig. I-9). The $\alpha+\beta$ structure in the matrix is much more complex than that of the Ti-6Al-4V conditions described above. The nature of the α-plates is shown in Fig. I-21(a). The plates contain a dense internal structure. Recently it has been shown that these plates each contain as many as six individual variants of α-phase; the variation in diffraction conditions between these variants results in the mottled contrast seen in the interior of the plates in Fig. I-21(a) and (b). The primary α is recrystallized, but contains some sub-boundaries as shown in Fig. I-21(b).

Condition 9 (Ti-6Al-2Sn-4Zr-6Mo) - This structure also consists of equiaxed primary α particles in an $\alpha+\beta$ matrix (Fig. I-10). The primary α particles are seen in Fig. I-22(a). The primary α particles also contain features which are not seen in Ti-6Al-4V (Fig. I-22(b)). The appearance of these features is sensitive to contrast conditions and these features can appear to be β-phase laths, as in Fig. I-22(b), a figure which also shows the small size of the α-plates in the matrix. The origin of these features is not altogether clear at present, however, these features appear to consist of thin

13

regions of β-phase which contain interface phase (Fig. I-22(c) and (d)). Similar features have been seen in Ti-6Al-6V-2Sn.

Condition 10 (Ti-6Al-2Sn-4Zr-6Mo) - This condition consists of Widmanstätten primary α-plates in an $\alpha+\beta$ matrix, Fig. I-11. The structure of this condition is quite similar to Condition 9 except that the primary α is elongated due to the β-forging. The primary α-plates contain extensive internal structure (Fig. I-23(a) and (b)). The $\alpha+\beta$ matrix structure consists of very fine α-plates (Fig. I-23(b) and (c)). As in Condition 9, the appearance of the internal features in the primary α depends on contrast conditions; Fig. I-23(c) shows these features when they appear to be continuous laths, whereas Fig. I-23(d) shows that the regions contain discrete precipitates. As in Fig. I-22(c) and (d), these features have been shown to be largely interface phase.

Texture and Modulus Measurements

The basal pole figures obtained from specimens of each of the microstructural conditions of the two alloys are shown in Fig. I-24 through I-33. Examination of these pole figures shows that all of the materials were only weakly textured. The maximum concentration of basal poles observed was four times random, and, in the samples where this concentration was observed, there were typically several orientations which contained such concentrations. Young's modulus values were determined for each condition at

14

80 KHz using a resonance technique. These values are shown in Table I-V, all lie between 110 and 117 GPa (16 and 17 x 10^6 psi), that is, they show a maximum variation of ~6%. These variations are consistent with the pole figure data. The data also are consistent with the fact that the samples have been stabilized at approximately the same temperature which leads to essentially constant volume fractions of α and β phases. The modulus predicted by the Rule of Mixtures would, therefore, be expected to be comparable for all conditions.

Tensile Properties and Hardness

The tensile properties of the ten conditions of the two alloys are shown in Table I-VI. From this table it can be seen that all of the yield strengths are somewhat lower than are often quoted for these alloys in the heat treatment conditions selected. This is qualitatively accounted for by the low oxygen content of the billet selected for forging as shown in Table I-II. Apart from this, there is at least one other inconsistency in the tensile property data. The overaged (Condition 7) material is stronger than the Condition 6 material which was aged for a shorter time at 1100^0F. The reason for this is not altogether clear, but it is possible that the low oxygen material has a different aging response than the more widely used higher oxygen material.

The Rockwell C hardness of the ten conditions of the two alloys are shown in Table I-VII. These data correlate reasonably well with the ultimate

15

strengths shown in Table I-VI. There are a few inconsistencies; for example, Conditions 3 and 4 have ultimate strengths of 908 MPa (132 ksi) and 852 MPa (124 ksi), respectively, whereas the R_c hardnesses are 30.2 and 30.7, respectively. Since hardness is related to flow stress at $\sim$6-8% strain, the uniform strain which corresponds to the ultimate strengths shown in Table I-VI are helpful in reconciling these data. Condition 3 shows a 9.2% strain at ultimate whereas Condition 4 shows an 8.7% strain. Thus, the work hardening capacity of Condition 3 is not as fully exhausted in the hardness test as compared to Condition 4.

Fatigue Life and Cyclic Stress-Strain Behavior

The fatigue life behavior of the ten conditions for the two alloys showed fatigue strengths at 10^7 cycles which varied between about 550 and 375 MPa for the smooth bars. The notched bars showed fatigue strengths which varied between about 225 and 125 MPa. Condition 1 consistently had the lowest fatigue strength, both smooth and notched. Condition 10 consistently had the highest smooth and notched fatigue strength. Of the other conditions of Ti-6Al-4V, Condition 6 had the highest smooth bar fatigue strength, whereas Condition 2 had the highest notched fatigue strength. Of the other conditions of Ti-6Al-2Sn-4Zr-6Mo, Condition 9 had the lowest smooth and notched bar strength. The S-N curves for all ten conditions are shown in Fig. I-34 and I-35. The ranking of these fatigue strengths does not lend itself to simple analysis. Moreover, there does not even seem to be any discernible

16

correlation between good smooth bar life and equiaxed microstructures or between acicular* microstructures and good notched bar life. Such correlations have been suggested previously,[2] but these do not appear to be supported by the data of the current program. The reasons for this will be briefly considered in the discussion.

The cyclic stress-strain curves for the ten conditions are shown together with their monotonic stress-strain curves in Fig. I-36 through I-45. Most of the conditions exhibit cyclic softening, that is, their cyclic curves lie below the monotonic curve. Such behavior is consistent with the cyclic stability index[3] which predicts softening when the ratio of tensile strength (UTS) to yield strength (YS) is less than 1.2, whereas hardening is predicted if the ratio is greater than 1.4. The relevant property data including the extent of softening at 1% strain are summarized in Table I-VIII The (UTS/YS) column in this table shows that all conditions except Condition 1 exhibit a ratio less than 1.2.

The cyclic stress-strain curves for Conditions 1, 2, and 4 (Fig. I-36, I-37, and I-39) cross the monotonic curve. This is relatively uncommon although curves which exhibit cyclic softening often show a trend which would lead to crossing at some higher strain. The crossing strains observed here are quite low, always less than 1%. These strains are also

_____

*The term acicular is used to describe the metallographic appearance of the microstructures and does not infer particle shape. It is well recognized from extensive work on titanium alloys that the Widmanstätten α particles are plates.

shown in Table I-VIII. This behavior is not understood in a mechanistic sense
at present. However, the conditions which exhibit crossing are regarded as
having cyclically stable flow properties.

Fracture Toughness

Fracture toughness of each of the ten conditions was determined.
These results are shown in Table I-IX. These data show that the Conditions 1,
2, and 4 were so tough that the tests resulted in invalid values. While it is
not reasonable to speculate about K_{Ic} values using K_Q data, it is clear
that all conditions of Ti-6Al-4V exhibit adequate toughness whereas two of the
conditions of Ti-6Al-2Sn-4Zr-6Mo exhibit fairly low toughness. The generally
high toughness values are consistent with and typical of the low oxygen
content of the two lots of material tested in this program. The general
trends in toughness are similar to those seen earlier by Sparks and Long,[4]
whose data has been analyzed and discussed elsewhere.[5] In general,
predominantly or wholly acicular microstructures (Conditions 2, 4, 6, 7
and 10) have superior toughness compared to the equiaxed microstructures. The
most obvious exception to this trend is Condition 5. Some possible
observations which account for this will be presented below in the
fractography section.

Fractography and Fracture Path of Toughness Specimens

The fractography of Conditions 1, 4, 5, 7, 8 and 10 are shown in
Fig. I-46 through I-51. These figures show the fatigue precrack to rapid

18

fracture transition at two magnifications (100 and 500X) and the rapid
fracture at point ~2.5 mm past the end of the fatigue precrack at the same
magnifications. Figures I-46 through I-48 show the fracture topography of
Conditions 4, 5 and 10. These conditions are the fully acicular
microstructures and consequently exhibit very undulating, tortuous fracture
paths, as discussed elsewhere.[5] Additional interpretation of the
fractographs is made possible by a technique reported earlier[1] which
permits simultaneous examination of the fracture surface and underlying
microstructure. The additional results obtained using this technique are
shown in Fig. I-52 through I-55. Comparison of Fig. I-46 and I-52 shows that
the large shallow dimples which contain serpentine glide occur when the crack
propagates along the long dimension of the Widmanstätten colony. Comparison
of Fig. I-46 and I-47 shows that the dimples are generally smaller in
Condition 5 compared to Condition 4 and that there is much less large scale
tearing in Condition 5. Comparison of Fig. I-48 and I-51 shows that the crack
path is very flat in the equiaxed microstructure of Ti-6Al-2Sn-4Zr-6Mo
(Condition 8, Fig. I-51) while the acicular microstructure (Condition 10,
Fig. I-48) causes extensive crack branching and secondary cracking. The
increase in toughness in Condition 10 is thus not surprising. Figure I-49
shows that the equiaxed microstructure of Ti-6Al-4V, Condition 1, fractures by
hole growth and tearing. Figure I-54 shows that many of the tear ridges
correspond to the α/β interfaces. The correlation between tear ridges and
primary α/acicular matrix boundaries is even more obvious in Condition 7
(Fig. I-50 and I-55). In this mixed equiaxed and acicular microstructure

19

numerous holes are formed in the acicular regions whereas the equiaxed primary α fails by stretching and tearing. All of the above fractures are consistent with extensive plasticity and would be characterized as highly ductile. The differences in toughness seem to qualitatively correlate with crack path tortuosity and with the size of the dimples.

DISCUSSION

The above data represents a reasonably complete characterization of ten microstructural conditions of Ti-6Al-4V and Ti-6Al-2Sn-4Zr-6Mo. The relative lack of texture permits the properties of these materials to be compared as a function of microstructure. The strengths of the materials were generally on the lower edge of the normal range of values for these alloys. This probably reflects the low oxygen content and the lack of any texture strengthening contribution. As mentioned earlier, the fracture toughness values were consistently high, again reflecting the somewhat lower than usual yield strengths of the material. The modulus values of all conditions were essentially constant. This is consistent with the very weak texture and will prove valuable when the FCP rates are compared for the various conditions since no modulus normalization of stress intensity of crack opening displacement will be required.

Perhaps the most difficult data to account for is the S-N fatigue data. The apparent lack of correlation between smooth life and strength or tensile ductility and the inconsistent correlation between notched life and low da/dN is perplexing. Since crack initiation is very sensitive to local

20

grain orientation at the specimen surface, it is not surprising that
Condition 1 (RA), which is very coarse grained, shows low smooth bar fatigue
strength. However, it seems that the remaining data is hard to explain. In
the absence of the biasing influence of texture, we can only suggest that the
biasing influence of texture would reduce the scatter in fatigue properties.
In the virtual absence of texture the present results may represent true
scatter and are not, therefore, statistically interpretable.

The low cycle fatigue behavior (see Table I-VIII and Fig. I-36
through I-45) seems to correlate with microstructure if viewed in the
following way. The three microstructures which exhibit coarse, well-annealed
microstructures are Conditions 1, 2 and 4. In these conditions, the cyclic
and monotonic stress-strain curves cross suggesting that an increasingly dense
and stable substructure is being formed. In all of the remaining conditions,
the microstructural scale is small enough and the residual dislocation
densities are high enough that cyclic softening might be expected. Additional
TEM studies of these samples would be required before any detailed
interpretation can be made.

The microstructure and base-line properties of ten microstructural
conditions of Ti-6Al-4V and Ti-6Al-2Sn-4Zr-6Mo have been characterized. The
strengths of the materials are relatively low and the fracture toughness and
ductility values relatively high owing to their low oxygen content and lack of
texture. The S-N type fatigue properties do not exhibit any particular trends
relative to microstructure. The cyclic work hardening behavior has been
qualitatively accounted for on the basis of microstructure.

21

REFERENCES

1. J. C. Chesnutt and R. A. Spurling, Met. Trans. A, 1977, Vol. 8A, pp. 216-18

2. D. Eylon and C. M. Pierce, Met. Trans. A, 1976, Vol. 7A, pp. 111-121

3. R. W. Smith, M. H. Hirschberg, and S. S. Manson, NASA TND-1574 (April 1963)

4. R. B. Sparks and J. R. Long, "Improved Manufacturing Methods for Producing High Integrity More Reliable Forgings," AFML-TR-73-301, Air Force Materials Laboratory, Wright-Patterson AFB, Ohio, February 1974

5. J. C. Chesnutt, C. G. Rhodes and J. C. Williams, in Fractography-Microscopic Cracking Processes, ASTM STP 600, 1975, pp. 99-138

TABLE I-I

DETAILS OF FORGING VARIABLES USED FOR FABRICATING
Ti-6Al-4V AND Ti-6Al-2Sn-4Zr-6Mo PANCAKE FORGINGS

Alloy	S/N	Quantity	First Upset				Second Upset			
			Temperature (F)	Furnace Time (Hours)	Cooling Method	Thickness Reduction (%)	Temperature (F)	Furnace Time (Hours)	Cooling Method	Thickness Reduction (%)
Ti-6Al-4V	1	2	1725	3	AC	30	1700	3	AC	43
(Heat 991174-RMI)	2	2	1750	3	AC	30	1775	3	AC	43
	3	2	1725	3	AC	30	1700	3	AC	43
	4	2	1875	3	AC	30	1875	3	AC	43
	5	2	1875	3	AC	30	1875	3	WQ	43
	6	2	1725	3	AC	30	1725	3	AC	43
	7	2	1725	3	AC	30	1725	3	AC	43
Ti-6Al-2Sn-4Zr-6Mo	8	2	1625	3	AC	30	1700	3	AC	43
(Heat N-0241-TMCA)	9	2	1625	3	AC	30	1625	3	AC	43
	10	2	1800	3	AC	30	1800	3	AC	43

TABLE I-II

COMPOSITION OF TITANIUM ALLOY FORGING BILLET

Alloy	Source	Heat	Composition weight percent									
			Al	V	Sn	Zr	Mo	Fe	C	O	N	H
Ti-6Al-4V	RMI	991174	6.2	4.1	-	-	-	0.22	0.010	0.122	0.012	0.003
Ti-6Al-2Sn-4Zr-6Mo	TMCA	N-0291	5.8	-	2.0	4.1	6.0	0.04	0.026	0.10	0.006	0.007

TABLE I-III

FORGING AND HEAT TREATMENT SUMMARY

Ti-6Al-4V		RMI Heat 991174	$(\beta_t \cong 1800^oF)$
Condition		Fabrication	Heat Treatment
Re-X Anneal	(1)	$\alpha-\beta$ Forge (β_t-75)/AC	1700°F/4h/Cool @ 90°F/h to 1400°F/AC
		$\alpha-\beta$ Finish (β_t-100)/AC	
10-20% Primary α	(2)	$\alpha-\beta$ Forge (β_t-50)/AC	1750°F/1h/AC + 1300°F/2h/AC
		$\alpha-\beta$ Finish (β_t-25)/AC	
40-50% Primary α	(3)	$\alpha-\beta$ Forge (β_t-75)/AC	1600°F/2h/AC + 1300°F/2h/AC
		$\alpha-\beta$ Finish (β_t-100)/AC	
β-Forge	(4)	β Forge (β_t+75)/AC	1300°F/2h/AC
		β Finish (β_t+75)/WQ	
β-Quench	(5)	β Forge (β_t+75)/AC	1900°F/30 min/WQ + 1300°F/2h/AC
		β Finish (β_t+75)/AC	
Solution Treat and Age (STA)	(6)	$\alpha-\beta$ Forge (β_t-75)/AC	1750°F/1h/WQ + 1100°F/4h/AC
		$\alpha-\beta$ Finish (β_t-75)/AC	
Solution Treat and Overage (STOA)	(7)	$\alpha-\beta$ Forge (β_t-75)/AC	1750°F/1h/WQ + 1100°F/24h/AC
		$\alpha-\beta$ Finish (β_t-75)/AC	
Ti-6Al-2Sn-4Zr-6Mo		TMCA Heat N-0291	$(\beta_t \cong 1725^oF)$
10-20% Primary α	(8)	$\alpha-\beta$ Forge (β_t-100)/AC	1625°F/1h/AC + 1100°F/8h/AC
		$\alpha-\beta$ Finish (β_t-25)/AC	
40-50% Primary α	(9)	$\alpha-\beta$ Forge (β_t-100)/AC	1625°F/1h/AC + 1300°F/1h/AC
		$\alpha-\beta$ Finish (β_t-100)/AC	
β Process	(10)	β Forge (β_t+75)/AC	1625°F/1h/AC + 1100°F/8h/AC
		β Finish (β_t+75)/AC	

24

TABLE I-IV

VOLUME FRACTION OF PHASES IN $\alpha+\beta$ ALLOYS

Condition	Volume Fraction Primary α, Observed	Volume Fraction α, Goal	Retained β, Observed	Remainder
1	0.89	~ 0.9	0.08	(1)
2	0.13	0.1-0.2	0.16	(2)
3	0.54	0.4-0.5	0.13	(2)
4	--	---	0.09	(2)
5	--	---	0.11	(3)
6	0.28	---	0.09	(4)
7	0.25	---	0.07	(4)
8	0.10	0.1-0.2		
9	0.51	0.4-0.5		
10	--	---		

(1) Interface α
(2) Interface α and Widmanstätten α
(3) Interface α, Widmanstätten α, and α'
(4) Interface α, Widmanstätten α, and precipitated β

TABLE I-V

YOUNG'S MODULUS, CIRCUMFERENTIAL DIRECTION

Condition	Modulus, 10^6 psi	Modulus, GPa
1	16.69	115.1
2	16.56	114.2
3	16.52	113.9
4	16.90	116.6
5	16.01	110.4
6	16.45	113.4
7	16.36	112.8
8	16.65	114.8
9	16.25	112.1
10	16.79	115.8

TABLE I-VI

TENSILE PROPERTIES

Condition	0.2% Yield		Ultimate Strength		True Fracture Strength		ε_u, %*	RA, %	Total Elong., %
	ksi	MPa	ksi	MPa	ksi	MPa			
1	103	707	127	873	173	1190	8.7	36	12.4
2	118	814	129	892	178	1229	7.9	36	12.0
3	124	857	132	908	196	1352	9.2	47	15.3
4	112	774	124	852	149	1024	8.7	23	11.2
5	125	862	135	931	140	966	5.7	6	5.9
6	127	877	136	939	170	1170	8.4	34	15.2
7	132	909	142	982	211	1458	7.4	47	15.5
8	173	1196	187	1287	234	1612	3.9	29	7.7
9	153	1055	165	1134	233	1605	7.2	42	11.8
10	157	1080	177	1223	194	1337	4.7	9	4.9

*True strain to maximum load (uniform strain)

TABLE I-VII

ROCKWELL HARDNESS
(Average of Triplicate Tests)

Condition	Hardness (R_c)
1	30.5
2	31.6
3	30.2
4	30.7
5	32.9
6	33.2
7	33.0
8	39.3
9	38.4
10	39.9

TABLE I-VIII

CYCLIC STRESS-STRAIN BEHAVIOR

Condition	UTS/YS	Softens	Crosses	Crossing Strain, %	Softening at 1% Strain, MPa
1	1.23		X	0.6	
2	1.10		X	0.8	
3	1.06	X			17
4	1.10		X	0.55	
5	1.08	X			47
6	1.07	X			39
7	1.07	X			60
8	1.08	X			64
9	1.07	X			21
10	1.13	X			74

TABLE I-IX

FRACTURE TOUGHNESS RESULTS

Condition	K_Q ksi$\sqrt{in}^{\frac{1}{2}}$	MPa·m$^{\frac{1}{2}}$	Valid	Required Thickness for Validity (cm)
1	109.3	120.1	No (1)	7.15
	110.6	121.5		7.31
2	111.0	122.0	No (1)	5.62
	114.0	125.3		5.92
3	102.5	112.8	No (2)	
	99.2	109.1		
4	108.9	119.8	No (1)	6.00
	106.7	117.4		5.76
5	91.6	100.8	Yes	
	92.2	101.3		
6	77.5	85.2	No (2)	
	75.1	82.6		
7	69.5	76.4	Yes	
	68.7	75.5		
8	39.4	43.3	Yes	
	38.5	42.3		
9	36.9	40.5	Yes	
	36.4	40.1	No (2)	
10	64.4	70.8	Yes	
	65.5	72.1		

(1) Failed thickness requirement

(2) Failed precrack curvature requirement

28
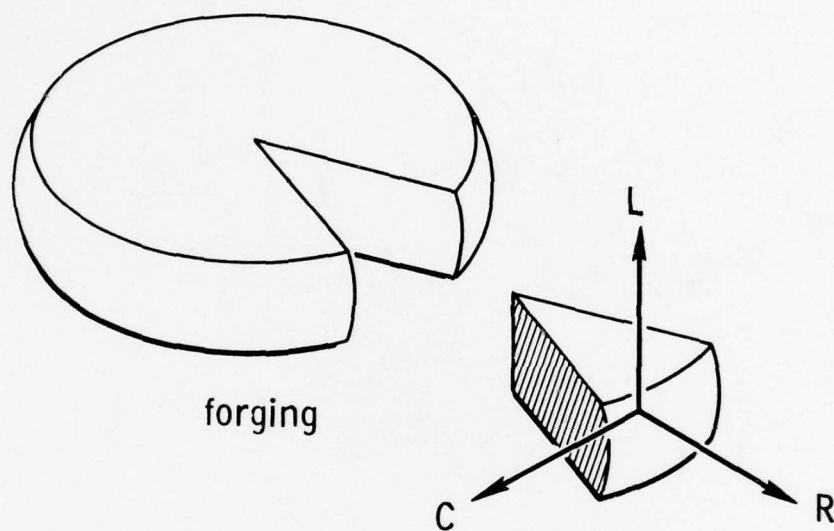
forging

Fig. I-1 Nomenclature for directions in forgings, following ASTM 399
recommendations (L = longitudinal, R = radial, C = circumferential).
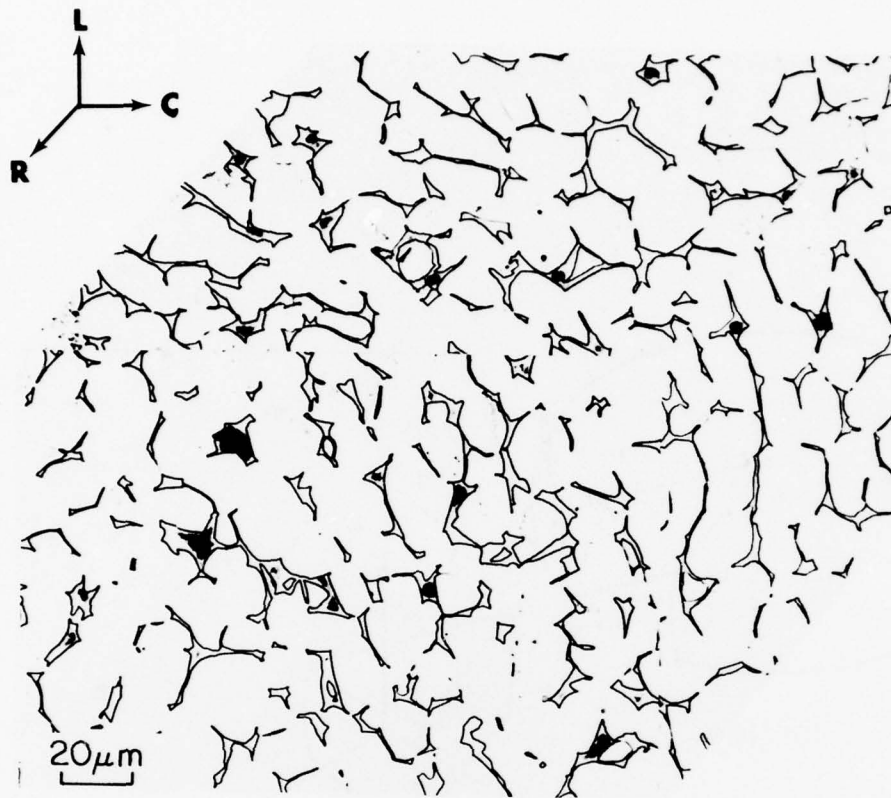
Fig. I-2 Microstructure of Ti-6Al-4V, Condition 1 heat treatment. Note nomenclature for directions in forgings.
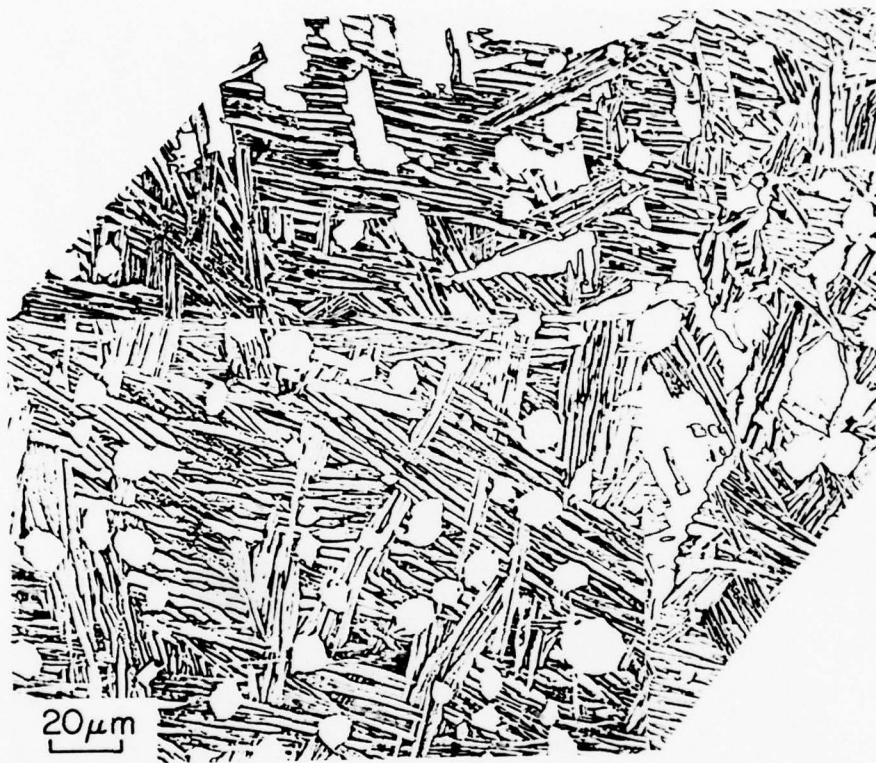
Fig. I-3 Ti-6Al-4V, Condition 2 heat treatment.
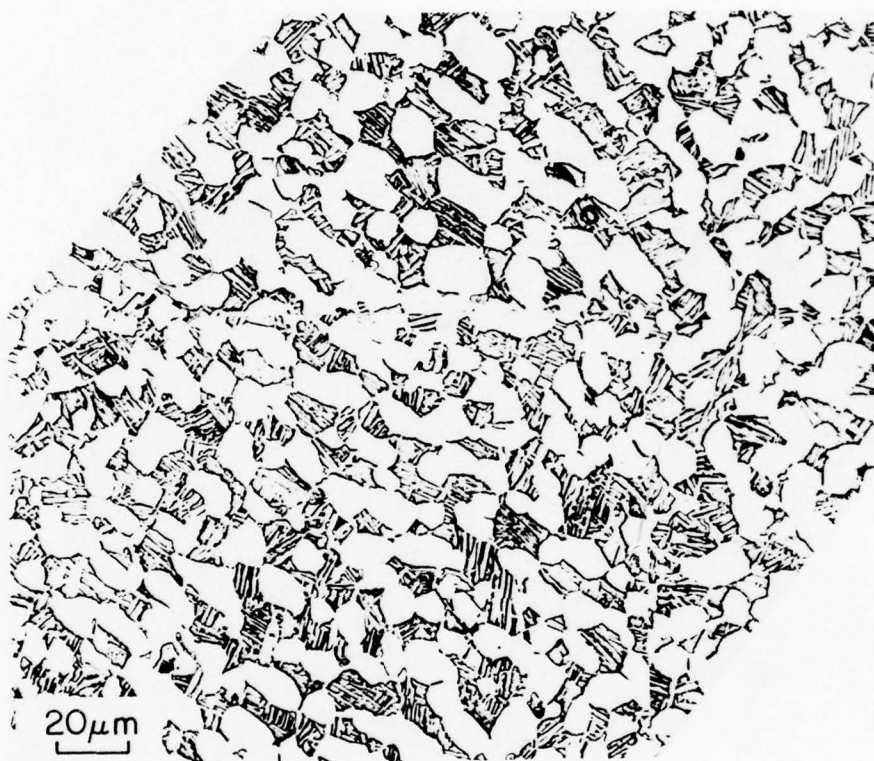
Fig. I-4 Ti-6Al-4V, Condition 3 heat treatment.
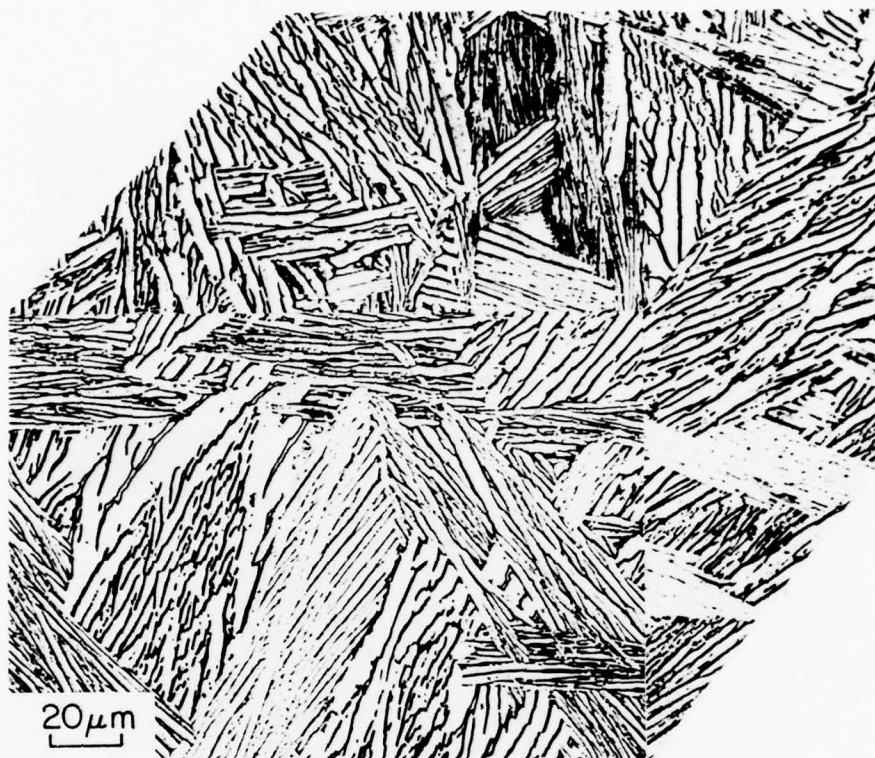
Fig. 1-5 Ti-6Al-4V, Condition 4 heat treatment.
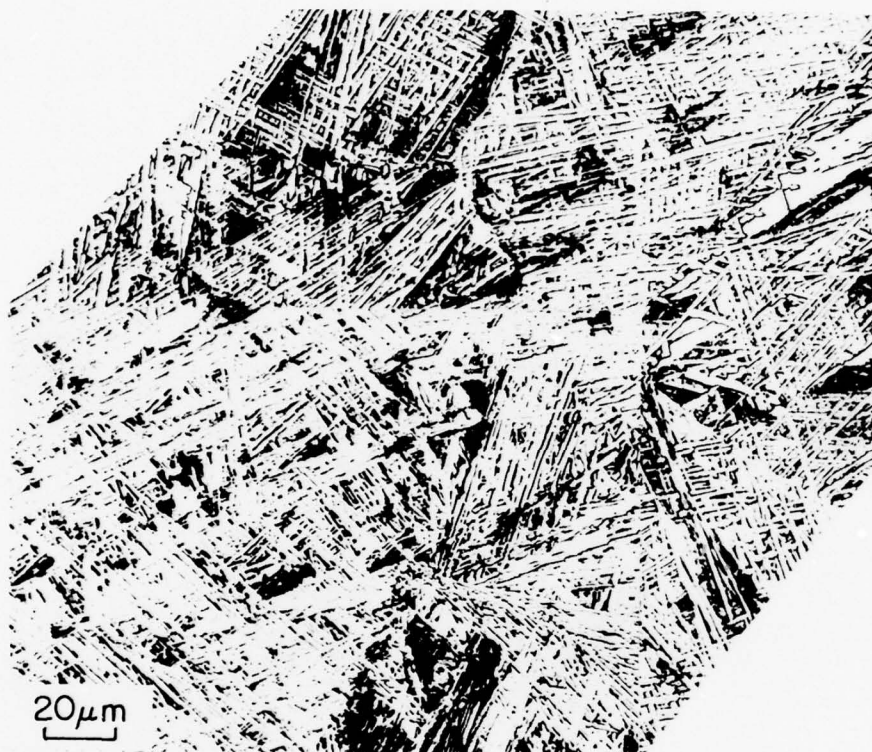
Fig. I-6 Ti-6A1-4V, Condition 5 heat treatment.

34

20μm
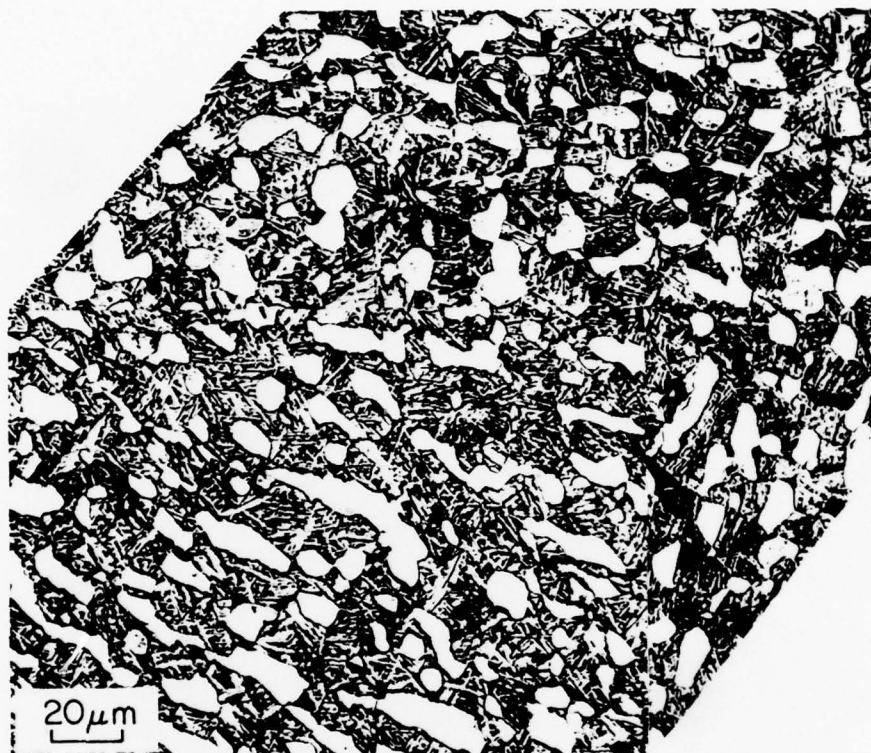
Fig. I-7   Ti-6Al-4V, Condition 6 heat treatment.
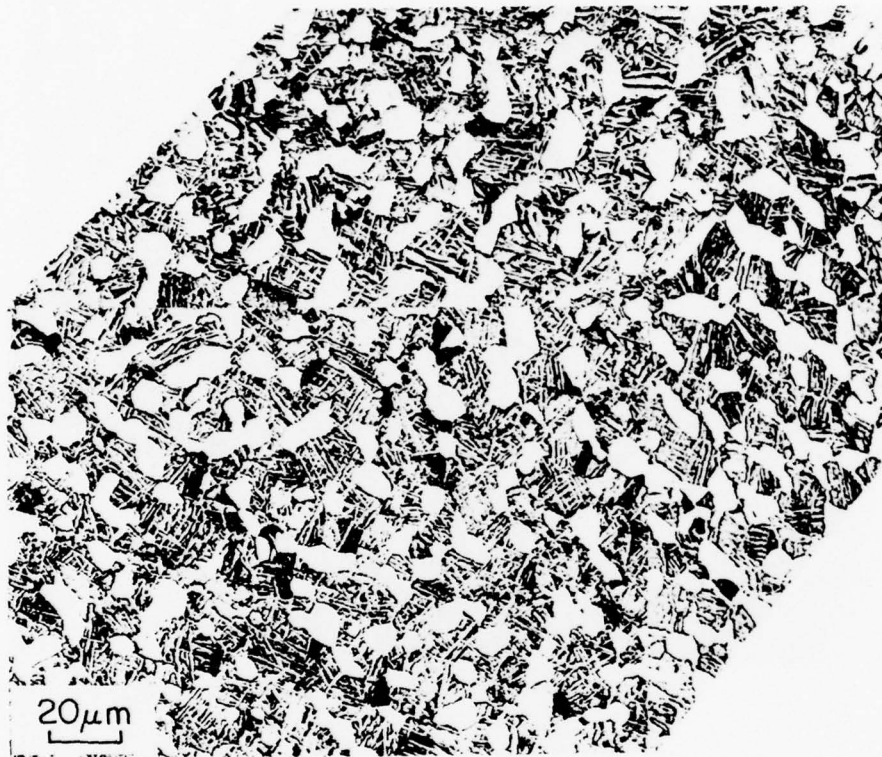
Fig. I-8 Ti-6Al-4V, Condition 7 heat treatment.
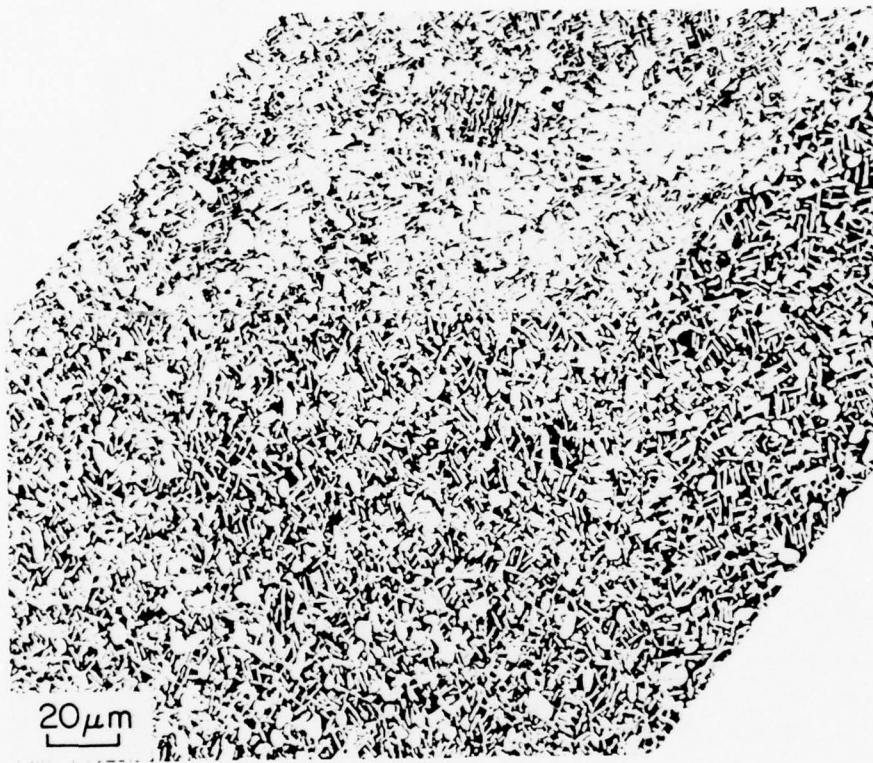
Fig. I-9 Ti-6Al-2Sn-4Zr-6Mo, Condition 8 heat treatment.

20μm
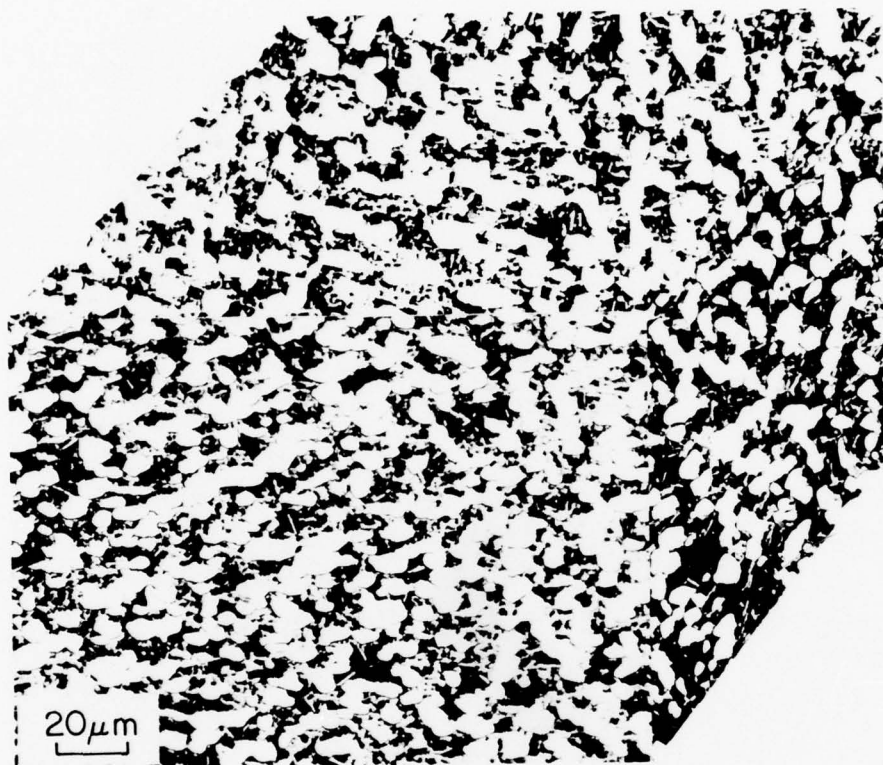
Fig. I-10   Ti-6Al-2Sn-4Zr-6Mo, Condition 9 heat treatment.
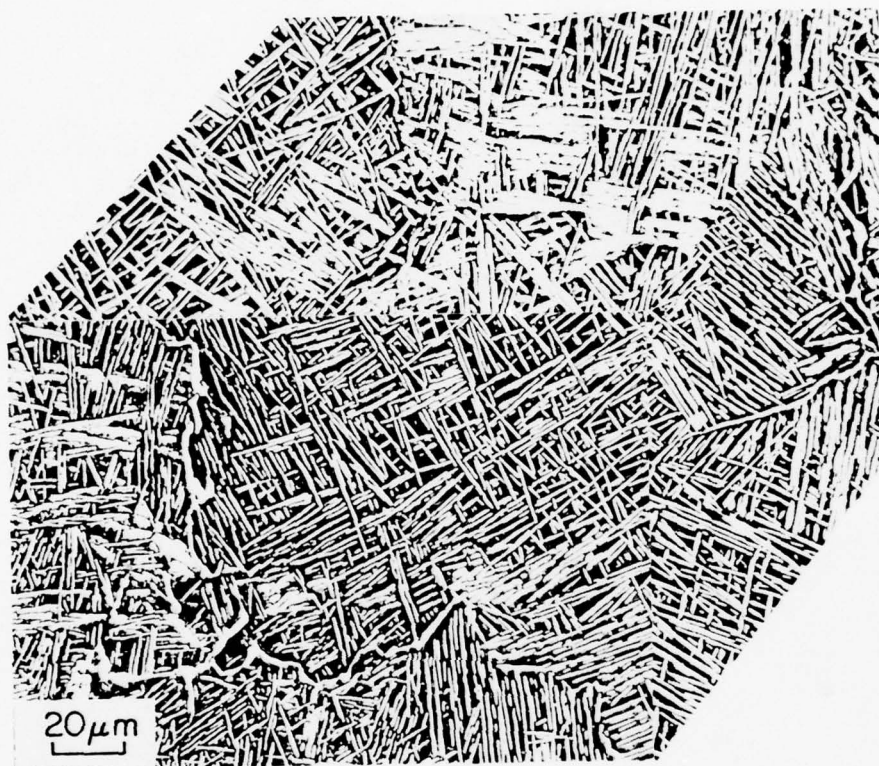
Fig. I-11   Ti-6Al-2Sn-4Zr-6Mo, Condition 10 heat treatment.
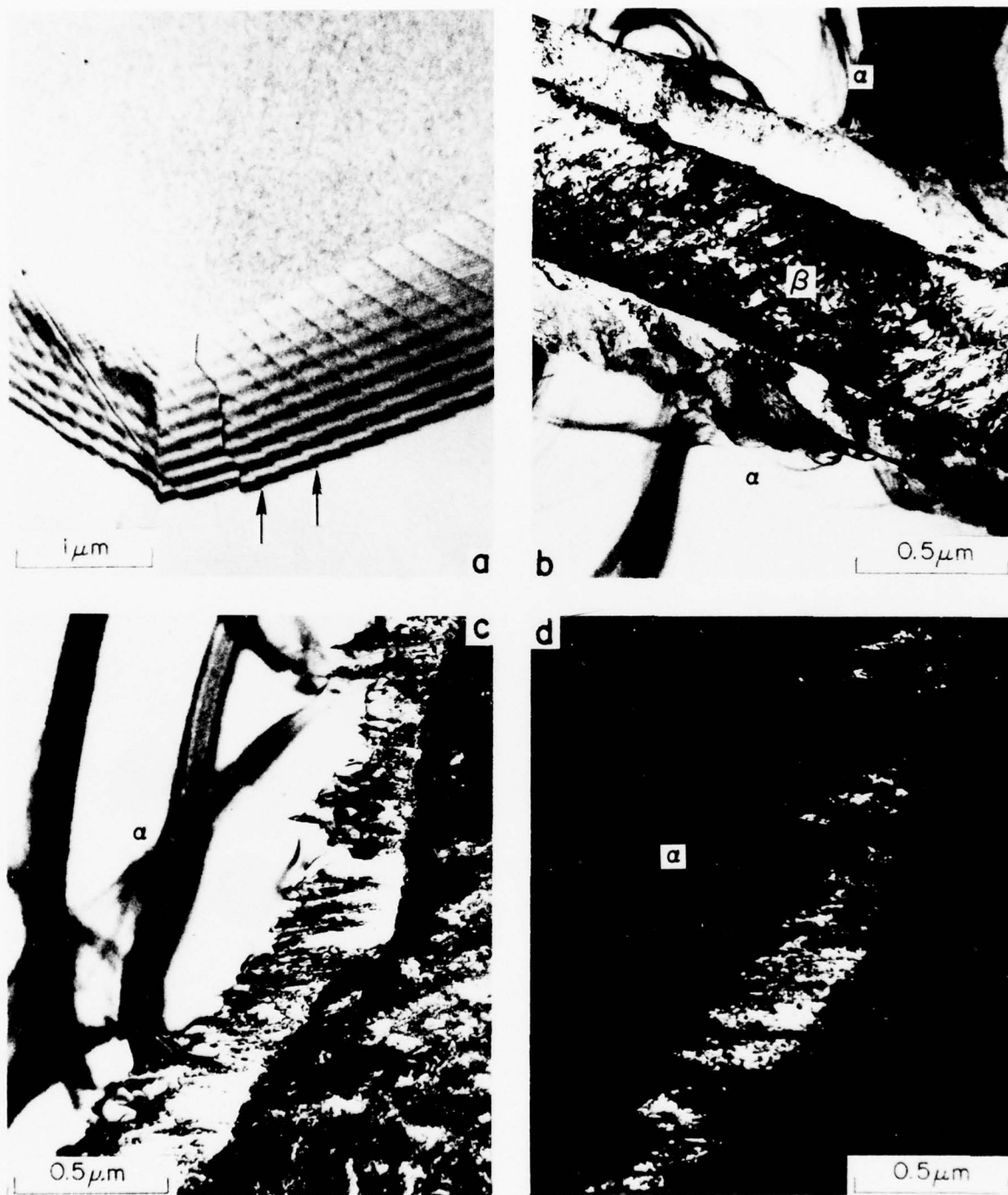
Fig. I-12 Condition 1 electron microscopy, showing boundary ledges in (a), arrowed; a strip of β between primary α grains, (b); and the interface phase between α and β, (c) and (d).
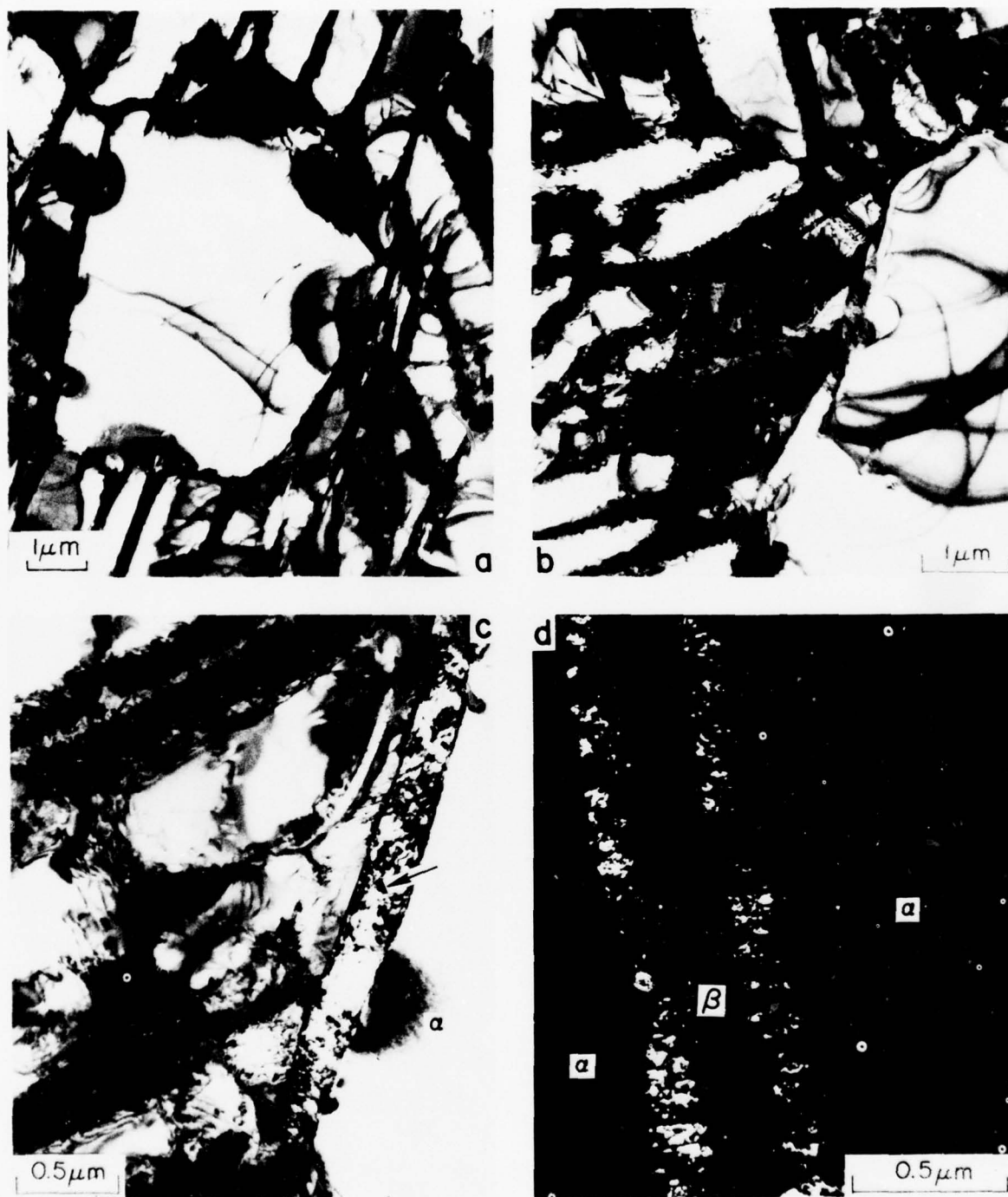
Fig. I-13 Condition 2 electron microscopy, showing primary α particle surrounded by Widmanstätten $\alpha + \beta$, (a) and (b); strip of interface phase surrounding primary α, (c); and interface phase along β strips in Widmanstätten $\alpha + \beta$ (d).

41
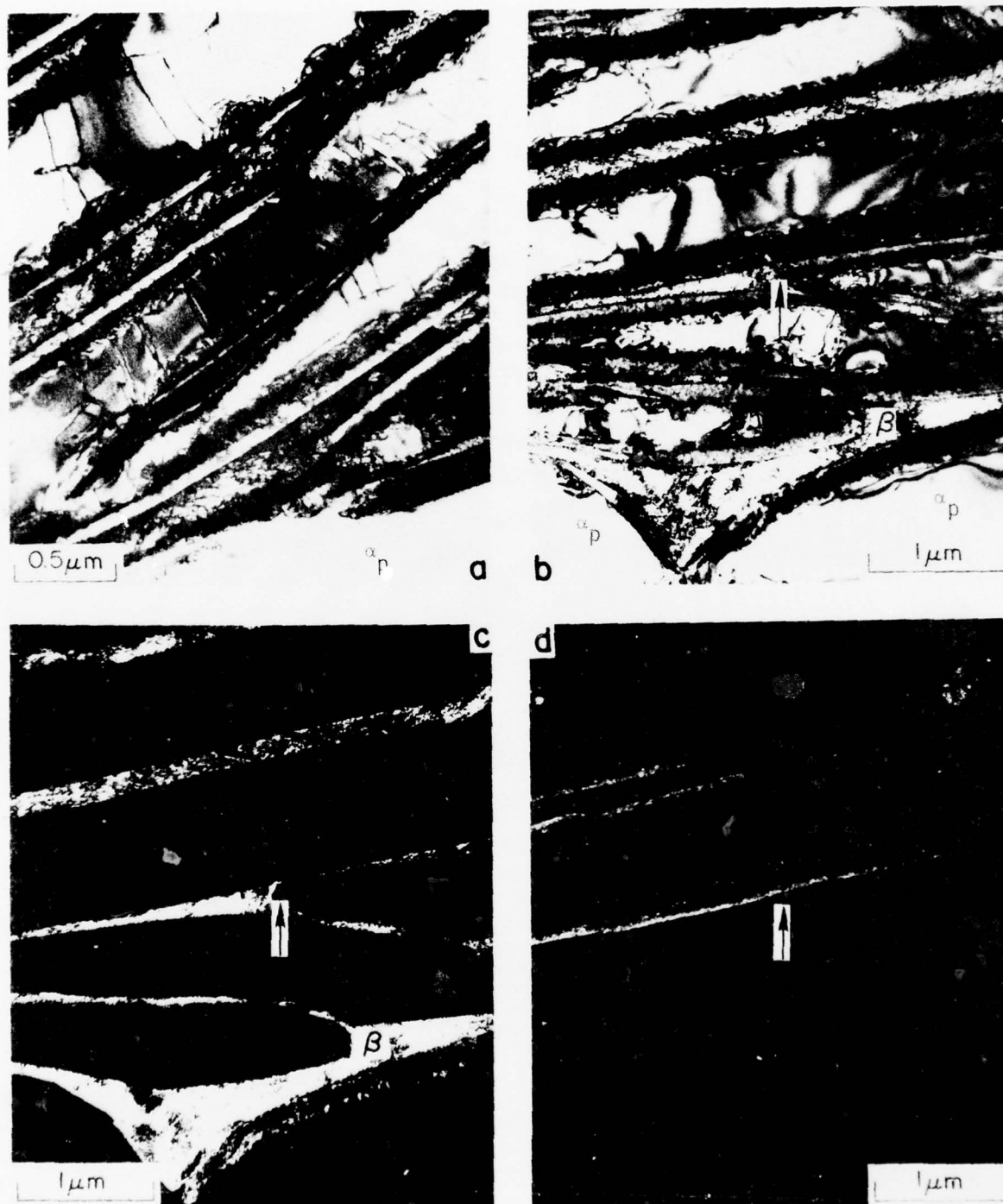
Fig. I-14 Condition 3 electron microscopy, showing Widmanstätten structure near primary α particle at bottom, (a); and a sequence of a single area, (b), showing β phase (c) and interface phase (d) in dark field. The corresponding point is arrowed in (b), (c), and (d).
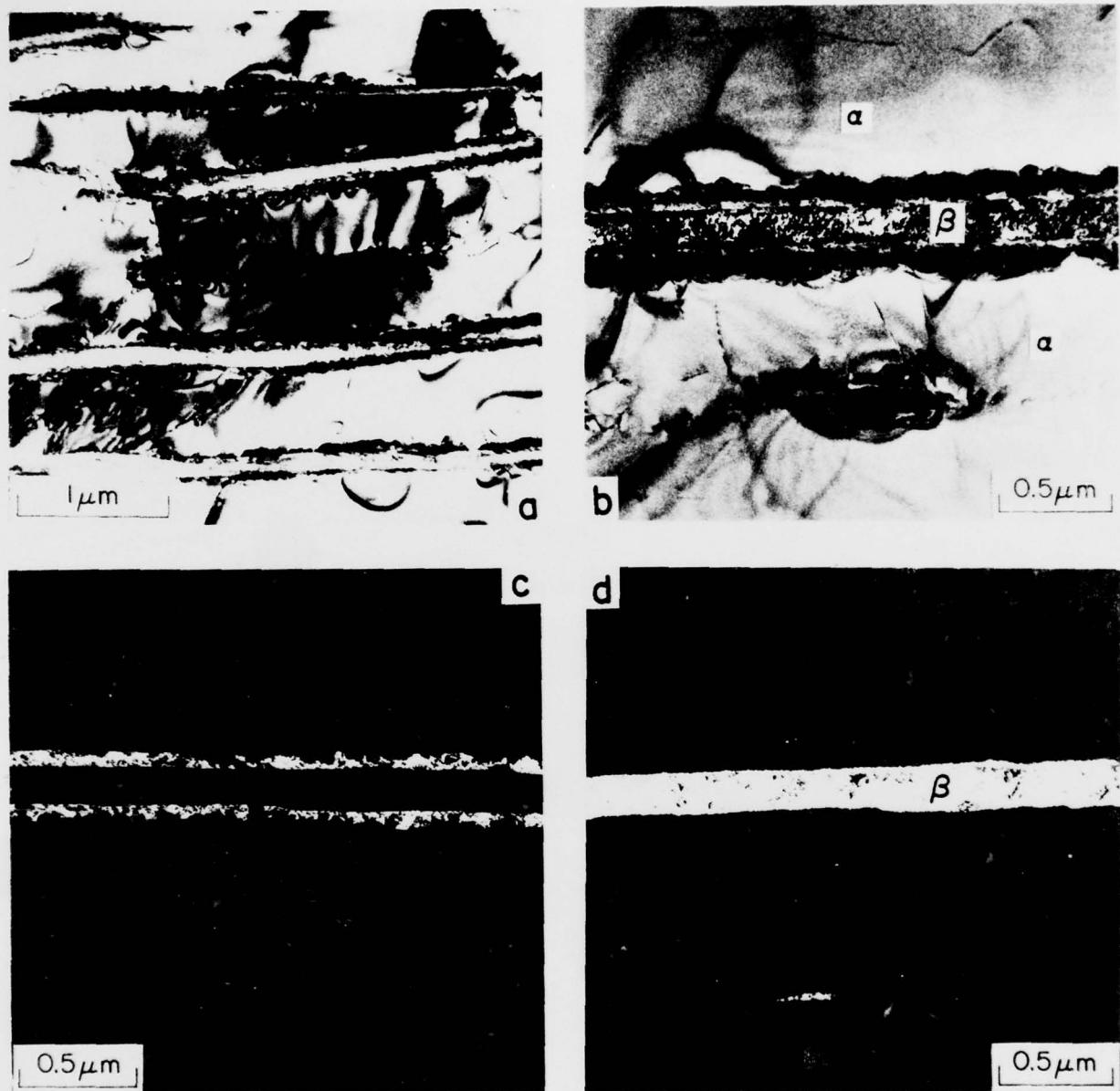
Fig. I-15 Condition 4 electron microscopy, showing the overall Widmanstätten structure, (a); and the interface phase along β strips (b), shown in dark field in (c) and the β itself in (d).

43
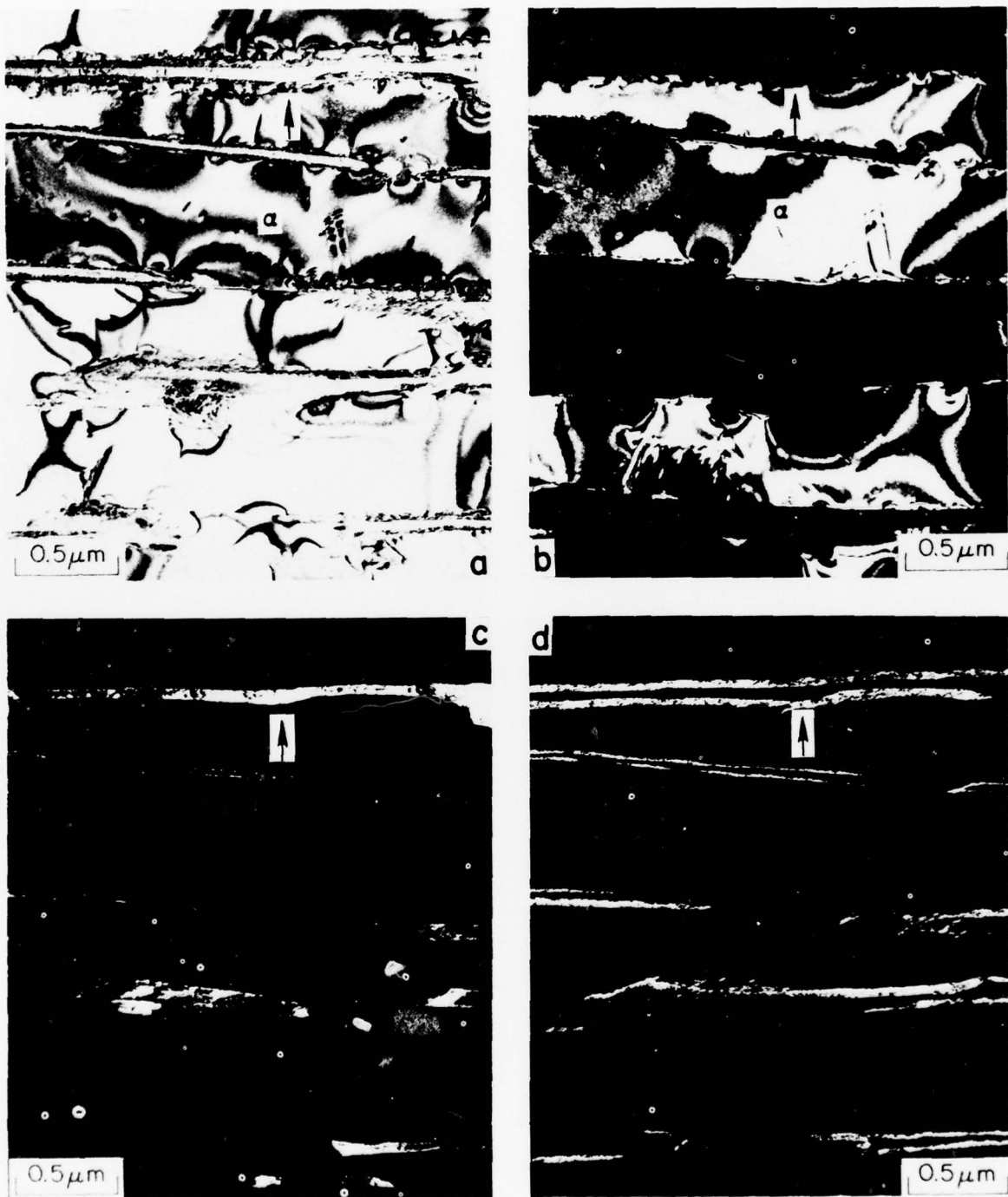
Fig. I-16 Condition 5 electron microscopy, illustrating the fine Widmanstätten structure, (a); the α plates in (a) in dark field, (b); the β of (a) in dark field, (c); and interface phase in (d).
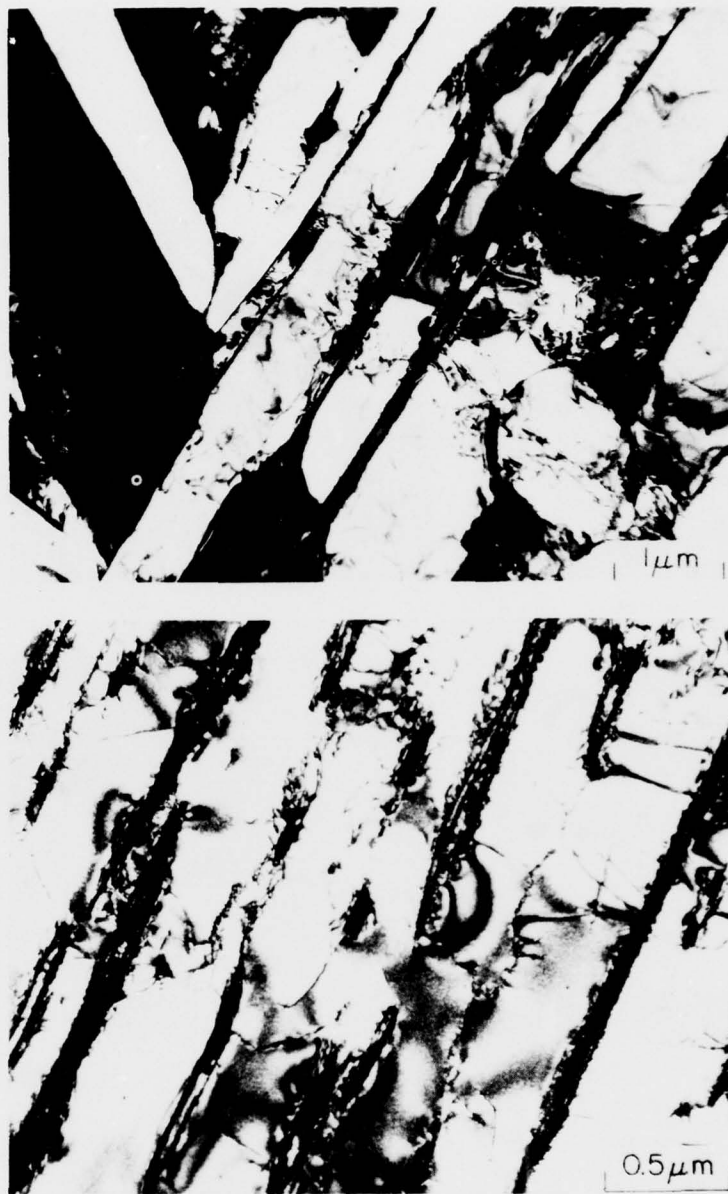
Fig. I-17 Details of Condition 5 microstructure at lower magnification described in text.
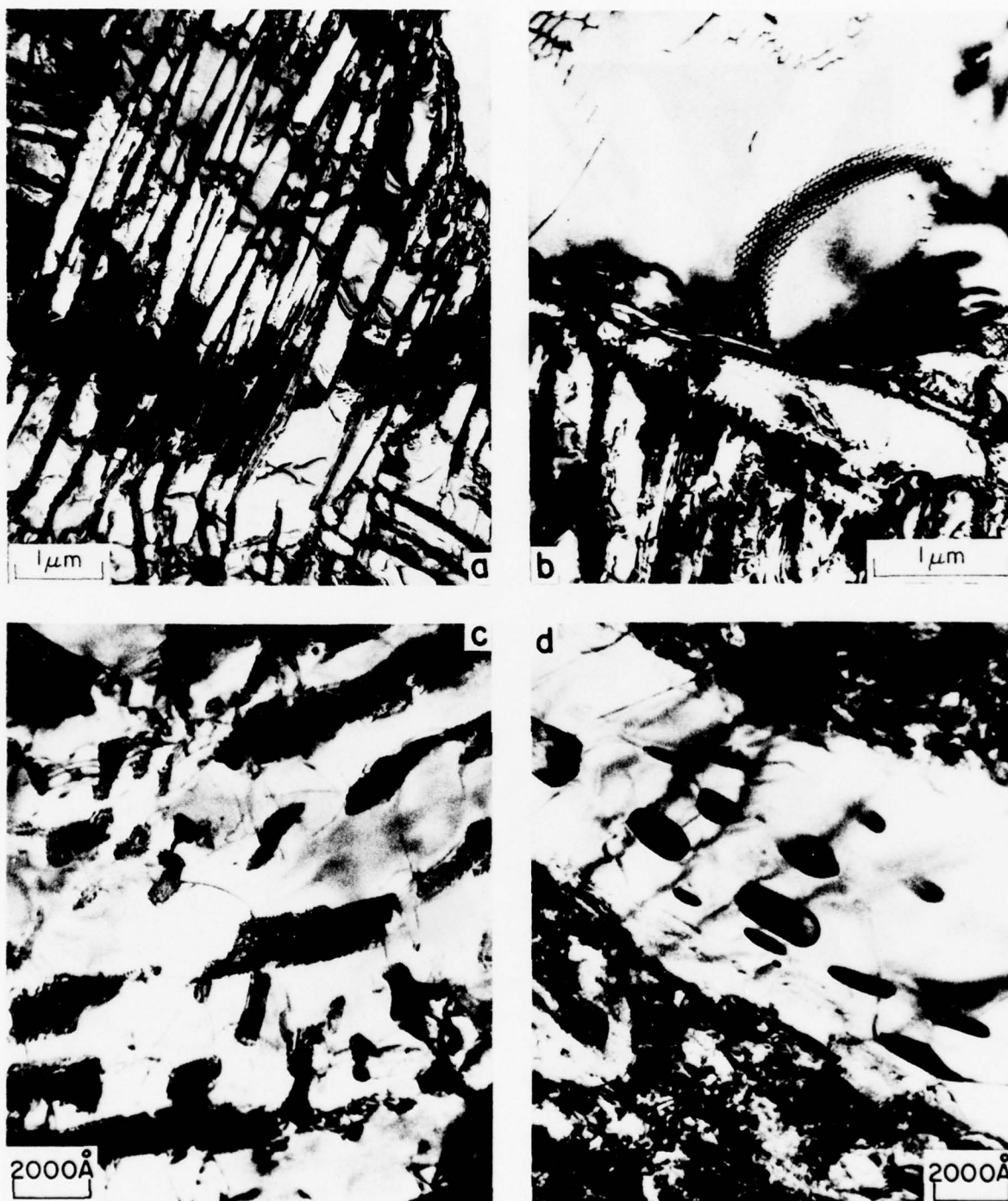
Fig. I-18 Condition 6 electron microscopy, showing fine acicular structure near primary α particle at upper right, (a); relaxed dislocation network in primary α, (b); interfacial structure on β precipitates, (c); and equiaxed β morphology, (d).

46
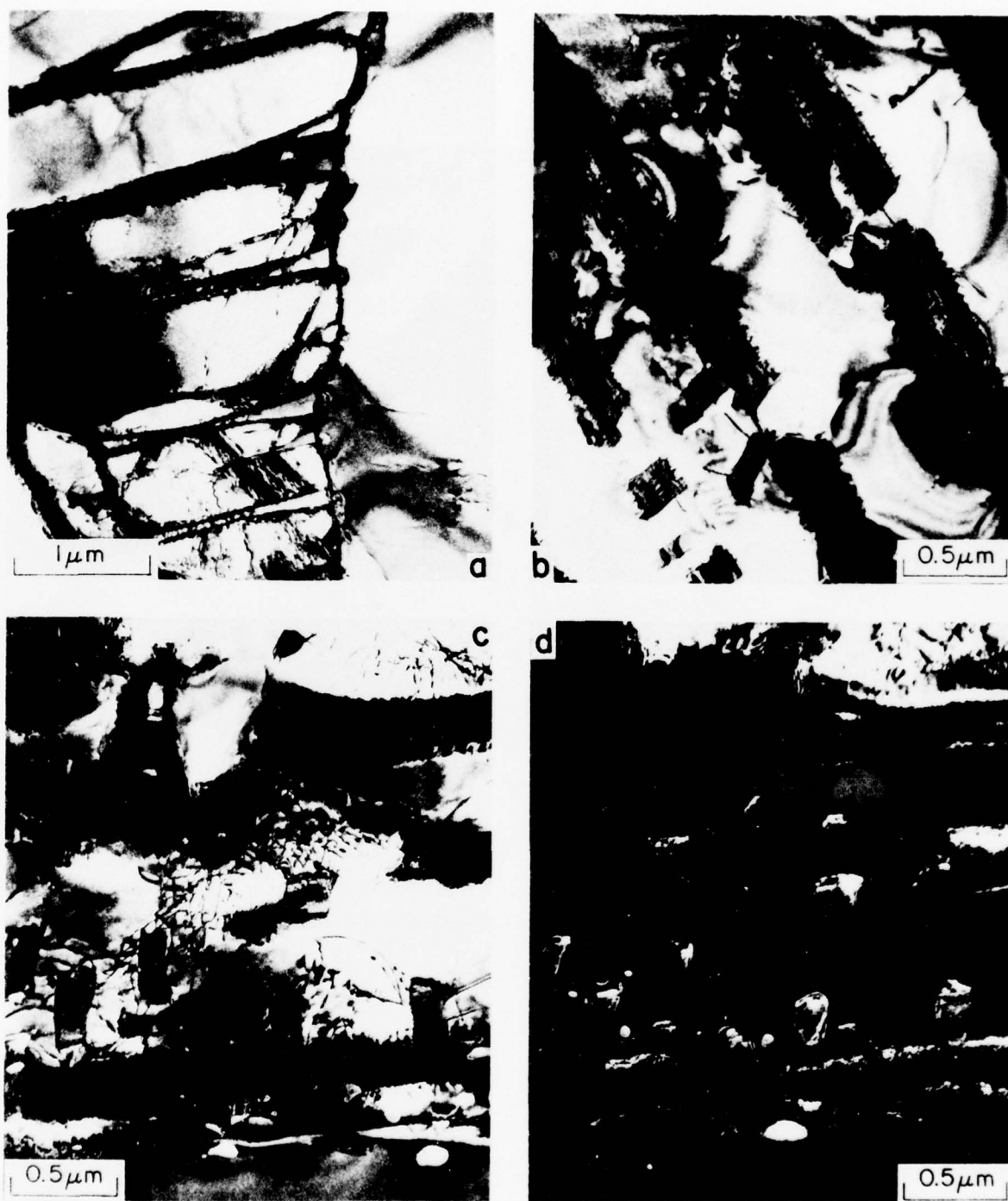
Fig. I-19 Condition 7 electron microscopy, again showing structure at a primary α
particle at right, (a); interfaces on β,(b); and extensive β
precipitates in bright field (c) and dark field (d).

47
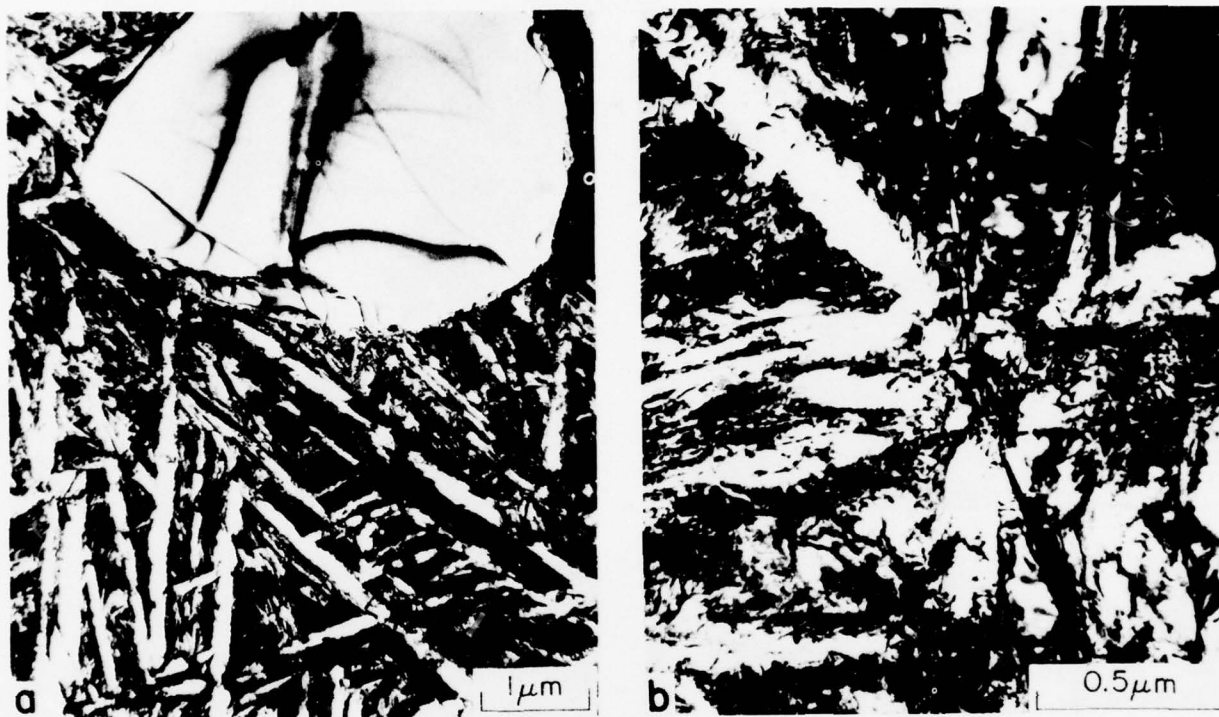
Fig. I-20 Thin section of Condition 7, water quenched as described in text to produce martensitic structure (a) with high dislocation density (b).

48
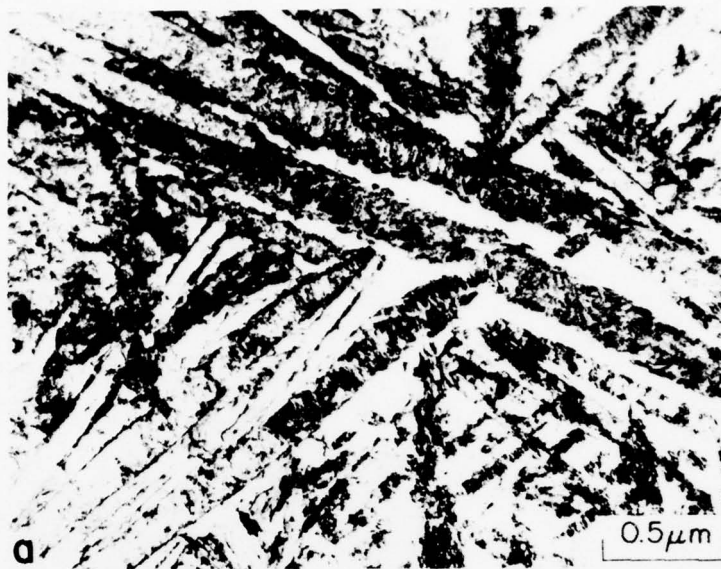
Fig. I-21 Condition 8 electron microscopy, showing fine substructure in
Widmanstätten $\alpha+\beta$, (a), and relaxed primary α at right (b).

49
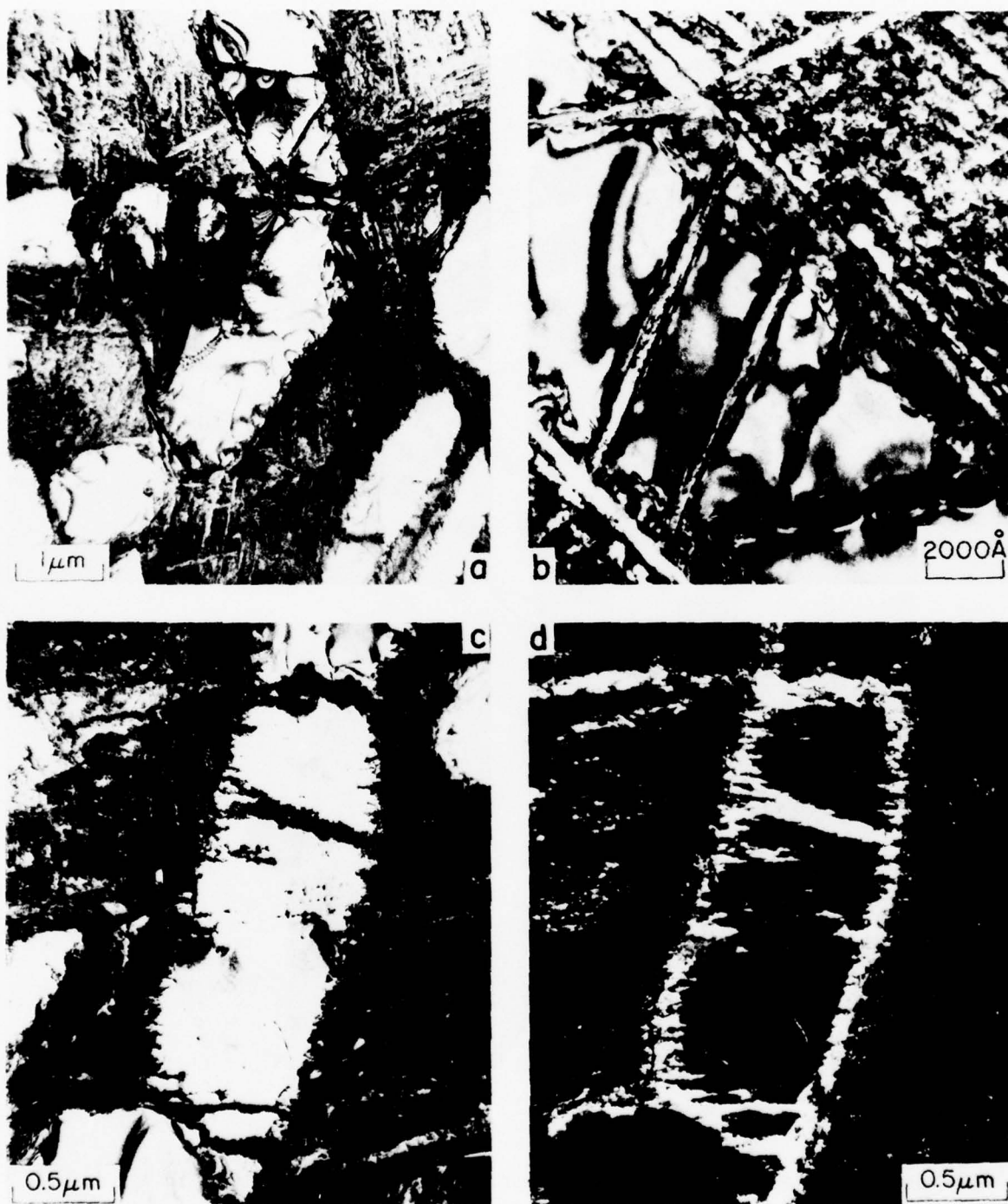
Fig. I-22 Condition 9 electron microscopy, showing primary α particles in (a); substructure within α in (b); and evidence that lath-appearing structure in (b) is interface phase, in bright field (c) and dark field (d).

50
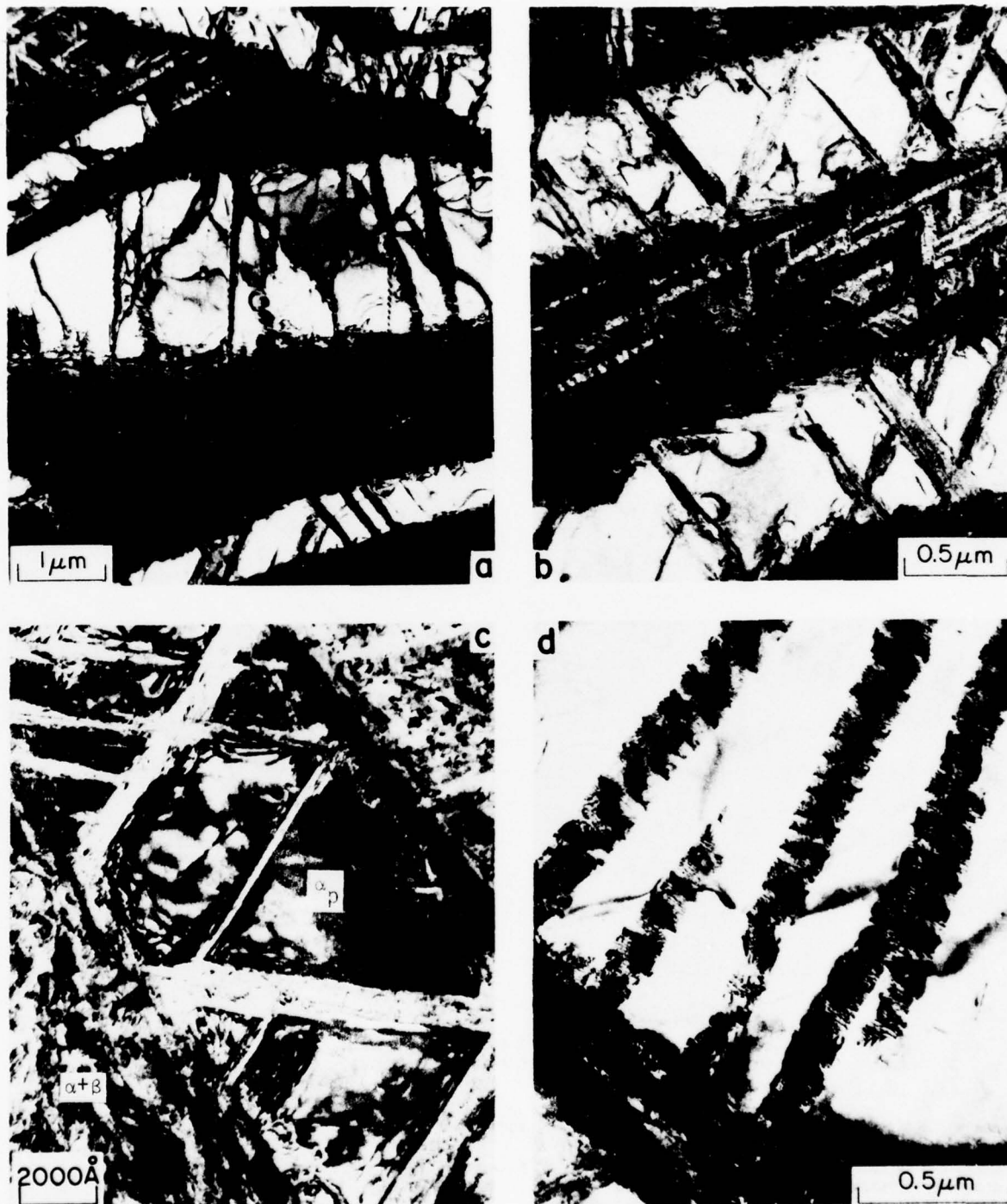
Fig. I-23   Condition 10 electron microscopy, illustrating elongated primary
            (Widmanstätten) α, (a); fine $\alpha+\beta$ mixtures and substructure in α, (b)
            and (c); and evidence that "strips" in the α, such as in (a), are
            discrete precipitates (d).

51

1	.5000	2	1.0000	3	1.5000	4	2.0000	5	4.0000
6	8.0000	7	14.0000	9	20.0000	9	25.0000	0	30.0000

JOB NO. BTS 464-2   SAMPLE 1-1-3   DATE 05/13/75
RADIATION CU AT 35 KV 28 MA COUNTER TUBE PROP AT   1.9125 KV
SLITS 2 H 1V ENTRANCE 5 H 1V RECEIVING   ENGINEER R. L. WINGERT
SCAN RATE 1 PSI/MIN 72 ALPHA/MIN   (0002) HKL
PHA 5 V BASE 12 V WINDOW CALIBRATION SAMPLE SILVER
RANDOM INTENSITY   212.1   K(A)   -.394 CALC DATE 05/14/75

Fig. I-24 Basal (0002) pole figure for Condition 1, 1-1-3.
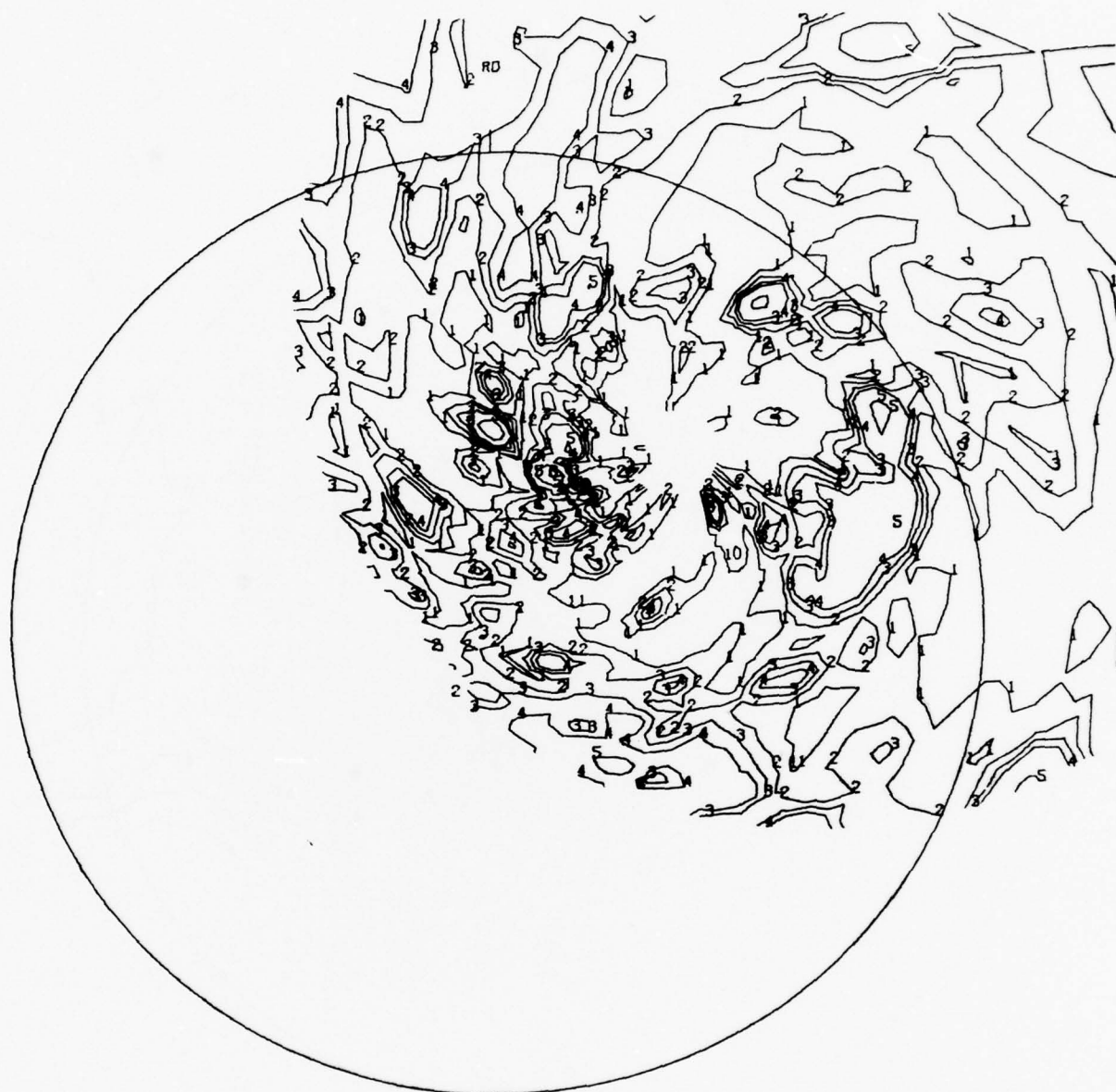
52

| 1 | .5000 | 2 | 1.0000 | 3 | 1.5000 | 4 | 2.0000 | 5 | 4.0000 |
| 6 | 8.0000 | 7 | 14.0000 | 8 | 20.0000 | 9 | 25.0000 | 0 | 30.0000 |

JOB NO. BTS 464-2   SAMPLE 1-2-4   DATE 05/13/75
RADIATION CU AT 35 KV 28 MA COUNTER TUBE PROP AT   1.8125 KV
SLITS 2 H 1V ENTRANCE 5 H 1 V RECEIVING   ENGINEER A. L. WINGERT
SCAN RATE 1 PSI/MIN 72 ALPHA/MIN   (0002) HKL
PHA 6 V BASE 12 V WINDOW CALIBRATION SAMPLE SILVER
RANDOM INTENSITY   211.8   K(A)   -9.490 CALC DATE 05/14/75

Fig. I-25 Basal pole figure for Condition 2, 1-2-4.

| 1 | .5000 | 2 | 1.0000 | 3 | 1.5000 | 4 | 2.0000 | 5 | 4.0000 |
| 6 | 8.0000 | 7 | 14.0000 | 8 | 20.0000 | 9 | 25.0000 | 0 | 30.0000 |

JOB NO. BTS 464-2   SAMPLE 1-3-8   DATE 05/04/75
RADIATION CU AT 35 KV 29 MA COUNTER TUBE PROP AT   1.915 K
SLITS 2 H 1V ENTRANCE 5 H 1 V RECEIVING   ENGINEER A. L. WINGERT
SCAN RATE 1 PSI/MIN 72 ALPHA/MIN   (0002)HKL
PHA 5 V BASE 12 V WINDOW CALIBRATION SAMPLE SILVER
RANDOM INTENSITY   237.6   K(A) -17.279 CALC DATE 05/14/75

Fig. I-26 Basal pole figure for Condition 3, 1-3-8.

54

| 1 | .5000 | 2 | 1.0000 | 3 | 1.5000 | 4 | 2.0000 | 5 | 4.0000 |
| 6 | 8.0000 | 7 | 14.0000 | 8 | 20.0000 | 9 | 25.0000 | 0 | 30.0000 |

JOB NO. BTS 464-2   SAMPLE 1-4-3   DATE 05/10/75
RADIATION CU AT 35 KV 28 MA COUNTER TUBE PROP AT   1.810KV
SLITS 2 H 1V ENTRANCE 5 H 1V RECEIVING   ENGINEER A. L. WINGERT
SCAN RATE 1 PSI/MIN 72 ALPHA/MIN   (0002) HKL
PHA 6 V BASE 12 V WINDOW CALIBRATION SAMPLE SILVER
RANDOM INTENSITY   252.8   K(A) -26.777 CALC DATE 05/14/75

Fig. I-27 Basal pole figure for Condition 4, 1-4-3.
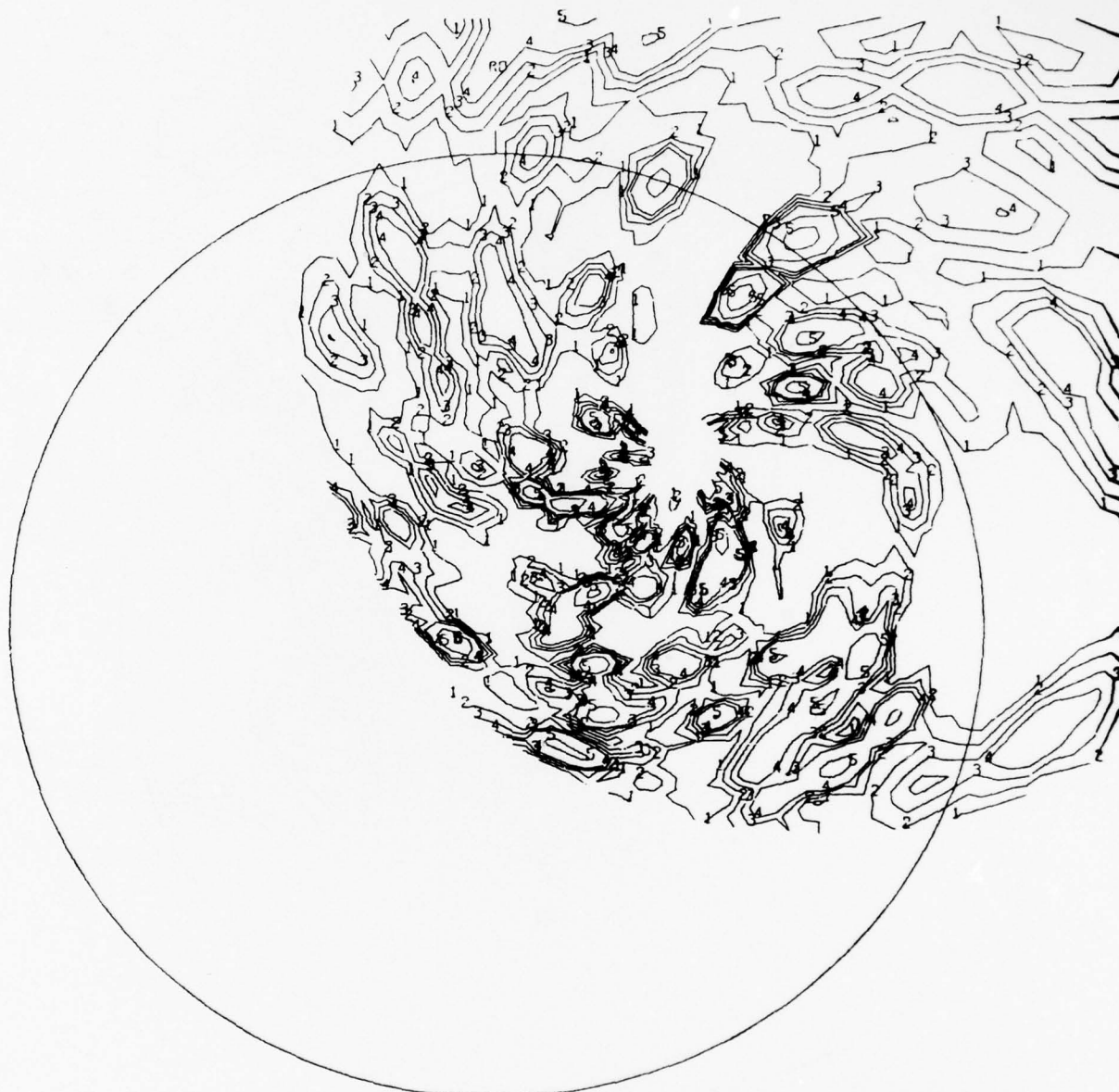
| 1 | .5000 | 2 | 1.0000 | 3 | 1.5000 | 4 | 2.0000 | 5 | 4.0000 |
| 6 | 8.0000 | 7 | 14.0000 | 8 | 20.0000 | 9 | 25.0000 | 0 | 30.0000 |

```
JOB NO. BTS 464-2    SAMPLE 1-5-5              DATE 05/04/75
RADIATION CU AT 35 KV  29 MA  COUNTER TUBE PROP AT        1.315 K
SLITS 2 H IV ENTRANCE  5 H IV RECEIVING   ENGINEER A. L. WINGERT
SCAN RATE 1 PSI/MIN  72 ALPHS/MIN                   (0002) HKL
PHA 5 V BASE  12 V WINDOW CALIBRATION SAMPLE SILVER
RANDOM INTENSITY    239.3        K(A)   -15.992 CALC DATE 05/14/75
```

Fig. I-28 Basal pole figure for Condition 5, 1-5-5.

56

1   .5000   2   1.0000   3   1.5000   4   2.0000   5   4.0000
6   8.0000   7   14.0000   8   20.0000   9   25.0000   0   30.0000

JOB NO 6TS 464-2   SAMPLE 1-6-3   DATE 05/19/75
RADIATION CU AT 35 KV 29 MA COUNTER TUBE PROP AT   1.910KV
SLITS 2 H 1V ENTRANCE 5 H 1 V RECEIVING   ENGINEER A. L. WINGERT
SCAN RATE 1 PSI/MIN 72 ALPHA/MIN   (00021 HKL
PHA 5 V BASE 12 V WINDOW CALIBRATION SAMPLE SILVER
RANDOM INTENSITY   303 0   K'A1 -19.52' CALC DATE 05/14/75

Fig. I-29 Basal pole figure for Condition 6, 1-6-3.
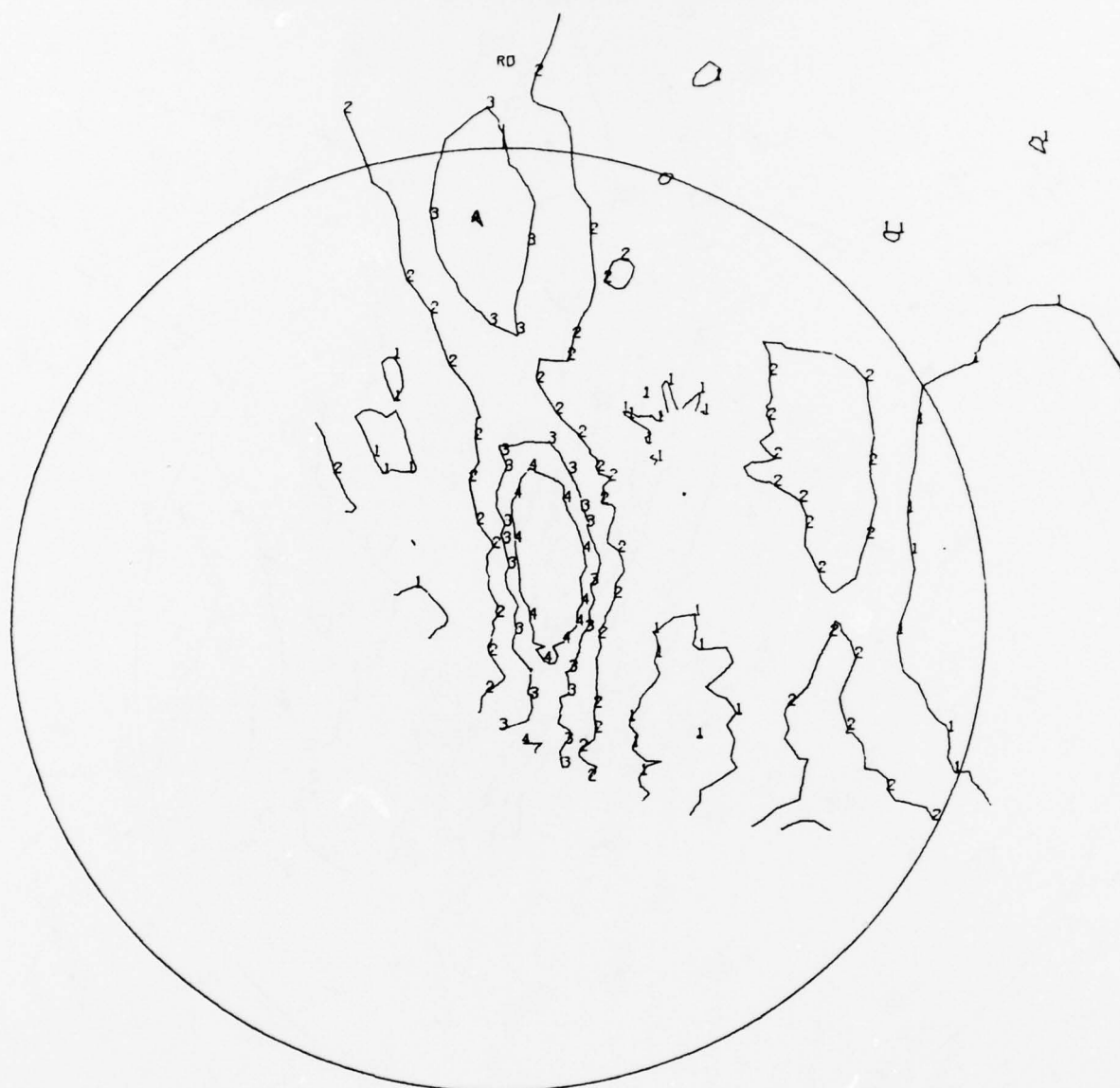
57

RD

A

| 1 | .5000 | 2 | 1.0000 | 3 | 1.5000 | 4 | 2.0000 | 5 | 4.0000 |
| 6 | 8.0000 | 7 | 14.0000 | 8 | 20.0000 | 9 | 25.0000 | 0 | 30.0000 |

JOB NO. BTS 464-2   SAMPLE 1-7-5   DATE 05/10/75
RADIATION CU AT 35 KV 29 MA   COUNTER TUBE PROP AT   1.910 K
SLITS 2 H 1V ENTRANCE 5 H 1 V RECEIVING   ENGINEER A. L. WINGERT
SCAN RATE 1 PSI/MIN 72 ALPHA/MIN   (0002) HKL
PHA 6 V BASE 12 V WINDOW CALIBRATION SAMPLE SILVER
RANDOM INTENSITY   337.2   K(A)   -23.814 CALC DATE 05/14/75

Fig. I-30 Basal pole figure for Condition 7, 1-7-5.

| 1 | .5000 | 2 | 1.0000 | 3 | 1.5000 | 4 | 2.0000 | 5 | 4.0000 |
| 6 | 8.0000 | 7 | 14.0000 | 8 | 20.0000 | 9 | 25.0000 | 0 | 30.0000 |

JOB NO. BTS 464-2   SAMPLE 2-8-0   DATE 05/10/75
RADIATION CU AT 35 KV 28 MA COUNTER TUBE PROP AT   1.910 K
SLITS 2 H 1V ENTRANCE 5 H 1V RECEIVING   ENGINEER A. L. WINGERT
SCAN RATE 1 PSI/MIN 72 ALPHA/MIN   (0002) HKL
PHA 6 V BASE 12 V WINDOW CALIBRATION SAMPLE SILVER
RANDOM INTENSITY   289.1   K(A)   -38.446 CALC DATE 05/14/75

Fig. I-31   Basal pole figure for Condition 8, 2-8-0.
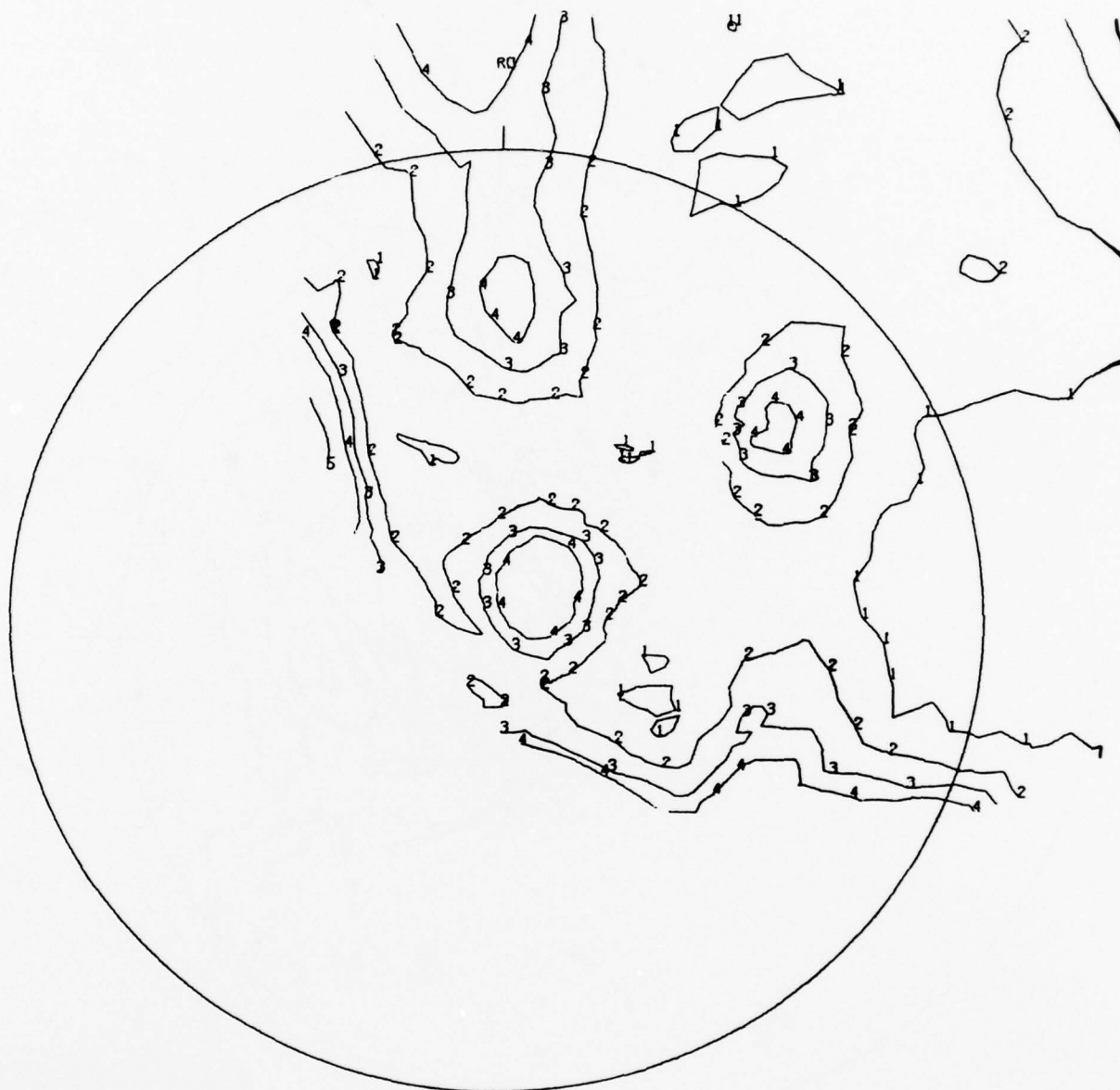
1	.5000	2	1.0000	3	1.5000	4	2.0000	5	4.0000
6	8.0000	7	14.0000	8	20.0000	9	25.0000	0	30.0000

JOB NO. BTS 464-2   SAMPLE 2-9-2   DATE 05/04/75
RADIATION CU AT 35 KV 29 MA COUNTER TUBE PROP AT   1.915 K
SLITS 2 H 1V ENTRANCE 5 H 1 V RECEIVING   ENGINEER A. L. WINGERT
SCAN RATE 1 PSI/MIN 72 ALPHA/MIN   (0002) HKL
PHA 6 V BASE 12 V WINDOW CALIBRATION SAMPLE SILVER
RANDOM INTENSITY   241.7   K(A) -29.172 CALC DATE 05/14/75

Fig. I-32 Basal pole figure for Condition 9, 2-9-2.
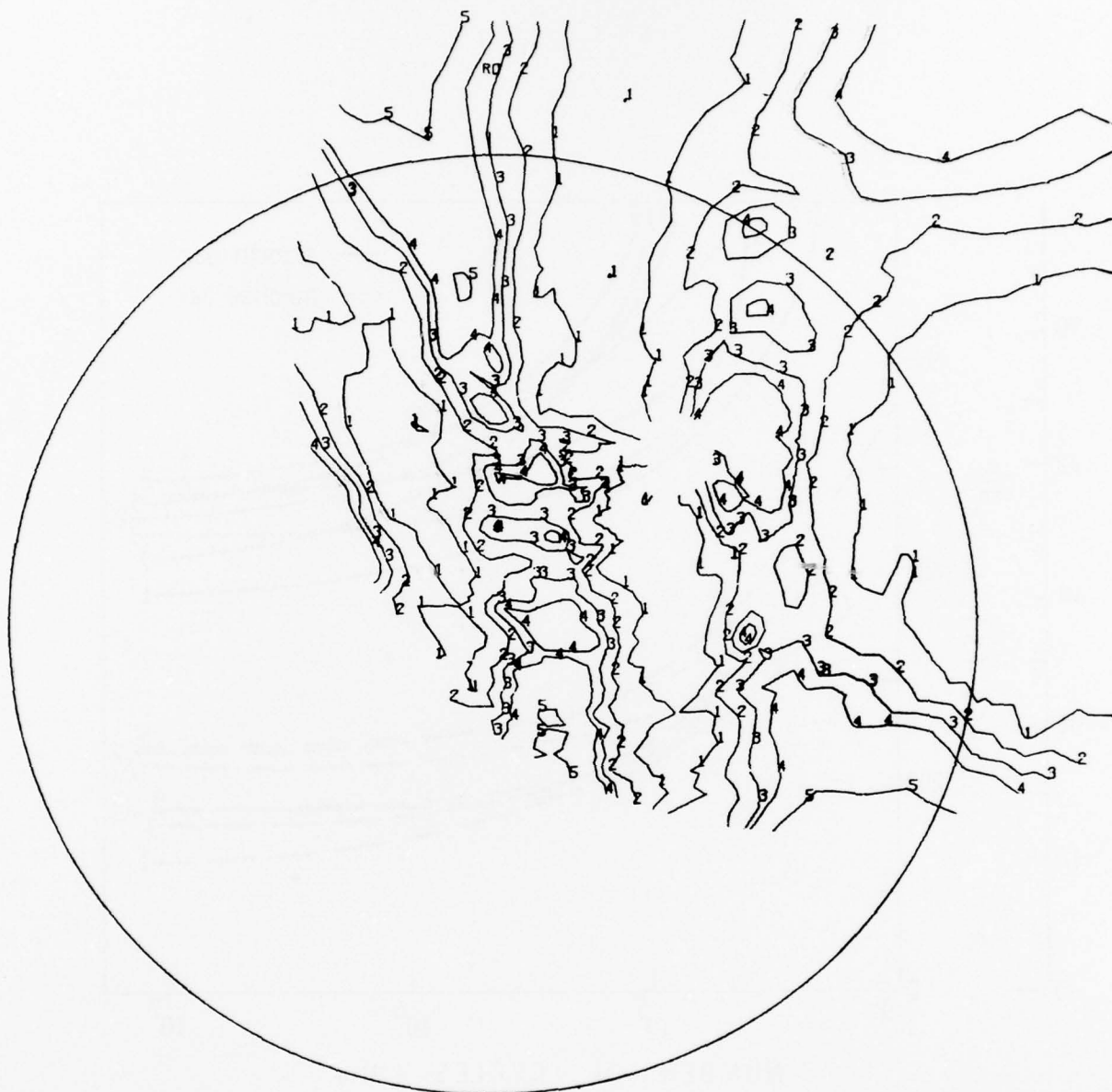
60

| 1 | .5000 | 2 | 1.0000 | 3 | 1.5000 | 4 | 2.0000 | 5 | 4.0000 |
| 6 | 8.0000 | 7 | 14.0000 | 8 | 20.0000 | 9 | 25.0000 | 0 | 30.0000 |

JOB NO. BTS 464-2   SAMPLE 2-10-2   DATE 05/10/75
RADIATION CU AT 35 KV 29 MA COUNTER TUBE PROP AT   1.910KV
SLITS 2 H 1V ENTRANCE 5 H 1V RECEIVING   ENGINEER A. L. WINGERT
SCAN RATE 1 PSI/MIN 72 ALPHA/MIN   (0002) HKL
PHA 6 V BASE 12 V WINDOW CALIBRATION SAMPLE SILVER
RANDOM INTENSITY   234.0   K(A)   -11.921 CALC DATE 05/14/75

Fig. I-33 Basal pole figure for Condition 10, 2-10-2.

61
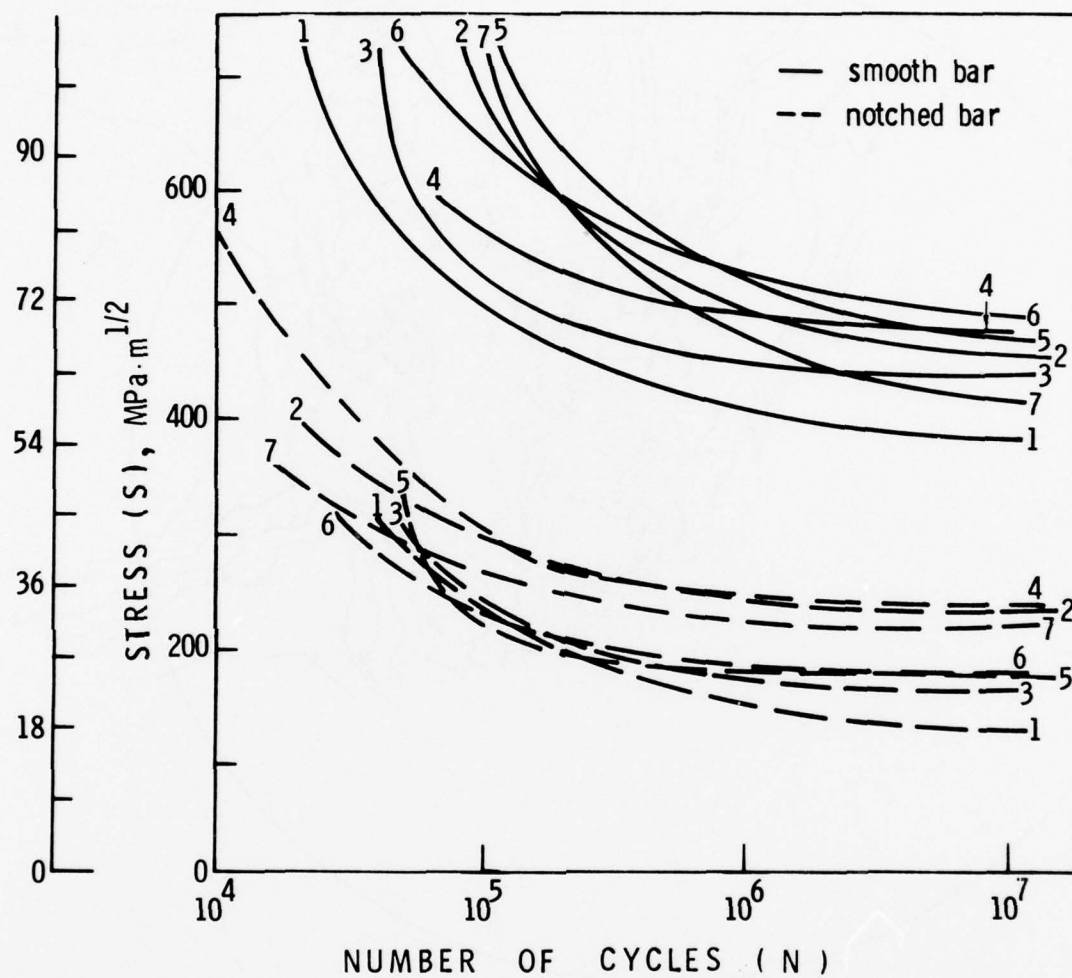
Fig. I-34 S-N curves for smooth and notched (K_t=3.4) bars of Ti-6A1-4V.
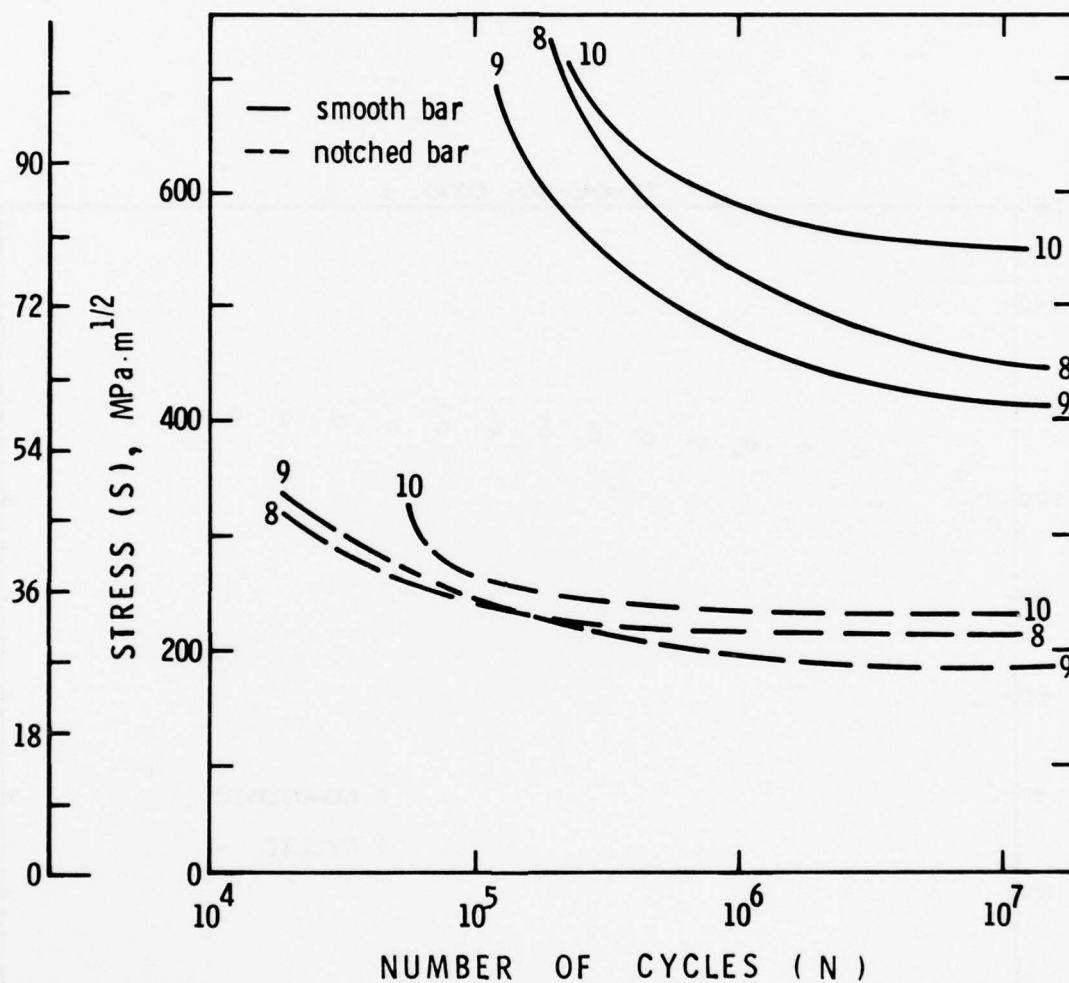
Fig. I-35 S-N curves for smooth and notched (K_t=3.4) bars of Ti-6Al-2Sn-4Zr-6Mo.

63
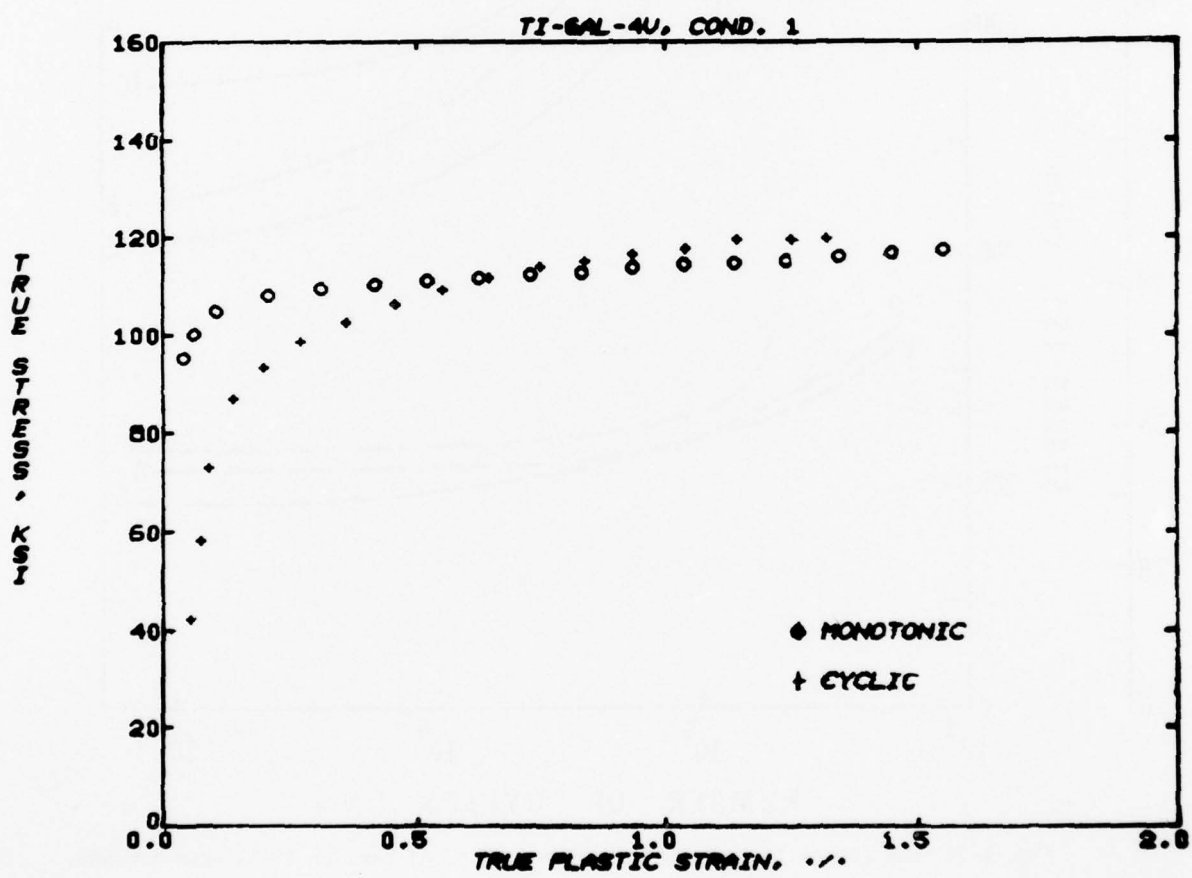
Fig. I-36 Cyclic stress-strain because of Condition 1 at 68°F.
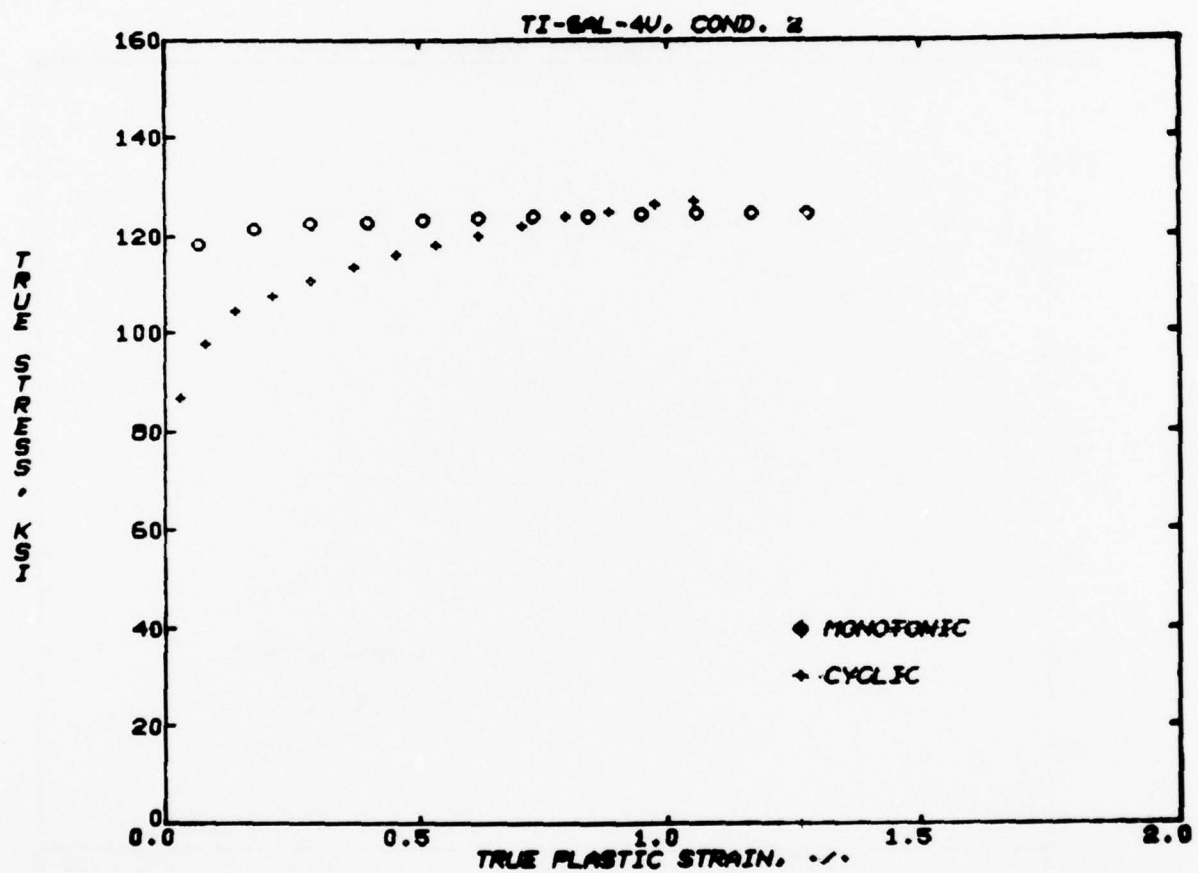
Fig. I-37 Cyclic stress-strain because of Condition 2 at 68°F.

65
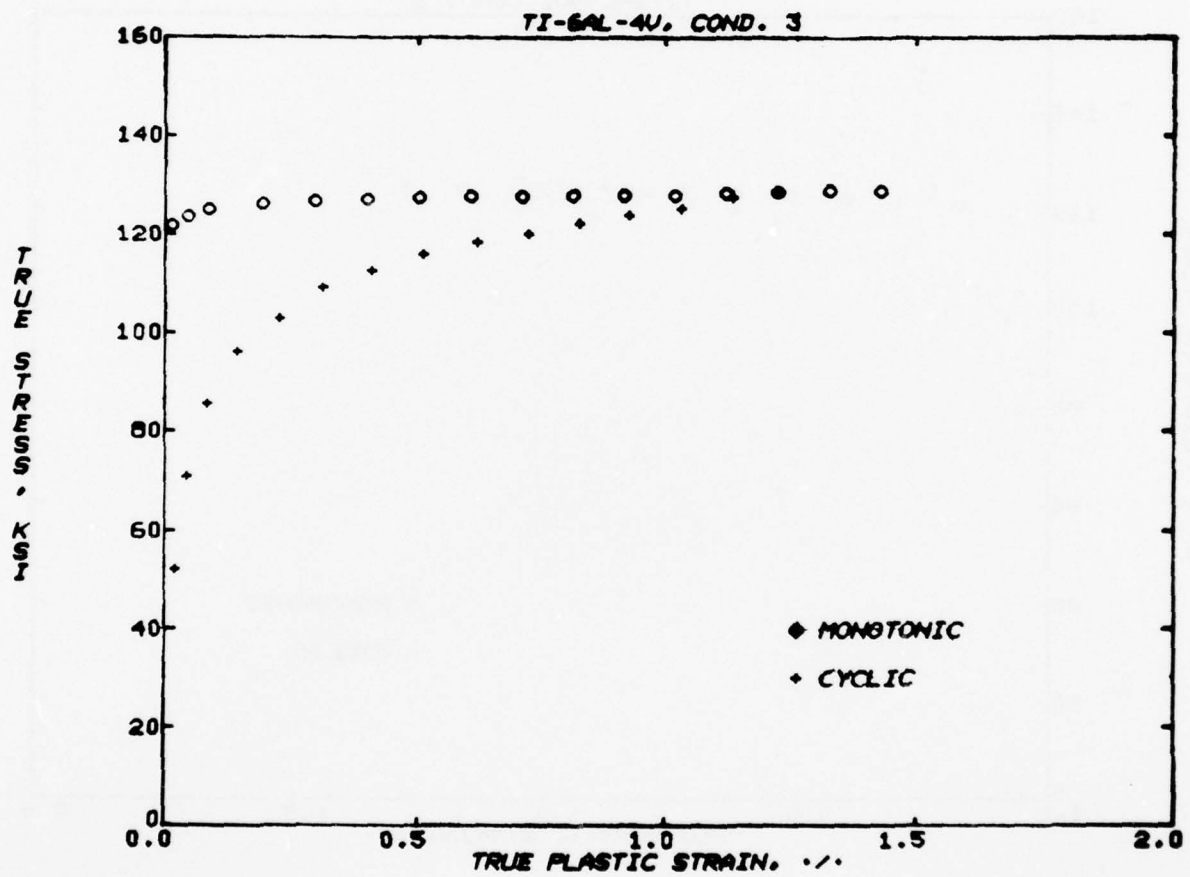
Fig. I-38 Cyclic stress-strain because of Condition 3 at 68°F.
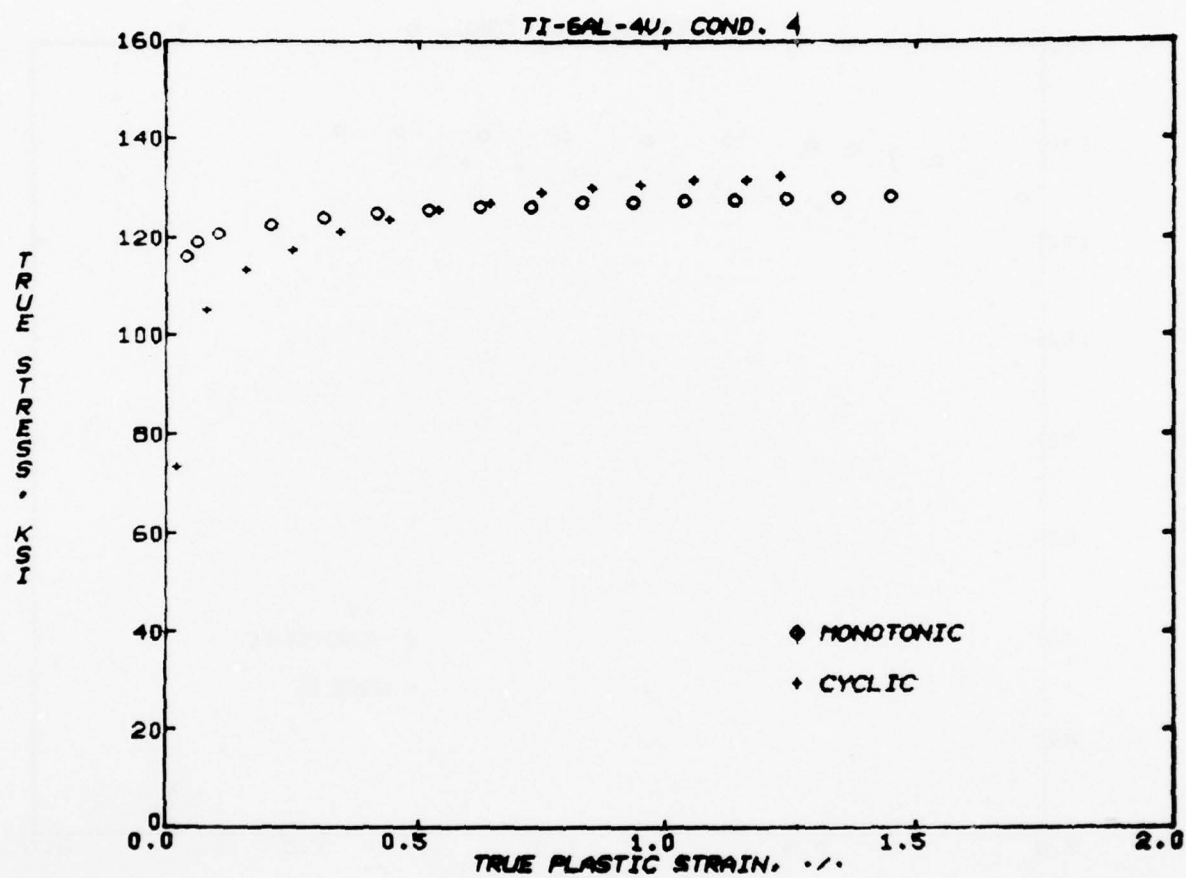
Fig. I-39 Cyclic stress-strain because of Condition 4 at 68°F.
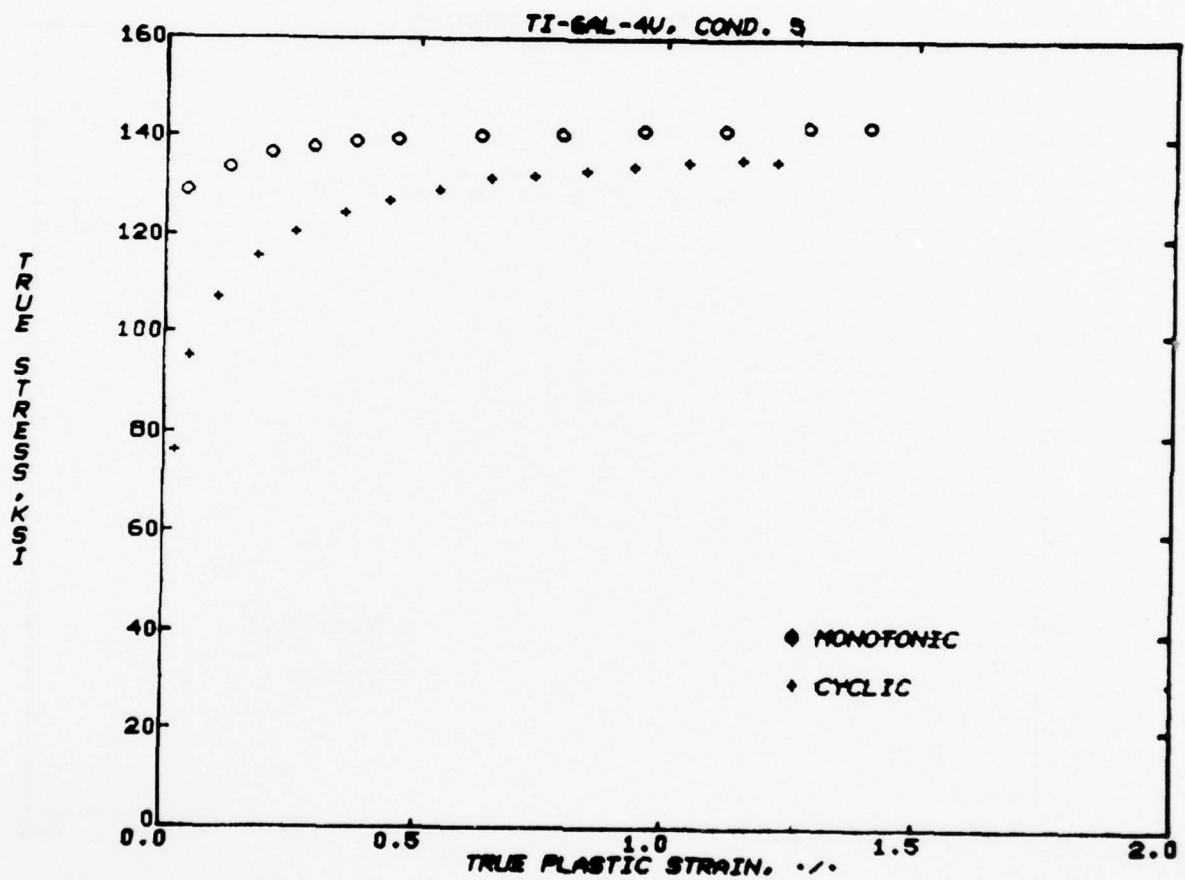
Fig. I-40 Cyclic stress-strain because of Condition 5 at 68°F.
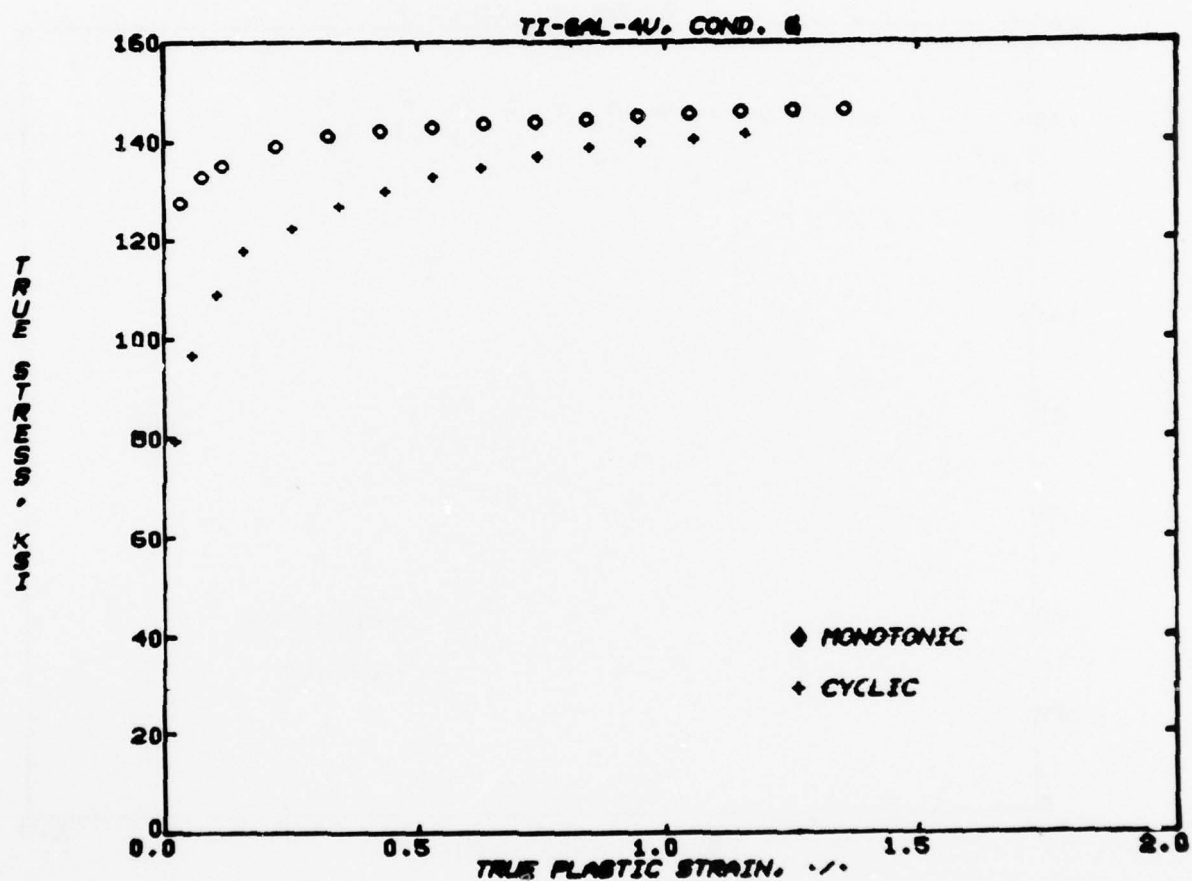
Fig. I-41   Cyclic stress-strain because of Condition 6 at 68°F.

69
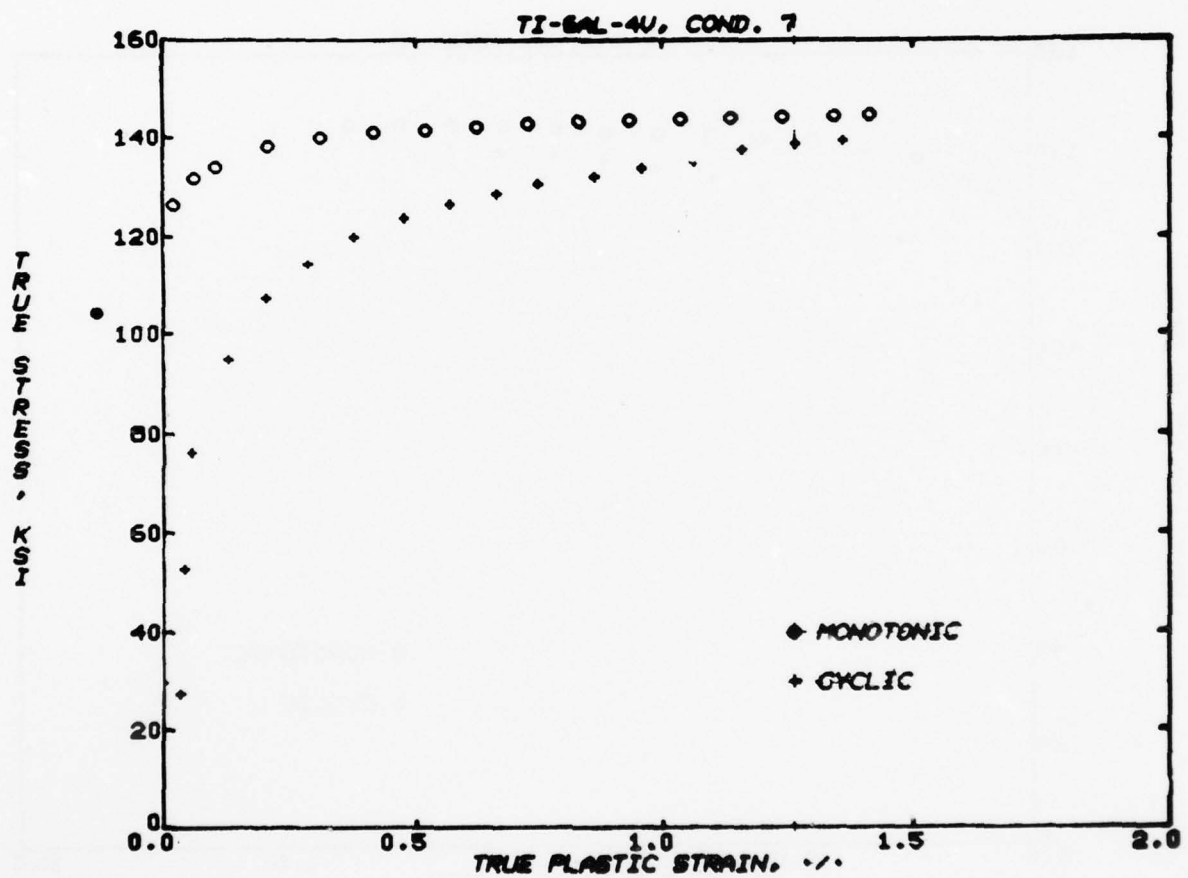
Fig. I-42 Cyclic stress-strain because of Condition 7 at 68°F.

1.0

4.5
5.0
5.6

2.8 2.5

3.2 2.2

3.6

1.1

4.0 2.0

1.8

1.25 1.4 1.6
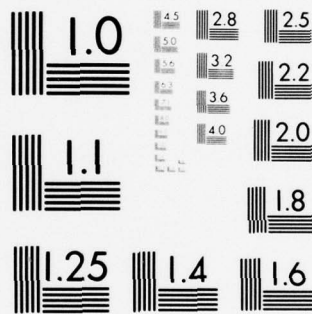
MICROCOPY RESOLUTION TEST CHART
NATIONAL BUREAU OF STANDARDS-1963-A
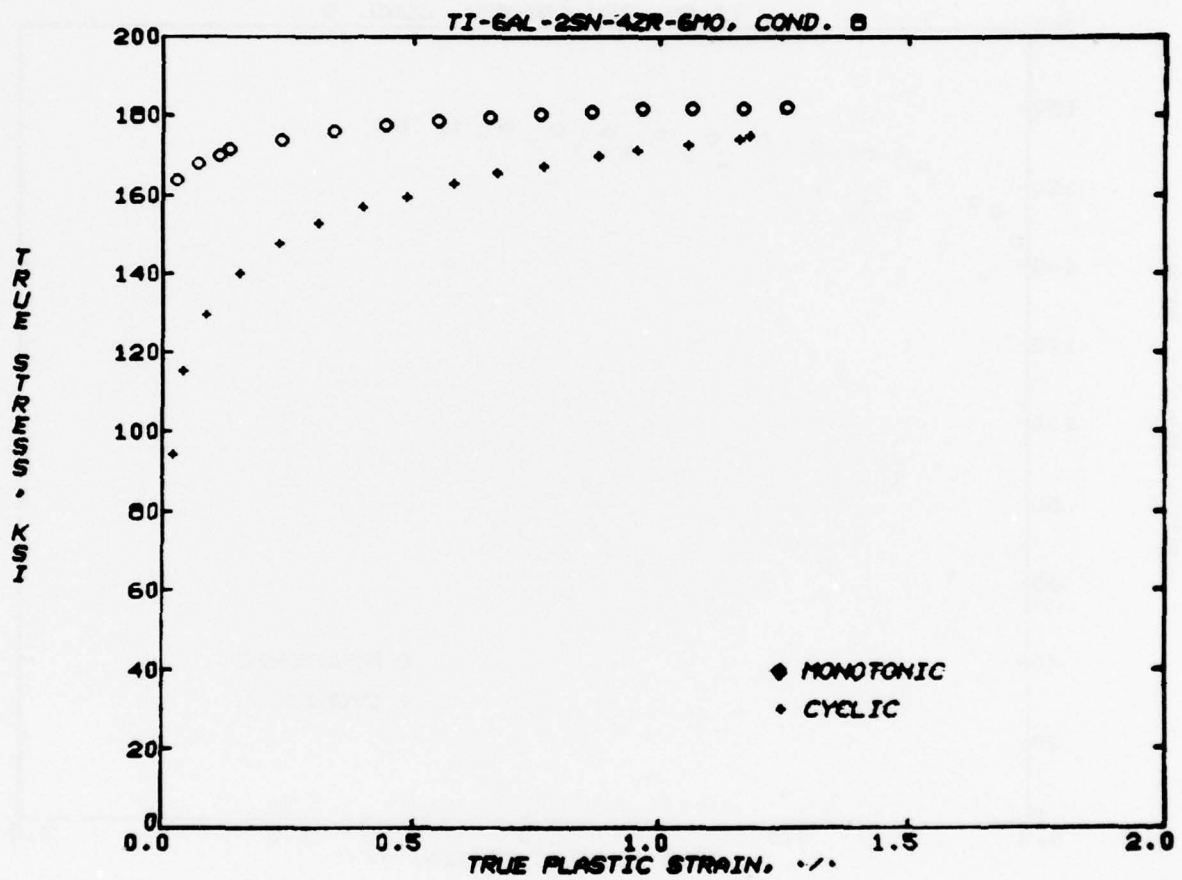
Fig. I-43 Cyclic stress-strain because of Condition 8 at 68°F.

71
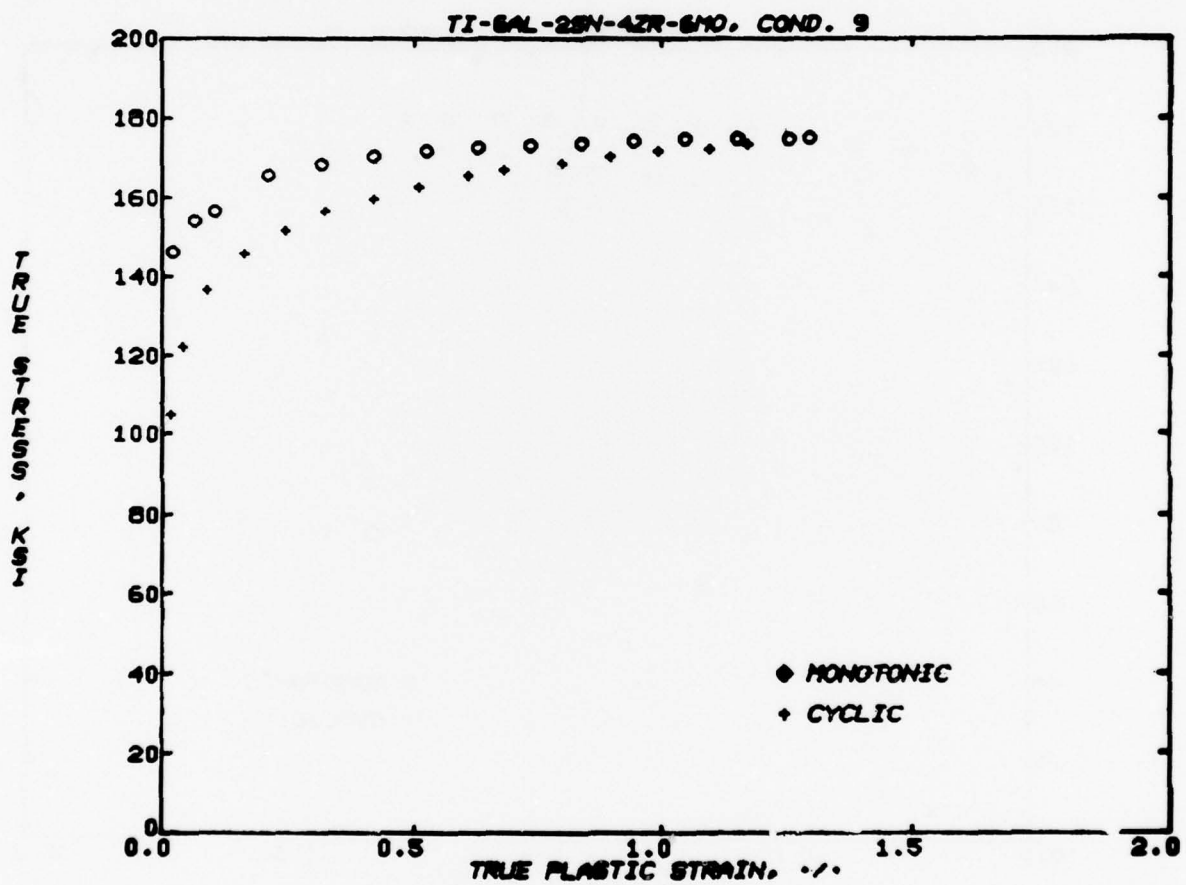
Fig. I-44 Cyclic stress-strain because of Condition 9 at 68°F.
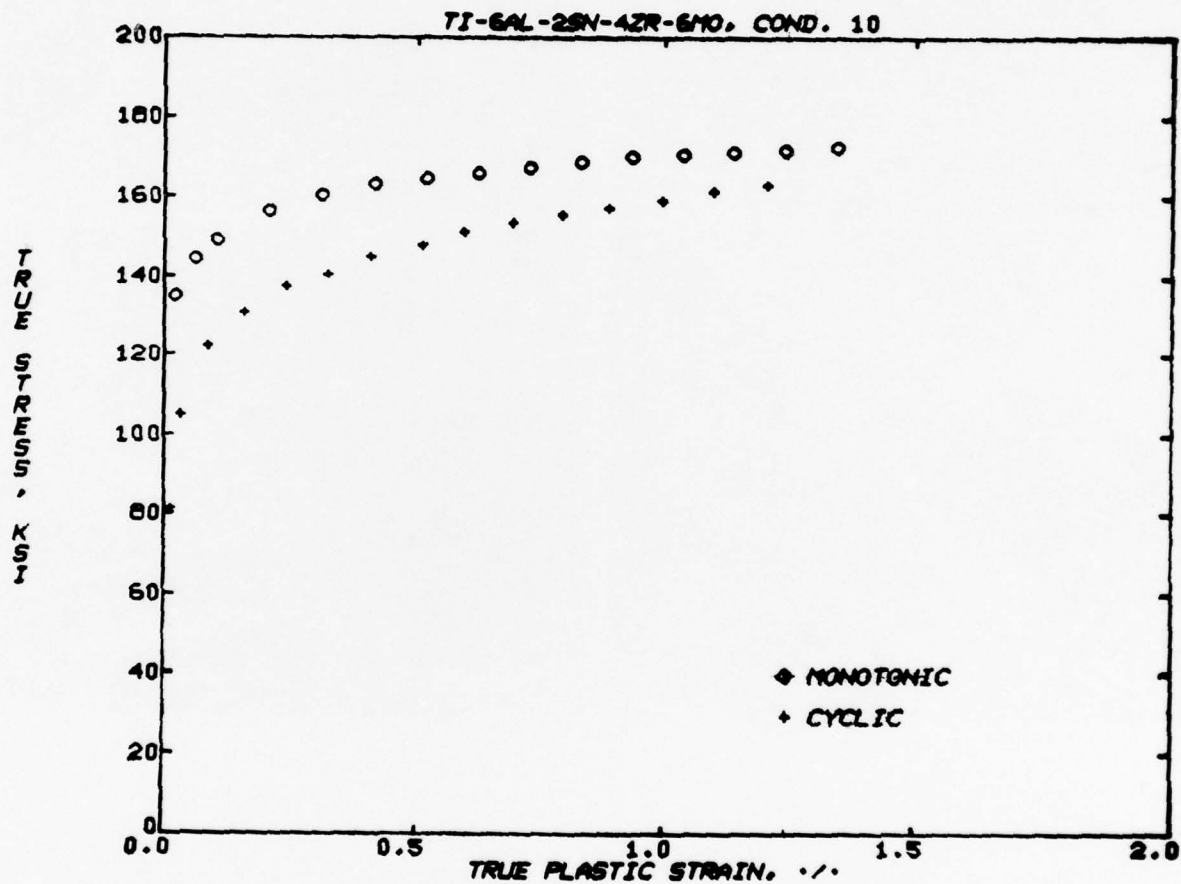
Fig. I-45 Cyclic stress-strain because of Condition 10 at 68°F.
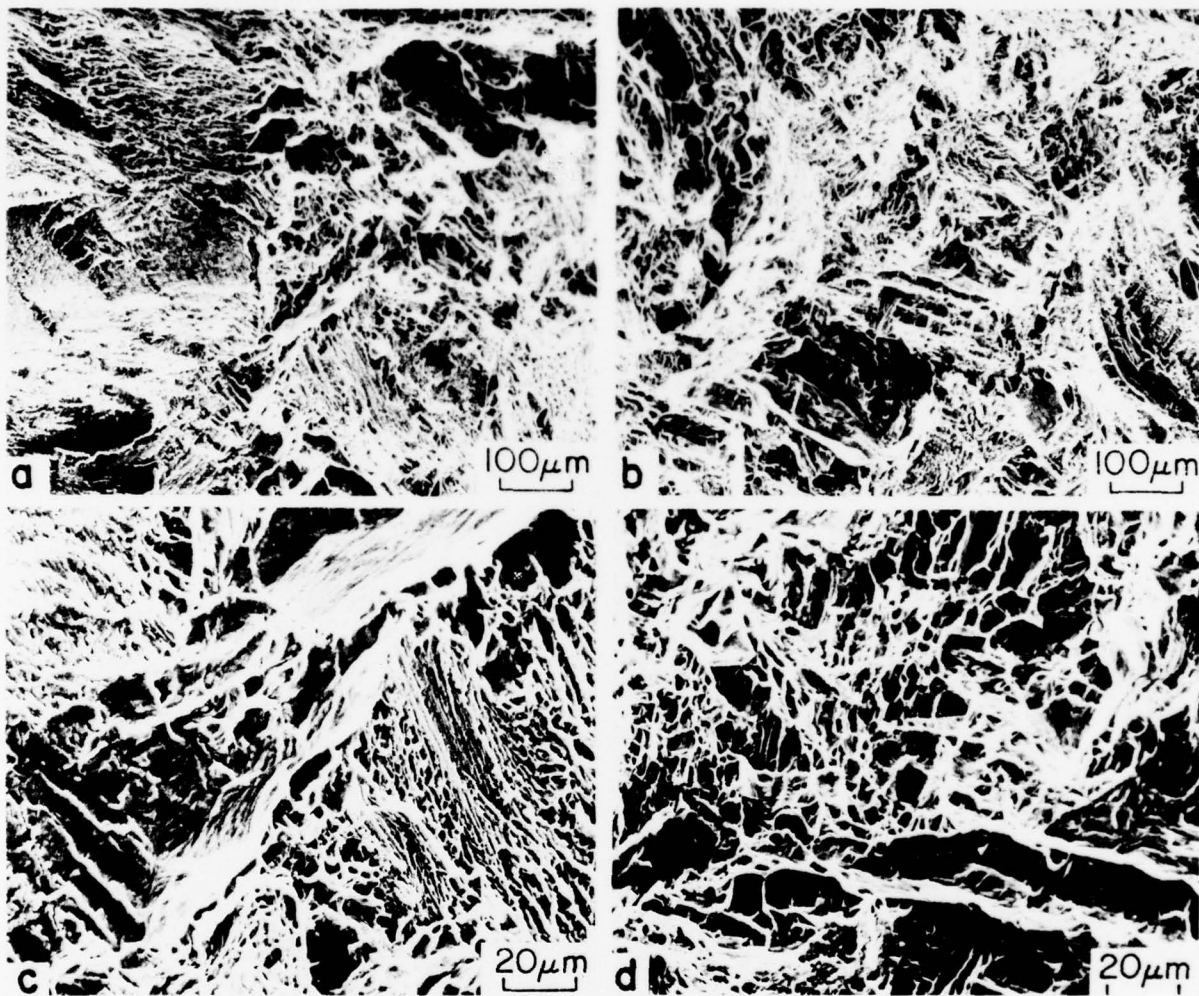
Fig. I-46   Fracture surface of Condition 4 K_{IC} specimen: (a,c) fatigue
precrack to rapid fracture transition; (b,d) rapid fracture.

74
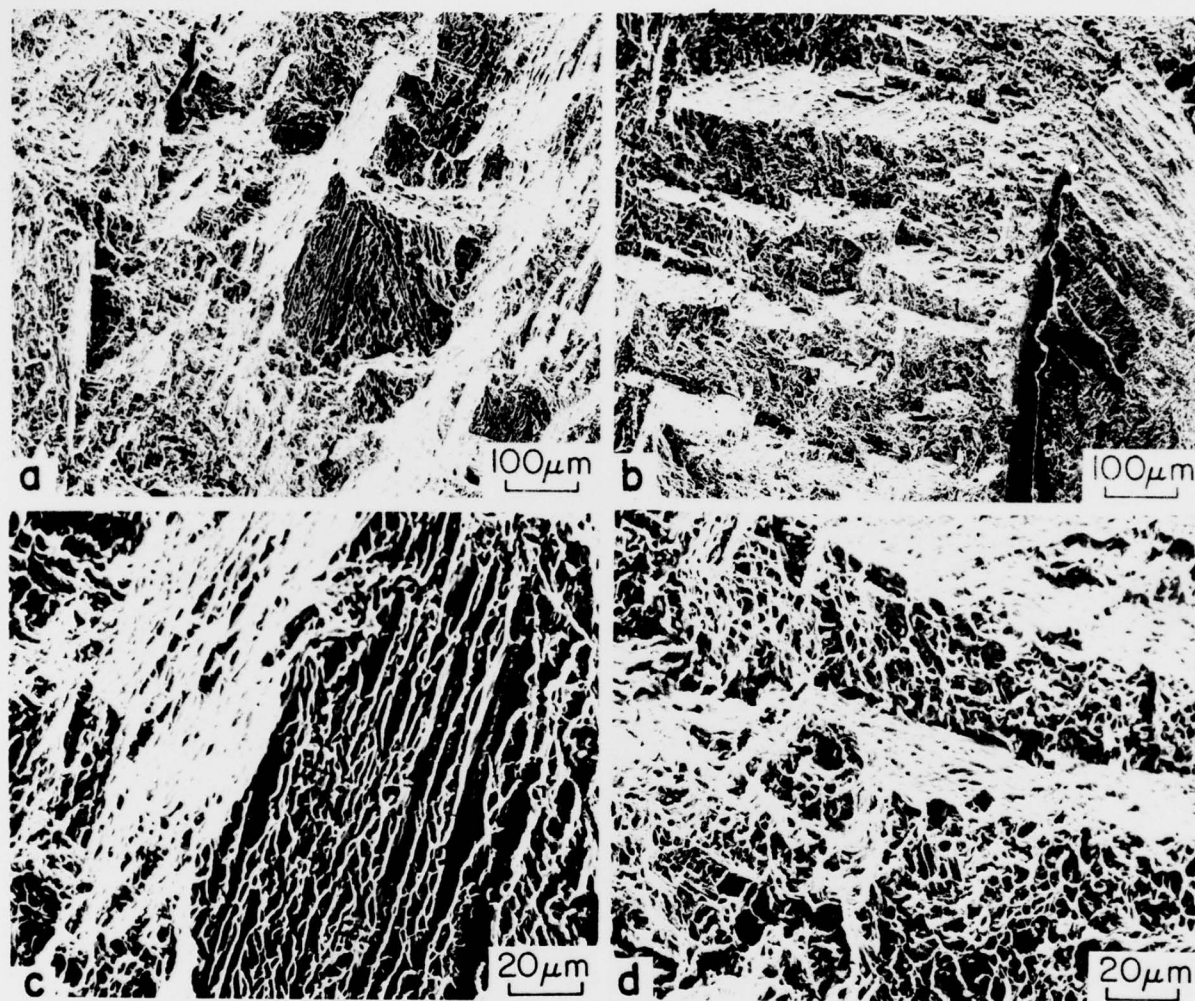
Fig. I-47 Fracture surface of Condition 5 K_{IC} specimen: (a,c) fatigue precrack to rapid fracture transition; (b,d) rapid fracture.
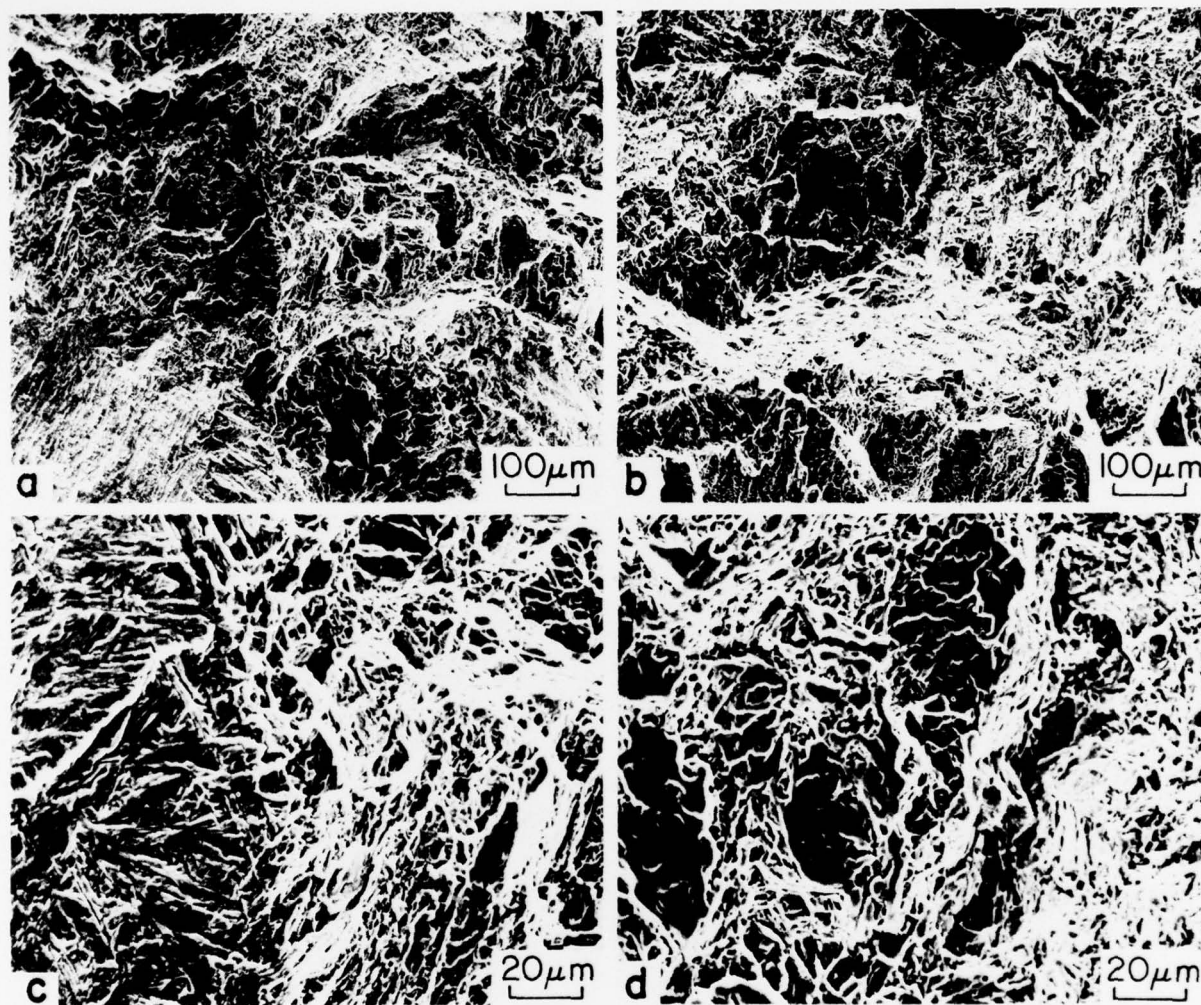
Fig. I-48 Fracture surface of Condition 10 K_{Ic} specimen: (a,c) fatigue precrack to rapid fracture transition; (b,d) rapid fracture.
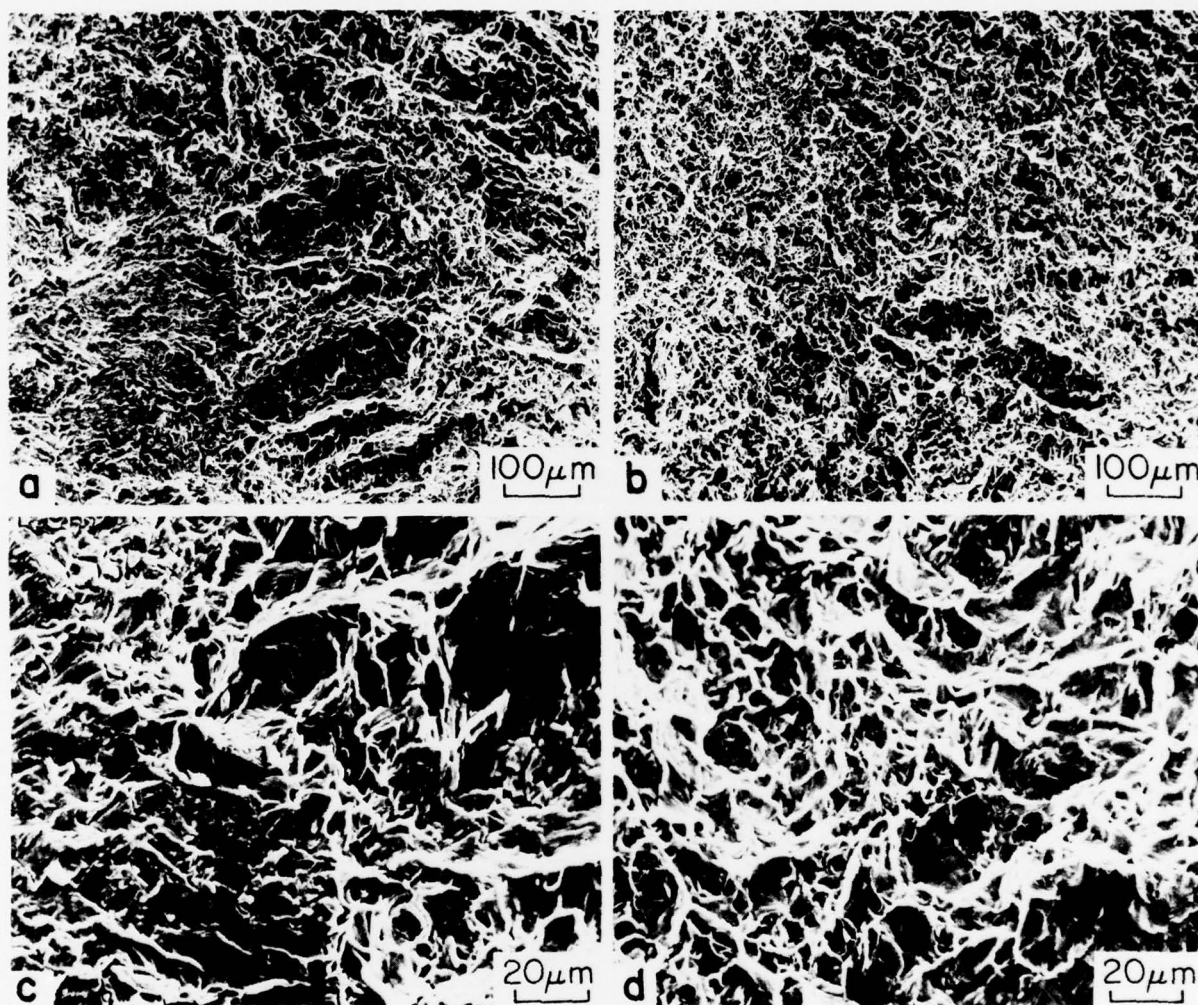
Fig. I-49   Fracture surface of Condition 1 K_{Ic} specimen: (a,c) fatigue
precrack to rapid fracture transition; (b,d) rapid fracture.

77
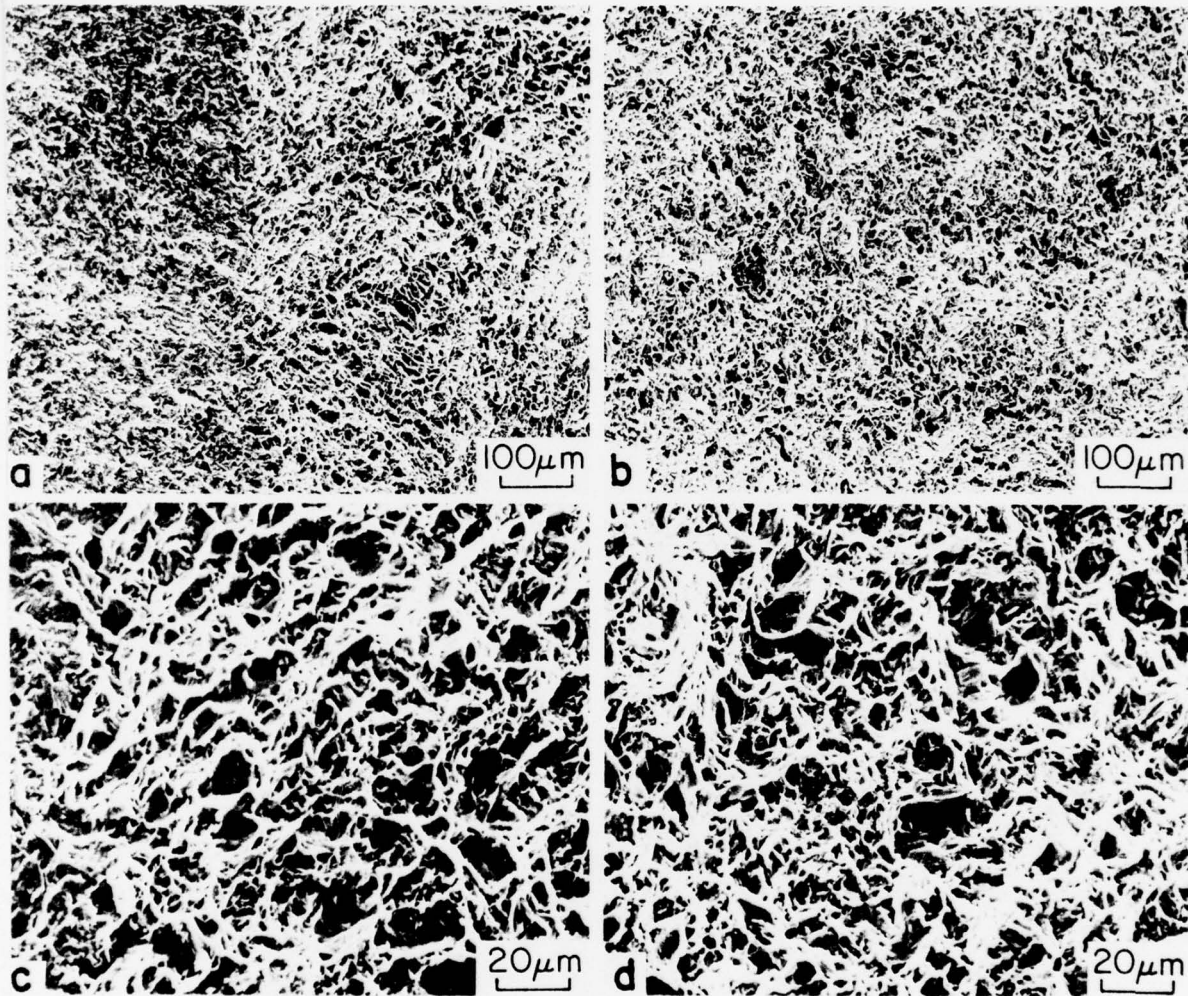
Fig. I-50 Fracture surface of Condition 7 K_{Ic} specimen: (a,c) fatigue
precrack to rapid fracture transition; (b,d) rapid fracture.

78
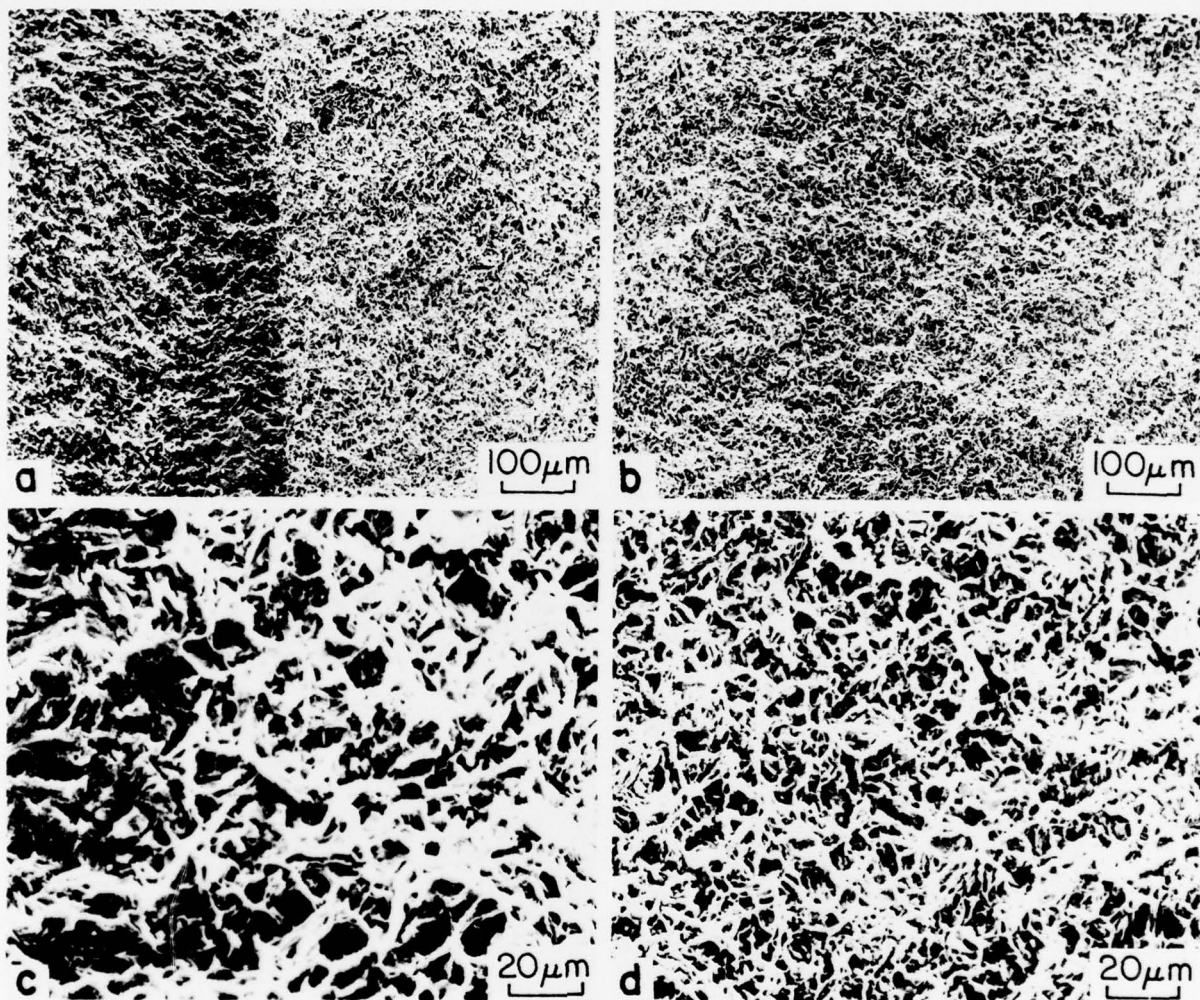
Fig. I-51 Fracture surface of Condition 8 K_{IC} specimen: (a,c) fatigue
precrack to rapid fracture transition; (b,d) rapid fracture.
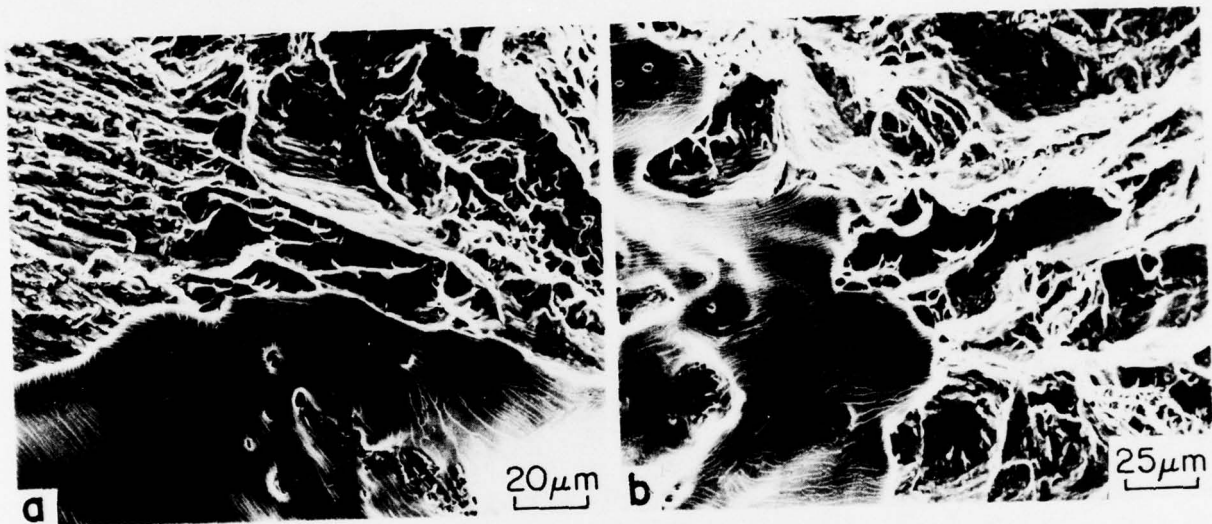
Fig. I-52 Scanning electron micrograph of the fracture path in Condition 4
K_{Ic} specimen: (a) fatigue precrack to rapid fracture transition;
(b) rapid fracture.
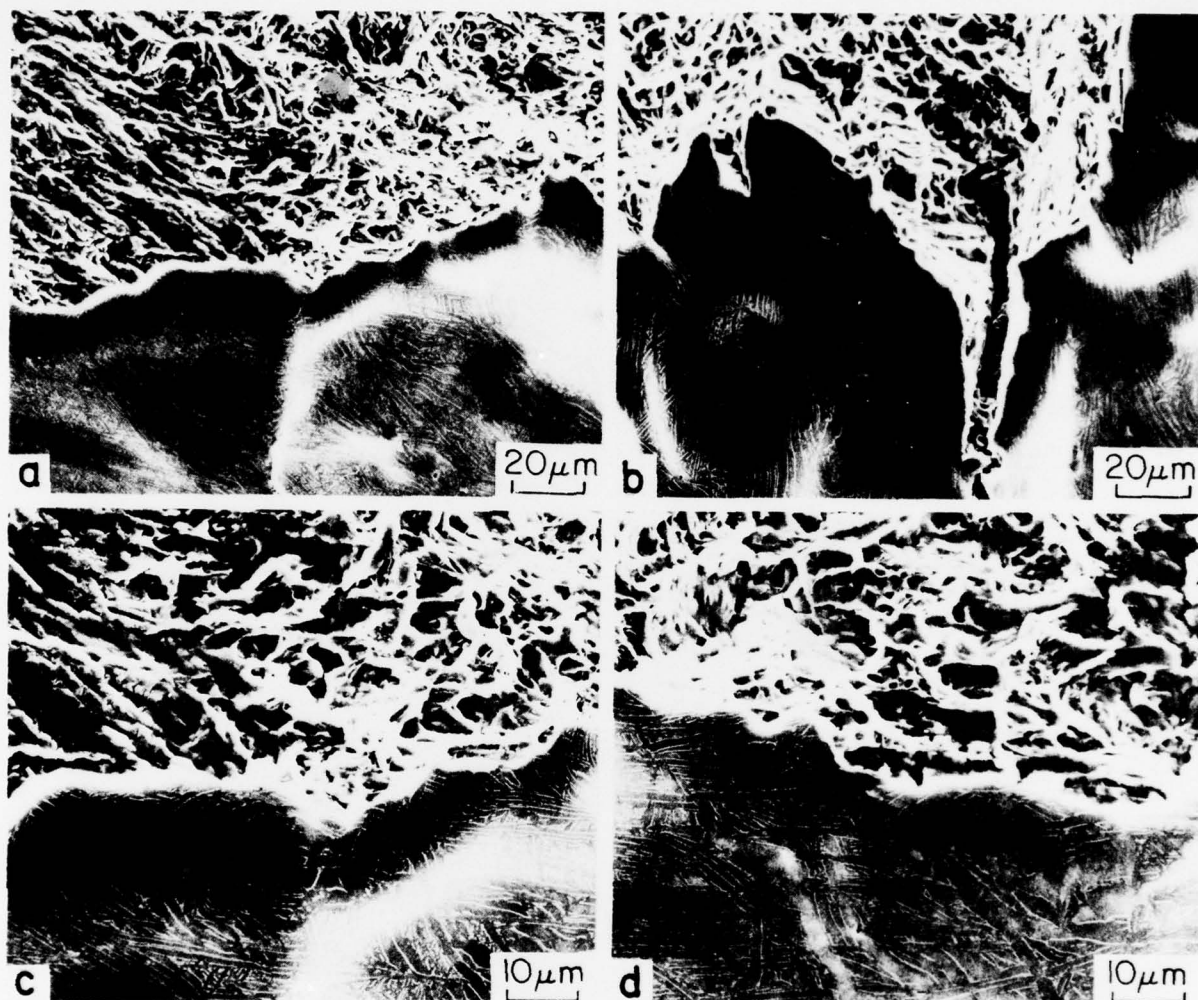
Fig. I-53 Scanning electron micrograph of the fracture path in Condition 5
K_{Ic} specimen: (a,c) fatigue precrack to rapid fracture transition;
(b,d) rapid fracture.
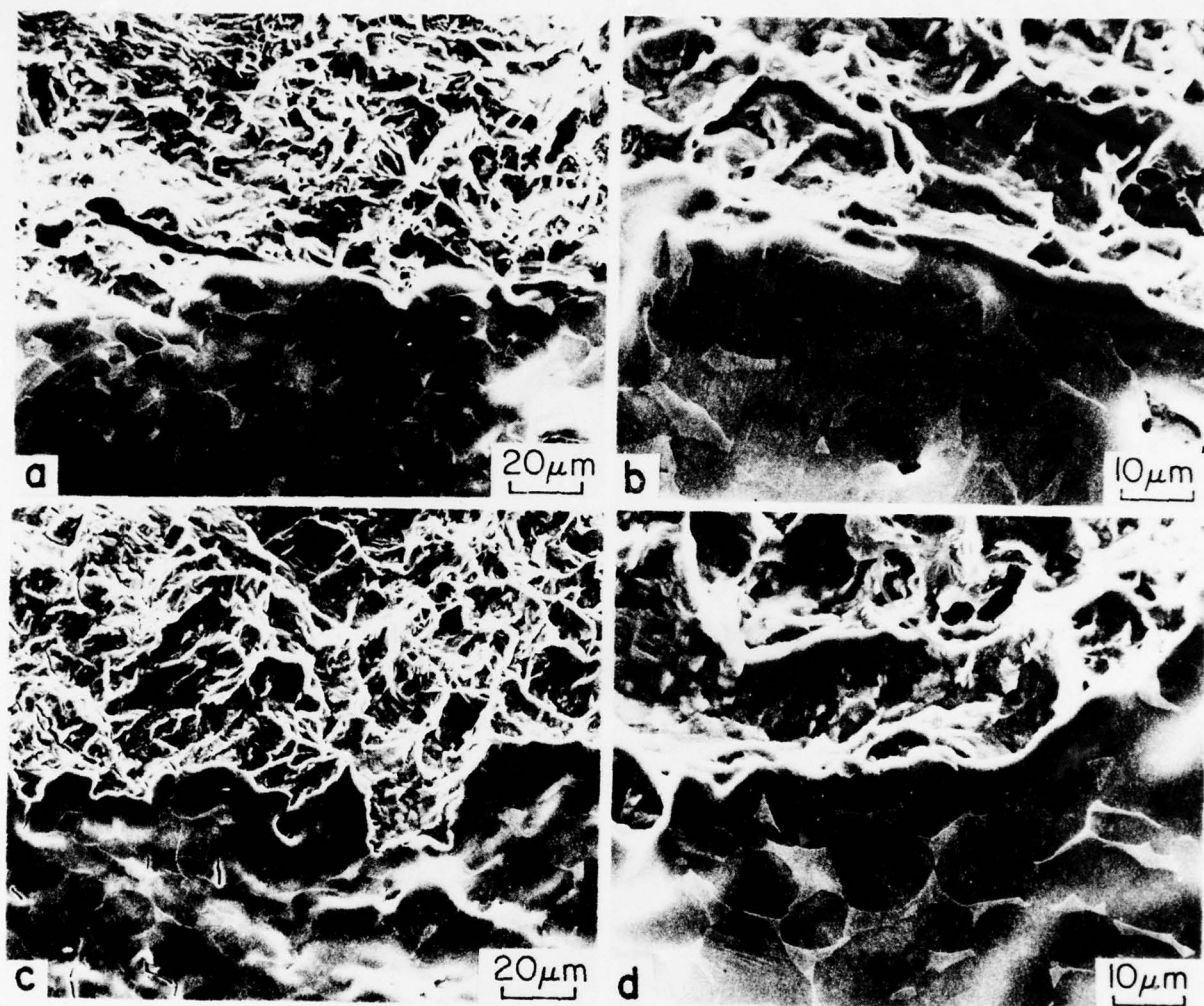
Fig. I-54 Scanning electron micrograph of the fracture path in Condition 1 K_{Ic} specimen: (a,c) fatigue precrack to rapid fracture transition; (b,d) rapid fracture.
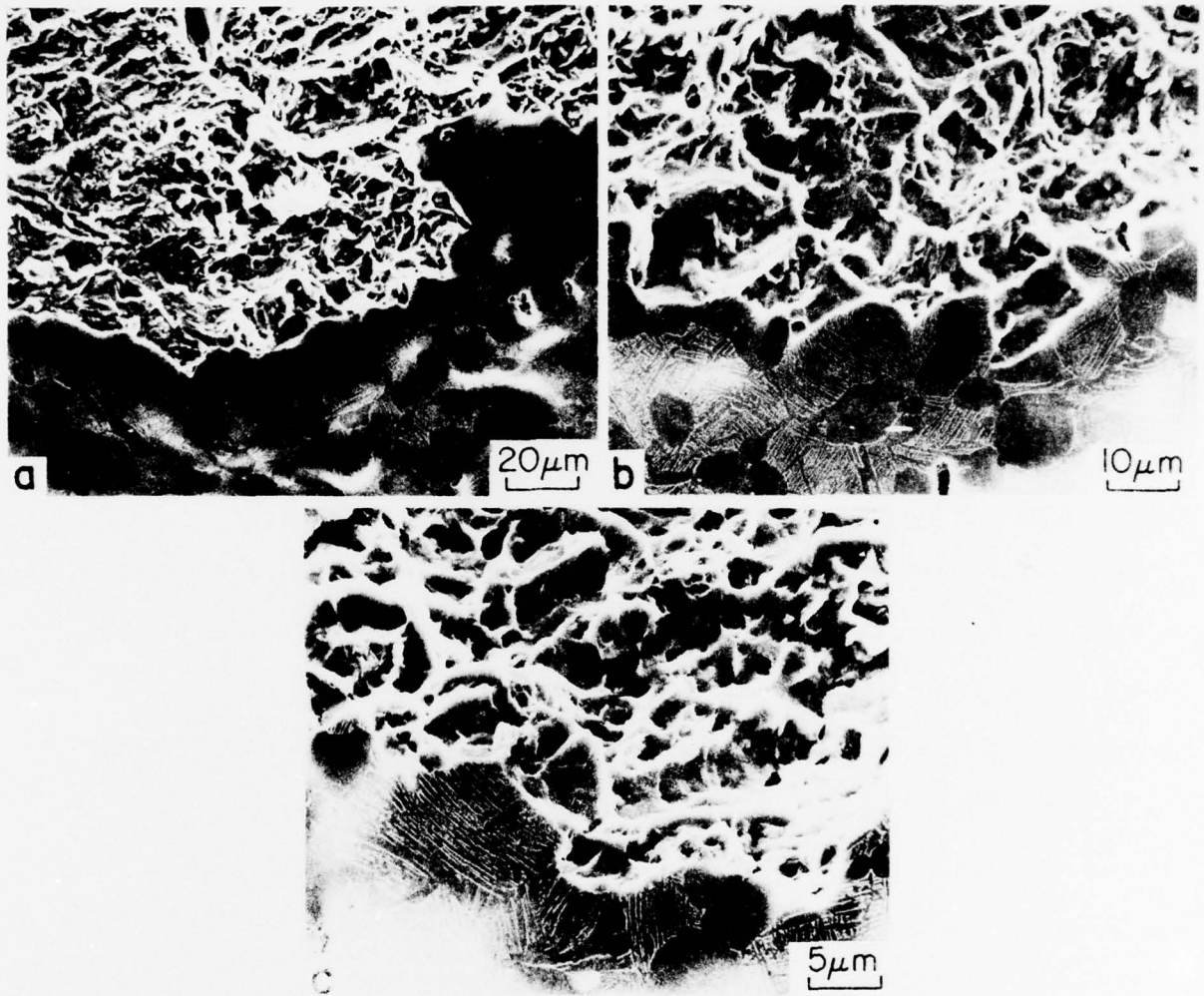
Fig. I-55 Scanning electron micrograph of the fracture path in Condition 7 K_{Ic} specimen: (a) fatigue precrack to rapid fracture transition; (b,c) rapid fracture.

PART II: CRACK PROPAGATION IN Ti-6Al-4V AND Ti-6Al-2Sn-4Zr-6Mo

INTRODUCTION

It has been evident almost since the formulation of the Paris law[1] that there is a range of fatigue crack propagation rates over which metallurgical variables play a weak or negligible role;[2,3] steels are among the best known examples of this.[4] Nevertheless, it is of interest to determine whether this is true for other alloys, such as the $\alpha+\beta$ titanium alloys of the present paper. As is described in the following, there have been preliminary indications of a distinct microstructural effect on fatigue cracking in these alloys.

For practical structures, design of critical parts must include assumption of flaws in the part before it enters service. The design variable then becomes the rate of growth of a flaw by fatigue, i.e., the period of service before it becomes large enough to cause failure. The fatigue parameter of interest is thus the fatigue crack propagation (FCP) rate, which must be known for reliable and efficient design. Such data are required regardless of the effect of microstructure. However, microstructure effects would be of particular interest for two reasons: to ensure reproducibility of results on a given material and to enhance progress toward improved materials. Information of this type is most reliable when acquired from material which has been characterized in considerable detail as to both

84

microstructural character and as to mechanical properties. These data were presented for the present program in the previous part, hereinafter called Part I.

Frequent observations that FCP rate is not correlated with such variables as yield strength,[4] grain size,[5-7] and other metallurgical variables[3] have led some workers to the view that microstructure is not significant in affecting FCP. But other observations, particularly for alpha-beta titanium alloys, have shown that certain metallurgical variables do affect FCP. The most significant early study on the effect of microstructure was that of Amateau, et al.[8] They found variations in FCP rate as a function of microstructure in Ti-6Al-6V-2Sn; these could not be correlated with either yield strength or fracture toughness. Examination of the data also shows that the FCP variations observed cannot be correlated with modulus values. The existing theories for FCP failed to predict the experimental data, probably because the theories do not account for crack path interactions with elements of microstructure. Amateau, et al. observed slower FCP when cracks were diverted to follow primary alpha boundaries, or to follow changes in orientation at prior beta boundaries.

Work at about the same time on Ti-6Al-2Sn-4Zr-6Mo, an alloy with comparable beta stabilization to Ti-6Al-6V-2Sn, showed[9] that an acicular alpha microstructure resulting from cooling from the beta had slower FCP than a microstructure containing equiaxed primary alpha. This result agrees with the correlation of Amateau et al.[8] Data from another report[10] on

Ti-6Al-4V indicate that a recrystallization anneal, which increases the amount of primary alpha, decreased FCP rate relative to solution treated and aged material. Still another report[11] on Ti-6Al-4V found that material cooled from the beta region was better in FCP resistance than was recrystallization-anneal (RA) material. The authors did not make this observation, but a crossplot of their data illustrates the point. This last report has complications due to texture effects, as will be discussed later, but the comparison should correctly rank the microstructures: as with the other studies cited, acicular or Widmanstätten α provided the most resistance to FCP.

There is some disagreement in past work on texture effects. Strongly textured Ti-6Al-4V sheet showed little FCP rate change from moderately textured sheet,[12] but texture can affect FCP of Ti-6Al-4V plate.[11,13,14] Textured Ti-6Al-2Sn-4Zr-6Mo plate also shows marked effects.[10] In view of these conflicts and complications, it was decided to conduct the present program on forged material deliberately processed to have as weak and uniform a texture as possible, independent of the final microstructure, as documented in Part I. In this way, the microstructure variable can be separated from that of texture, a separation not possible in earlier work.[8-14] Concurrent research on the role of texture[15] has not entirely resolved the question of the absolute magnitude of texture effects.

EXPERIMENTAL PROCEDURE

The composition, forging process history, microstructure development, mechanical properties, and textures of the Ti-6Al-4V and Ti-6Al-2Sn-4Zr-6Mo were described in Part I. The specimens for FCP measurement were sawed as rough blanks from the forgings, heat treated to produce the final microstructure, and machined to final dimensions. In every case, specimens were oriented so the crack growth plane corresponded to the RL plane (see Part I). The compact tension specimens (Fig. II-1) were, in all cases, 12.7-mm (0.5-in.) thick, and conformed to ASTM E399 suggestions as to specimen proportions, except that H/W = 0.486.

Prior to testing, all specimens were fatigue precracked at 20 Hz at a load ratio of R = 0.1 in laboratory air. Loads were stepped down every 1.3 mm (0.050 in.) such that the final 0.8 mm (0.030 in.) of growth occurred at a maximum stress intensity equal to that at which subsequent testing was started. Crack length measurements were made at 800X in a microscope focused on the specimen surface while the specimen was unloaded. Crack length was measured to ±0.003 mm (±0.0001 in.), with the aid of a FILAR eyepiece, for $0.3 \leqslant a/w \leqslant 0.75$. Three or four data points were taken at a constant maximum load after which the load was increased by 445 N (100 lb); the load was thus increased incrementally until the onset of unstable crack growth.

Testing was conducted in a dry air atmosphere (nominal humidity 5% RH) obtained by passing the air through anhydrous Ca_2SO_4 (Drierite) into a sealed polyethelyene bag surrounding the specimen. The stress ratio R,

87

defined as $\sigma_{min}/\sigma_{max}$, was controlled for both precracking and FCP measurements at values of 0.1, 0.3, 0.5, and 0.7. Cyclic frequency was 20 Hz.

Previous work[16] has shown that a correlation exists between ultrasonic measurements of crack closure and the nonlinearity in a load-displacement (compliance) curve. On this basis, careful compliance curve determinations were made in order to establish the R value corresponding to an open crack throughout the stress cycle. This value was found to lie between 0.28 and 0.30 for all of the ten microstructures tested and, accordingly, $R \geqslant 0.3$ is taken as open crack conditions.

Room temperature hold-time tests were performed by employing a 5-min hold time at maximum K on each cycle, with 20 Hz unload-load sequences separating the holds. This hold time was chosen on the basis of evidence[17] that maximum effects occur for such times, provided that they are observed at all. Stubbington's study[7] was performed on textured material in the as-formed condition; he found appreciably decreased hold time effects when a solution treatment was applied to material after forming. Results were obtained near cyclic growth rates of about 2×10^{-5}, 2×10^{-4}, and 2×10^{-3} mm/cycle (1×10^{-6}, 1×10^{-5} and 1×10^{-4} in./cycle), using a programmable function generator. Hold-time data include 2 or 3 values for each growth rate, taken for a block of 100-300 hold cylces.

Spike overload effects were evaluated near cyclic growth rates of about 2×10^{-5} mm/cycle (1×10^{-6} in./cycle) in dry air, for six selected microstructures. The overloads were chosen as a 75% increase in maximum load

above that being applied just prior to overloading, and a block of 20 such cycles of 75% overload were applied. Subsequent response of the specimens, including the number of cycles required for the specimen to return to the base line crack growth rate, was monitored.

Upon termination of FCP measurements, the specimens were fractured at high ΔK and fractographic examination was conducted in a scanning electron microscope (SEM). In addition to conventional fractography, several specimens were also prepared by the "plateau etching" technique originally suggested by Shechtman[18] and subsequently refined by Chesnutt and Spurling[19] to permit direct observation of the relation between crack path and microstructure.

RESULTS

FCP Measurements

FCP data for all ten microstructures of the two alloys, for four R values, are difficult to present concisely. Illustrative data will thus be used with the intent of increased clarity. A primary observation for the seven microstructures of Ti-6Al-4V is that three groupings are evident: (1) The fastest FCP over most of the ΔK range studied was associated with the structures comprising equiaxed α particles in a Widmanstätten matrix (Conditions 2, 3, 6, and 7), of which the STOA Condition 7 is selected as representative; (2) an intermediate FCP rate was associated with the equiaxed α or RA (Condition 1) and the coarse Widmanstätten or βA (Condition 4)

89

structures; (3) the slowest FCP was associated with the fine Widmanstätten or
βQ (Condition 5) structure. Data for Conditions 1, 4, 5, and 7 at each R
value is shown as Fig. II-2 through II-5. In the case of Ti-6Al-2Sn-4Zr-6Mo,
the fine primary α (Condition 8) showed somewhat faster FCP than the coarse
primary α (Condition 9) or the Widmanstätten α (Condition 10). Data for all
three are shown for R = 0.1 and 0.3 in Fig. II-6 and II-7, while Conditions 8
and 10 are depicted in Fig. II-8 and II-9 at higher R.

The general pattern in all these data, as would be expected, is that
for a particular microstructure increasing R tends to increase FCP rate
(Fig. II-10 through Fig. II-15). However, this is not marked at higher FCP
rates, e.g., above about 10^{-4} mm/cycle, and in Condition 10, Fig. II-15,
there is little effect of R over the whole FCP rate range. The largest effect
seen is for the change between R = 0.3 and R = 0.5. Increasing R from 0.5 to
0.7 has little or no additional effect on any condition, except perhaps at the
lowest FCP rates (e.g., with Conditions 1 and 4). The differences between
R = 0.1 and R = 0.3 are slight, as would be expected because R = 0.3
corresponds closely to the R value for crack closure, i.e., the crack just
closes for R = 0.3, for all ten conditions. The overall pattern of results as
a function of R resembles that shown by Yuen, et al.,[20] whose material was
very similar to Condition 2 of this study.

The important conclusion from Fig. II-2 through II-9 is that
microstructure does have a distinct effect on FCP in weakly textured Ti-6Al-4V
and Ti-6Al-2Sn-4Zr-6Mo, and that this effect can be discerned at R values
ranging from 0.1 to 0.7. The only clear-cut effect of R $\geqslant$ 0.3 (open crack) is
to reduce data scatter in these results.

90

Fractography

Fracture surfaces were examined for all ten microstructures, but only the representative cases (Conditions 1, 4, 5, 7, 8, and 10) will be reported here, except where exceptional observations were made on the other microstructures. The examination was conducted at two ΔK levels, corresponding to crack growth rates of 2.54×10^{-6} mm/cycle and 2.54×10^{-4} mm/cycle. There is an element of ambiguity to this procedure, however, because of the changes in da/dN-ΔK curves with R. As shown in Fig. II-16, either low or high growth rates may correspond to regions of quite different ΔK. (This effect has been well documented in steels by Ritchie[21] and others, and can readily be discerned in Fig. II-10 through II-15.)

Emphasis is on fractography for R = 0.1. Although all FCP specimens were examined, fractographic examples are omitted here for the cases which exhibited little or no load ratio effect, or which exhibited little difference in fracture topography between the R = 0.5 or 0.7 specimen, and the R = 0.1 specimen. The results in Figs. II-17 through II-23 are presented so that the crack propagation direction is from left to right. The accompanying optical micrograph shows the microstructure in an RL section which corresponds to the crack growth plane. It and the fracture face macrophotograph are presented in identical orientation. The smallest interval on the macrograph scale is 1 mm.

(i)   <u>Ti-6Al-4V</u>

The fastest FCP microstructure in Ti-6Al-4V was the STOA, Condition 7. Fig. II-17 illustrates this for R = 0.1. At low growth rates, Fig. II-17(c), it appears that FCP occurs by mixed modes consisting of striation formation, "cleavage" of the primary α particles or at the primary α-Widmanstätten $\alpha+\beta$ interfaces, and/or "cleavage" of the Widmanstätten $\alpha+\beta$ packet interfaces. At the intermediate growth rates, Fig. II-17(d) through (f), FCP occurs primarily by striation formation in or around the primary α particles accompanied by ductile tearing of the β. Considerable secondary cracking at $\alpha - \alpha+\beta$ interfaces and Widmanstätten $\alpha+\beta$ packet boundaries evidently occurs, especially at the intermediate growth rate. Similar observations were made for the other primary α-Widmanstätten matrix microstructures, Conditions 2, 3, and 6.

The two microstructures having similar, intermediate FCP rates, Conditions 1 and 4, nevertheless exhibit strikingly different microstructures and fracture surface topographies. At the low growth rate in RA material, Condition 1, Fig. II-18(c), crack propagation is by a mixed mode of cleavage and striation formation. Regions of cleavage and striation formation, the smooth areas in Fig. II-18(c), correspond to the primary α particle size and morphology (Fig. II-18(b)). At the intermediate growth rate, well defined striation formation on transgranular facets corresponding to the primary α particles occurs. Secondary cracking is pronounced at the edges of these facets (Fig. II-18(d)), and such locations correspond to the regions of

92

β phase and α/α grain boundaries. The βA, Condition 4, on the other hand, exhibits considerable intergranular cracking, both at the low and intermediate growth rates, with very good correlation between the colonies of Widmanstätten α plates and the flat facets on the fracture surface for the low growth rate (compare Fig. II-19(b), (c), and (d)).

At the intermediate growth rate for βA Condition 4, the low magnification correlation of Fig. II-19 between fracture topography and microstructure is less obvious, although some facets similar to those shown in Fig. II-19 are present, for instance at "B" in Fig. II-20(a). Higher magnification examination of areas "A" and "B," Fig. II-20(a), are shown in Fig. II-20(b) and (c), respectively. These figures show that shallow but discernible striations are present in both areas A and B and that local crack propagation is occurring in two orthogonal directions, Fig. II-20(b). In Fig. II-20(c) a series of indistinct ridges is seen which runs from lower left to upper right; they are also evident at B in Fig. II-20(a). The origin of these ridges is thought to be connected with the Widmanstätten plates; in any case, these ridge features should not be confused with striations, since the examples shown here illustrate that they are different from each other.

For βQ, Condition 5, which exhibited the lowest growth rate, the crack path was seen to follow prior β grain boundaries at the low growth rate (cf Fig. II-21(c) with (b)) with smooth straight features evidently corresponding to α platelet morphology also evident. At the intermediate growth rate, Fig. II-21(d), little correlation with the microstructure is

93

seen, indicating a primarily transgranular mode of propagation accompanied by extensive secondary cracking. The lower growth rate of this condition compared to Condition 4 (both of which have β treatment microstructures) probably results from a combination of the more tortuous prior β grain boundary path at low growth rates, and more extensive secondary cracking at intermediate growth rates. The tortuosity is evident in a comparison of Fig. II-21(a) with Fig. II-19(a) and II-17(a).

(ii)   Ti-6Al-2Sn-4Zr-6Mo

Turning to the behavior of the Ti-6Al-2Sn-4Zr-6Mo alloy at R = 0.1, the general microstructures of the primary α Conditions 8 and 9 showed similar fracture topographies; this is illustrated for Condition 8 in Fig. II-22. The topography can be characterized as a fairly smooth fracture surface at both growth rates examined, with the microstructure, i.e., the size, morphology and distribution of the primary α, being evident at comparable magnification. At the intermediate growth rate, crack propagation by striation formation is evidenced by poorly defined striations in or at the interface of the primary α particles. In both conditions, considerable secondary cracking was seen. The forging flow lines in the macrograph of Condition 8 (Fig. II-22(a)) can also be seen on the fracture surface at low magnification in the SEM but appear to have no effect on fracture topography when examined at higher magnification (Fig. II-20(c)).

94

For the β processed material, Condition 10, the fracture topography at low growth rate exhibits features corresponding to the elongated primary α in the microstructure; compare Fig. II-23(c) with (b). At the intermediate growth rate, the correspondence is seen to hold also, with the striking result (when the surface is observed at high magnification) that striation formation occurs in the α platelets accompanied by some ductile tearing of the β (Fig. II-23(d)).

In all the microstructures presented, there seems to be, especially at low growth rates where the most pronounced FCP rate differences were observed, a marked correspondence between microstructural features and fractographic features. The inclusion of light micrographs in the figures was intended to help illustrate this. Another point which can be made here is that the results for the predominantly acicular microstructures, Conditions 4, 5, and 10, suggest an analogy to laminated structures. The toughness and cracking resistance of a structure can be considerably increased at little sacrifice in strength by interleaving thin sheets of soft, ductile material between plates of the strong structural material;[22] this is thought to occur because of the difficulty of re-initiating the crack in the strong material. The β lying between the α plates may play this role in the acicular microstructures (see Figs. II-21(d) and II-23(d)).

95

(iii)   Load Ratio Effects

Turning now to the effect of increased R, the fracture characteristics are shown in Fig. II-24 through II-28. For Condition 1 (RA), at the lower crack growth rate, increasing R (R = 0.5 and 0.7) causes an increasing amount of "cleavage-like" fracture on the same scale as the primary α particle size, Fig. II-24(a), with the greatest amount occurring in the R = 0.7 specimen, Fig. II-24(b). At the higher crack growth rate only, a small R effect is noted and crack propagation is by striation formation and ductile tearing, Fig. II-24(c) and (d), as it was in the R = 0.1 case. Both the R = 0.5 and the R = 0.7 specimen of Condition 4 were similar to each other; the R = 0.5 specimen is shown in Fig. II-25, with the fracture path for this load ratio being less faceted than for R = 0.1, cf Fig. II-25(a) to II-19(c), probably resulting from a higher mean load promoting a more transgranular or transcolony (Widmanstätten α colony) path.

The βQ or Condition 5 exhibited, at low growth rates, the greatest load ratio effect, Fig. II-12, as a result of a transition from an intergranular path at R = 0.1 to a highly transgranular path at R = 0.5 and 0.7, Fig. II-26(a) and (b). These figures demonstrate the way in which fracture topography reflects the microstructure. At the higher growth rate some R effect is seen, especially at R = 0.5, but little difference in fracture topography was noted. As in the case of R = 0.1 propagation is predominately by ductile tearing.

96

Condition 7 also shows a significant load ratio effect at low growth rate, Fig. II-14, but the R = 0.5 and R = 0.7 fractures have different appearance, cf Fig. II-27(a) with II-27(b). For R = 0.5, a considerable amount of "cleavage-like" fracture of the primary α particles, Fig. II-27(a), is observed, a condition which was not observed in the R = 0.1 specimen. At the higher load ratio, R = 0.7, the fracture topography also reflects the microstructure, Fig. II-27(b), but fracture of the α particles appears less planar. In addition, the Widmanstätten α in the transformed β is more clearly delineated at the higher R value.

The load ratio effect is much less pronounced in Ti-6Al-2Sn-4Zr-6Mo than in Ti-6Al-4V with the exception of Condition 8 at the higher crack growth rate (Fig. II-15). Examination of this specimen showed fracture by microvoid growth and coalescence, Fig. II-28(a), reminiscent of that seen in a fracture toughness specimen of this condition. This type of fracture would be expected at the high load ratios, at which K_{max} approaches $K_{critical}$. The β-processed Condition 10 at both R values exhibited fracture topography similar to that at R = 0.1, with the Widmanstätten α of this condition clearly discernible on the fracture face, Fig. II-28(b).

A general observation worth noting is that at the higher load ratios, the fracture surface more strongly reflects the underlying microstructure than it does at the lower load ratios. This probably results from secondary cracking along microstructural constituents, especially interfaces between Widmanstätten α and retained β, as a result of the higher mean loads.

97

Although this secondary cracking absorbs some crack energy, the tendency for transgranular propagation at high load ratios generally overwhelms the secondary cracking, producing a crack acceleration, or equivalently, a constant crack growth rate at lower ΔK.

(iv)   Crack Path

FCP crack path determination was performed by use of the plateau etching technique, Chesnutt and Spurling.[19] The technique allows simultaneous observation in the scanning electron microscope (SEM) of both the fracture surface and the underlying microstructure. Examples drawn from Ti-6Al-4V and Ti-6Al-2Sn-4Zr-6Mo FCP specimens tested at 20 Hz in dry air at room temperature are shown in Figs. II-29 through II-31. Normal contrast conditions in the SEM cause the primary and/or secondary α of the electropolished and etched microstructure to appear dark gray while the transformed β matrix appears lighter. The direction of crack propagation is from left to right in all micrographs.

For Ti-6Al-4V, the RA, βA and STOA material (Conditions 1, 4, and 7) are used to illustrate the effect of volume fraction primary α and the effect of beta processing on fracture path. In RA, Condition 1 (Fig. II-29(a), (b), and (c)), the fracture path is primarily transgranular and the fracture contains large areas of fairly flat surface. At high ΔK (Fig. II-29(c)), these flat regions extend across several primary α particles while at lower ΔK

98

(Fig. II-29(a) and (b)) the path becomes more sensitive to crystallographic orientation. The flat features are even smoother, with characteristics similar to cleavage facets, but are inclined at different angles with respect to the macroscopic crack plane. Behavior at R = 0.3 is quite similar. In STOA, Condition 7 (Fig. II-29(d) and (e)), the path is again transgranular with respect to primary α particles, with smooth features on the fracture face corresponding to these particles. Cracking of the transformed beta matrix is seen to take a much more tortuous path. In the Widmanstätten $\alpha+\beta$ microstructure of βA, Condition 4 (Fig. II-29(f)), the fracture path is seen to follow individual α laths and the crack to branch at or near colony boundaries.

For Ti-6Al-2Sn-4Zr-6Mo, two microstructural conditions, primary α and β-process (Conditions 8 and 10), are used to show the effect of $\alpha +\beta$ processing vs. β processing, and Condition 10 is used to show the effect of load ratio (R) on fracture path. In Condition 8 (Figs. II-30(a) and (b)), the path is transgranular and is macroscopically flat. Some small regions on the order of the primary α particle size appear microscopically flat and probably represent propagation either through a primary α particle or through a coarse Widmanstätten α particle aligned parallel to the crack plane. The occurrence of these flat features increases with decreasing ΔK (Fig. II-30(a)). In the β-processed material, Condition 10, the path is also essentially transgranular (Fig. II-30(c) and (d)) although some secondary cracking along Widmanstätten α plates is observed, resulting in the facets seen in Fig. II-30(c). At

higher load ratios (R = 0.3), Fig. II-30(e) and (f), Condition 10 is seen to undergo more extensive secondary cracking. As seen in Fig. II-30(f), this cracking occurs along the boundary between a large Widmanstätten α particle and the adjacent transformed β, raising a question as to a possible role of the interface phase[23] in the occurrence of secondary cracking.

Additional observations by this technique further clarify the role of microstructural constituents in the FCP process. For Ti-6Al-4V, Conditions 2 and 3 demonstrate the effect of volume fraction primary α on fracture path. Condition 2, which contains 0.13 volume fraction primary α, exhibits fracture topography which is essentially independent of the primary α particles (Fig. II-31(a) and (b)), but which is very sensitive to the orientation of the coarse Widmanstätten α plates. In Fig. II-31(a), where the plates are aligned with the macroscopic crack propagation plane, large areas of flat "cleavage-like" fracture are observed in conjunction with tearing across the platelets aligned perpendicular to this plane. This latter feature can be observed near the edge of the polished portion of the micrograph. In the case where the Widmanstätten α packets are less favorably aligned (Fig. II-31(b)), considerable tearing coupled with crack branching along packet boundaries is observed.

When the volume fraction of primary α is increased to 0.54, as in Condition 3, the effect of this primary α in providing a preferential crack path becomes evident (Fig. II-31(c) and (d)). At low ΔK, the path goes

100

through or around the α particles, producing the smooth-appearing features in Fig. II-31(c). At higher ΔK, the crack propagates through the primary α particles by striation formation (Fig. II-31(d)).

The crack path in the β-quenched microstructure, Condition 5, was similar to that in β-air cooled material, Condition 4, with cracking along Widmanstätten α laths, Fig. II-31(e), and along prior β grain boundaries, Fig. II-31(f), even more accentuated. Although somewhat difficult to discern at magnifications used in the SEM, the facets of the type seen in Fig. II-31(f) are on the scale of the prior β grain size and are those which produce the faceted appearance in fractures of β-quenched material when viewed without electron-optical magnification. The fracture paths in STA, Condition 6, were found to be identical with those of STOA, Condition 7. For Ti-6Al-2Sn-4Zr-6Mo, a similar identity exists between the primary Conditions 9 and 8.

Hold-Time Measurements

The room temperature hold time results for Conditions 1, 4, 5, and 7 of Ti-6Al-4V and Conditions 8 and 10 of Ti-6Al-2Sn-4Zr-6Mo are plotted in Fig. II-32 through II-37. Conditions 1, 7, 8, and 10 all exhibit growth rates under hold-time conditions which can be considered to lie within the scatter band for that condition while for βA, Condition 4 (Fig. II-33), there is clearly no effect of hold time. In βQ, Condition 5 (Fig. II-34), there appears to be a marked effect which will be addressed in the following paragraph on fractography.

101

The fracture surfaces of hold-time specimens for all six conditions were examined and compared with the fracture surfaces of comparable specimens tested at R = 0.3 and 20 Hz. The RA material, Condition 1, exhibited modest acceleration at low ΔK and lesser acceleration at intermediate ΔK. At low ΔK, considerable cleavage-like propagation across primary α particles was evident in the hold-time specimen, Fig. II-38, although the cleavage appears less well delineated than that formed in 20 Hz specimens at lower growth rates. For the intermediate ΔK (20.9 MPa·m$^{\frac{1}{2}}$), the hold-time cycling caused little acceleration; the fractures were quite similar, Fig. II-39. The only discernible difference was the improved resolution of striations in the hold-time specimen shown in Fig. II-39(b). This would be expected if the hold produced deeper striations, which would enhance their resolution in the SEM. Condition 4, β-annealed Ti-6Al-4V and Condition 10, β-annealed Ti-6Al-2Sn-4Zr-6Mo, both showed no effect of hold time on the fatigue crack growth rate and, as expected, identical fracture surface topography.

Condition 5 (β-quenched) showed considerable acceleration at low ΔK as a result of the hold promoting transgranular propagation at a lower ΔK than in a 20 Hz specimen. This effect can be seen by comparing Fig. II-40(a) and (b) with Fig. II-40(c) and (d). The fracture topographies are essentially the same, although the Fig. II-40(a) and (b) represent ΔK = 13.8 MPa·m$^{\frac{1}{2}}$ in the hold-time specimen, compared with ΔK = 16.8 MPa·m$^{\frac{1}{2}}$ in the 20 Hz (Fig. II-40(c) and (d)).

At low ΔK, Conditions 7 and 8 experienced minimal acceleration and minimal retardation, respectively, due to hold time. In the former, the acceleration probably resulted from an increased amount of cleavage-like fracture of the primary α particles (cf Fig. II-41(a) and (b) with Fig. II-41(c) and (d)). The cause of the retardation in Condition 8 is not clear from the fractography but may have resulted from a slightly more tortuous path in the hold-time specimen, Fig. II-42(a) and (b).

For the intermediate ΔK in Condition 1 and for the low ΔK situation in Conditions 7 and 8, it should be noted that the effect is small and may be within the scatter band for that condition. Therefore, the fractography relating to these cases should not be taken as a description of major effects, but as an indication of possible microstructural effects on small changes in crack growth rate.

Overload Measurements

The other potential acceleration/retardation effect studied was that involving a spike overload. The results for Conditions 1, 4, 5, and 7 of Ti-6Al-4V and Conditions 8 and 10 of Ti-6Al-2Sn-4Zr-6Mo are shown in Fig. II-43 through II-48. In all six plots, the baseline data previously obtained are shown as circles (note expanded ΔK scale), and the overload test data both prior to and following the overload block as crosses, with specimen numbers also shown. The pattern of behavior is essentially the same in each figure, with a strong retardation ("downspike") following the overload block

103

(which is not shown), and a subsequent recovery to about the baseline curve. What is not shown is the "width" of the downspike in cycles, and that leads to the second way of presenting the results, Table II-I. Here the number of cycles required to return to essentially the baseline da/dN rate is tabulated. The figures and the table both suggest that the behavior of all six conditions was similar, except that Conditions 1 and 4 required significantly longer to recover to the baseline da/dN, Table II-I.

DISCUSSION

The data presented above clearly illustrate that microstructure can affect FCP rate in α-β alloys such as Ti-6Al-4V and Ti-6Al-2Sn-4Zr-6Mo. Moreover, particularly at low growth rates or high R values, it is evident that fracture surface appearance can reflect the influence of microstructure. Finally, as noted above, it appears possible to understand the correlations of FCP and microstructure in terms of crack path observations. The most significant microstructural conclusion, which is indirectly supported by fatigue life studies also,[24-28] is that acicular-type microstructures, particularly when refined in size, are most resistant to FCP. Although others have reached similar conclusions,[8,9,11,29,30] the present work appears to be the first unequivocal determination inasmuch as texture effects are clearly separated from effects of microstructure (cf Part I).

The foregoing results have implicitly been rationalized in microstructural terms through detailed fractography. As shown in Part I, the cyclic work hardening behavior of nearly all these microstructures corresponds to essentially stable behavior, i.e., neither hardening nor softening, and accordingly little insight into FCP behavior is afforded by consideration of hardening within the plastic zone. The fracture process(es) thus remain as the most likely avenue to rationalizing the data.

The rationale pursued here relies on a rather simple view: the energy provided to the specimen plastic zone by the cyclic stresses can be dissipated in a variety of ways, and the relative efficiency of these determines the FCP rate. One dissipative process is hardening, but these (largely) cyclically stable materials are quite similar in that regard. A second, fracture-related process is the relative crack length; assuming a reasonably constant energy requirement per unit length of a given fracture mode, increasing crack length, i.e., tortuosity, will reduce net FCP. Secondary cracking will have the same effect.

There have been earlier reports which attempted to rationalize FCP behavior in microstructural terms. It was noted[20] that the fatigue plastic zone size of Ti-6Al-4V coincided with the alpha grain size at about the point during FCP at which a fracture topography change occurred. The authors then suggested a change from predominantly single slip within the grain, to multiple slip, as the cause of the transition to a faster fracture mode. Although deserving further investigation, the correlation appears

105

fortuitous, for three reasons. First, the rationale predicts that increased grain size would decrease FCP by postponing the transition to the faster cracking mode, but in the mid-growth rate regime in planar slip materials like Ti-6Al-4V, grain size has no effect on FCP.[5,6,31] Second, metallographic evidence rules against fracture-mode control by the first grain cracked.[32,33] Third, the materials of this study exhibit varying amounts and sizes of primary α grains, including zero primary α in Conditions 4, 5, and 10, yet all show very similar fracture mode transitions. This third point also illustrates the limitations of the Yoder, et al rationale,[30] which is based on Widmanstätten packet size: the RA (Condition 1) and primary α-Widmanstätten matrix (Conditions 2, 3, 6-9) behave generally similarly to all-Widmanstätten microstructures as far as curve shape is concerned. Curve shape is emphasized by Yoder, et al [30] as pivotal in understanding FCP rate, but the present results show that curve shape is not significantly sensitive to microstructure.

The hold time and spike overload data can be rationalized in a consistent fashion using the above approach. For the hold time tests, the maximum increase in FCP rate (a factor of two) was found in βQ, Condition 5 and this increase was associated fractographically with a transition to a more transgranular failure under hold-time conditions. Conversely, Bania and Eylon[34] have shown that hold-time tests in textured Ti-6Al-4V can cause a decrease in growth rate of a factor of two to four. Those results combined with the results of the present study would suggest that the increase or

106

decreases of crack growth rates may result from local interaction of microstructure, texture and hold time at maximum load. An additional factor may be the sequence of loading as suggested by Bania and Eylon,[34] but that subject was outside the scope of the present program. The conclusion reached after hold-time testing at room temperature is that hold-time effects are small for the uniformly and weakly textured microstructures of this study. This conclusion is also consistent with the preliminary results of Stubbington,[17] which showed that post-forging heat treatment appreciably lessened hold-time effects even in textured material.

Turning to the overload data, the rate of return of FCP rate to the baseline level, Table II-I, is perhaps the most suggestive result. It would appear that the effect of the overloads is to enlarge the plastic zone at the crack tip, and the crack subsequently grows more slowly because the hardened zone exerts a compressive residual stress on the crack tip. Put another way, the crack closure load is raised and the effective (open crack) ΔK is reduced, thus reducing da/dN, until the crack grows through most of the overload zone. The extent to which all this happens will depend on the plastic response of the zone during the subsequent cycling. As shown previously, Conditions 5, 7, 8, and 10 all cyclically soften slightly, and thus the material ahead of the moving crack more quickly assumes the character of the normal fatigue plastic zone. Conditions 1 and 4 are fully stable; further, the RA Condition 1 has a markedly higher hardening capacity than Condition 4 (UTS/YS = 1.23 vs 1.10) and this magnifies the retardation due to the overload zone. This is

107

consistent with the results in Table II-I, and with the results of studies in other materials.[35]

In summary, fatigue crack propagation (FCP) rate in seven microstructures of Ti-6Al-4V and three microstructures of Ti-6Al-2Sn-4Zr-6Mo with uniform, weak texture depends significantly upon microstructure. Acicular-appearing or Widmanstätten microstructures were most resistant to FCP, with RA material also fairly resistant. Microstructures containing primary α in a Widmanstätten matrix were least resistant. These results can be rationalized in terms of the extent of secondary cracking and the relative tortuosity of the crack path; cyclic hardening behavior varied little among these ten microstructures. The same approach encompasses the results on hold-time tests (in which little effect was found) and spike overload tests.

REFERENCES

1. P. C. Paris and F. Erdogan, J. Basic Engr., 1963, Vol. 85, p. 528

2. A. J. McEvily and T. L. Johnston, Proc. First Int. Conf. on Fracture, Vol. II, pp. 515-45, Sendai, Japan (1966)

3. A. R. Rosenfield, Eng. Fract. Mech., 1977, Vol. 9, pp. 509-520

4. J. Barsom, E. J. Imhof, and S. T. Rolfe, Eng. Fract. Mech., 1970, Vol. 2, pp. 301-17

5. A. W. Thompson, J. D. Frandsen and J. C. Williams, Met. Sci., 1975, Vol. 9, pp. 46-48

6. A. W. Thompson, Eng. Fract. Mech., 1975, Vol. 7, pp. 61-67

7. G. Birkbeck, A. E. Inckle, and G. W. J. Waldron, J. Mater. Sci., 1971, Vol. 6, pp. 319-23

8. M. F. Amateau, W. D. Hanna, and E. G. Kendall, "The Effects of Microstructure on Fatigue Crack Propagation in Ti-6Al-6V-2Sn Alloy," Report TR-0172(2250-10)-3, Aerospace Corp., El Segundo, California, October 1971

9. J. C. Williams, N. E. Paton, P. J. Stocker, and H. L. Marcus, Space Shuttle Materials, Vol. 3, pp. 643-51, Proc. Nat'l SAMPE Conf., Huntsville, Alabama (1971)

10. A. W. Sommer and C. H. Hamilton, "Thermomechanical Processing of Titanium Alloys," Report NA-73-277, LAA Division, Rockwell International, Los Angeles, California, April 1973

11. D. E. Pettit, W. E. Krupp, J. T. Ryder, and D. W. Hoeppner, "Investigation of the Effects of Stress and Chemical Environments on the Prediction of Fracture in Aircraft Structural Materials," Report LR 26026, Lockheed-California Co., Burbank, California, July 1973

12. F. L. Parkinson, "Titanium Alloy 6Al-4V Sheet," Report FAA-SS-72-01, The Boeing Co., Seattle, Washington, July 1972

13. A. W. Bowen, Proc. Third Int. Conf. on Strength of Metals and Alloys, pp. 446-50, Cambridge, U.K. (1973); see also Acta Met., 1975, Vol. 23, p. 1401

14. A. W. Sommer, private communication: meeting summary memorandum, "Recent Results on Ti-6Al-4V RA Material," June 20, 1973

15. A. W. Sommer, and M. Creager, "Research Toward Developing an Understanding of Crystallographic Texture on Mechanical Properties of Titanium Alloys," AFML-TR-77-222, Air Force Materials Laboratory, Wright-Patterson AFB, Ohio, January 1977

16. J. D. Frandsen and H. L. Marcus, Science Center, Rockwell International, Thousand Oaks, California, unpublished research (1973)

17. C. A. Stubbington, Royal Aircraft Establishment, Farnborough, U.K., personal communication, 1975

18. D. Shechtman, Met. Trans. A, 1976, Vol. 7A, pp. 151-2

19. J. C. Chesnutt and R. A. Spurling, Met. Trans. A, 1977, Vol. 8A, pp. 216-8

20. A. Yuen, S. W. Hopkins, G. R. Leverant, and C. A. Rau, Met. Trans., 1974, Vol. 5, p. 1833-42

21. R. O. Ritchie, J. of Engineering Materials and Technology (Trans. ASME Series H), 1977, Vol. 99, p. 195

22. J. D. Embury, N. J. Petch, A. E. Wraith, and E. S. Wright, Trans. TMS-AIME, 1967, Vol. 239, pp. 114-18

23. C. G. Rhodes and J. C. Williams, Met. Trans. A, 1975, Vol. 6A, pp. 1670-76

24. C. A. Stubbington and A. W. Bowen, Proc. Second Int. Conf. on Titanium, Vol. 2, pp. 1283-96, Plenum Press, New York (1973); also RAE Report 72091, August 1972

25. A. W. Bowen and C. A. Stubbington, Proc. Second Int. Conf. on Titanium, Vol. 3, pp. 2097-2108, Plenum Press, New York (1973); also RAE Report 73019, May 1973

26. C. A. Stubbington and A. W. Bowen, "Some Observations on Stage I Fatigue in Ti-6Al-4V; Synthesis of a High Fatigue Strength Microstructure," Report 73036, Royal Aircraft Establishment, Farnborough, Hants, U.K., May 1973

27. D. Eylon, J. A. Hall, C. M. Pierce, and D. L. Ruckle, Met. Trans., 1976, Vol. 7A, pp. 1817-26

28. D. Eylon and J. A. Hall, Met. Trans., 1977, Vol. 8A, pp. 981-90

29. N. E. Paton, J. C. Williams, J. C. Chesnutt and A. W. Thompson, Alloy Design for Fatigue and Fracture Resistance (Report CP-185), AGARD/NATO, Brussels, paper 4 (1976)

30. G. R. Yoder, L. A. Cooley, and T. W. Crooker, Met. Trans., 1977, Vol. 8A, pp. 1737-43

31. A. W. Thompson and R. J. Bucci, Met. Trans., 1973, Vol. 4, pp. 1173-74

32. A. W. Thompson and W. A. Backofen, Acta Met., 1971, Vol. 19, pp. 597-606

33. A. W. Thompson, Acta Met., 1972, Vol. 20, pp. 1085-94 (1972)

34. P. J. Bania and D. Eylon, Met. Trans., 1978, Vol. 9A, pp. 847-55

35. M. W. Mahoney and N. E. Paton, Met. Trans., in press

TABLE II-I

POST-SPIKE RECOVERY

Condition	Number of Cycles to Recover to Baseline da/dN
1	34,000
4	24,500
5	11,000
7	12,000
8	11,500
10	11,500
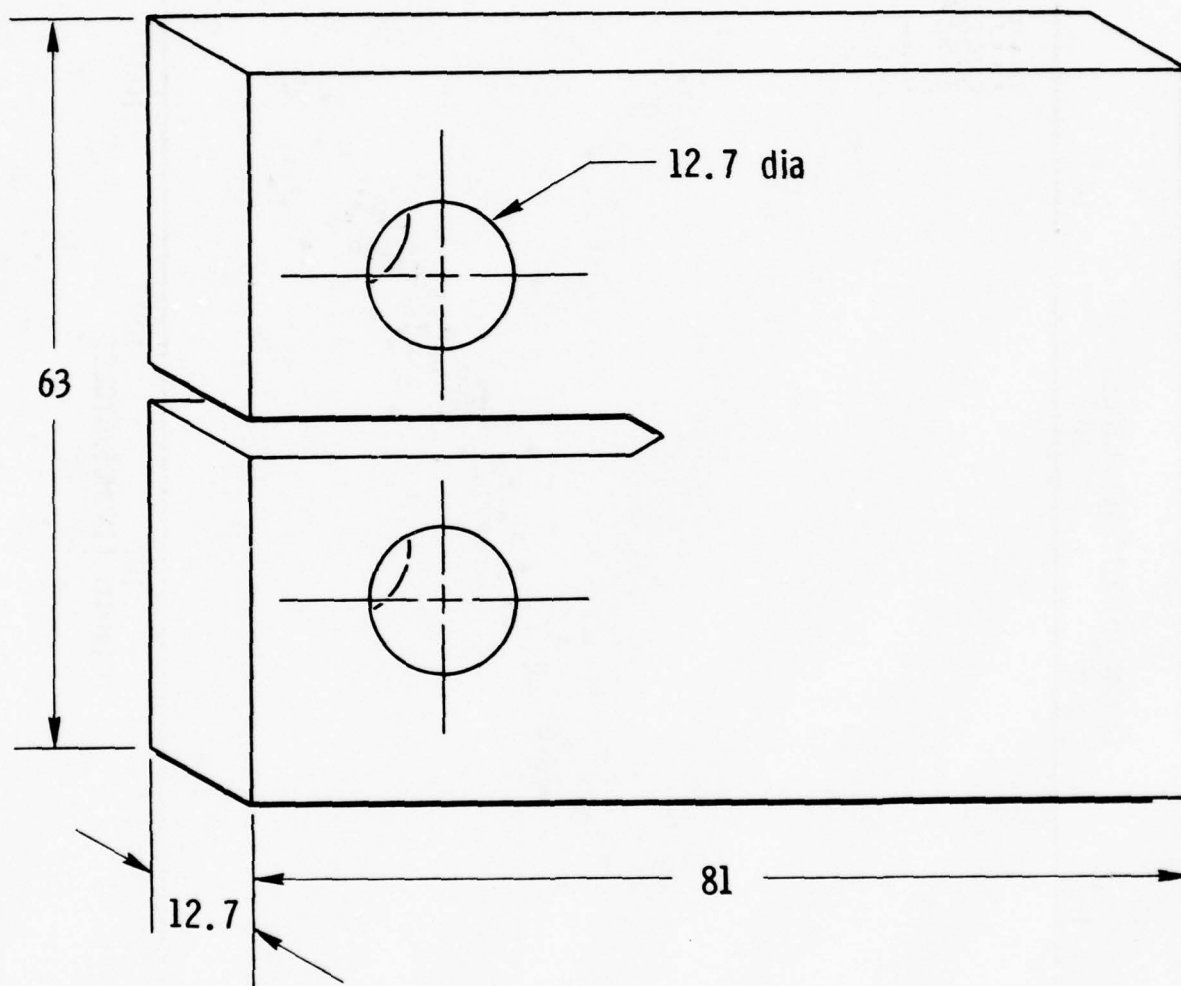
Fig. II-1 Compact tension specimen for fatigue crack propagation measurement. Dimensions in mm.

TI-6AL-4V, 68F, DRY AIR, 20HZ, R-0.1
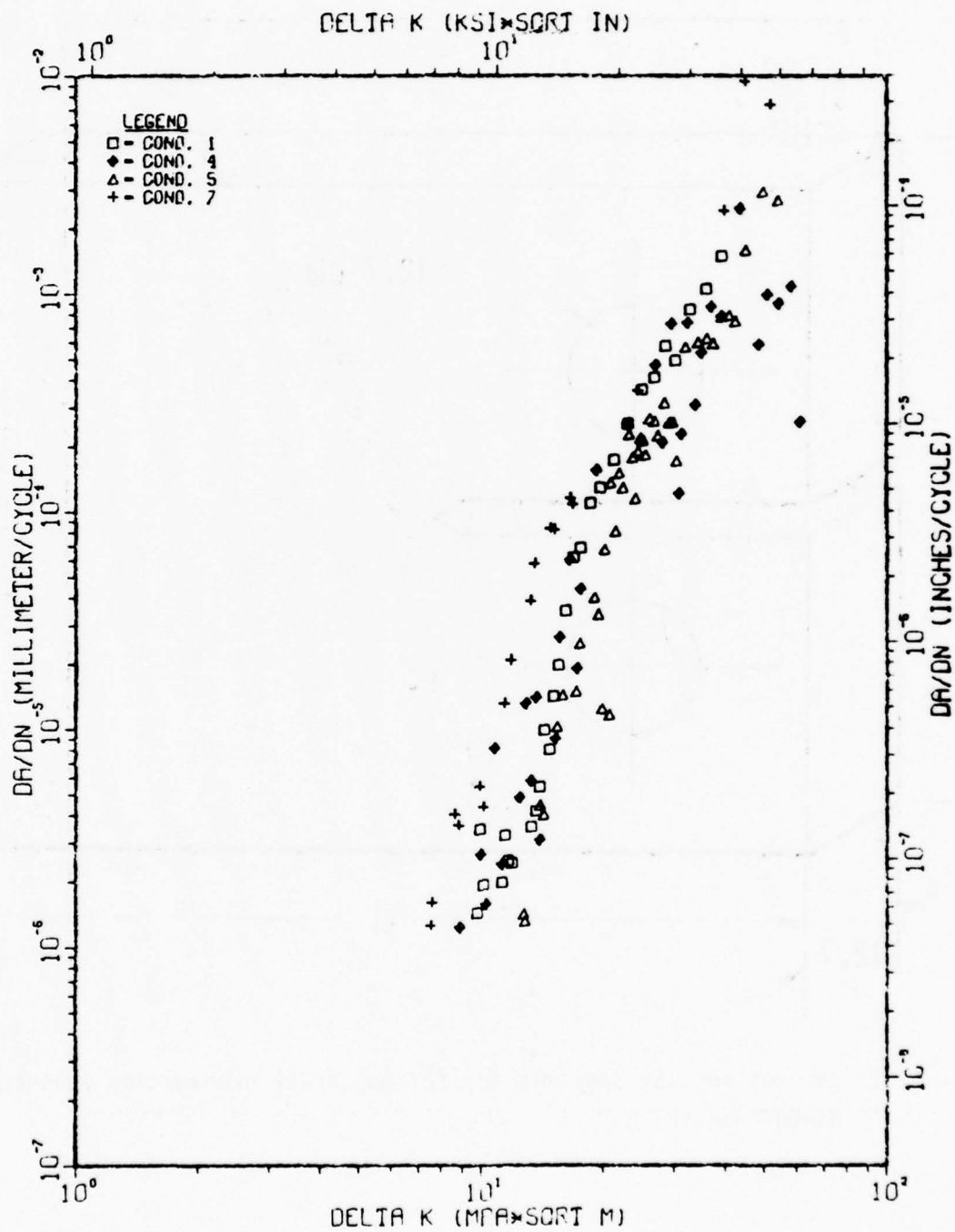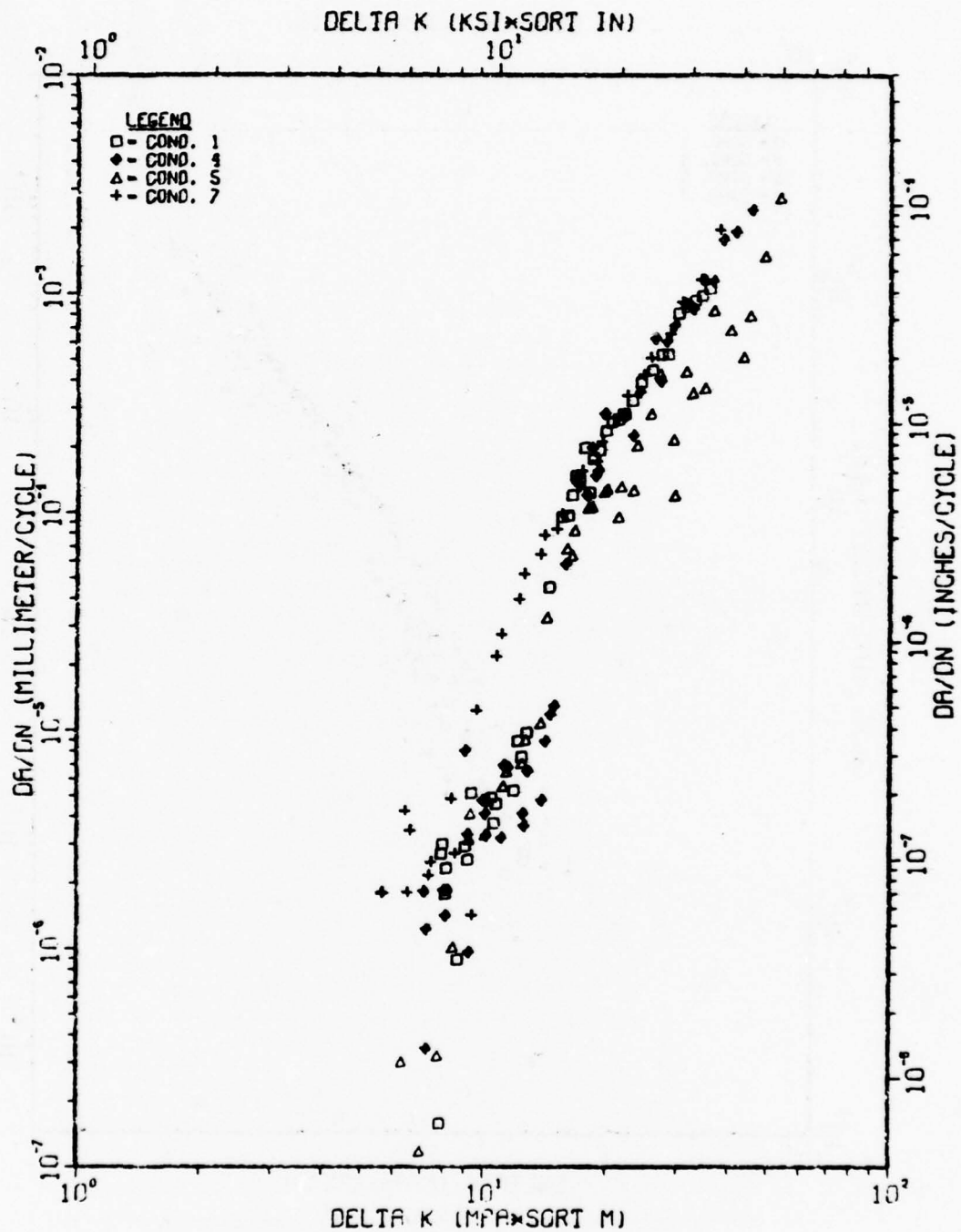
Fig. II-2 Dependence of FCP in Ti-6Al-4V on microstructure at R = 0.1.

114

Fig. II-3 Dependence of FCP in Ti-6Al-4v on microstructure at R = 0.3.
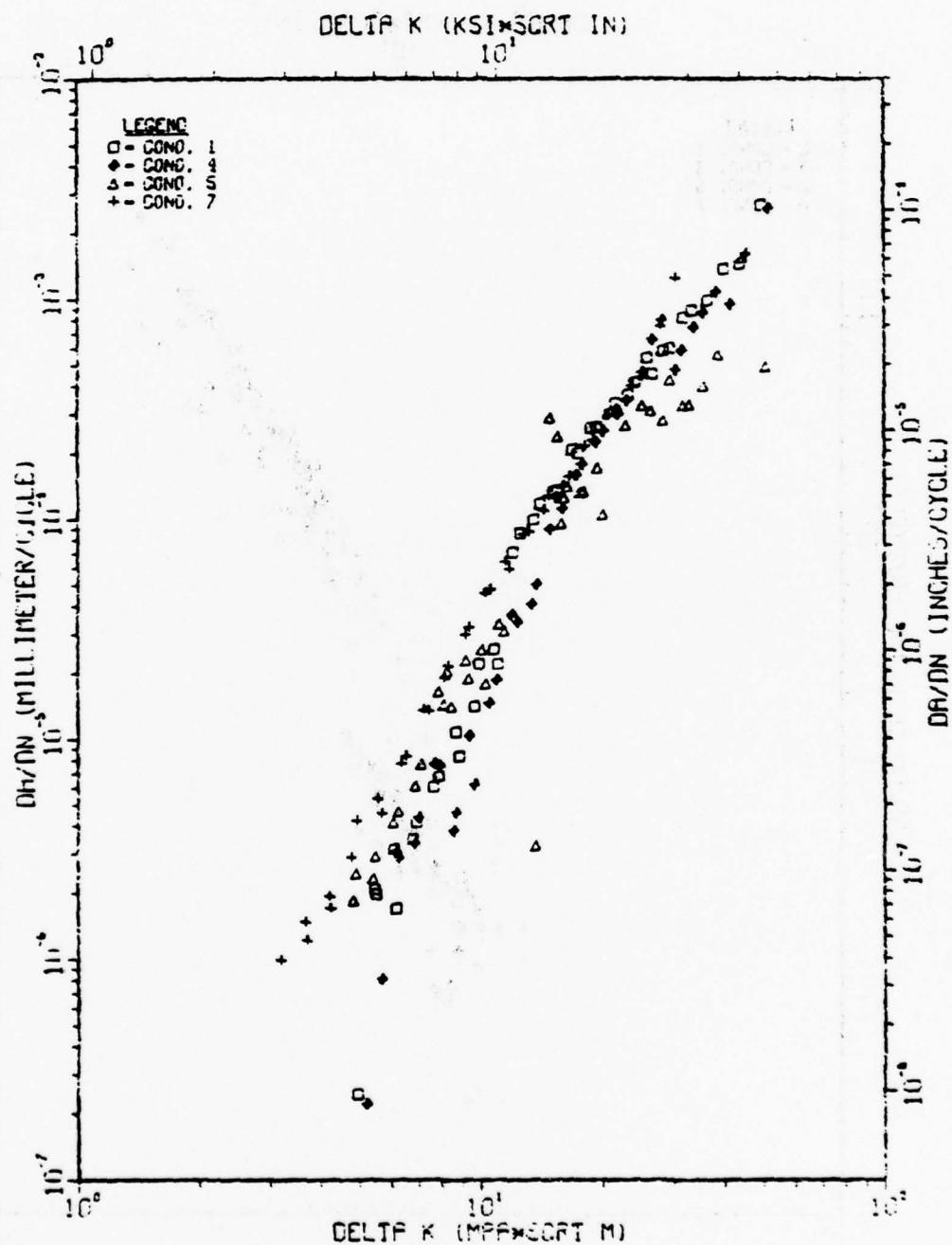
Fig. II-4 Dependence of FCP in Ti-6Al-4V on microstructure at R = 0.5.

TI-6AL-4V, 69F, DRY AIR, 2GHZ, R=0.7
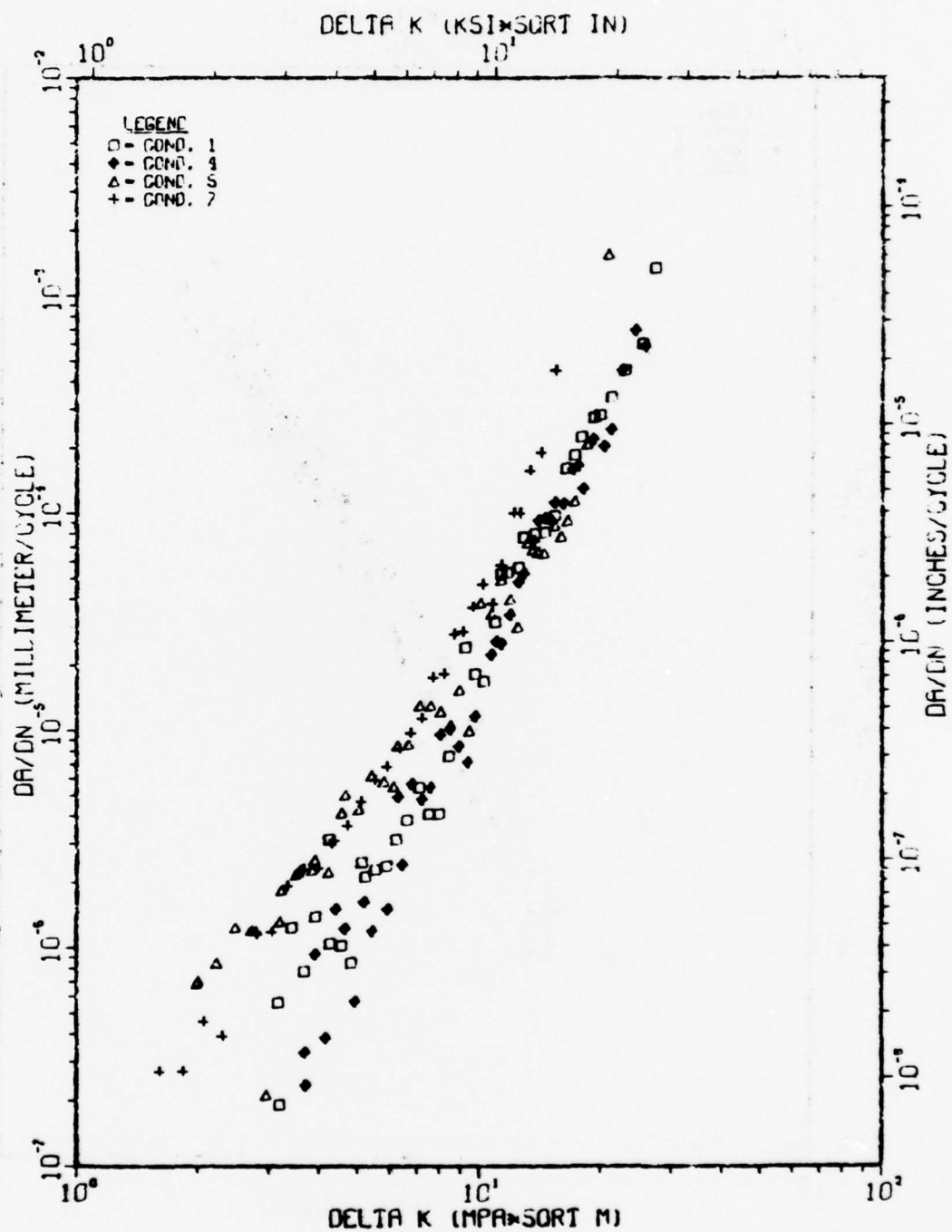
Fig. II-5 Dependence of FCP in Ti-6Al-4V on microstructure at R = 0.7.

117
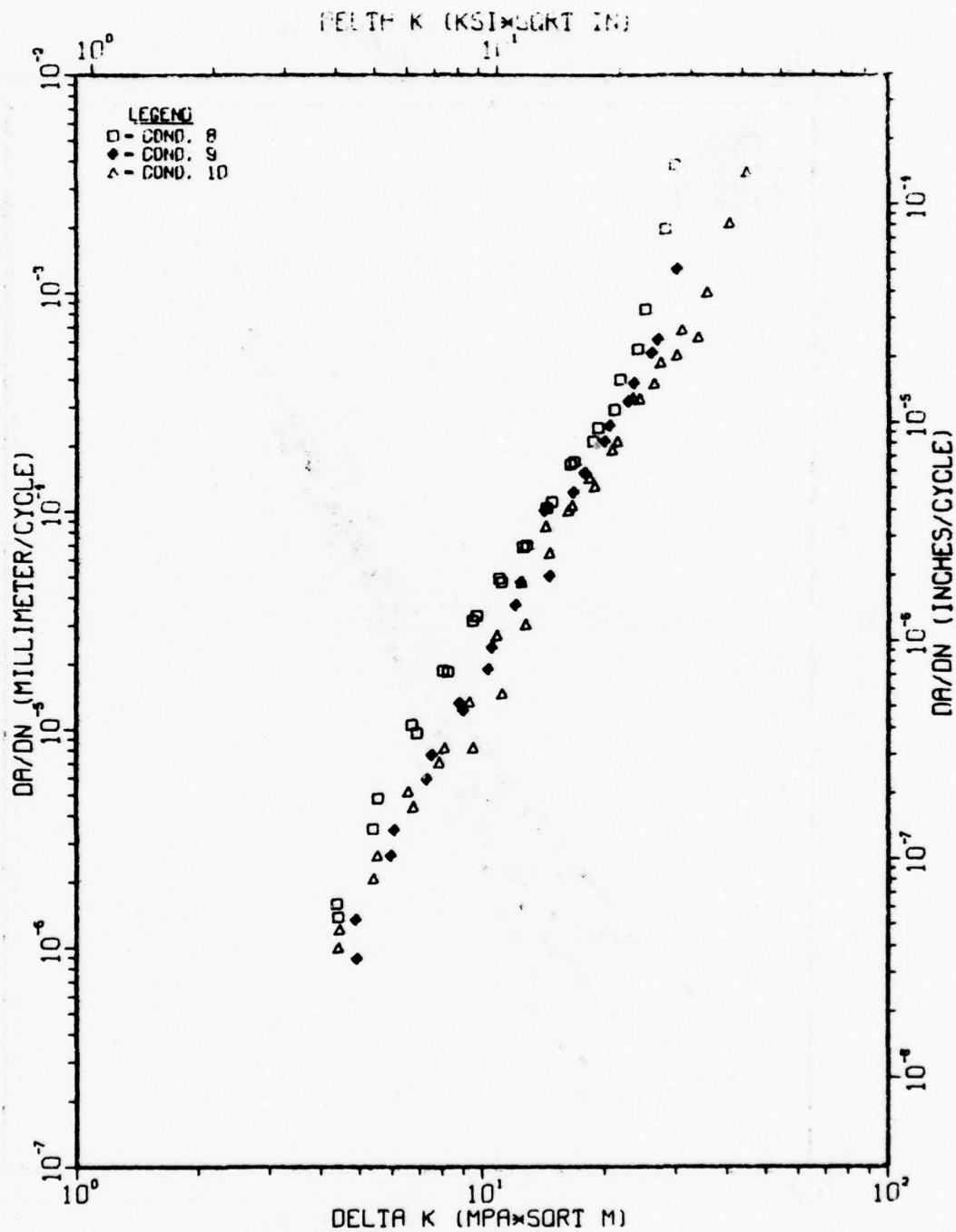
Fig. II-6 Dependence of FCP in Ti-6Al-2Sn-4Zr-6Mo on microstructure at R = 0.1.

TI-6AL-2SN-4ZR-6MO, 68F, DRY AIR, 20HZ, R-0.3
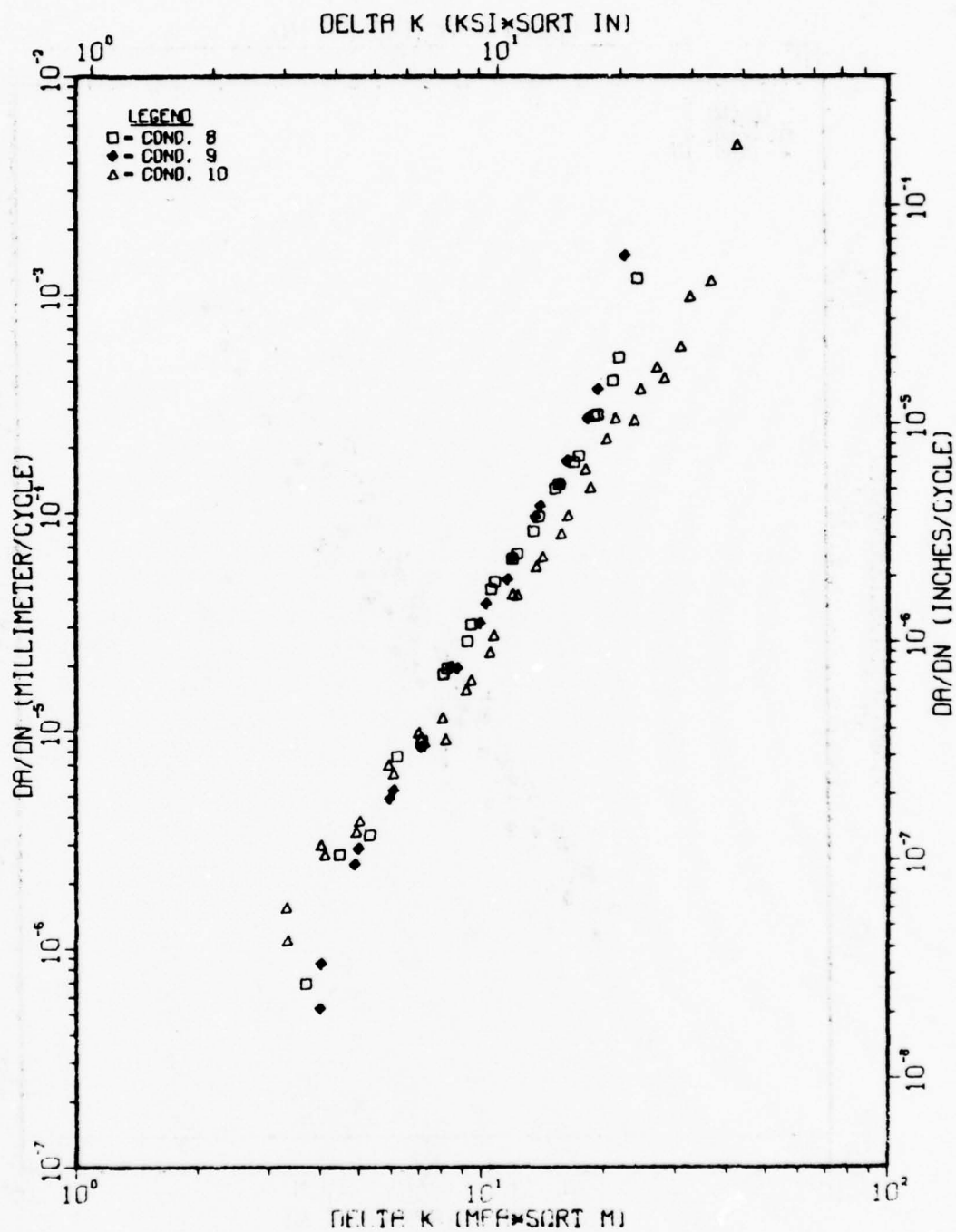
Fig. II-7 Dependence of FCP in Ti-6Al-2Sn-4Zr-6Mo on microstructure at R = 0.3.

119

TI-6AL-2SN-4ZR-6MO, 68F, DRY AIR, 20HZ, R-0.5
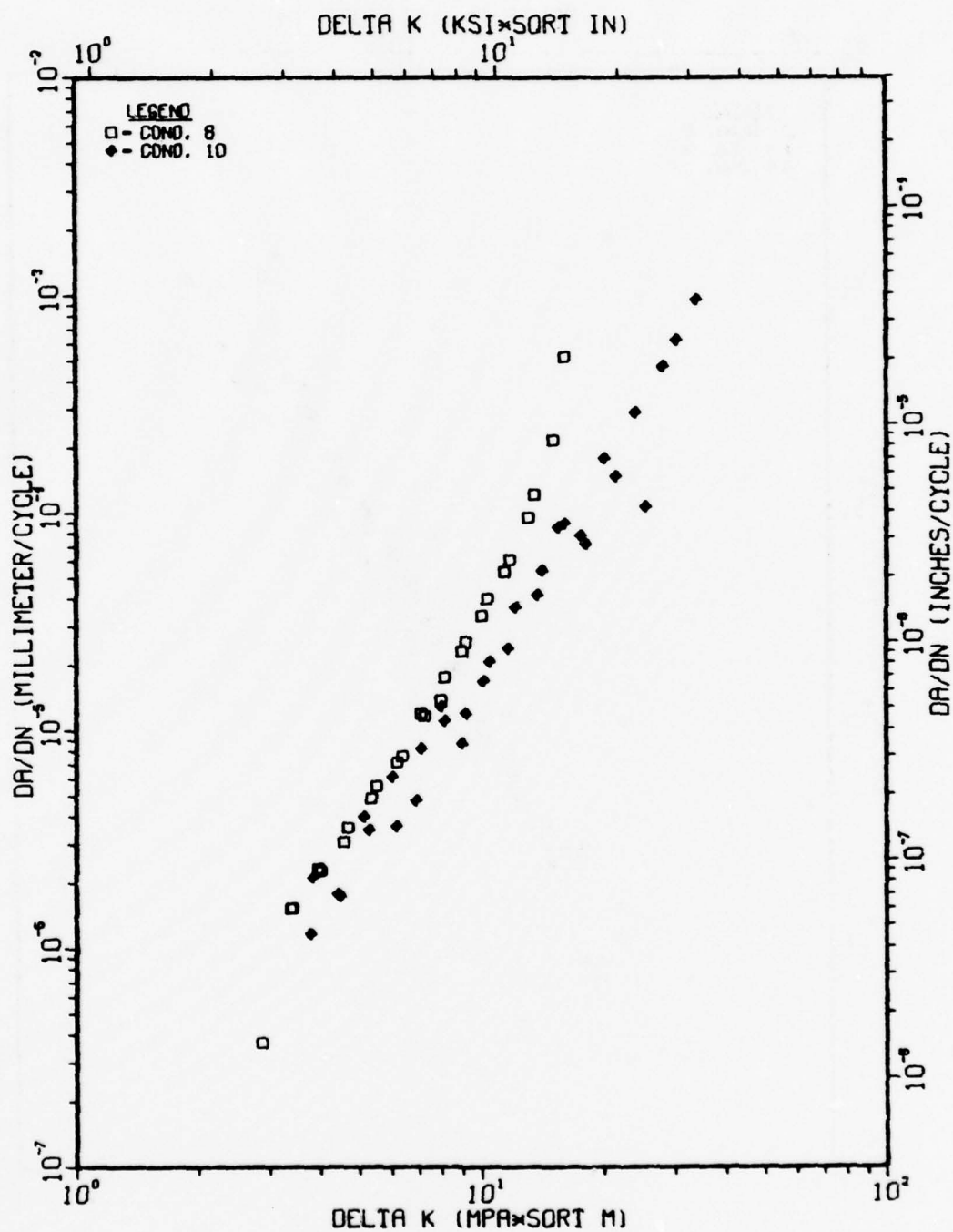
Fig. II-8 Dependence of FCP in Ti-6Al-2Sn-4Zr-6Mo on microstructure at
R = 0.5.

120

TI-6AL-2SN-4ZR-6MO, 68F, DRY AIR, 20HZ, R-0.7
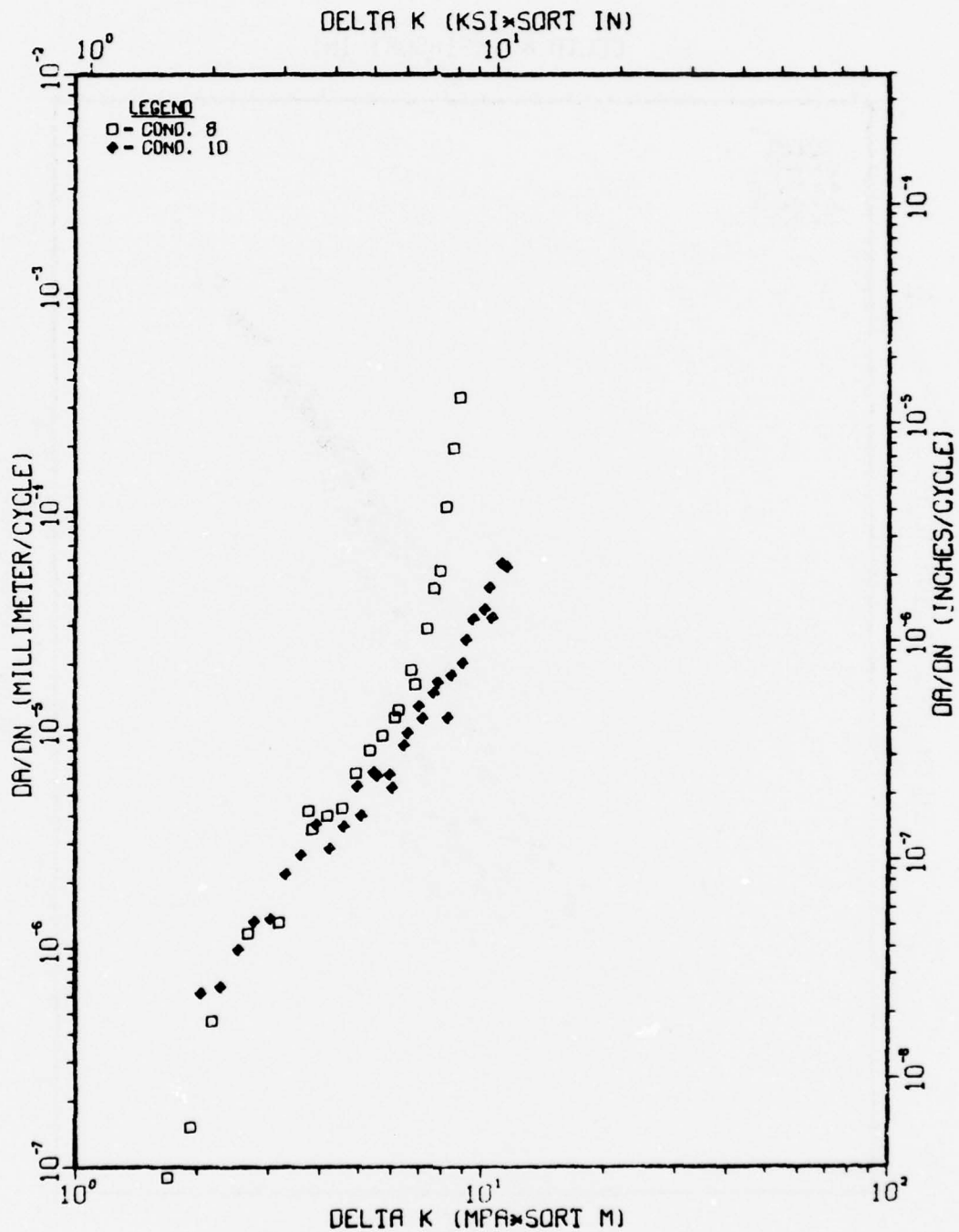
Fig. II-9 Dependence of FCP in Ti-6Al-2Sn-4Zr-6Mo on microstructure at R = 0.7.

121

TI-6AL-4V(COND. 1), 68F, DRY AIR, 20HZ
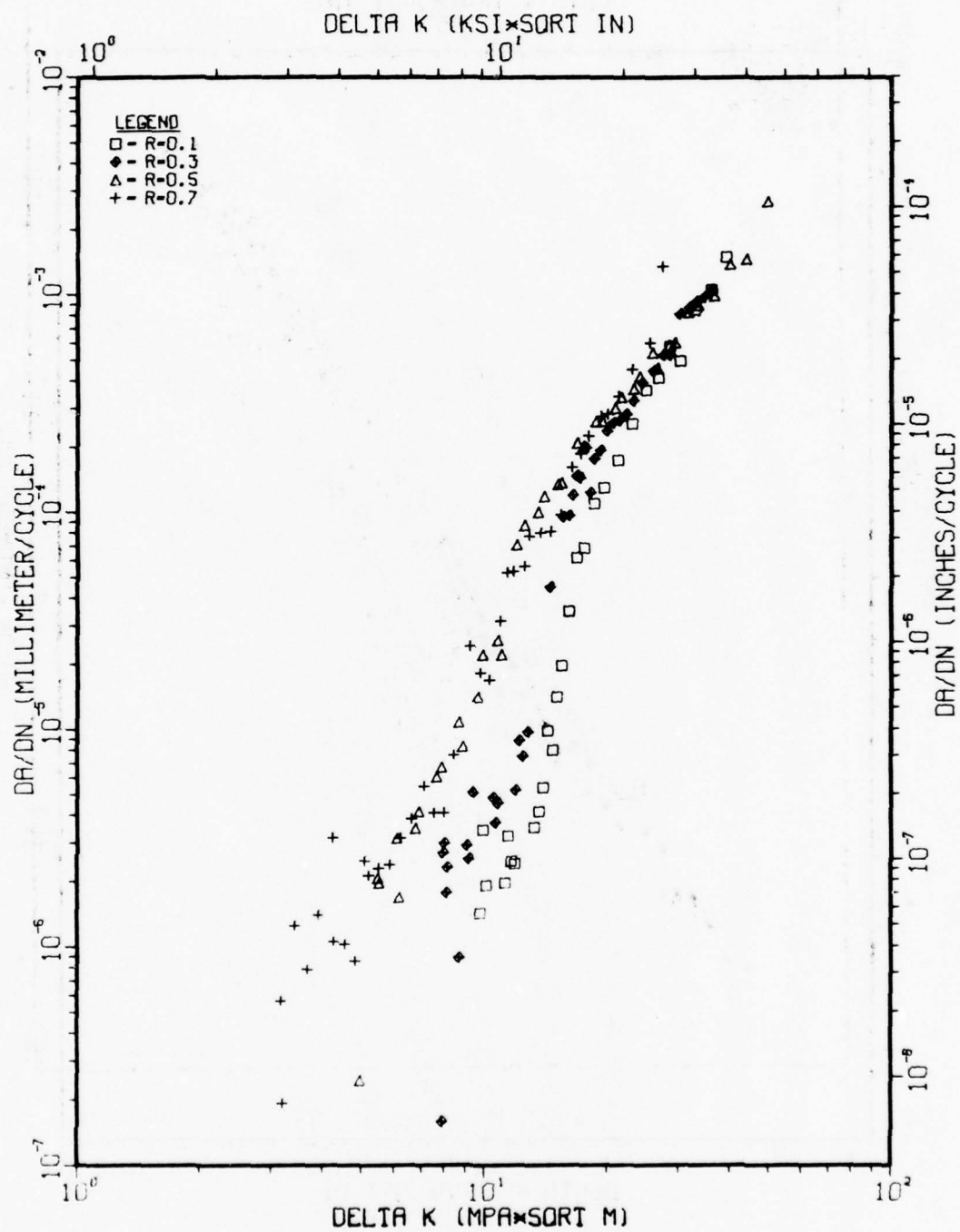
Fig. II-10 Dependence of FCP in Ti-6Al-4V, Condition 1, on load ratio, R.

122

TI-6AL-4V(COND. 4), 68F, DRY AIR, 20HZ
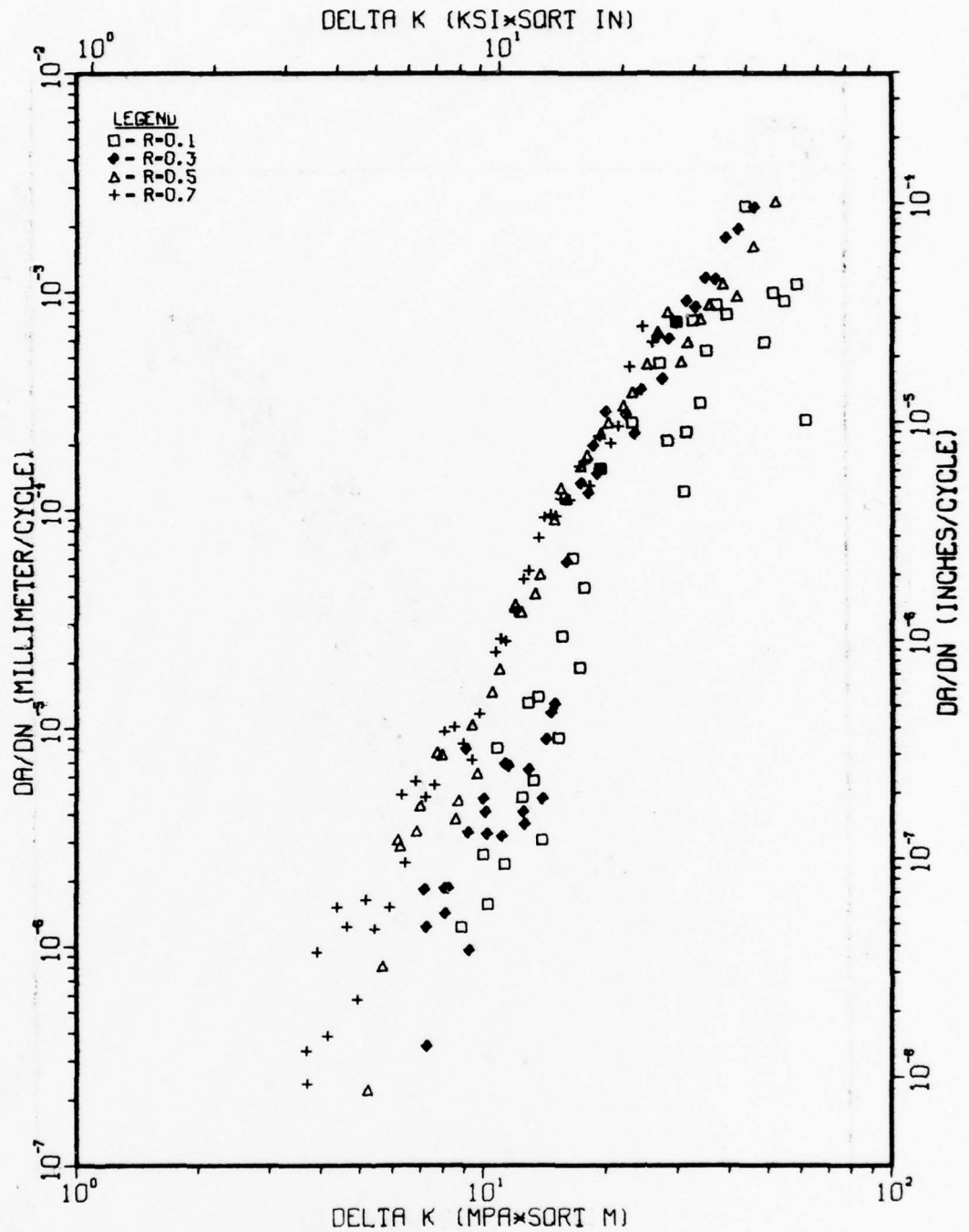
Fig. II-11   Dependence of FCP in Ti-6Al-4V, Condition 4, on load ratio, R.

TI-6AL-4V(COND. 5), 68F, DRY AIR, 20HZ
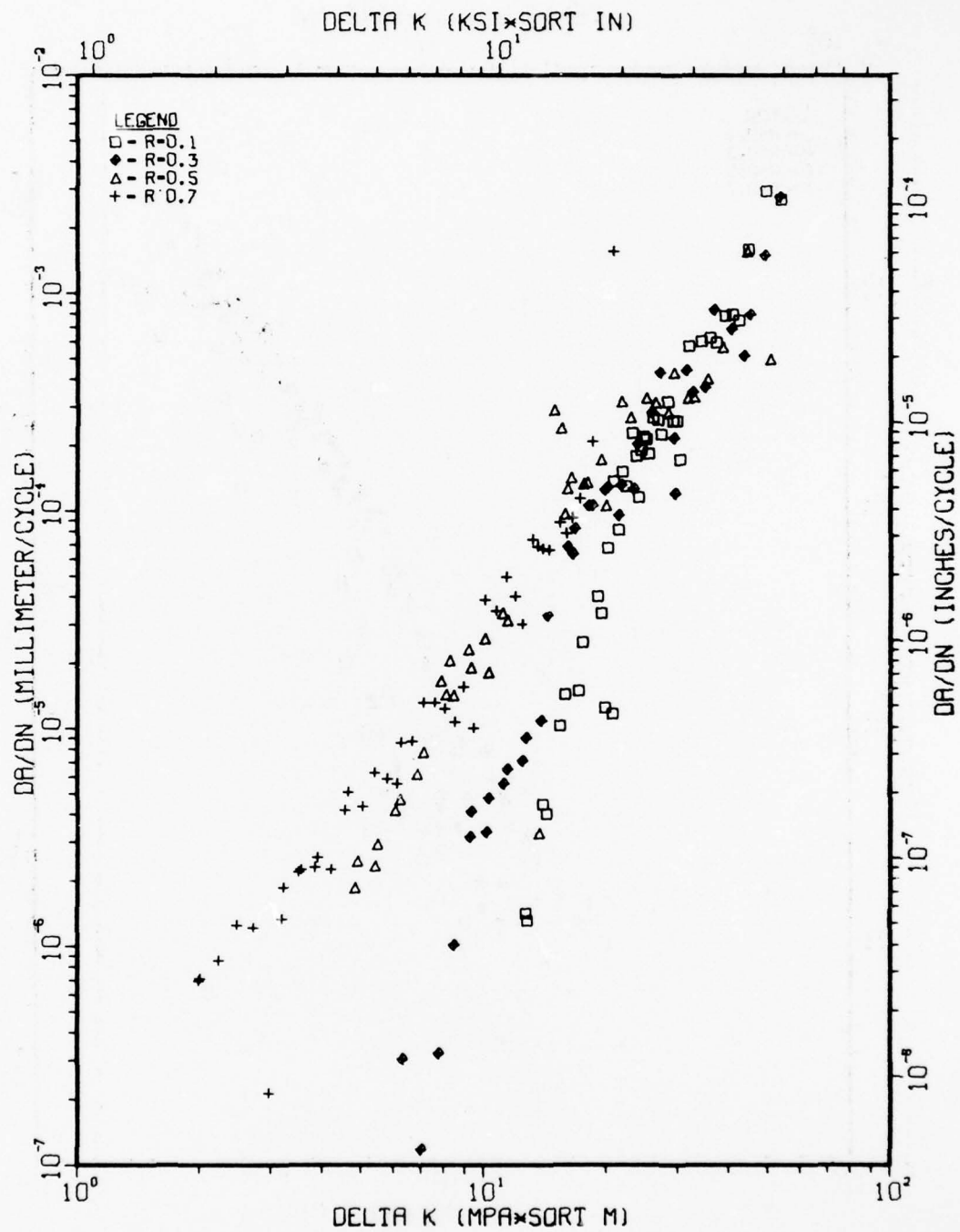
Fig. II-12 Dependence of FCP in Ti-6Al-4V, Condition 5, on load ratio, R.

124

TI-6AL-4V(COND. 7), 68F, DRY AIR, 20HZ
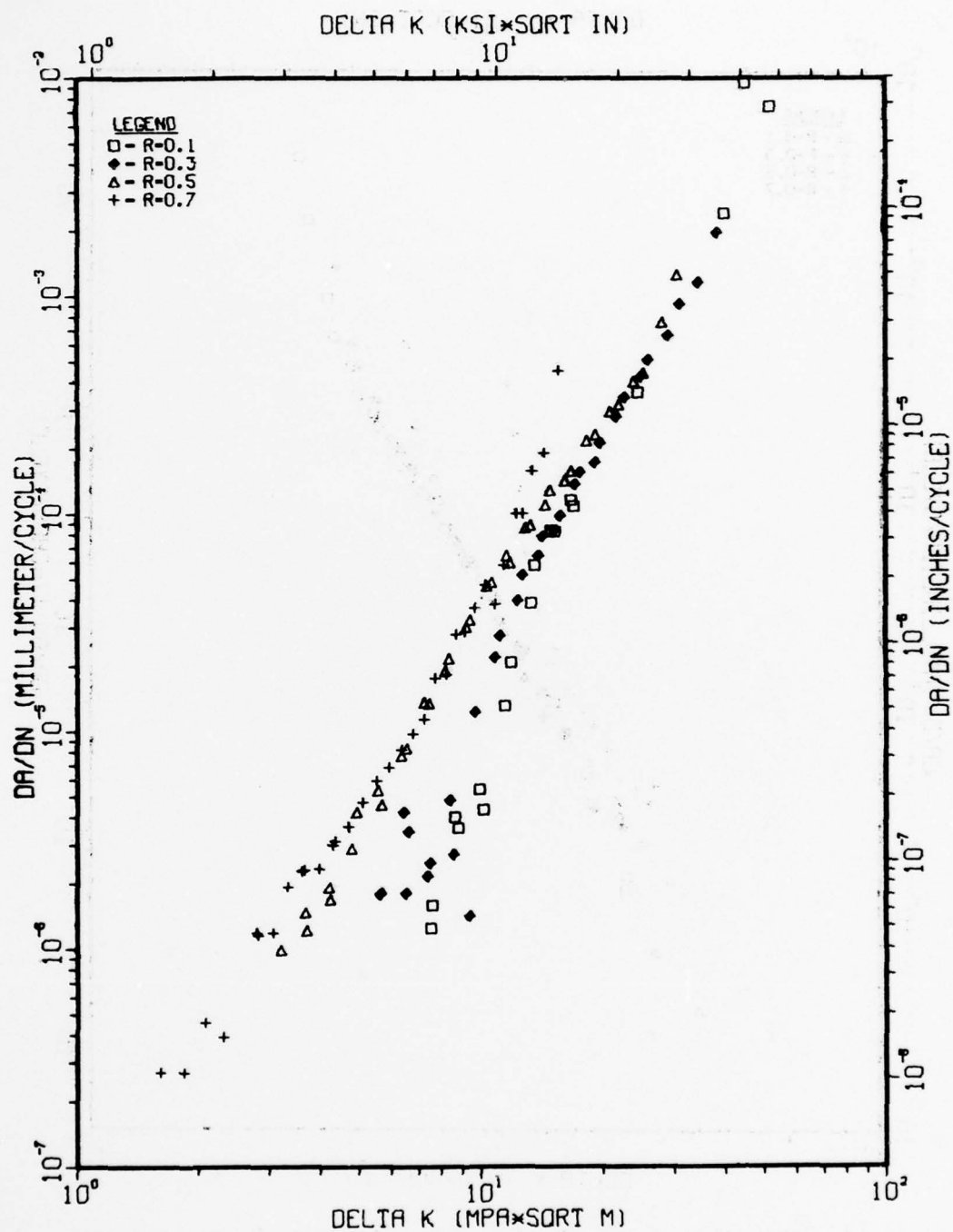
Fig. II-13   Dependence of FCP in Ti-6Al-4V, Condition 7, on load ratio, R.

TI-6AL-2SN-4ZR-6MO(COND. 8), 68F, DRY AIR, 20HZ
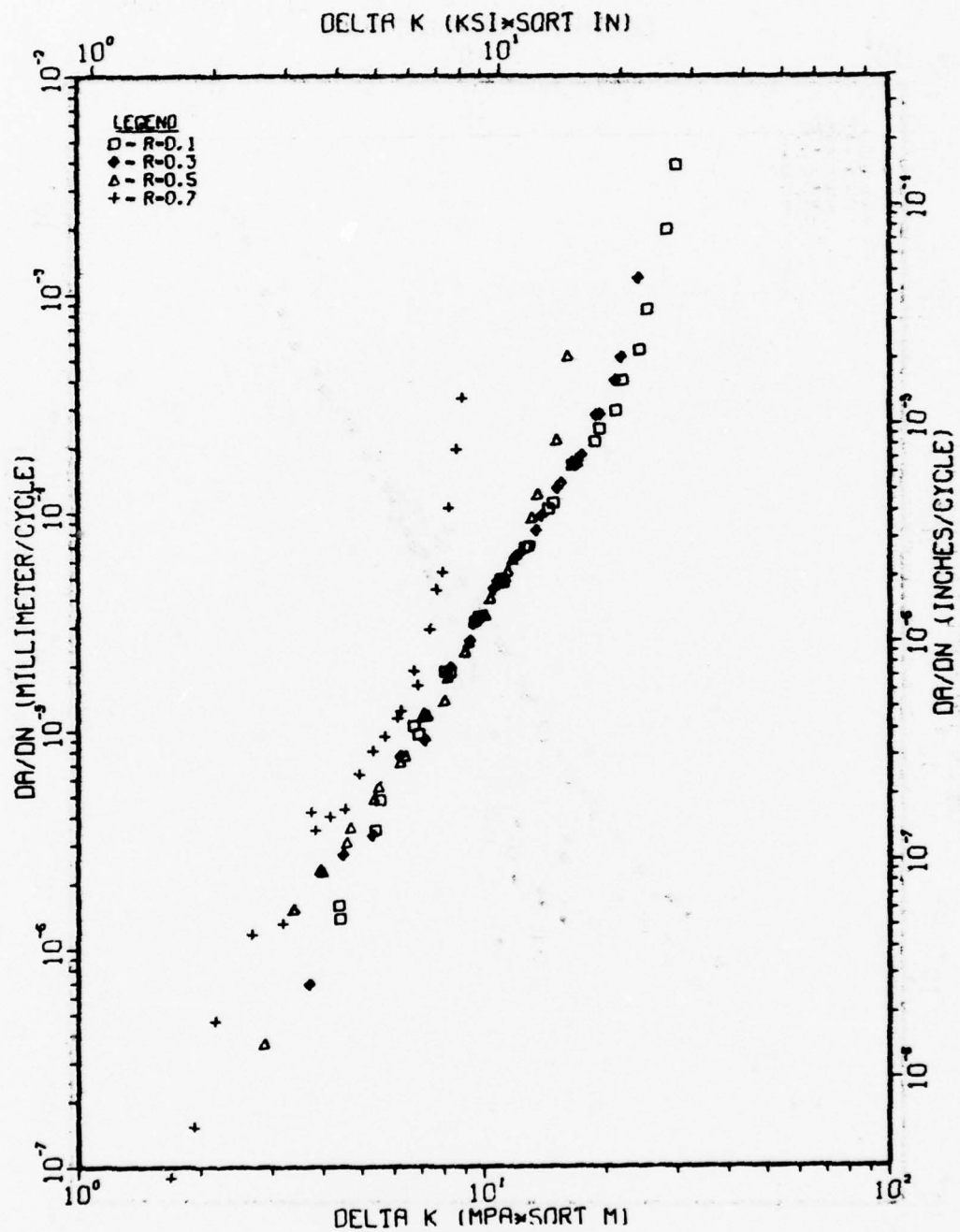
Fig. II-14   Dependence of FCP in Ti-6Al-4V, Condition 8, on load ratio, R.

126
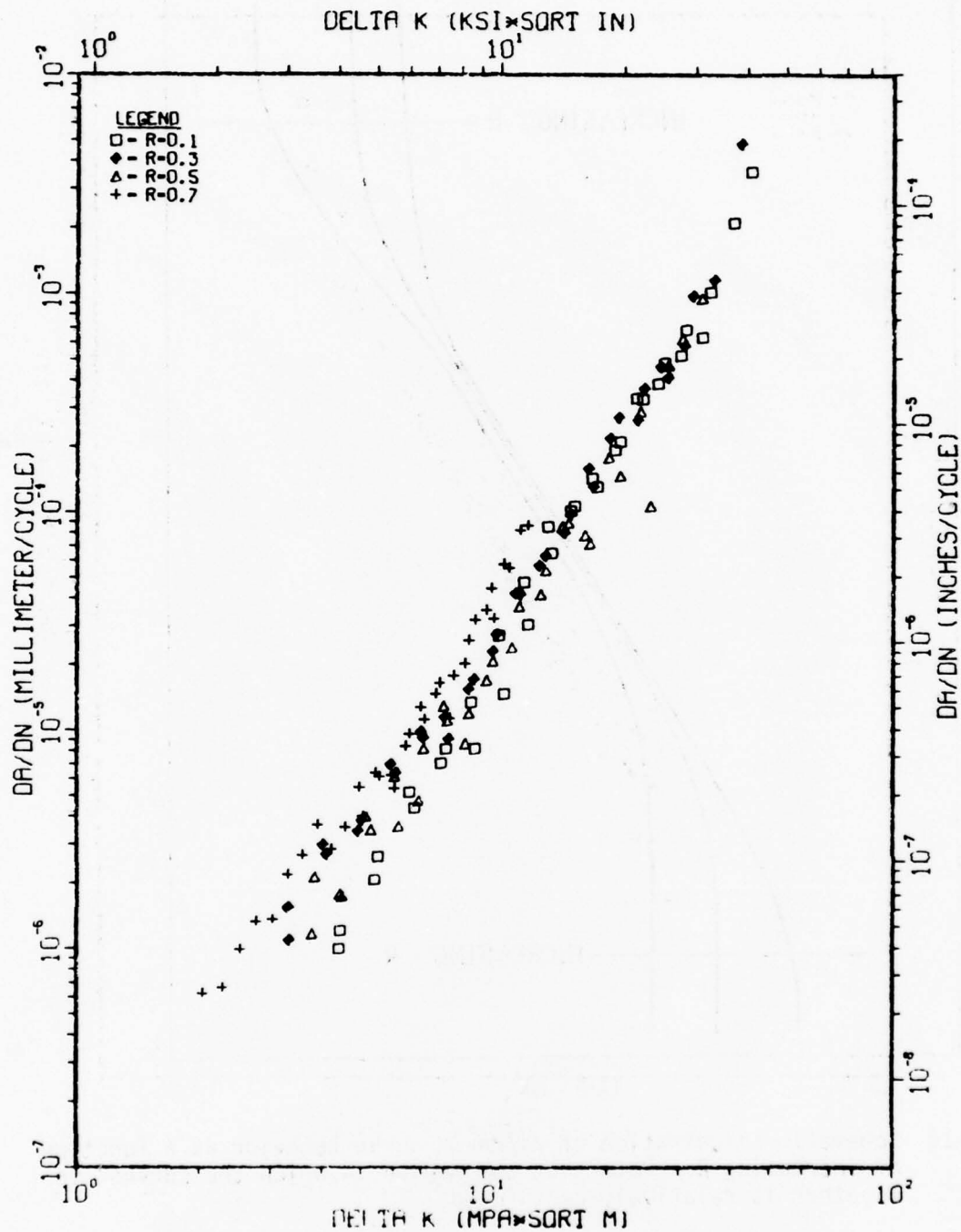
Fig. II-15 Dependence of FCP in Ti-6Al-4V, Condition 10, on load ratio, R.
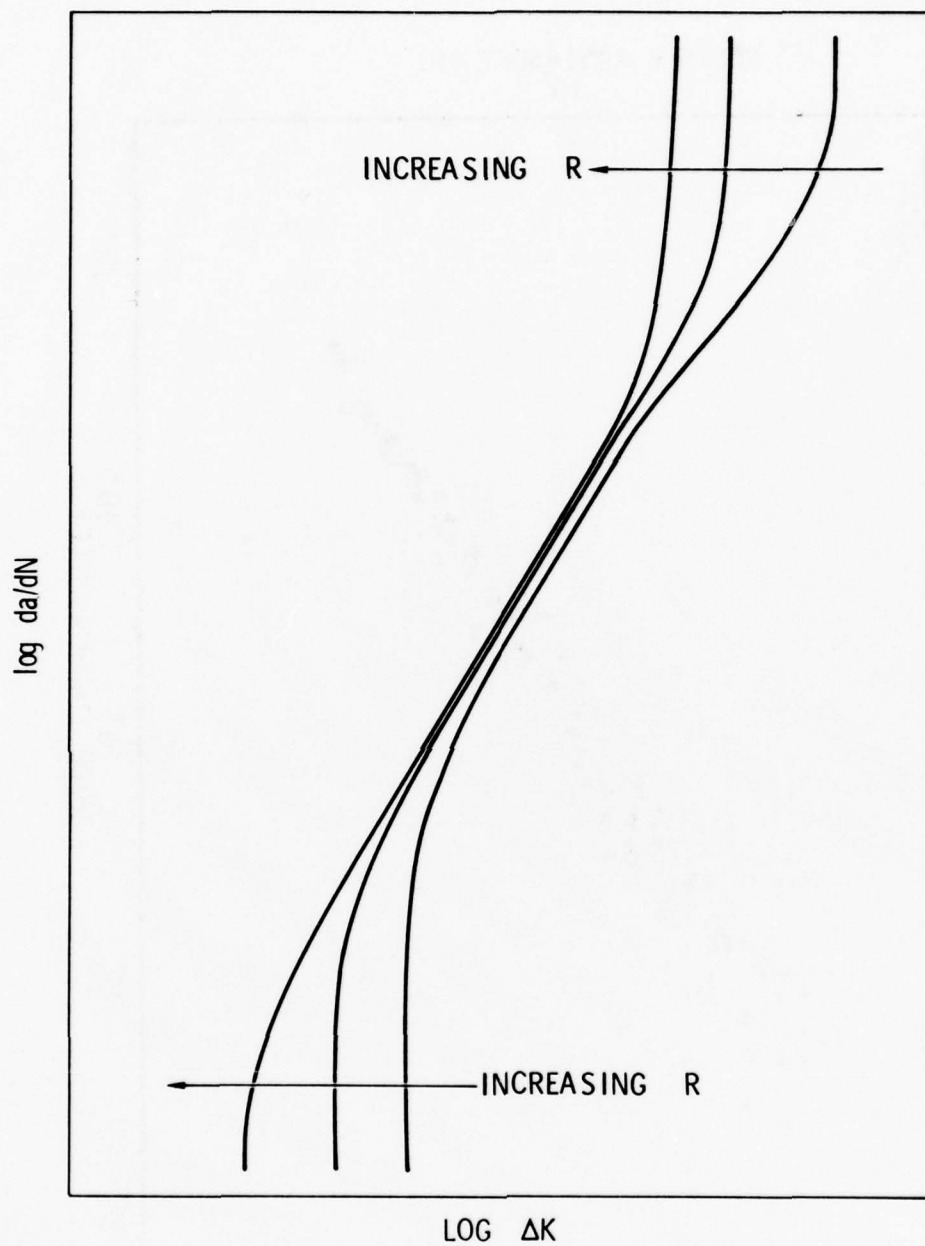
Fig. II-16   Schematic illustration of da/dN-ΔK curve behavior as a function
of increasing R. Note that the region in which the curves lie
together is relatively restricted.

128
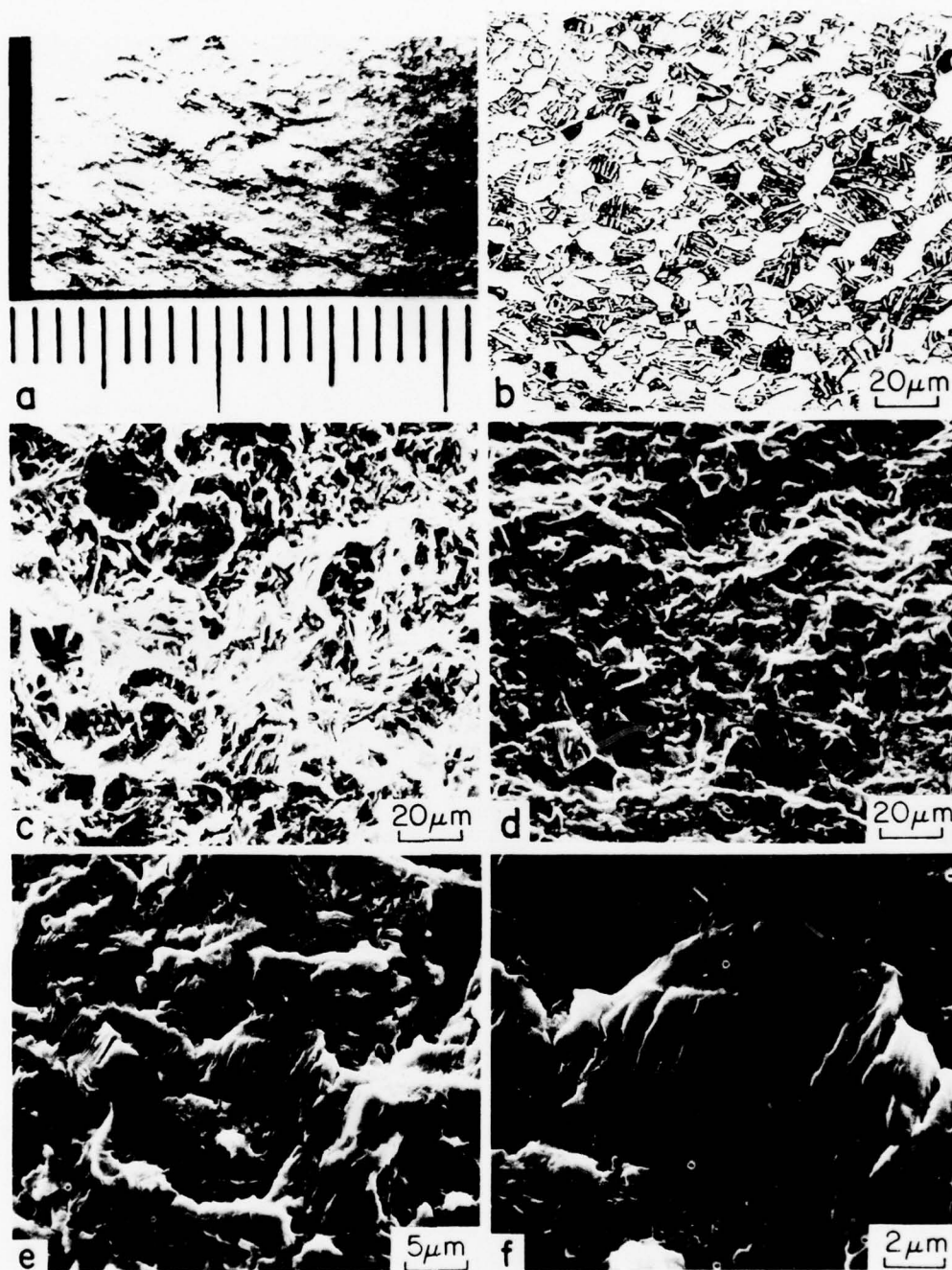
Fig. II-17 Fractography of Condition 7, R = 0.1. (a) macrograph, (b) light microgrph, (c) SEM of fracture surface for ΔK = 8.0 MPa·m$^{\frac{1}{2}}$ and da/dN = 2.5 x 10^{-6} mm/cycle, (d), (e) and (f) fracture surface for ΔK = 21.3 MPa·m$^{\frac{1}{2}}$ and da/dN = 2.5 x 10^{-4} mm/cycle.
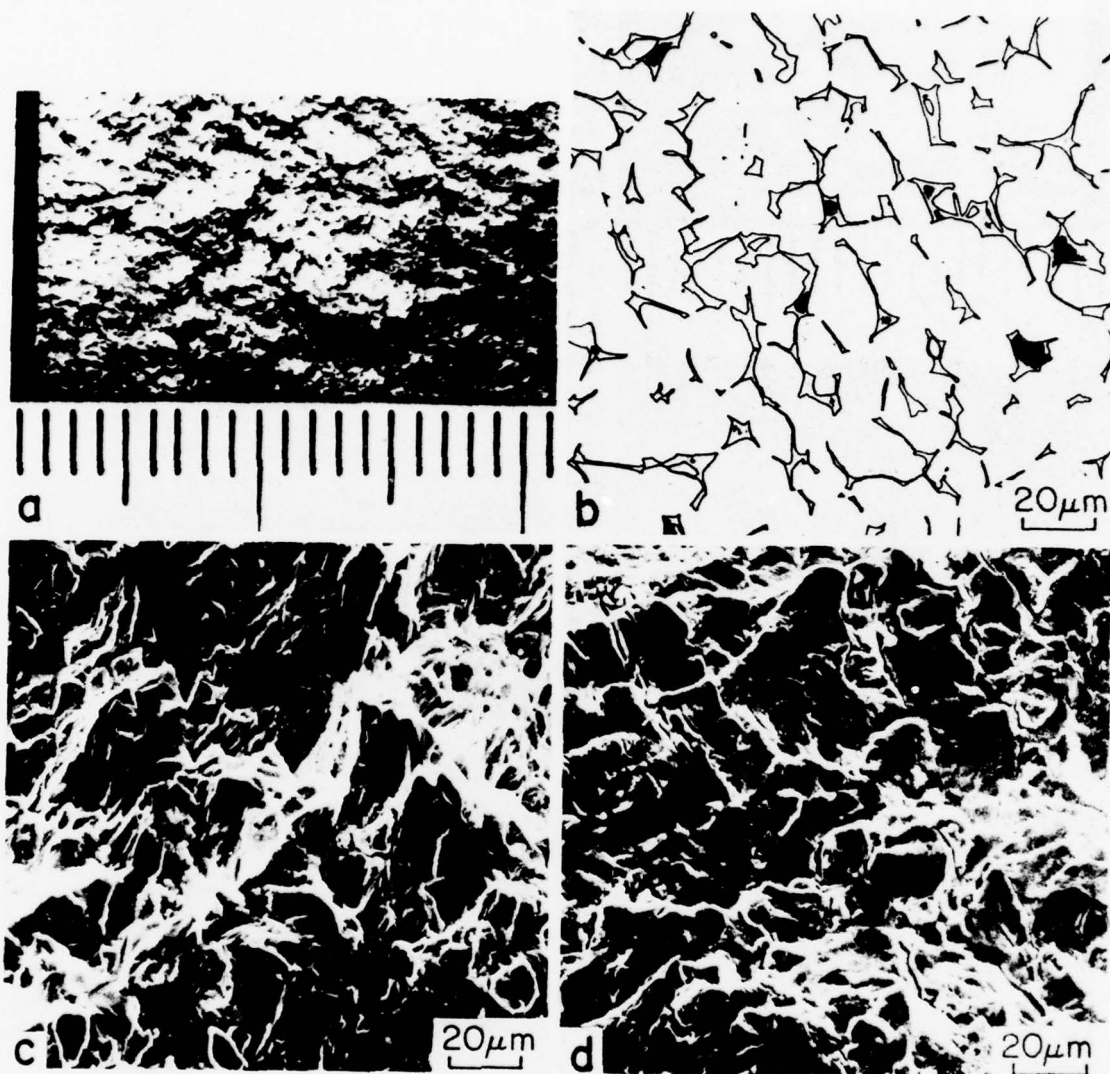
Fig. II-18 Fractography of Condition 1, R = 0.1. (a) macrograph, (b) light micrograph, (c) fracture surface for $\Delta K = 11.9$ MPa·m$^{\frac{1}{2}}$ and $da/dN = 2.5 \times 10^{-6}$ mm/cycle, (d) fracture surface for $\Delta K = 23.1$ MPa·m$^{\frac{1}{2}}$ and $da/dN = 2.5 \times 10^{-4}$ mm/cycle.
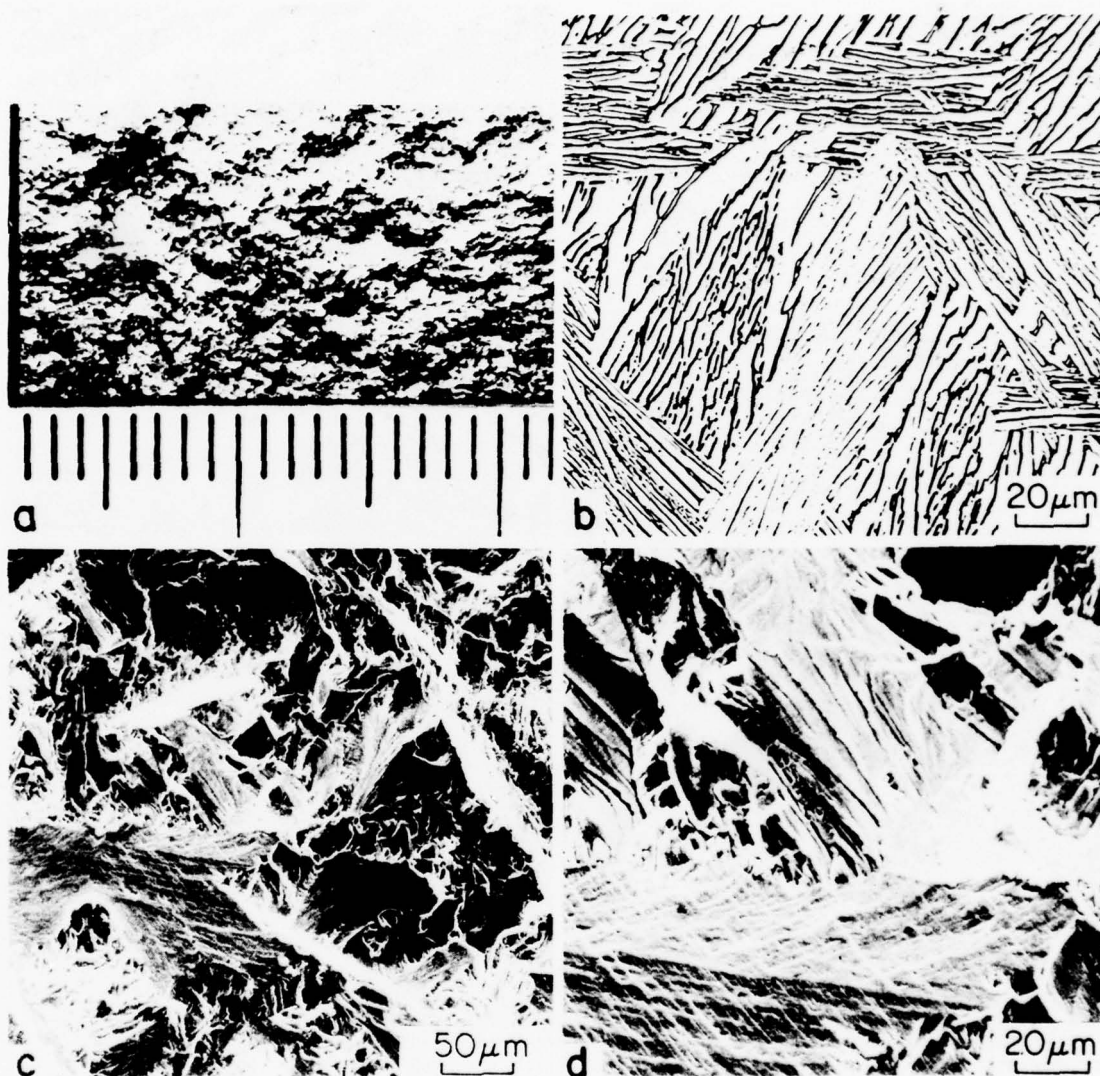
Fig. II-19   Fractography of Condition 4, R = 0.1 for ΔK = 11.4 MPa·m$^{\frac{1}{2}}$ and
da/dN = 2.5 x 10^{-6} mm/cycle. (a) macrograph, (b) light micrograph
at 500X (c), (d) fracture surface at 200X and 500X, respectively.

131
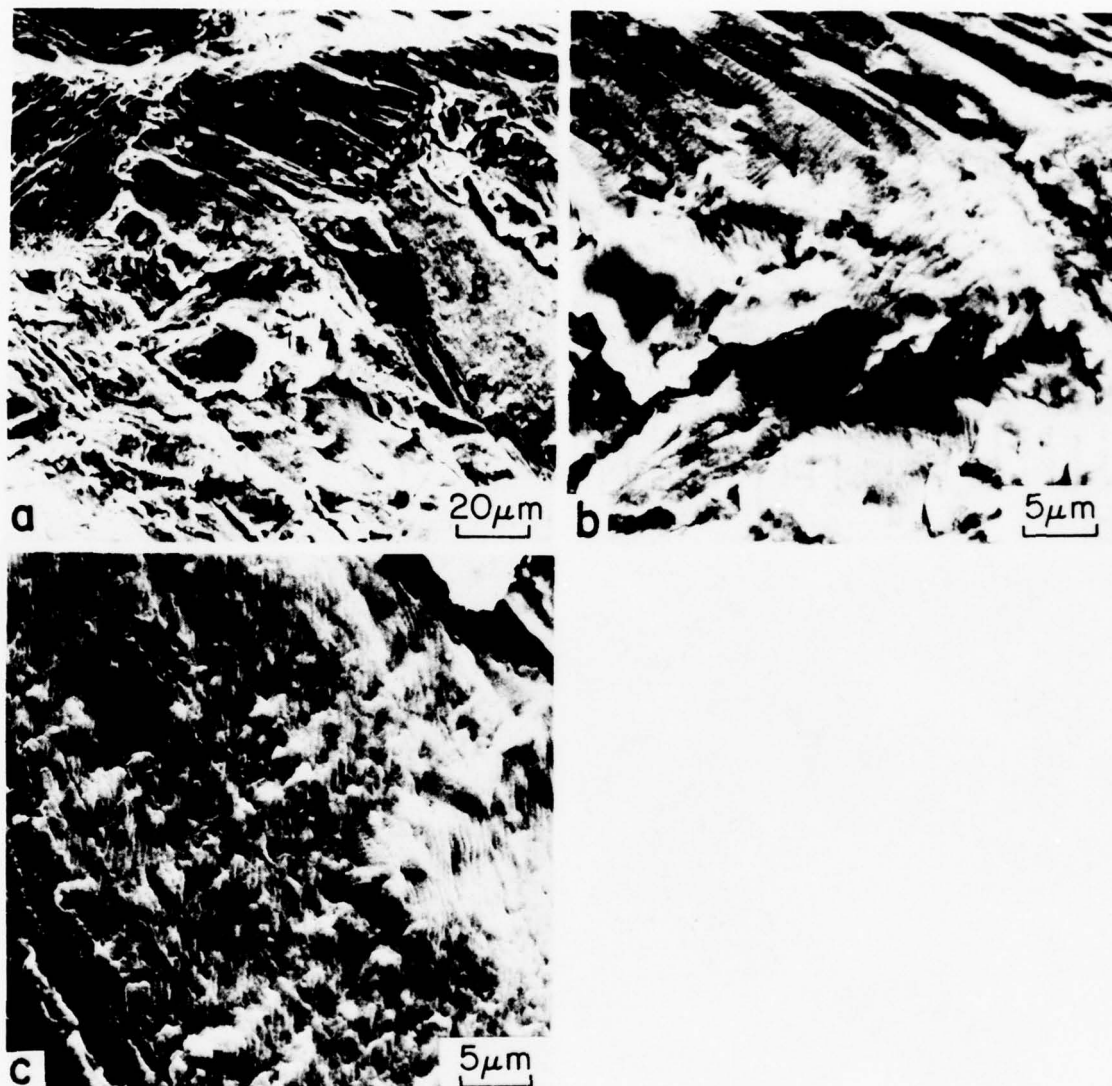
Fig. II-20 Fractography of Condition 4, R = 0.1 for ΔK = 27.5 MPa·m$^{\frac{1}{2}}$ and da/dN = 2.5 x 10^{-4} mm/cycle. (a) portion with type "A" and type "B" areas, (b) details of type "A" area, (c) details of type "B" area.
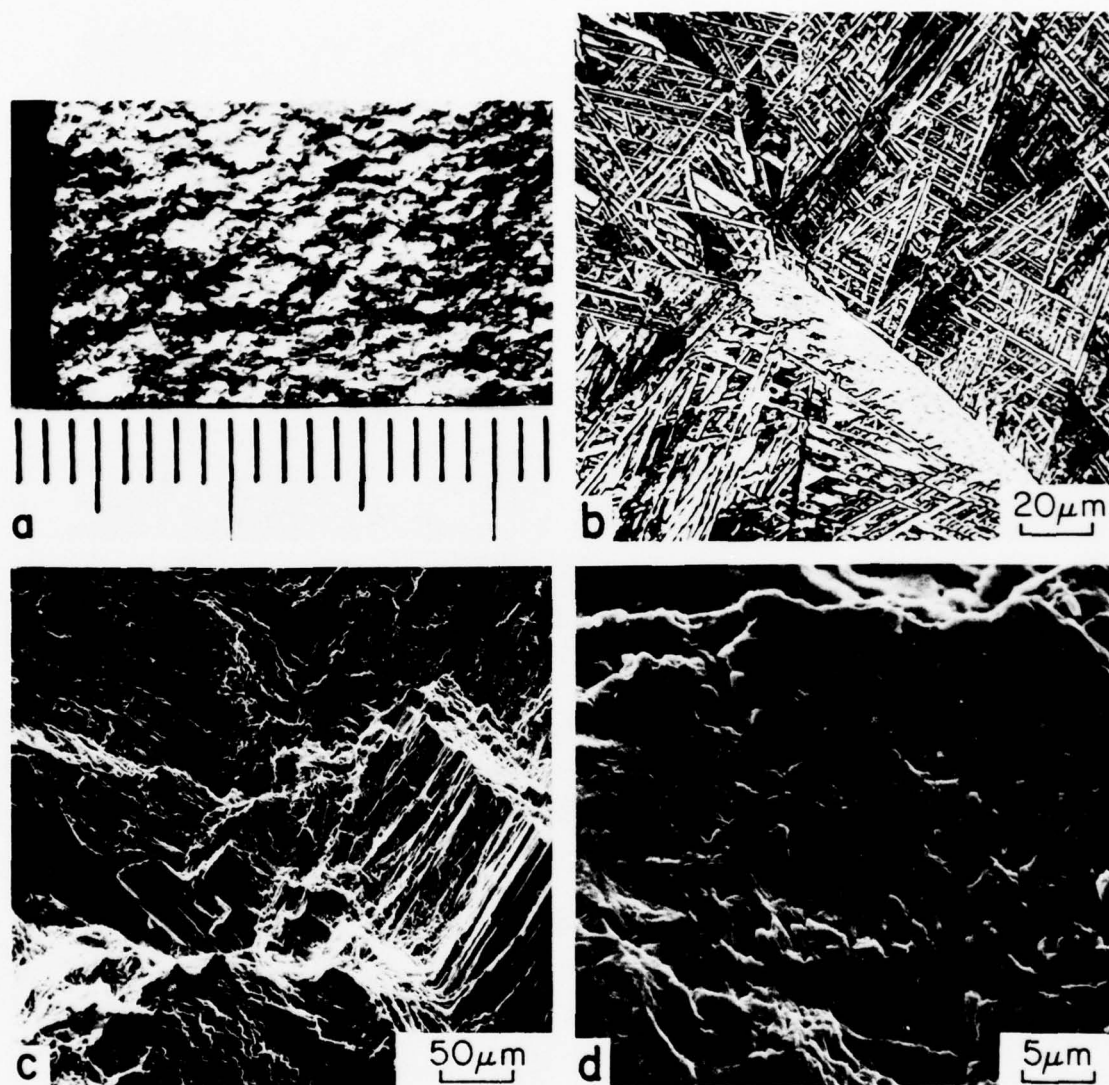
Fig. II-21   Fractography of Condition 5, R = 0.1. (a) macrograph, (b) light micrograph, (c) fracture surface for ΔK = 13.3 MPa·m$^{\frac{1}{2}}$ and da/dN = 2.5 x 10^{-6} mm/cycle, (d) fracture surface for ΔK = 25.9 MPa·m$^{\frac{1}{2}}$ and da/dN = 2.5 x 10^{-4} mm/cycle.
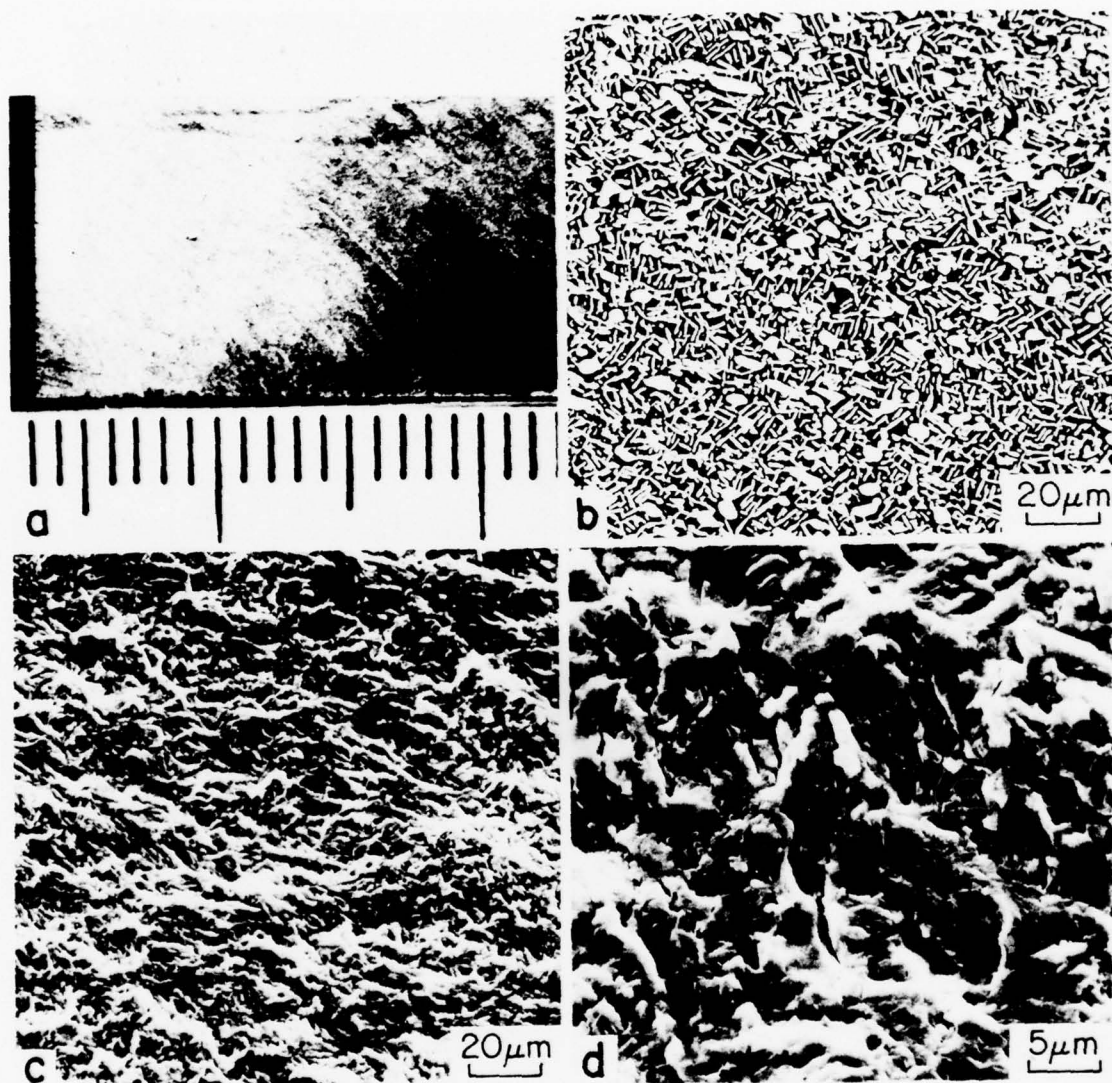
Fig. II-22 Fractography of Condition 8, R = 0.1. (a) macrograph, (b) light micrograph, (c) fracture surface for $\Delta K = 5.0$ MPa·m$^{\frac{1}{2}}$ and da/dN = 2.5 x 10^{-6} mm/cycle, (d) fracture surface for $\Delta K = 19.7$ MPa·m$^{\frac{1}{2}}$ and da/dN = 2.5 x 10^{-4} mm/cycle.

134
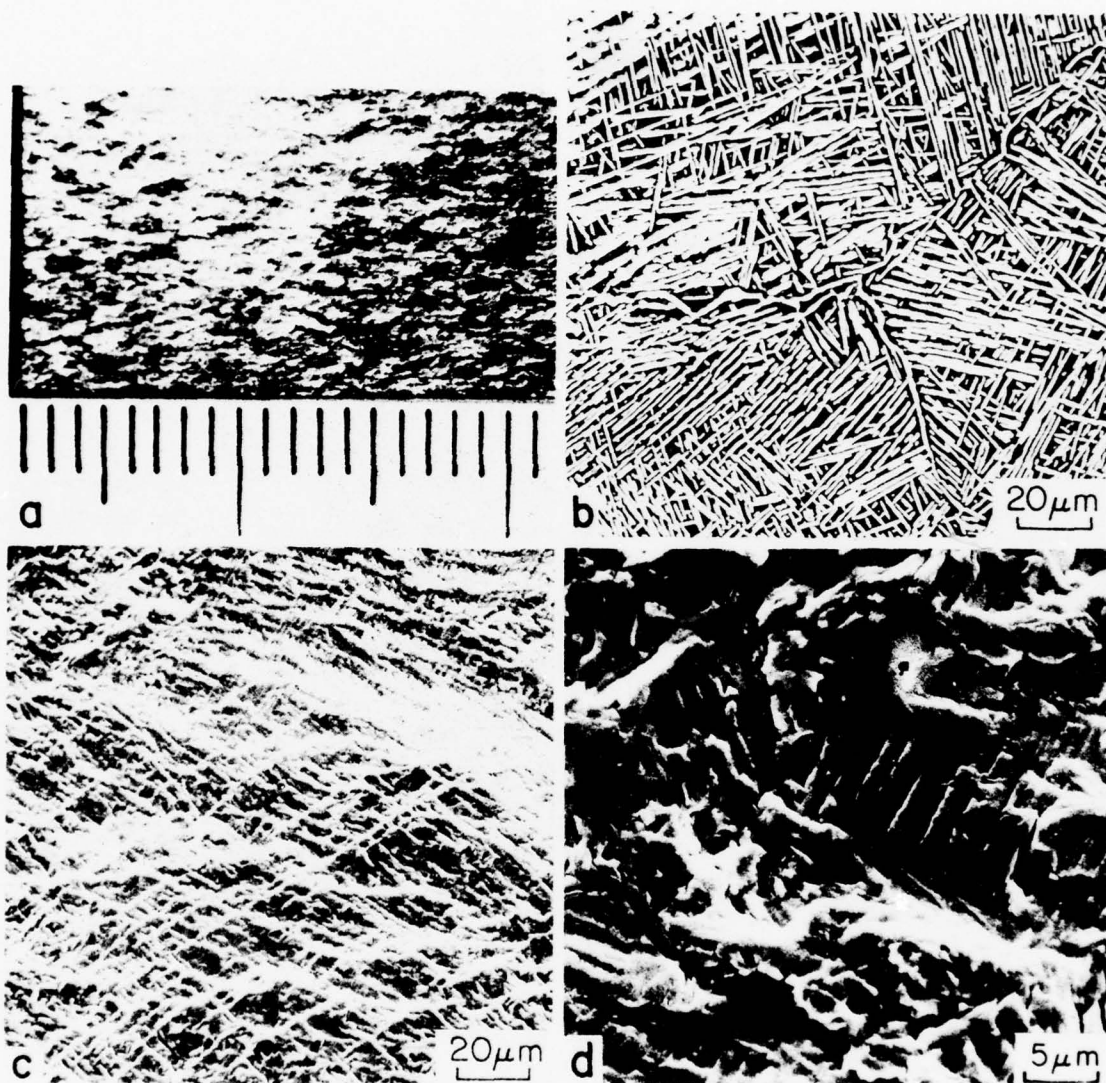
Fig. II-23 Fractography of Condition 10, R = 0.1. (a) macrograph, (b) light micrograph, (c) fracture surface for $\Delta K = 5.5$ MPa·m$^{\frac{1}{2}}$ and $da/dN = 2.5 \times 10^{-6}$ mm/cycle, (d) fracture surface for $\Delta K = 22.2$ MPa·m$^{\frac{1}{2}}$ and $da/dN = 2.5 \times 10^{-4}$ mm/cycle.
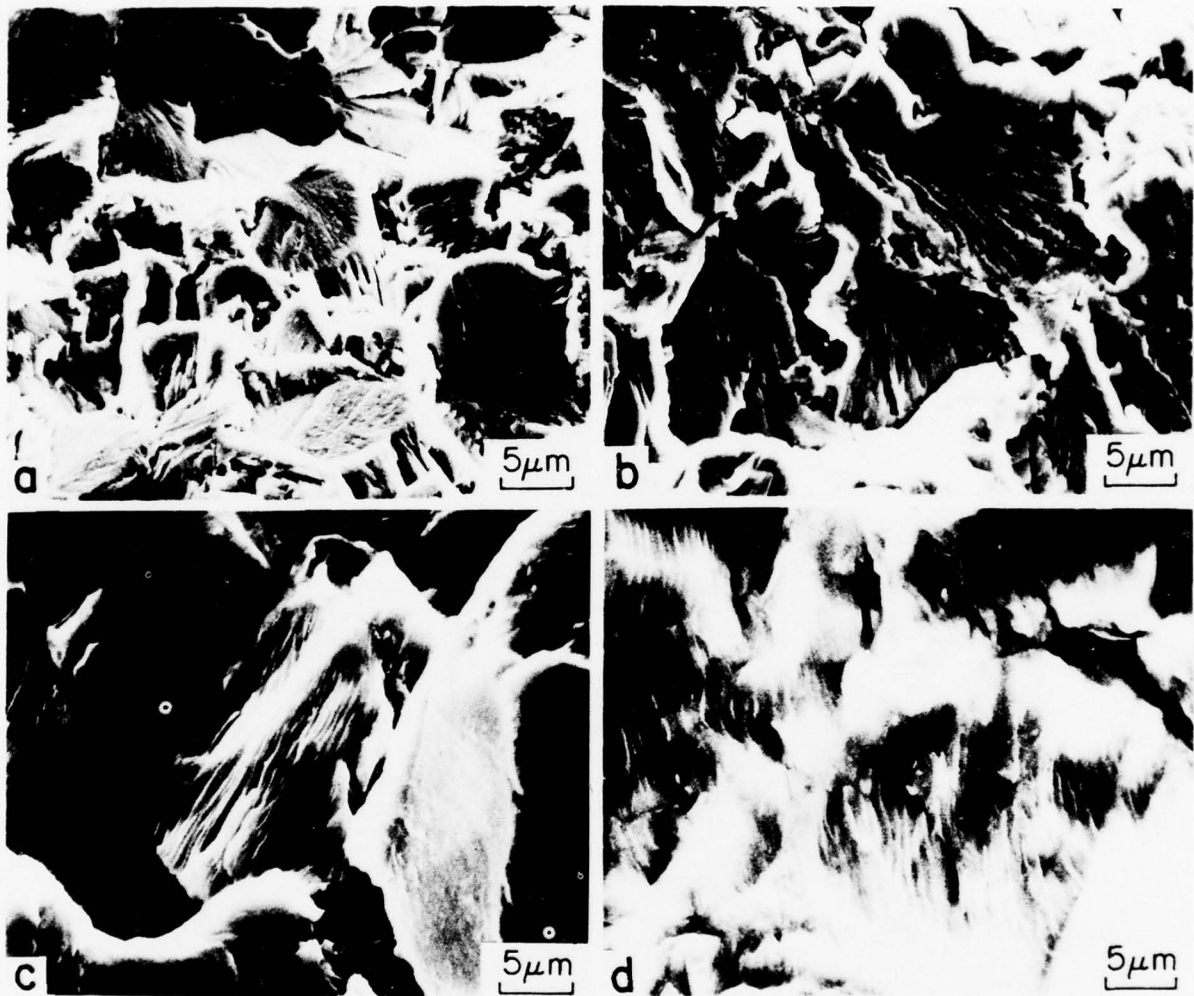
Fig. II-24 Fracture surface for Condition 1 tested at 20 Hz in dry air.
(a) R = 0.5, ΔK = 6.5 MPa·m$^{\frac{1}{2}}$, da/dN = 2.5 x 10^{-6} mm/cycle;
(b) R = 0.7, ΔK = 5.9 MPa·m$^{\frac{1}{2}}$, da/dN = 2.5 x 10^{-6} mm/cycle;
(c) R = 0.5, ΔK = 18.7 MPa·m$^{\frac{1}{2}}$, da/dN = 2.5 x 10^{-4} mm/cycle;
(d) R = 0.7, ΔK = 18.8 MPa·m$^{\frac{1}{2}}$, da/dN = 2.5 x 10^{-4} mm/cycle.
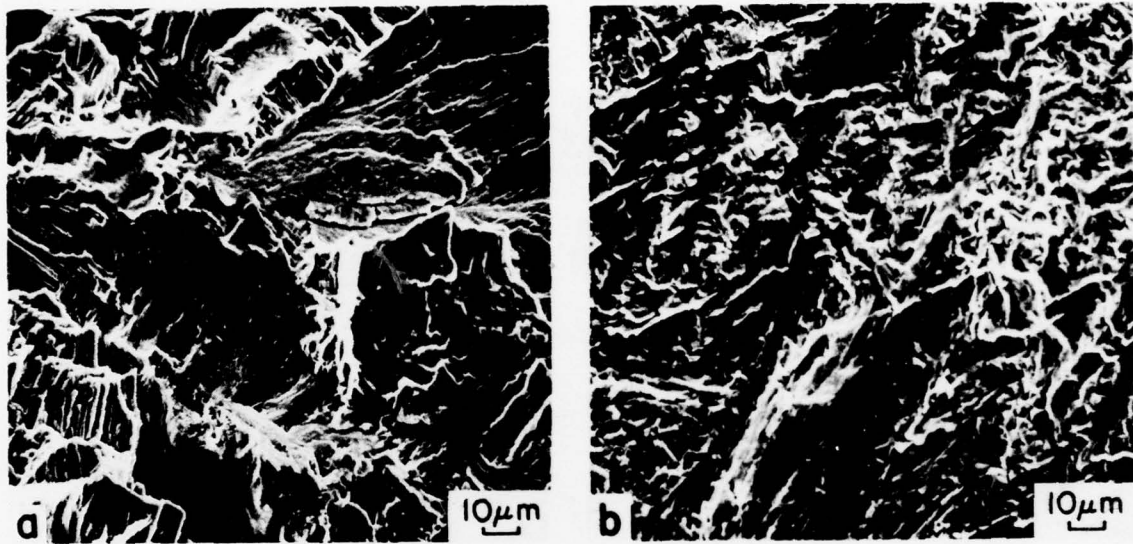
Fig. II-25 Fracture surface of Condition 4 tested at R = 0.5 and 20 Hz in dry air (a) ΔK = 6.1 MPa·m$^{1/2}$, da/dN = 2.5 x 10^{-6} mm/cycle; (b) ΔK = 20.3 MPa·m$^{1/2}$, da/dN = 2.5 x 10^{-4} mm/cycle.
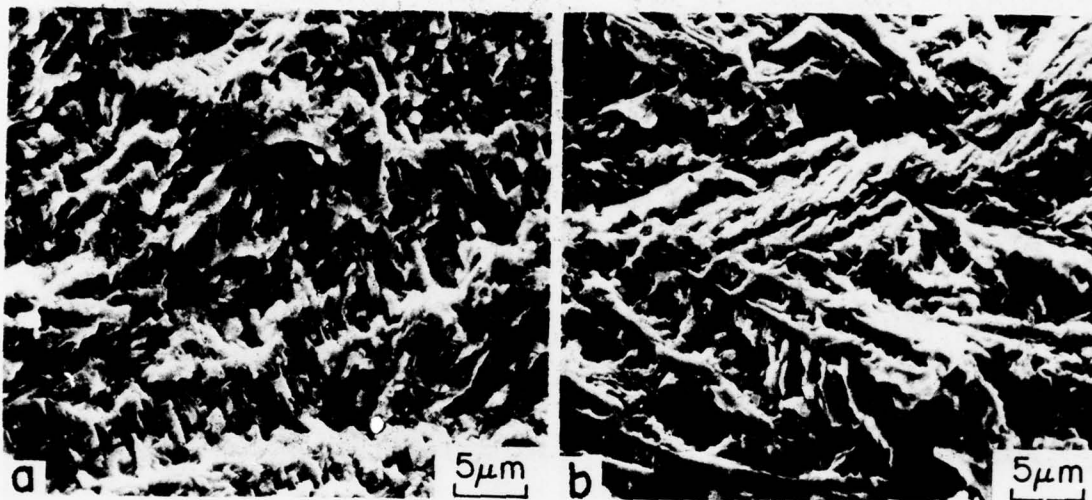
Fig. II-26   Fracture surface of Condition 5 tested at 20 Hz in dry air.
  (a) R = 0.5, ΔK = 5.5 MPa·m$^{\frac{1}{2}}$, da/dN = 2.5 x 10^{-6} mm/cycle;
  (b) R = 0.7, ΔK = 3.9 MPa·m$^{\frac{1}{2}}$, da/dN = 2.5 x 10^{-6} mm/cycle.

138
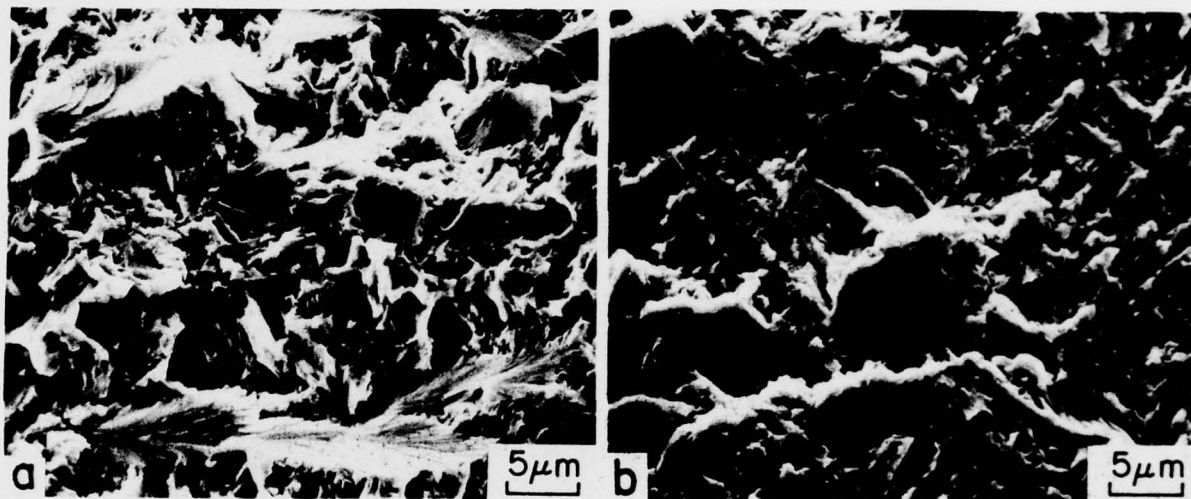
Fig. II-27 Fracture surface of Condition 7 tested at 20 Hz in dry air.
(a) R = 0.5, ΔK = 4.6 MPa·m$^{\frac{1}{2}}$, da/dN = 2.5 x 10^{-6} mm/cycle;
(b) R = 0.7, ΔK = 4.1 MPa·m$^{\frac{1}{2}}$, da/dN = 2.5 x 10^{-6} mm/cycle.

139

5μm

b 20μm
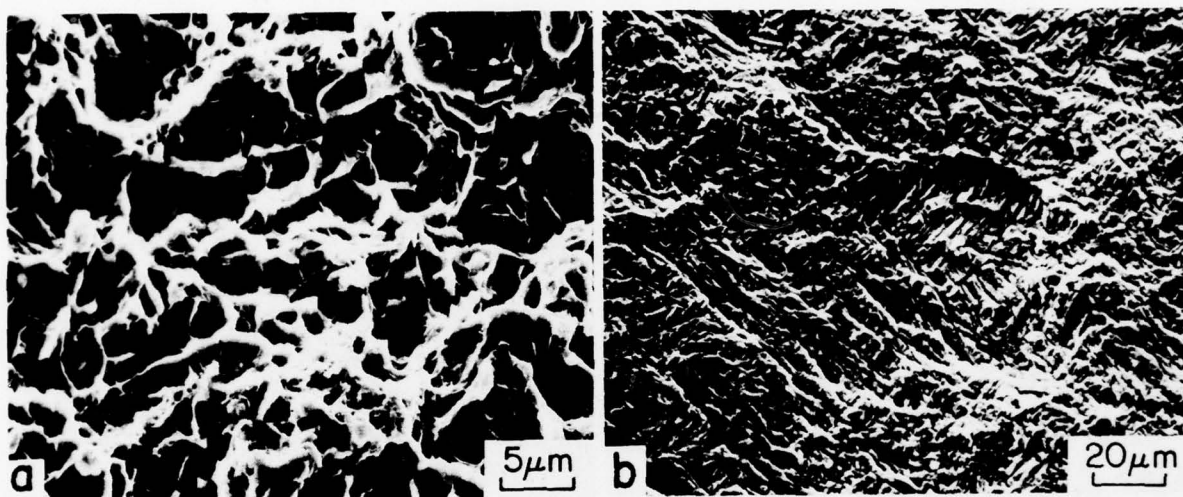
Fig. II-28 Fracture surface of Conditions 8 and 10 tested at 20 Hz in dry air.
(a) Condition 8, R = 0.7, ΔK = 15.2 MPa·m$^{\frac{1}{2}}$,
da/dN = 2.5 x 10^{-4} mm/cycle; (b) Condition 10, R = 0.5,
ΔK = 4.7 MPa·m$^{\frac{1}{2}}$, da/dN = 2.5 x 10^{-6} mm/cycle.
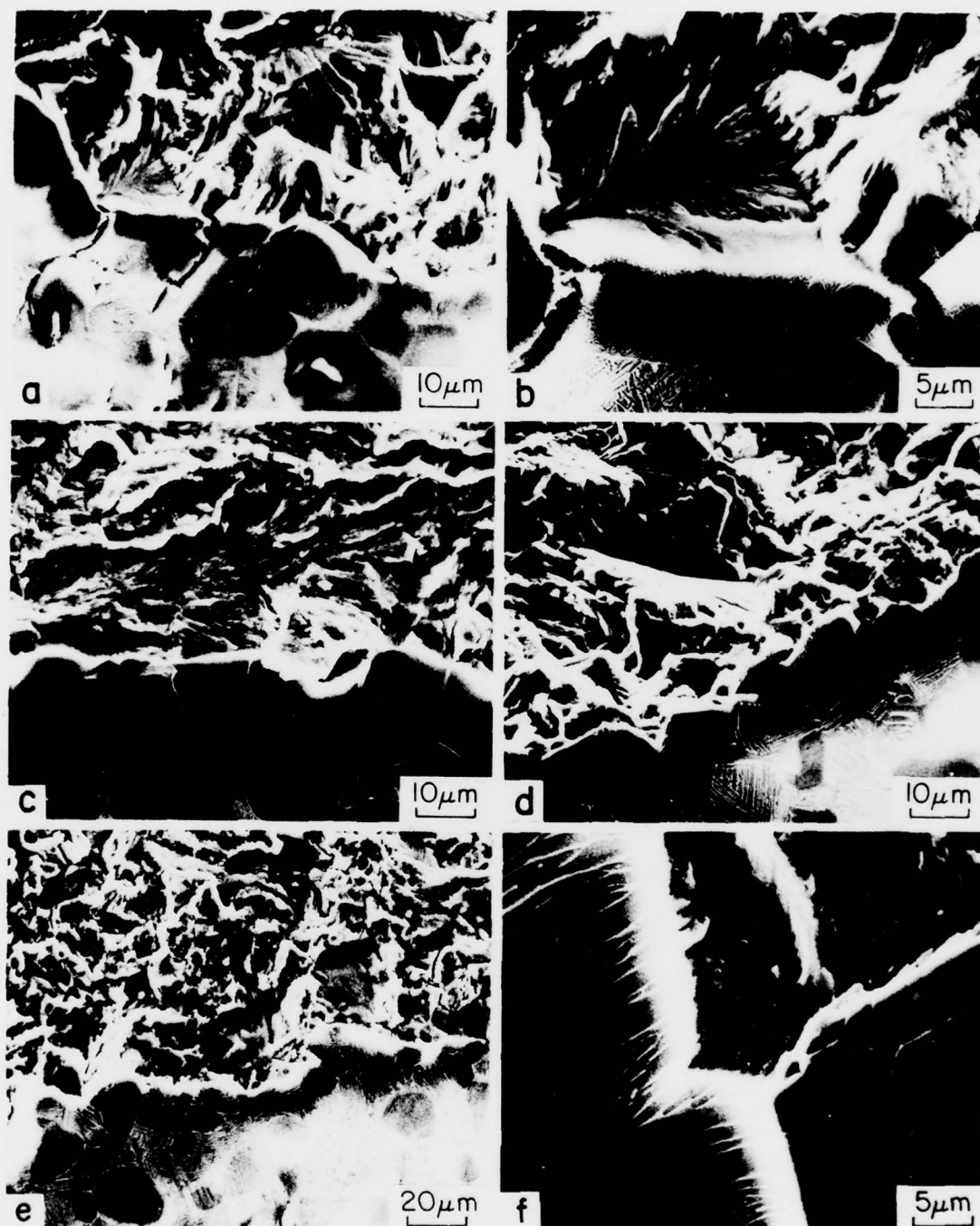
Fig. II-29 Scanning electron micrographs of the fracture paths in Ti-6Al-4V FCP specimens: (a,b) Condition 1, R = 0.1, da/dN = 2.5 x 10^{-6} mm/cycle (ΔK = 9.9 MPa·m$^{\frac{1}{2}}$); (c) Condition 1, R = 0.1, da/dN = 2.5 x 10^{-4} mm/cycle (ΔK = 22.8 MPa·m$^{\frac{1}{2}}$); (d) Condition 7, R = 0.1, da/dN = 2.5 x 10^{-6} mm/cycle (ΔK = 7.9 MPa·m$^{\frac{1}{2}}$); and (f) Condition 4, R = 0.1, da/dN 2.5 x 10^{-6} mm/cycle (ΔK = 11.3 MPa·m$^{\frac{1}{2}}$).

141
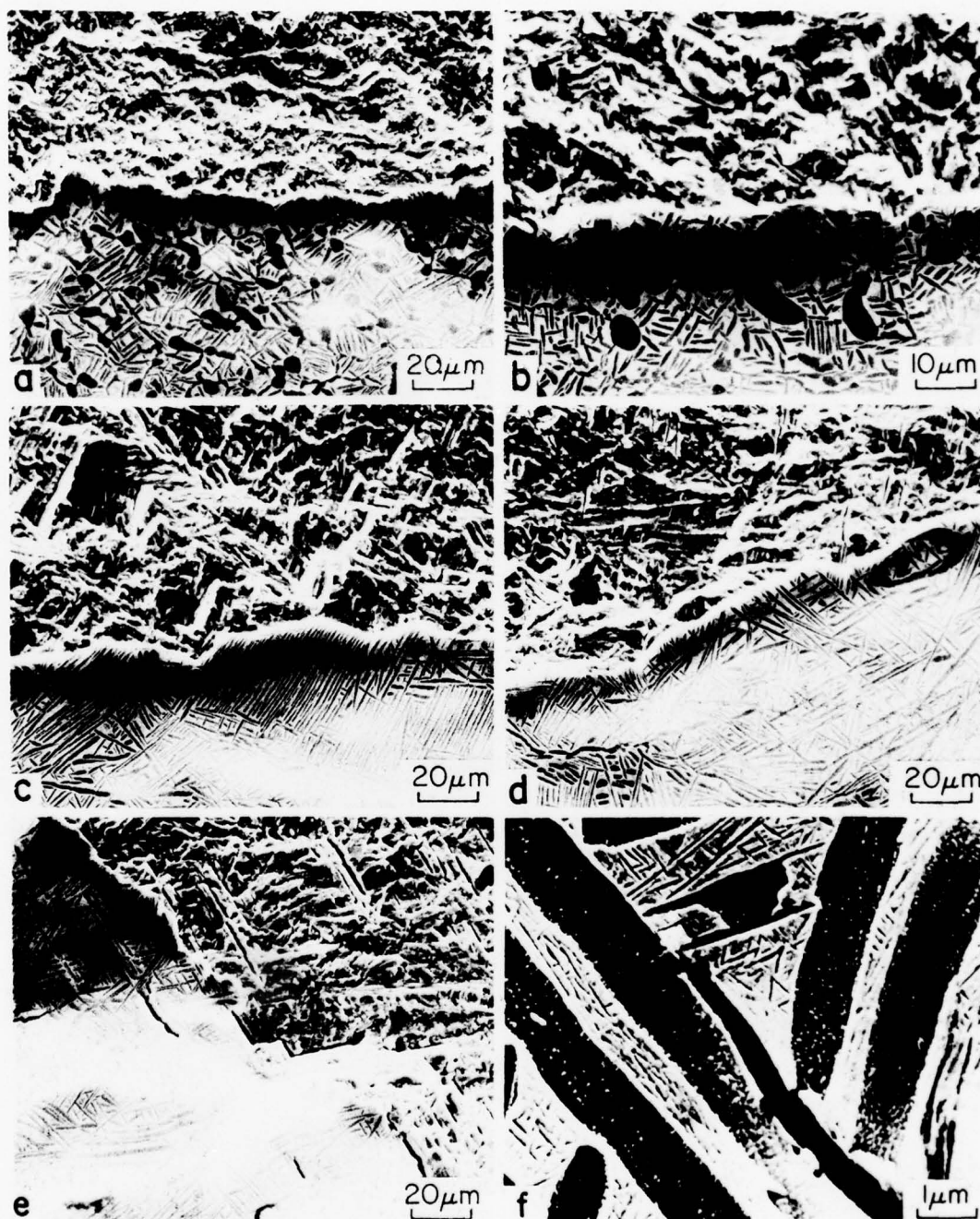
Fig. II-30 Scanning electron micrographs of the fracture paths in Ti-6Al-2Sn-4Zr-6Mo FCP specimens: (a) Condition 8, R = 0.1, da/dN = 2.5 x 10^{-6} mm/cycle (ΔK = 4.9 MPa·m$^{\frac{1}{2}}$); (b) Condition 8, R = 0.1, da/dN = 2.5 x 10^{-4} mm/cycle (ΔK = 19.5 MPa·m$^{\frac{1}{2}}$); (c,d) Condition 10, R = 0.1, da/dN = 2.5 x 10^{-4} mm/cycle (ΔK = 22.0 MPa·m$^{\frac{1}{2}}$); and (e,f) Condition 10, R = 0.3, da/dN = 2.5 x 10^{-4} mm/cycle (ΔK = 20.8 MPa·m$^{\frac{1}{2}}$).

142
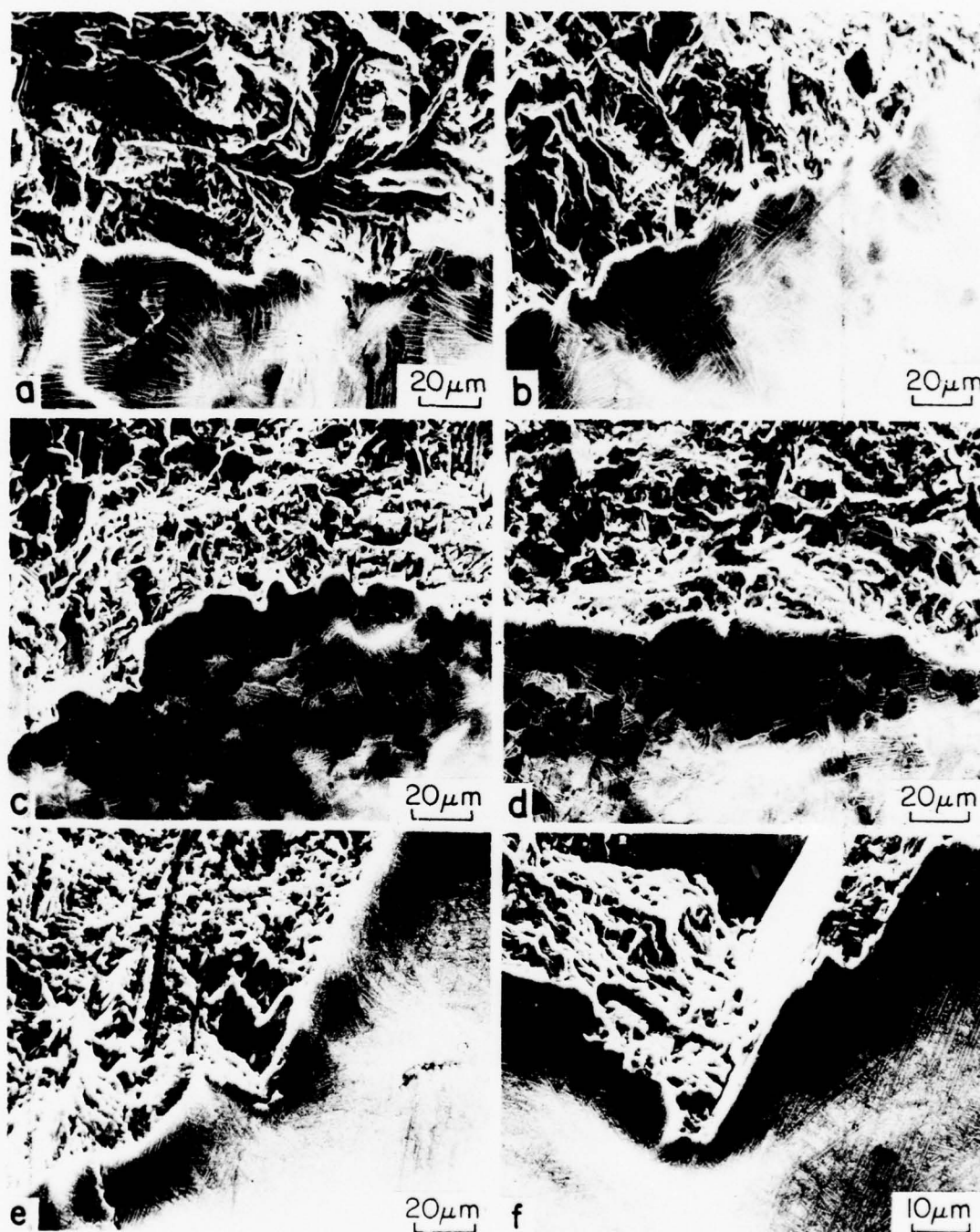
Fig. II-31 Scanning electron micrographs of the fracture paths in Ti-6Al-4V FCP
specimens: (a,b) Condition 2, R = 0.1, da/dN = 2.5 x 10^{-6} mm/cycle
(ΔK = 8.8 MPa·m$^{\frac{1}{2}}$); (c) Condition 3, R = 0.1,
da/dN = 2.5 x 10^{-6} mm/cycle (ΔK = 10.9 MPa·m$^{\frac{1}{2}}$); (d) Condition 3,
R = 0.1, da/dN = 2.5 x 10^{-4} mm/cycle (ΔK = 20.9 MPa·m$^{\frac{1}{2}}$); and
(e,f) Condition 5, R = 0.3, da/dN = 2.5 x 10^{-6} mm/cycle
(ΔK = 9.0 MPa·m$^{\frac{1}{2}}$). Note: the direction of crack propagation in
(f) is from right to left.

143

TI-6AL-4V (COND. 1), 68F, DRY AIR, R-0.3
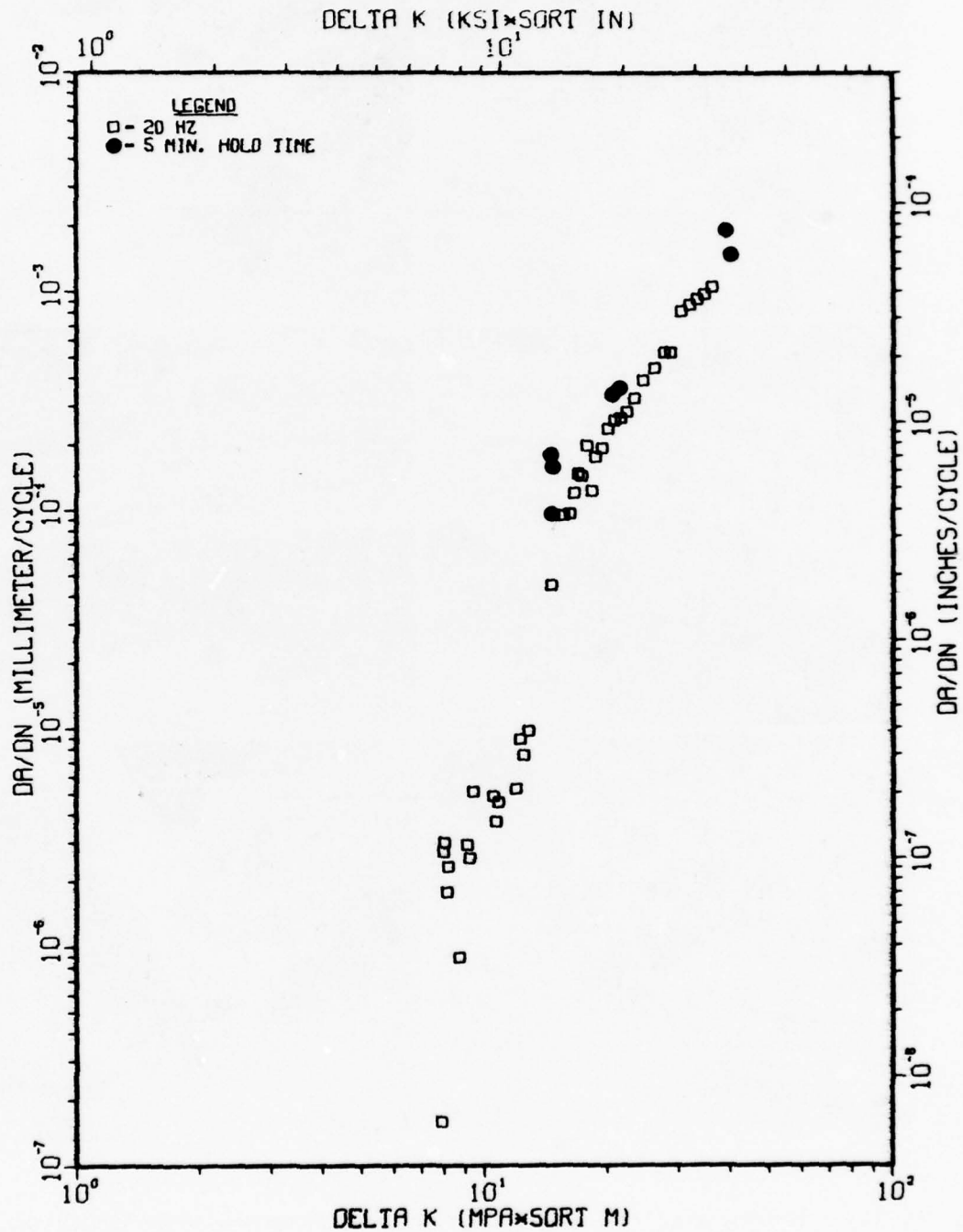
Fig. II-32 FCP data for Condition 1 (1-1-3/10), 68°F, dry air, 20 Hz,
R = 0.3; including 5 min. hold-time data at approximately
2.5×10^{-5}, 2.5×10^{-4}, and 2.5×10^{-3} mm/cycle.
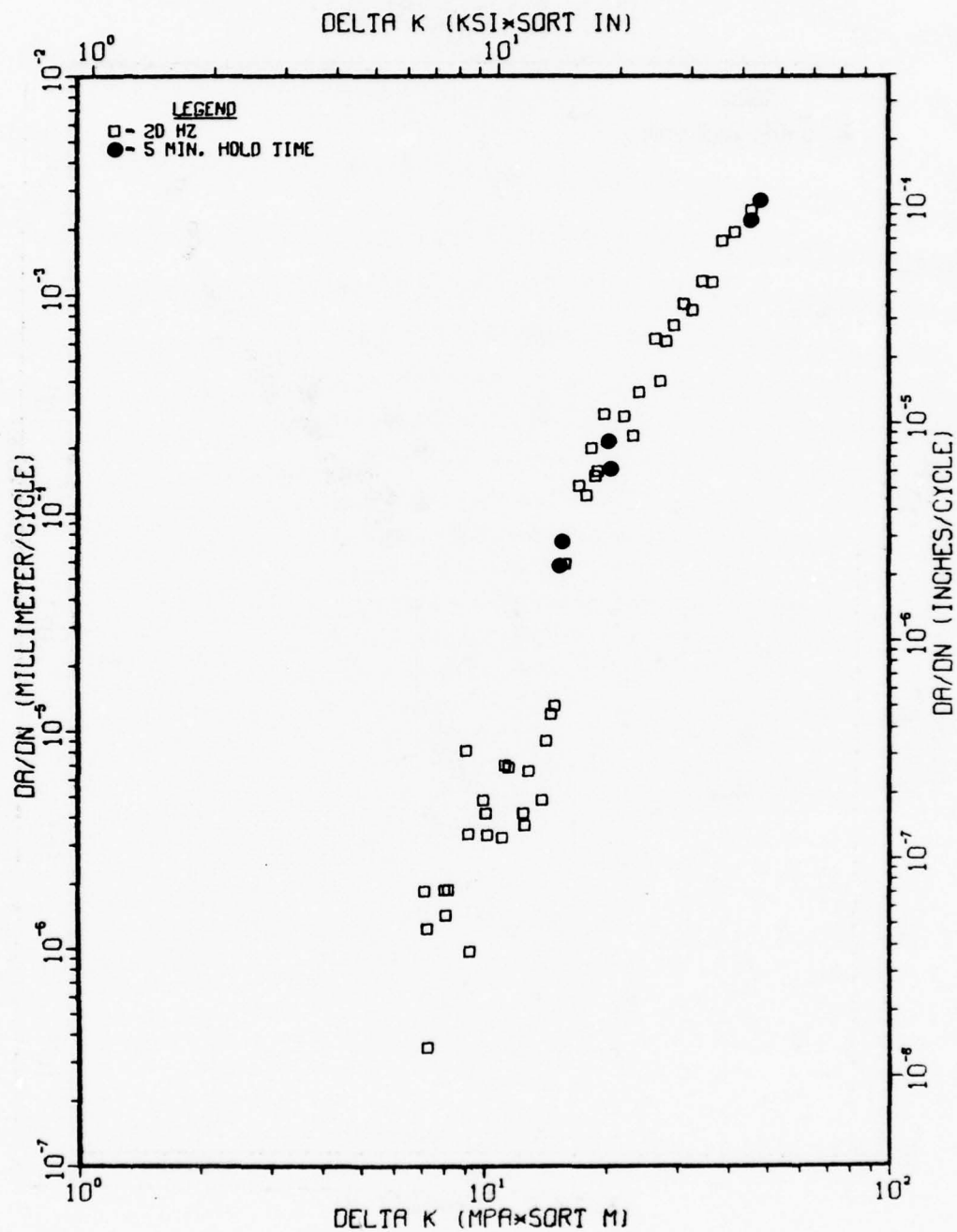
Fig. II-33 FCP data for Condition 4 (1-4-3/22), 68°F, dry air, 20 Hz,
R = 0.3; including 5 min hold-time data at approximately
2.5×10^{-5}, 2.5×10^{-4}, and 2.5×10^{-3} mm/cycle.

145

TI-6AL-4V (COND. 5), 68F, DRY AIR, R-0.3
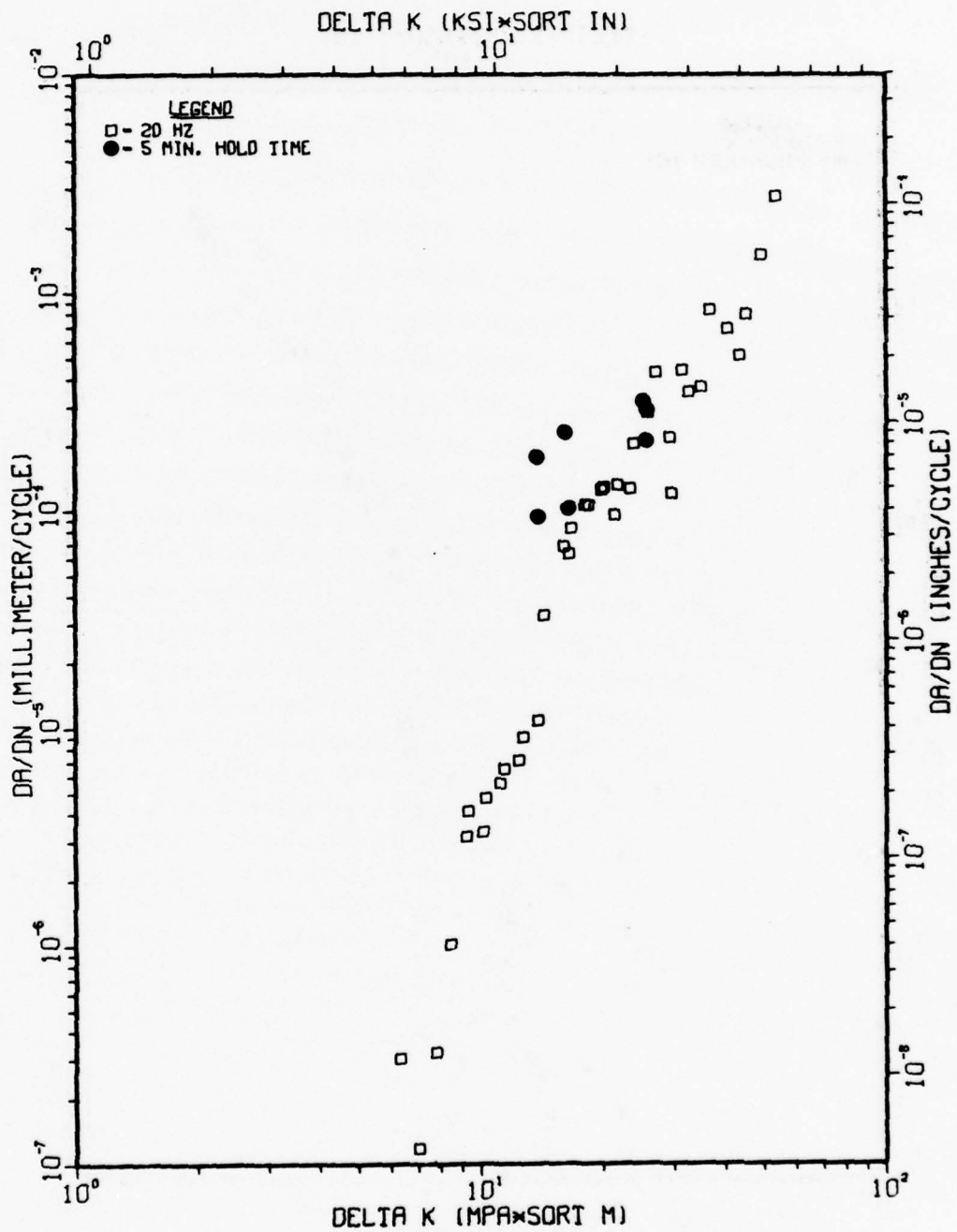
Fig. II-34 FCP data for Condition 5 (1-5-1/21), 68°F, dry air, 10 Hz,
R = 0.3; including 5 min. hold-time data at approximately
2.5 x 10⁻⁵, 2.5 x 10⁻⁴, and 2.5 x 10⁻³ mm/cycle.

146

TI-6AL-4V (COND. 7), 68F, DRY AIR, R-0.3
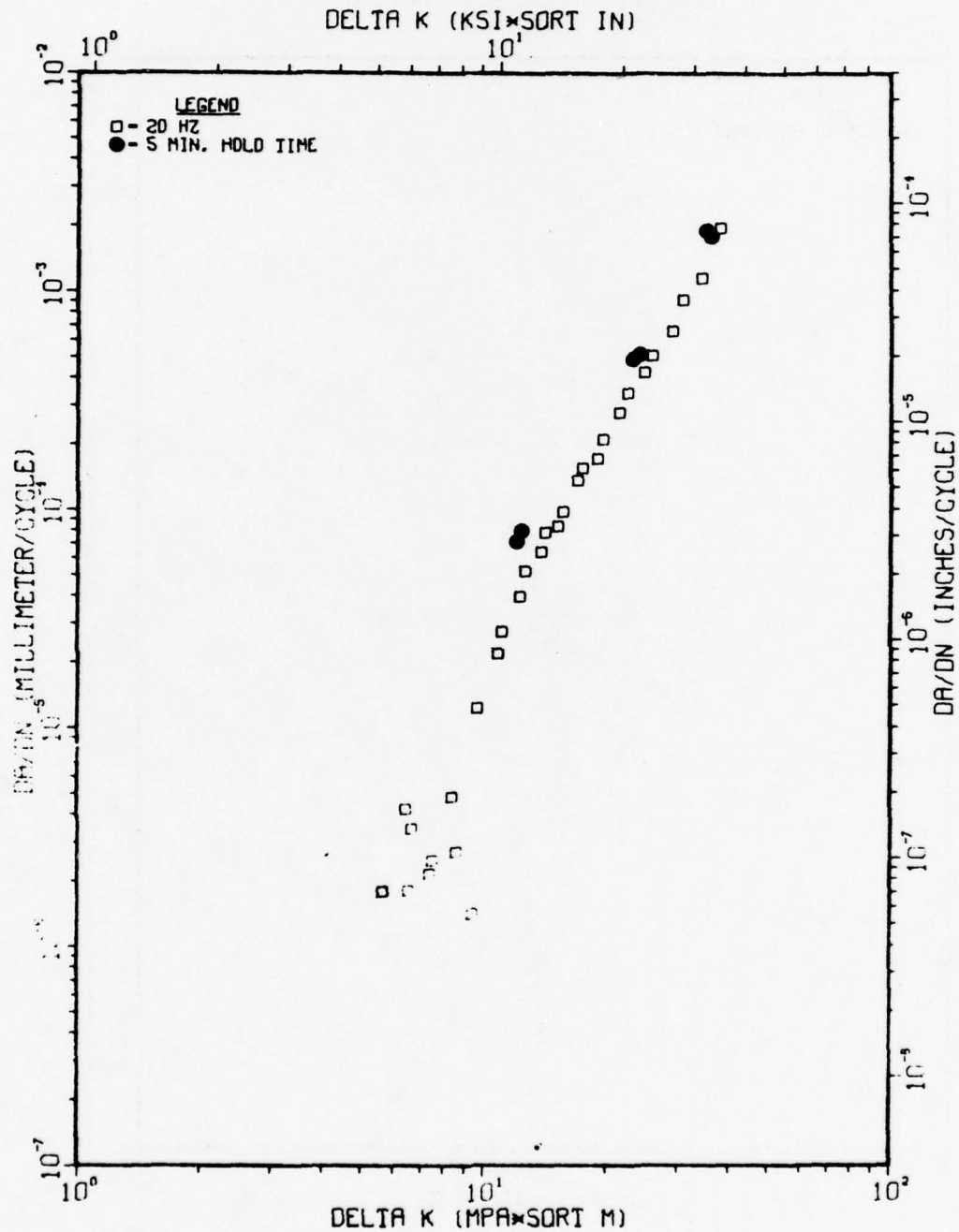
Fig.II-35   FCP data for Condition 7 (1-7-0/26), 68°F, dry air, 20 Hz,
             R = 0.3; including 5 min. hold-time data at approximately
             2.5 x 10⁻⁵, 2.5 x 10⁻⁴, and 2.5 x 10⁻³ mm/cycle.

147

TI-6AL-2SN-4ZR-6MO (COND. 8), 68F, DRY AIR, R-0.3
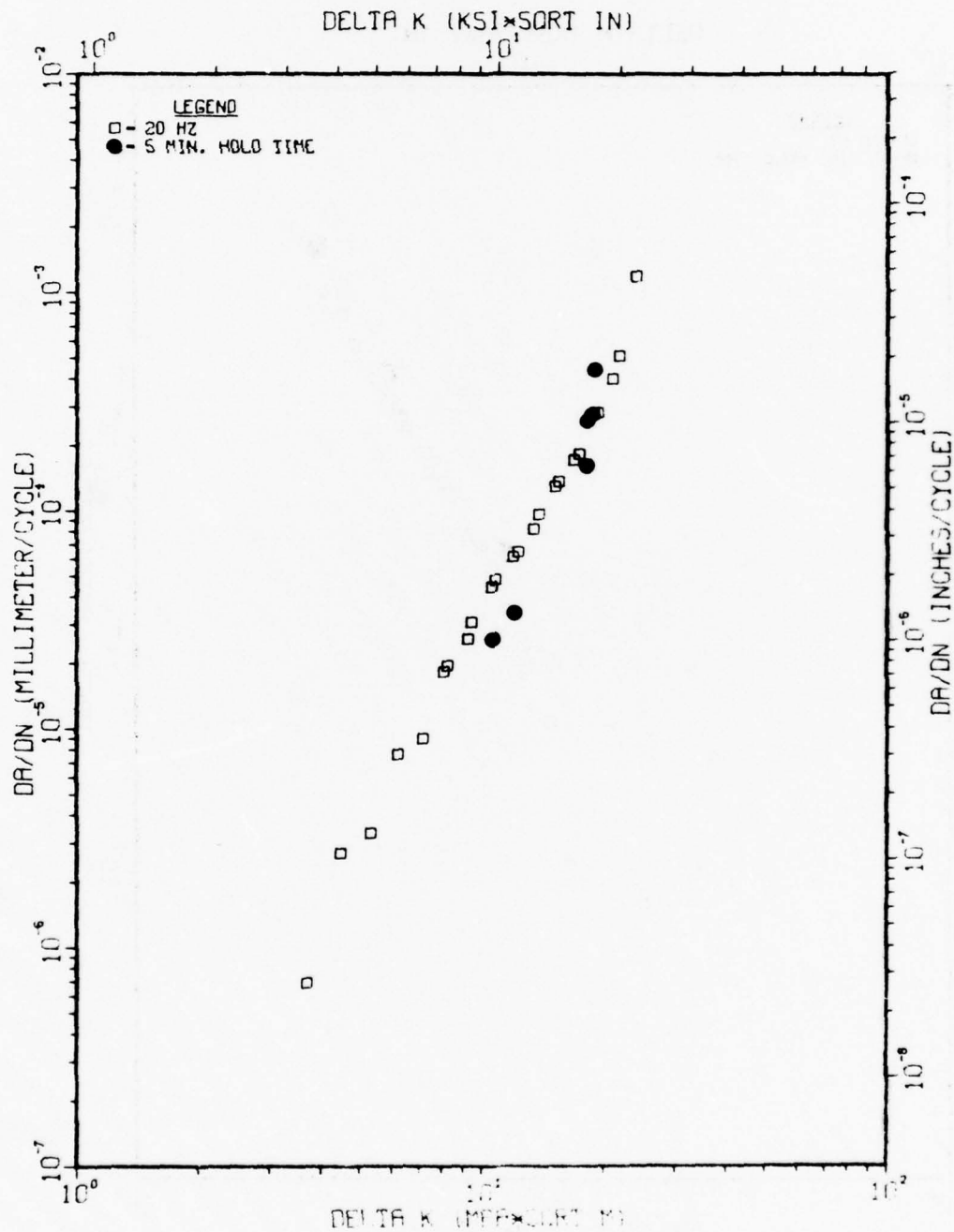
Fig. II-36 FCP data for Condition 8 (2-8-3/9), 68°F, dry air, 20 Hz,
R = 0.3; including 5 min hold-time data at approximately
2.5 x 10⁻⁵, 2.5 x 10⁻⁴, and 2.5 x 10⁻³ mm/cycle.

148

TI-6AL-2SN-4ZR-6MO (COND. 10), 68F, DRY AIR, R-0.3
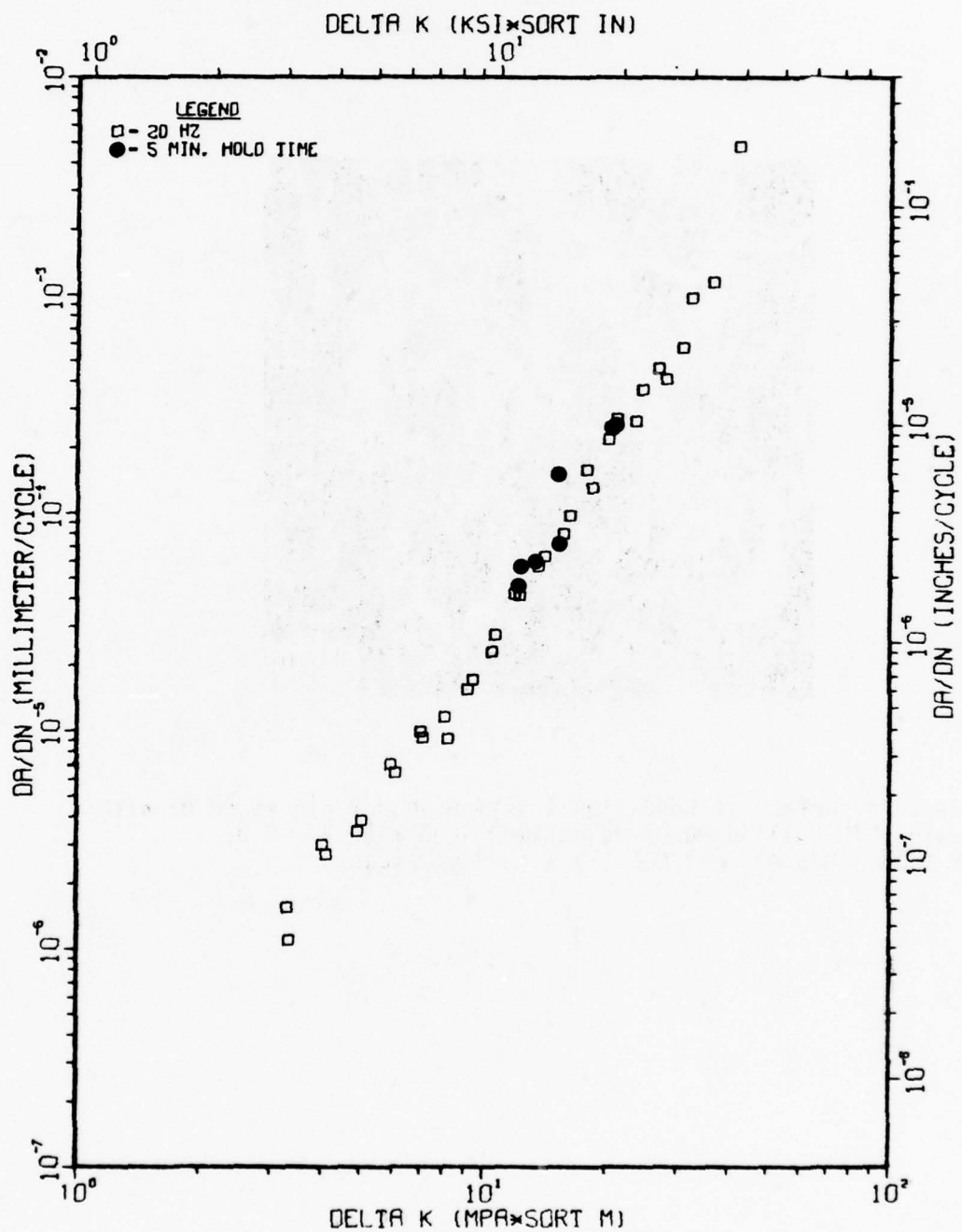
Fig. II-37 FCP data for Condition 10 (2-10-2/24), 68°F, dry air, 20 Hz, R = 0.3; including 5 min. hold-time data at approximately 2.5×10^{-5}, 2.5×10^{-4}, and 2.5×10^{-3} mm/cycle.
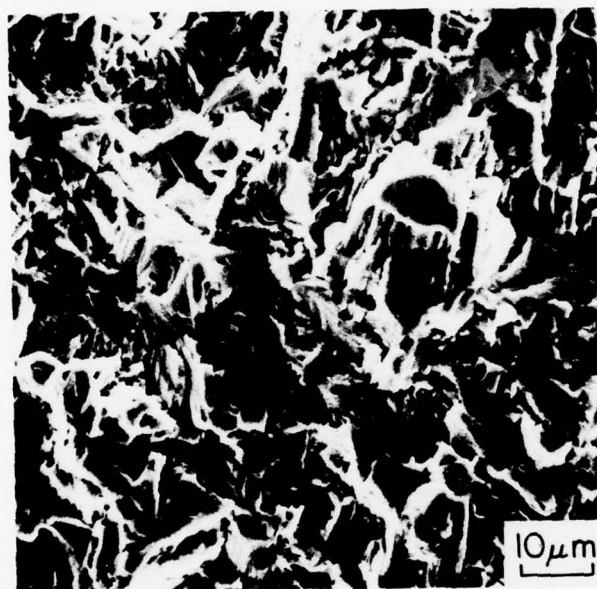
Fig. II-38 Fracture surface of Condition 1 tested in dry air at 20 Hz with a 5-min hold (called HOLD) at maximum load with R = 0.3, ΔK = 14.3 MPa·m$^{\frac{1}{2}}$, da/dN = 1.5 x 10^{-4} mm/cycle.
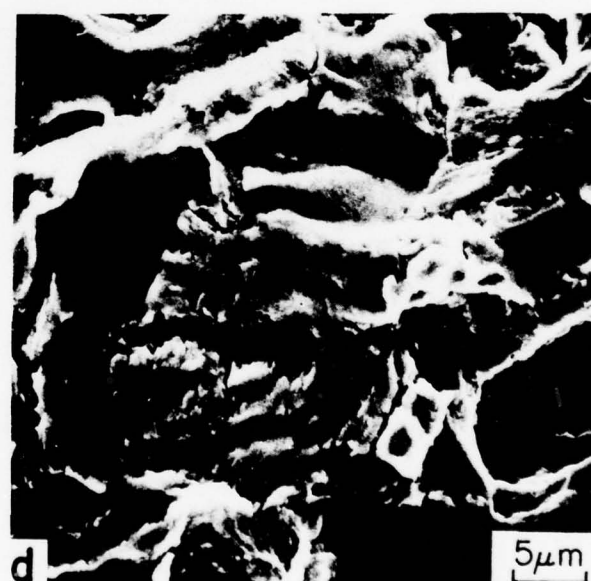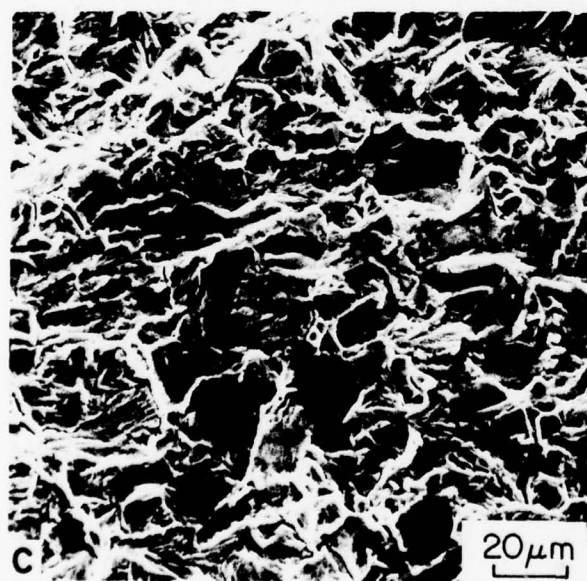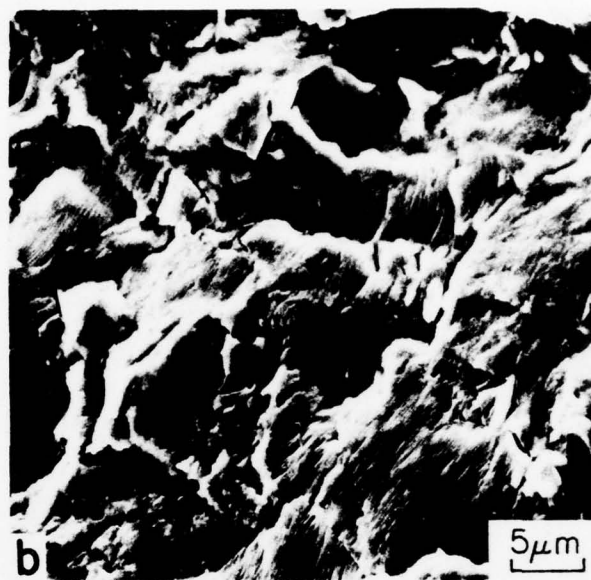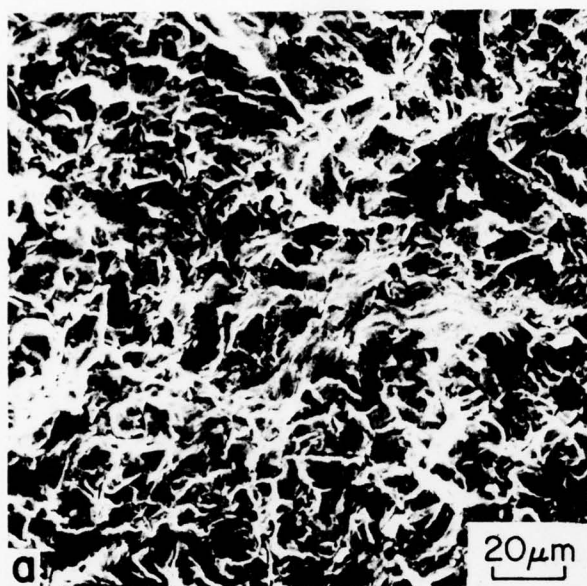
Fig. II-39 Fracture surface of Condition 1 tested at R = 0.3 in dry air.
(a,b) HOLD: ΔK = 20.9 MPa·m$^{\frac{1}{2}}$, da/dN = 3.6 x 10^{-4} mm/cycle;
(c,d) 20 Hz: ΔK = 20.8 MPa·m$^{\frac{1}{2}}$, da/dN = 2.6 x 10^{-4} mm/cycle.

151
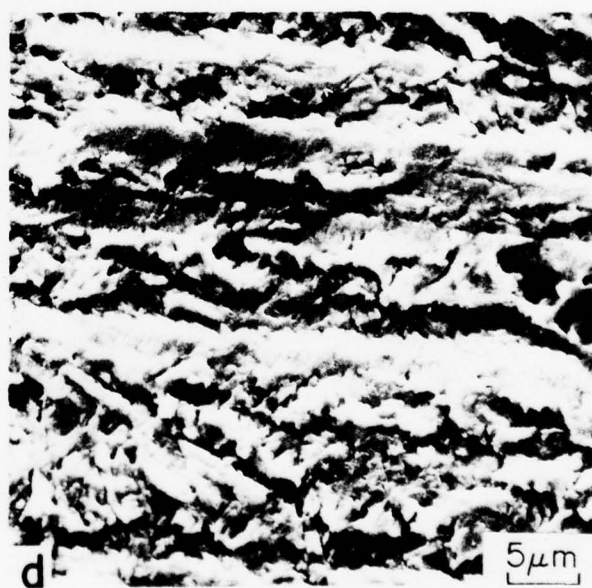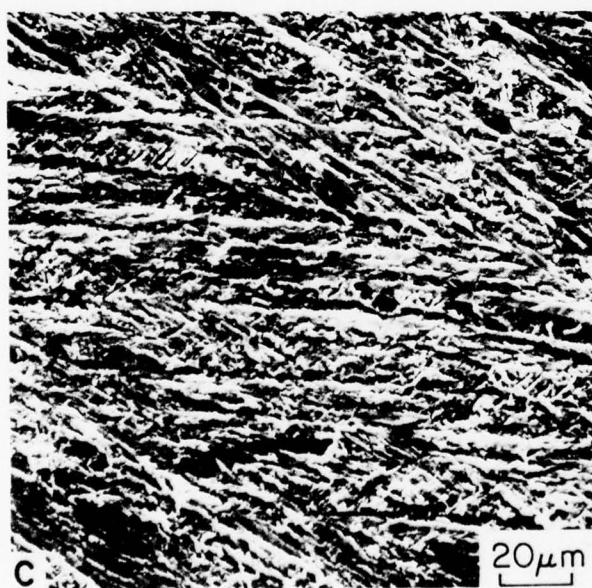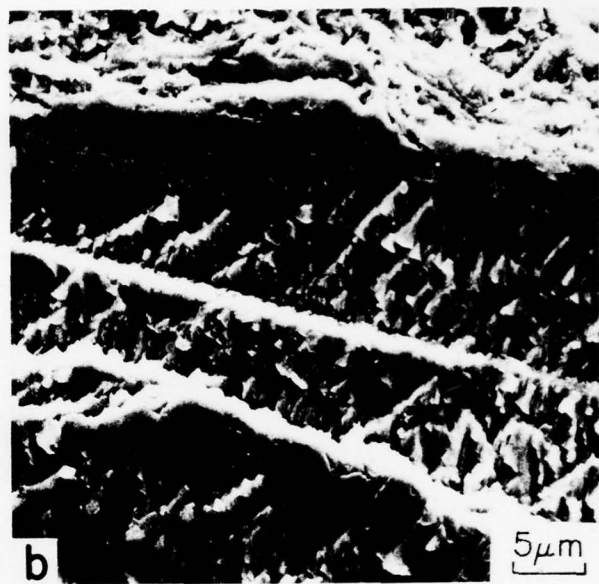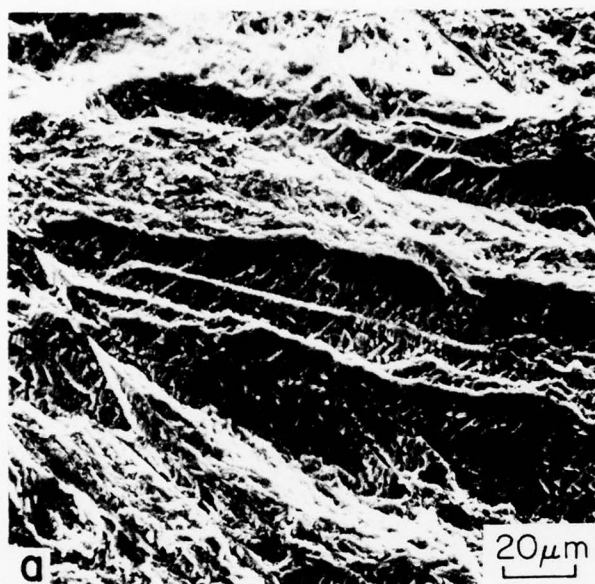
Fig. II-40   Fracture surface of Condition 5 tested at R = 0.3 in dry air.
(a,b) HOLD: ΔK = 13.8 MPa·m$^{\frac{1}{2}}$, da/dN = 9.4 x 10^{-5} mm/cycle;
(c,d) 20 Hz: ΔK = 16.8 MPa·m$^{\frac{1}{2}}$, da/dN = 8.2 x 10^{-5} mm/cycle.
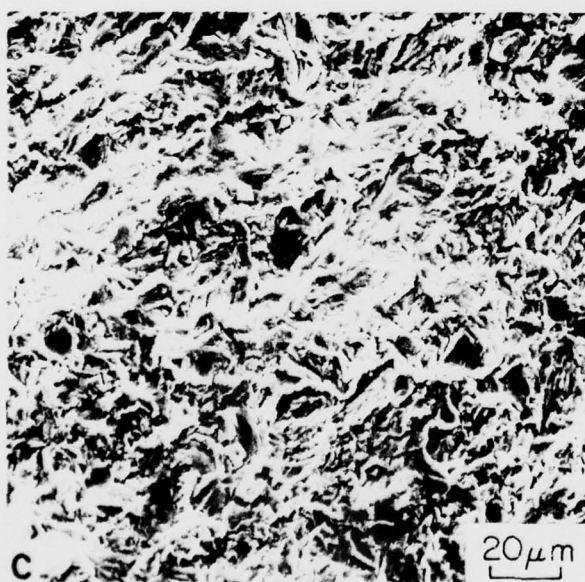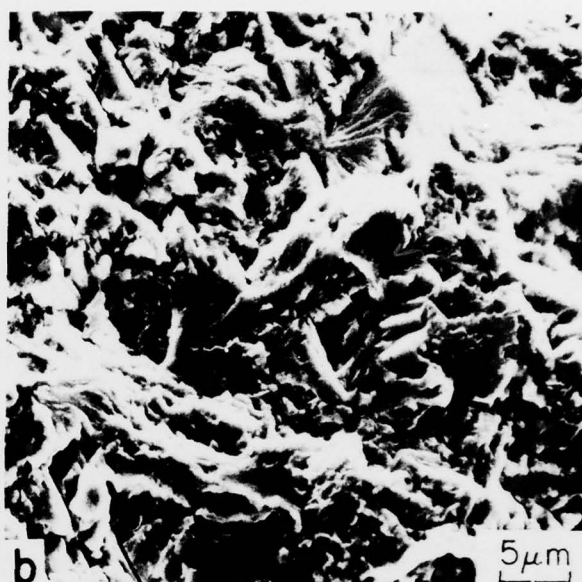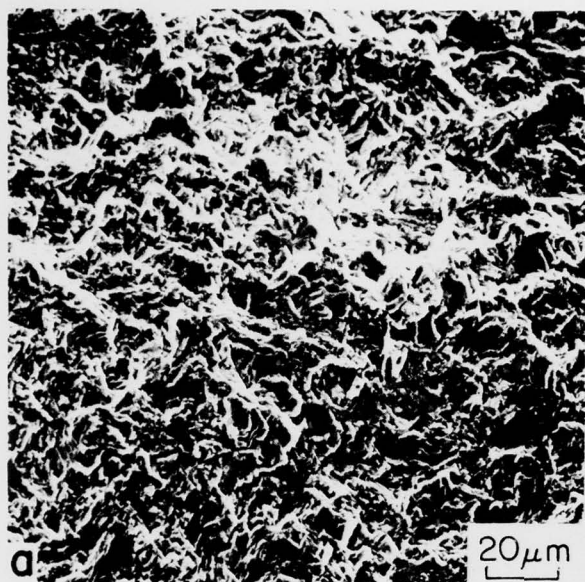
Fig. II-41 Fracture surface of Condition 7 tested at R = 0.3 in dry air.
(a,b) HOLD: ΔK = 12.3 MPa·m$^{\frac{1}{2}}$, da/dN = 8.0 x 10^{-5} mm/cycle;
(c,d) 20 Hz: ΔK = 12.3 MPa·m$^{\frac{1}{2}}$, da/dN = 3.9 x 10^{-5} mm/cycle.
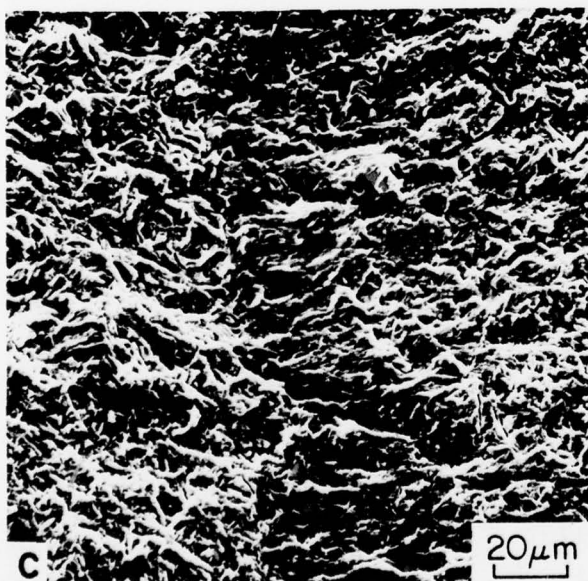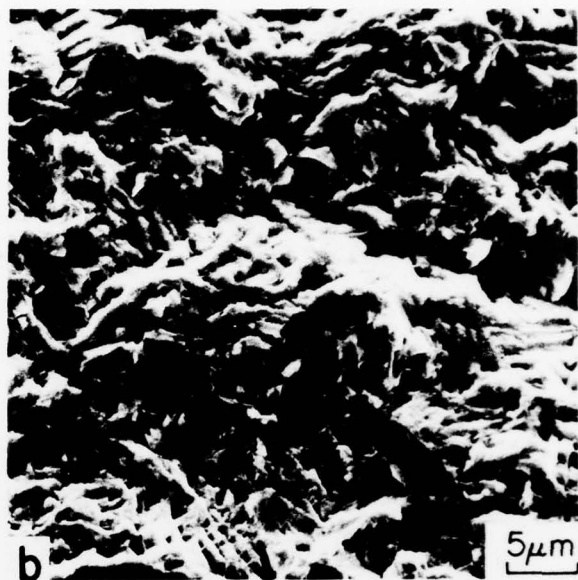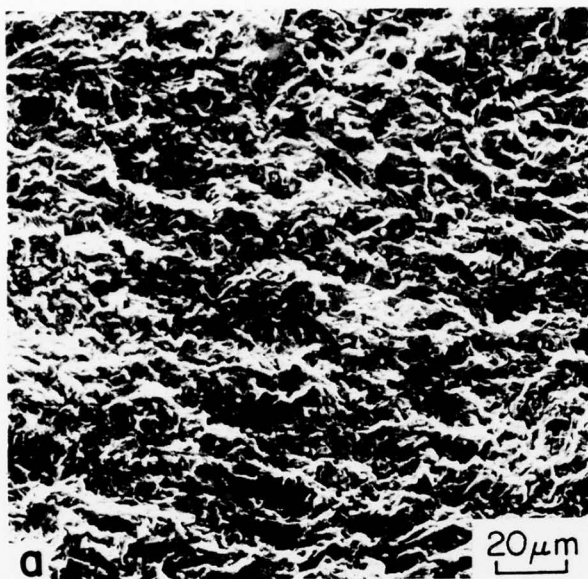
Fig. II-42   Fracture surface of Condition 8 tested at R = 0.3 in dry air.
(a,b) HOLD: ΔK = 10.6 MPa$\cdot$m$^{\frac{1}{2}}$, da/dN = 2.5 x 10^{-5} mm/cycle;
(c,d) 20 Hz: ΔK = 10.8 MPa$\cdot$m$^{\frac{1}{2}}$, da/dN = 4.8 x 10^{-5} mm/cycle.

154
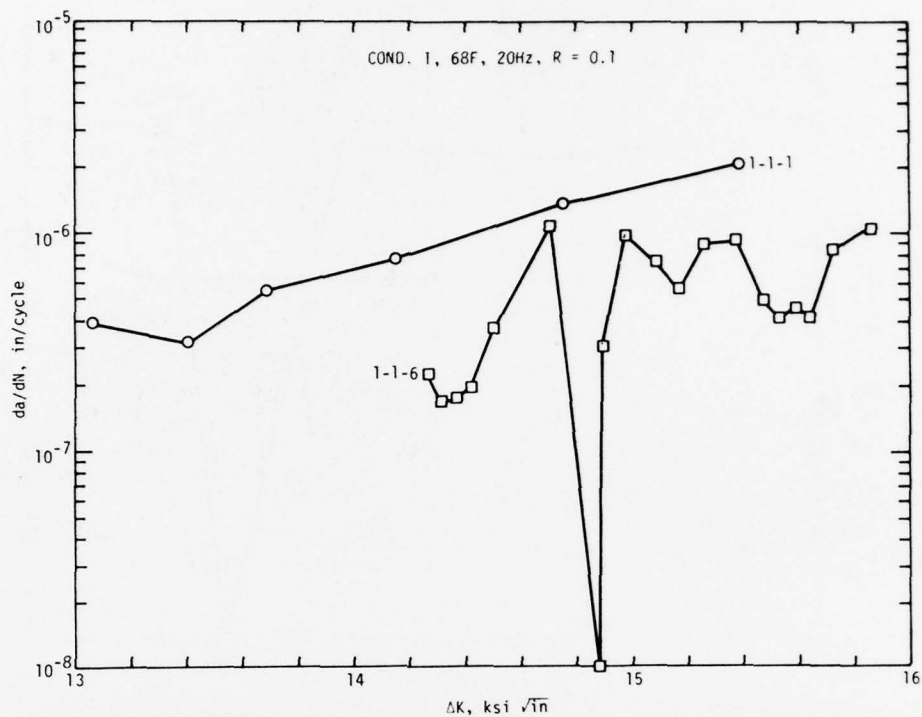
Fig.II-43 FCP data for Condition 1 (1-1-6), subjected to 1.75 σ max overload for 20 cycles, 68°F, dry air, 20 Hz, R = 0.1.
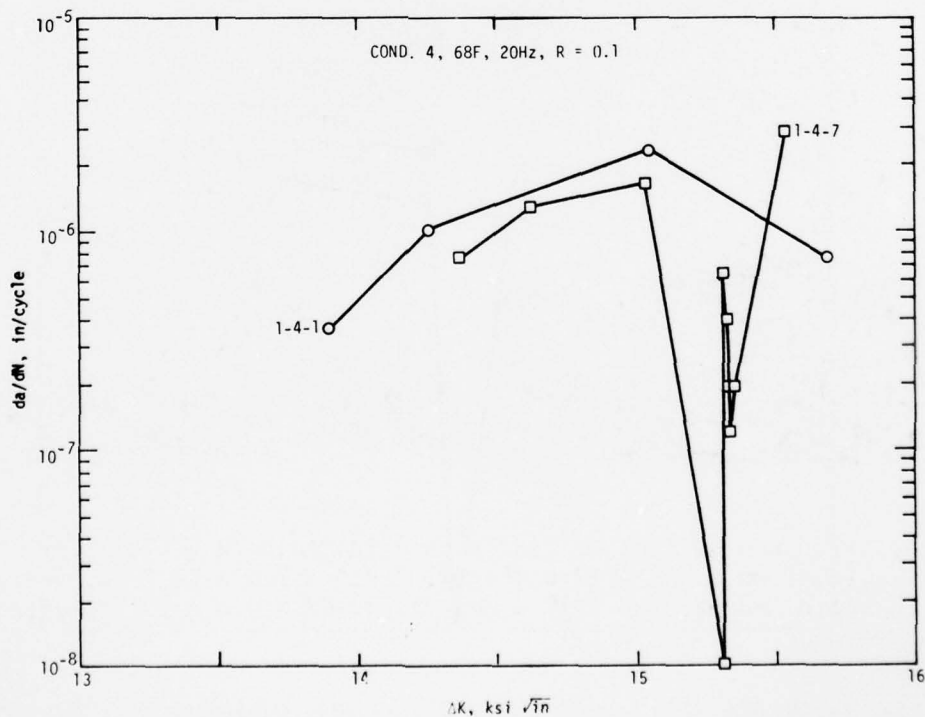
Fig.II-44 FCP data for Condition 4 (1-4-7), subjected to 1.75σ max overload for 20 cycles, 68°F, dry air, 20 Hz, R = 0.1.

155
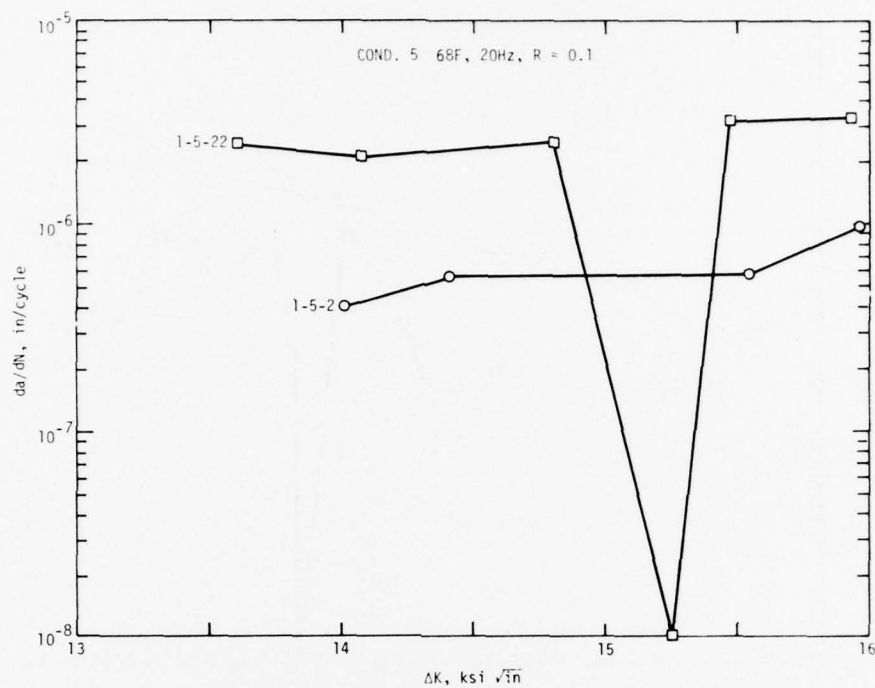
Fig. II-45   FCP data for Condition 5 (1-5-22), SUBJECTED TO 1.75σ max
overload for 20 cycles, 68°F, dry air, 20 Hz, R = 0.1.
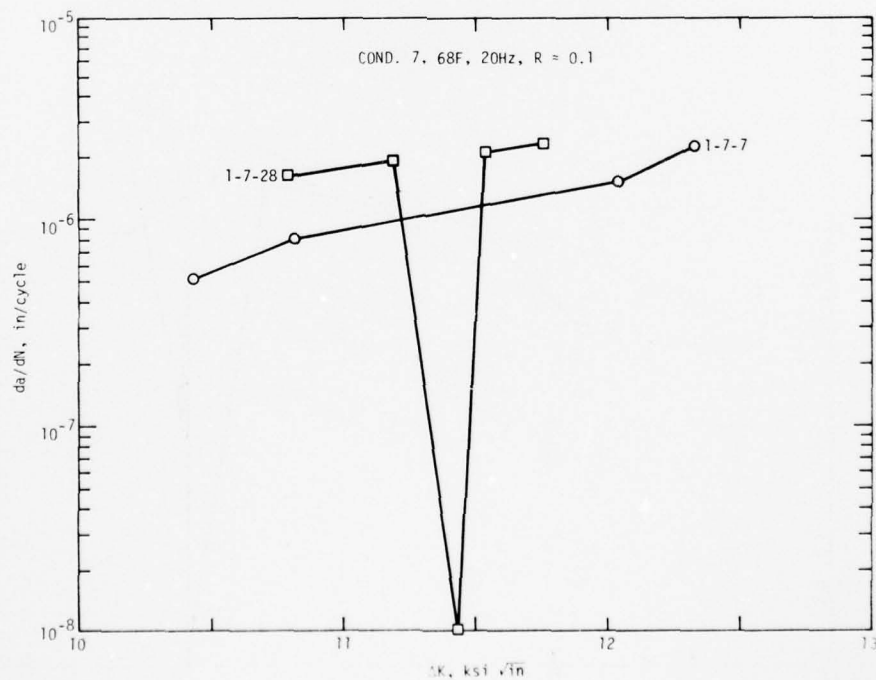
Fig. II-46   FCP data for Condition 7 (1-7-28), subjected to 1.75σ max
overload for 20 cycles, 68°F, dry air, 20 Hz, R = 0.1.

156
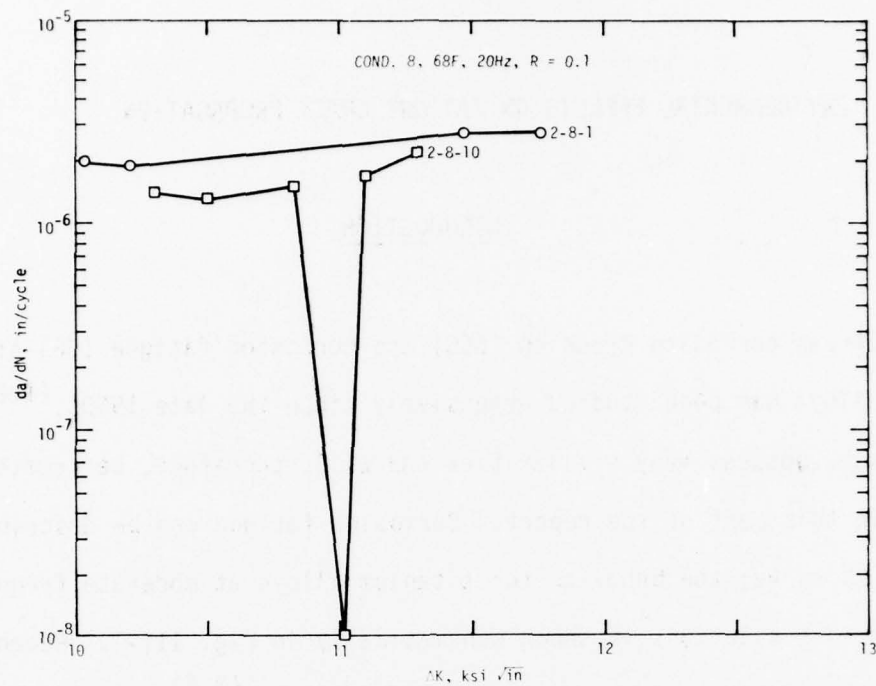
Fig. II-47   FCP data for Condition 8 (2-8-10), subjected to 1.75σ max overload
for 20 cycles, 68°F, dry air, 20 Hz, R = 0.1.
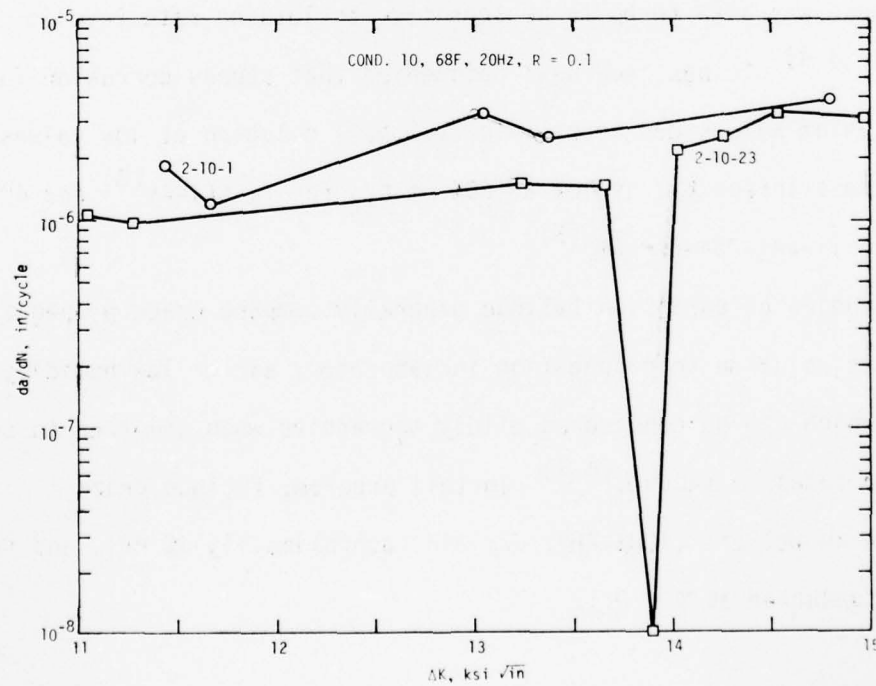
Fig. II-48   FCP data for Condition 10 (2-10-23), subjected to 1.75σ max overload
for 20 cycles, 68°F, dry air, 20 Hz, R = 0.1.

157

PART III: ENVIRONMENTAL EFFECTS ON FATIGUE CRACK PROPAGATION

INTRODUCTION

Stress corrosion cracking (SCC) and corrosion fatigue (CF) of titanium alloys has been studied extensively since the late 1960s.[1,2] The two processes possess many similarities and will, therefore, be treated together in this part of the report. Corrosion fatigue can be described by a da/dN vs. ΔK curve; the behavior for titanium alloys at moderate frequencies in aqueous salt solutions is shown schematically in Fig. III-1. Recent work has shown that fatigue crack propagation in Ti-6Al-4V[3,4] and Ti-6Al-2Sn-4Zr-6Mo[5] can be accelerated significantly by an aqueous salt environment. This response was also found to be sensitive to loading rate (cyclic frequency).[3,4] It has been well documented that stress corrosion failures of $\alpha + \beta$ titanium alloys can occur in a 3.5% NaCl solution at low values of initial stress intensity; as low as 50% of K_{Ic} for Ti-6Al-4V[6] and 40% for K_{Ic} for Ti-6Al-2Sn-4Zr-6Mo[5].

Studies of corrosion fatigue generally compare crack propagation in aqueous salt solution to propagation in laboratory air or low humidity air either of which can be considered mildly aggressive when compared to crack propagation rates in vacuum.[4,7] In this program, fatigue crack propagation in wet air (100% RH), dry air (approximately 5% RH), and pure, dry argon was evaluated at R = 0.1.

158

Microstructure[1,5,6] and texture,[6,8] especially in microstructures containing a large volume fraction primary alpha, can significantly effect the stress corrosion cracking and corrosion fatigue behavior of titanium alloys. This study was, therefore, conducted on pancake forgings deliberately processed to as weak and as uniform a texture as possible permitting emphasis on microstructural effects alone.

EXPERIMENTAL PROCEDURE

The composition, forging process history, microstructure development, mechanical properties and texture of the Ti-6A1-4V and Ti-6A1-2Sn-4Zr-6Mo were described in Part I. All ten microstructures were evaluated in this portion of the program. The specimens for FCP measurement were prepared and precracked as detailed in the part of the report dealing with baseline FCP, Part II.

Crack length measurements were made optically on the specimen surface while the specimen was unloaded; measurements were made for $0.3 \leqslant a/W \leqslant 0.75$. Testing was conducted in wet air (100% RH), dried air (approximately 5% RH), and pure, dry argon at 20 Hz and a load ratio $R = \sigma_{min}/\sigma_{max}$ of 0.1. The latter two environments were dried by passing the gas through anhydrous $CaSO_4$ (Drierite) into a sealed polyethylene bag surrounding the specimen. Testing in the 3.5% NaCl solution at $R = 0.1$ was done at both 1 and 20 Hz.

Upon termination of FCP measurements, the specimen was fractured at high ΔK and fractographic examination was conducted in a scanning electron microscope (SEM).

K_{Iscc} in 3.5% NaCl was determined in a 100 h stress corrosion test using a wedge-opening-loaded, double-cantilever-beam (DCB) specimen shown in Fig. III-2. Details of the specimen design and the method of compliance analysis and calibration are given in a paper by Williams and Nelson.[11] K_{Iscc} specimens were precracked to $0.6 \leqslant a \leqslant 0.8$ and bolt loaded to a crack opening displacement (δ) equivalent to $0.9 \, K_{Ic}$. For some of the conditions for which K_{IC} had not been determined, the initial stress intensity level, $(K_I)_i$, was subsequently found to be less than $0.9 \, K_{Ic}$; these specimens were reprecracked and reloaded to $0.9 \, K_{Ic}$. Loading was accomplished with 3.5% NaCl solution in contact with the crack tip; specimens were then immersed in salt solution for 100 h after which the crack length was measured by the compliance technique. For those specimens in which no crack growth was measured and for those in which $(K_I)_i$ was less than $0.9 \, K_{Ic}$, the specimens were reprecracked and retested. After testing, the specimens were broken open under cyclic loading and the initial and final crack position measured on the fracture face. SEM analysis of the fracture face for crack position and fracture mode was conducted.

RESULTS

FCP Measurements

FCP data obtained for Conditions 1, 4, 5, and 7 of Ti-6Al-4V and
Conditions 8 and 10 of Ti-6Al-2Sn-4Zr-6Mo in argon, dry air, and wet air are
shown in Fig. III-3 through III-8. In general, the differences in the three
environments is not very significant, particularly for the alloys containing
equiaxed primary alpha (Conditions 1, 7, and 8) but trends differ from
condition to condition. For Condition 1, for example (Fig. III-3), argon
produces the slowest growth rate at very low ΔK, while in Condition 4
(Fig. III-4), the argon and wet air data agree well, and essentially lie in
the center of the more scattered dry air data (we have shown in Part II that
appreciable crack branching occurs in Condition 4). Yet in Condition 7
(Fig. III-6), the wet air data exhibits higher growth rates over the ΔK range
of 7-20 MPa·$m^{\frac{1}{2}}$. Condition 8 (Fig. III-7) appears highly insensitive to the
three environments. The two microstructures that appear most sensitive to
these three environments are beta-quenched Ti-6Al-4V, Condition 5, and
beta-forged Ti-6Al-2Sn-4Zr-6Mo, Condition 10, although the results for the two
beta processed structures are reversed. For Condition 5, argon produces an
increase in growth rate relative to dry air and wet air over most of the
growth rate range while for Condition 10, argon produces a decrease in crack
growth rate relative to dry air and wet air. The difference in behavior of
these two conditions in the argon environment will be discussed in terms of
fracture path in the fractography section.

161

Testing in 3.5% NaCl solution has been performed at two frequencies to determine whether the lower frequency, 1 Hz, might show additional effects due to stress corrosion cracking, the combined behavior being known as corrosion fatigue. The data is shown in Fig. III-9 through III-18. It can also be noted with the exception of RA Condition 1 that the lower loading rate (1 Hz) did not effect the growth rates at low growth rates ($\Delta K <$ approximately 20 MPa$\cdot$m$^{\frac{1}{2}}$) but that significant increases occur for the high growth rate end of the curve when testing at 1 Hz. Fatigue crack propagation in the material of this program is in general only mildly accelerated (less than a factor of two or three) and in some cases is not accelerated at all by testing in a 3.5% NaCl solution. This is true for testing at 20 and 1 Hz with the following exceptions for Ti-6Al-4V: (1) RA Condition 1 at both 20 and 1 Hz (Fig. III-9), (2) Condition 3 (50% primary α) at 20 Hz (Fig. III-11), (3) βQ Condition 5 at 20 Hz (Fig. III-13), and (4) Condition 6 (STA) and Condition 7 (STOA) at 20 Hz and low ΔK (Fig. III-14 and III-15). For Ti-6Al-2Sn-4Zr-6Mo the only significant acceleration occurred for Condition 9 (50% primary α) and Condition 10 (beta heat treat + STA) at $\Delta K >$ approximately 20 MPa$\cdot$m$^{\frac{1}{2}}$ (Fig. III-17 and III-18). It should be noted that the maximum increase for either alloy was a factor of ten, see βQ Condition 5, Fig. III-13.

Examining the effect of microstructure in the 3.5% NaCl solution, the following trends are observed. For Ti-6Al-4V at 20 Hz, Fig. III-19, the most resistant Conditions are 1, 4, and 5, with 5 showing a slight superiority at low ΔK. A distinctly less resistant group includes Conditions 2, 3, 6, and 7, with 7 the least resistant at intermediate values of ΔK. For

162

Ti-6Al-2Sn-4Zr-6Mo at 20 Hz, Fig. III-20, Condition 10 is more resistant than
are Conditions 8 and 9. Thus, the 20 Hz data in salt water largely follow the
trends in air, and FCP rates are only mildly accelerated relative to data in
air (e.g., Condition 5 at ΔK = 20 MPa·$m^{\frac{1}{2}}$ shows da/dN increased by less than
a factor of two). In a few cases, such as Condition 8, Fig. III-20, a
definite "S" curve is developed, which often indicates the onset of
significant environmental effects, although the FCP rate is not markedly
increased.

Results at 1 Hz, which do not extend to equally low da/dN values
because of the frequency difference, are shown in Fig. III-21 and III-22. For
Ti-6Al-4V, Fig. III-21, the groupings differ somewhat from those in air at
20 Hz. The least FCP resistant conditons are 6 and 7; 1, 2, and 3 are similar
and of intermediate resistance; and the most resistant are Conditions 4
and 5. At low ΔK values, Condition 5 exhibits the slowest FCP. For
Ti-6Al-2Sn-4Zr-6Mo, Fig. III-22, Condition 10 is somewhat more resistant than
are Conditions 8 and 9. These differences will be addressed below in terms of
fractography.

Stress Corrosion Cracking (K_{Iscc}) Tests

Stress corrosion cracking (SCC) tests have also been performed.
These were intended to be conducted at an initial K level of 90% K_{Ic}, with a
"threshold K" or K_{Iscc} being obtained as the K level due to crack growth in
100 h in 3.5% NaCl solution. As Table III-I shows, the relatively high K_{Ic}
values of these alloys led to the expected starting values $(K_I)_i$, in fact,

163

being below 90% K_{Ic}. Conditions 1, 4, 9, and 10 were reprecracked and retested; the results for all conditions are given in Table II-I.

Fractography

Fracture surface examination of Conditions 5 and 10 tested in argon, dry air and wet air were made to analyze the difference crack path morphology. The results are shown for βQ, Condition 5 in Fig. III-23 and for beta heat treated + STA, Condition 10 in Fig. III-24. In Condition 5, the beta quenched microstructure of Ti-6Al-4V, exhibits a behavior which is suggestive of interaction of the dry air and wet air environments with grain boundaries and colony boundaries. At low ΔK, the growth rates in both dry air and wet air are less than in argon and both the former exhibit considerably more crack branching and a more tortuous crack path, cf Fig. III-23(b) and (c) with III-23(a). Condition 10, which is beta processed Ti-6Al-2Sn-4Zr-6Mo also shows an effect of environment, although significantly smaller (factor of four versus a factor of ten) and one in which the aggressive environments (dry air and wet air) produce increases in growth rate. Associated with this increase in crack growth rate is a more planar fracture, cf Figs. III-24(b) and (c) with Fig. III-24(a). It would appear that for both these transformed beta type microstructures dry air and wet air interact with the crack tip, thereby influencing the crack growth rate. For Condition 5, the two environments promote grain boundary and colony boundary cracking and a net reduction in macroscopic crack growth rate. Conversely, for Condition 10 in which the strength differential between grain boundaries and the matrix is probably less

164

than in beta quenched Ti-6Al-4V, the moisture in the dry air and wet air adsorbed at the crack tip promotes a more planar, more rapid crack propagation.

It is instructive to consider the fracture behavior observed in salt water with that observed in air to illustrate the points discussed. Figure III-25 shows the FCP results for Condition 1 in air, and Fig. III-26 shows the results in 3.5% NaCl solution at 1 Hz for the same condition and with similar magnifications. Note in Fig. III-26 that areas of "cleavage-like" fracture are observed, with a size which appears to correspond to the α grain size. It is presumed that these facets correspond to the typical stress corrosion fracture morphology on basal planes or planes oriented about 15° away from the basal plane. As Fig. III-9 shows, the FCP rates are not greatly different in the growth range of Figs. III-25 and III-26, and this may occur because transgranular fracture with some secondary cracking occurs in each case.

The same comparison for Condition 4 is shown in Fig. III-27 (air) and Fig. III-28 (salt water, 1 Hz). Figure III-27 shows distinct striation formation and apparent tearing across Widmanstätten α plate colonies, which is less distinct at these intermediate FCP rates. In Fig. III-28, smoother fracture with some areas of striations is seen, and, at lower magnification, Fig. III-28(c), the fracture topography appears to be correlated with the microstructural size and morphology. Here, as in Condition 1, the fracture behavior is not greatly altered and no major change in FCP rate occurs relative to that in air.

165

Figure III-29 (air) and Fig. III-30 (salt water, 1 Hz) continue the comparison to Condition 6. In this case, Fig. III-29(b), FCP occurs in air by ductile tearing in the Widmanstätten $\alpha+\beta$, and striation formation in the primary α, although the correlation with microstructure is not pronounced. In salt water, a fracture surface of similar roughness is produced (cf Fig. III-29(c) and III-30(b) to recognize this) but "cleavage-like" areas are evident. In addition, energy absorption due to secondary cracking is less apparent in salt water. Thus, FCP rate is increased in salt water relative to air, by as much as a factor of three.

DISCUSSION

The argon tests show considerable similarity to the dry air results with the exception of RA Condition 1 at low ΔK and Conditions 5 and 10, suggesting that dry air is not an aggressive environment in Ti-6Al-4V or Ti-6Al-2Sn-4Zr-6Mo except that it is mildly aggressive in recrystallization annealed Ti-6Al-4V and in beta forged Ti-6Al-2Sn-4Zr-6Mo by producing a more transgranular, less tortuous path. Wet air is not an aggressive environment either, except in a few cases (e.g., Conditions 1 and 7 at low FCP rates). In summary it can be concluded, in general, that neither dry air nor wet air are very aggressive environments for the uniform and weakly textured Ti-6Al-4V and Ti-6Al-2Sn-4Zr-6Mo of this study. It is reasonable that environmental effects would be most evident at low FCP, so the above findings should not be interpreted as no effect of either dry or wet air. With the sole exception of Condition 10, however, these effects are generally modest.

166
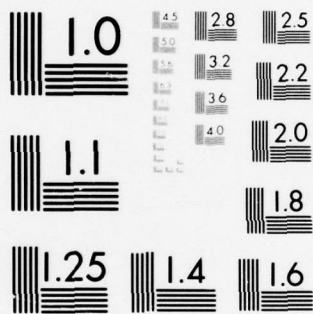
MICROCOPY RESOLUTION TEST CHART

NATIONAL BUREAU OF STANDARDS-1963-A

The FCP results for testing in 3.5% NaCl solution are not surprising and continue to point out the complex interactions between chemistry processing, microstructure, texture, environment and loading rate in controlling fatigue crack growth rate in titanium alloys.

If the results of this program are compared with several previous studies on corrosion fatigue,[10-13] it can be shown that one of the major factors affecting crack acceleration in 3.5% NaCl is texture. Hall, et al[10] studied Ti-6Al-4V in both the RA and βA conditions, and included two different oxygen levels for the βA material, 0.06 and approximately 0.11 wt%. The RA material was analyzed by the supplier as containing 0.13 wt% oxygen; by Boeing as 0.084 wt% oxygen. The βA material had a random texture, the RA material a "slight" basal transverse texture. In the study the only case in which FCP acceleration at R = 0.1 was significantly greater than a factor of three was for the RA condition at 0.1 Hz, in which case the growth rate in 3.5% NaCl was a factor of ten greater than that at the same frequency in distilled water. Ferguson and Berryman[11] in their study of B-1 materials evaluated Ti-6Al-4V in many product forms and microstructural conditions. FCP rates were measured in a variety of atmospheres, including low humidity air (LHA) and fuel tank sump residue water (STW) containing a 0.12% metal chloride solution. Such a solution is reported by others[13] to be somewhat less aggressive than 3.5% NaCl, the effect depending on loading frequency. Increases in crack growth rate up to a factor of four in STW were found, but of special interest are two cases in which LHA and STW results are identical (see Fig. 8.2.1.5-9 and 8.2.1.5-10 of Ref. 11). Textures were not

167

specified in this work, but an examination of the L and T tensile properties indicate that most material had a random texture.

Sommer and Creager[12] intentionally produced material of a very strong basal transverse texture (14 to 20 times random) and found a factor of five to ten increase of growth rate in 3.5% NaCl compared to laboratory air. The large increases in FCP were associated with TL specimens, ones in which the crack is propagating parallel to the maximum concentration of basal planes of the α phase. The effect was also found to be frequency dependent, with the largest accelerations occurring at 1 Hz. Finally, the work of Ryder et al[13] on "strongly" textured, RA Ti-6Al-4V showed similar accelerations for material tested in the TL orientation. In this work, samples were tested in 3.5% NaCl at 10, 1, and 0.1 Hz FCP was compared to that at 10 Hz in laboratory air. It was found that growth rate increased with decreasing frequency (a factor of 10, 50, and 100 for 10, 1, and 0.1 Hz, respectively). Some "weakly" textured sheet was also tested, and a factor of ten increase in FCP for 0.1 Hz loading in 3.5% NaCl compared to 10 Hz loading in high humidity ($\geqslant$ 85% RH) air was measured.

Oxygen effects were evaluated in two studies, 0.06 vs 0.11 wt% oxygen in the work by Hall, et al[11] and 0.09 vs 0.16 wt% oxygen in the work by Sommer and Creager.[12] At 1 Hz in the former and at 1 and 10 Hz in the latter study, "low" oxygen and "standard" oxygen material behaved essentially the same in 3.5% NaCl.

From the preceeding studies and the current program, it can be concluded, that in the absence of a strong texture, only modest increases in

FCP (less than a factor of ten) might be expected for the alloy microstructures of this study. Accelerated propagation when found in this program is often associated with "cleavage-like" fracture of primary alpha particles in equiaxed primary alpha microstructures, Fig. III-26 and III-30, or a more transgranular propagation path in beta processed microstructures such as Conditions 4, 5, and 10. These trends presumably reflect the existence of a stress corrosion crack velocity which is smaller than the imposed da/dN in air.

The K_{Iscc} results suggest that all the microstructural conditions studied are resistant to stress corrosion cracking, the worst case being Condition 10 with a $K_{Iscc} = 0.78 K_{Ic}$. This behavior could be attributed in part to the high inherent toughness of the microstrucural conditions and in part to the uniform and weak texture.

It should be pointed out that there are reports of more severe sustained load cracking at lower K levels, when more nearly plane strain conditions exist.[14] In the present program using salt water, however, K/K_Q values as low as 0.5 (Condition 4), 0.65 (Condition 1), and 0.71 (Condition 10) did not result in any crack movement. Condition 10 was certainly in plane strain at the 0.71 ratio.

In conclusion, it can be observed that the $\alpha + \beta$ microstructures are not significantly sensitive to environment and that the beta microstructures (beta annealed and beta quenched Ti-6Al-4V and beta forged Ti-6Al-2Sn-4Zr-6Mo) are only weakly effected by the environments used in this study.

169

REFERENCES

1. D. N. Fager and W. F. Spurr, Trans. ASM, 1968, Vol. 61, pp. 283-92

2. D. E. Piper, S. H. Smith and R. V. Carter, Metals Eng. Quart., 1968, Vol. 8, pp. 50-63

3. D. B. Dawson and R. M. Pelloux, Met. Trans., 1974, Vol. 5, pp. 723-731

4. H. Döker and D. Munz, "Influence of Environment onthe Fatigue Crack Propatation of Two Titanium Alloys," Proceedings of the Conference on the Influence of Environment on Fatigue, Mechanical Engineering Publications, London, 1977, pp. 123-130

5. J. C. Williams, N. E. Paton, P. J. Stocker and H. L. Marcus, Space Shuttle Materials, Vol. 3, SAMPE, Azusa, California, 1971, pp. 643-651

6. M. J. Blackburn, J. A. Feeney, and T. R. Beck, in "Advances in Corrosion Science and Technology," Vol. 3, 1973, Plenum, New York, pp. 67-292

7. P. E. Irving and C. J. Beevers, Met. Trans., 1974, Vol. 5, pp. 391-398

8. C. A. Stubbington, Alloy Design for Fatigue and Fracture Resistance, pp. 3-1 to 3-19, Report AGARD-CP-185, NATO, Brussels, January 1976

9. D. P. Williams and H. G. Nelson, Met. Trans., 1972, Vol. 3, pp. 2107-2113

10. L. R. Hall, R. W. Finger, and W. F. Spurr, "Corrosion Fatigue Crack Growth in Aircraft Structural Materials," AFML-TR-73-204, Wright-Patterson AFB, Ohio, September 1973

11. R. R. Ferguson and R. G. Berryman, "Fracture Mechanics Evaluation of B-1 Materials," AFML-TR-76-137 (Volume I), Air Force Materials Laboratory, Wright-Patterson AFB, Ohio, October 1976

12. A. W. Sommer and M. Creager, "Research Toward Developing an Understanding of Crystallographic Texture on Mechanical Properties of Titanium Alloys," AFML-TR-76-222, Air Force Materials Laboratory, Wright-Patterson AFB, Ohio, January 1977

13. J. T. Ryder, W. E. Krupp, D. E. Pettit, and D. W. Hoeppner, in Corrosion Fatigue Technology, ASTM-STP 642, 1978, pp. 202-22

14. D. N. Williams, Mater. Sci. Eng., 1975, Vol. 18, p. 149

TABLE III-I
STRESS CORROSION CRACKING DATA

Condition	K_Q, ksi in$^{\frac{1}{2}}$	K_Q, MPa·m$^{\frac{1}{2}}$	Valid	(K_I) ksi in$^{\frac{1}{2}}$	(K_I) MPa·m$^{\frac{1}{2}}$	$(K_I)_i/K_Q$	(K_I) 100 h ksi in$^{\frac{1}{2}}$	K_{Iscc} MPa·m$^{\frac{1}{2}}$	K_{Iscc}/K_Q
1	109.3 / 110.6	120.1 / 121.5	No(1) / No(1)	71.0 / 99.0	78.0 / 108.8	0.65 / 0.90	(3) / (3)	(3) / (3)	0.90
2	111.0 / 114.0	122.0 / 125.3	No(1) / No(1)	101.0	111.0	0.90	94.1	103.4	0.84
3	102.5 / 99.2	112.8 / 109.1	No(2) / No(2)	90.8	99.8	0.90	89.5	98.4(3)	0.89
4	108.9 / 106.7	119.8 / 117.4	No(1) / No(1)	64.0 / 97.0	70.3 / 106.6	0.59 / 0.90	(3) / 96.6	(3) / 106.2	0.90
5	91.6 / 92.2	100.8 / 101.3	Yes / Yes	80.0	87.9	0.87	74.9	82.3	0.82
6	77.5 / 75.1	85.2 / 82.6	No(2) / No(2)	69.0	75.8	0.90	68.5	75.3(3)	0.90
7	69.5 / 68.7	76.4 / 75.5	Yes / Yes	75.0	82.4	1.09	71.0	78.0	"1.03"
8	39.4 / 38.5	43.3 / 42.3	Yes / Yes	34.0	37.4	0.87	32.0	35.2	0.82
9	36.9 / 36.4	40.5 / 40.1	Yes / No(2)	33.0 / 33.0	36.3 / 36.3	0.90 / 0.90	(3) / 32.9	(3) / 36.2	0.90
10	64.4 / 65.5	70.8 / 72.1	Yes / Yes	46.0 / 58.5	50.6 / 64.3	0.71 / 0.90	(3) / 51.0	(3) / 56.0	0.78

(1) Failed thickness requirement.

(2) Failed precrack curvature requirement.

(3) No conclusive evidence either from compliance measure or fractography that crack extended.
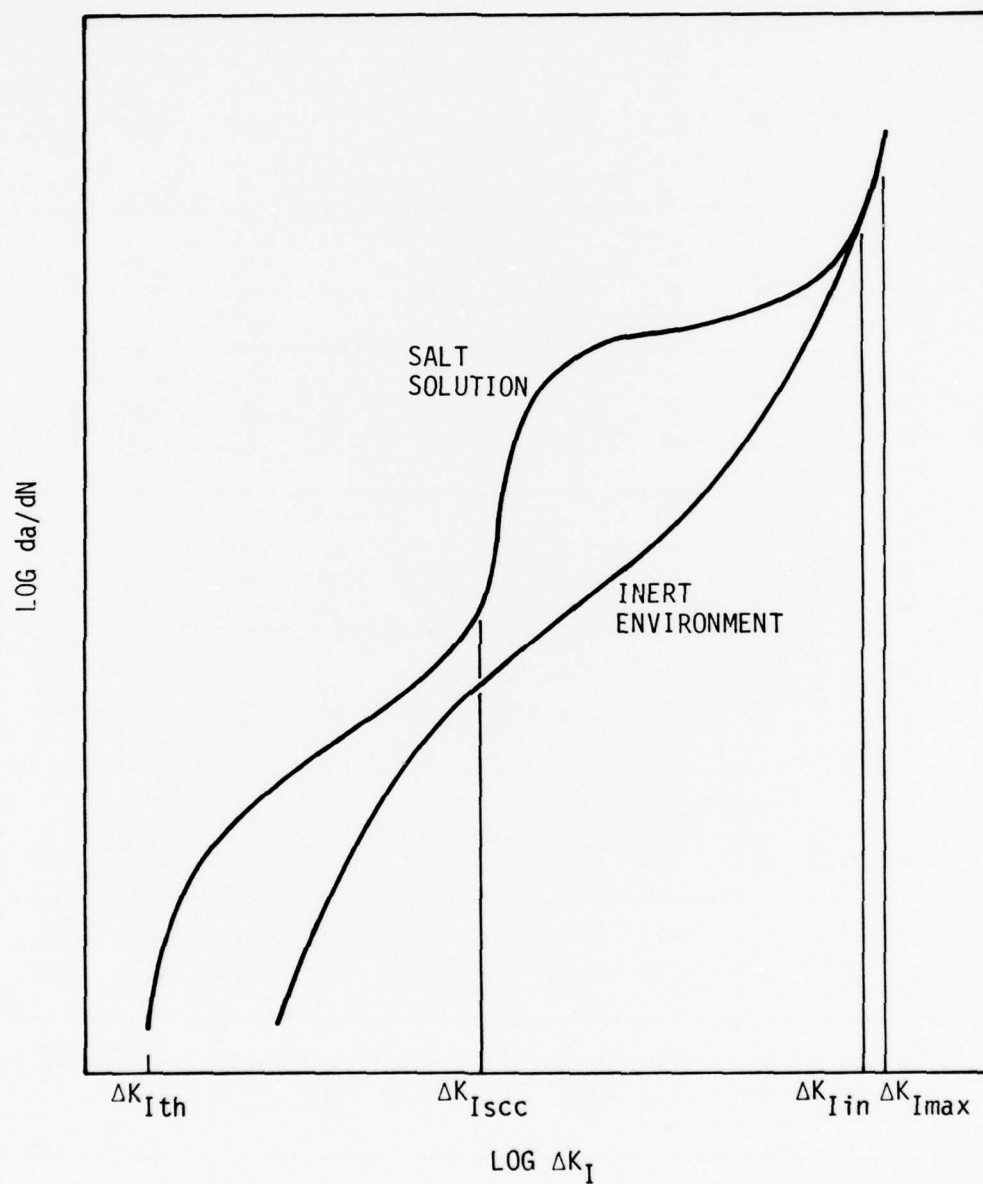
Fig. III-1 Schematic log da/dN - log ΔK_I curve for a titanium alloy in salt solution and an inert environment.

172
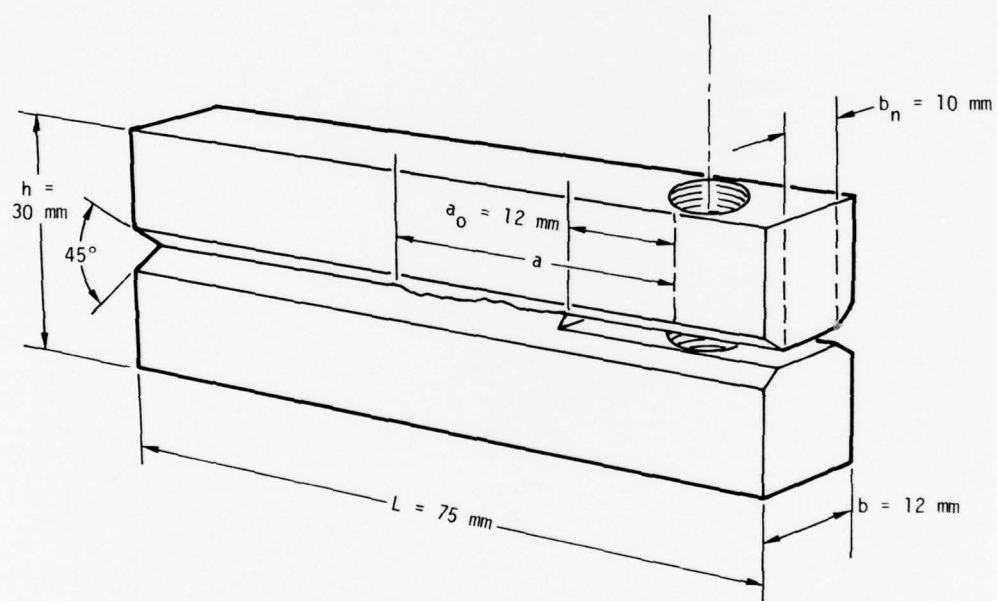
Fig. III-2 Double-cantilever-beam (DCB) specimen used for stress corrosion
cracking tests.

173
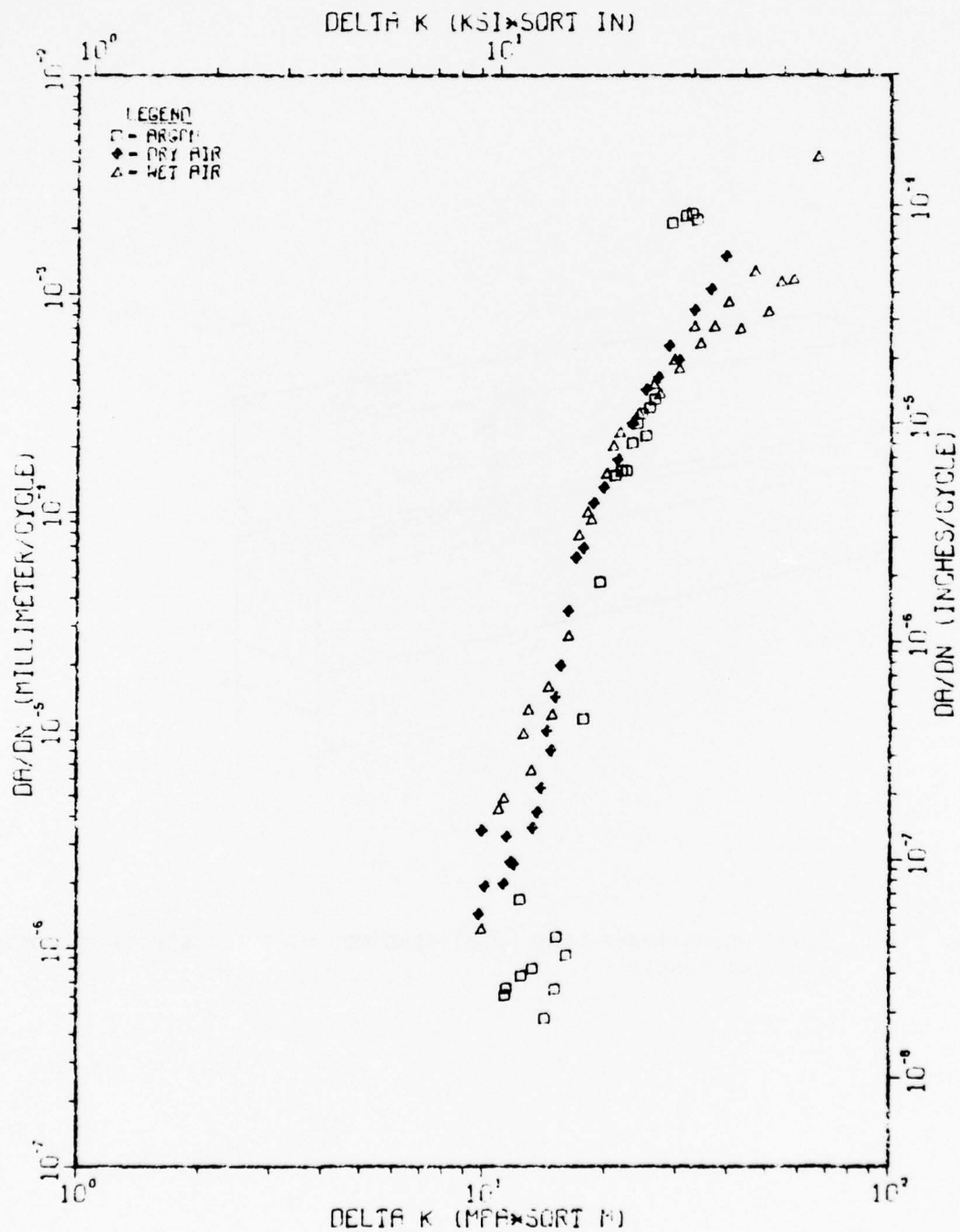
Fig. III-3 Dependence of FCP in Condition 1 on gaseous environment (wet air vs. dry air vs. argon) at 20 Hz, R = 0.1.
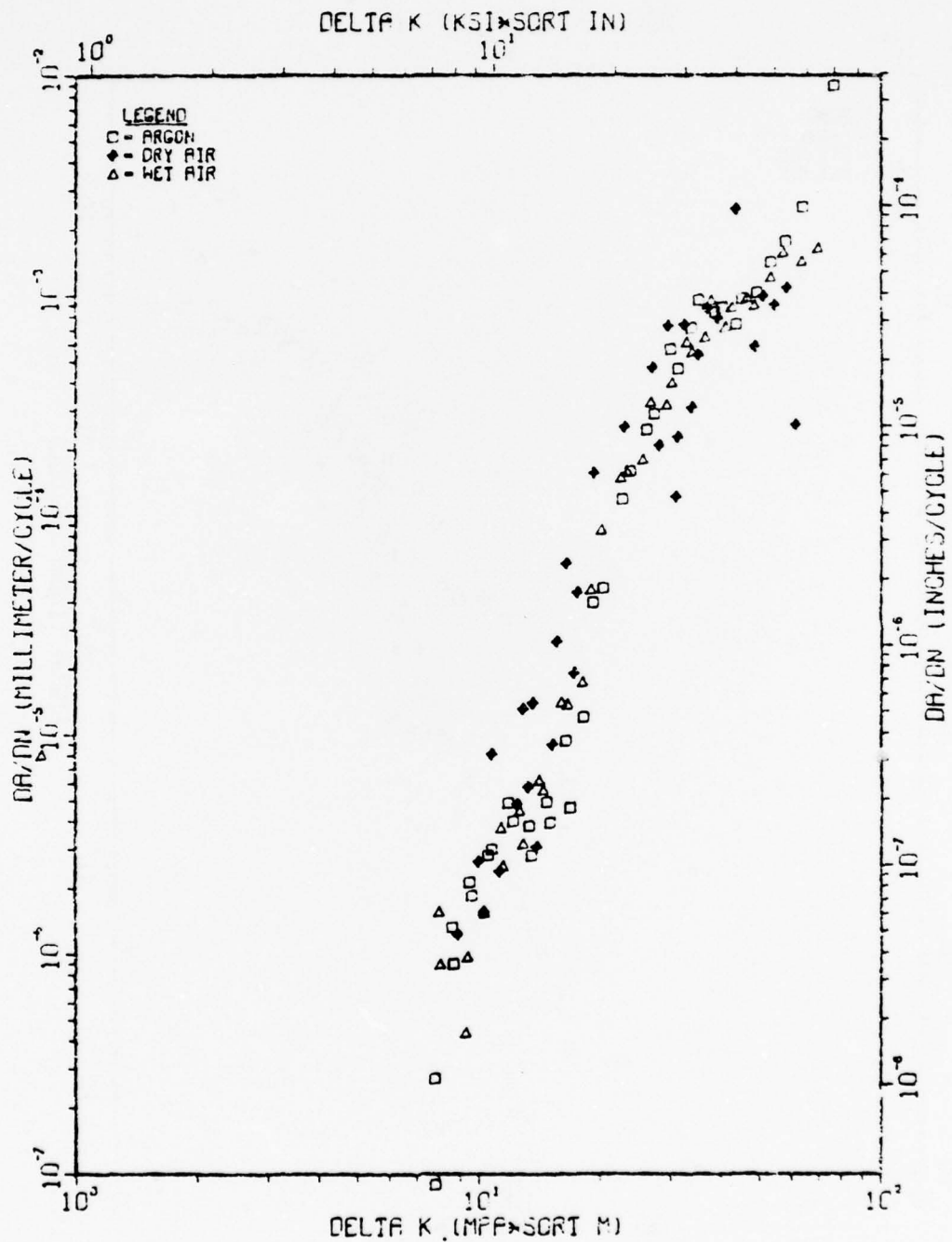
Fig. III-4 Dependence of FCP in Condition 4 on gaseous environment at 20 Hz, R = 0.1.

175
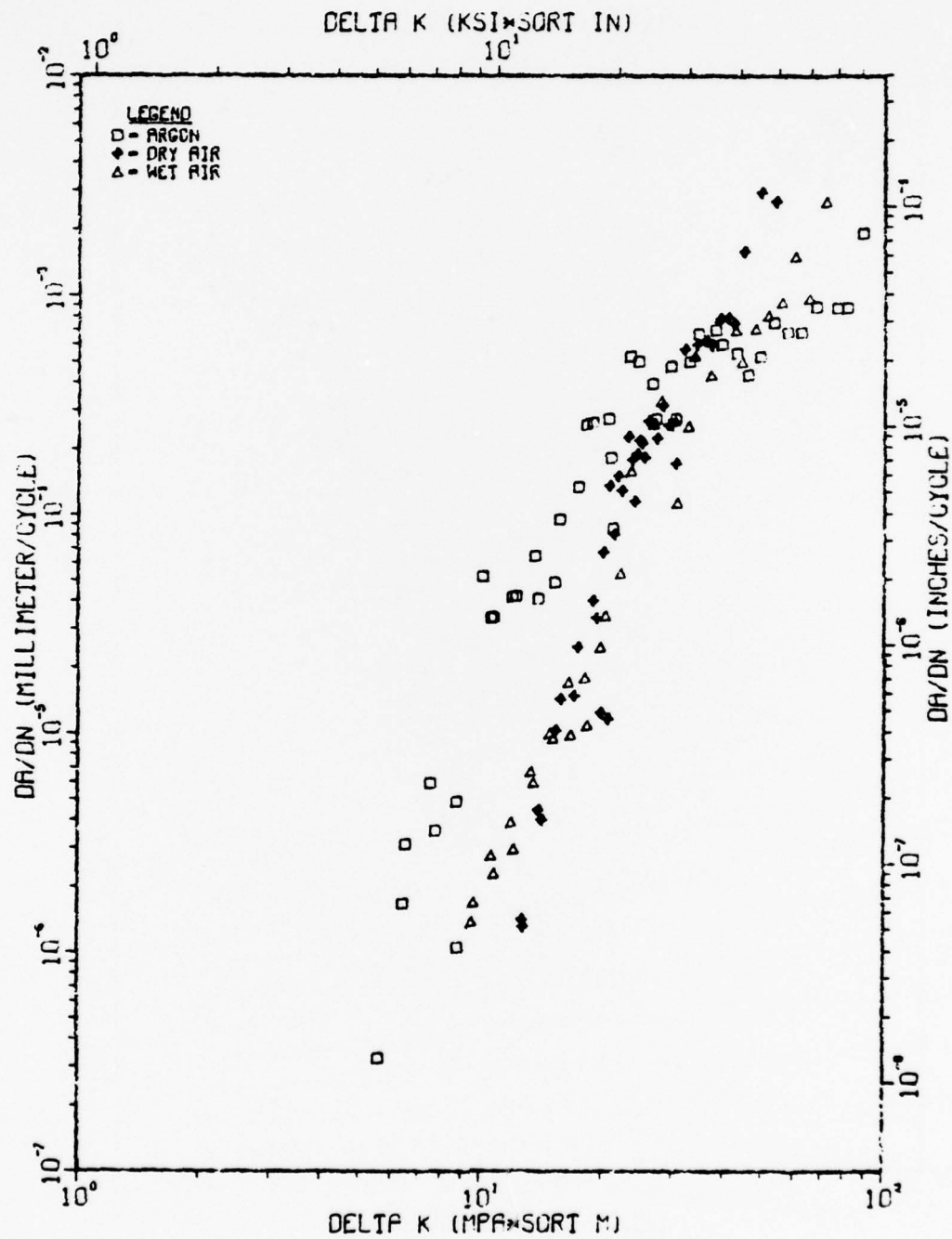
Fig. III-5 Dependence of FCP in Condition 5 on gaseous environment at 20 Hz, R = 0.1.

DELTA K (KSI*SORT IN)

LEGEND
□ - ARGON
◆ - DRY AIR
△ - WET AIR

DA/DN (MILLIMETER/CYCLE)

DA/DN (INCHES/CYCLE)

DELTA K (MPA*SORT M)

Fig. III-6 Dependence of FCP in Condition 7 on gaseous environment at 20 Hz, R = 0.1.

Fig. III-7   Dependence of FCP in Condition 8 on gaseous environment at
20 Hz, R = 0.1.

TI-6AL-2SN-4ZR-6MO(COND. 10), 6°F, 20HZ, R=0.1
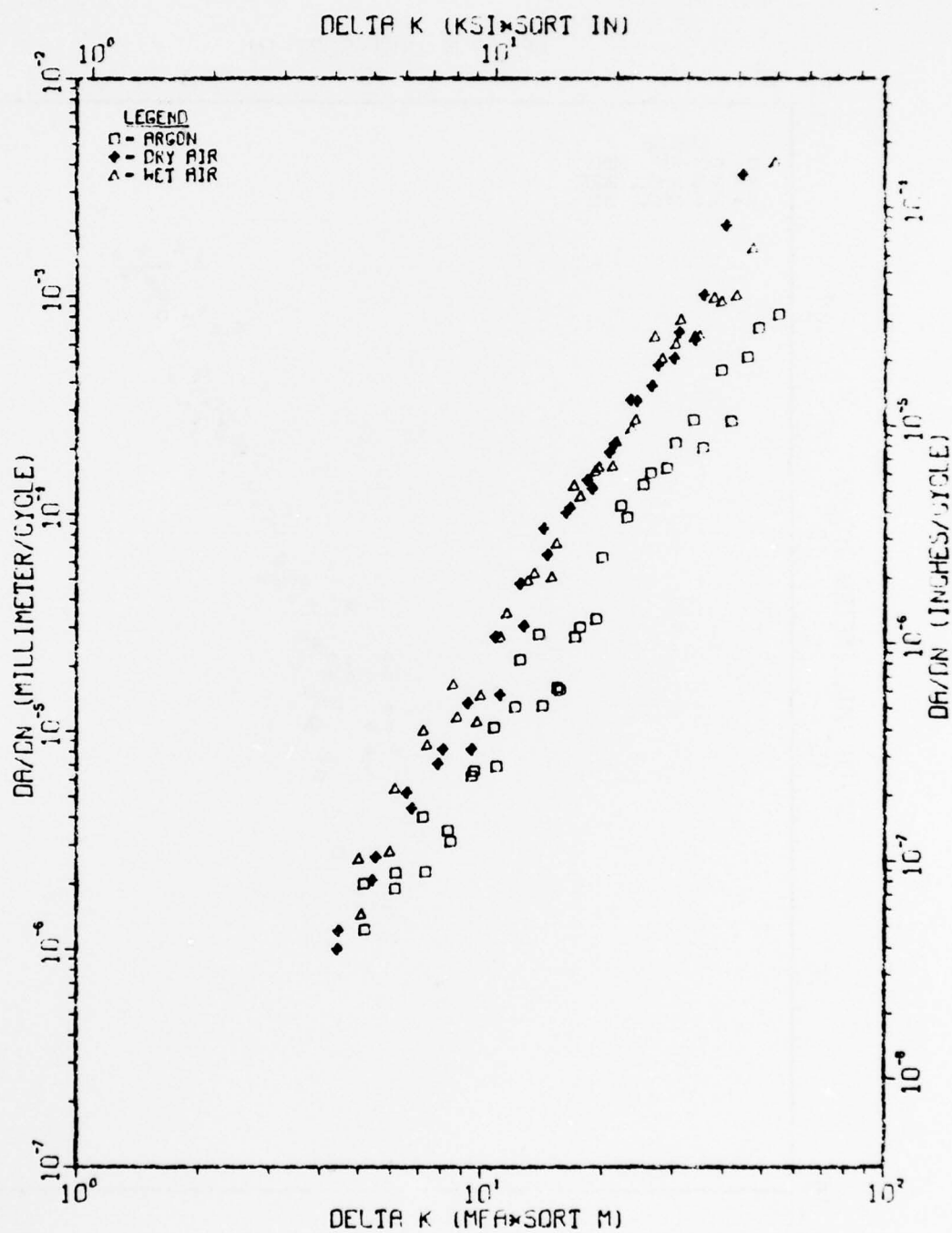
Fig. III-8 Dependence of FCP in Condition 10 on gaseous environment at
20 Hz, R = 0.1.

TI-6AL-4V(COND. 1), 68F, R-0.1
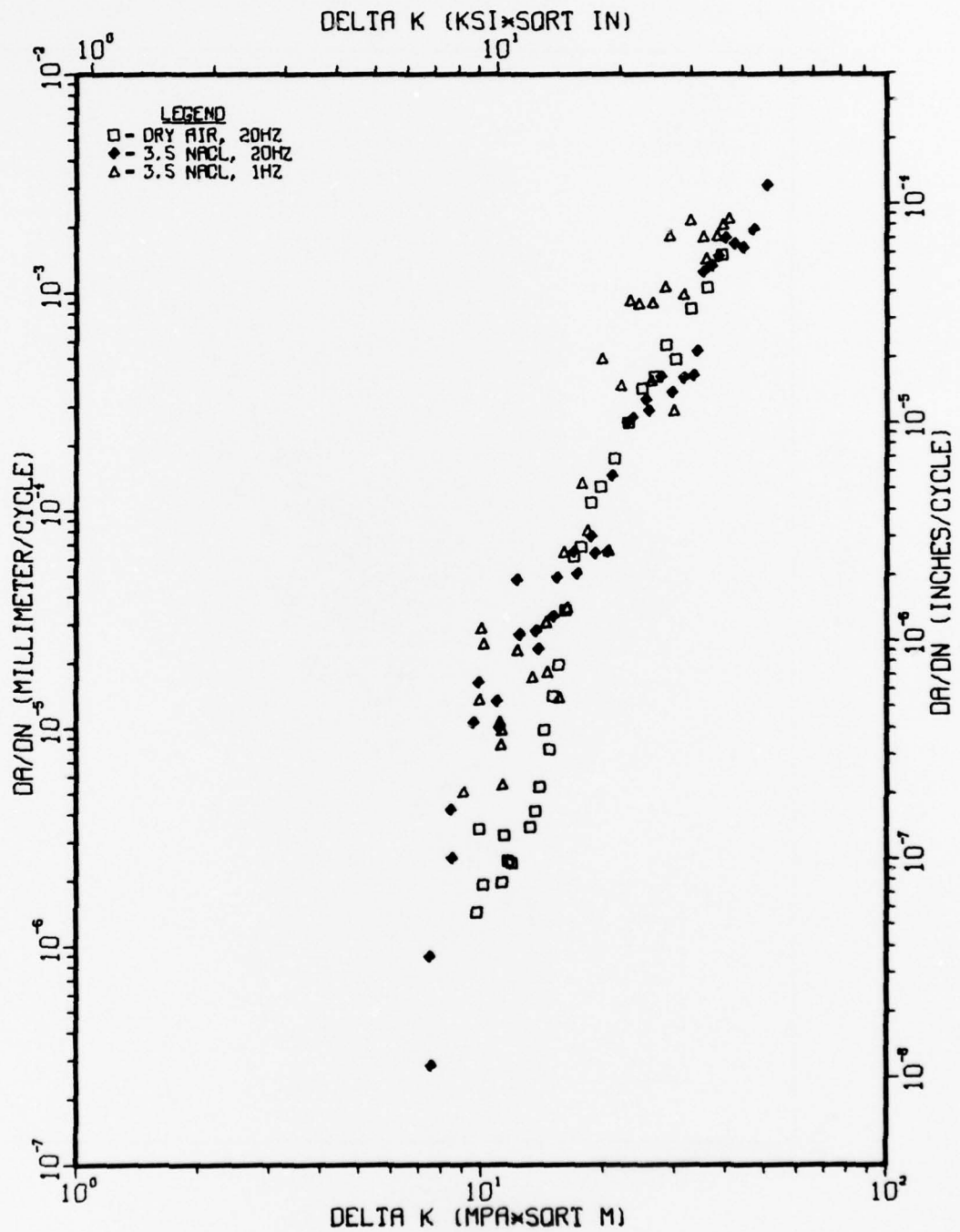
Fig. III-9 Dependence of FCP in Condition 1 on aqueous environment
(3.5% NaCl at 1 and 20 Hz vs. dry air at 20 Hz) at R = 0.1.

180

TI-6AL-4V(COND. 2), 68F, R-0.1
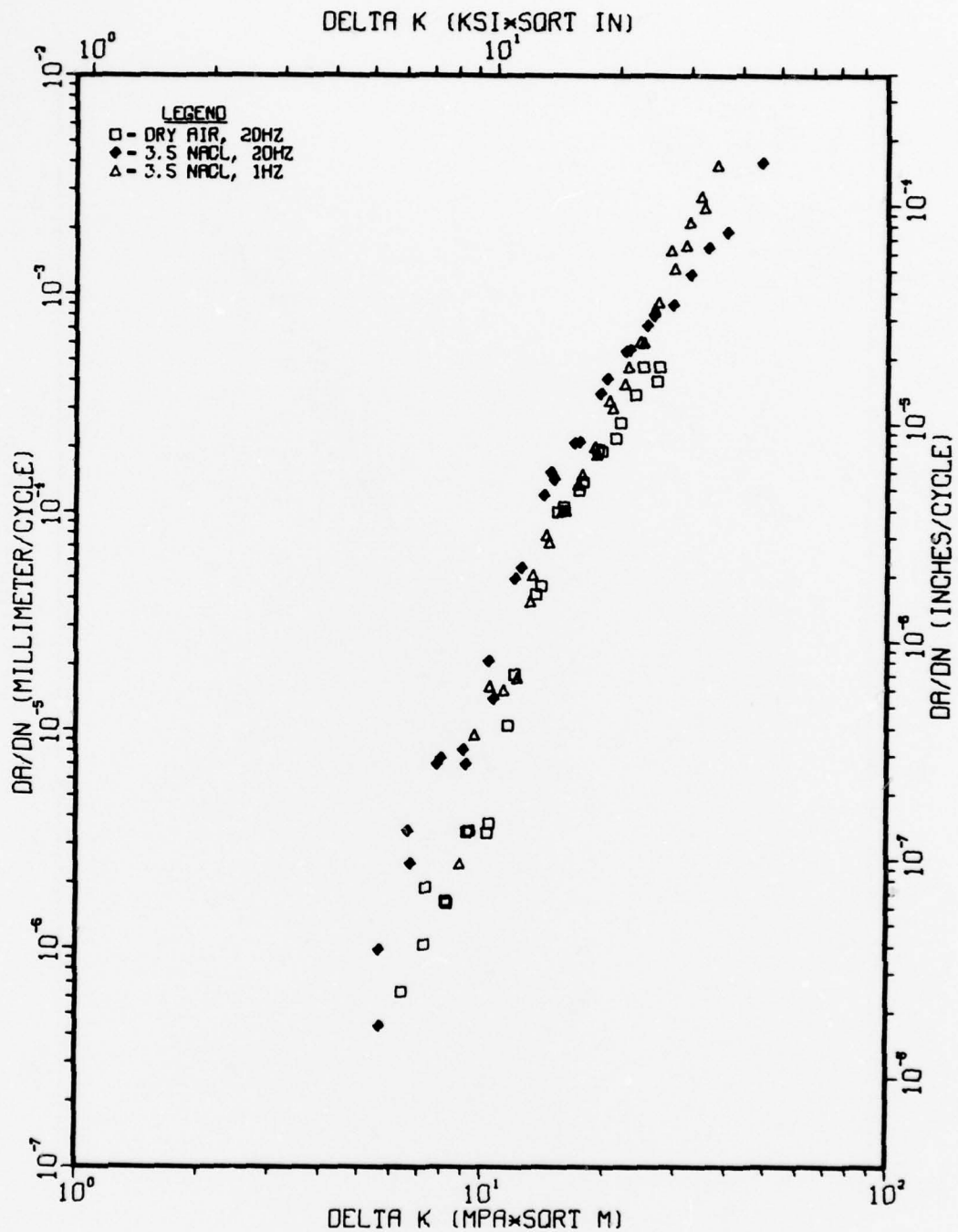
Fig. III-10   Dependence of FCP in Condition 2 on aqueous environment at
              R = 0.1.

TI-6AL-4V(COND. 3), 68F, R-0.1
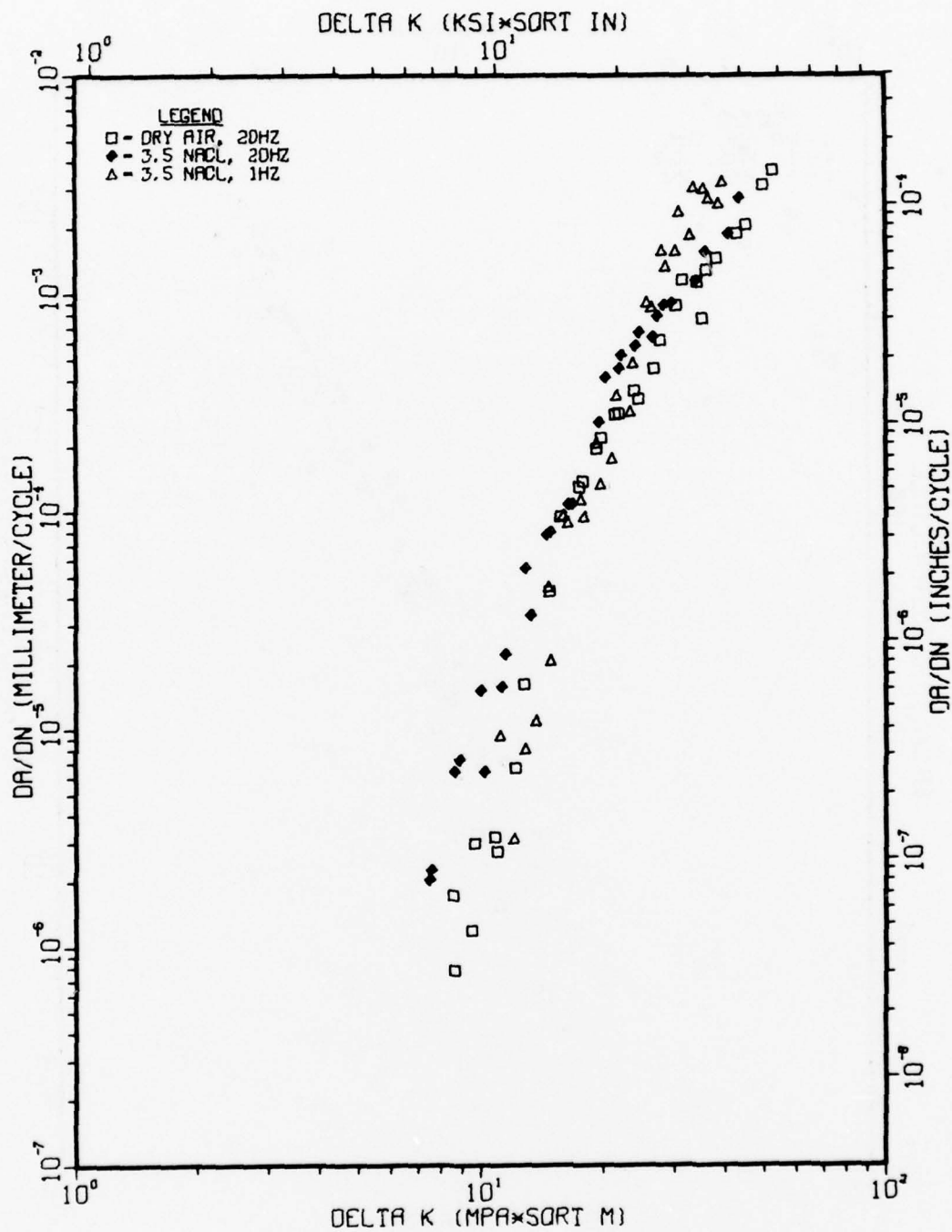
Fig III-11 Dependence of FCP in Condition 3 on aqueous environment
at R = 0.1.
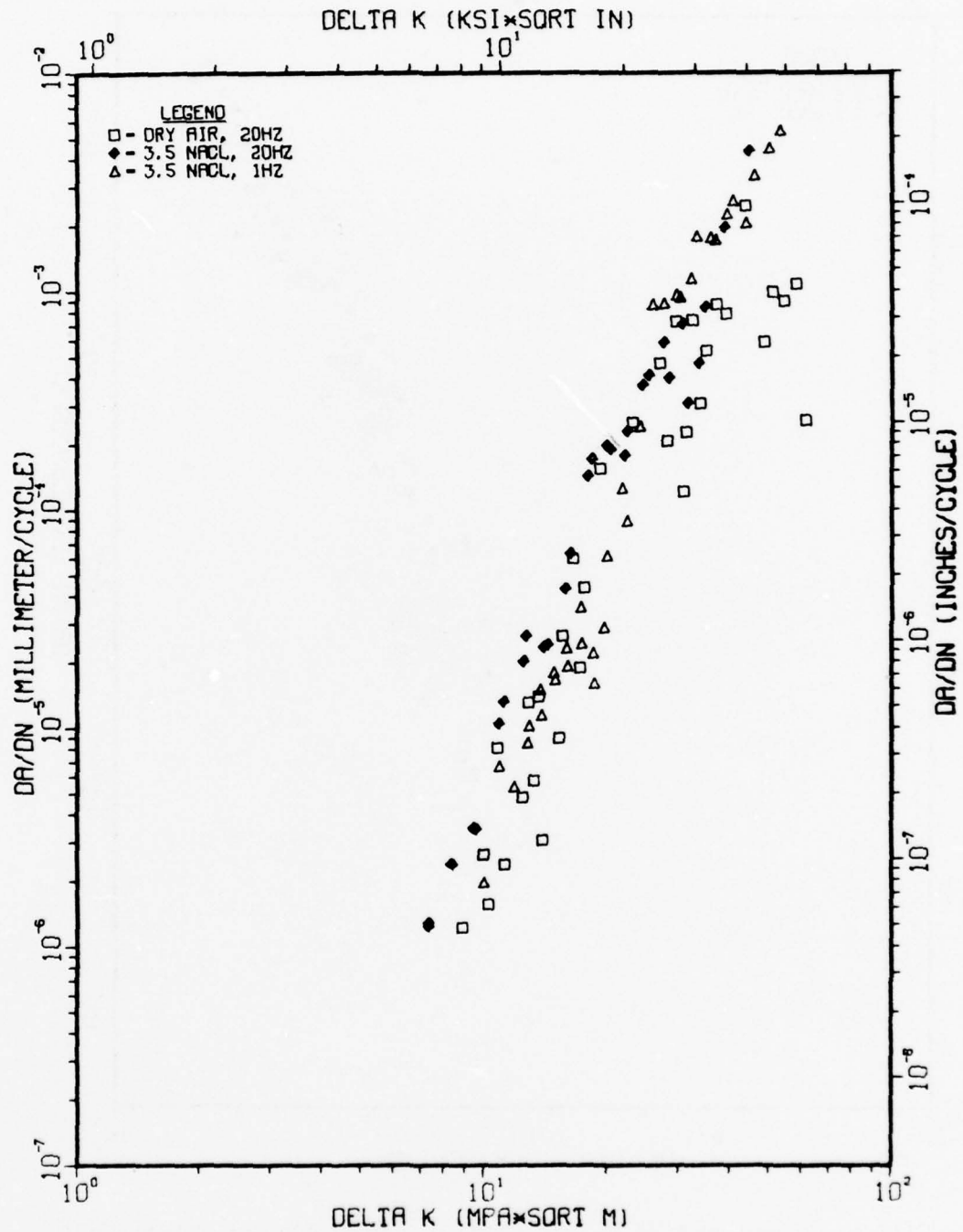
Fig. III-12 Dependence of FCP in Condition 4 on aqueous environment
at R = 0.1.
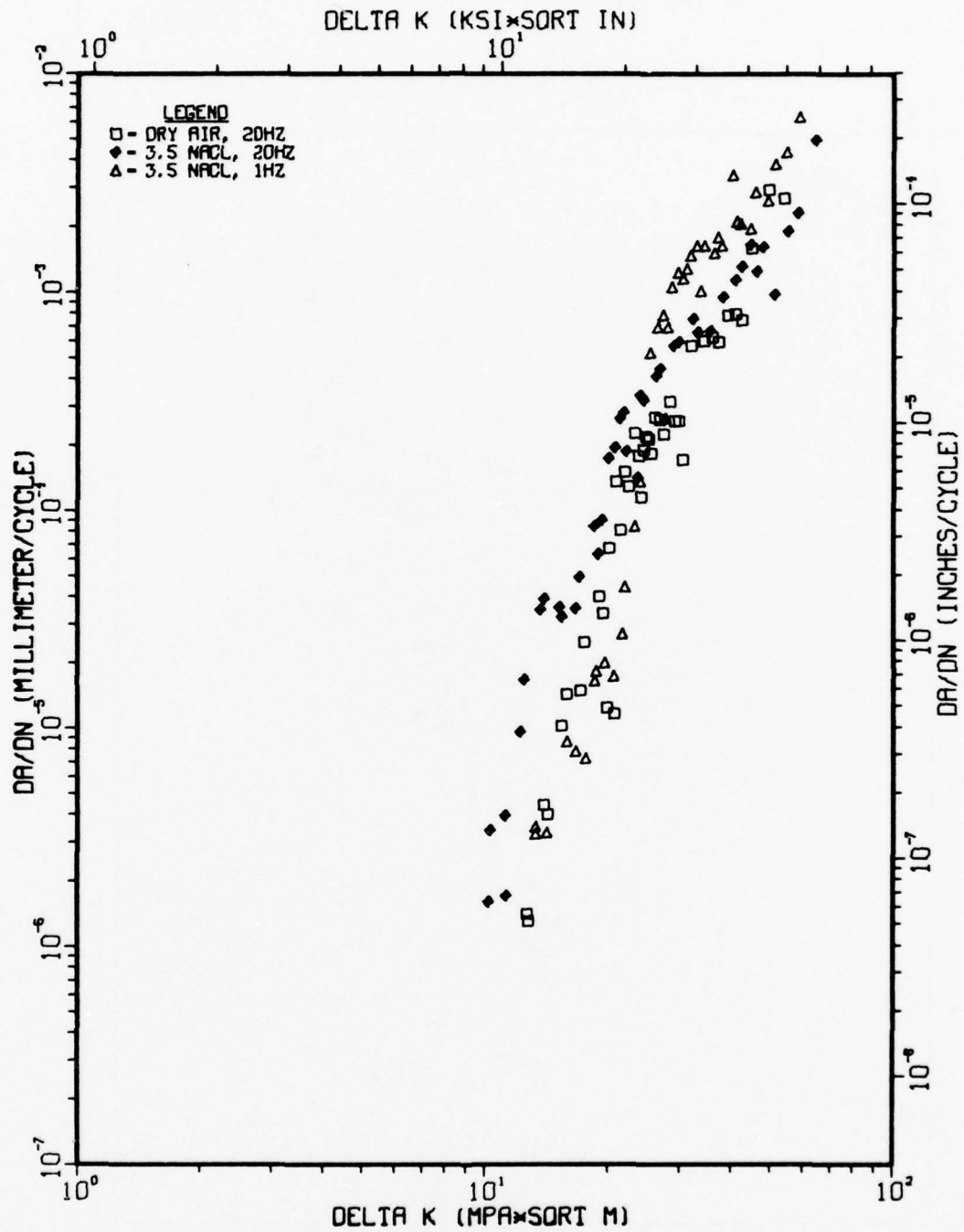
Fig. III-13 Dependence of FCP in Condition 5 on aqueous environment
at R = 0.1.

134

TI-6AL-4V(COND. 6), 68F, R-0.1
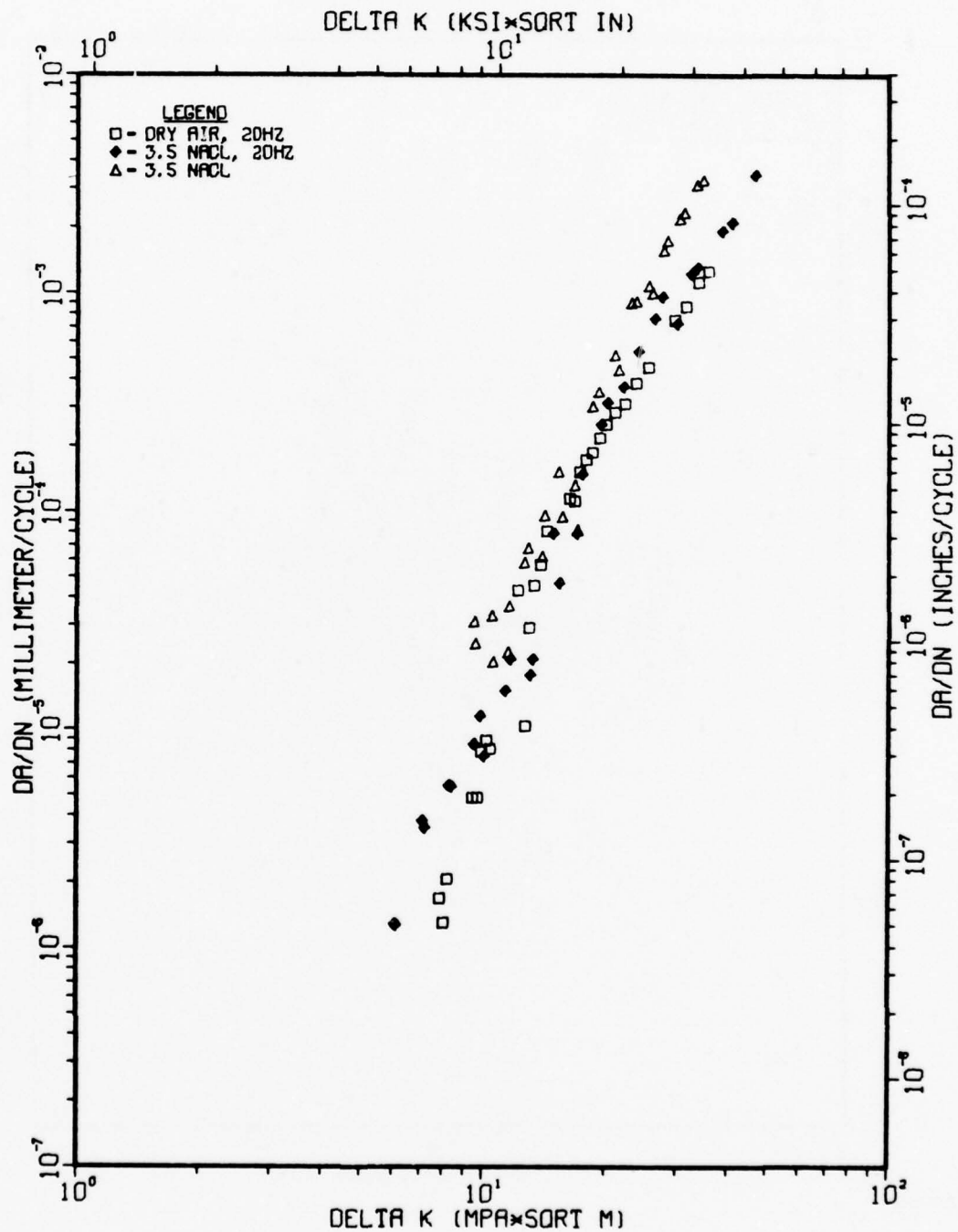
Fig. III-14 Dependence of FCP in Condition 6 on aqueous environment
at R = 0.1.
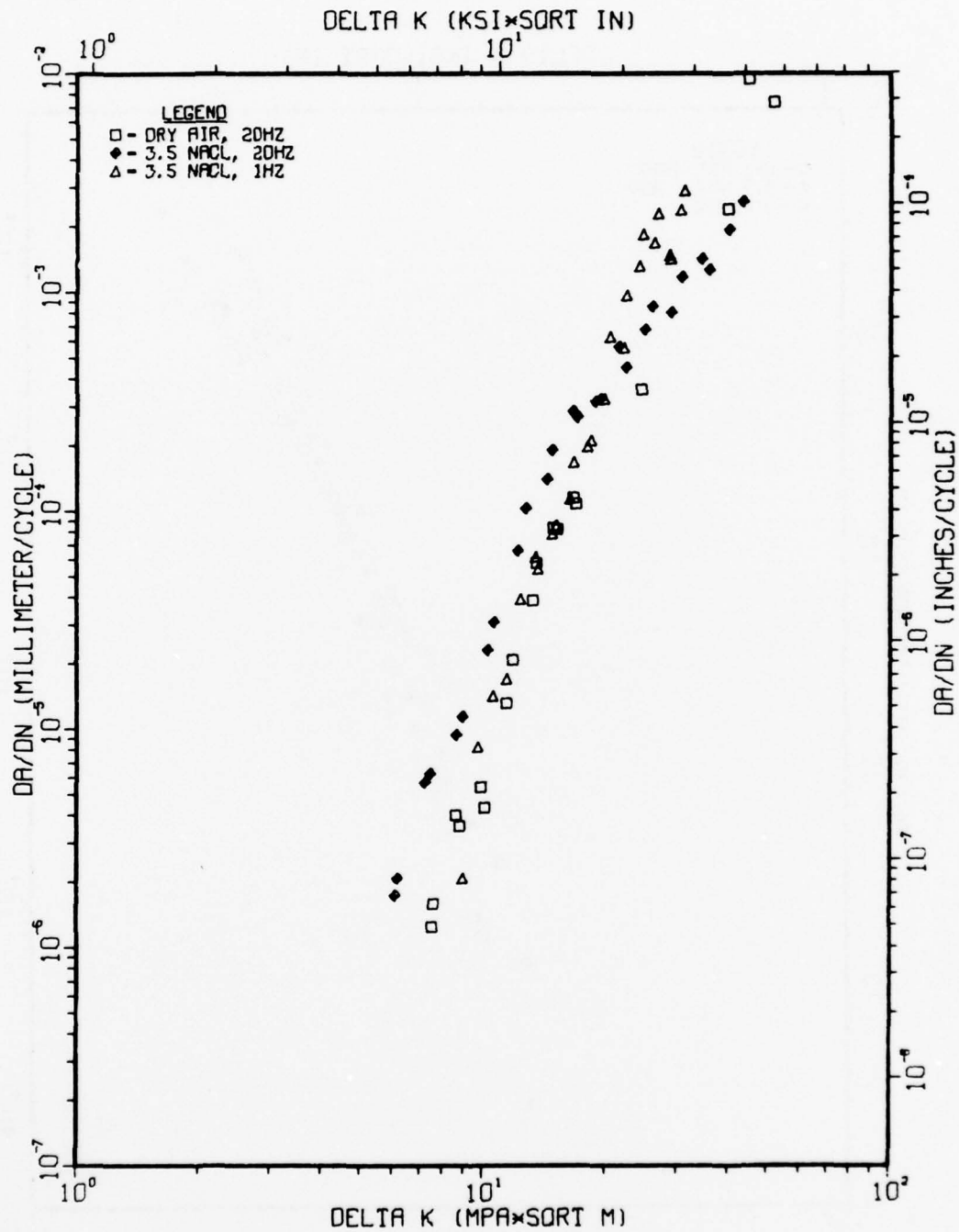
Fig. III-15 Dependence of FCP in Condition 7 on aqueous environment at R = 0.1.

TI-6AL-2SN-4ZR-6MO(COND. 8), 68F, R-0.1
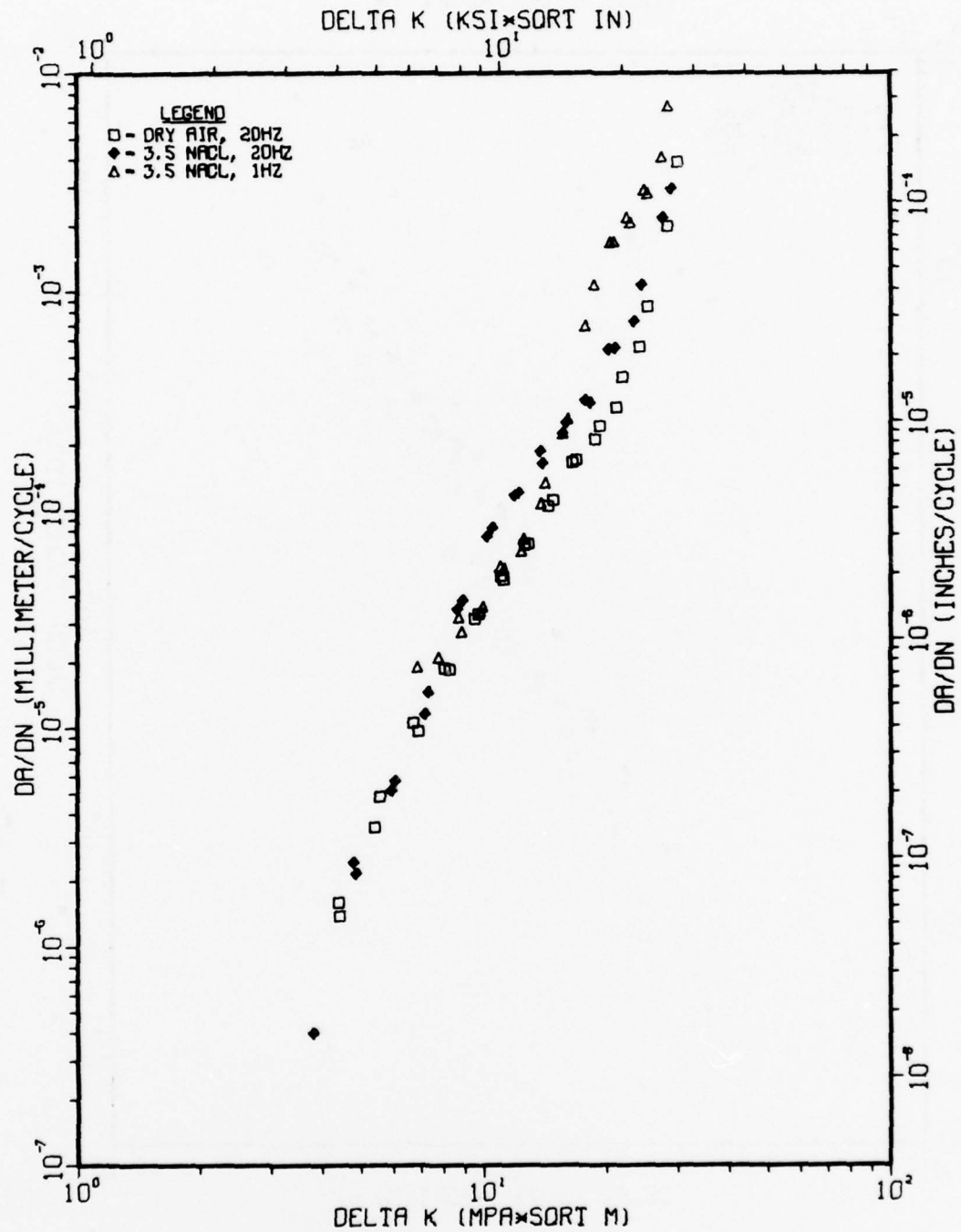
Fig. III-16 Dependence of FCP in Condition 8 on aqueous environment at
R = 0.1.

137

TI-6AL-2SN-4ZR-6MO(COND. 9), 68F, R-0.1
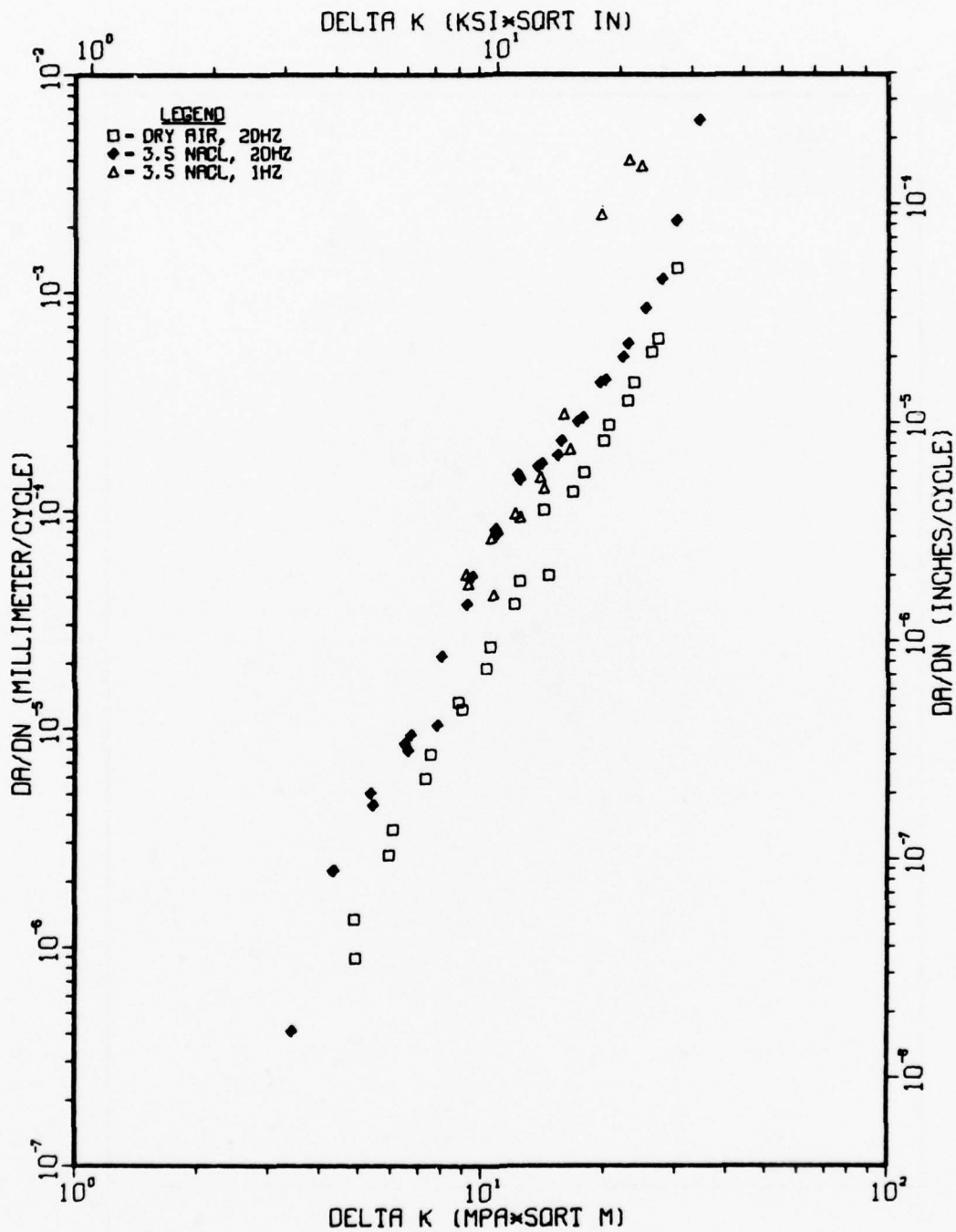
Fig. III-17 Dependence of FCP in Condition 9 on aqueous environment at
R = 0.1.

188

TI-6AL-2SN-4ZR-6MO(COND. 10), 68F, R-0.1
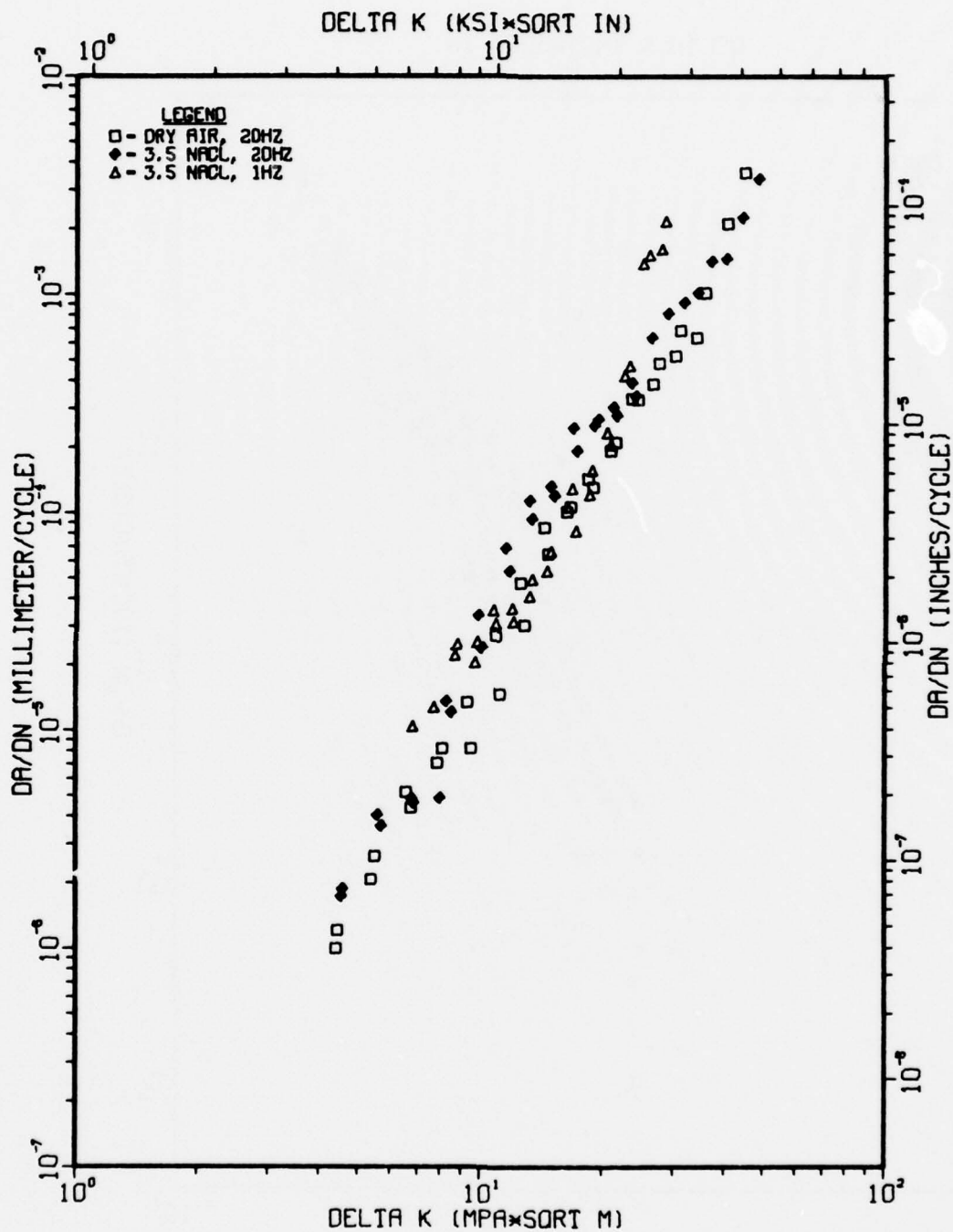
Fig. III-18 Dependence of FCP in Condition 10 on aqueous environment at R = 0.1.

189

TI-6AL-4V, 68F, 3.5 NACL, 20HZ, R-0.1
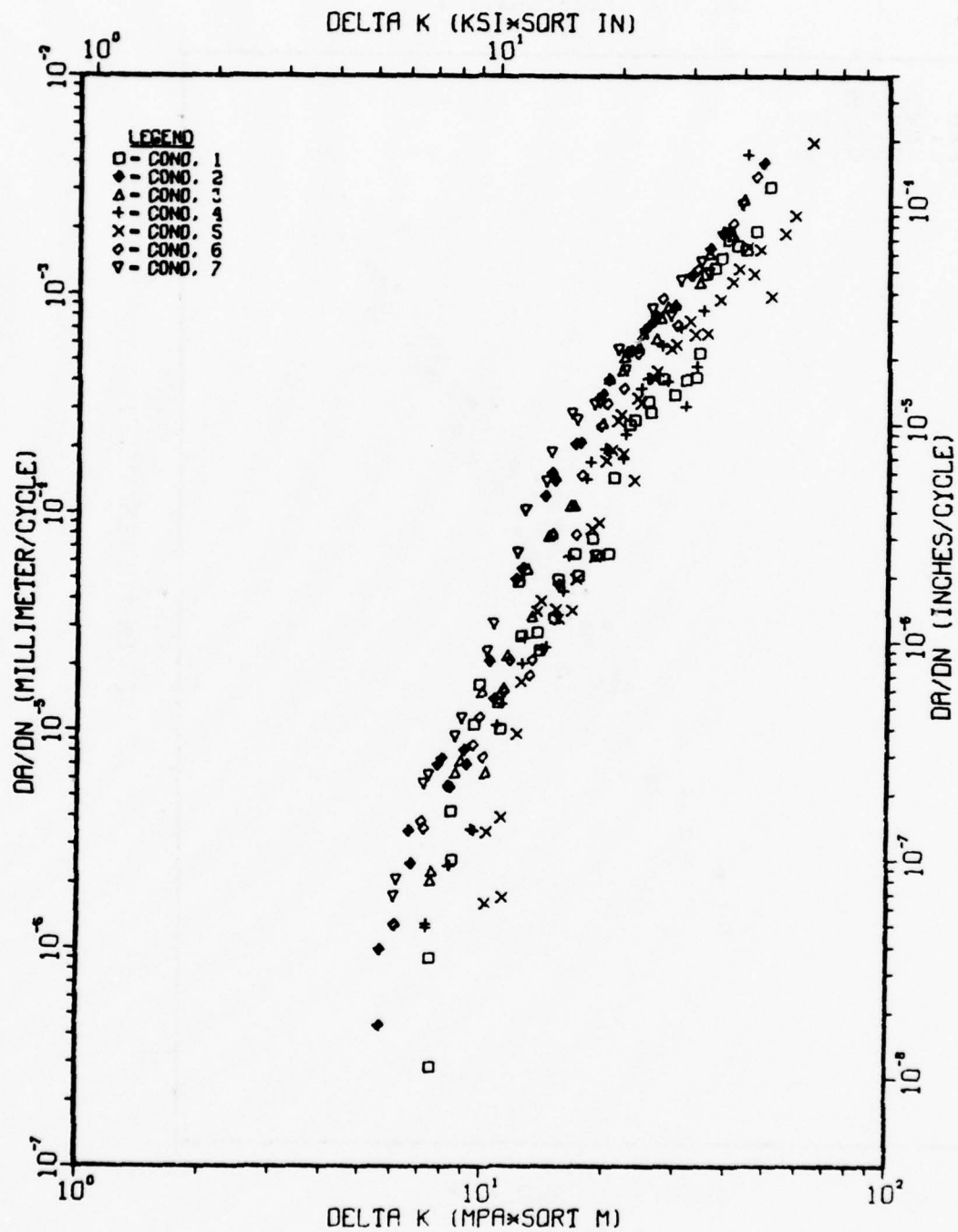
Fig. III-19 Dependence of FCP on microstructure for Ti-6-4 in 3.5% NaCl
at R = 0.1 and 20 Hz.

190

TI-6AL-2SN-4ZR-6MO, 68F, 3.5 NACL, 20HZ, R-0.1
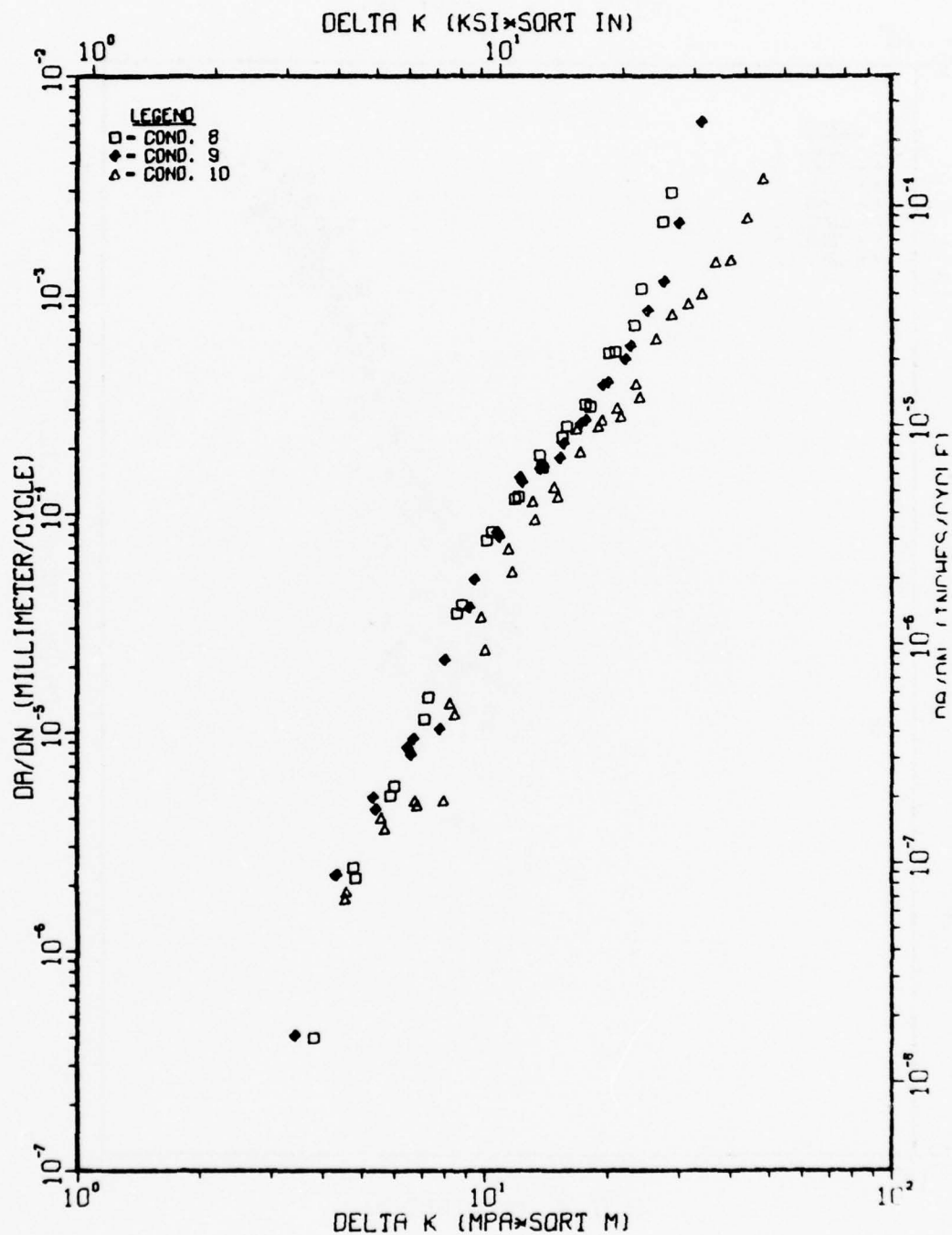
Fig. III-20   Dependence of FCP on microstructure for Ti-6-2-4-6 in 3.5%
NaCl at R = 0.1 and 20 Hz.
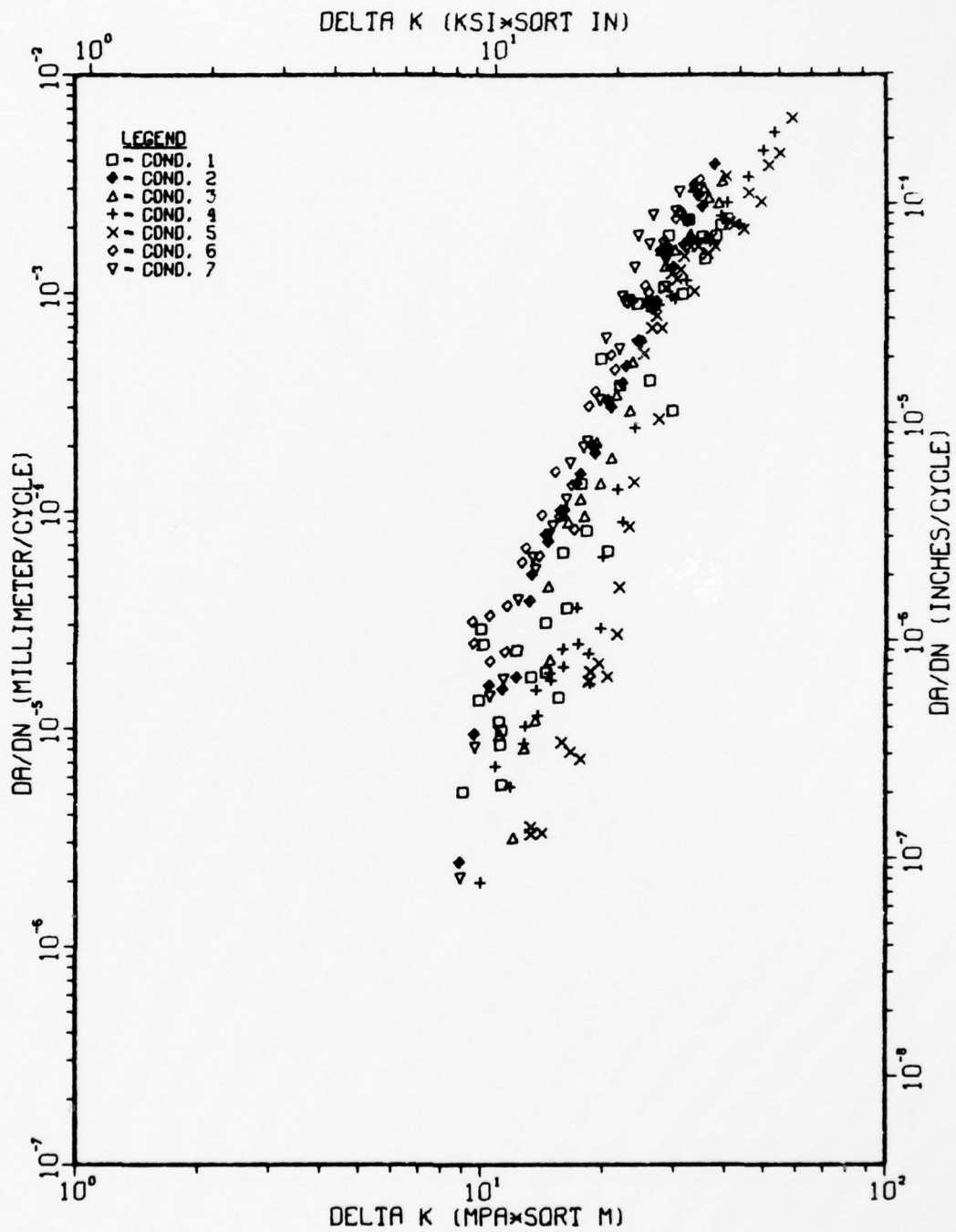
Fig. III-21 Dependence of FCP on microstructure for Ti-6-4 in 3.5%
NaCl at R = 0.1 and 1 Hz.

TI-6AL-2SN-4ZR-6MO, 68F, 3.5 NACL, 1HZ, R-0.1
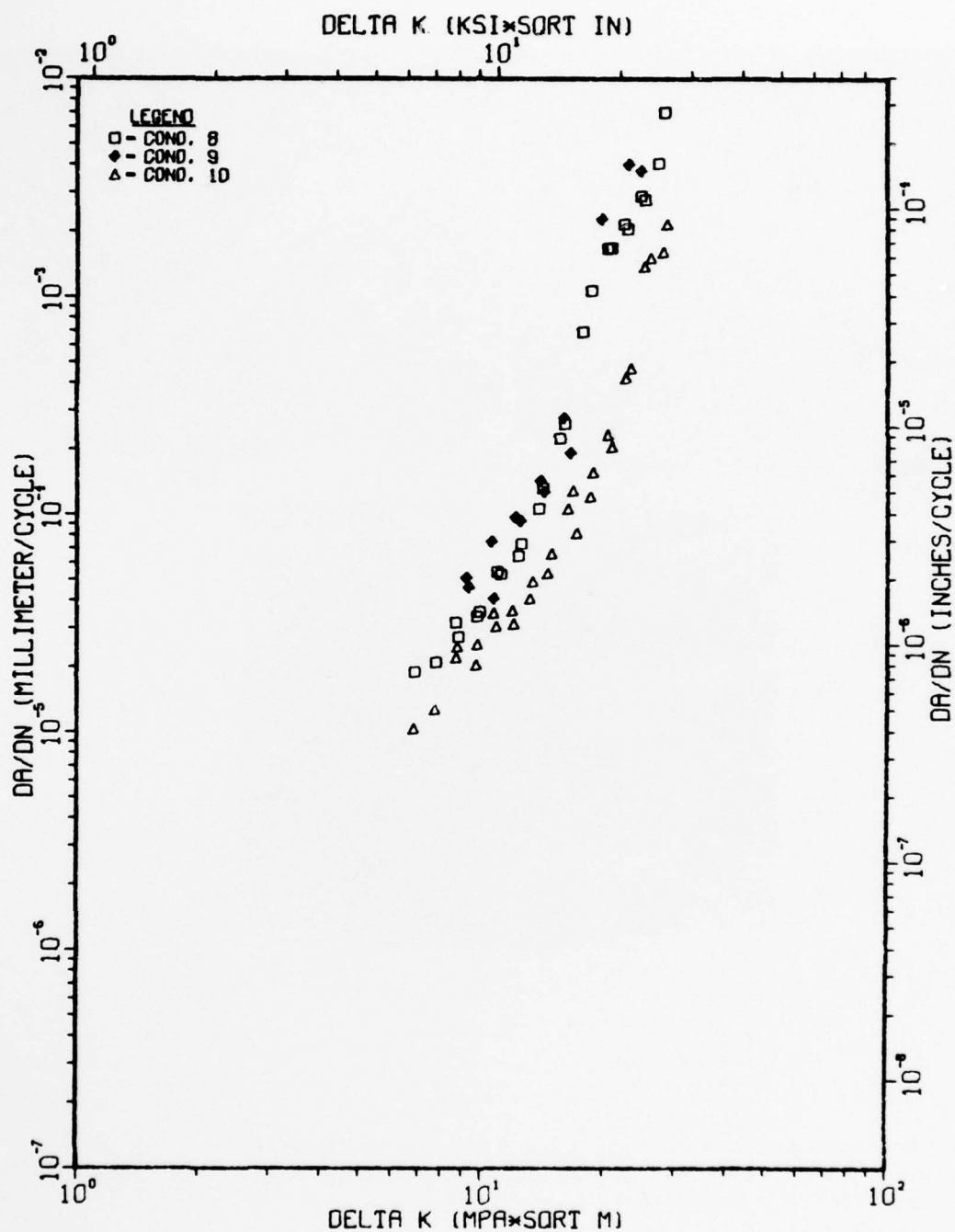
Fig. III-22   Dependence of FCP on microstructure for Ti-6-2-4-6 in 3.5%
             NaCl at R = 0.1 and 1 Hz.
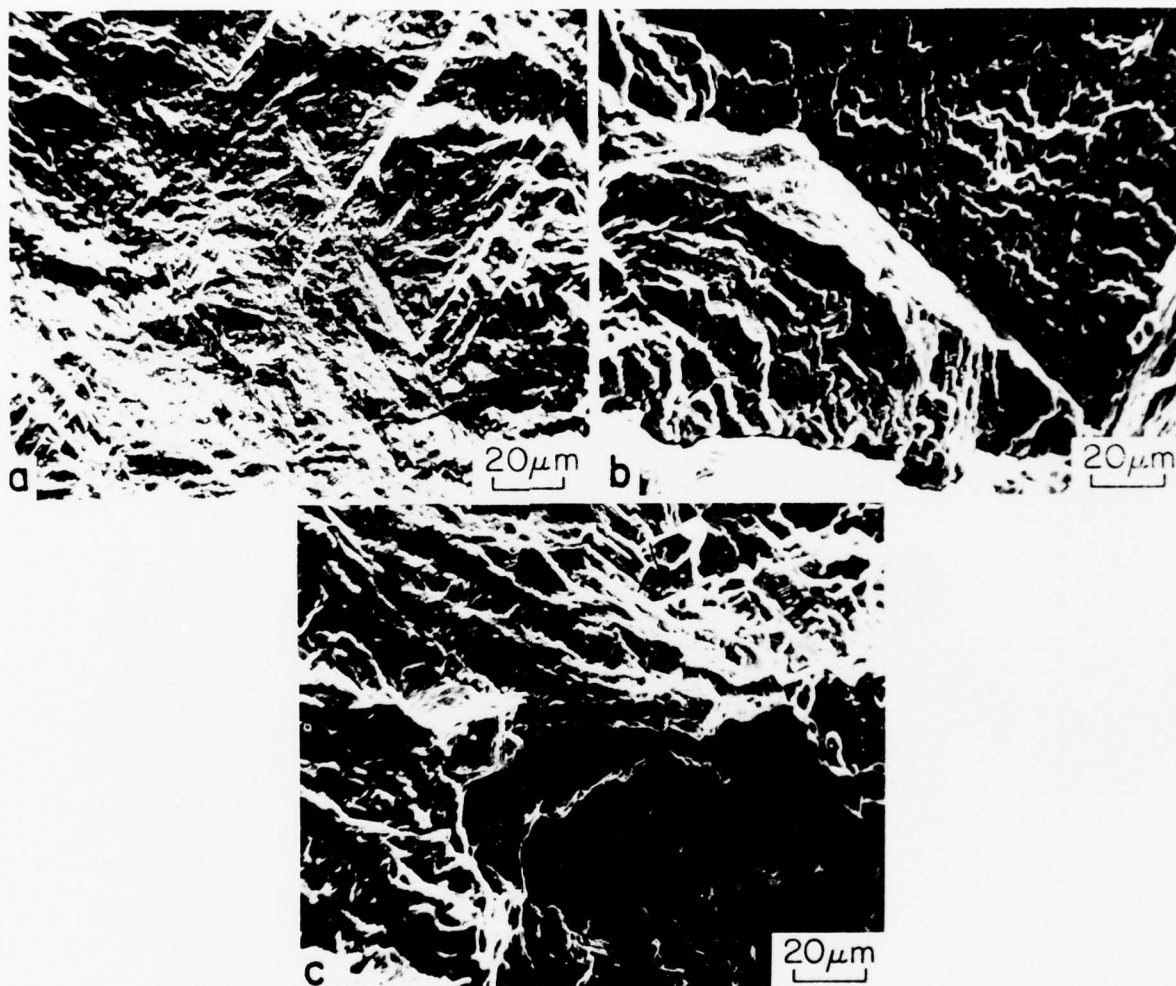
Fig. III-23 Fracture surface of Condition 5, R = 0.1, 20 Hz for
$\Delta K = 14$ MPa·m$^{\frac{1}{2}}$: (a) argon: da/dN = 4.1 x 10^{-5} mm/cycle, (b) dry
air: da/dN = 6.0 x 10^{-6} mm/cycle, (c) wet air:
da/dN = 4.5 x 10^{-6} mm/cycle.
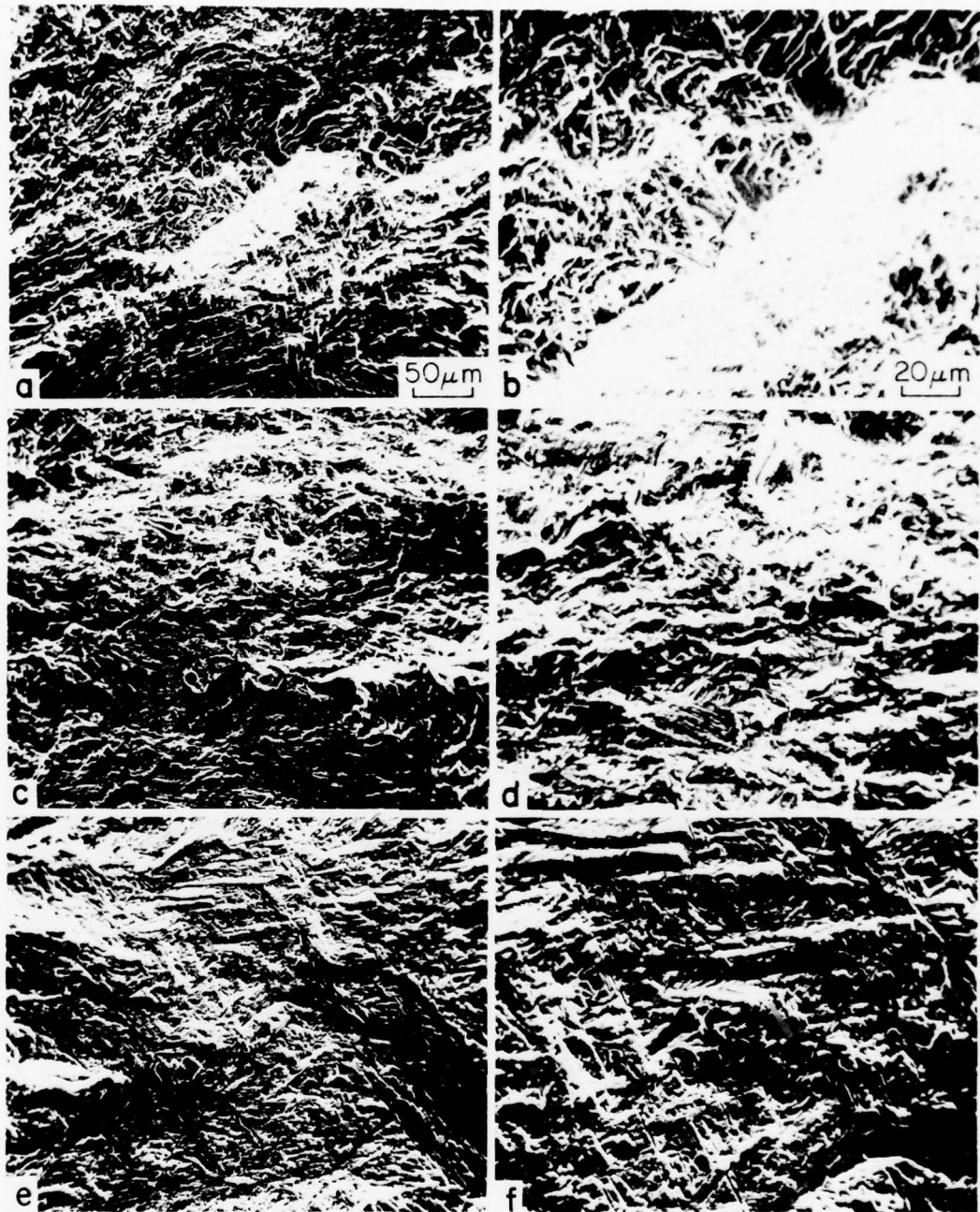
Fig. III-24   Fracture surface of Condition 10, R = 0.1, 20 Hz for
$\Delta K = 17$ MPa·m$^{\frac{1}{2}}$:   (a,b) argon: da/dN = 3.0 x 10^{-5} mm/cycle,
(c,d) dry air: da/dN = 1.1 x 10^{-4} mm/cycle, (e,f) wet air:
da/dN = 1.4 x 10^{-4} mm/cycle.
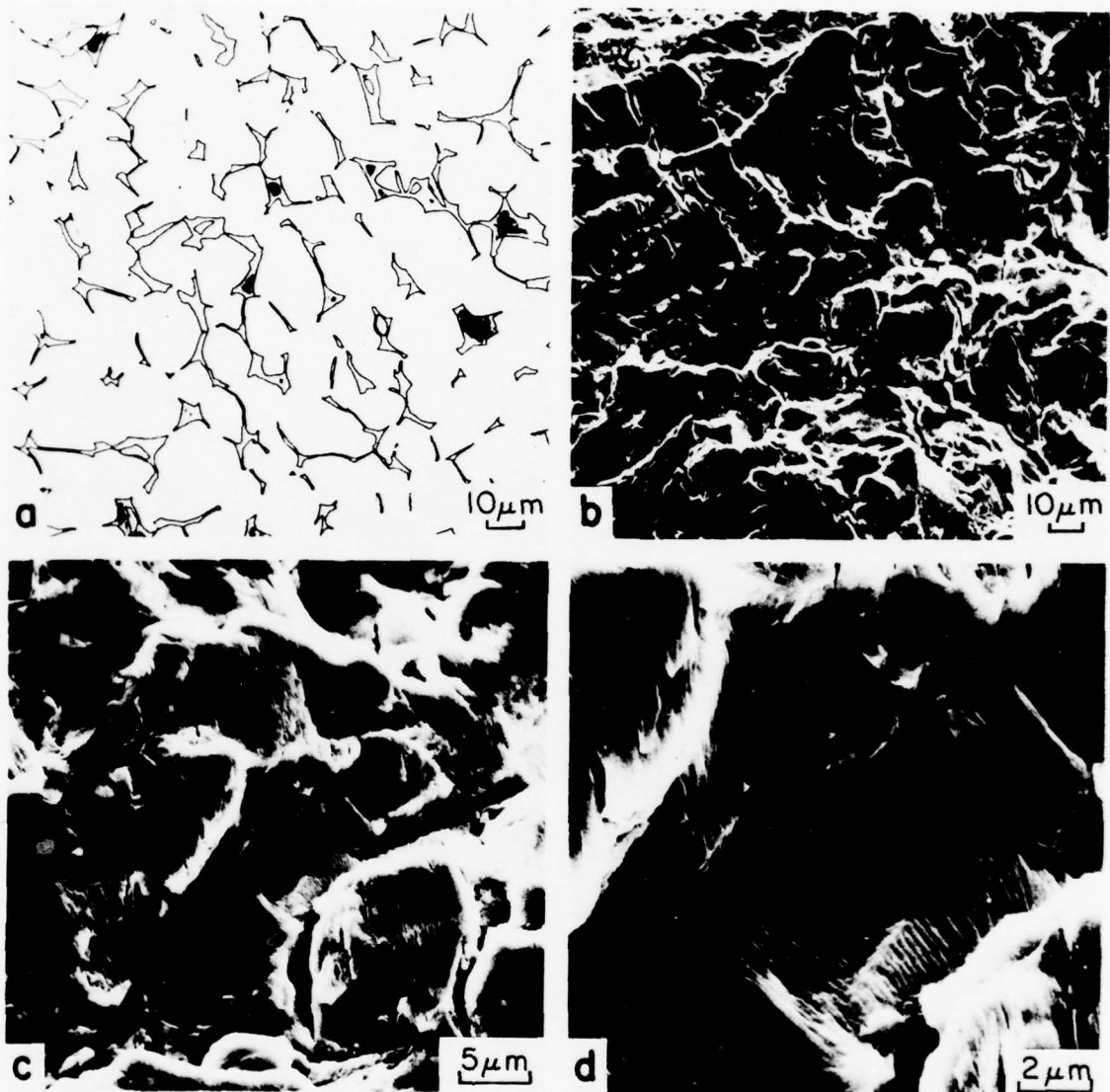
Fig. III-25 Fracture surface of Condition 1, R = 0.1, dry air, 20 Hz for
ΔK = 23.1 MPa·m$^{1/2}$ and da/dN = 2.5 x 10^{-4} mm/cycle: (a) light
micrograph; (b) SEM of fracture surface to show correlation with (a);
(c,d) transgranular cracking in α grains with distinct striations.
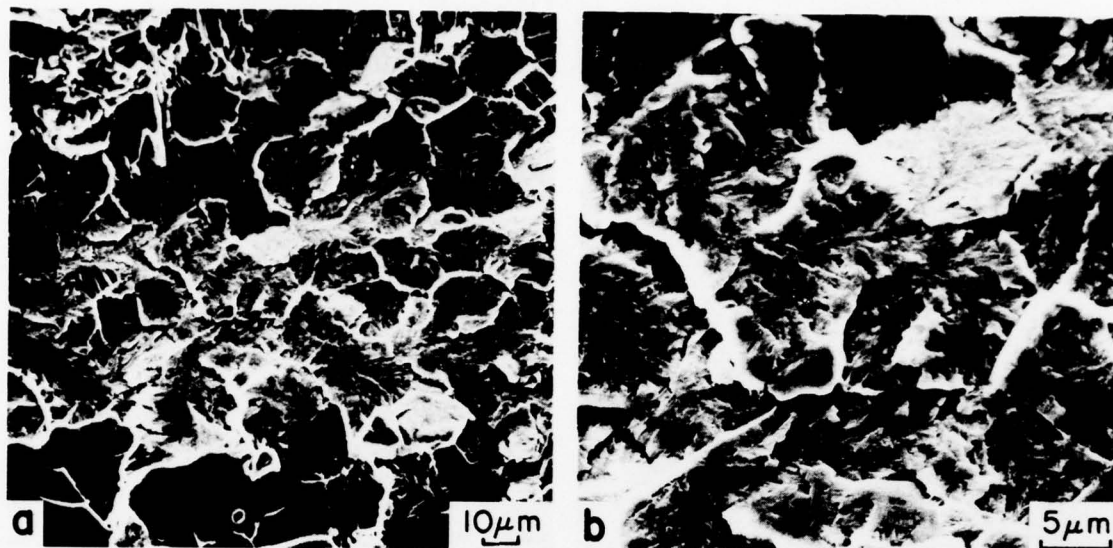
Fig. III-26 Fracture surface of Condition 1, R = 0.1, 3.5% NaCl solution, 1 Hz
for ΔK = 20.0 MPa·$m^{\frac{1}{2}}$ and da/dN = 2.5 x 10^{-4} mm/cycle:
(a,b) "cleavage-like" facets in primary α.
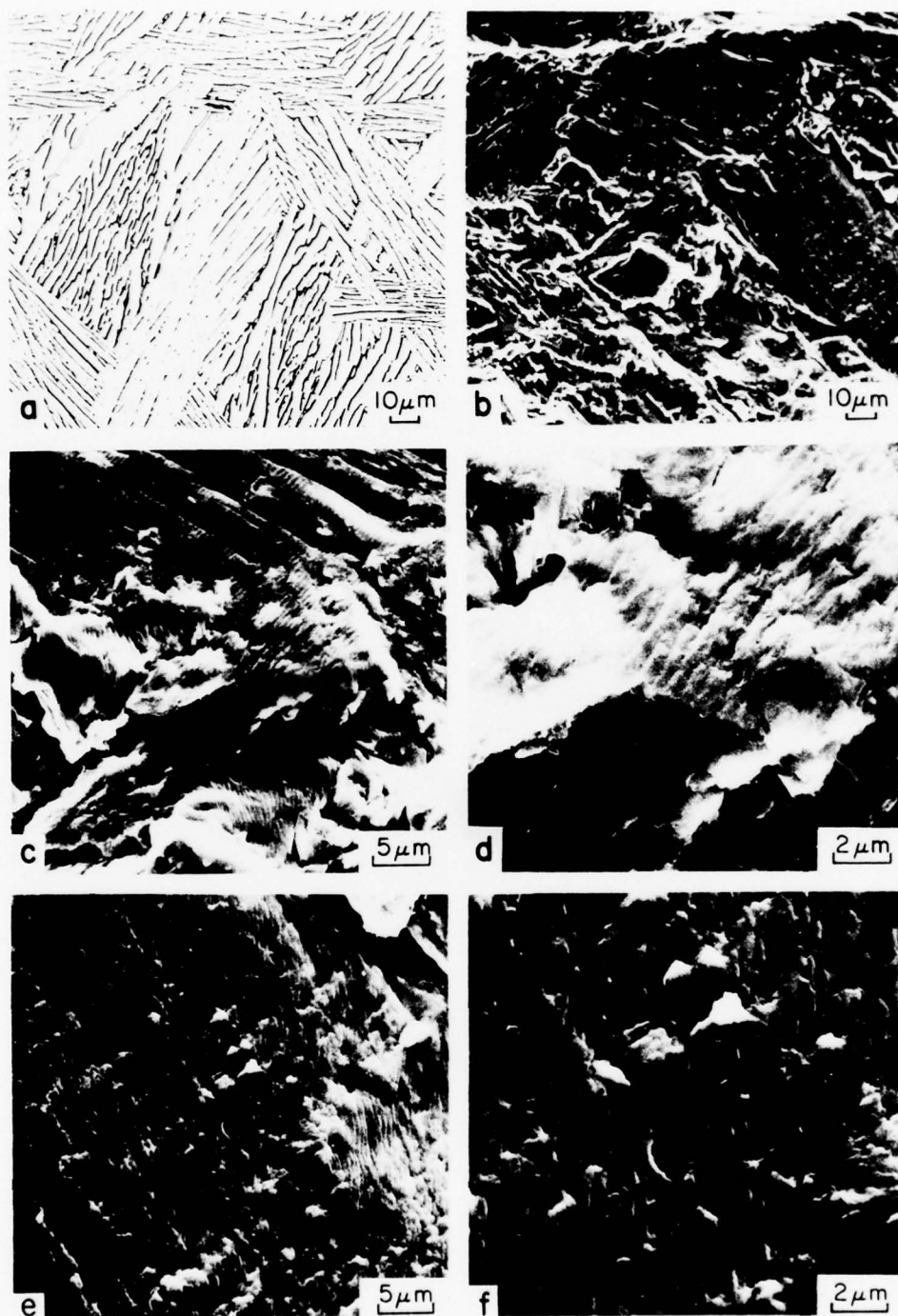
Fig. III-27 Fracture surface of Condition 4, R = 0.1, dry air, 20 Hz for $\Delta K = 27.5$ Mpa·m$^{\frac{1}{2}}$ and da/dN = 2.5 x 10^{-4} mm/cycle: (a) light micrograph; (b) SEM of fracture, with type "A" and type "B" areas; (c,d) details of type "A" area, note different local crack directions in (c); (e,f) details of type "B" area.

198
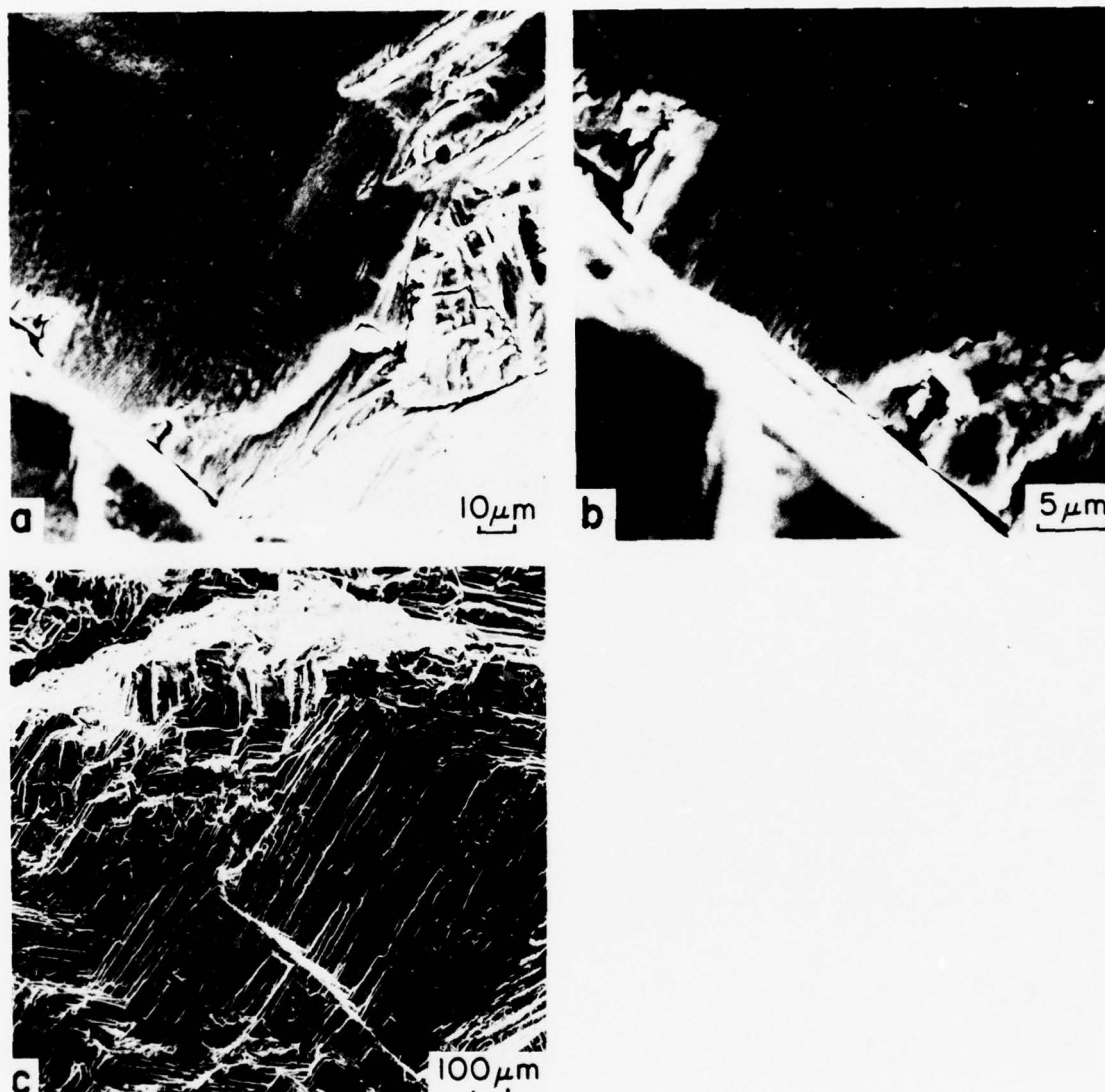
Fig. III-28   Fracture surface of Condition 4, R = 0.1, 3.5% NaCl solution, 1 Hz
for $\Delta K = 19.7$ MPa$\cdot$m$^{\frac{1}{2}}$ and da/dN = 2.5×10^{-4} mm/cycle:
(a,b) local striation formation; (c) low magnification suggesting
intergranular path.

199
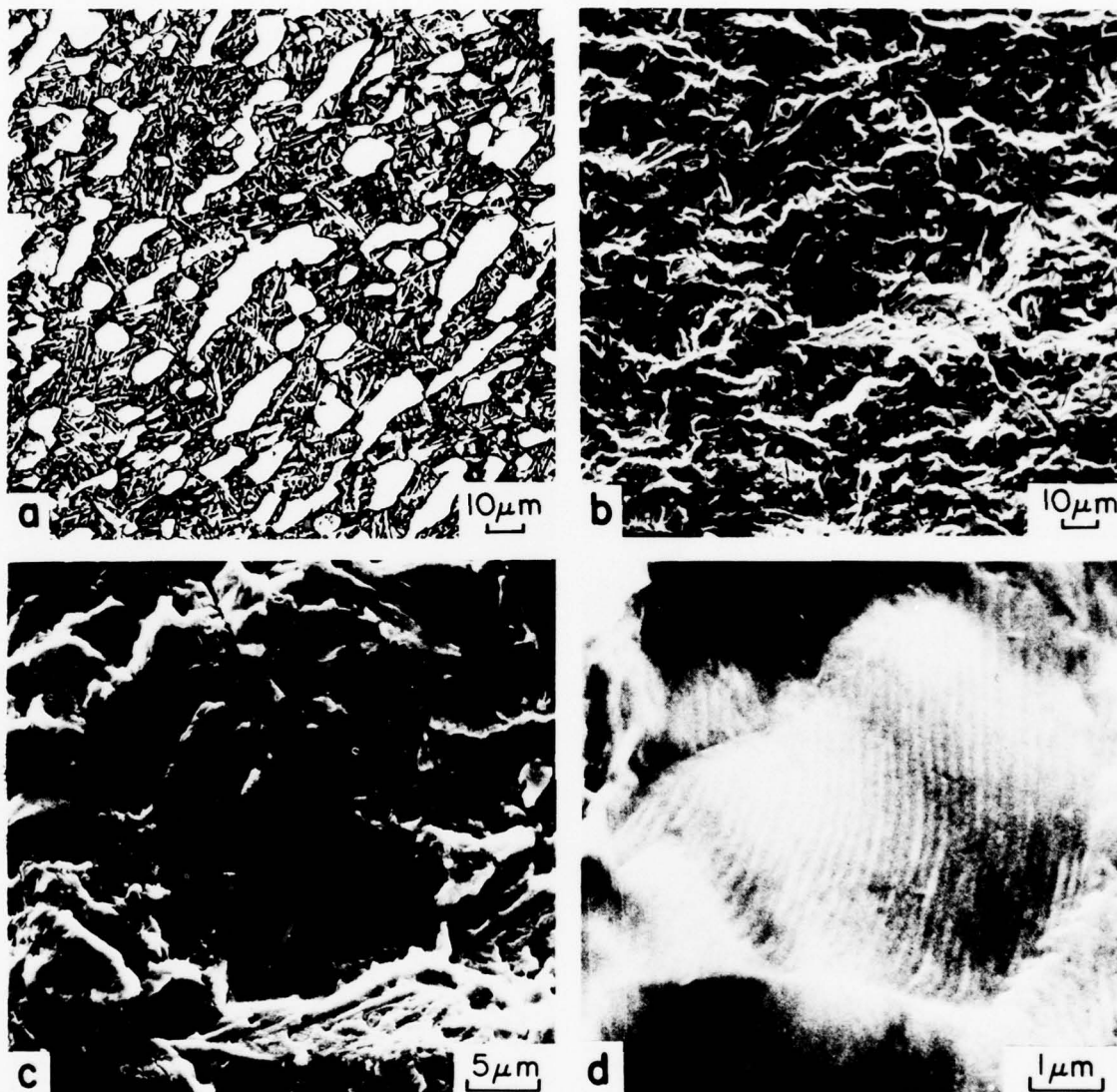
Fig. III-29 Fracture surface of Condition 6, R = 0.1, dry air, 20 Hz for
ΔK = 18.7 MPa·m$^{\frac{1}{2}}$ and da/dN = 2.5 x 10^{-4} mm/cycle. (a) light
micrograph; (b) SEM fracture surface to show correlation;
(c,d) striation formation in primary α.
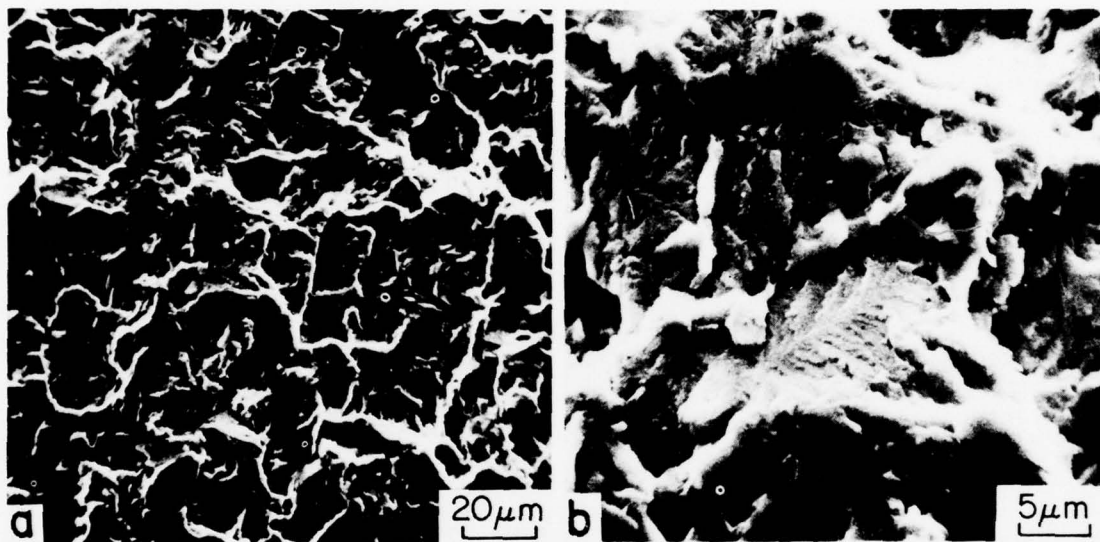
Fig. III-30 Fracture surface of Condition 6, R = 0.1, 3.5% NaCl solution, 1 Hz
for $\Delta K = 18.2$ MPa·m$^{\frac{1}{2}}$ and da/dN = 2.5 x 10^{-4} mm/cycle:
(a,b) "cleavage-like" facets in primaryα.

PART IV: TEMPERATURE AND INTERSTITIAL EFFECTS ON FATIGUE CRACK PROPAGATION

INTRODUCTION

Numerous investigators have studied the effect of the interstitial elements oxygen and hydrogen on fatigue crack propagation (FCP) and fracture in titanium alloys,[1-5] but little systematic study of the effect of elevated temperatures on FCP is found. The effects of oxygen and hydrogen are complicated and are dependent on microstructure, texture, loading rate and stress intensity level ΔK. A general trend seems to be that increased oxygen and/or hydrogen content cause an increase in growth rate especially at low ΔK. The approach in this part was a systematic study of the effect of oxygen and hydrogen on two microstructures of Ti-6Al-4V, recrystallization annealed (Condition 1) and beta quenched (Condition 5). FCP studies at 1 and 20 Hz and at room temperature and 600°F (316°C) were included.

The limited studies on the effect of temperature on FCP in titanium alloys have concentrated on mill-annealed or STA, Ti-6Al-4V plate.[6-8] These studies have shown little effect of temperature on FCP at temperatures up to 650°F (343°C). None of these studies have addressed the subject of microstructure or texture and the interaction of these with temperature effects on FCP.

Additionally, there has been some disagreement in past work on the texture effect on FCP in general. Strongly textured Ti-6Al-4V sheet showed

202

little difference in FCP rate from moderately textured sheet,[9] but texture can affect FCP of Ti-6Al-4V plate.[10-12] Textured Ti-6Al-2Sn-4Zr-6Mo plate also shows marked effect.[13] In view of these conflicts and complications, the present program as well as those in the preceding three parts was conducted on forged material deliberately processed to have as weak and as uniform a texture as possible, independent of final microstructure. In this way, the microstructure, temperature and interstitial variables can be separated from that of texture, a separation not possible in earlier work.

EXPERIMENTAL PROCEDURES

Ingot material of two additional oxygen levels (0.082 and 0.185 wt% oxygen) was obtained for this part of the study and was pressed forged into 5.08 cm (2 in.) thick pancakes. Additional 0.122 wt% oxygen material from the Part I ingot material was also forged at this time. Two pancakes of each oxygen level were forged, one for Condition 1 (RA) and one for Condition 5 (βQ); forging temperatures were adjusted to allow for oxygen effects on the β transus temperature. The details of forging temperatures and reductions are shown in Table IV-I. The chemical composition and β transus of the starting materials are shown in Table IV-II.

Specimens were hydrogen charged in a Sieverts apparatus at 1300°F (704°C) for approximately 17 h and cooled in vacuum. The 1300°F charging temperature was chosen to be at or below the final heat treatment temperature of both Condition 1 and Condition 5. Spot check chemical analysis indicated

203

the actual hydrogen contents were within 25% of the values calculated from the charging. Tensile testing as a function of oxygen and hydrogen content and as a function of temperature were conducted using the same specimen geometry and strain rate (1.67×10^{-4} s^{-1}) as in Part I. Elevated temperature tensile tests were done in a vacuum (p = 10^{-5} Torr) muffle furnace; specimen temperature was controlled to $\pm5^{O}$C. Cyclic stress-strain measurements both as a function of temperature and interstitial content were conducted in a closed-loop electrohydraulic system in strain control using an axial extensometer. Specimen heating for the elevated temperature testing utilized an electric heat gun; specimen temperature was maintained at $\pm10^{O}$C. Fracture toughness tests were conducted using compact tension which were designed and tested in accordance with ASTM E399.

The specimens for FCP measurements were fabricated and precracked as described in Part II. Elevated temperature fatigue crack propagation measurements were made at 250°F (121°C) and 600°F (316°C) in a closed-loop electrohydraulic system in load control. The specimens were heated in air in a small resistance furnace fabricated for the purpose, and temperature was controlled to $\pm5^{O}$C. Crack growth was monitored and measured to the nearest ±0.001 in. through a quartz window in the furnace using a cathatometer; specimens were precracked in air at room temperature. All other details of FCP testing matched those for Part II. Elevated temperature hold-time measurements included: (1) 5-min holds at 2.5×10^{-4} mm/cycle for specimens tested at 250°F and R = 0.3, (2) 1-min holds at 1.3×10^{-4} mm/cycle and 1- and 5-min holds at 2.5×10^{-4} mm/cycle for

204

specimens tested at $600^{o}F$ and R = 0.3, and (3) 1-min holds at 1.3 and
2.5×10^{-4} mm/cycle. Hold-time data includes 2 or 3 data points at each
growth rate taken for a block of 100-300 hold cycles.

Upon termination of FCP testing, selected fractographic examination
was conducted in a scanning electron microscope (SEM).

RESULTS

The results will be presented in three sections: (1) effect of
temperature and interstitials on tensile, cyclic stress-strain and fracture
toughness properties of Conditions 1, 5, and 7, RA, Q, and STOA,
respectively; (2) effect of temperature on fatigue crack propagation (FCP) on
these same conditions; and (3) effect of interstitials on FCP in RA,
Condition 1, and βQ, Condition 5.

Tensile, Cyclic σ-ϵ, K_{IC} Properties

Tensile tests fall into three groups: (1) tests at 250 and $600^{o}F$
(121 and $316^{o}C$) on Conditions 1, 5, and 7, to determine the effect of
temperature; (2) tests at room temperature and $600^{o}F$ on specimens of low
(0.082%) and high (0.185%) oxygen content in Conditions 1 and 5; and (3) tests
at room temperature and $600^{o}F$ on Conditions 1 and 5 specimens containing 100
and 300 ppm hydrogen, to determine the effect of hydrogen content. The
results are summarized in Table IV-III.

205

The data have also been plotted in Fig. IV-1 and IV-2; Fig. IV-1 illustrates the effects of temperature and oxygen content on yield strength, while Fig. IV-2 is a similar plot for hydrogen. Room temperature data for the "standard" oxygen (0.122%) and hydrogen (Condition 1: 3 ppm; Condition 5: 20 ppm) content material are taken from Part I. Several things can be noted in this figure. First, the temperature dependence is roughly independent of microstructure but is a function of oxygen content; low and standard oxygen material exhibits about 0.85 MPa/^{o}C strength reduction, while for high oxygen it is 1.10 MPa/^{o}C. Second, the effects of oxygen and microstructure are less pronounced at 600°F, in part because of the differences in temperature dependence. Third, increased oxygen content strengthens the Condition 5 microstructure more than it does Condition 1; in fact, low and standard oxygen in Condition 1 give essentially the same strength. These conclusions are self-consistent and are consistent with earlier work at this laboratory on Ti-6Al;[14] the same is true of the UTS and ductility results in Table IV-I. The hydrogen effects on yield strength follow similar trends with increased hydrogen content producing modest strength increases in Condition 1 both at room temperature and 600°F and in Condition 5 at room temperature. The effect of hydrogen on the temperature dependence of the yield strength is dependent on microstructure; Condition 1 is independent of hydrogen and exhibits about 0.85 MPa/^{o}C strength reduction, while for Condition 5 containing 100 and 300 ppm hydrogen, the slope is 0.93 MPa/^{o}C.

Differences among the microstructures in Table IV-III and Fig. IV-1 should not be due directly to the effect of oxygen on the β transus since heat

206

treatments were adjusted to take this into account. Condition 1 is slowly cooled from β_t - 100°F, and Condition 5 is quenched from β_t + 100°F. For the low, standard and high oxygen contents, the respective β_t values are 1775, 1800 and 1820°F. The only microstructural effect noted was an increase in the primary alpha grain size with oxygen content in slow cooled, Condition 1 (RA), Fig. IV-3. In the case of the more rapidly cooled Condition 5 (βQ), oxygen content did not significantly alter the microstructure, Fig. IV-4.

Cyclic stress-strain curves for Conditions 1, 5, and 7 at 250 and 600°F are presented in Fig. IV-5 through IV-10. The curves for the standard material are presented in Part I. Curves for Conditions 1 and 5 for the two additional oxygen contents and for the two additional hydrogen contents are shown in Fig. IV-11 through IV-18.

It is interesting to note in Fig. IV-5, IV-6, IV-11, IV-12, IV-15, and IV-16 that the cyclic curve crosses the monotonic curve for Condition 1 (RA) as they did in the "standard" material in Part I. This is relatively uncommon, although curves which exhibit cyclic softening commonly have a trend toward crossing at some higher strain. As listed in Table IV-II, however, the crossing strains here are modest. Condition 1, therefore, may be regarded as approximately cyclically stable. Both βQ, Condition 5 and STOA, Condition 7 cyclically soften for all conditions tested; the extent of softening in Conditions 5 and 7 is estimated in the last column of Table IV-IV, as the difference in monotonic and cyclic flow stress at 1% strain.

207

Thus, Condition 1 exhibits crossing behavior and Conditions 5 and 7

softening consistent with the "standard" material of Part I. This is expected

from the "cyclic stability index:"[15] that cyclic softening is expected

when the ratio of ultimate tensile strength (UTS) to yield strength (YS) is

less than 1.2, while hardening is expected when the ratio exceeds 1.4. As

Table IV-II shows, all the conditions exhibit a ratio below 1.2 except

Condition 1 at 68 and $600^{\circ}F$.

Fracture toughness testing of Conditions 1 and 5 at two additional

oxygen levels and two additional hydrogen levels was conducted in compliance

to ASTM E399-74. The results are given in Tables IV-V and IV-VI. The tables

have been footnoted to make them self-explanatory. For all intents and

purposes, the three oxygen contents of Condition 5 (βQ) exhibit valid K_{Ic}

values, and as would be expected, K_{Ic} increases with decreasing oxygen

content. The same trend can be inferred for Condition 1 (RA), but the invalid

toughness values for two oxygen contents make the comparison only

approximate. The toughness in 0.122 and 0.082% oxygen material can be ranked

by their R curves, however, permitting a valid inference to be drawn.

Temperature Effects

FCP Measurements - FCP data for Conditions 1, 5, and 7 for two R

values each (R = 0.3 and 0.7) as a function of temperature are shown in

Fig. IV-19 through IV-24. For Condition 1 at R = 0.3, the effect of

temperature was negligible (Fig. IV-19); at R = 0.7 the effect was significant

at low ΔK. The order of the curves was surprising in that the $250^{\circ}F$ growth

208

rate was less than the room temperature growth rate (Fig. IV-20). For Condition 5 at R = 0.3, the temperature effects were somewhat greater than for Condition 1 (cf Fig. IV-21 and IV-19). At R = 0.7, the temperature effect for βQ, Condition 5 (Fig. IV-21) was comparable to that in RA, Condition 1 at the same R value. Temperature effects in Condition 7 were negligible at R = 0.3 (Fig. IV-23) while at R = 0.7 the effect was similar to that of Condition 1 at the same R value (cf Fig. IV-24 and IV-20).

Selected fractography was performed on fracture surfaces from the specimens used to generate Fig. IV-20, IV-21, and IV-24 as being representative of the temperature effects in Conditions 1, 5, and 7, respectively. The examination was conducted at lower ΔK ($<$11 MPa·m$^{\frac{1}{2}}$) where the effects were most pronounced; the results are shown in Fig. IV-25 through IV-27.

For Condition 1 tested at 20 Hz and R = 0.7, the anomalously lower crack growth rate at 250^{0}F is accompanied by a more tortuous path (cf Fig. IV-25(c) and (a));[*] while the path at 600^{0}F is more transgranular, Fig. IV-25(e) and (f). At room temperature and 250^{0}F, considerable cleavage-like fracture of the primary alpha is observed (Fig. IV-25(b) and (d)); at 600^{0}F the amount of cleavage-like fracture is smaller and evidence of propagation by striation formation is present, Fig. IV-25(g). The Widmanstätten alpha microstructure of Condition 5 does not exhibit as striking

---

*In Fig. IV-25 through IV-27 micrographs in each column are at the same magnification which is indicated by the micron marker at the top of the column. The pair in each row are taken from the same area of the specimen.

a fracture mode transition as Condition 1 but a transition to a more transgranular mode at elevated temperature can be discerned by comparing Fig. IV-26(b) and (c) with Fig. IV-26(a).

In Condition 7 a similar increased tortuosity of crack path to that in Condition 1 occurs for the $250^{o}F$ specimen (cf Fig. IV-24(a) with IV-27(c) and (e)) although the effect is not as obvious because Condition 7 contains a considerably smaller volume fraction of primary alpha. The increased tortuosity of the fracture path at $250^{o}F$ for both conditions is probably related to crack tip blunting in the oxidizing atmosphere at $250^{o}F$. At $600^{o}F$, the crack blunting benefit of the environment is overwhelmed by the decrease in yield strength with temperature, and more rapid, transgranular propagation occurs. The yield strength decrease from room temperature for Condition 1 is 5.9 and 32.8% for $250^{o}F$ and $600^{o}F$, respectively; for Condition 7 it is 7.5 and 26.8%.

During the generation of the elevated temperature data, hold-time data was also taken for comparison to hold-time data taken at room temperature. The hold-time data is presented in the following section.

Hold-Time Measurements - Hold-time data for Conditions 1, 5, and 7 at 250 and $600^{o}F$ is plotted along with the baseline (no-hold) data in Fig. IV-28 through IV-36. In general, increases or decreases in crack growth rate with hold-time at elevated temperature were less than a factor of two and such changes are consistent with hold-time behavior at room temperature. In the room temperature case, the maximum increase (a factor of two) was found in

210

Condition 5 and this increase was associated fractographically with a transition to a more transgranular failure under hold-time conditions. Conversely, Bania and Eylon[16] have shown that hold-time tests in textured Ti-6Al-4V can cause a decrease in growth rate of a factor of two to four. These results combined with the result of the present study would suggest that the increases or decreases of crack growth rates may result from local interaction of microstructure, texture and hold time at maximum load. An additional factor may be the sequence of loading as suggested by Bania and Eylon but that subject was outside the scope of the present program. The conclusion reached after hold-time testing at room temperature, 250°F and 600°F, is that hold-time effects are small for the uniformly, weakly textured microstructures of this study.

Interstitial Effects

FCP Measurements - FCP data at 68 and 600°F for Conditions 1 and 5 are plotted as a function of oxygen content in Fig. IV-37 through IV-40 and as a function of hydrogen content in Fig. IV-41 through IV-44. Oxygen effects were minor for Condition 1 at both room temperature and 600°F (Fig. IV-37 and IV-38) although there is some scatter in the 1 Hz data for the high oxygen material. This probably resulted from a larger primary alpha grain size (Fig. IV-3) in the high oxygen material and localized acceleration related to alpha grain orientation. Such orientation sensitive propagation would be enhanced by the 1 Hz loading. Condition 5 at room temperature, Fig. IV-39, exhibited more pronounced oxygen effects with the low oxygen material tested

211

at 1 Hz giving the lowest growth rate in the range 10 MPa·m$^{\frac{1}{2}}$ ≤ ΔK ≤ 25 MPa·m$^{\frac{1}{2}}$. At ΔK levels less than 10 MPa·m$^{\frac{1}{2}}$, the nominal oxygen material (0.122%) exhibits the lowest growth rate; reasons for this behavior will be addressed in the fractography section. At 600°F similar oxygen effects are observed, Fig. IV-40, but are less pronounced.

Hydrogen effects in Condition 1 (Fig. IV-41 and IV-42) were generally small with the exception of material containing 296 ppm hydrogen tested at room temperature and 1 Hz. For Condition 5 (Fig. IV-43 and IV-44), the hydrogen effects were most pronounced for low ΔK levels at room temperature. Fractographic analysis of the specimens used to produce the room temperature curves is presented in the following section.

Fractography - Detailed fractography was performed on the specimens used to generate Fig. IV-39 and IV-43 in order to better understand the oxygen and hydrogen effects in Condition 5. At low ΔK (ΔK = 6.4 MPa·m$^{\frac{1}{2}}$), the "standard" oxygen (0.122%) material had the slowest growth rate and had the most tortuous fracture topography (cf Fig. IV-45(b) with IV-45(a) and (c)). In the ΔK range 10-25 MPa·m$^{\frac{1}{2}}$, the low oxygen (0.082%) tested at 1 Hz had the slowest crack growth rate. The fracture surface in this specimen exhibited a coarse, tortuous path (Fig. IV-46(a)); as the test frequency and oxygen content was increased, a more planar fracture mode (cf Fig. IV-46(c) and (e) with 46(a)) resulted in increased crack growth rate.

Examination of the hydrogen data for Condition 5 (at ΔK = 6.4 MPa·m$^{\frac{1}{2}}$) revealed that a low ΔK an increase of a factor of five in

crack growth rate occurred for material containing 300 ppm hydrogen tested at 1 Hz when compared to material containing nominal hydrogen (20 ppm) tested at 20 Hz. This increase in growth rate was accompanied by a striking transition in fracture mode from intergranular to transgranular propagation, cf Fig. IV-47(a) and (b). A similar, though less striking, transition was seen as the hydrogen content was increased (Fig. IV-48) in specimens tested at 20 Hz and $\Delta K = 11$ MPa$\cdot$m$^{\frac{1}{2}}$.

It was concluded that, for Condition 5, the effect of oxygen and hydrogen was principally associated with a change in fracture path morphology and that the most significant increases in crack growth rate at a given ΔK level occurred for loading at the lower rate, 1 Hz.

DISCUSSION

The tensile results have shown that considerable oxygen strengthening is dependent on microstructure, the effect being largest in Condition 5, the beta quenched microstructure. The hydrogen effects are much less significant, with a small effect at room temperature and none at 600°F. At nominal hydrogen levels, the temperature dependence is roughly independent of microstructure but is a function of oxygen content. For material containing 0.122% oxygen, and variations in hydrogen content, the temperature dependence is sensitive to hydrogen only for Condition 5. Condition 1, therefore, can be considered more tolerant from a strength standpoint to variations in interstitial content than Condition 5.

213

The cyclic stress-strain behavior for Conditions 1 and 5 both as a function of temperature and as a function of interstitial content exhibit small changes from the room temperature, "standard" material. Condition 1 exhibits crossing behavior for all test conditions, while Condition 5 cyclic softens for all test conditions. This behavior both for Condition 1 and 5 is as would be expected from the "cyclic stability index"[15] which is less than 1.2 for all specimens tested except Condition 1 at 68 and 600°F. For these two specimens the UTS/YS ratio is still less than 1.4, the value above which cyclic hardening is expected; the crossing behavior would, therefore, be consistent with the "cyclic stability index" approach.

The trend in both Condition 1 and Condition 5 of increasing fracture toughness with decreasing oxygen content is in agreement with trends previously reported for titanium alloys.[17,18]

In contrast to the results of other investigators,[6-8] temperature effects on crack growth were found to be significant for all three microstructures evaluated in this program; this effect was most pronounced at low ΔK levels although it persisted to higher ΔK levels for some of the microstructure load ratio (R) combinations. It should be noted that the previous investigation had been conducted at load ratios of 0.05 and 0.1 and that the data in this program was taken as a function of temperature at R = 0.3 and 0.7. For Conditions 1 and 7 the effect was greatest for R = 0.7, the high mean load situation; for Condition 5, the effect was similar for R = 0.3 and 0.7. Conditions 1 and 7, also exhibited analogous behavior in

214

that the 250°F curve fell below rather than in between the 68 and 600°F curves. Associated with this behavior was a more tortuous crack path which is rationalized by crack tip blunting associated with the oxidizing atmosphere at 250°F. As the temperature is raised to 600°F, the decrease in yield strength with temperature offsets the crack tip blunting effect and results in an increase in growth rate.

Hold time at maximum load had little effect on crack growth rate at either of the test temperatures (250 and 600°F), the change in growth rate being less than a factor of two; the only exception being a decrease in growth rate by a factor of 2.7 in Condition 1 at 600°F and R = 0.3. Since this isolated exception is less than a factor of three, it is concluded that hold-time effects are negligible for the uniformly, weakly textured microstructures of this study.

The FCP behavior of Conditions 1 and 5 as a function of interstitial content follows the pattern for the tensile behavior in that Condition 5 is more sensitive than Condition 1 to oxygen and hydrogen content. The change in crack growth rate in Condition 5 was associated with transitions from tortuous, faceted growth to a more planar, transgranular propagation as interstitial content was increased. Transgranular propagation with increased interstitial content is consistent with the increased yield strength and an associated tendency to planar slip in the alpha phase of these conditions.

215

REFERENCES

1. R. J. H. Wanhill, J. Inst. Met., 1973, Vol. 101, p. 258

2. A. W. Thompson, J. D. Frandsen, and J. C. Williams, Met. Sci., 1975, Vol. 9. p. 46

3. J. L. Robinson and C. J. Beevers, Met. Trans., 1973, Vol. 5, p. 391

4. C. J. Beevers, Fract. 1977, Vol. 1, 1977, pp. 239-60

5. D. A. Meyn, Met. Trans., 1974, Vol. 5, p. 2405

6. R. P. Wei and D. L. Ritter, J. Mater., 1972, Vol. 7, p. 240

7. T. T. Shih and R. P.Wei, Fatigue Crack Growth Under Spectrum Loads, ASTM STP 595, 1976, pp. 113-124

8. A. Yuen, S. W. Hopkins, G. R. Leverant and C. A. Rau, Met. Trans., 1974, Vol. 5, pp. 1833-42

9. F. L. Parkinson, "Titanium Alloy 6Al-4V Sheet," Report FAA-SS-72-01, The Boeing Co., Seattle, Washington, July 1972

10. D. E. Pettit, W. E. Krupp, J. T. Ryder, and D. W. Hoeppner, "Investigation of the Effects of Stress and Chemical Environments on the Prediction of Fracture in Aircraft Structural Materials," Report LR 26026, Lockheed-California Co., Burbank, California, July 1973

11. A. W. Bowen, Proc. Third Int. Conf. on Strength of Metals and Alloys, pp. 446-50, Cambridge, U.K. (1973)

12. A. W. Sommer, private communication: meeting summary memorandum, "Recent Results on Ti-6Al-4V RA Material," June 20, 1973

13. A. W. Sommer and C. H. Hamilton, "Thermomechanical Processing of Titanium Alloys," Report NA-73-277, LAA Division, Rockwell International, Los Angeles, California, April 1973

14. J. C. Williams, J. C. Chesnutt, and N. E. Paton, unpublished research

15. R. W. Smith, M. H. Hirschberg and S. S. Manson, NASA TN D-1574 (April 1973)

16. P. J. Bania and D. Eylon, Met. Trans., 1978, Vol. 9A, pp. 847-55

17. W. S. Hieronymous, Aviation Week and Space Technology, 1971, July, p. 42

18. R. J. Goode and R. W. Judy, Weld. Res. Supp. Bull. No. 134, 1968, October

TABLE IV-I

DETAILS OF FORGING VARIABLES USED FOR FABRICATING Ti-6Al-4V PANCAKE FORGINGS

Alloy	Heat Number	S/N	First Upset						Second Upset					
			Temp. (°F)	Furnace Time (h)	Cooling Method	Thickness Initial (in.)	Finish (in.)	Reduction (%)	Temp. (°F)	Furnace Time (h)	Cooling Method	Thickness Initial (in.)	Finish (in.)	Reduction (%)
Ti-6Al-4V 0.185 wt% O_2 (8-3/4 in. round billet)	K-8795 (TMCA)	D1	1745 (β_t-75)	3	AC	5.5	3.5	36	1720 (β_t-100)	3	AC	3.5	2	43
		D5	1895 (β_t+75)	3	AC	5.5	3.5	36	1895 (β_t+75)	3	AC	3.5	2	43
Ti-6Al-4V 0.122 wt% O_2 (9 in. round billet)	991174 (RMI)	C1	1725 (β_t-75)	3	AC	5	3.5	30	1700 (β_t-100)	3	AC	3.5	2	43
		C5	1875 (β_t+75)	3	AC	5	3.5	30	1875 (β_t+75)	3	AC	3.5	2	43
Ti-6Al-4V 0.082 wt% O_2 (8 in. rcs bloom)	R-50645C (Crucible)	E1	1700 (β_t-75)	3	AC	4.75	3.5	27	1675 (β_t-100)	3	AC	3.5	2	43
		E5	1850 (β_t+75)	3	AC	4.75	3.5	27	1850 (β_t+75)	3	AC	3.5	2	43

218

TABLE IV-II

COMPOSITION AND BETA TRANSUS TEMPERATURE OF TITANIUM ALLOY FORGING BILLET

Alloy	Source	Heat	Composition Weight Percent							$\alpha + \beta/\beta$ Transus $^\circ F$ ($^\circ C$)
			Al	V	Fe	C	O	N	H	
Ti-6Al-4V 0.185 wt% O_2 (8-3/4 in. round billet)	TMCA	K-8795	6.3	4.0	0.16	0.026	0.185	0.009	0.006	1820 (993)
Ti-6Al-4V 0.122 wt% O_2 (9 in. round billet)	RMI	991174	6.2	4.1	0.22	0.010	0.122	0.012	0.003	1800 (982)
Ti-6Al-4V 0.082 wt% O_2 (8 in. rcs bloom)	Crucible	R50645C	6.0	3.8	0.05	0.022	0.082	0.009	0.005	1775 (968)

219

TABLE IV-III

TENSILE PROPERTIES, Ti-6Al-4V

Condition	Content	Temperature °F	Yield Strength ksi	MPa	Ultimate Strength ksi	MPa*	Uniform True Strain %	Total Elong. in 25 mm, %	RA %
1	Standard Oxygen and Hydrogen	RT	103	707	127	873	8.7	12.4	36.0
1		250	96	665	107	735	8.6	16.2	42.0
1		600	69	475	90	620	14.0	23.0	52.0
5		RT	125	862	135	931	5.7	5.9	6.0
5		250	117	805	128	885	7.3	8.1	12.2
5		600	94	645	112	770	6.9	10.1	29.8
7		RT	132	909	142	982	7.4	15.5	47.0
7		250	122	840	134	925	9.9	22.4	54.5
7		600	96	665	115	790	6.4	18.4	37.4
1	Low Oxygen	RT	107	735	119	820	9.7	21.3	40.0
1		600	73	500	91	630	11.7	24.1	56.9
5		RT	118	815	130	895	6.3	7.3	14.8
5		600	86	590	103	710	6.7	10.0	23.9
1	High Oxygen	RT	124	855	133	920	12.3	24.9	34.8
1		600	75	520	95	655	16.8	24.3	40.5
5		RT	145	1000	157	1085	5.0	5.1	7.9
5		600	99	685	123	845	7.7	9.7	24.4
1	100 ppm Hydrogen	RT	116	800	123	848	9.2	17.3	29.8
1		600	83	574	100	692	10.3	15.9	48.4
5		RT	135	931	145	1000	6.8	7.6	9.6
5		600	94	650	112	775	6.8	10.2	15.8
1	300 ppm Hydrogen	RT	113	779	125	862	10.5	20.7	34.8
1		600	75	515	96	663	9.6	15.9	36.6
5		RT	129	889	148	1020	5.8	7.6	9.5
5		600	101	697	108	746	10.1	11.8	7.2

*Stresses in English units were originally calculated to the nearest 0.1 ksi and converted to SI units to the nearest MPa. Tabulated stresses in English units were rounded to the nearest 1 ksi.

TABLE IV-IV

CYCLIC STRESS-STRAIN BEHAVIOR

Condition	Temp °F	Inter-stitials	UTS/YS	Softens	Crosses	Crossing Strain %	Softening (MPa) at 0.5% ϵ_p	1.0% ϵ_p
1	68	nominal	1.23		X	0.60		
	250	nominal	1.11		X	0.74		
	600	nominal	1.31		X	0.65		
	68	low oxygen	1.12		X	0.62		
	68	high oxygen	1.08		X	0.60		
	68	100 ppm hydrogen	1.06		X	0.53		
	68	300 ppm hydrogen	1.11		X	0.37		
5	68	nominal	1.08	X			77	47
	250	nominal	1.10	X			70	
	600	nominal	1.19	X			46	
	68	low oxygen	1.10	X			72	
	68	high oxygen	1.09	X			33	
	68	100 ppm hydrogen	1.07	X			59	
	68	300 ppm hydrogen	1.15	X			20	
7	68	nominal	1.07	X			118	60
	250	nominal	1.10	X			112	
	600	nominal	1.19	X				63

221

TABLE IV-V

OXYGEN EFFECT ON FRACTURE TOUGHNESS

Condition	Oxygen Content %	K_Q Ksi·in$^{\frac{1}{2}}$	K_Q MPa·m$^{\frac{1}{2}}$	Valid	Required Thickness cm
1	0.185	77.8 73.2	85.5 80.4	Yes Yes	
1	0.122	109.3 110.6	120.1 121.5	No (1) No (1)	7.15 7.31
1	0.082	108.5 116.6	119.2 128.1	No (1) No (1)	6.57 7.59
5	0.185	62.0 62.3	68.2 68.5	No (3,4) Yes	
5	0.122	91.6 92.1	100.8 101.3	Yes Yes	
5	0.082	99.7 100.7	109.6 110.6	No (1) No (1,4)	4.605 (5)

(1) Failed thickness requirement

(2) Failed precrack curvature requirement

(3) Precrack load too high

(4) Compare with valid K_Q for duplicate specimen

(5) Actual specimen thickness 4.575 cm

TABLE IV-VI

HYDROGEN EFFECTS ON FRACTURE TOUGHNESS

Condition	Hydrogen Content ppm	K_Q Ksi·in$^{\frac{1}{2}}$	K_Q MPa·m$^{\frac{1}{2}}$	Valid	Required Thickness cm
1	3	109.3	120.1	No (1)	7.15
		110.6	121.5	No (1)	7.31
1	100	101.7	111.8	No (1)	4.90 (2)
1	300	60.0	65.9	Yes (3)	
5	20	91.6	100.8	Yes	
		92.1	101.3	Yes	
5	100	81.1	89.1	Yes	
5	300	90.5	95.5	No (4)	

(1) Failed thickness requirement

(2) Actual specimen thickness 4.46 cm

(3) Actual specimen thickness 2.54 cm

(4) Failed precrack curvature requirement

223
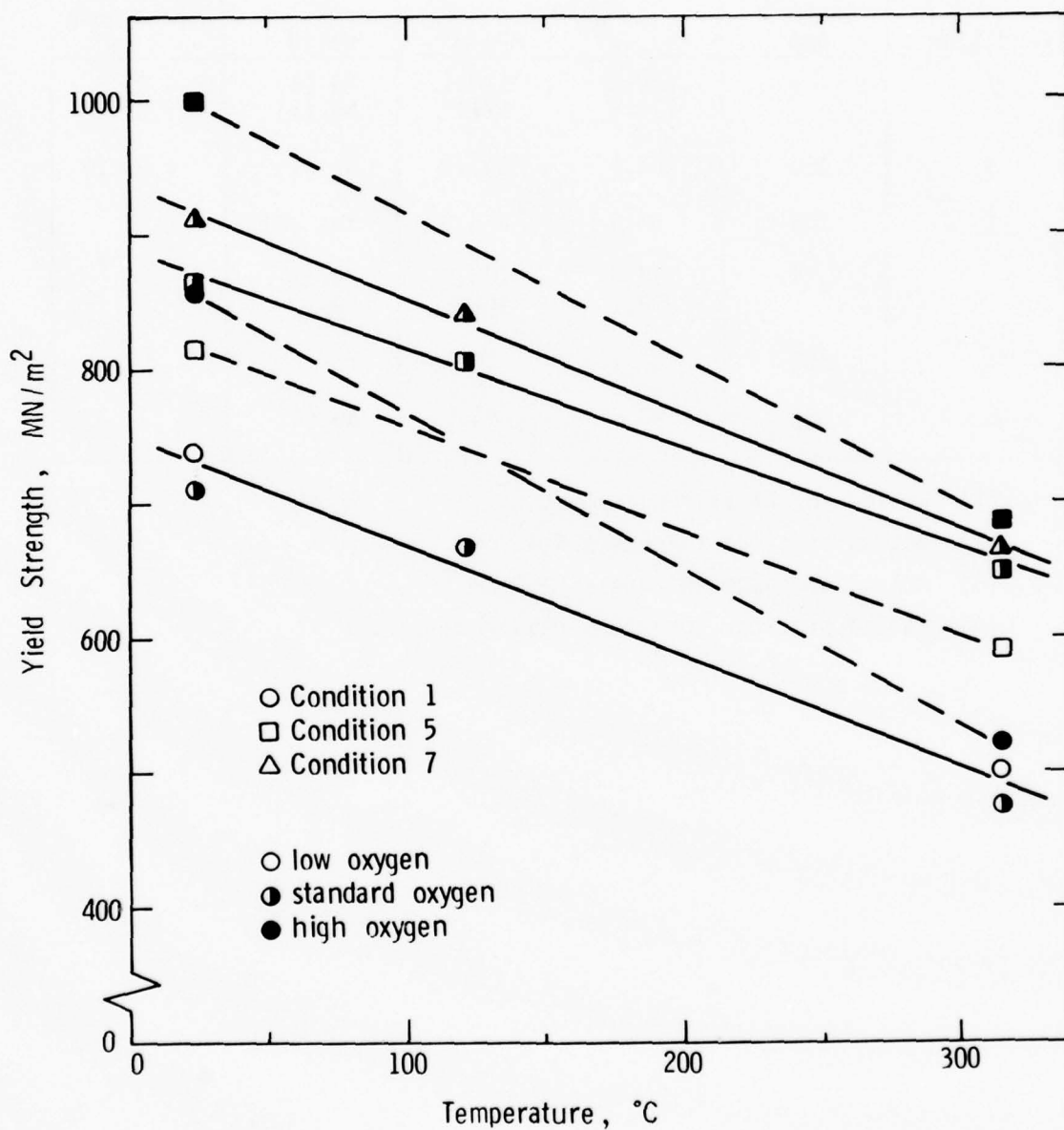
Fig. IV-1   Yield strength as a function of temperature and oxygen
content for Conditions 1, 5, and 7

224
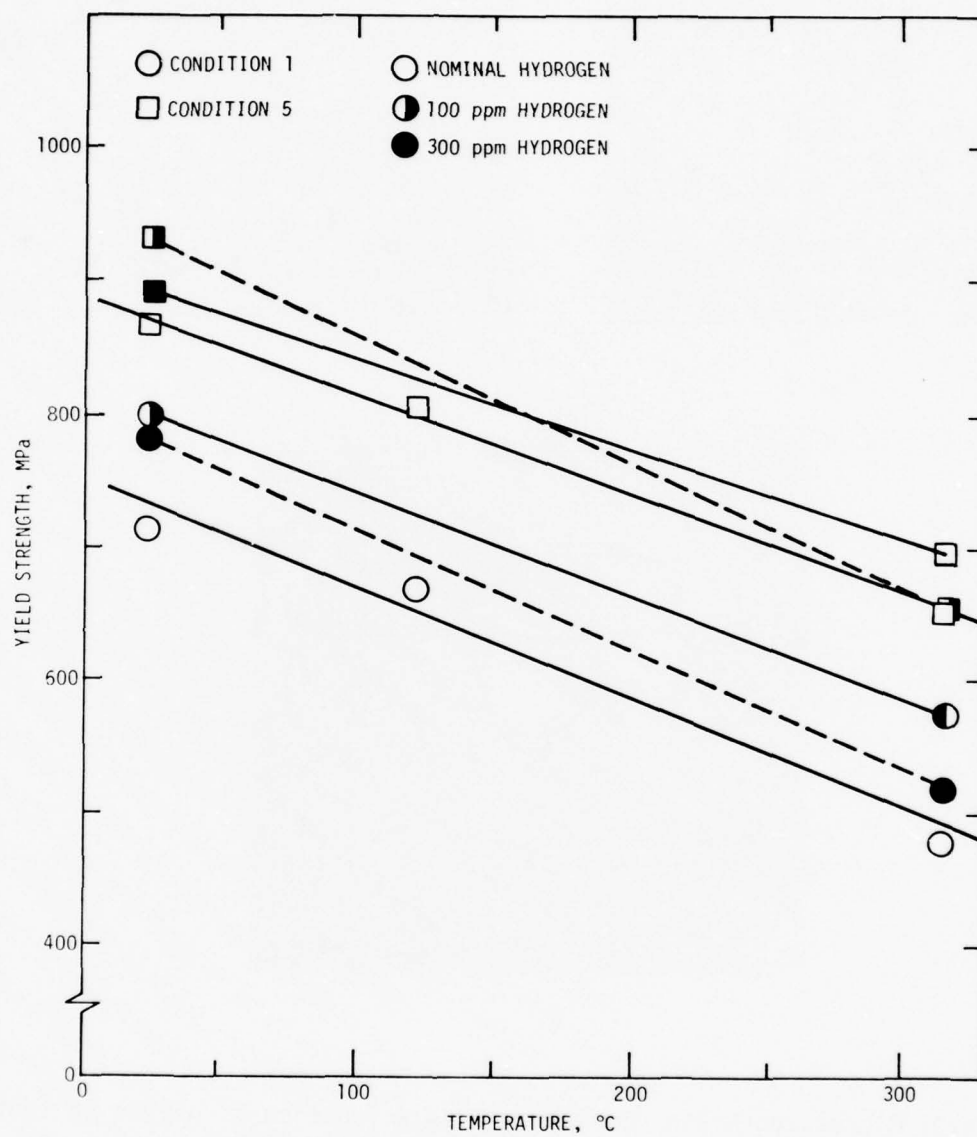
Fig. IV-2 Yield strength as a function of temperature and hydrogen content for Conditions 1 and 5.

225
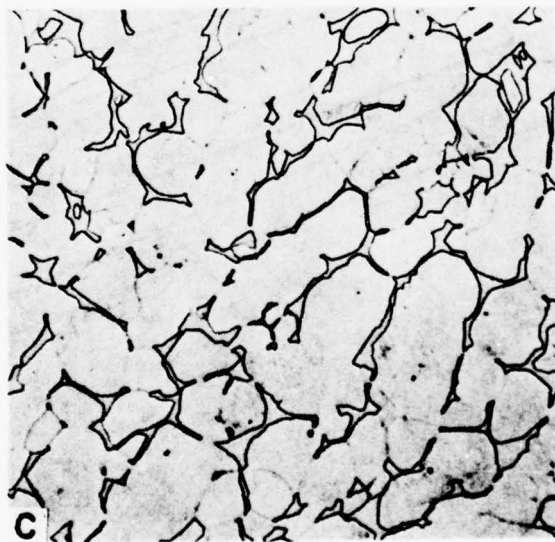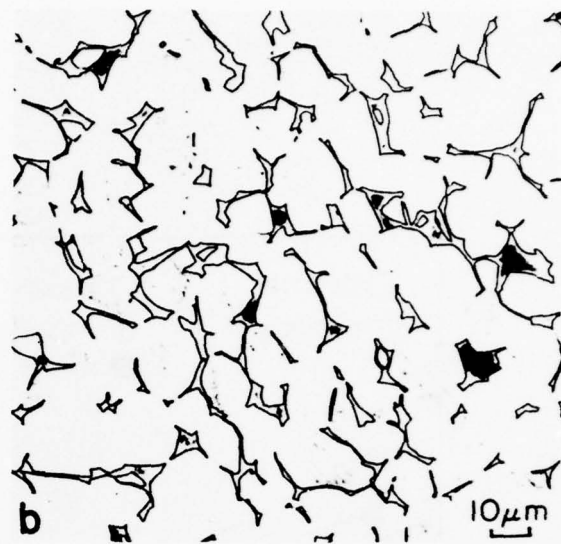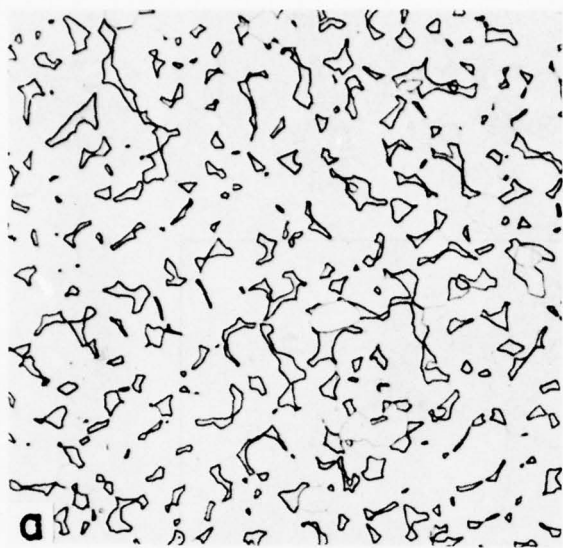
Fig. IV-3 Microstructure of Condition 1 as a function of oxygen content:
(a) 0.082% oxygen, (b) 0.122%, and (c) 0.185%.
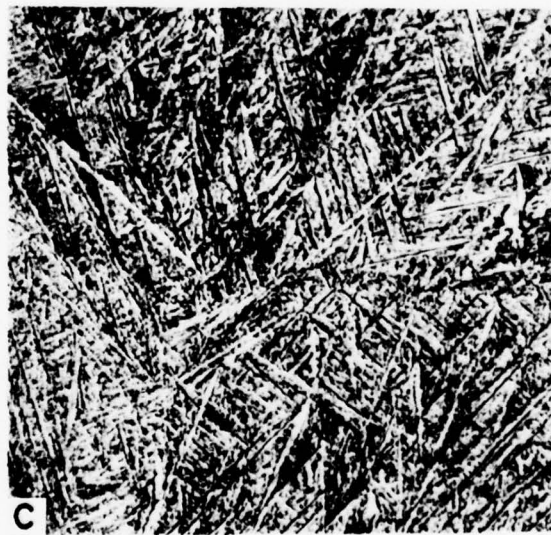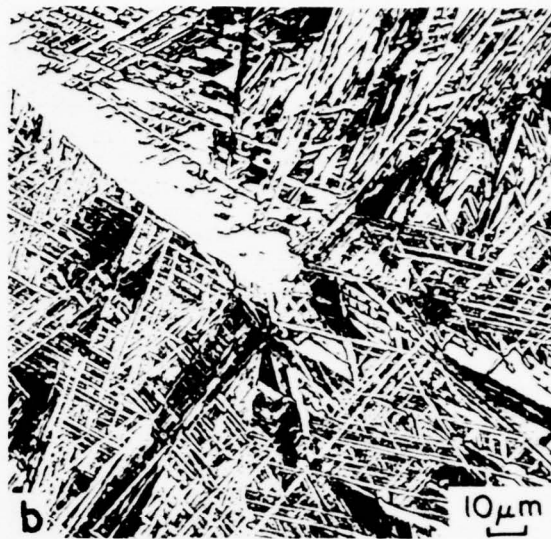
Fig. IV-4 Microstructure of Condition 5 as a function of oxygen content: (a) 0.082% oxygen, (b) 0.122%, and (c) 0.185%.
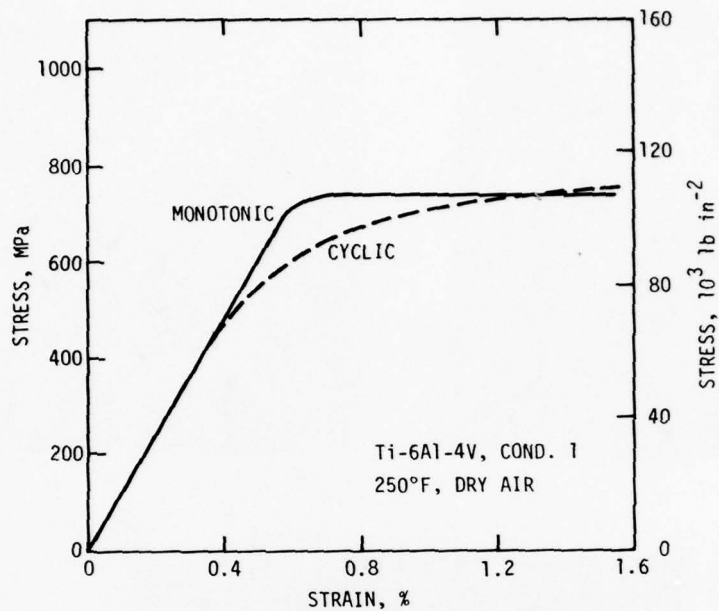
Fig. IV-5   Cyclic stress-strain behavior of Condition 1 at 250°F.
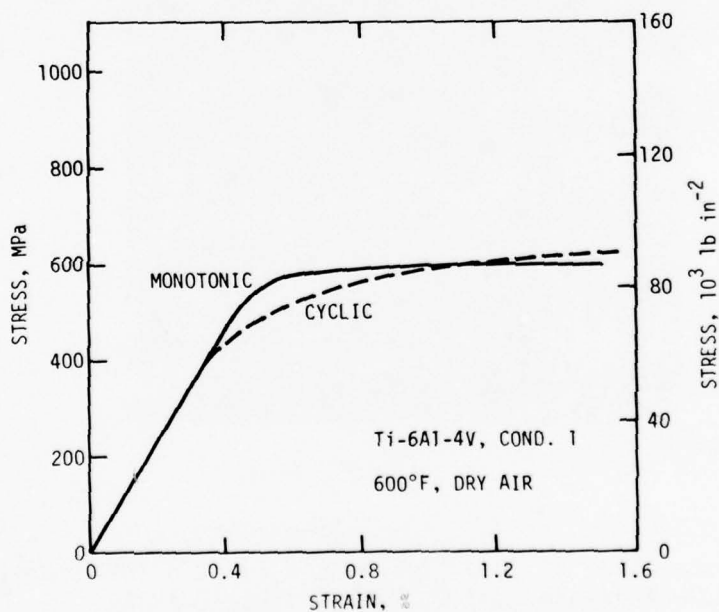
Fig. IV-6   Cyclic stress-strain behavior of Condition 1 at 600°F.
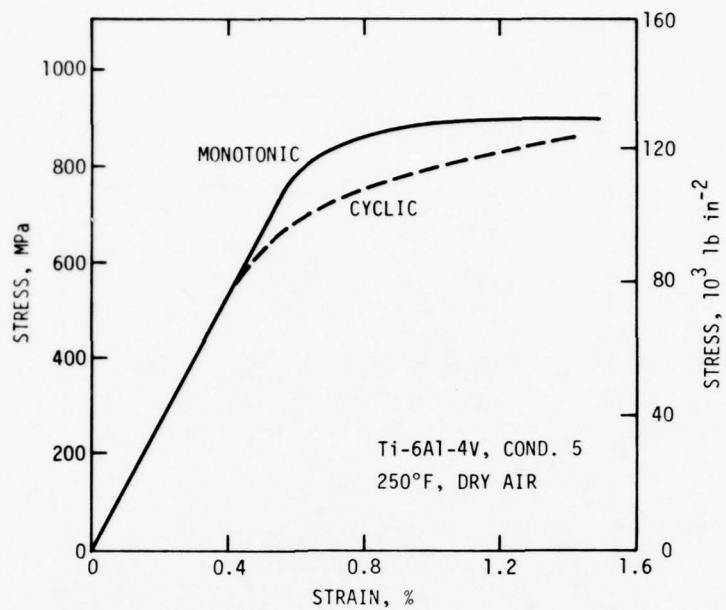
Fig. IV-7 Cyclic stress-strain behavior of Condition 5 at 250°F.
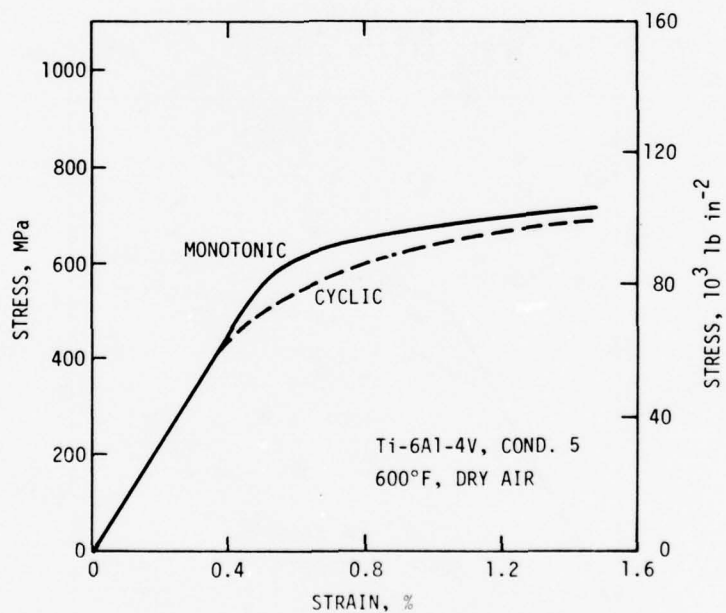
Fig. IV-8 Cyclic stress-strain behavior of Condition 5 at 600°F.

229
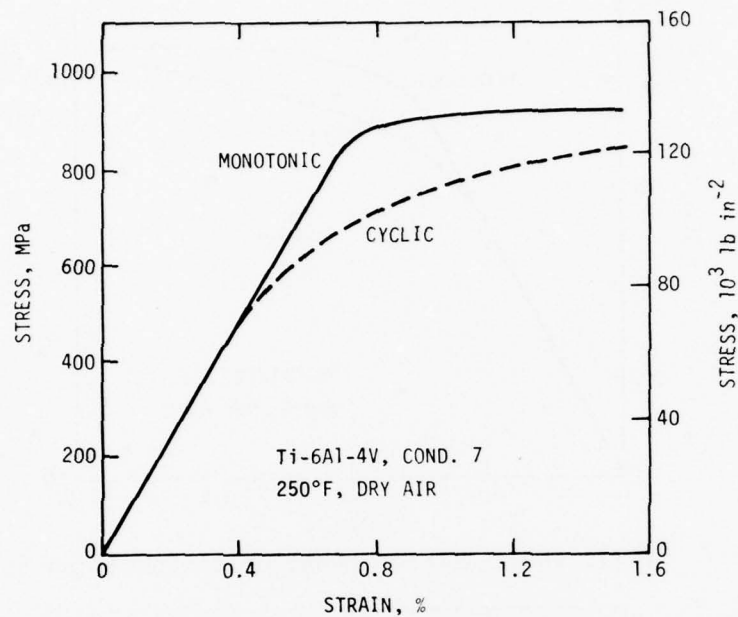
Fig. IV-9 Cyclic stress-strain behavior of Condition 7 at 250°F.
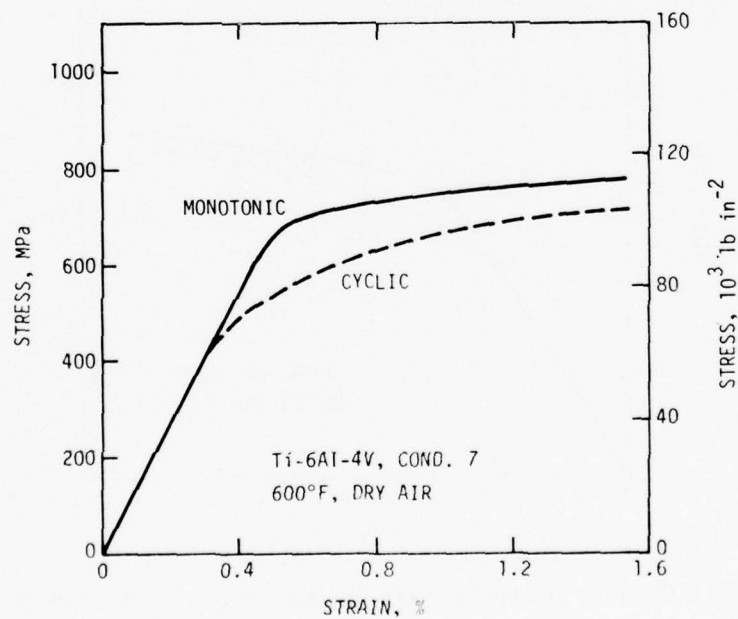
Fig. IV-10 Cyclic stress-strain behavior of Condition 7 at 600°F.

230
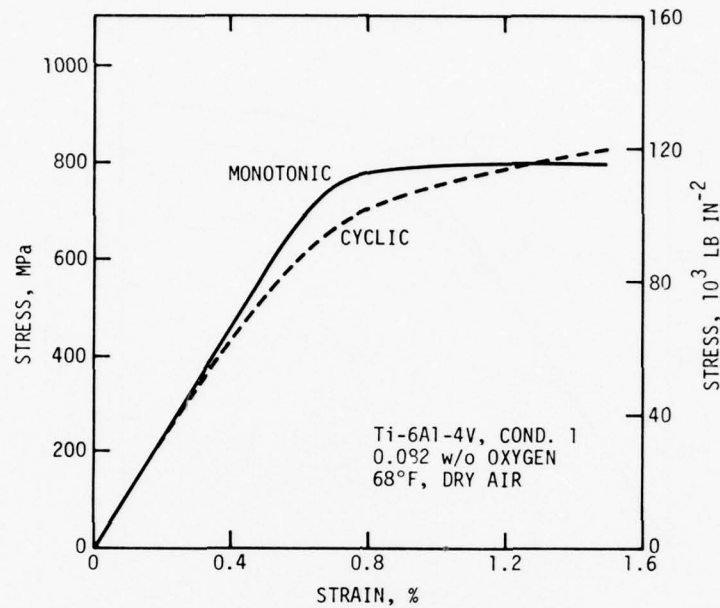
Fig. IV-11 Cyclic stress-strain behavior of Condition 1 (0.082 wt% oxygen).
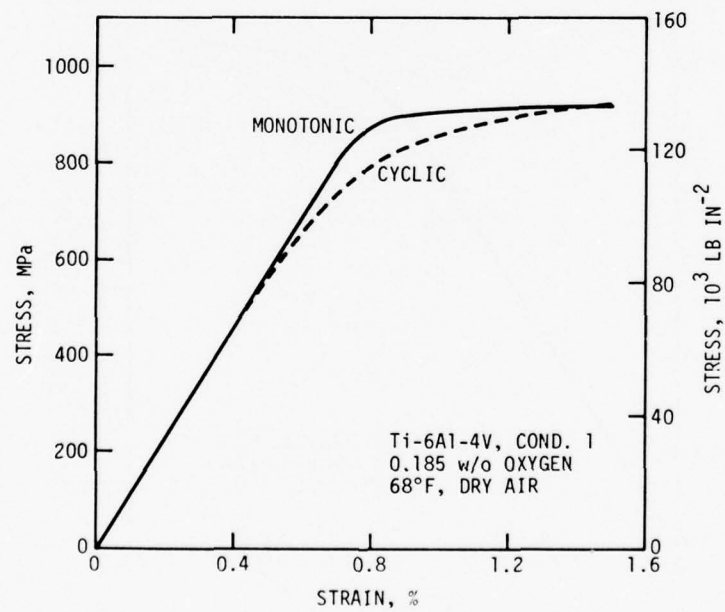
Fig. IV-12 Cyclic stress-strain behavior of Condition 1 (0.185 wt% oxygen).

231
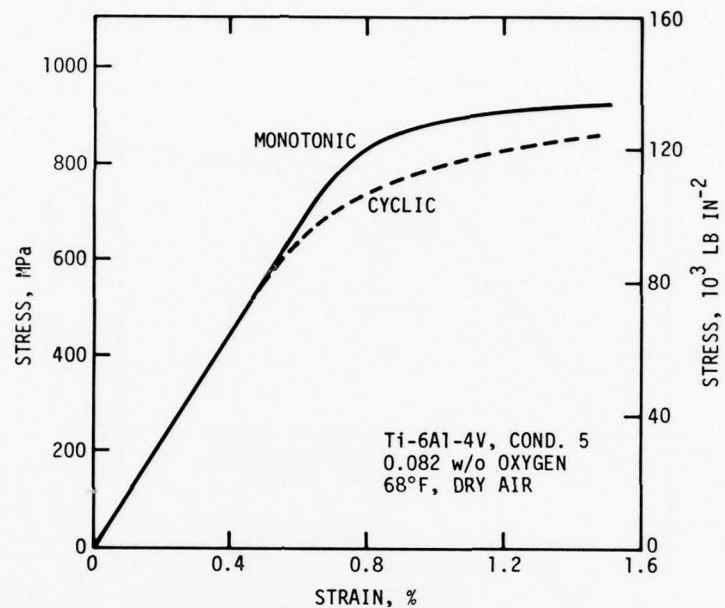
Fig. IV-13   Cyclic stress-strain behavior of Condition 5 (0.082% wt% oxygen).
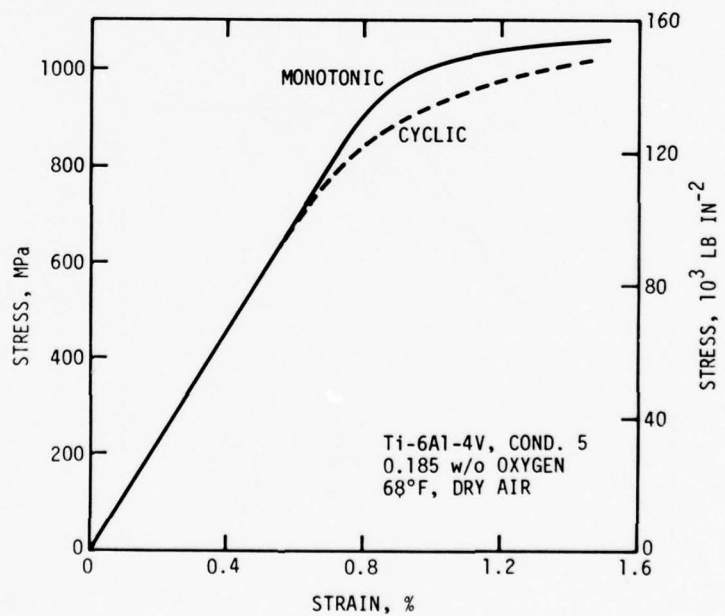
Fig. IV-14   Cyclic stress-strain behavior of Condition 5 (0.185 wt% oxygen).
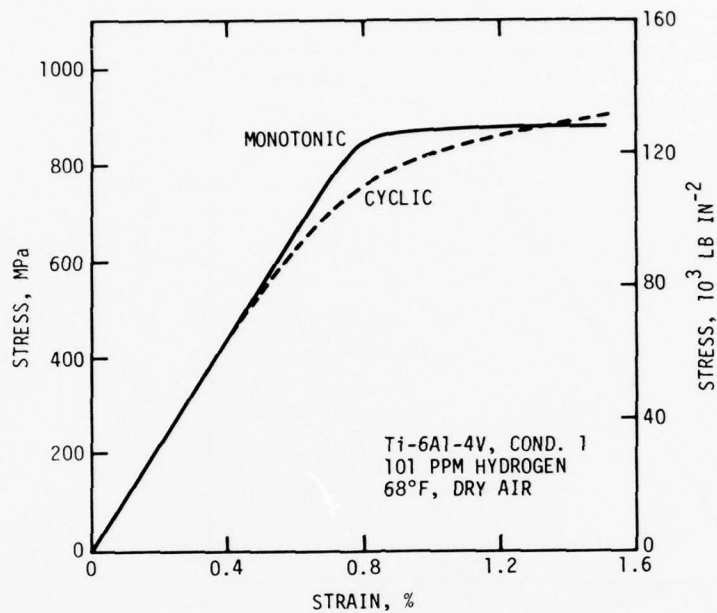
Fig. IV-15 Cyclic stress-strain behavior of Condition 1 (101 ppm hydrogen).
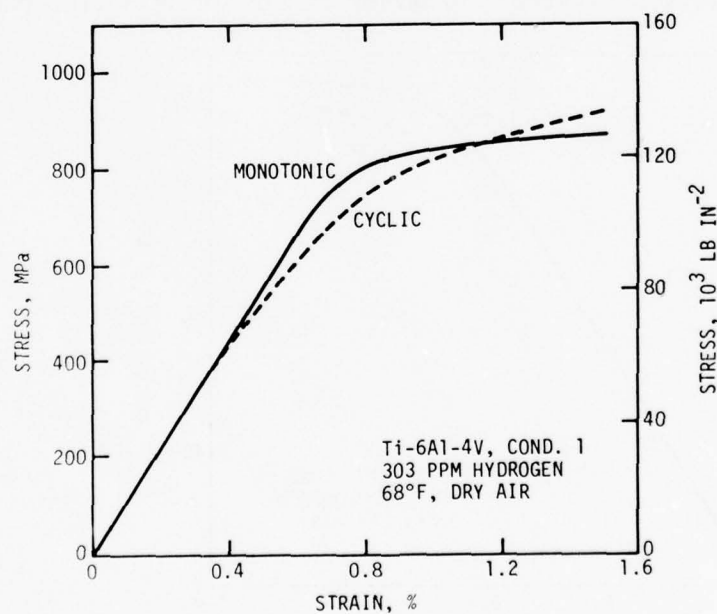
Fig. IV-16 Cyclic stress-strain behavior of Condition 1 (303 ppm hydrogen).
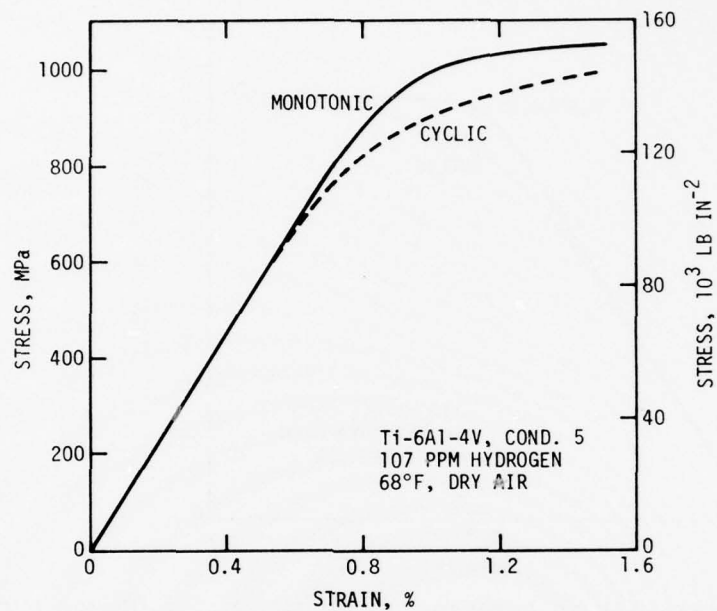
Fig. IV-17 Cyclic stress-strain behavior of Condition 5 (107 ppm hydrogen).
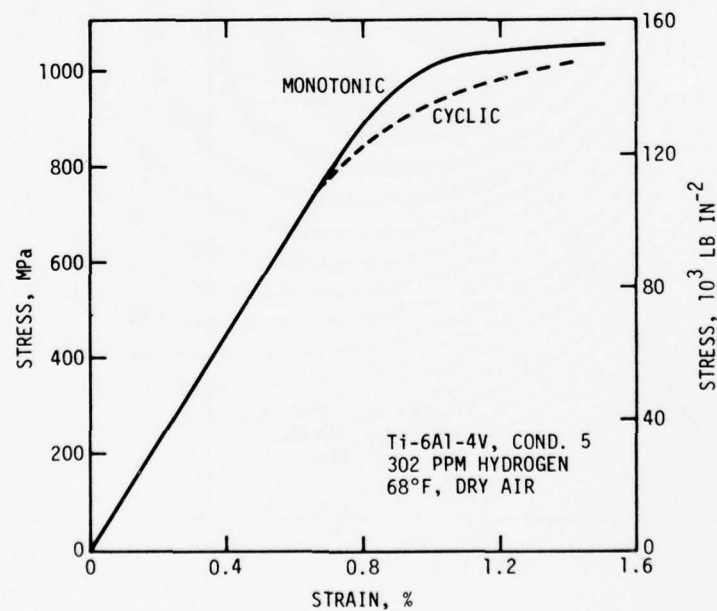
Fig. IV-18 Cyclic stress-strain behavior of Condition 5 (302 ppm hydrogen).

234

TI-6AL-4V(COND. 1), 20HZ, R-0.3
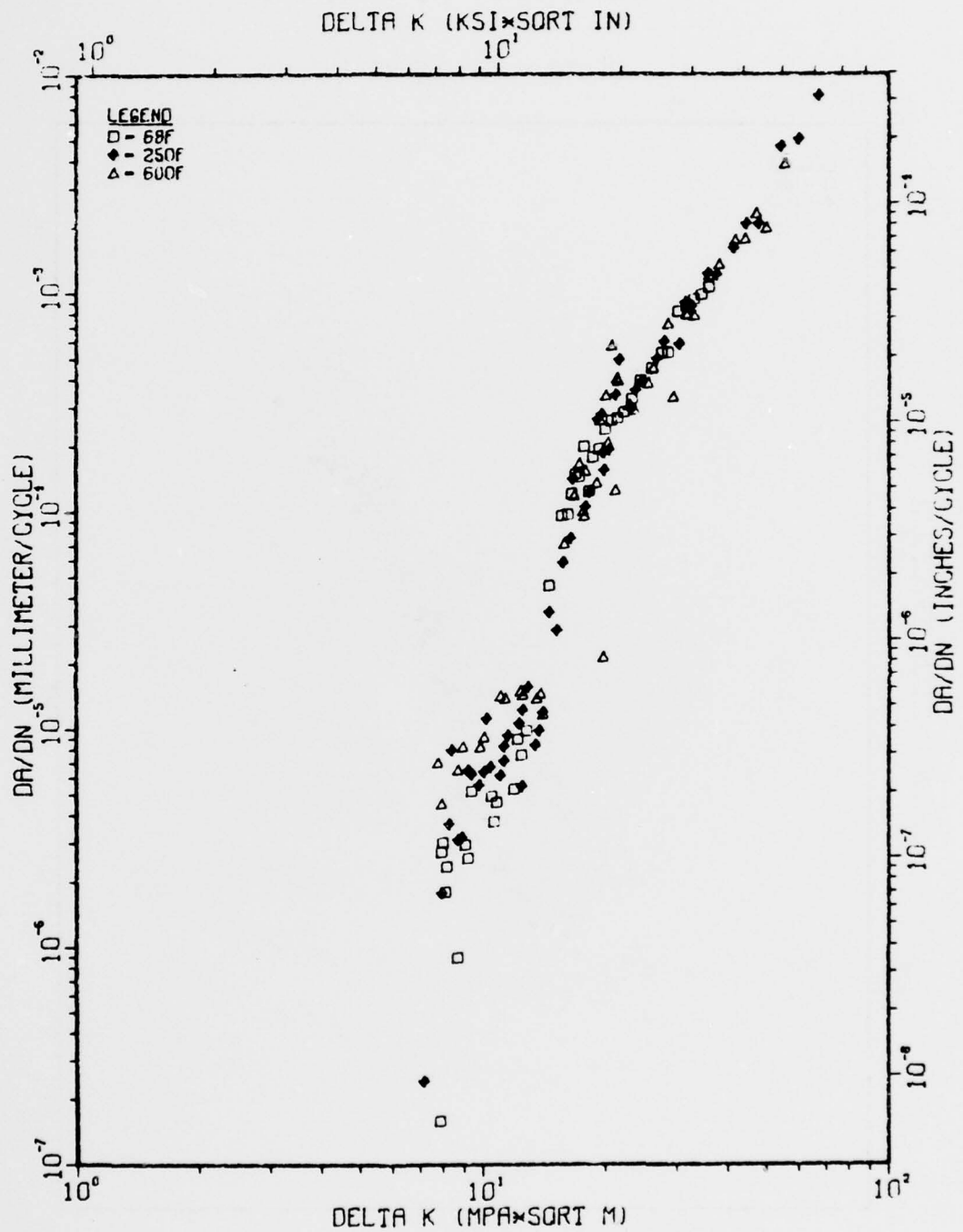
Fig. IV-19 Dependence of FCP in Condition 1 on temperature (68, 250 and 250°F) at 20 Hz, R = 0.3.

235

TI-6AL-4V(COND. 1), 20HZ, R-0.7
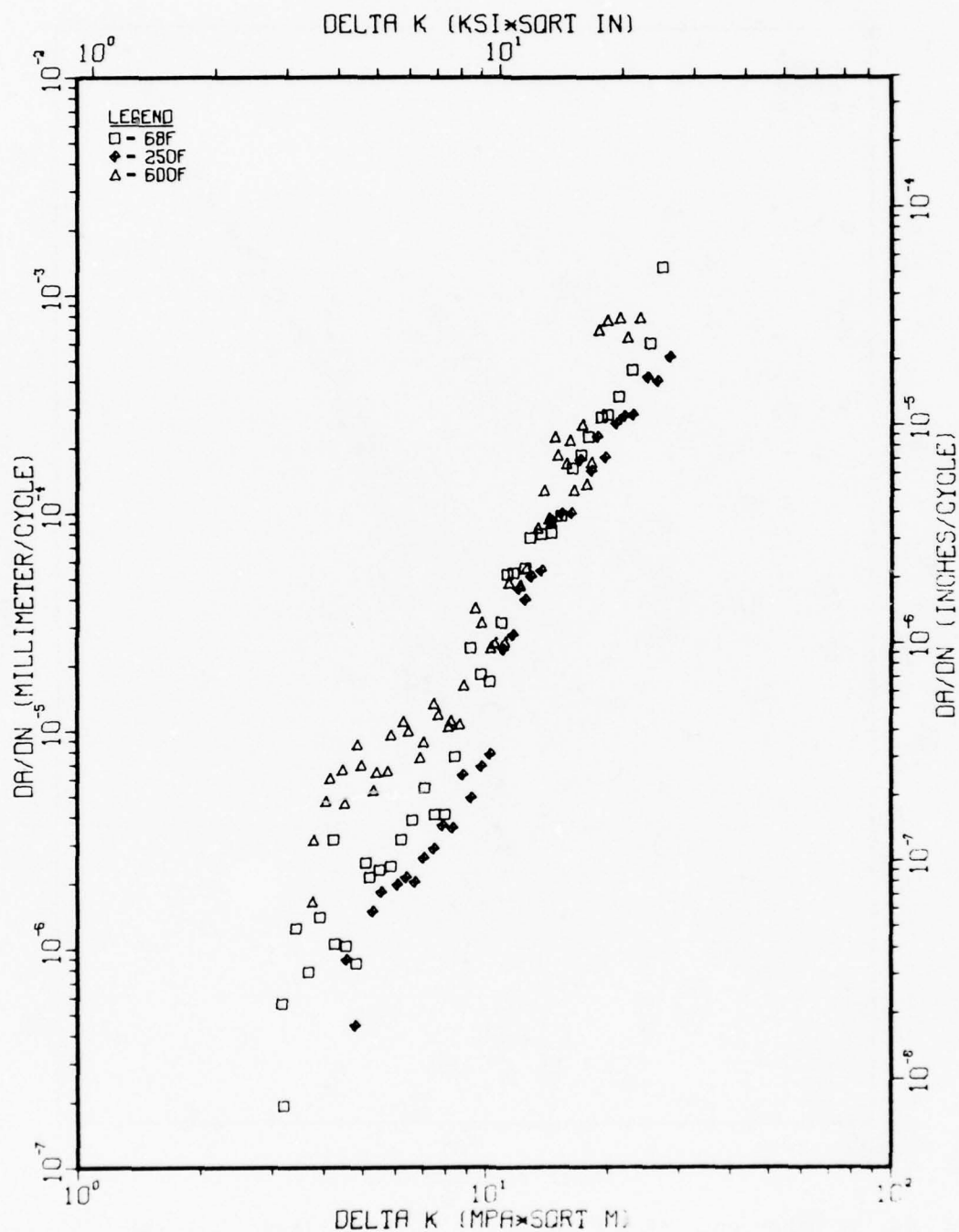
Fig. IV-20 Dependence of FCP in Condition 1 on temperature at 20 Hz, R = 0.7.

Fig. IV-21 Dependence of FCP in Condition 5 on temperature at 20 Hz, R = 0.3.

TI-6AL-4V(COND. 5), 20HZ, R-0.7
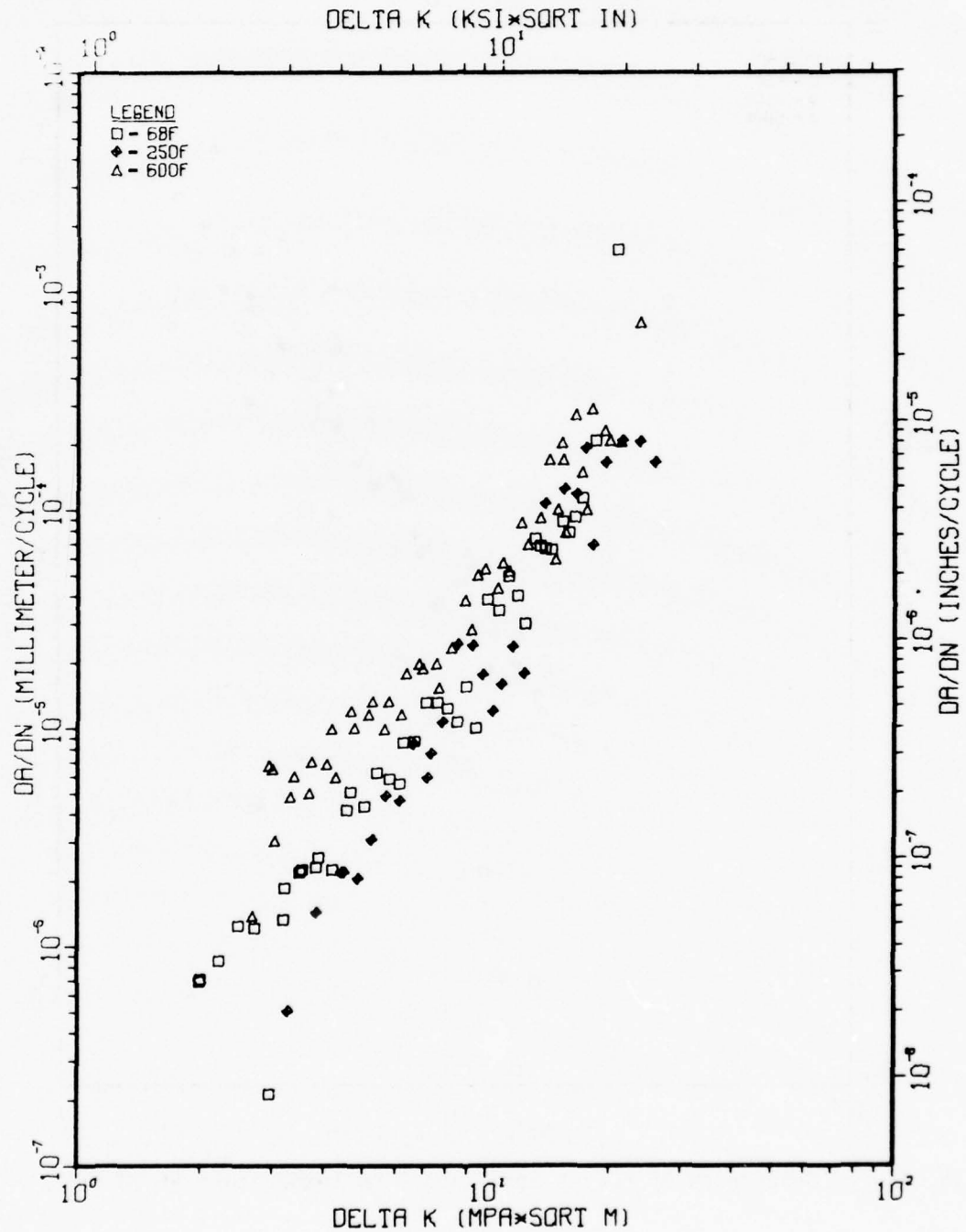
Fig. IV-22 Dependence of FCP in Condition 5 on temperature at 20 Hz, R = 0.7.

TI-6AL-4V(COND. 7), 20HZ, R-0.3
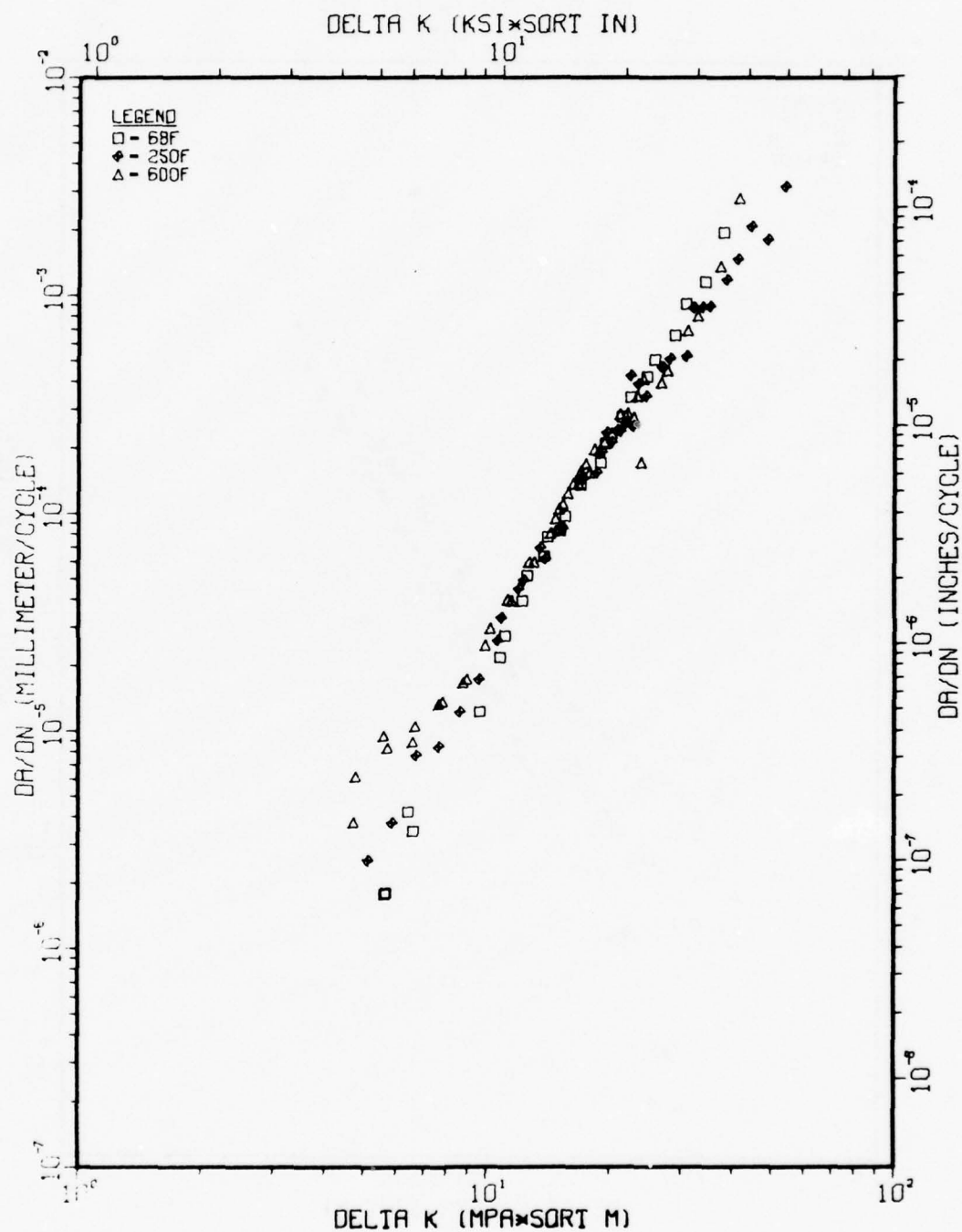
Fig. IV-23 Dependence of FCP in Condition 7 on temperature at 20 Hz, R = 0.3.

239

TI-6AL-4V(COND. 7), 20HZ, R-0.7
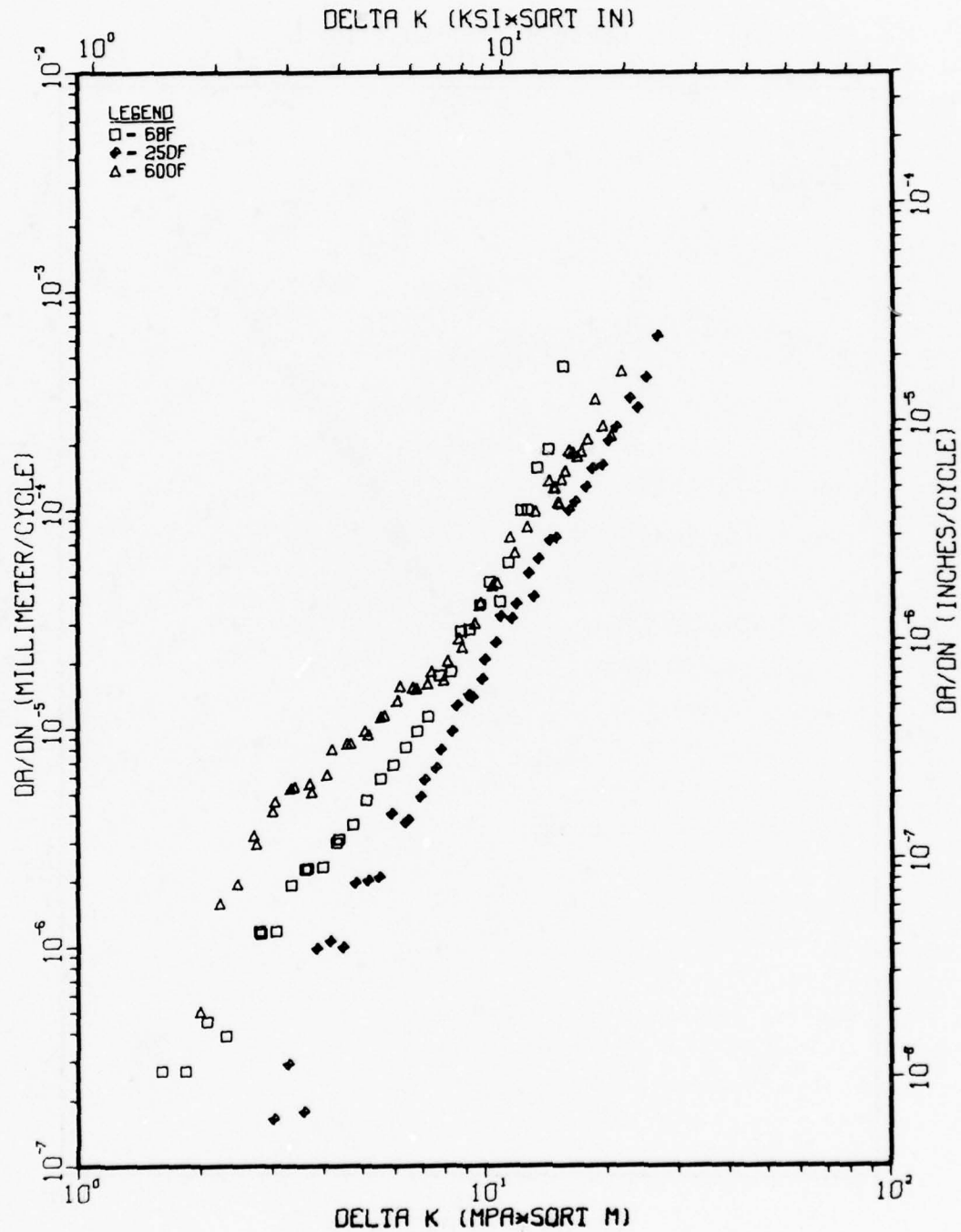
Fig. IV-24 Dependence of FCP in Condition 7 on temperature at 20 Hz, R = 0.7.
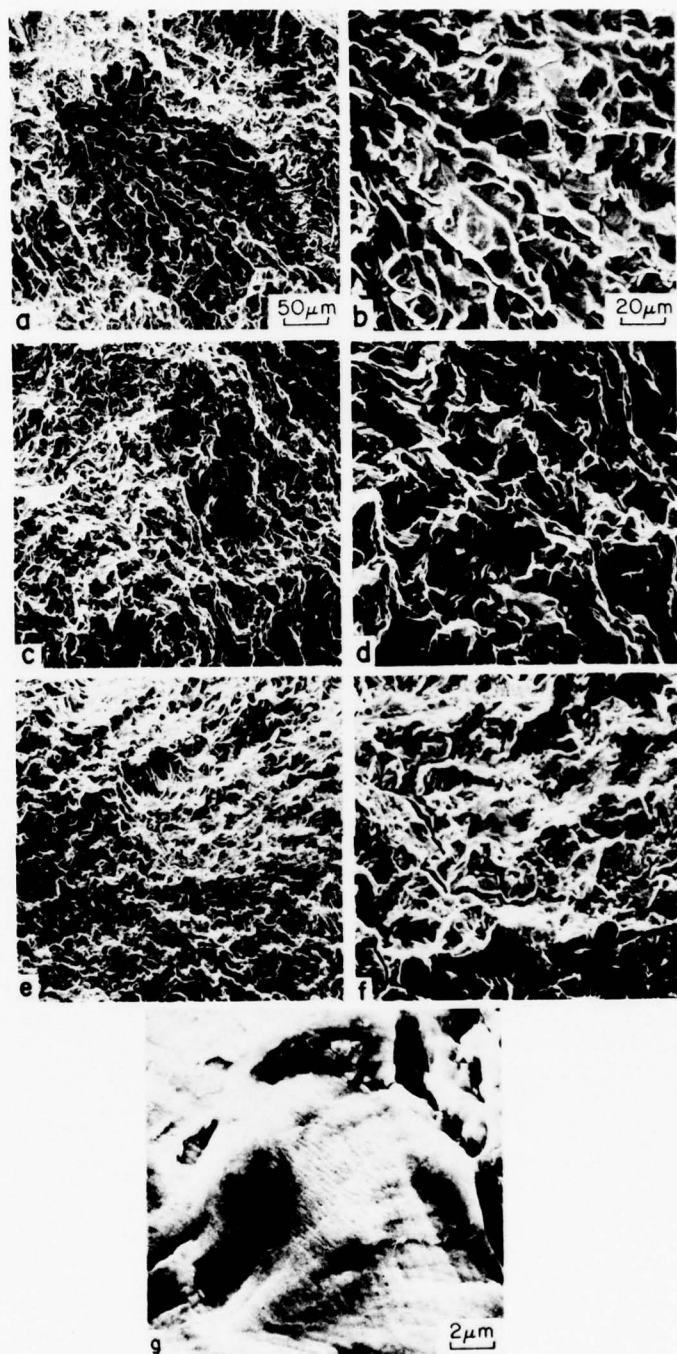
Fig. IV-25   Fracture surfaces of Condition 1 tested in dry air at 20 Hz and
R = 0.7 for ΔK = 6.2 MPa·m². (a,b) room temperature:
da/dN = 3.0 x 10^{-6} mm/cycle; (c,d) 250°F:
da/dN = 2.0 x 10^{-6} mm/cycle; (e, f, g) 600°F:
da/dN = 1.1 x 10^{-5} mm/cycle.

241
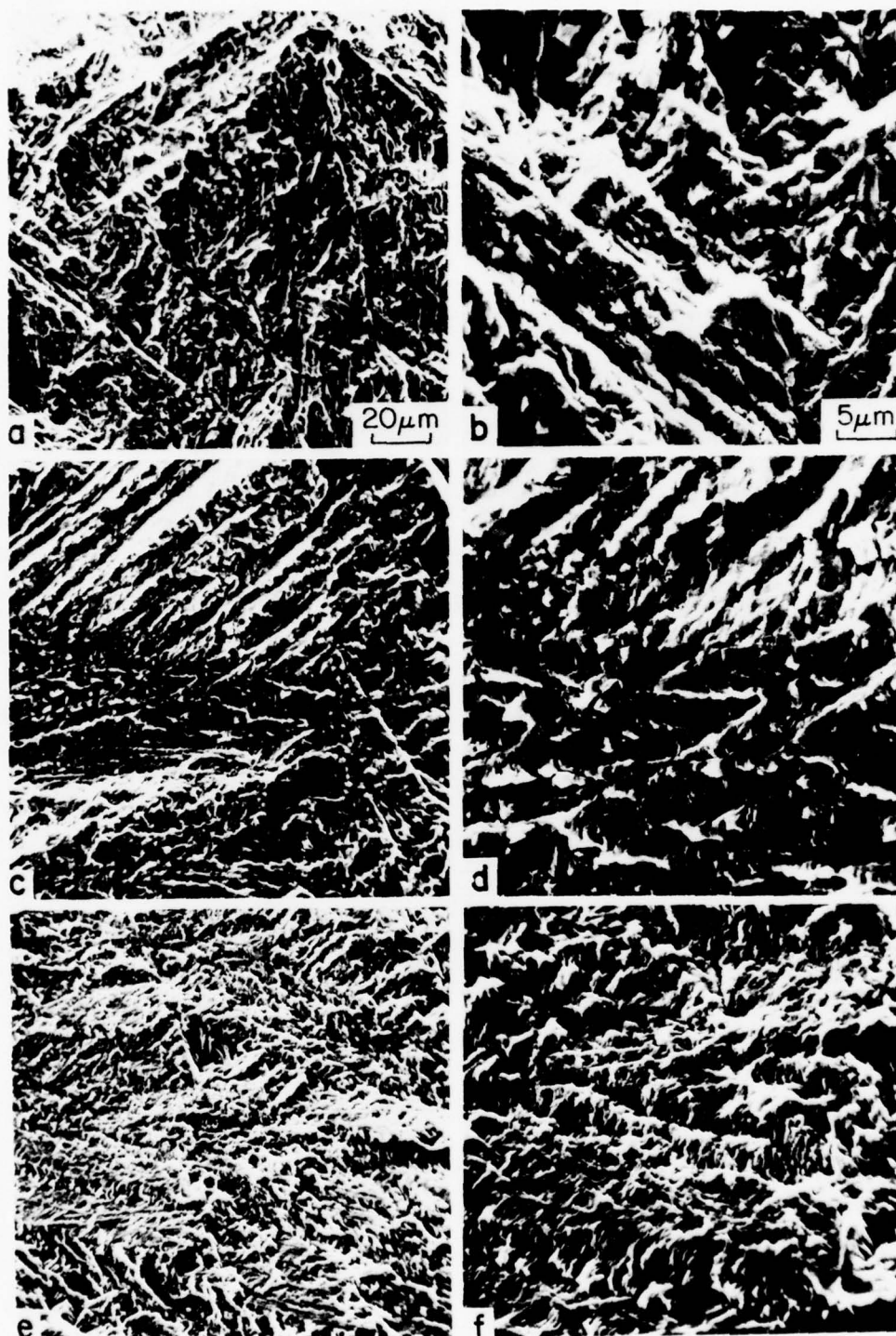
Fig. IV-26 Fracture surfaces of Condition 5 tested in dry air at 20 Hz and
R = 0.3 for $\Delta K = 11$ MPa·m$^{\frac{1}{2}}$. (a,b) room temperature:
da/dN = 5.4 x 10^{-6} mm/cycle; (c,d) 250^{0}F:
da/dN = 1.8 x 10^{-5} mm/cycle; (e,f) 600^{0}F:
da/dN = 3.6 x 10^{-5} mm/cycle.

242

Fig. IV-27 Fracture surfaces of Condition 7 tested in dry air at 20 Hz and
R = 0.7 for K = 5.1 MPa·m². (a,b) room temperature:
da/dN = 4.6 x 10⁻⁶ mm/cycle; (c,d) 250°F:
da/dN = 2.0 x 2.0 x 10⁻⁶ mm/cycle; (e,f) 600°F:
da/dN = 9.4 x 10⁻⁶ mm/cycle.

243
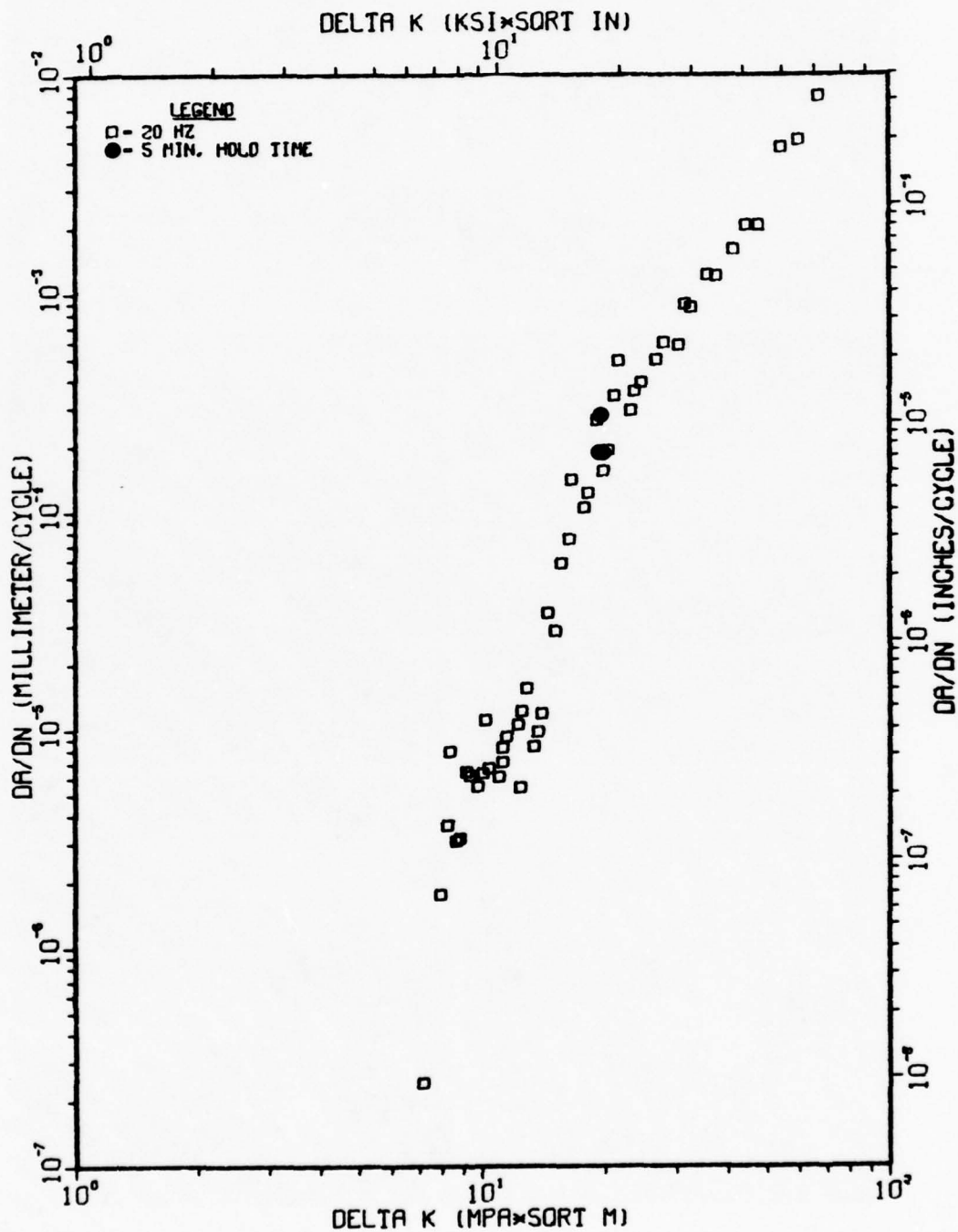
Fig. IV-28 FCP data for Condition 1 (1-1-31/38), 250°F, dry air, 20 Hz,
R = 0.3; including 5 min. hold-time data at approximately
2.5 x 10^{-4} mm/cycle.

TI-6AL-4V 1-1-33 STD. OX.
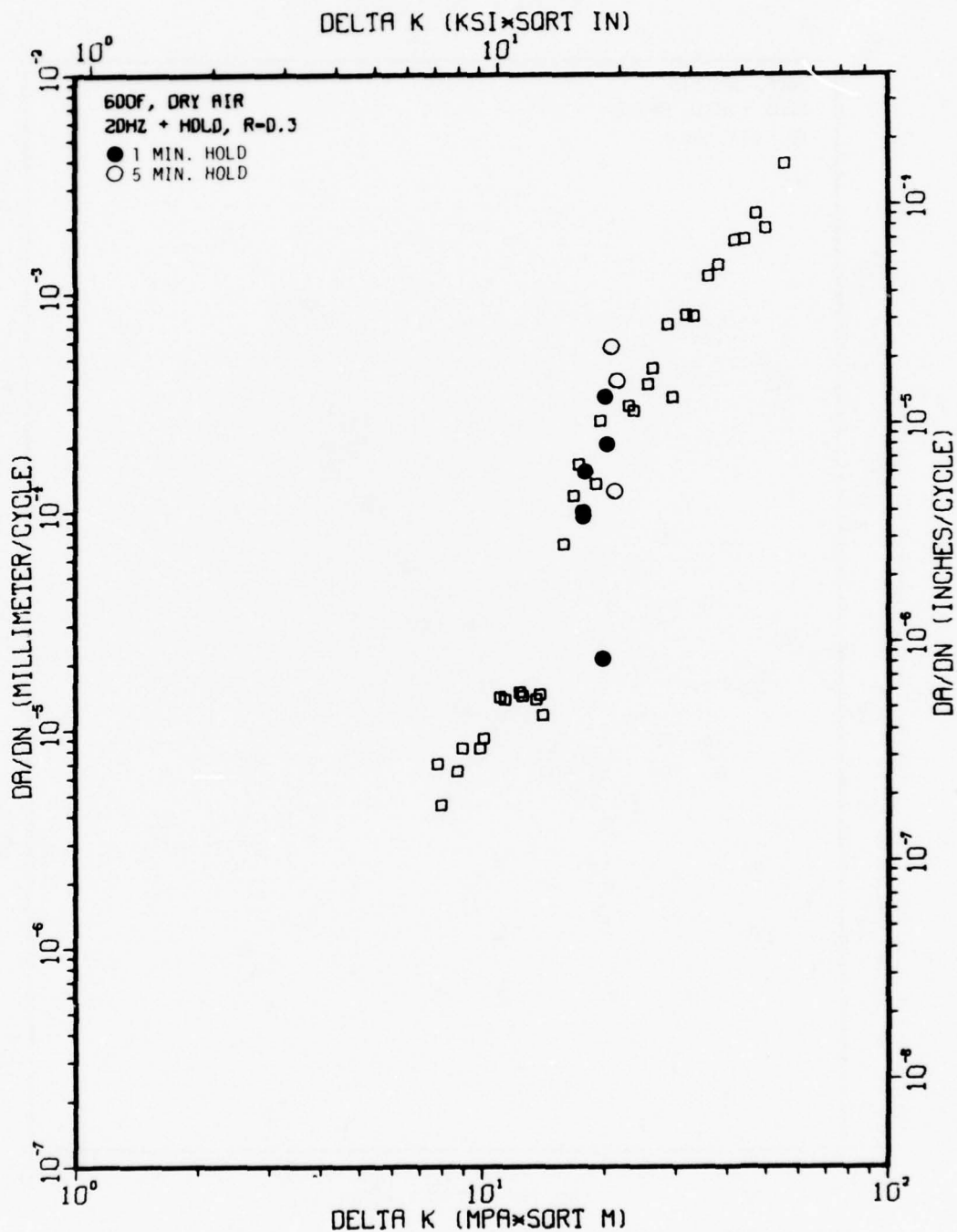
Fig. IV-29 FCP data for Condition 1 (1-1-33), 600°F, dry air, 20 Hz,
R = 0.3; including 1 min. hold-time data at approximately 1.3 and
2.5 x 10-4 mm/cycle and 5 min. hold-time data at approximately
2.5 x 10-4 mm/cycle.

245

Fig. IV-30 FCP data for Condition 1 (1-1-39), 600°F, dry air, 20 Hz,
R = 0.7; including 1 min. hold-time at 1.3 and
2.5 x 10⁻⁴ mm/cycle.

246

Fig. IV-31 FCP data for Condition 5 (1-5-31), 250°F, dry air, 20 Hz, R = 0.3; including 5 min. hold-time data at approximately 2.5 x 10⁻⁴ mm/cycle.

247
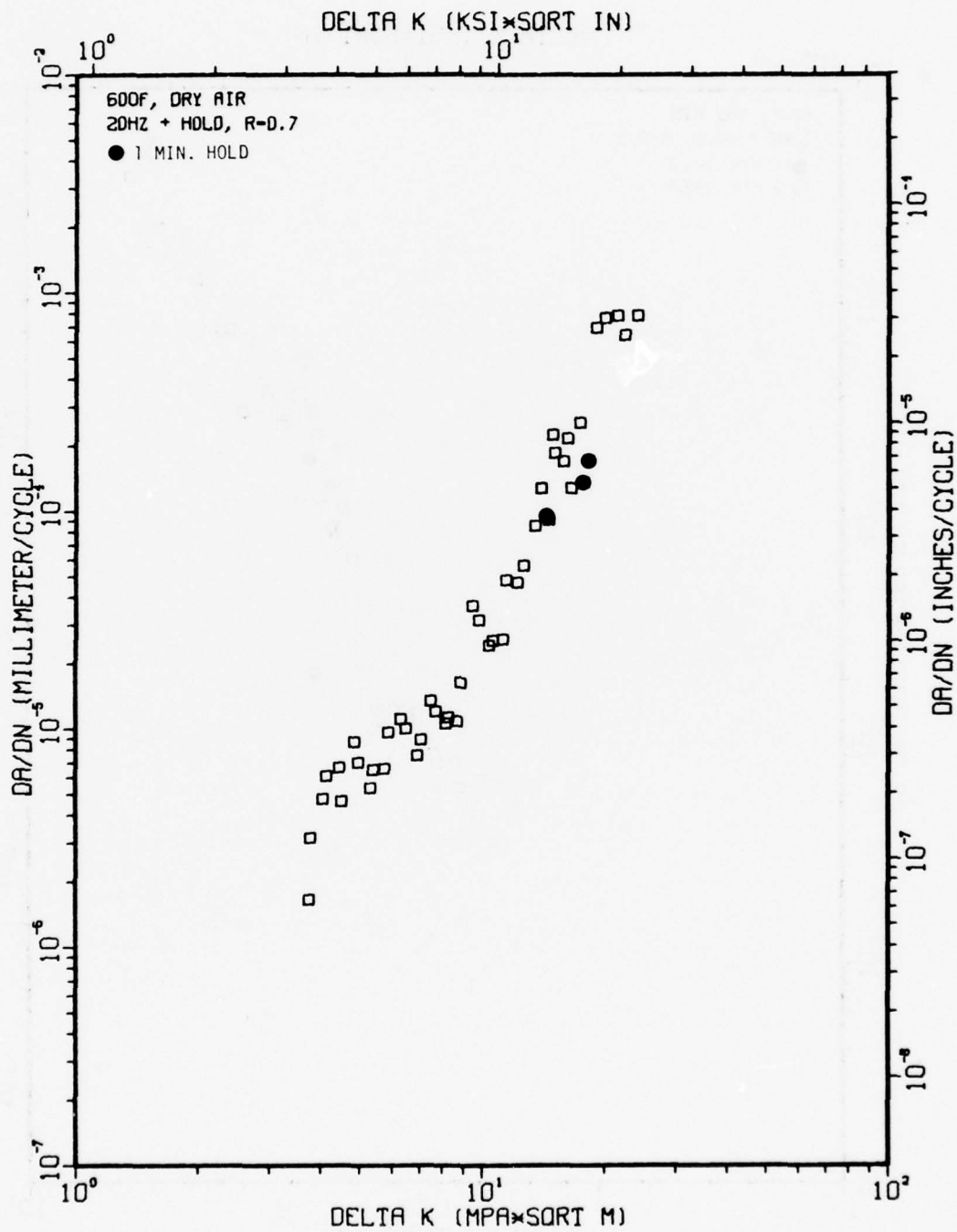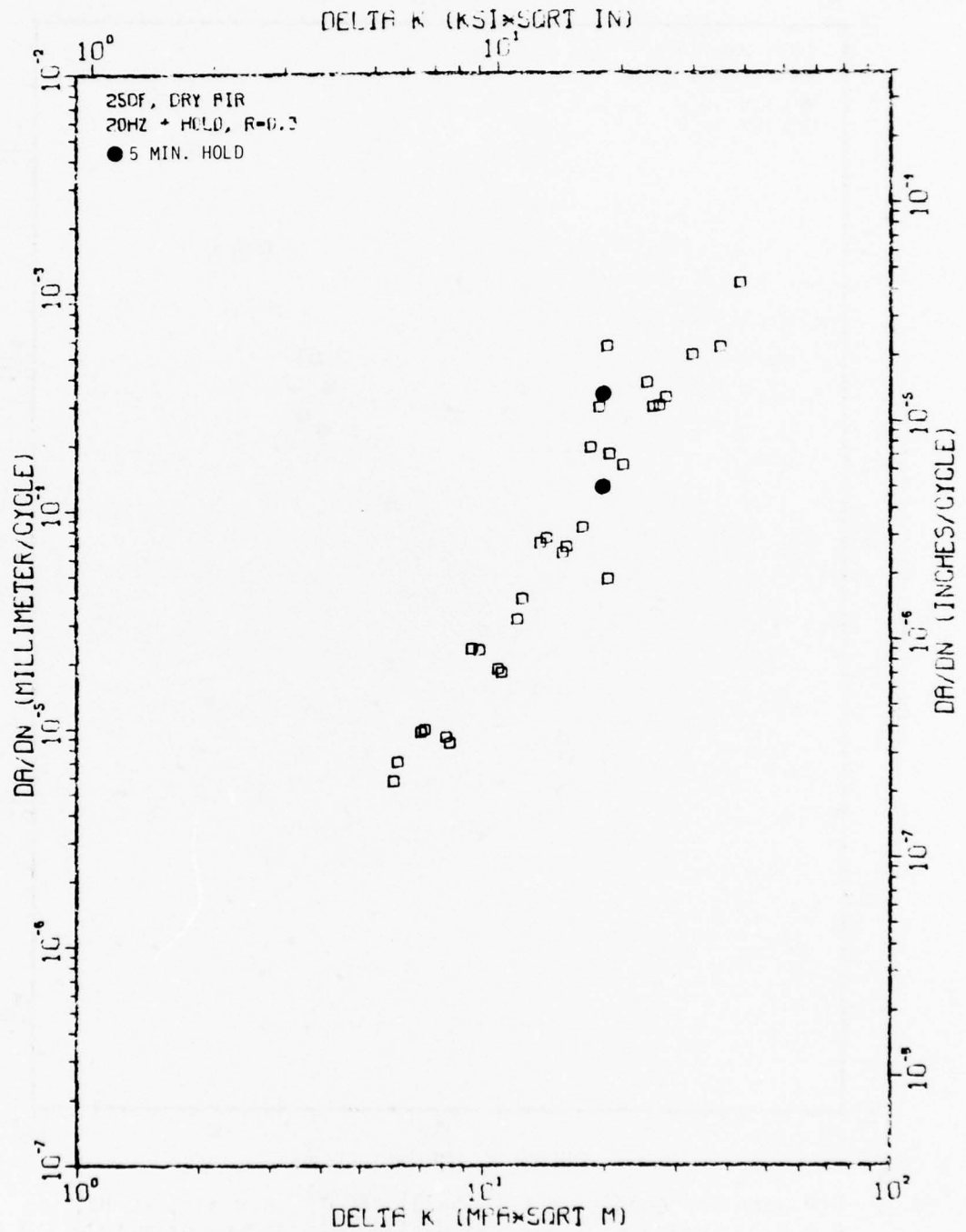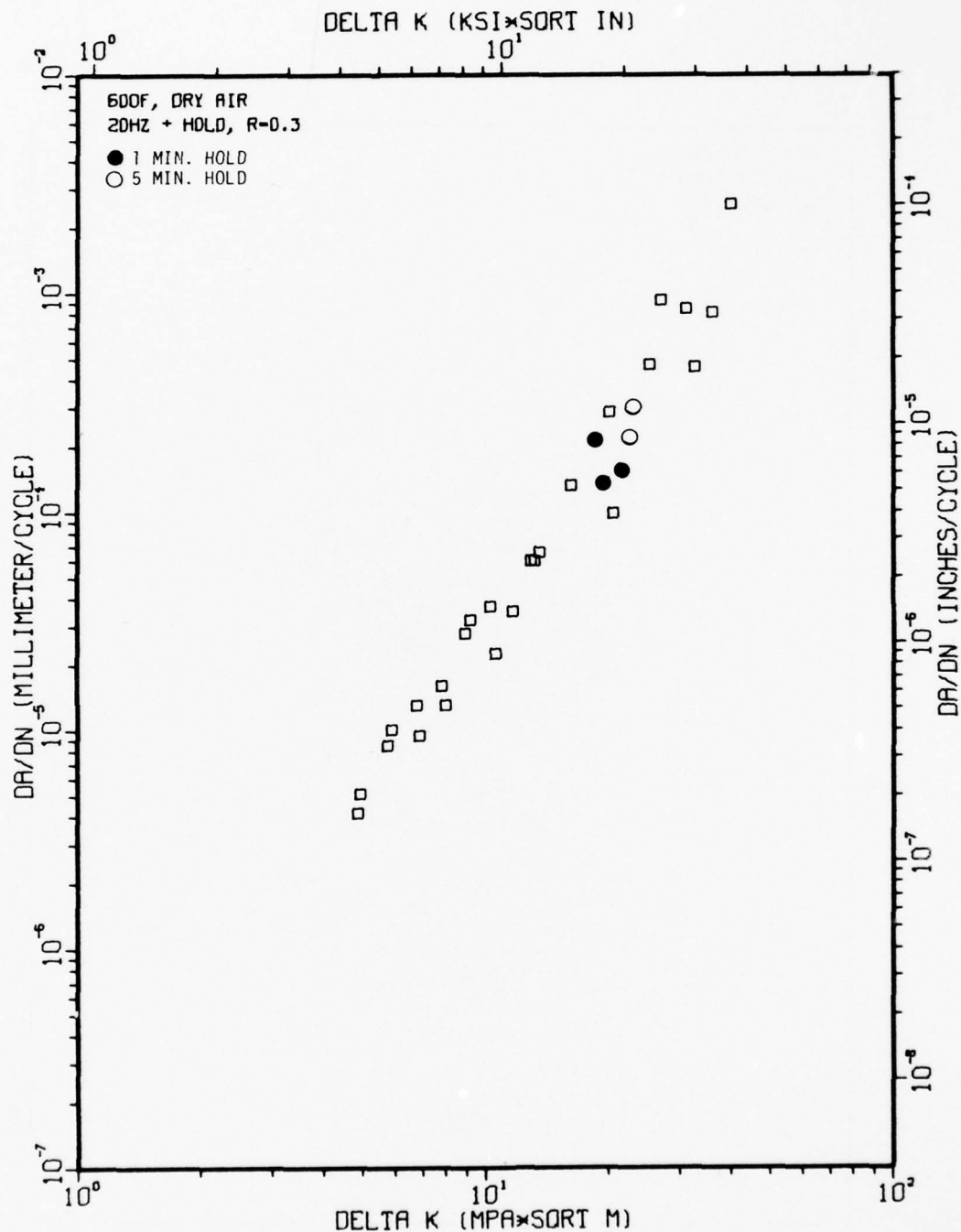
Fig. IV-32 FCP data for Condition 5 (1-5-33), 600°F, dry air, 20 Hz, R = 0.3; including 1 min. hold-time data at approximately 1.3 and 2.5 x 10⁻⁴ mm/cycles and 5 min. hold-time data at approximately 2.5 x 10⁻⁴ mm/cycles.

TI-6AL-4V 1-5-38

Fig. IV-33 FCP data for Condition 5 (1-5-38), 600°F, dry air, 20 Hz, R = 0.7; including 1 min. hold-time data at approximately 1.3 and 2.5 × 10⁻⁴ mm/cycles.
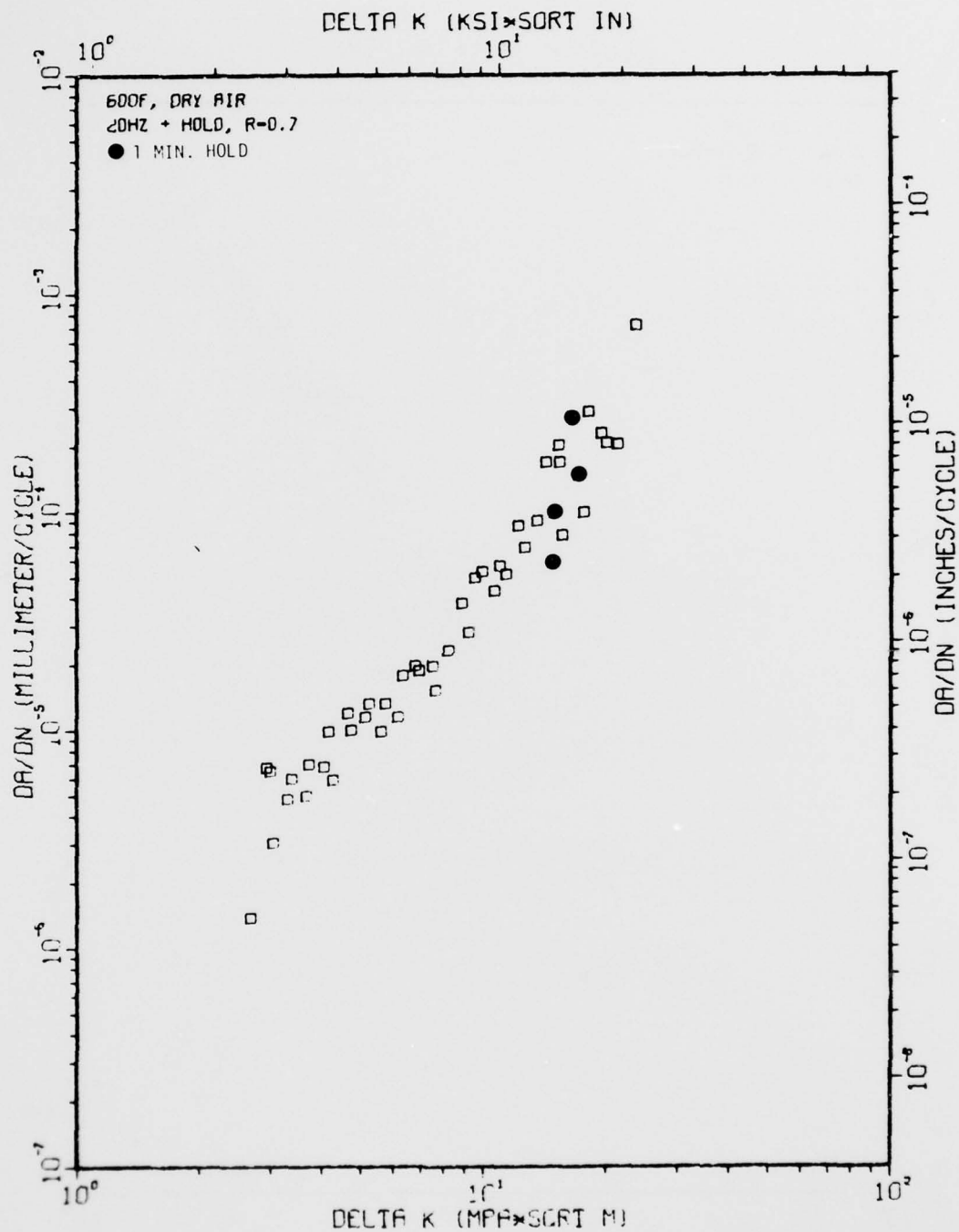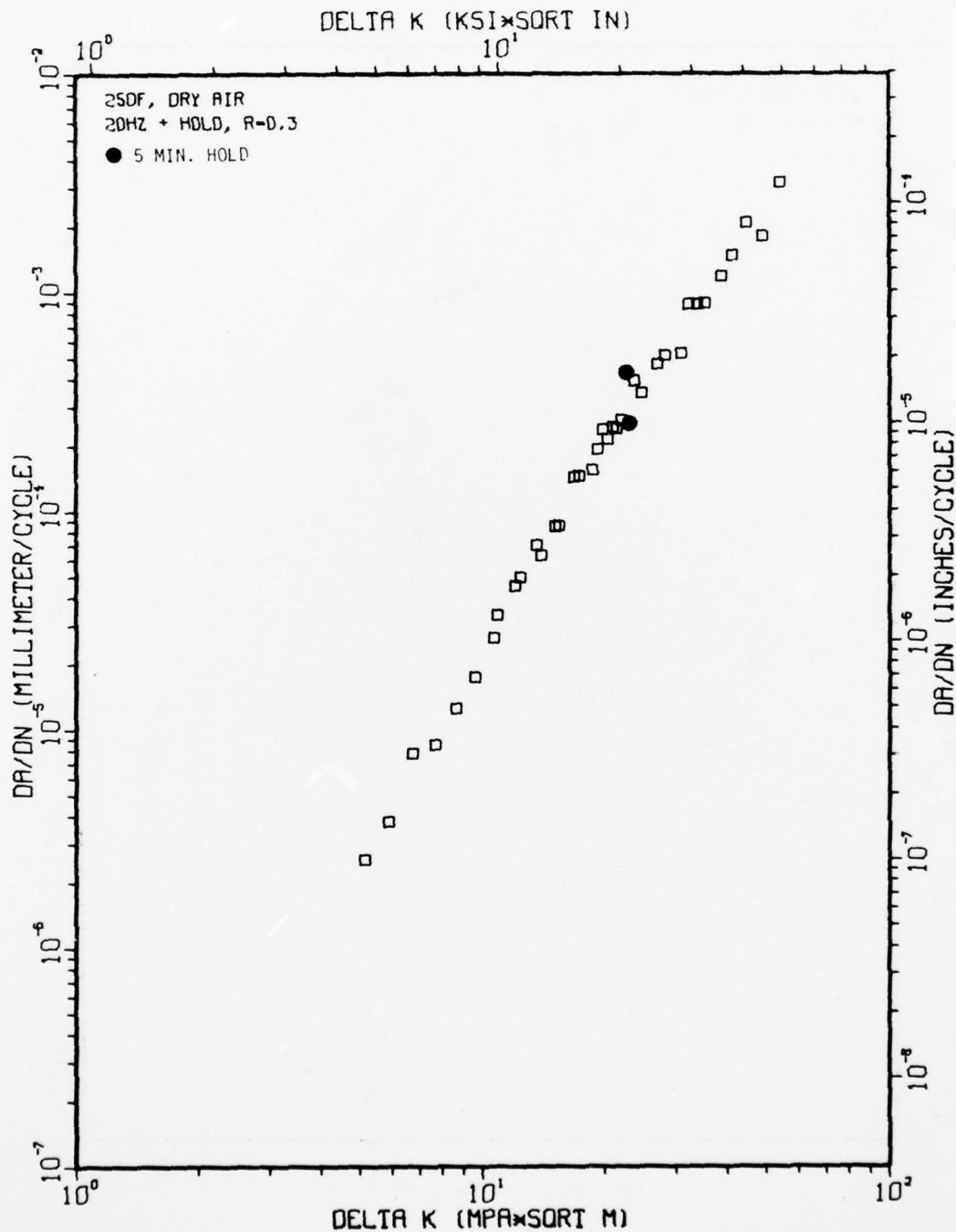
TI-6AL-4V   1-7-29

Fig. IV-34 FCP data for Condition 7 (1-7-29), 250°F, dry air, 20 Hz,
            R = 0.3; including 5 min. hold-time data at approximately
            2.5 x 10⁻⁴ mm/cycle.

250
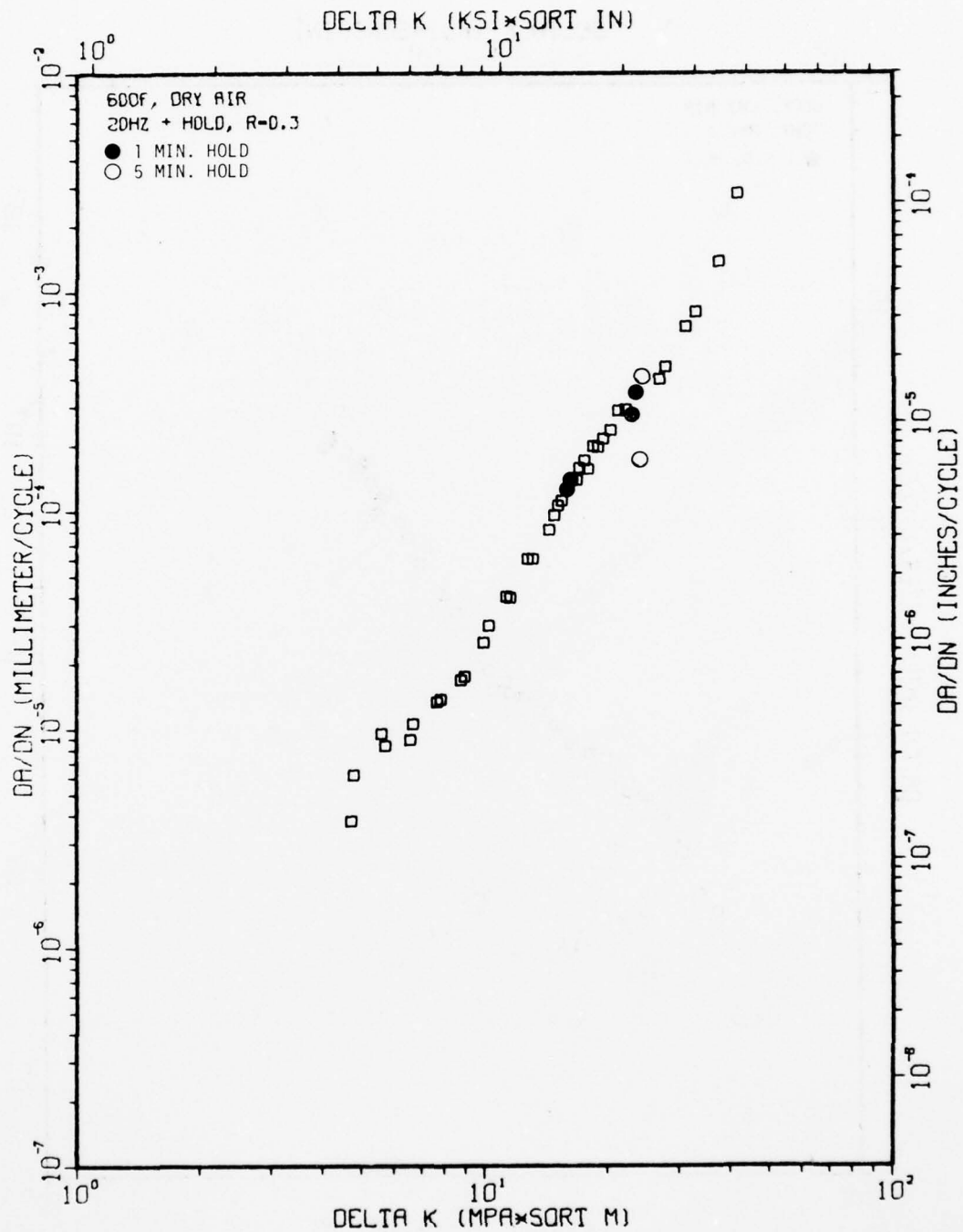
TI-6AL-4V 1-7-31

Fig. IV-35 FCP data for Condition 7 (1-7-31), 600°F, dry air, 20 Hz,
R = 0.3; including 1 min. hold-time data at approximately 1.3 and
2.5 x 10⁻⁴ mm/cycles and 5 min. hold-time data at approximately
2.5 x 10⁻⁴ mm/cycles.

251
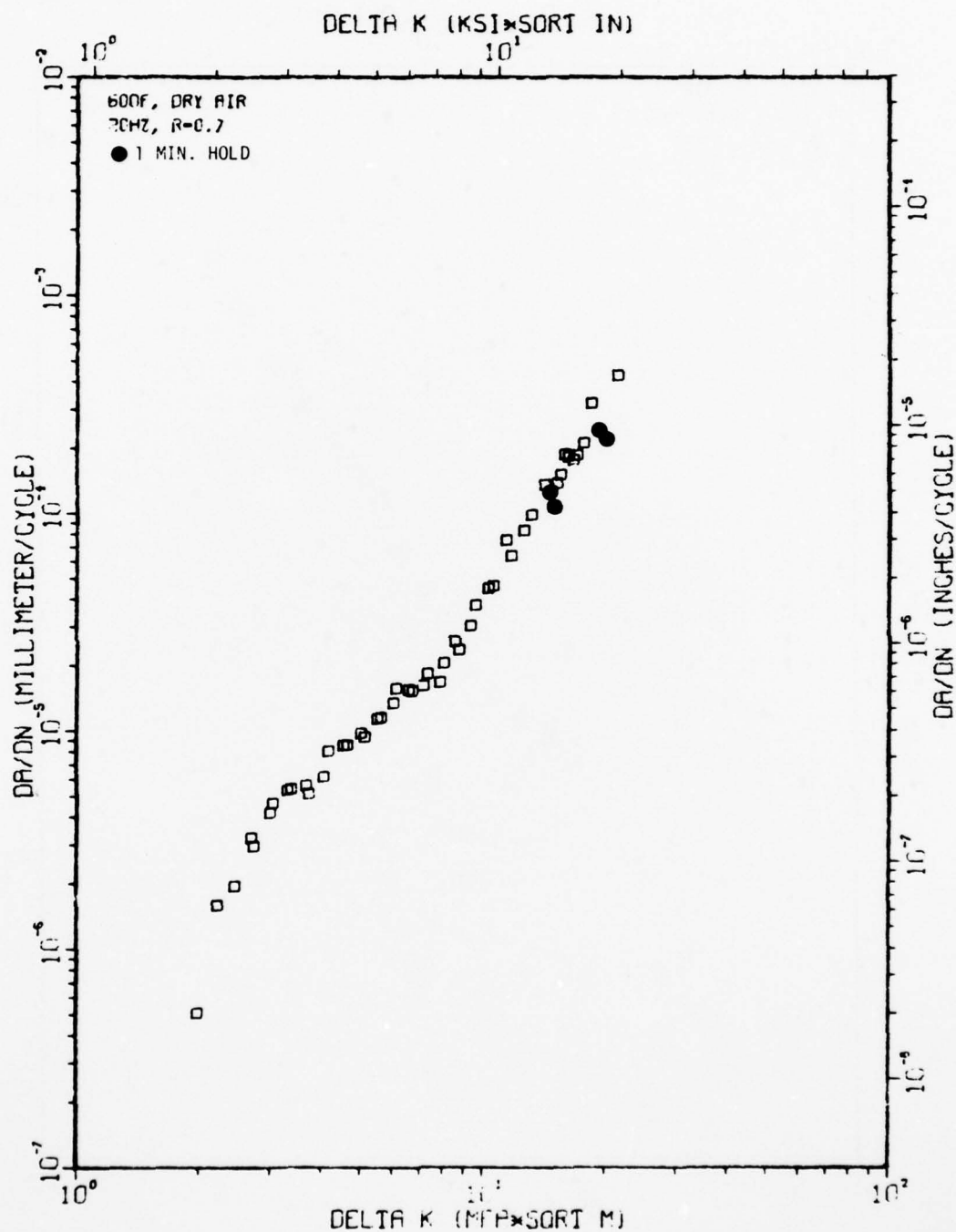
Fig. IV-36 FCP data for Condition 7 (1-7-32), 600°F, dry air, 20 Hz,
R = 0.7; including 1 min. hold-time data at approximately 1.3 and
2.5 x 10-4 mm/cycles.

252

TI-6AL-4V(COND. 1), 68F, DRY AIR, R-0.3
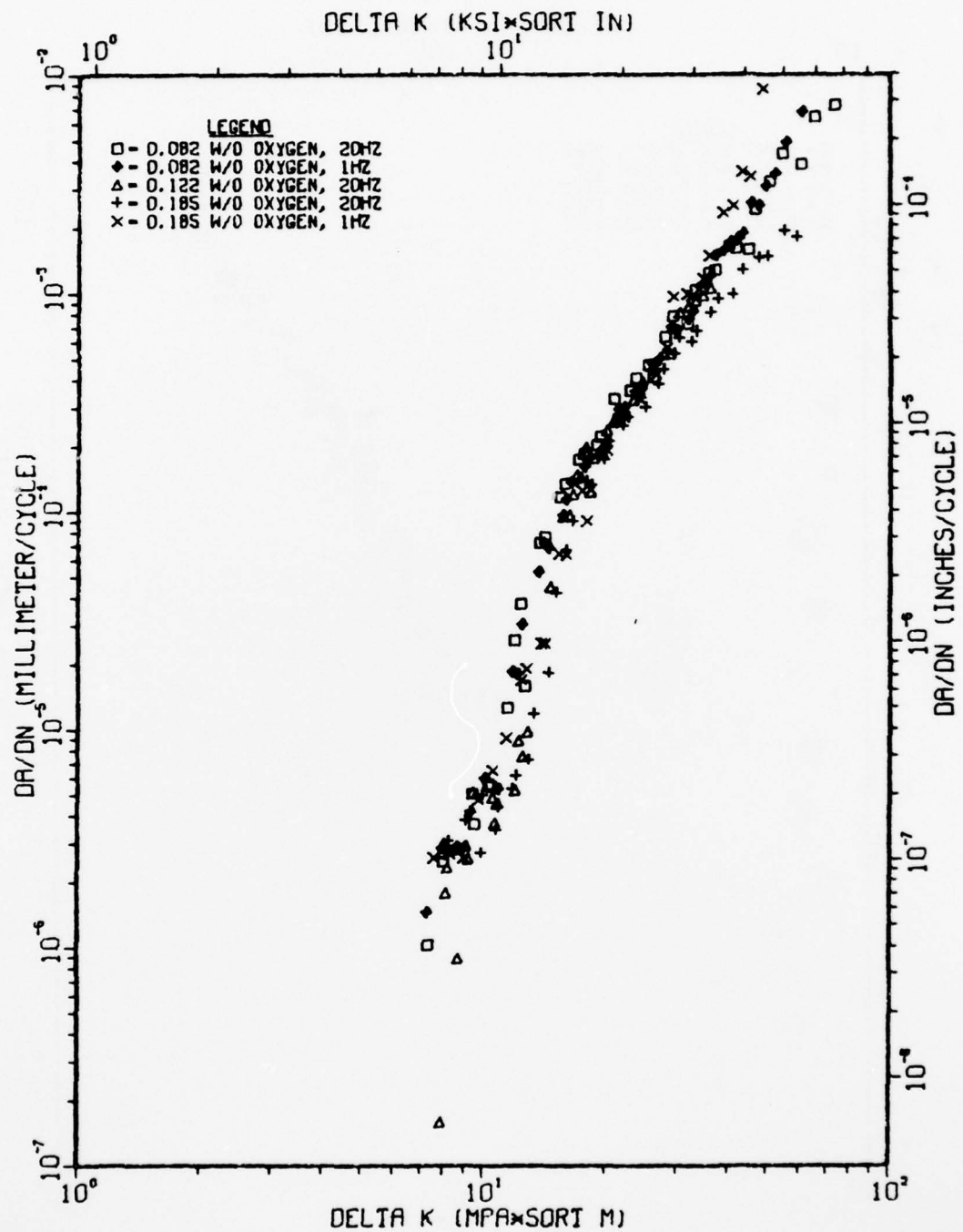
Fig. IV-37 Dependence of FCP in Condition 1 on oxygen content (0.082, 0.122 and 0.185 wt % oxygen) at 68°F, R = 0.3.

TI-6AL-4V(COND. 1), 600F, DRY AIR, R-0.3
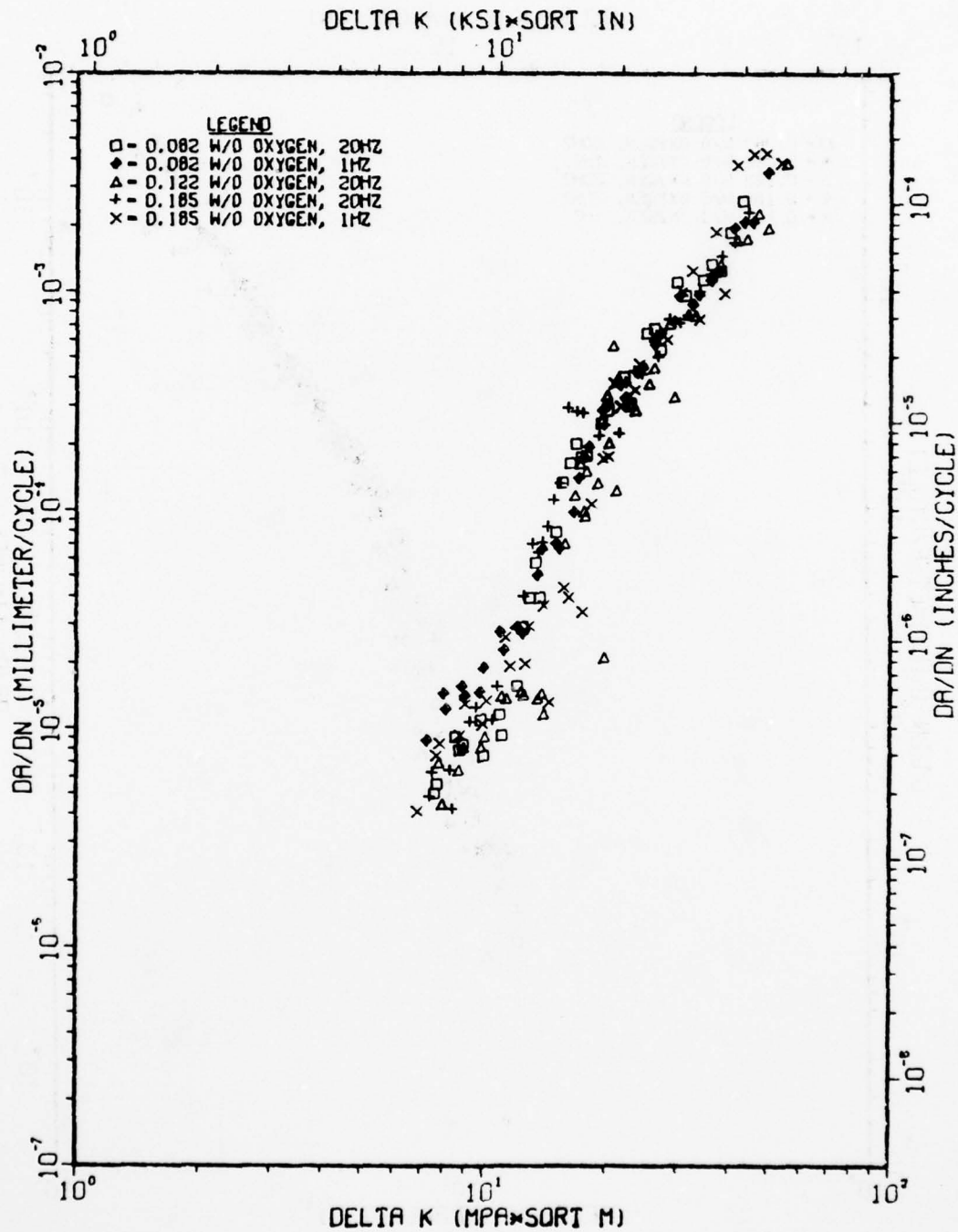
Fig. IV-38   Dependence of FCP in Condition 1 on oxygen content at 600°F, R = 0.3.

254

TI-6AL-4V(COND. 5), 68F, DRY AIR, R-0.3

DELTA K (KSI×SQRT IN)

Fig. IV-39 Dependence of FCP in Condition 5 on oxygen content at 68°F,
R = 0.3.

255
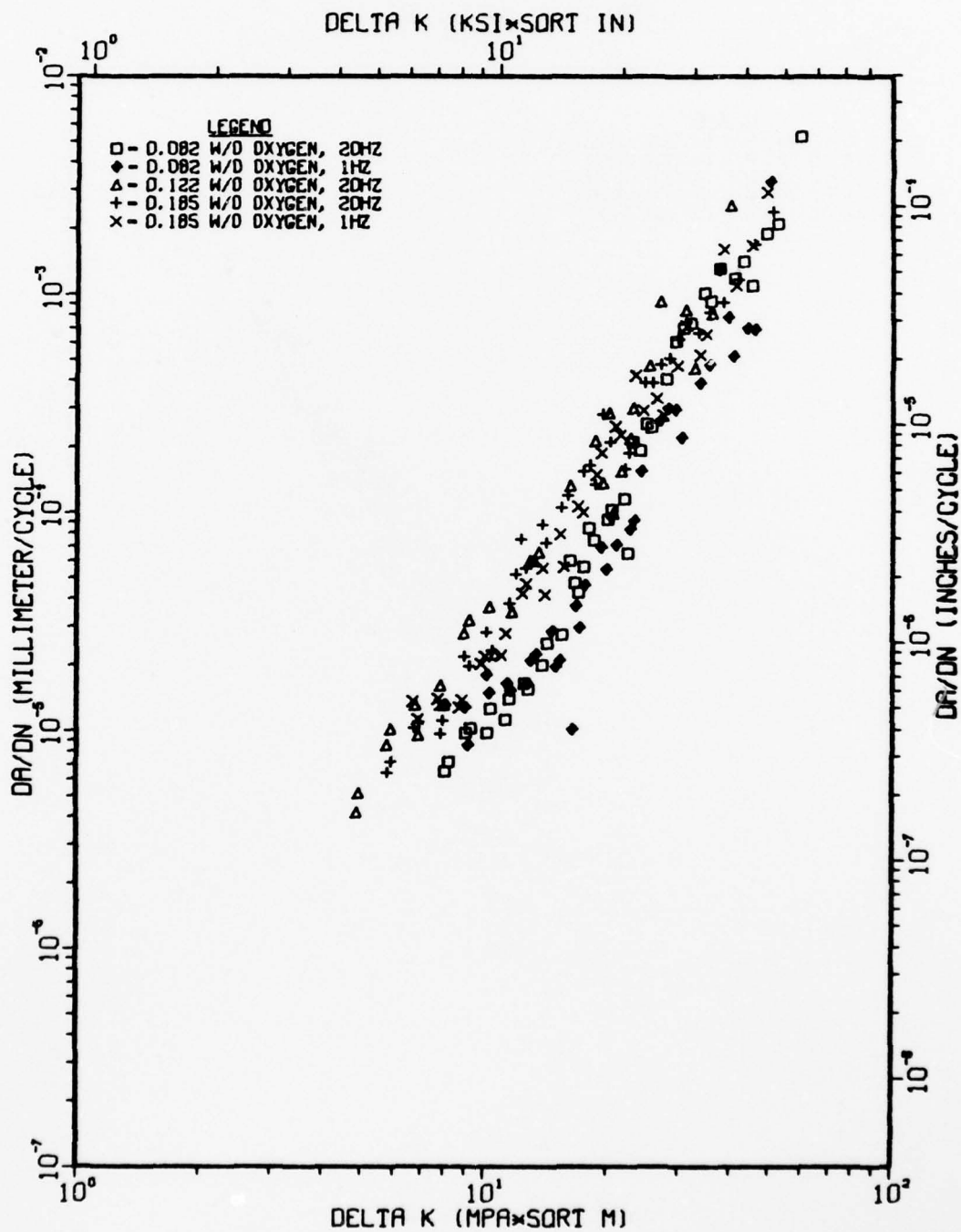
Fig. IV-40 Dependence of FCP in Condition 5 on oxygen content at 600°F, R = 0.3.

TI-6AL-4V(COND. 1), 68F, DRY AIR, R-0.3
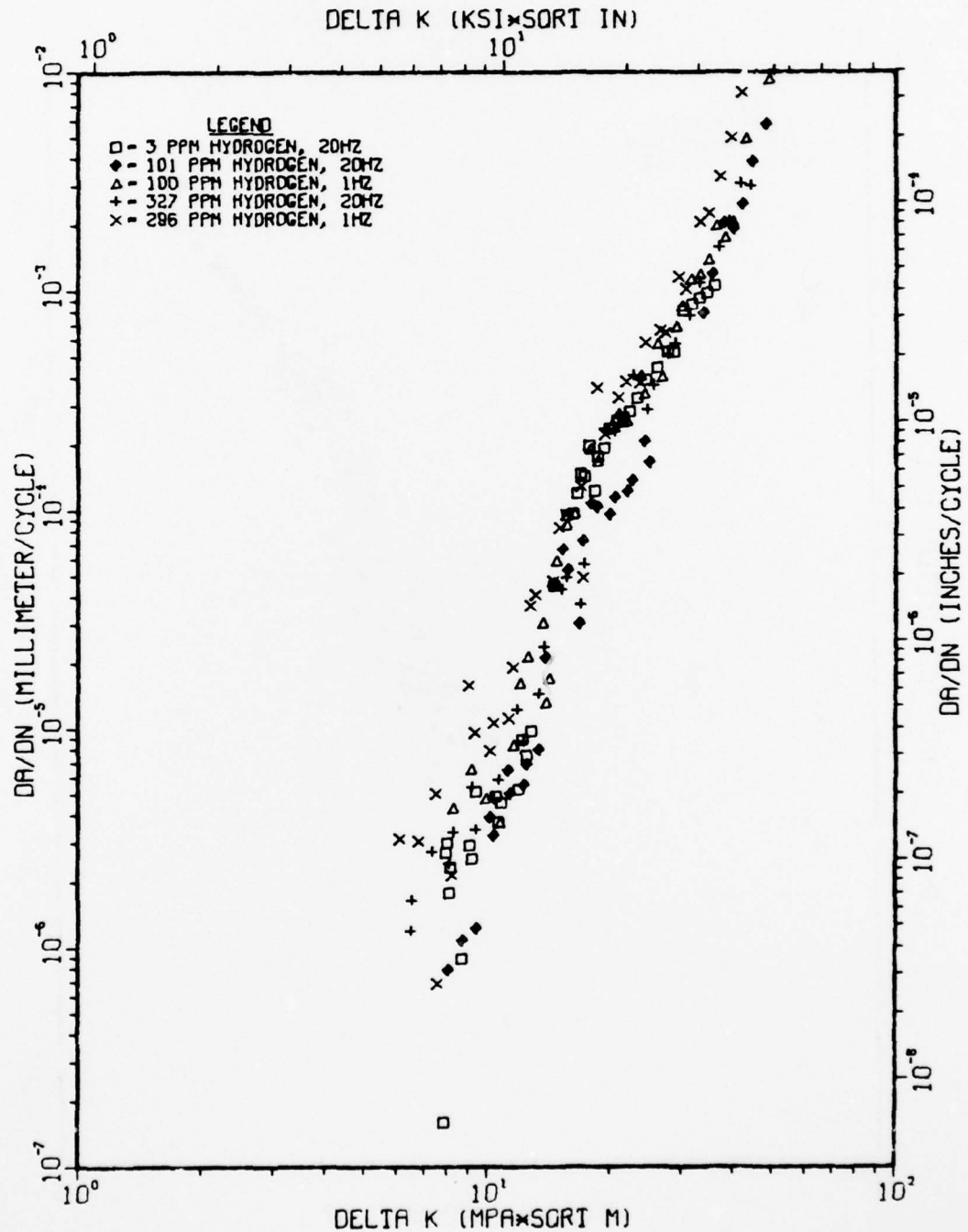
Fig. IV-41 Dependence of FCP in Condition 1 on hydrogen content (nom., 100 and 300 ppm by weight) at 68°F, R = 0.3.

257

Fig. IV-42 Dependence of FCP in Condition 1 on hydrogen content at 600°F, R = 0.3.

258

TI-6AL-4V(COND. 5), 68F, DRY AIR, R=0.3
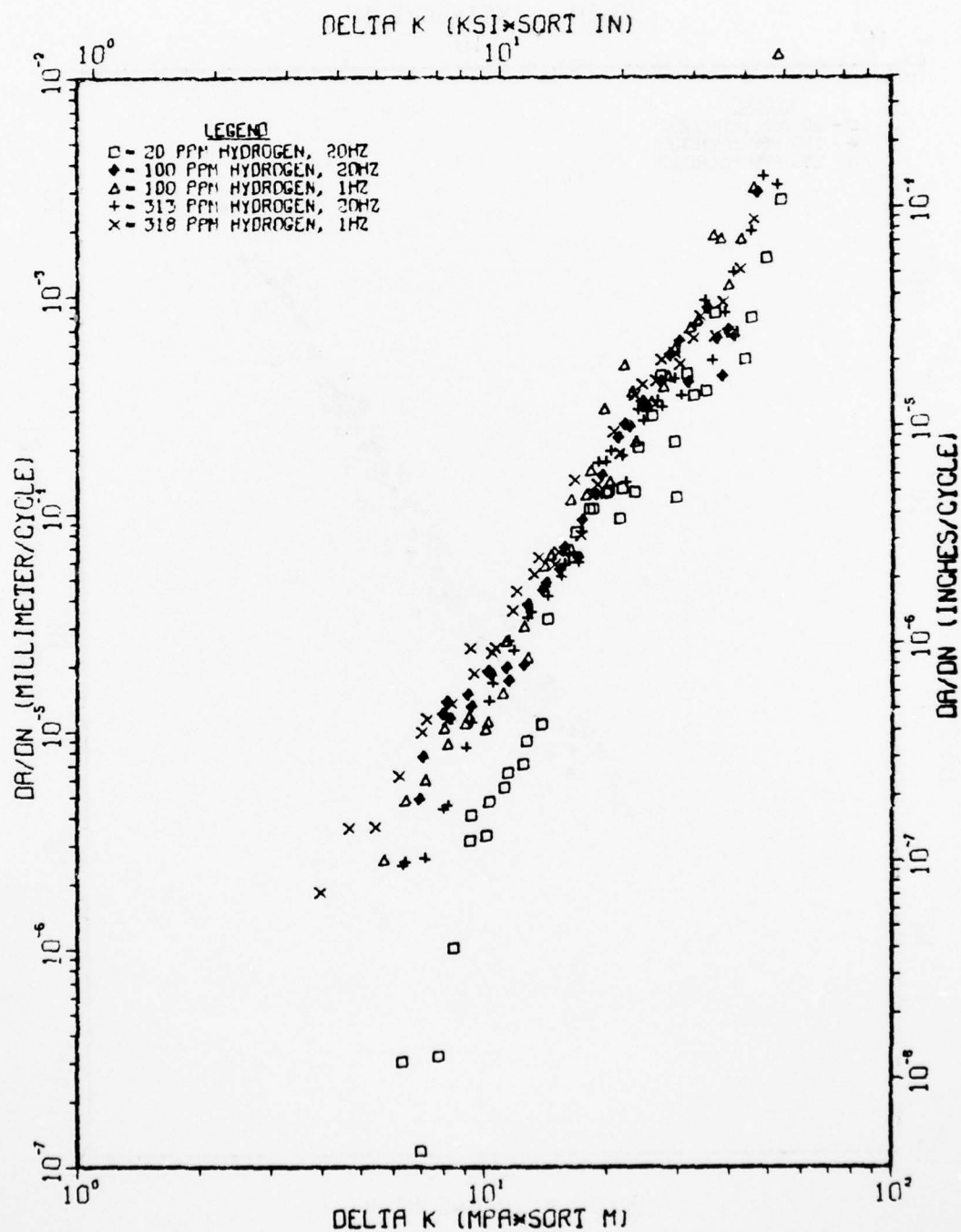
Fig. IV-43 Dependence of FCP in Condition 5 on hydrogen content at 68°F, R = 0.3.

259

TI-6AL-4V(COND. 5), 600F, DRY AIR, 20HZ, R-0.3
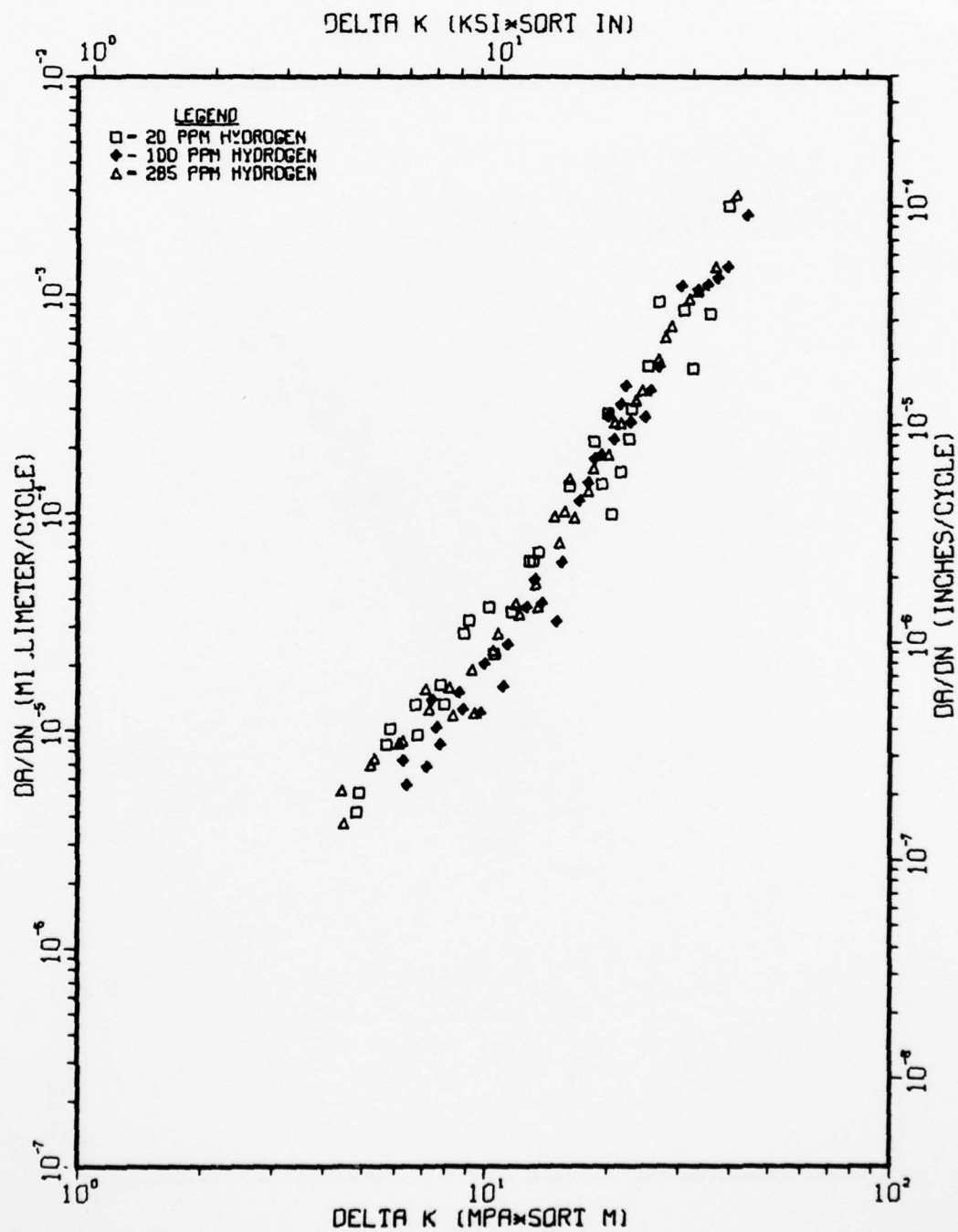
Fig. IV-44 Dependence of FCP in Condition 5 on hydrogen content at 600°F, R = 0.3.
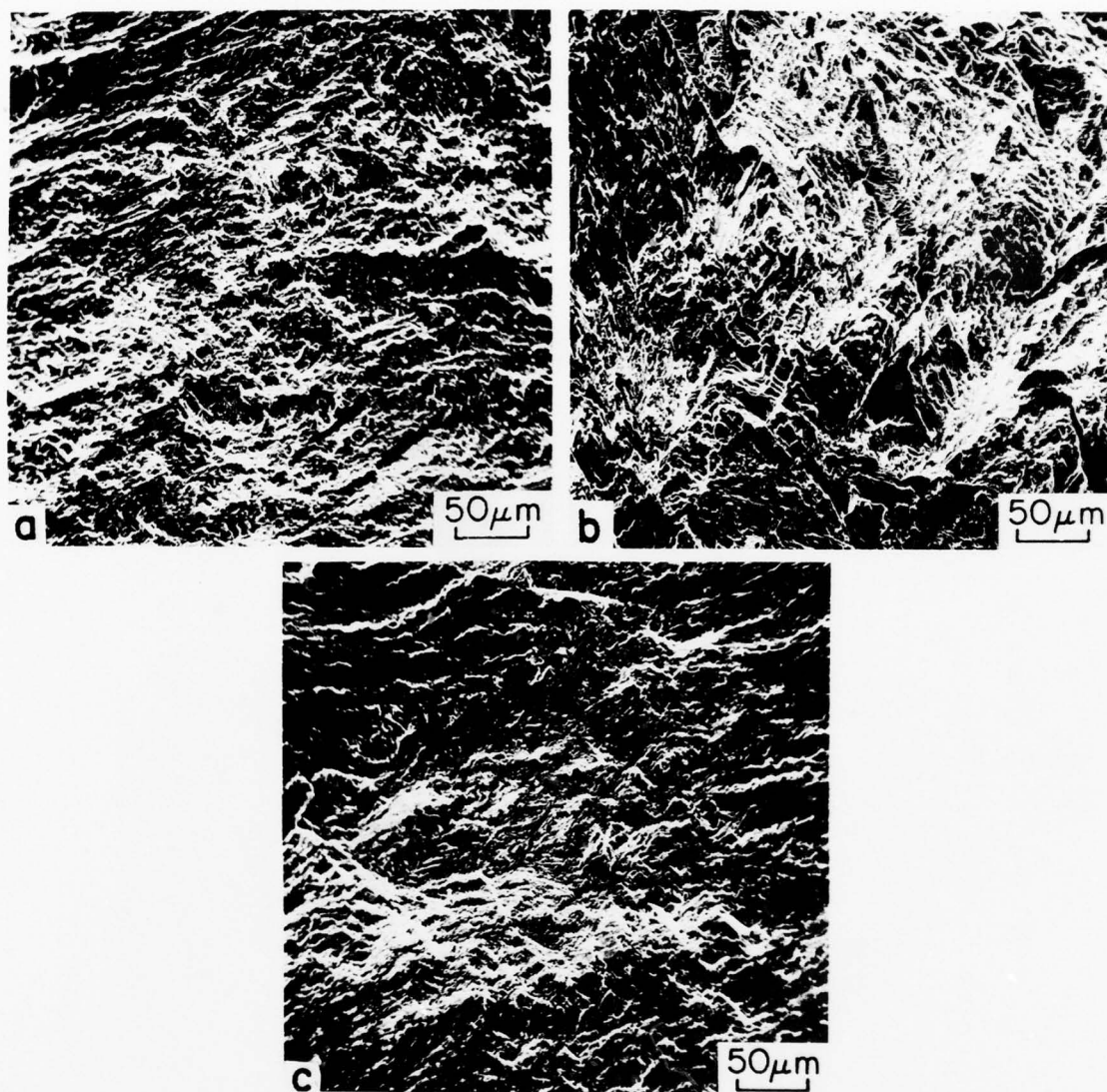
Fig. IV-45 Fracture surface of Condition 5 tested in dry air at 20 Hz and
R = 0.3 for ΔK = 6.4 MPa·m$^{\frac{1}{2}}$: (a) 0.082 wt% oxygen:
da/dN = 2.2 x 10^{-6} mm/cycle; (b) 0.122 wt% oxygen:
da/dN = 2.9 x 10^{-7} mm/cycle; (c) 0.185 wt% oxygen:
da/dN = 4.3 x 10^{-6} mm/cycle.
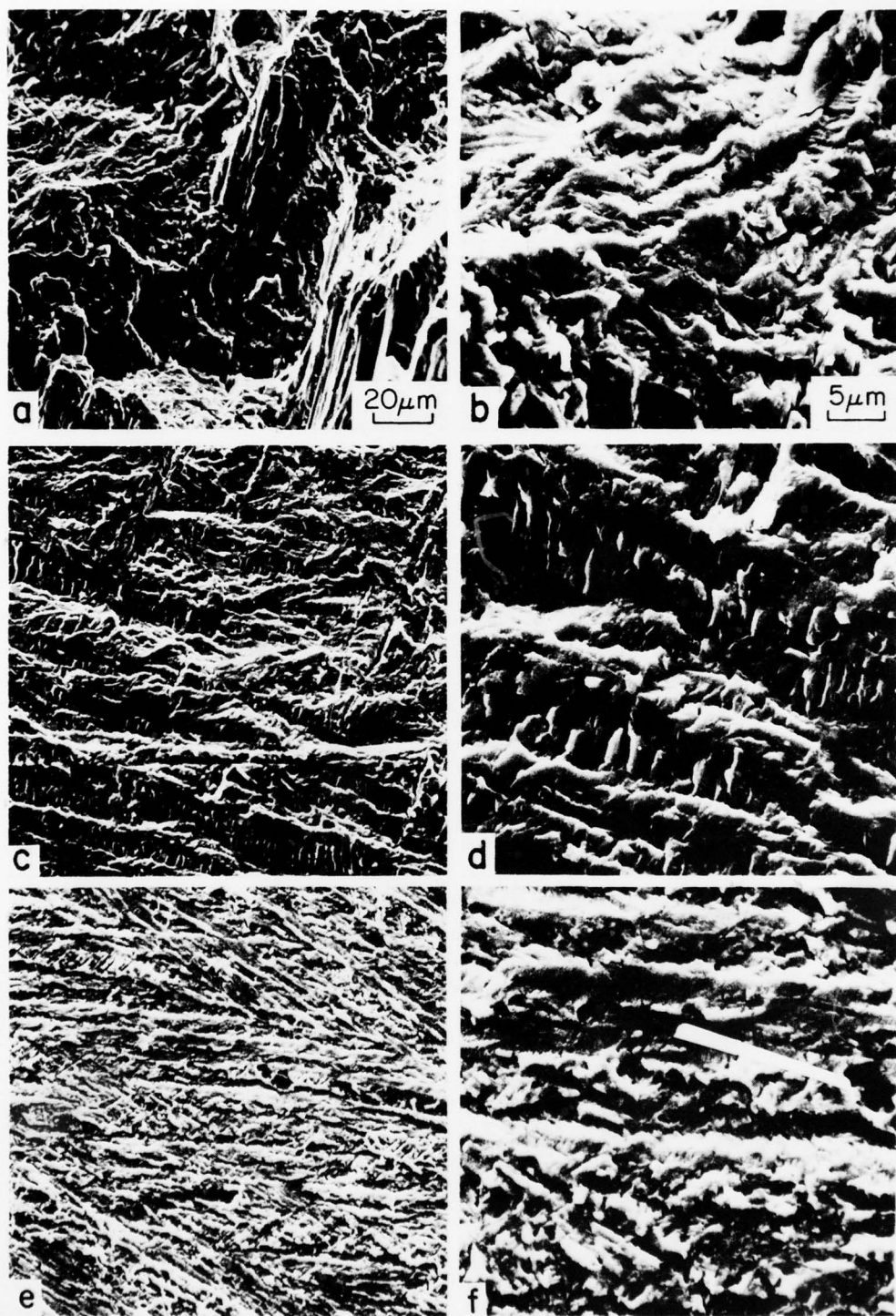
Fig. IV-46   Fracture surfaces of Condition 5 tested in dry air at room
             temperature and R = 0.3 for 17.6 MPa·m$^{\frac{1}{2}}$: (a,b) 0.082 wt% oxygen
             tested at 1 Hz: da/dN = 2.4 x 10^{-5} mm/cycle; (c,d) 0.082 wt%
             oxygen tested at 20 Hz: da/dN = 6.1 x 10^{-5} mm/cycle;
             (e,f) 0.122 wt% oxygen tested at 20 Hz:
             da/dN = 1.0 x 10^{-4} mm/cycle.

MICROCOPY RESOLUTION TEST CHART
NATIONAL BUREAU OF STANDARDS-1963-A
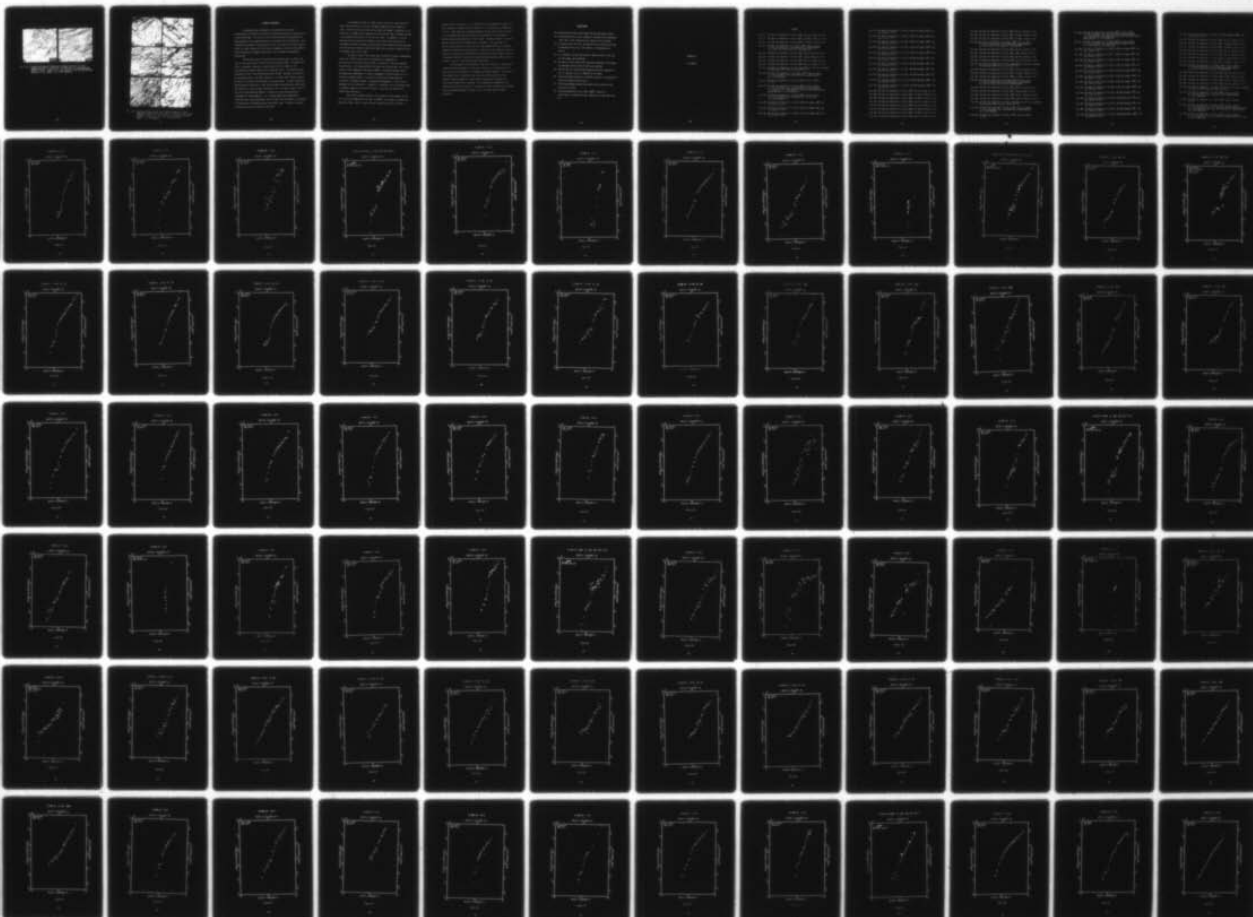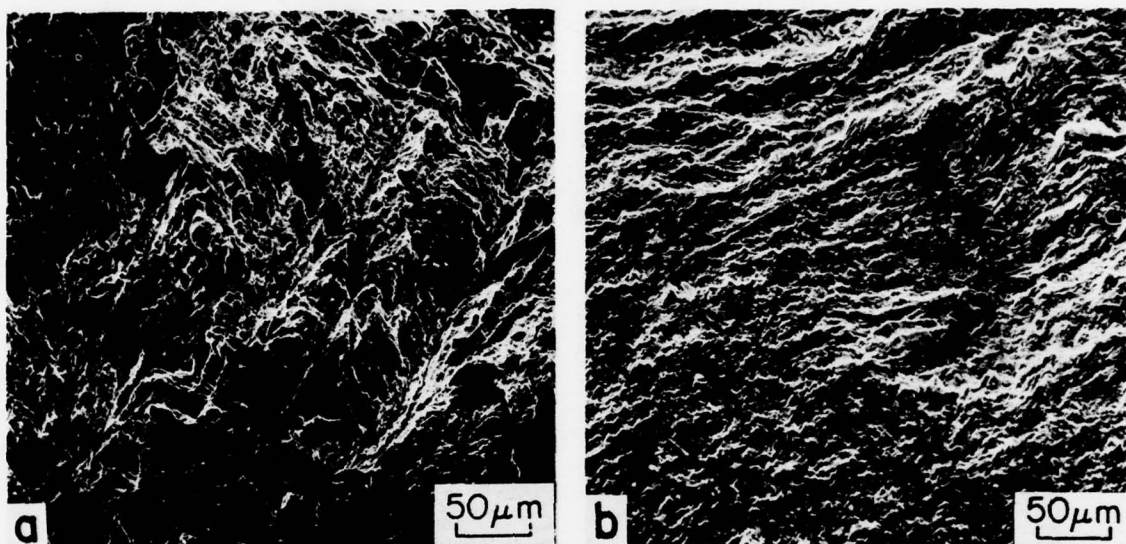
Fig. IV-47 Fracture surfaces of Condition 5 tested in dry air at room temperature and R = 0.3 for ΔK = 6.4 MPa·m$^{\frac{1}{2}}$; (a) 20 ppm hydrogen tested at 20 Hz: da/dN = 3.0 x 10^{-7} mm/cycle; (b) 318 ppm hydrogen tested at 1 Hz: da/dN = 6.4 x 10^{-6} mm/cycle.
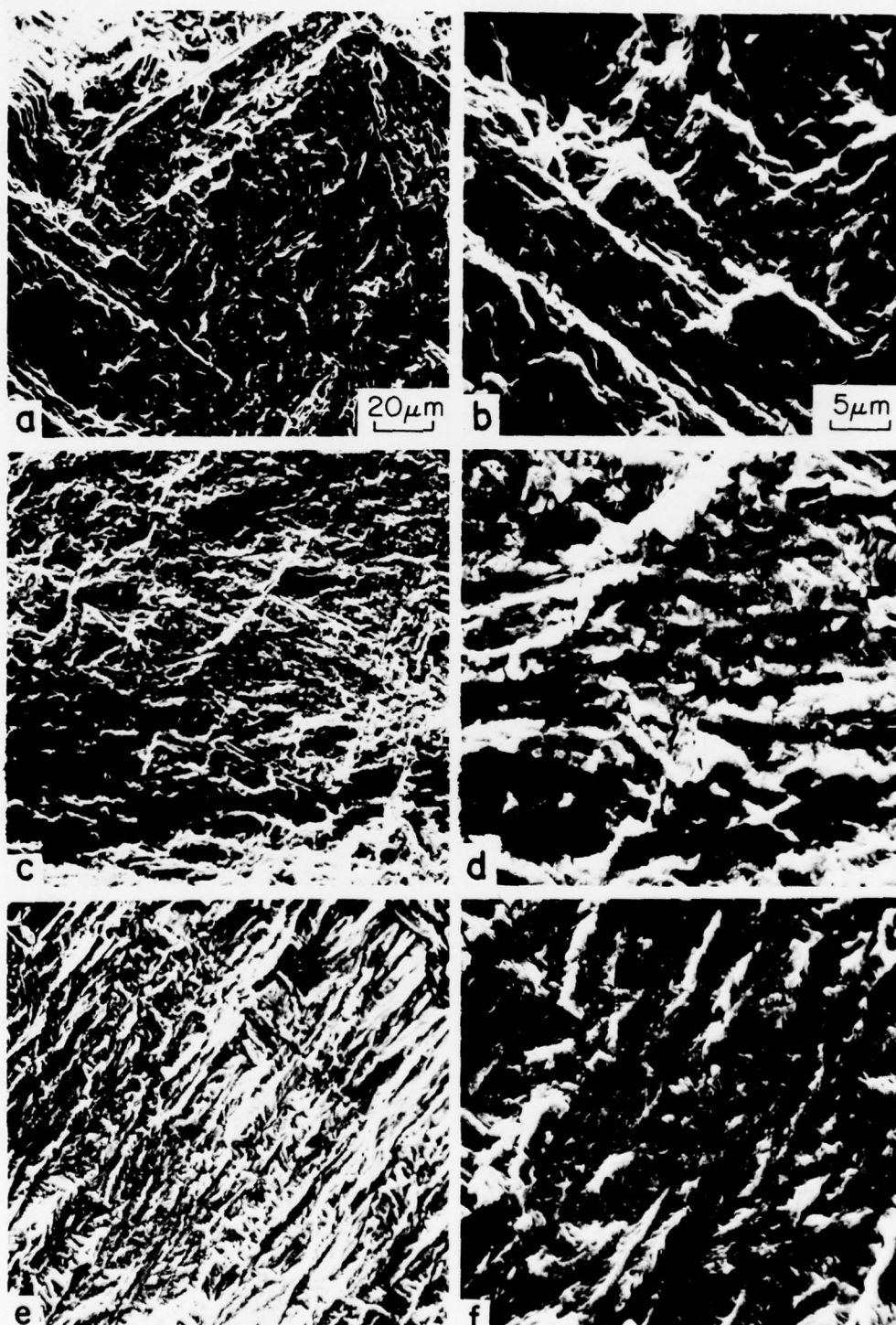
Fig. IV-48 Fracture surfaces of Condition 5 tested in dry air at room
temperature, 20 Hz and R = 0.3 for $\Delta K = 11$ MPa·m$^{\frac{1}{2}}$. (a,b) 20 ppm
hydrogen: da/dN = 5.6 x 10^{-6} mm/cycle; (c,d) 100 ppm hydrogen:
da/dN = 2.0 x 10^{-5} mm/cycle; (e,f) 318 ppm hydrogen:
da/dN = 2.1 x 10^{-5} mm/cycle.

264

GENERAL DISCUSSION

The preceding data represents a characterization of seven microstructural conditions of Ti-6Al-4V and three microstructural conditions of Ti-6Al-2Sn-4Zr-6Mo. The relative lack of texture permits the properties of these materials to be compared primarily on the basis of microstructure. The strength of the materials was generally on the low side of the normal range of values for these alloys while the fracture toughness values were consistently high, reflecting low oxygen content and a lack of texture strengthening contribution.

The FCP data clearly illustrate that microstructure can affect FCP rate in α-β alloys such as Ti-6Al-4V and Ti-6Al-2Sn-4Zr-6Mo. Increased load ratio, R, produced increases in crack growth rate for several of the microstructures studied, especially at lower ΔK levels. The effect was most pronounced in the Ti-6Al-4V microstructures studied. Moreover, particularly at low growth rates or at high R values, it is evident that fracture surface appearance can reflect the influence of microstructure. The most significant microstructural conclusion is that acicular-type microstructures, particularly when refined in size, are most resistant to FCP. As shown in Parts I and IV, the cyclic work hardening behavior of nearly all these microstructures corresponds to stable behavior, i.e., neither appreciable hardening or softening occurs, and accordingly little insight into FCP behavior is afforded by consideration of hardening within the plastic zone. Therefore, fracture processes were used to rationalize the data.

265

Environmental effects of argon, dry air and wet air were generally small and dry and wet air are not considered aggressive with respect to argon. The FCP acceleration due to salt water environment is moderate at low ΔK values; at higher ΔK the combined salt solution and lower frequency loading (1 Hz) modest accelerations in FCP rate are noted. In summary, it can be observed that the $\alpha + \beta$ microstructures are not significantly sensitive to environment and that the beta microstructures (beta annealed and beta quenched Ti-6Al-4V and beta forged Ti-6Al-2Sn-4Zr-6Mo) are only weakly affected by the environment used in this study.

The tensile results have shown that considerable oxygen strengthening occurs for Ti-6Al-4V and that the strengthening is dependent on microstructure, the effect being largest in Condition 5, the beta quenched microstructure. The hydrogen effects are much less significant, with a small effect at room temperature and none at $600^{\circ}F$. At nominal hydrogen levels, the temperature dependence is roughly independent of microstructure but is a function of oxygen content. For material containing 0.122% oxygen and variations in hydrogen content, the temperature dependence is sensitive to hydrogen only for Condition 5. Condition 1, therefore, can be considered from a strength standpoint to be more tolerant to variations in interstitial content than Condition 5.

Hold time at maximum load had little effect on crack growth rate at any of the test temperatures (68, 250, and $600^{\circ}F$), the change in growth rate being less than a factor of two; the only exceptions being an increase in

growth rate of a factor of 3.7 in Condition 5 at room temperature and R = 0.3 and a decrease in growth rate by a factor of 2.7 in Condition 1 at 600°F and R = 0.3. Since these two isolated exceptions are less than a factor of four, it is concluded that hold-time effects are negligible for the uniformly, weakly textured microstructures of this study. The delay (number of cycles to return to baseline crack growth rates) following a 1.75 σ_{max} block of 20 cycles was found to correlate with the room temperature cyclic hardening response of a particular microstructure. Condition 1 and Condition 4 both of which do not cyclically soften require a significantly larger number of cycles to recover; Condition 1 which has a higher hardening capacity than Condition 4 (UTS/YS = 1.23 vs. 1.10) exhibits the longest delay.

The FCP behavior of Conditions 1 and 5 as a function of interstitial content follows the pattern for the tensile behavior in that Condition 5 is more sensitive than Condition 1 to oxygen and hydrogen content. The change in crack growth rate in Condition 5 was associated with transitions from tortuous, faceted growth to a more planar, transgranular propagation as interstitial content were increased. The transgranular propagation with increased interstitial content is consistent with the increased yield strength and an associated tendency to planar slip in the alpha phase of these conditions.

267

CONCLUSIONS

The following conclusions can be made from the preceeding studies:

(1) Microstructure has a real influence on fatigue crack propagation (FCP) rate in the titanium alloys studied in this program.

(2) Increasing load ratio (R) incrases FCP rate in the low and high ΔK regimes but has very little effect at intermediate ΔK values.

(3) The 3.5% NaCl solution had at most a modest effect on FCP rate for the oxygen level examined.

(4) No effects of hold time on FCP rate were observed in the oxygen and hydrogen content material which was examined.

(5) FCP rate was not altered significantly by testing conducted in dry air (5% RH), moist air (95% RH) or dry argon.

(6) Increasing oxygen content in Ti-6Al-4V resulted in increased FCP rates at constant microstructure.

(7) Increasing hydrogen content had essentially no effect on FCP rate tests at 20 Hz.

(8) Increased temperature up to $316^{\circ}C$ ($600^{\circ}F$) resulted in significantly increased FCP rate, especially at high load ratio (R).

APPENDIX A

FCP CURVES

FIGURES

Fig. A71 FCP data for Condition 5 (1-5-63), 285 ppm hydrogen, 600°F, dry air, 20 Hz, R = 0.3.

Fig. A72 FCP data for Condition 6 (1-6-1), 68°F, dry air, 20 Hz, R = 0.1.

Fig. A73 FCP data for Condition 6 (1-6-3), 68°F, 3.5 NaCl, 20 Hz, R = 0.1.

Fig. A74 FCP data for Condition 6 (1-6-4), 68°F, 3.5 NaCl, 1 Hz, R = 0.1.

Fig. A75 FCP data for Condition 6 (1-6-2), 68°F, dry air, 20 Hz, R = 0.3.

Fig. A76 FCP data for Condition 7 (1-7-7), 68°F, dry air, 20 Hz, R = 0.1.

Fig. A77 FCP data for Condition 7 (1-7-9), 68°F, 3.5 NaCl, 20 Hz, R = 0.1.

Fig. A78 FCP data for Condition 7 (1-7-8), 68°F, 3.5 NaCl, 1 Hz, R = 0.1.

Fig. A79 FCP data for Condition 7 (1-7-0/26), 68°F, dry air, 20 Hz, R = 0.3; including 5 min. hold-time data at approximately 2.5×10^{-5}, 2.5×10^{-4}, and 2.5×10^{-3} mm/cycle.

Fig. A80 FCP data for Condition 7 (1-7-25), 68°F, wet air, 20 Hz, R = 0.1.

Fig. A81 FCP data for Condition 7 (1-7-21), 68°F, argon, 20 Hz, R = 0.1.

Fig. A82 FCP data for Condition 7 (1-7-23), 68°F, dry air, 20 Hz, R = 0.5.

Fig. A83 FCP data for Condition 7 (1-7-24), 68°F, dry air, 20 Hz, R = 0.7.

Fig. A84 FCP data for Condition 7 (1-7-28), subjected to $1.75\,\sigma$ max overload for 20 cycles, 68°F, dry air, 20 Hz, R = 0.1.

Fig. A85 FCP data for Condition 7 (1-7-29), 250°F, dry air, 20 Hz, R = 0.3; including 5 min. hold-time data at approximately 2.5×10^{-4} mm/cycle.

Fig. A86 FCP data for Condition 7 (1-7-30), 250°F, dry air, 20 Hz, R = 0.7.

Fig. A87 FCP data for Condition 7 (1-7-31), 600°F, dry air, 20 Hz, R = 0.3; including 1 min. hold-time data at approximately 1.3 and 2.5×10^{-4} mm/cycles and 5 min. hold-time data at approximately 2.5×10^{-4} mm/cycles.

Fig. A88 FCP data for Condition 7 (1-7-32), 600°F, dry air, 20 Hz, R = 0.3; including 1 min. hold-time data at approximately 1.3 and 2.5×10^{-4} mm/cycles.

275

Fig. A108 FCP data for Condition 10 (2-10-9), 68°F, dry air, 20 Hz, R = 0.5.

Fig. A109 FCP data for Condition 10 (2-10-8), 68°F, dry air, 20 Hz, R = 0.75.

Fig. A110 FCP data for Condition 10 (2-10-23), subjected to $1.75\,\sigma$ max overload for 20 cycles, 68°F, dry air, 20 Hz, R = 0.1.

TI-6AL-4V   1-1-1
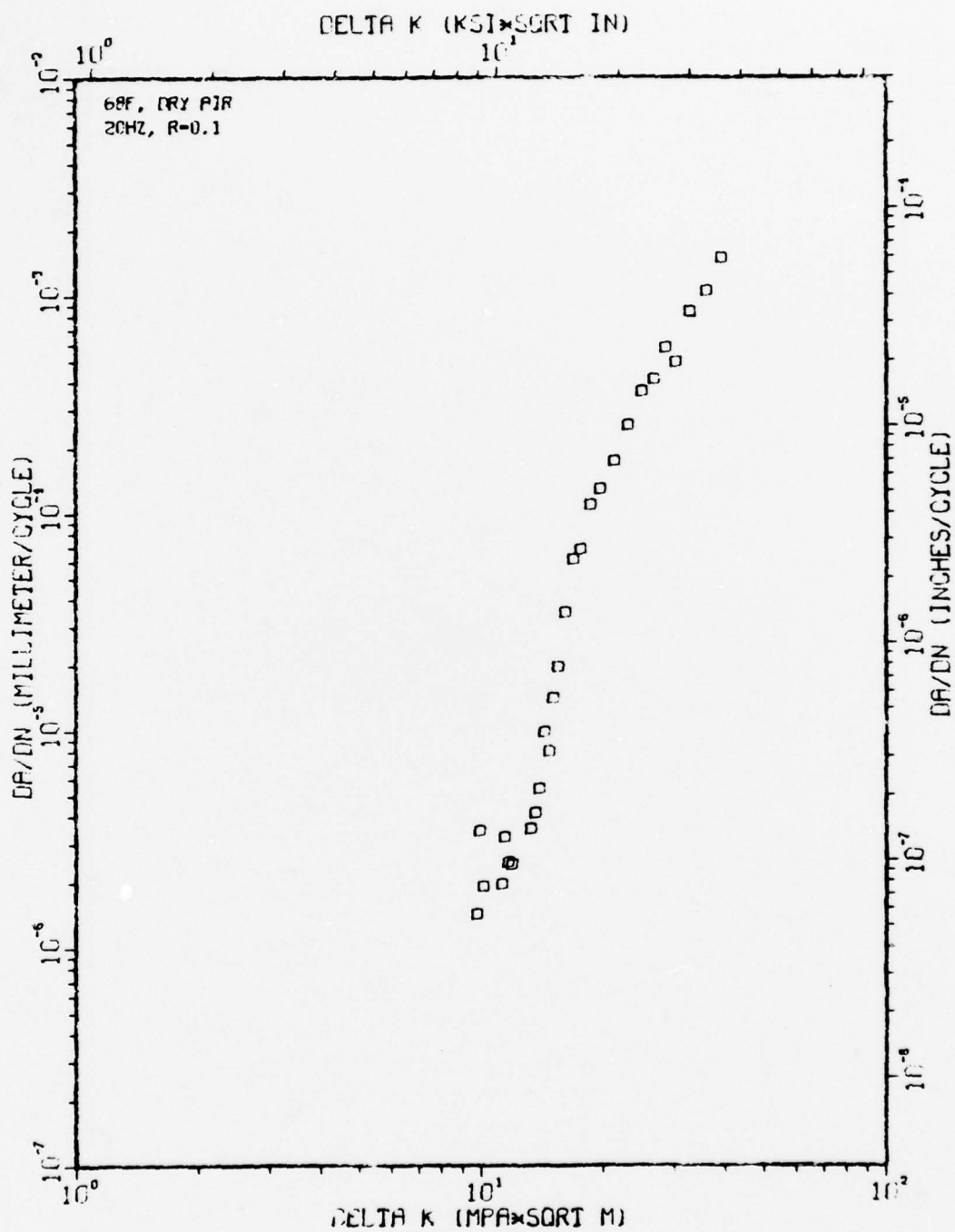
Figure A1

TI-6AL-4V 1-1-2
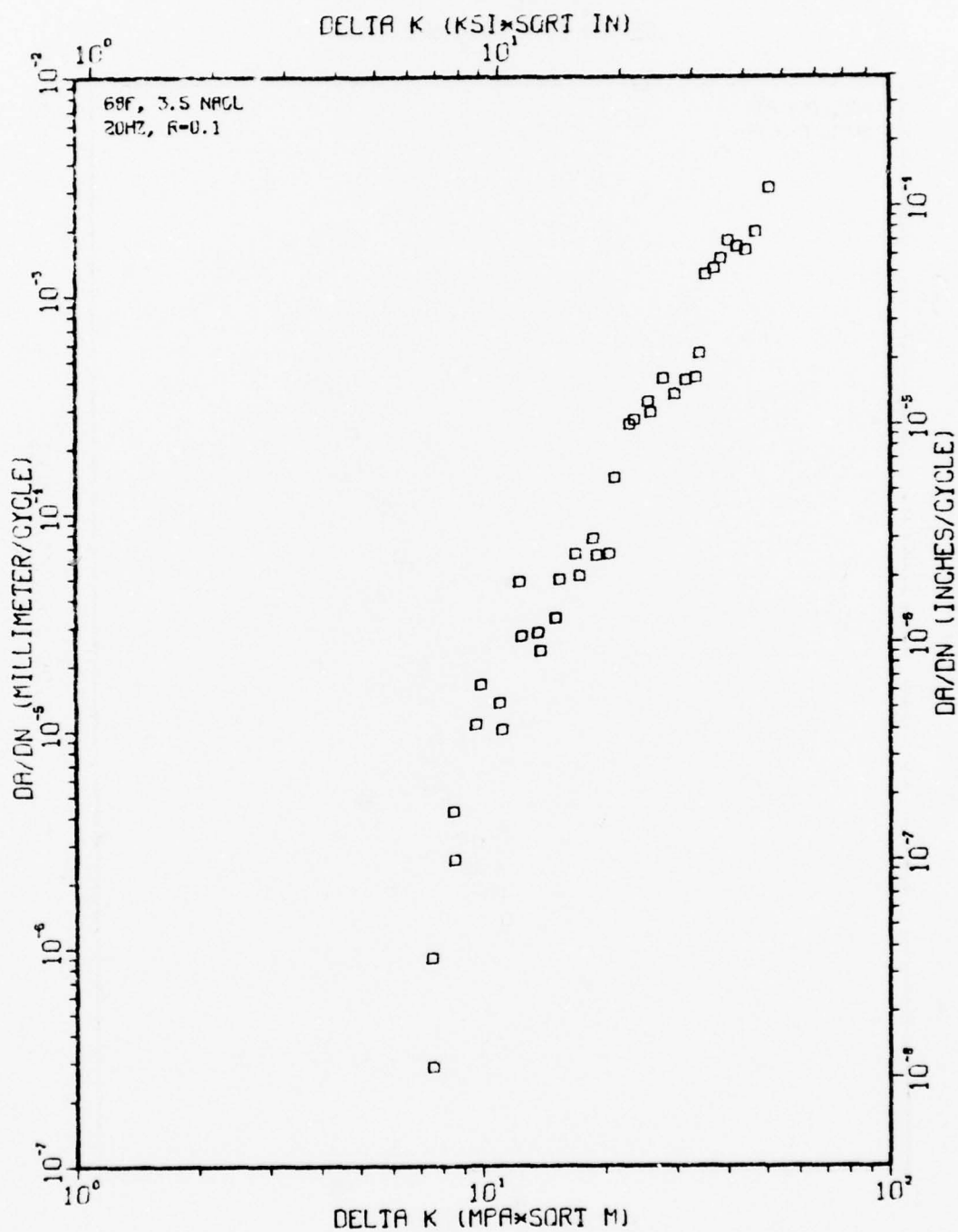
Figure A2

TI-6AL-4V 1-1-4
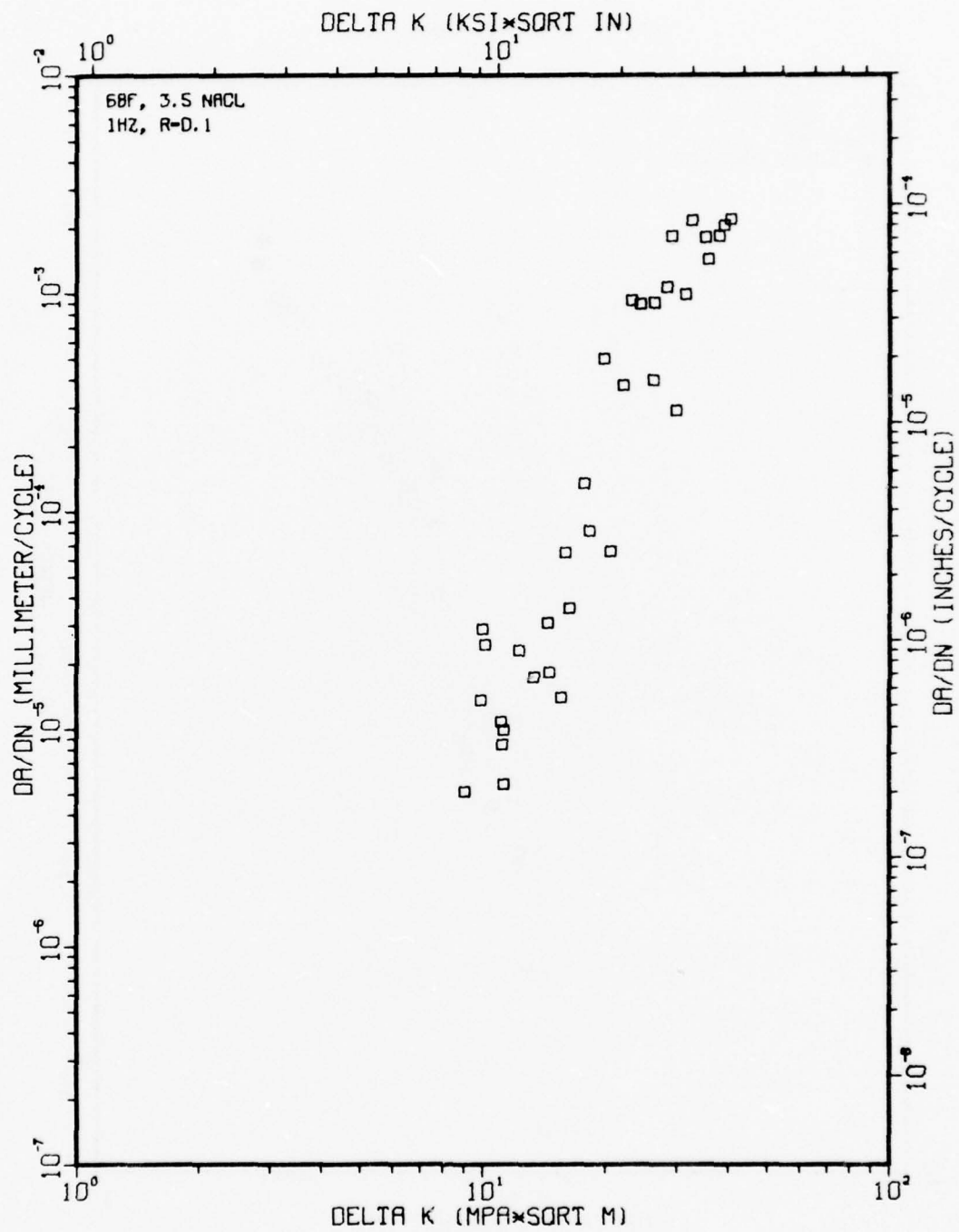
Figure A3

TI-6AL-4V (COND. 1), 68F, DRY AIR, R-0.3

Figure A4

280
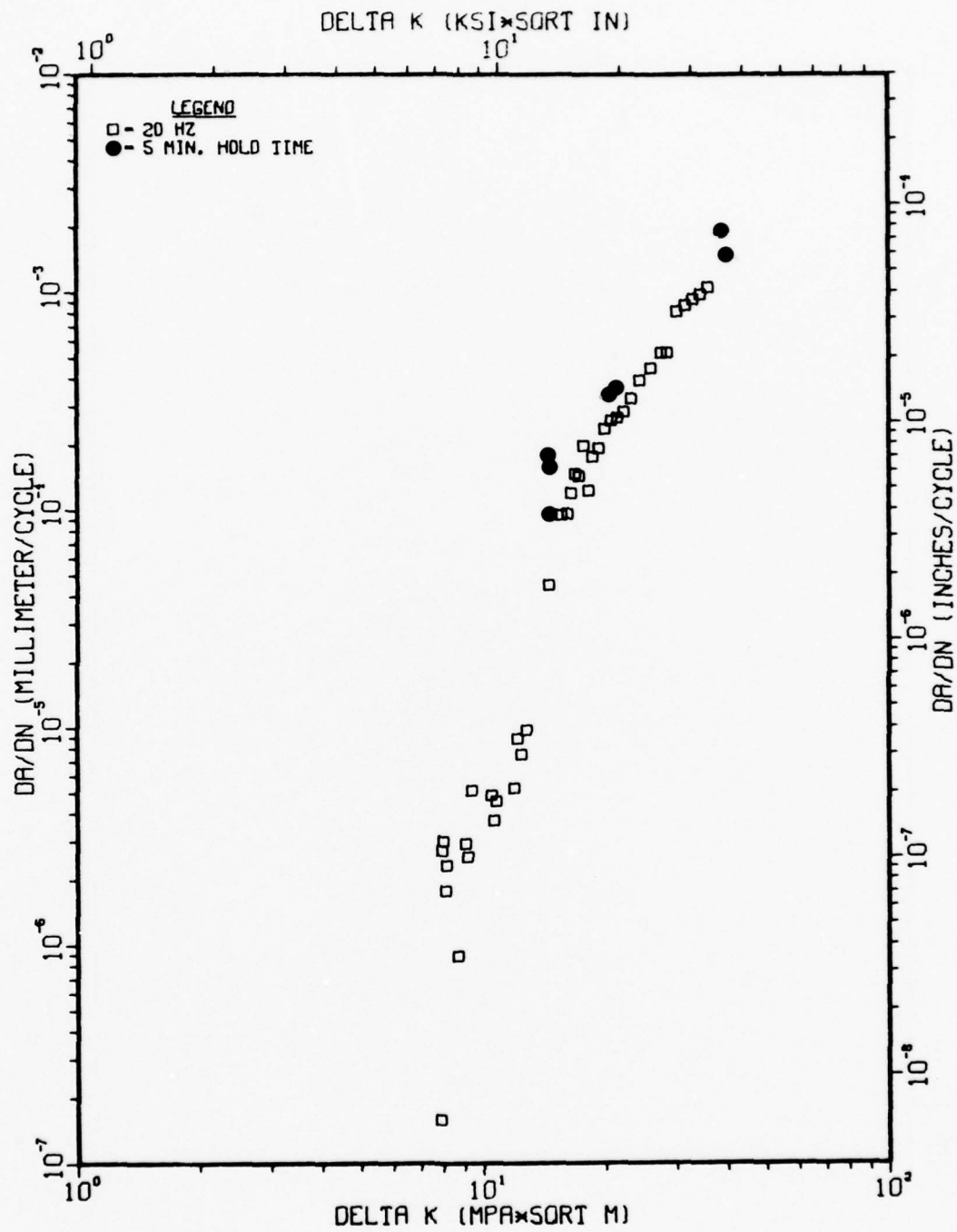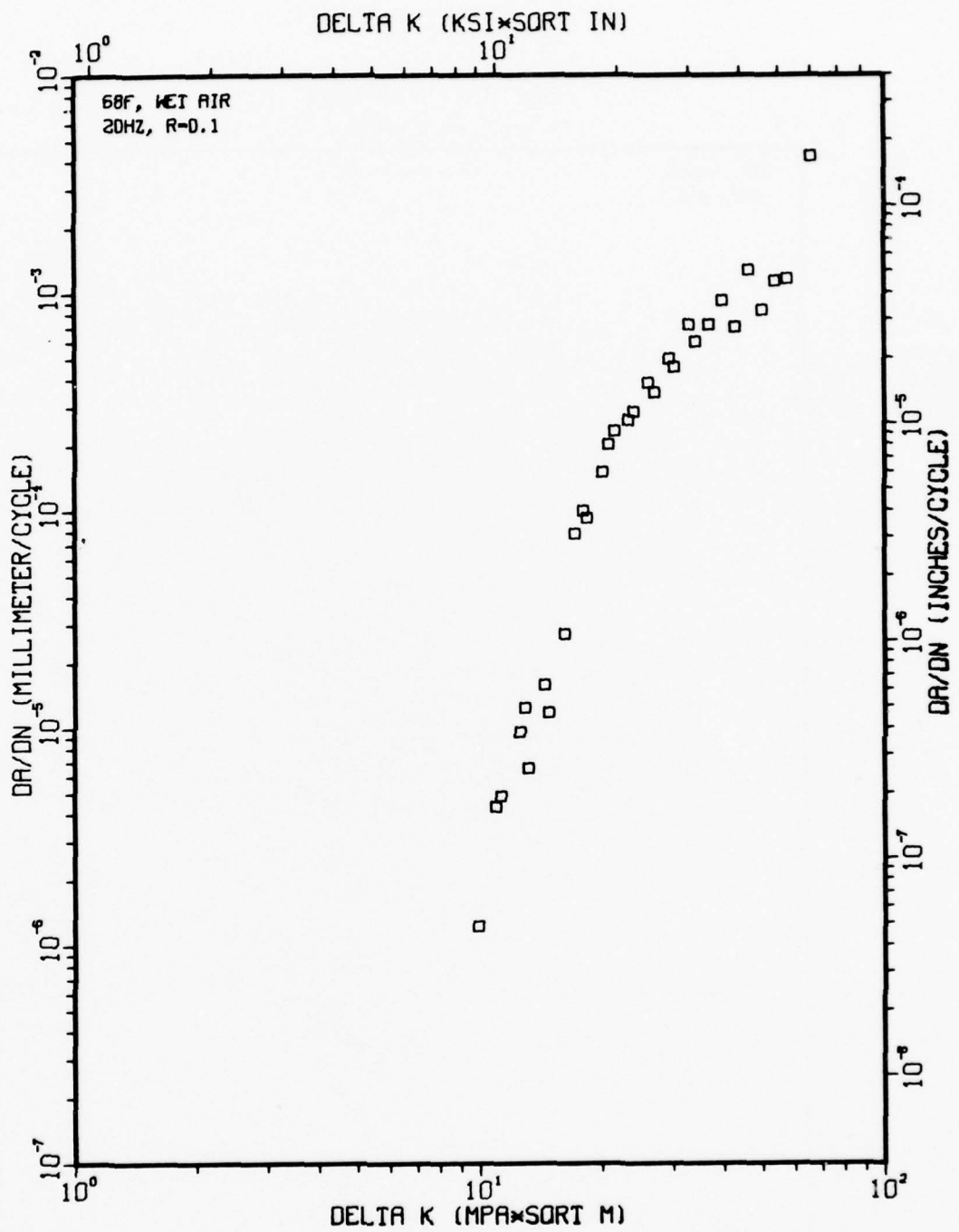
TI-6AL-4V   1-1-8

Figure A5

TI-6AL-4V 1-1-7
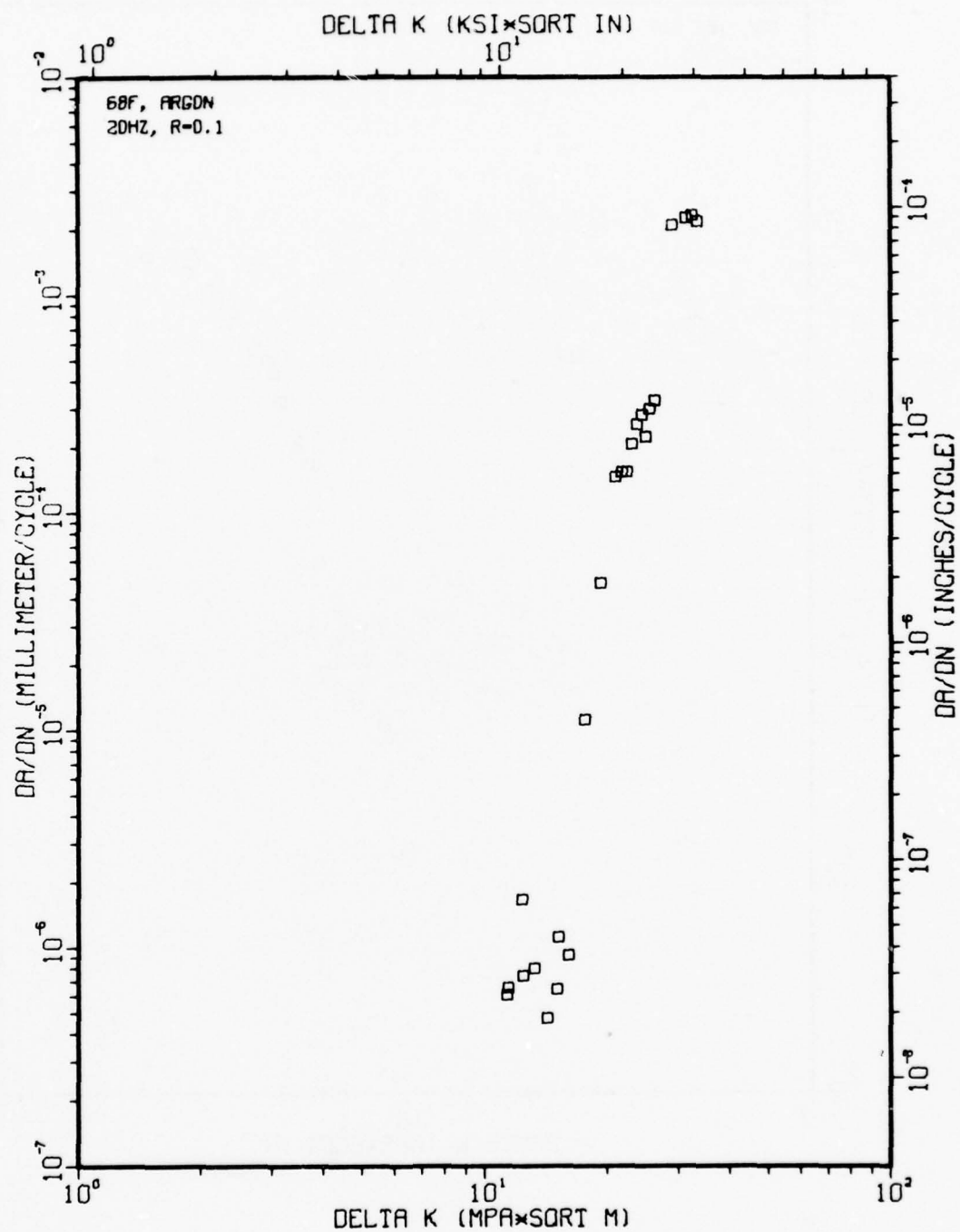
Figure A6

TI-6AL-4V 1-1-5
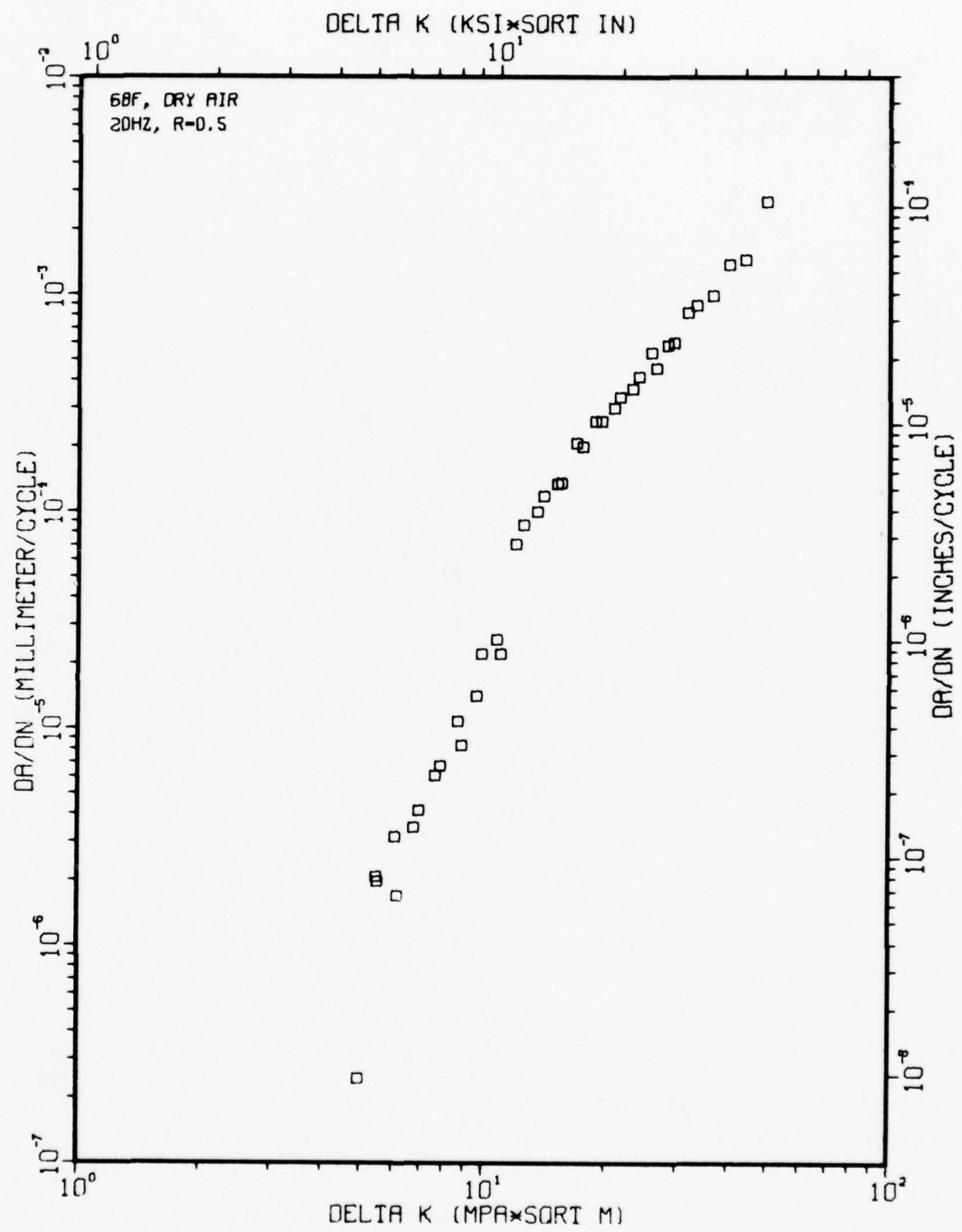
Figure A7

TI-6AL-4V   1-1-9
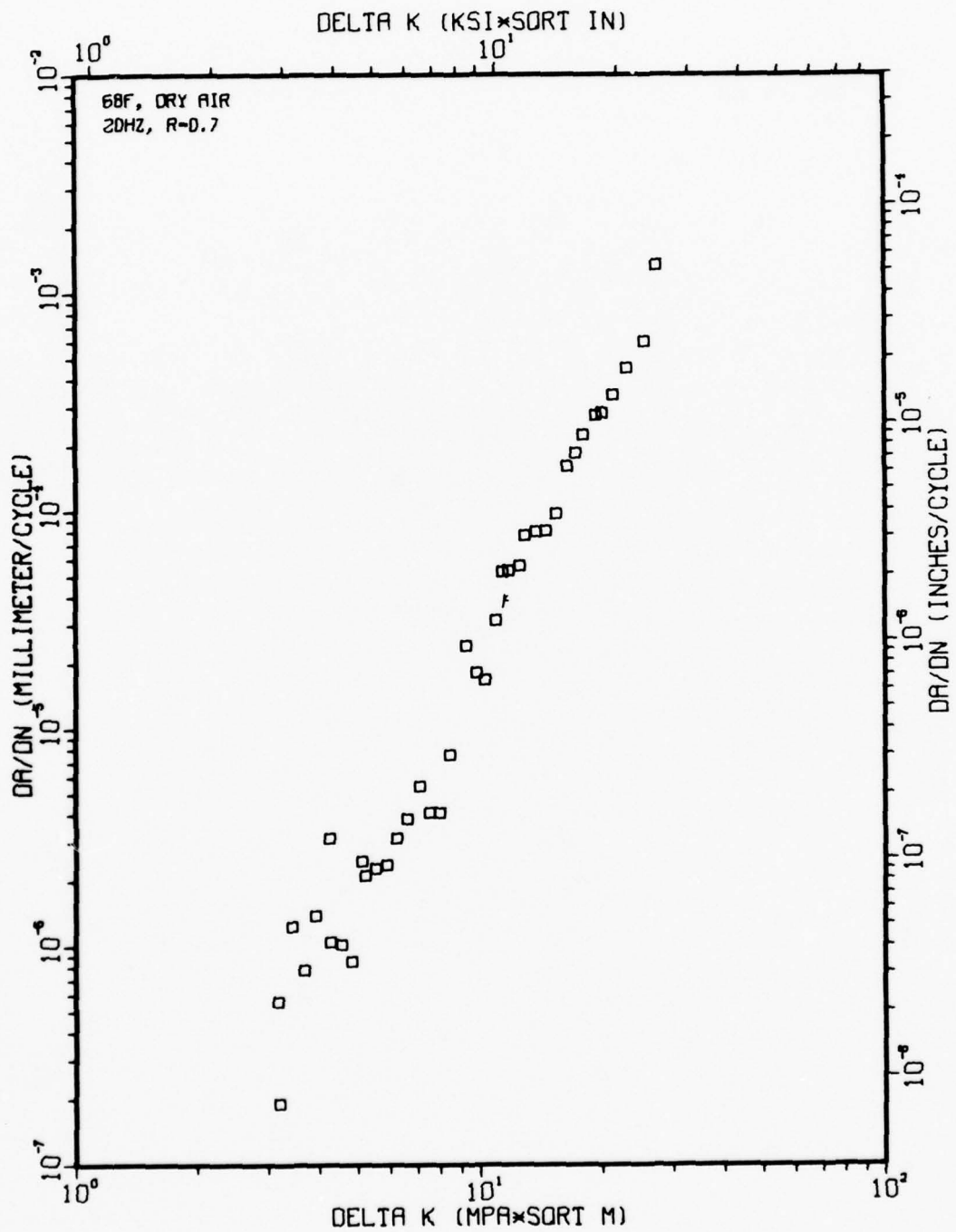
Figure A8

TI-6AL-4V   1-1-6
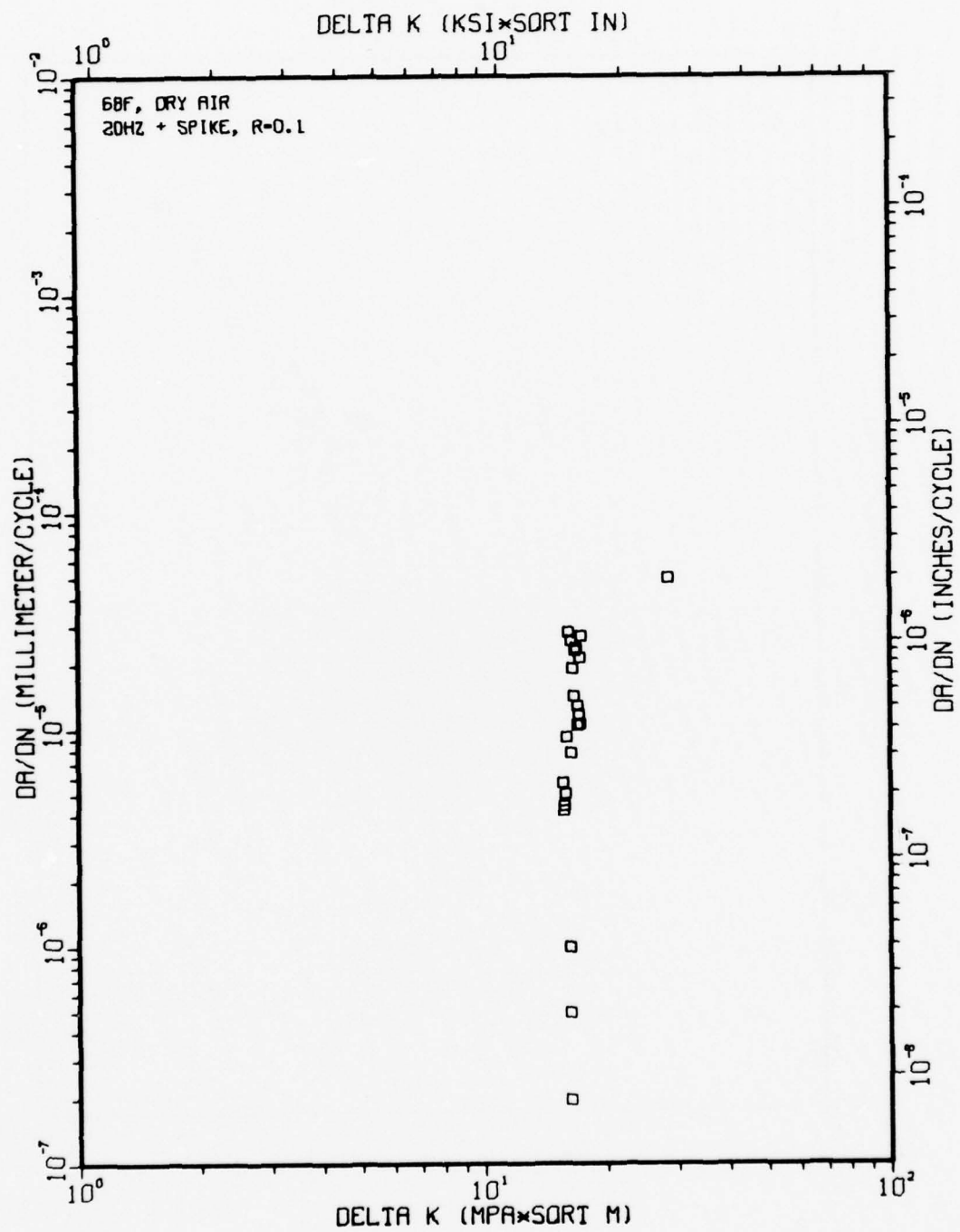
Figure A9

TI-6AL-4V 1-1-31/38, 250F, DRY AIR, R-0.3
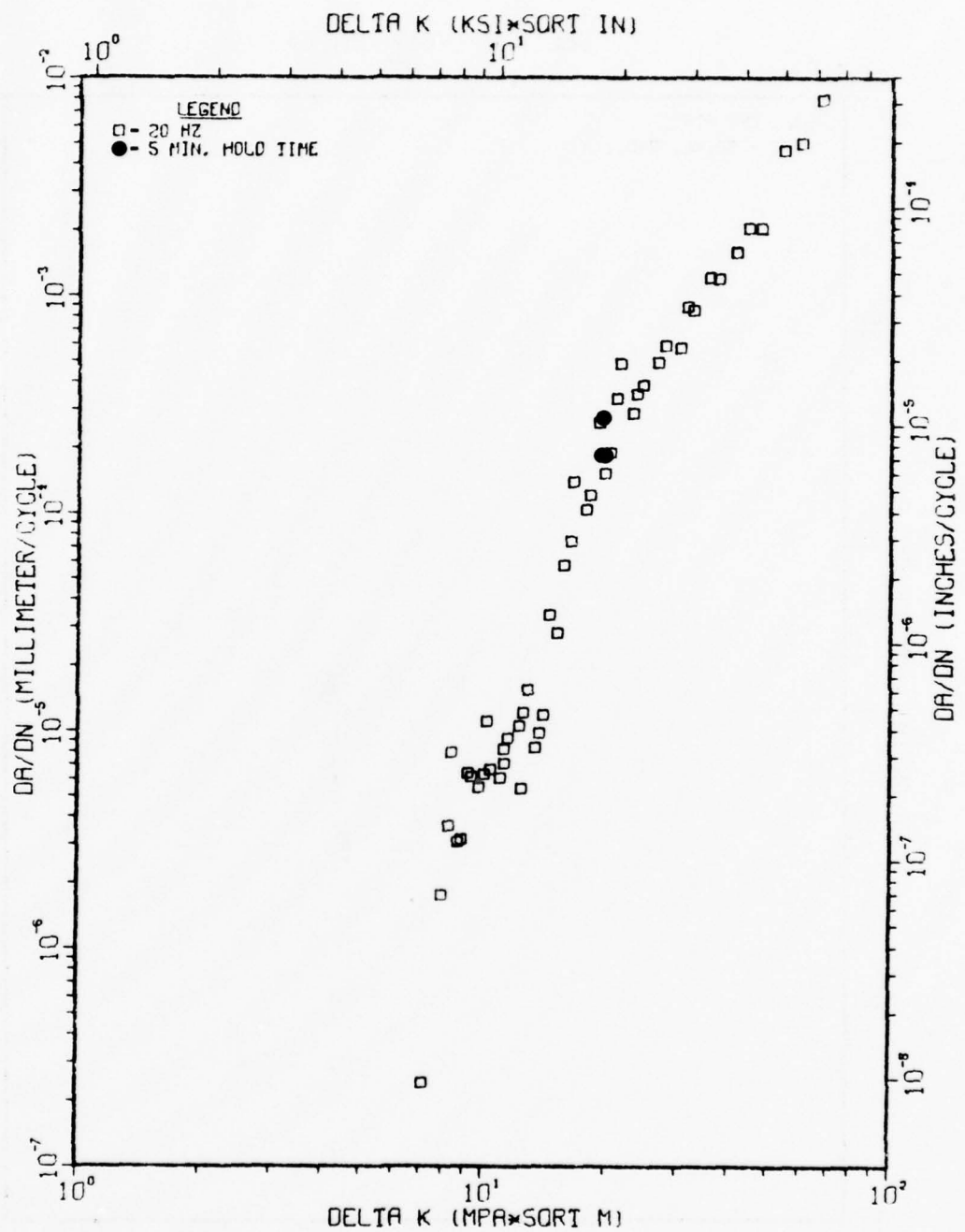
Figure A10

TI-6AL-4V 1-1-32 STD. OX.

Figure A11
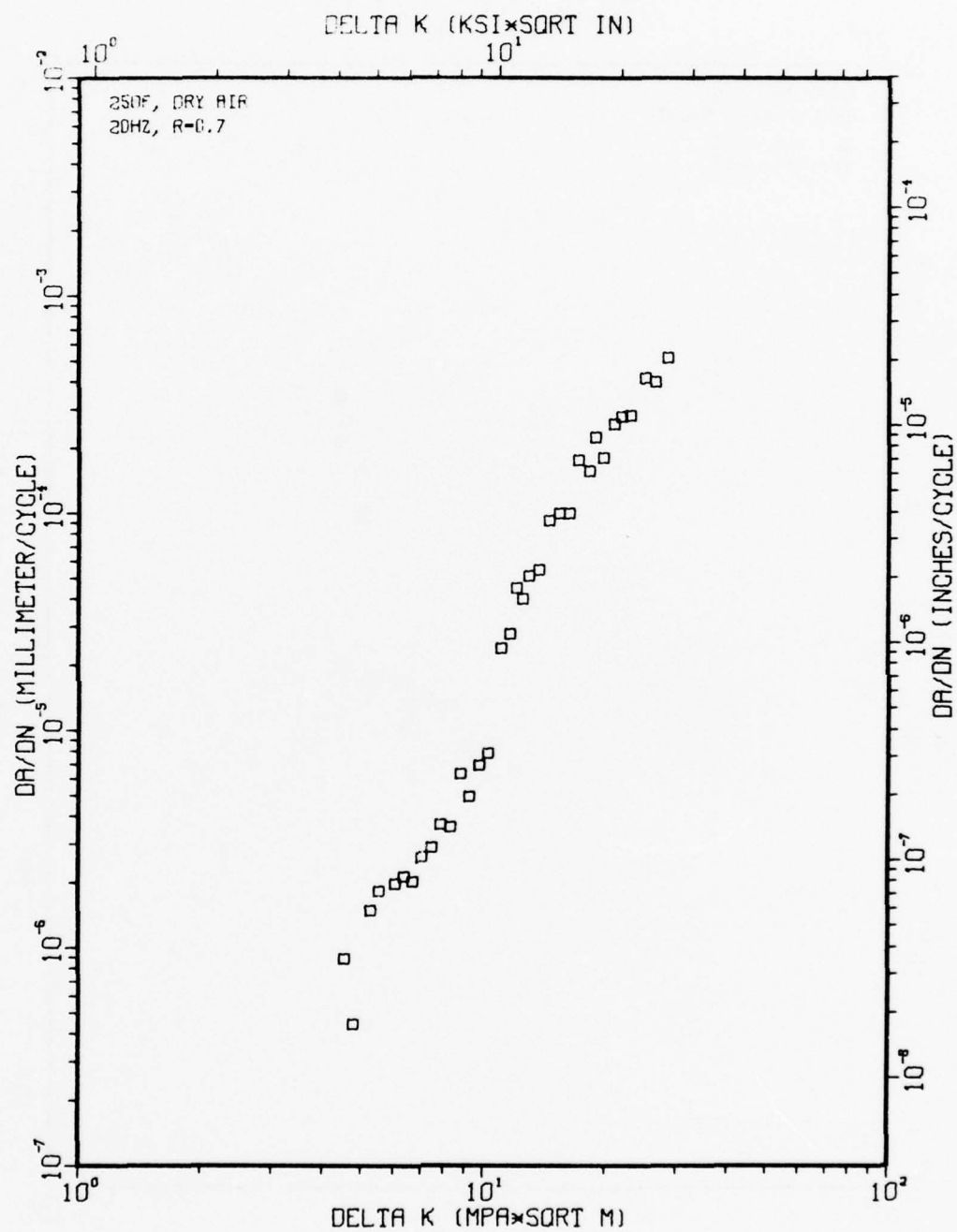
TI-6AL-4V 1-1-33 STD. OX.
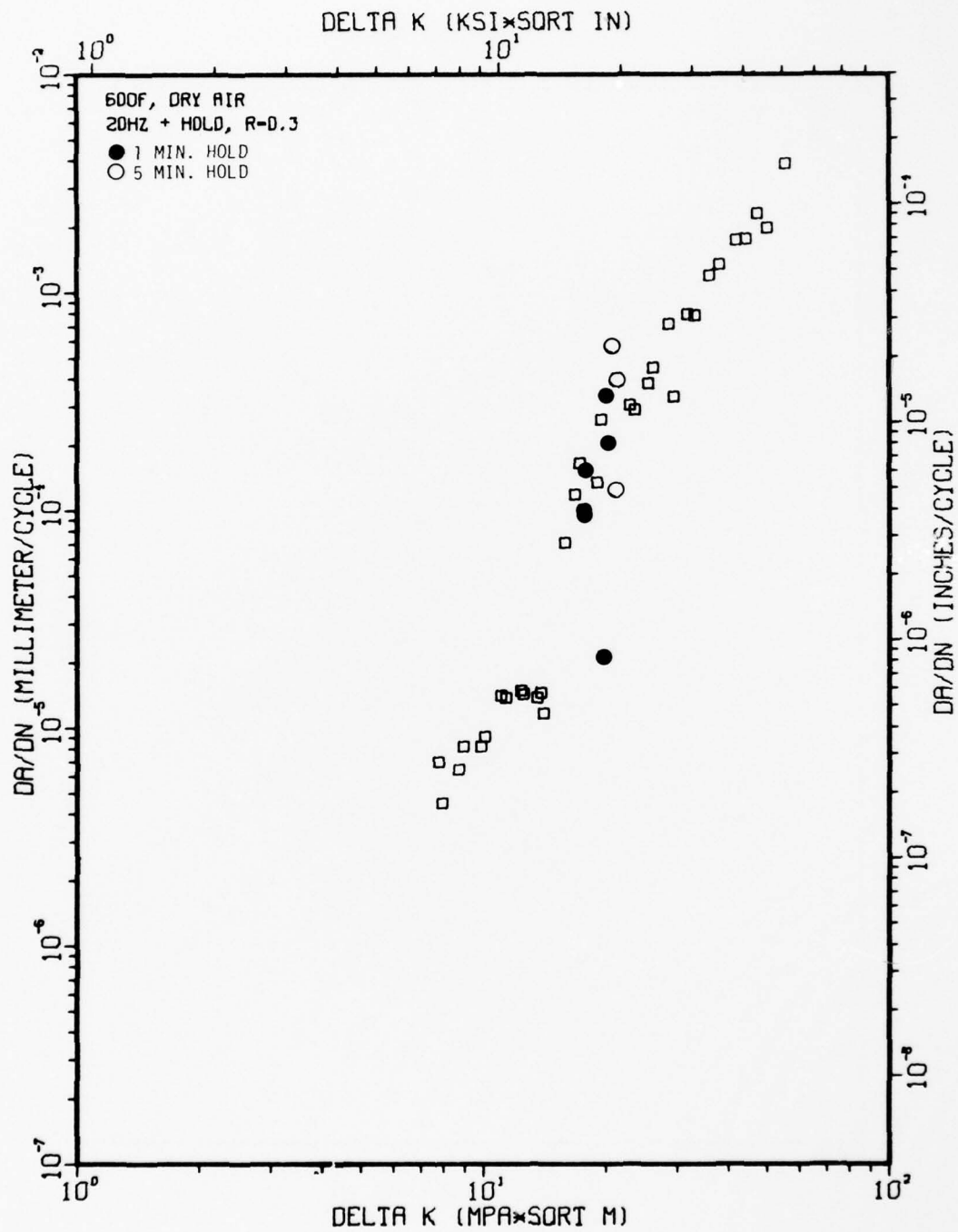
Figure A12

TI-6AL-4V 1-1-39 STD. OX.

Figure A13

289
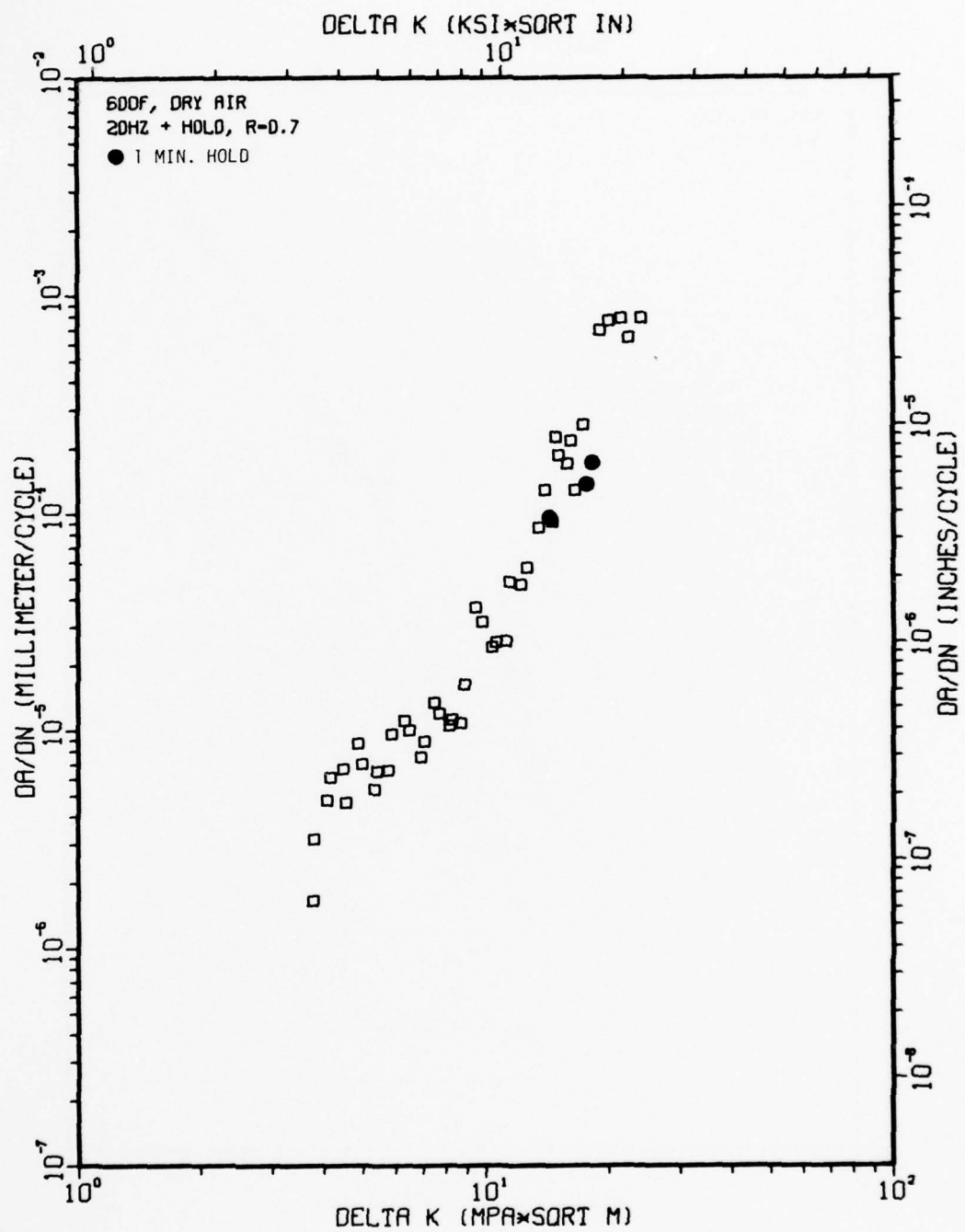
TI-6AL-4V 1-1-47 LO. OX.

Figure A14

290

TI-6AL-4V 1-1-48 LO. OX.

Figure A15

291
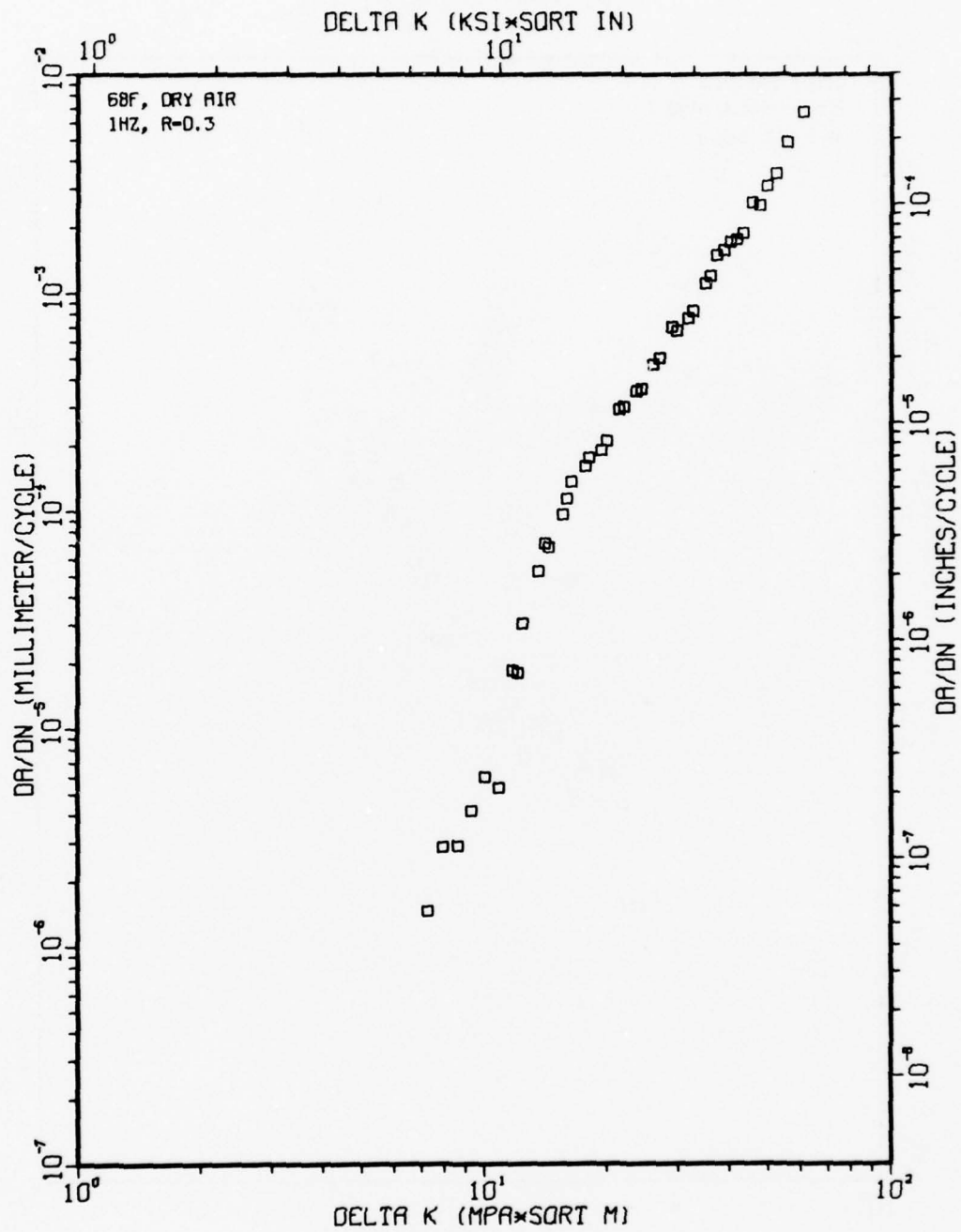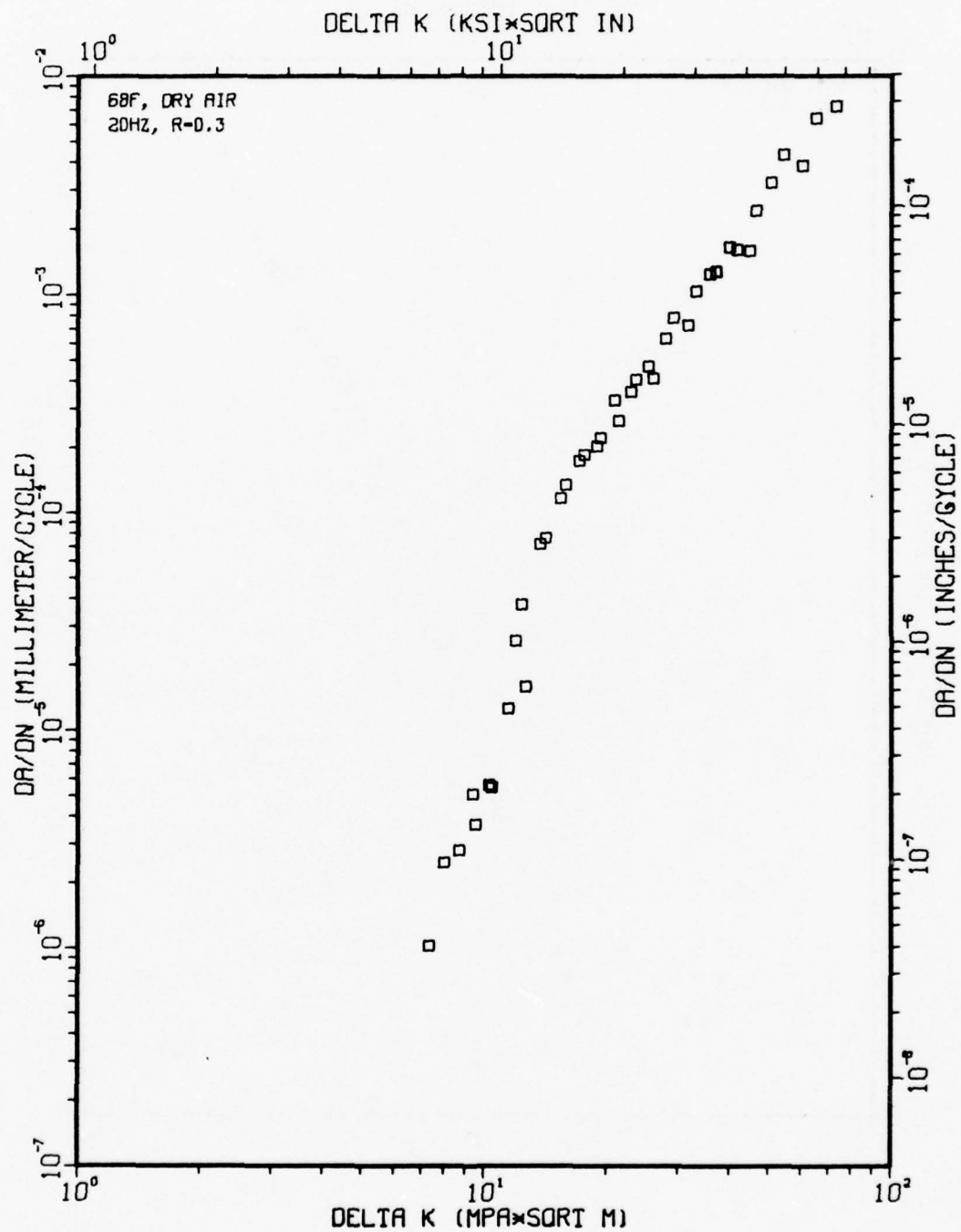
TI-6AL-4V   1-1-36   HI. OX.

Figure A16

292

TI-6AL-4V   1-1-34   HI. OX.

Figure   A17

293

TI-6AL-4V 1-1-45 LO. OX.

DELTA K (KSI*SORT IN)
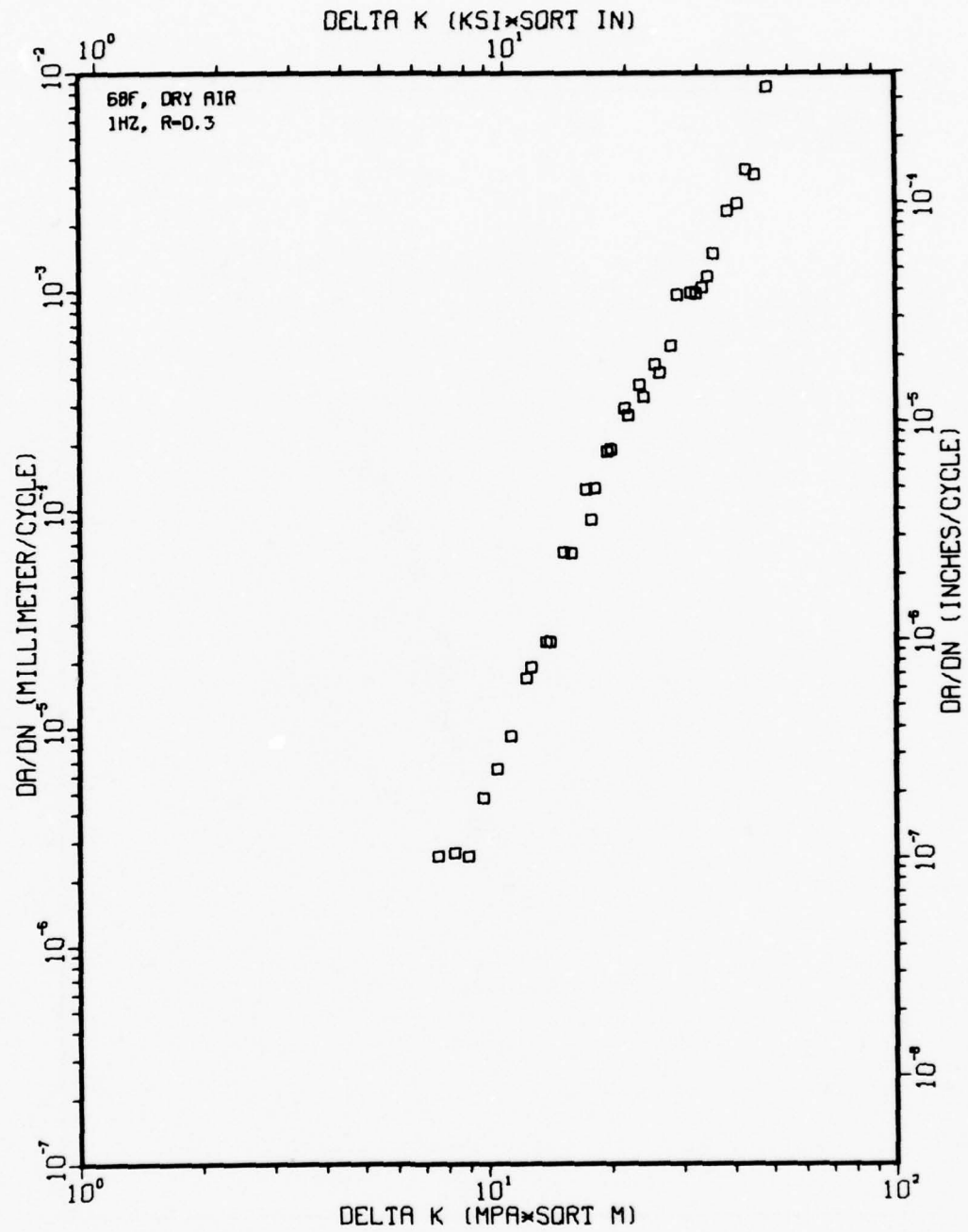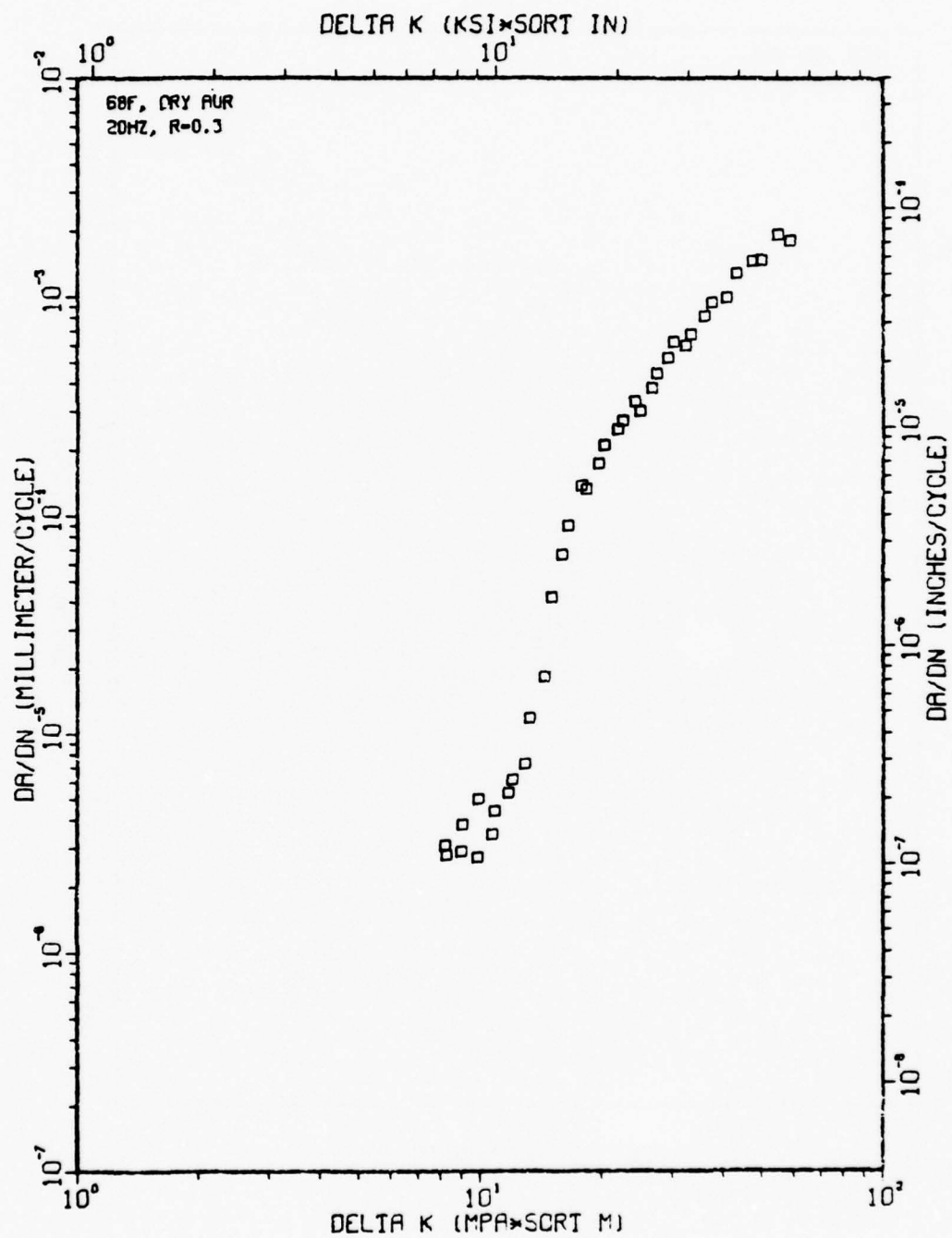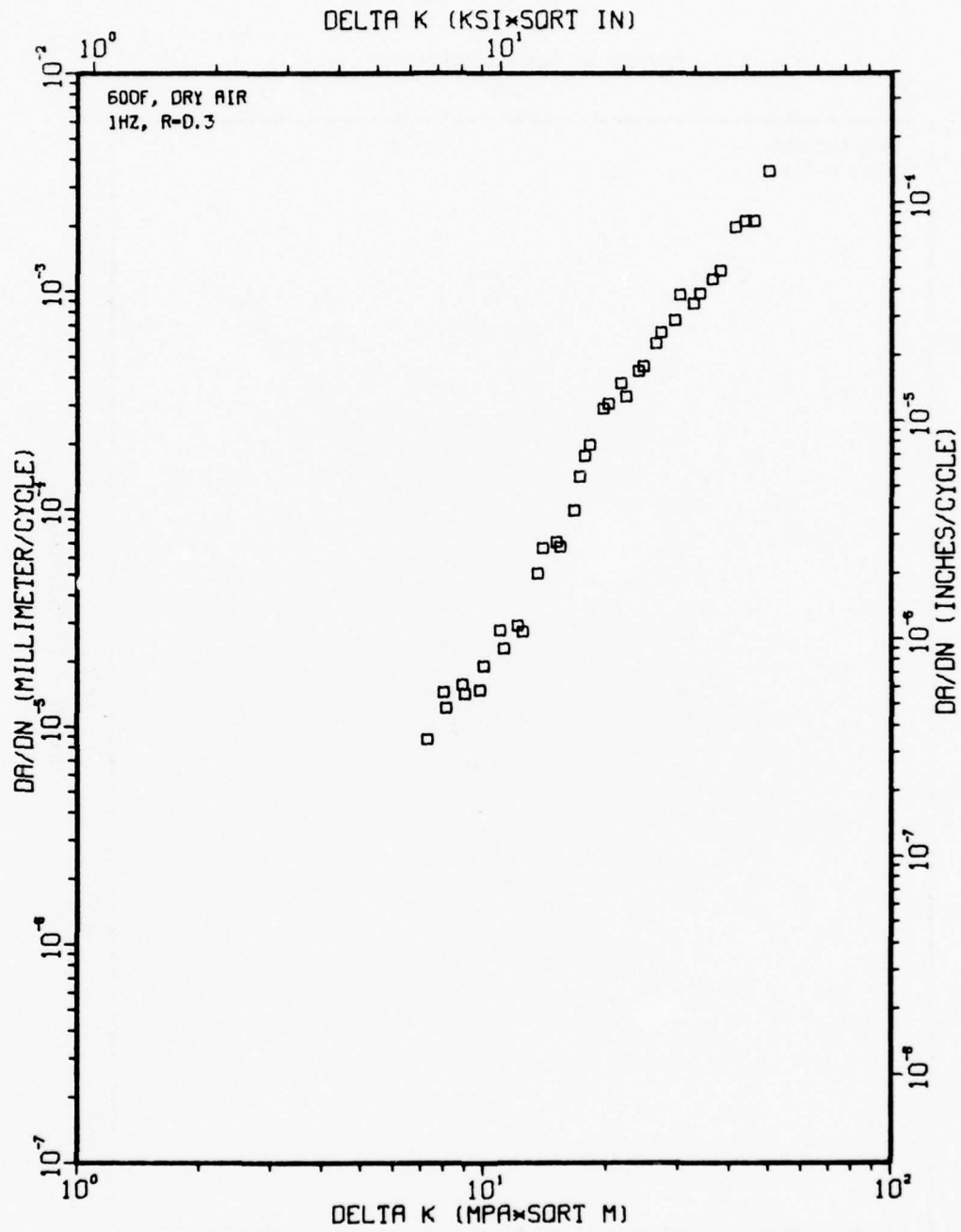
Figure A18

TI-6AL-4V 1-1-46 LO. OX.

Figure A19

295
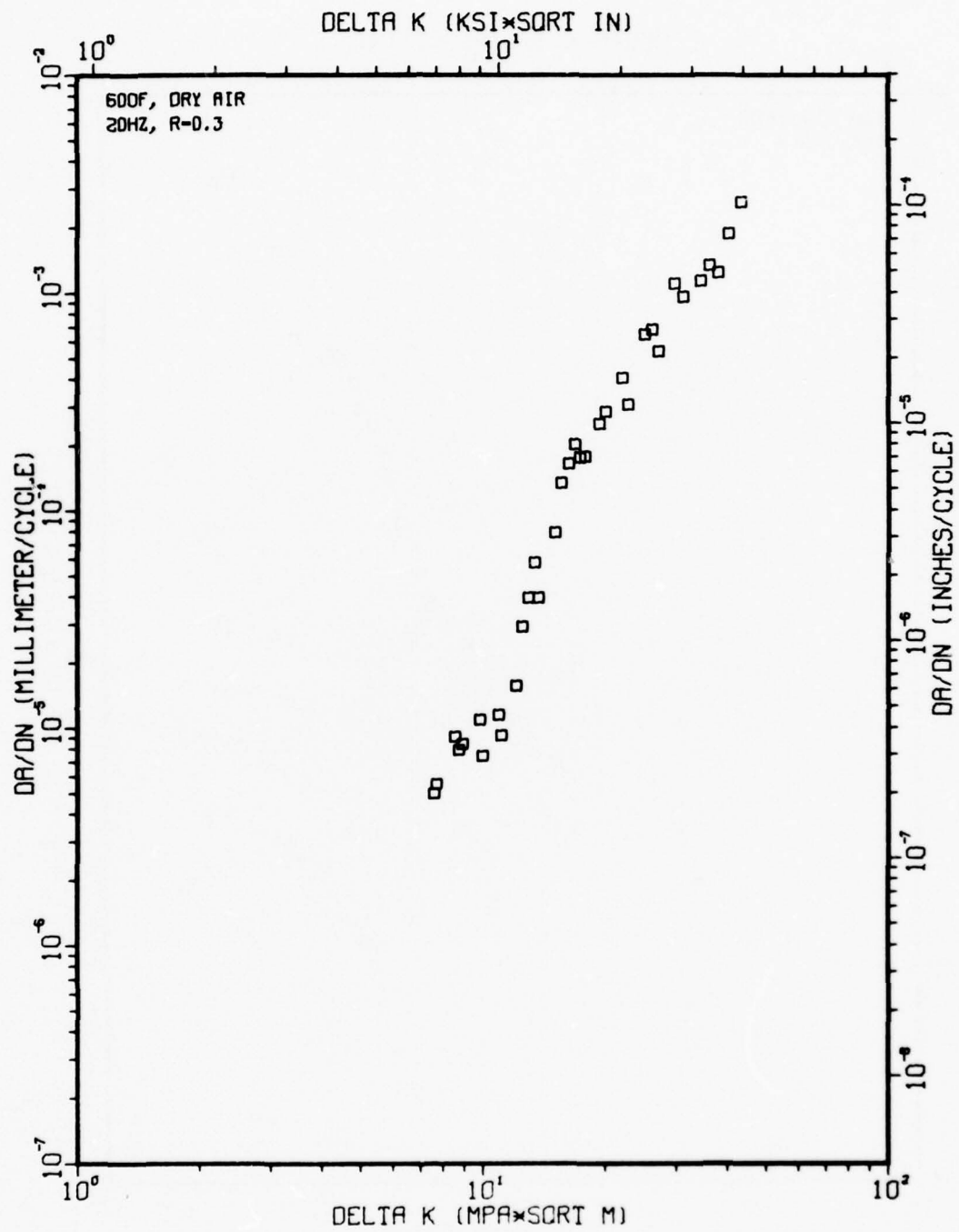
TI-6AL-4V 1-1-37 HI. OX.
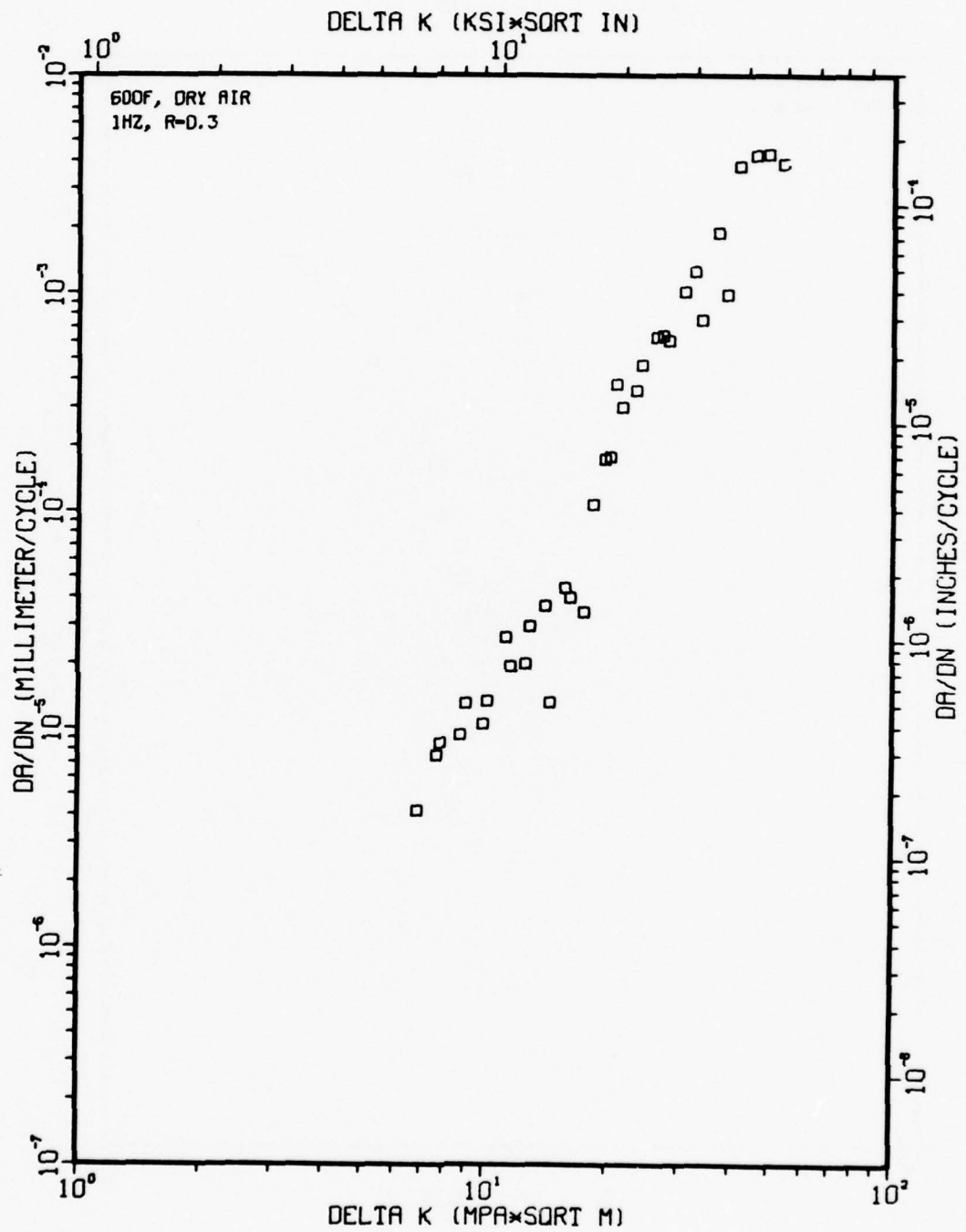
Figure A20

TI-6AL-4V 1-1-35 HI. OX.
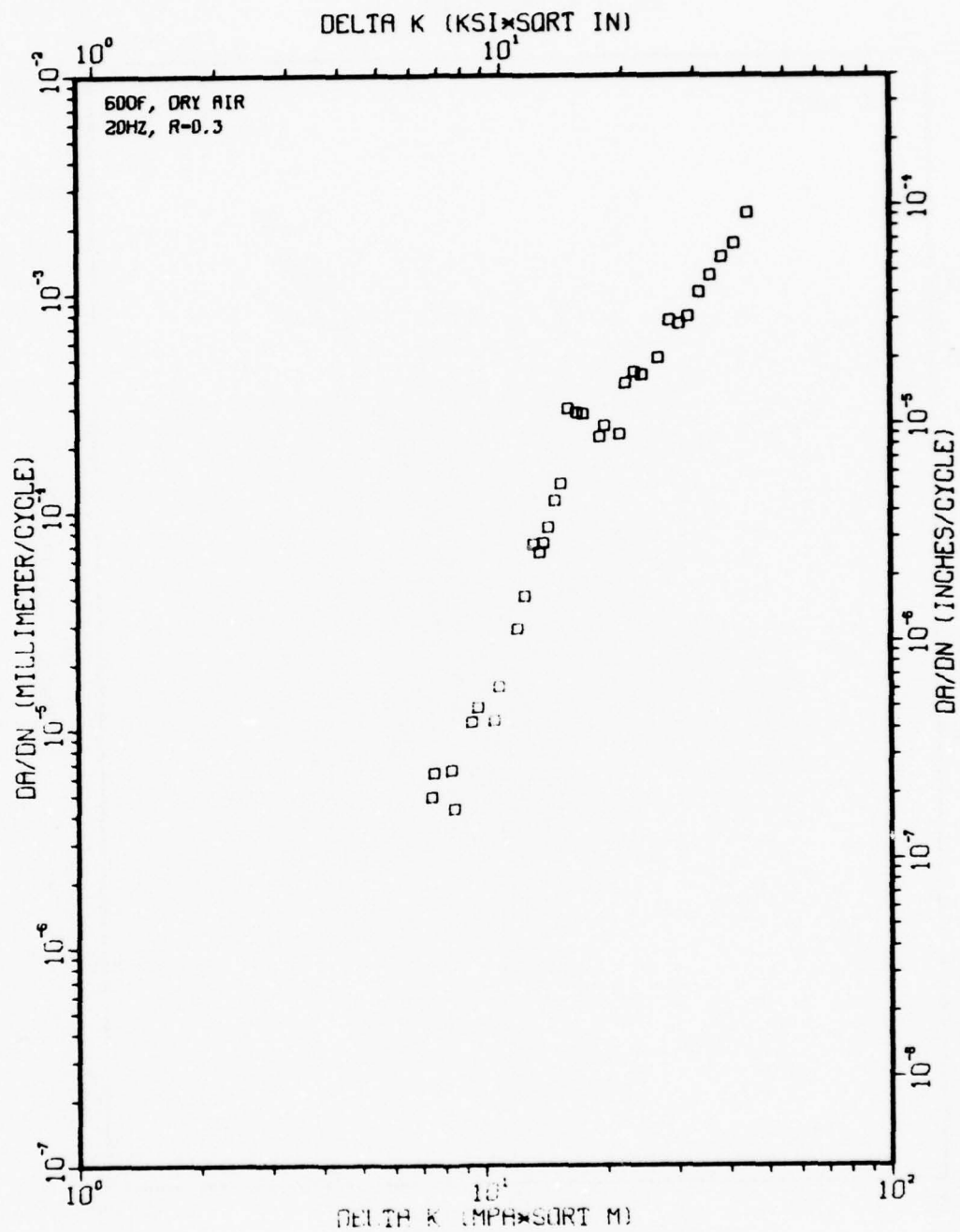
Figure A21

TI-6AL-4V 1-1-52 100H

Figure A22

298
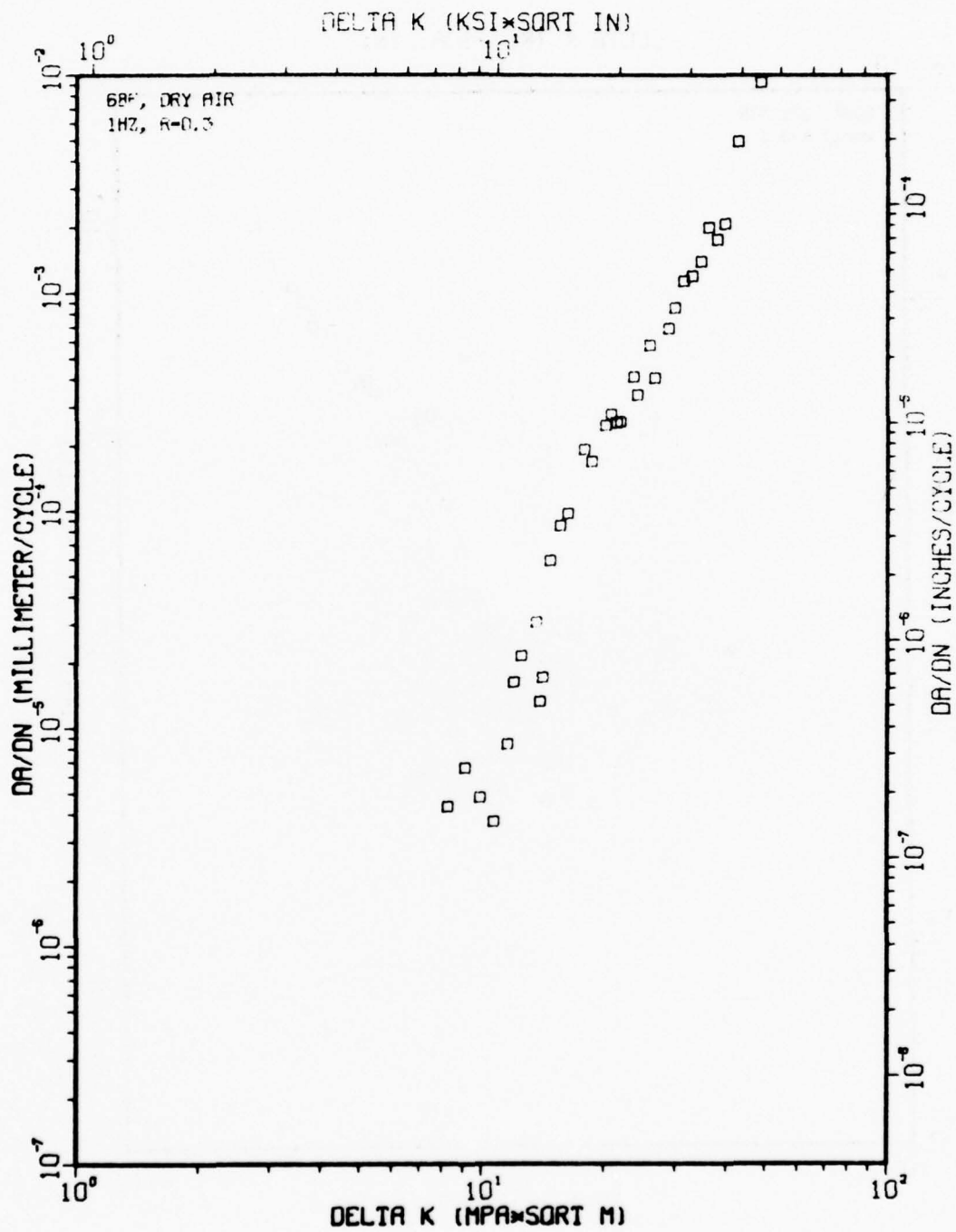
TI-6AL-4V 1-1-51 101H
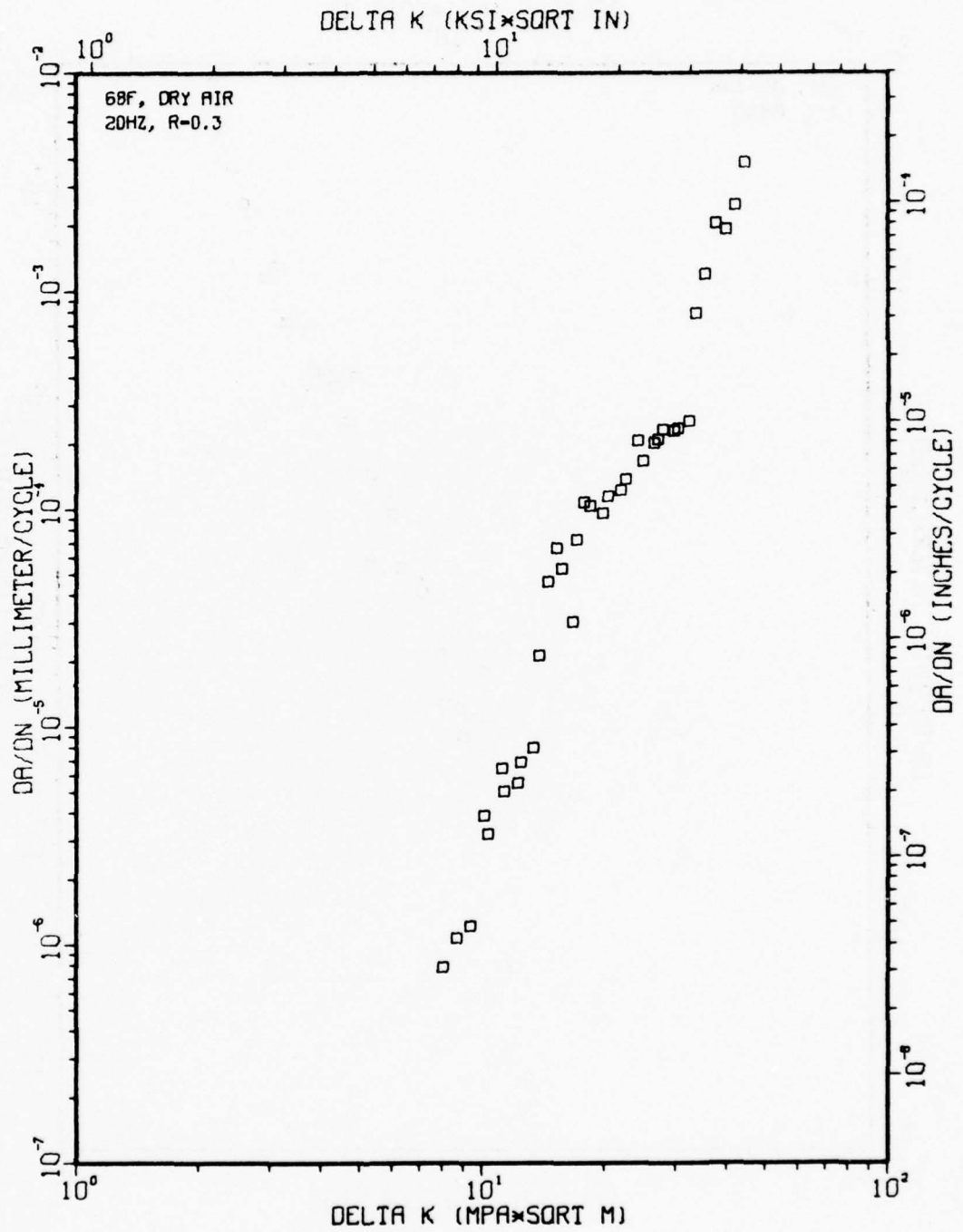
Figure A23

TI-6AL-4V 1-1-61 296H
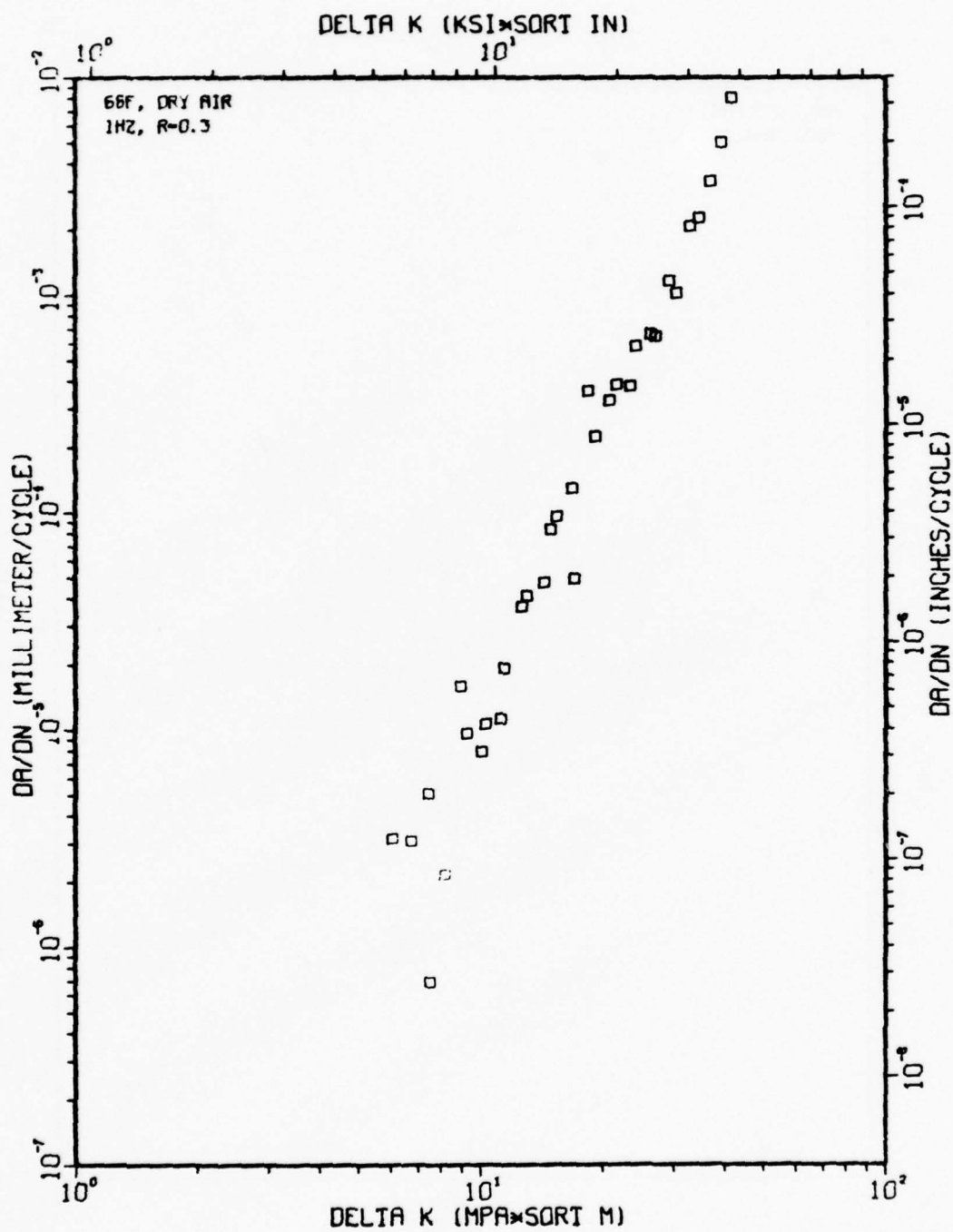
Figure A24

TI-6AL-4V 1-1-60 327H
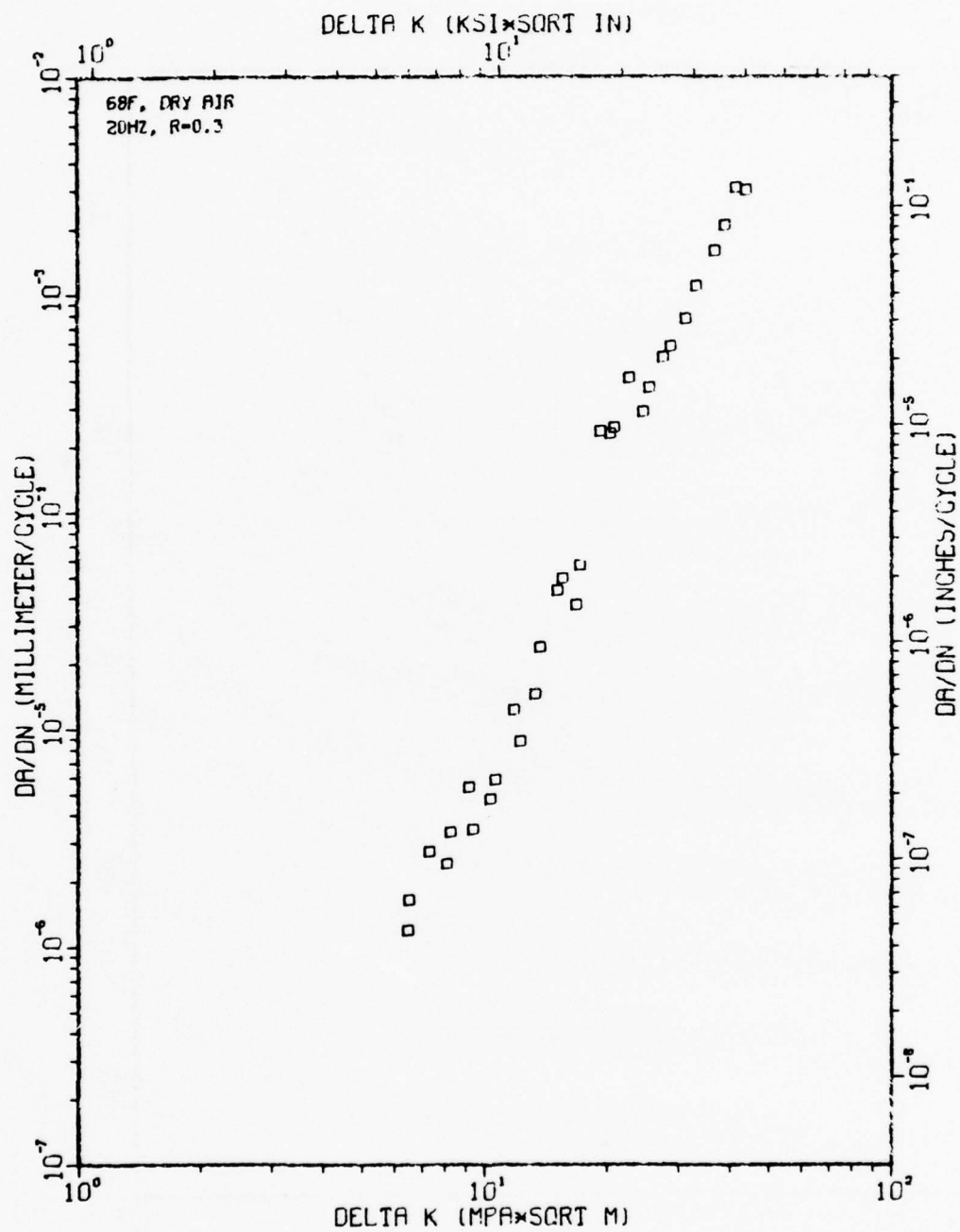
Figure A25

TI-6AL-4V 1-1-53 100H
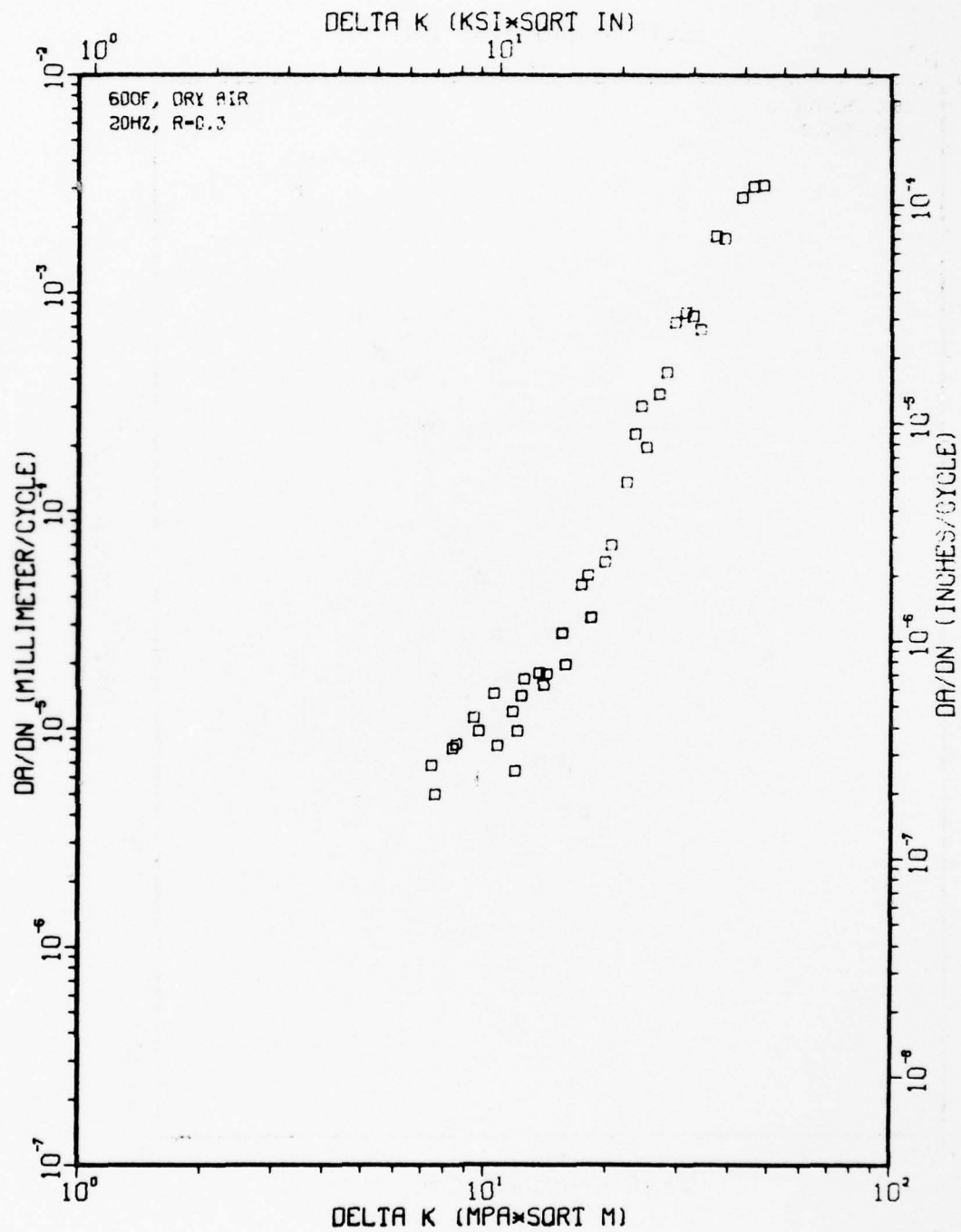
Figure A26

TI-6AL-4V   1-1-62   291H

Figure A27

303
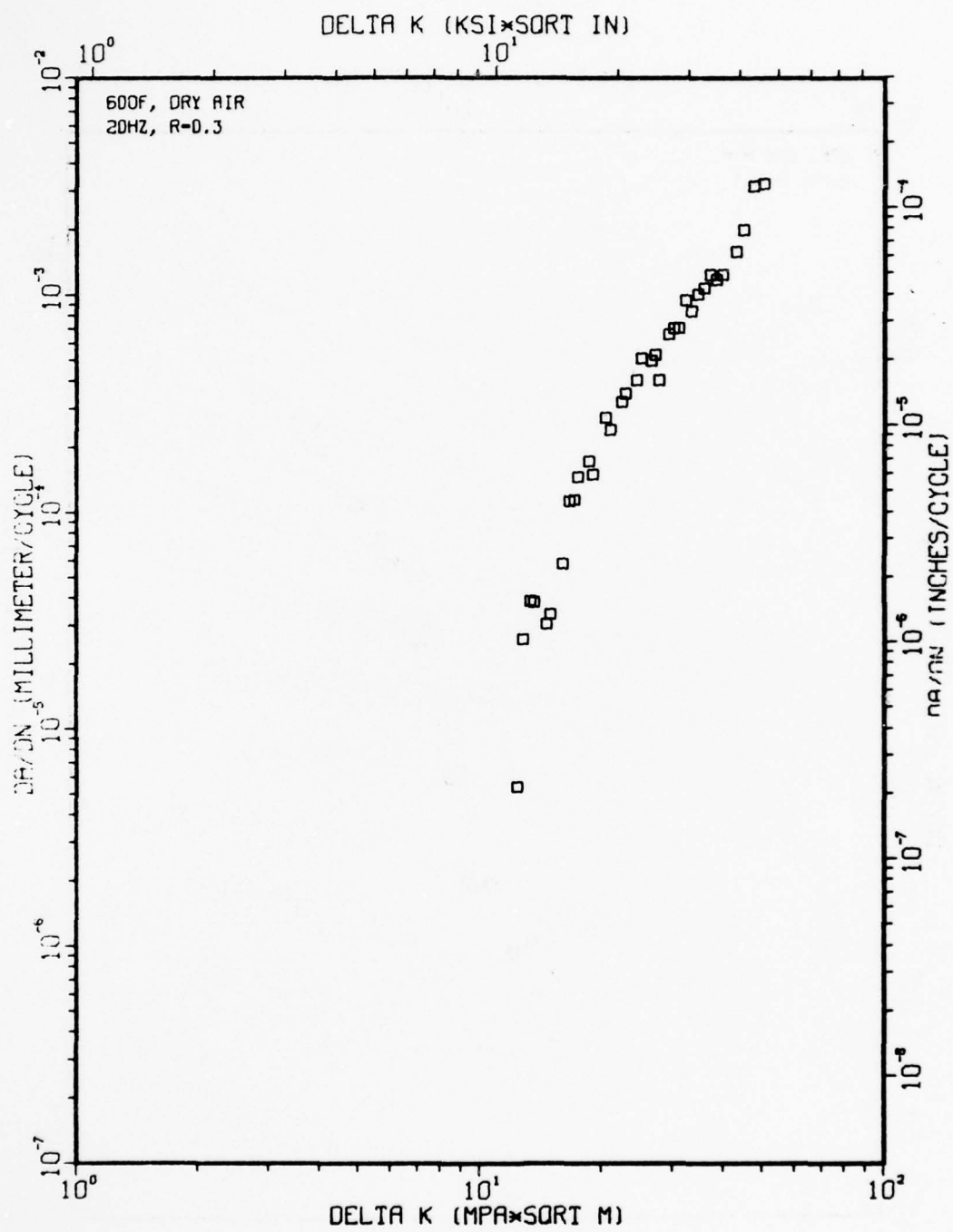
TI-6AL-4V 1-2-1

Figure A28
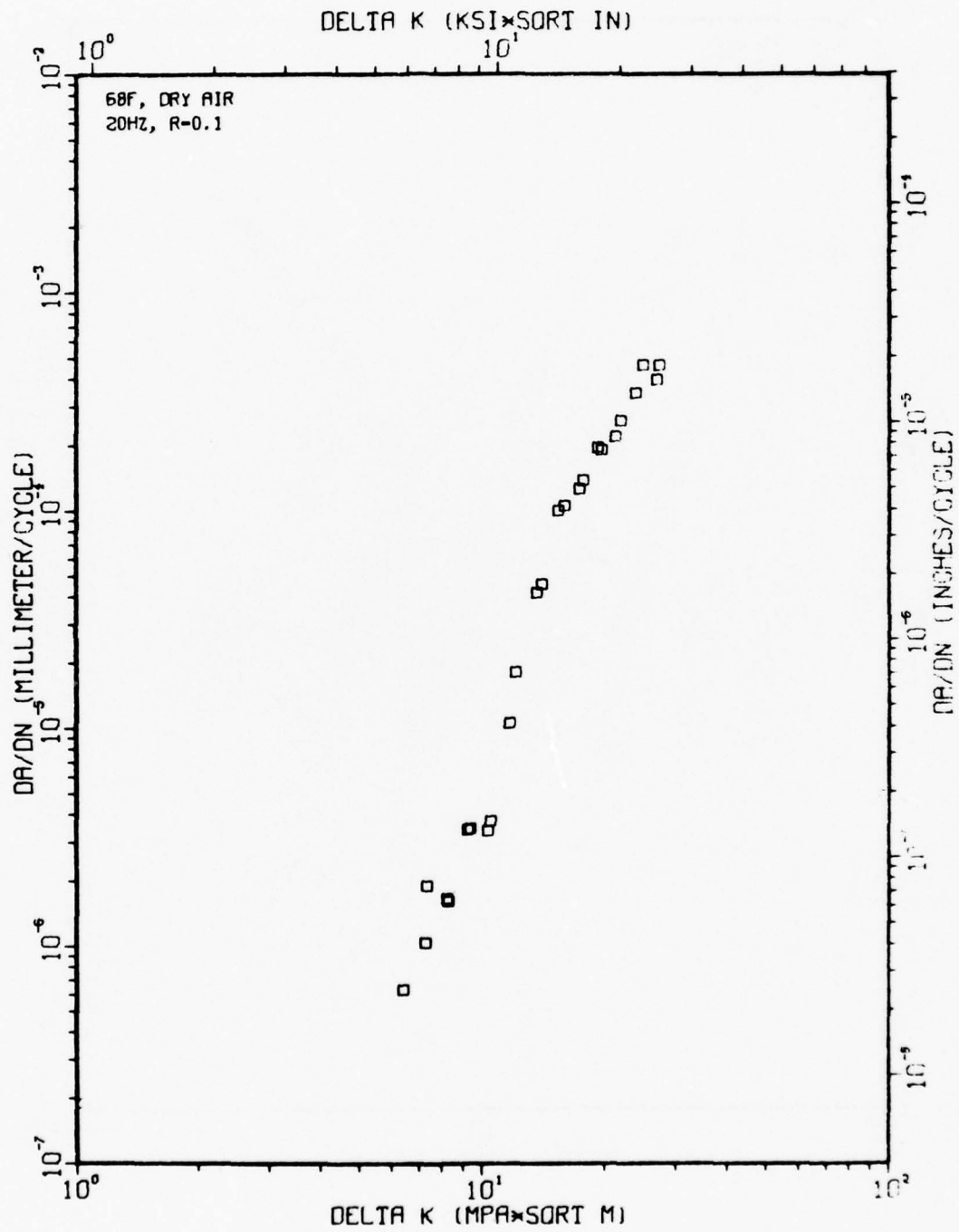
TI-6AL-4V   1-2-4
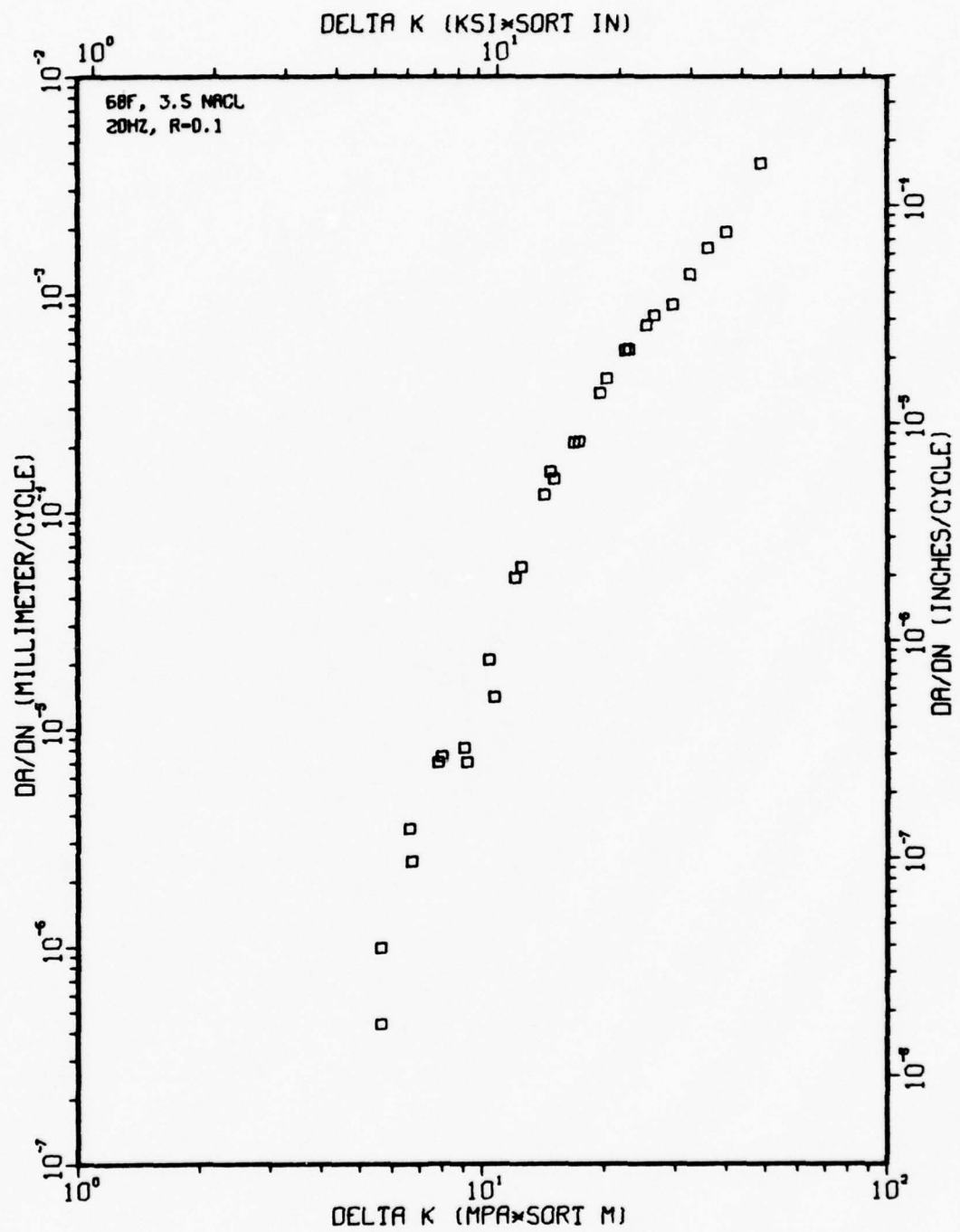
Figure A29
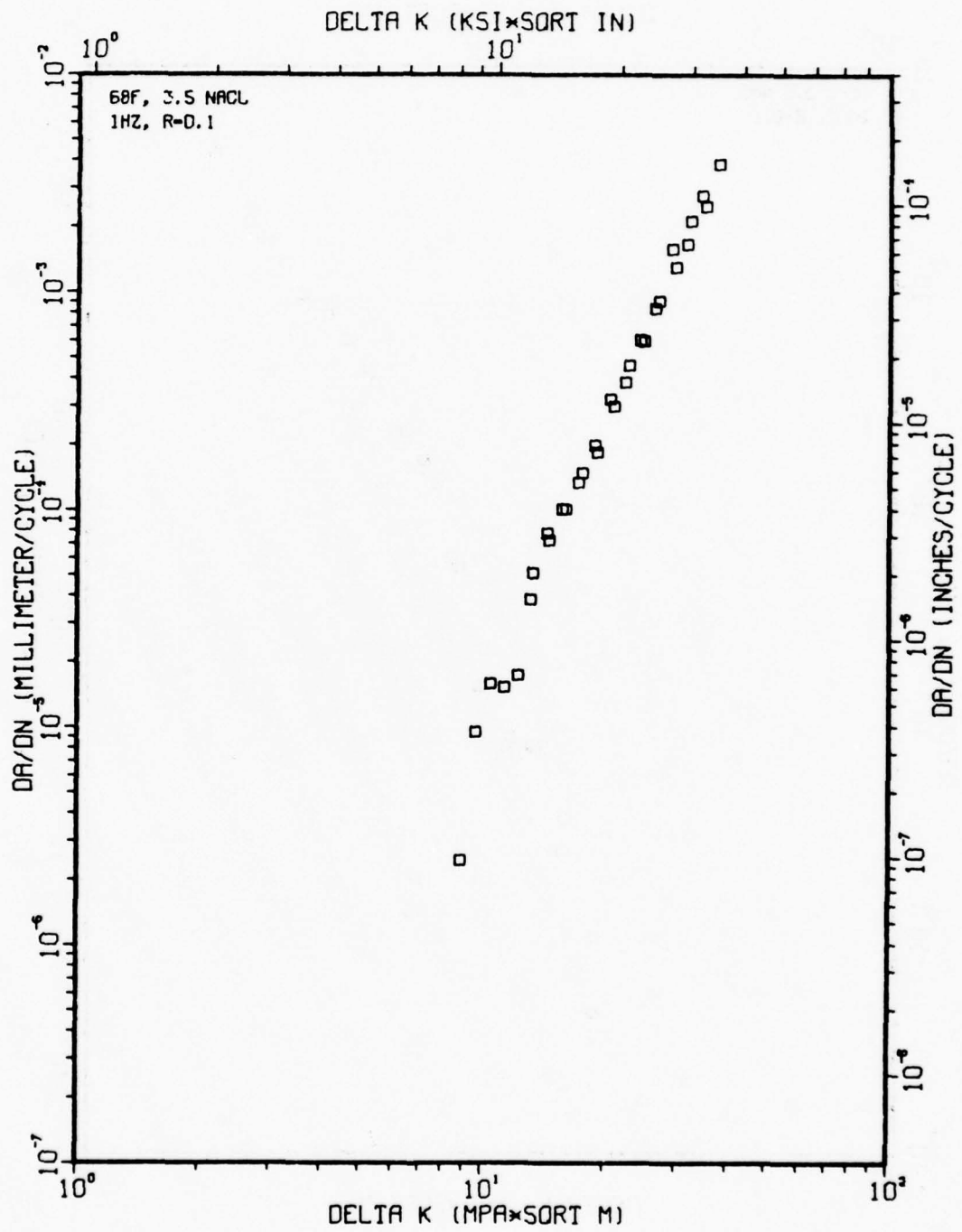
TI-6AL-4V 1-2-2

Figure A30

TI-6AL-4V 1-2-3

Figure A31

307
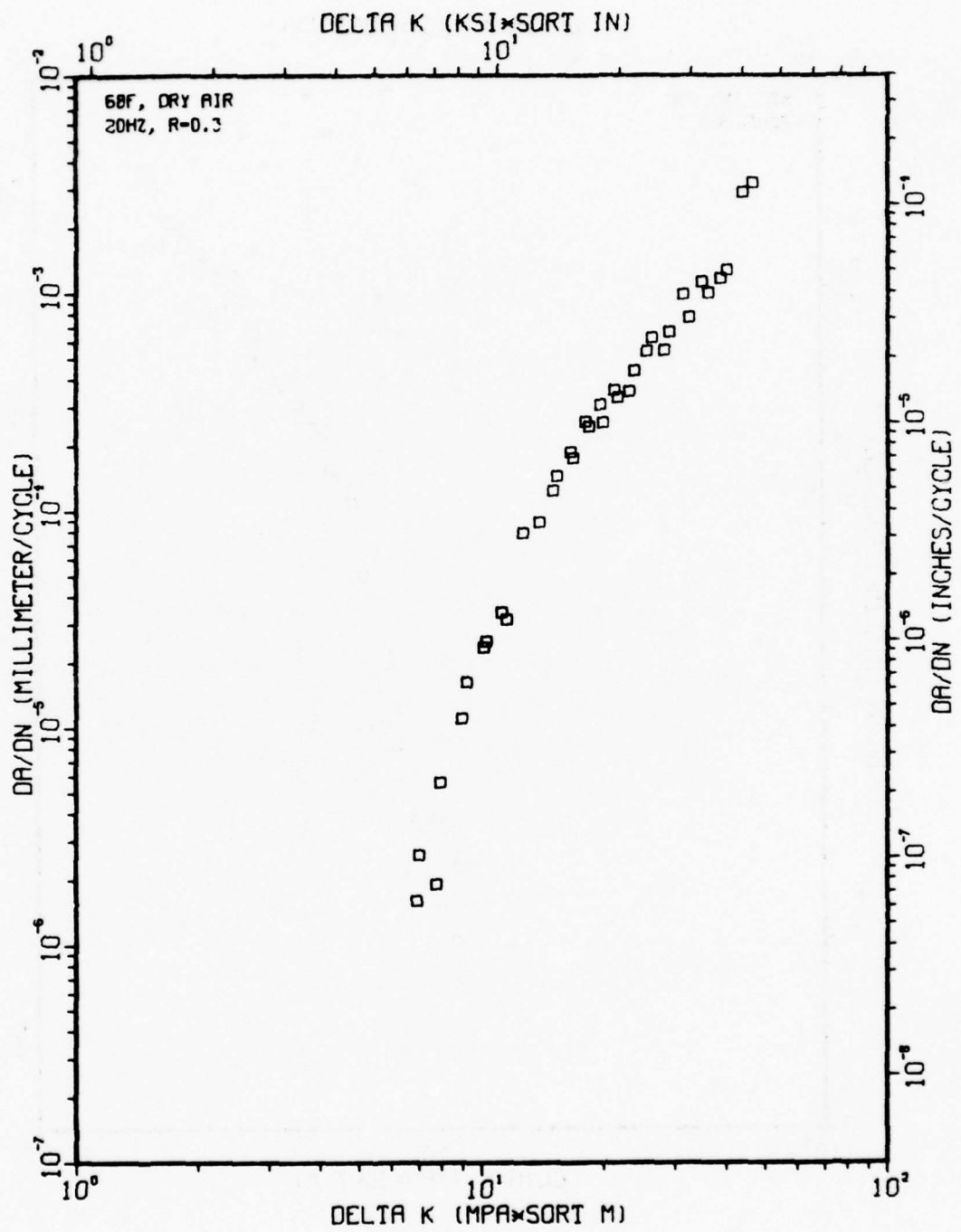
TI-6AL-4V 1-3-3

Figure A32

303
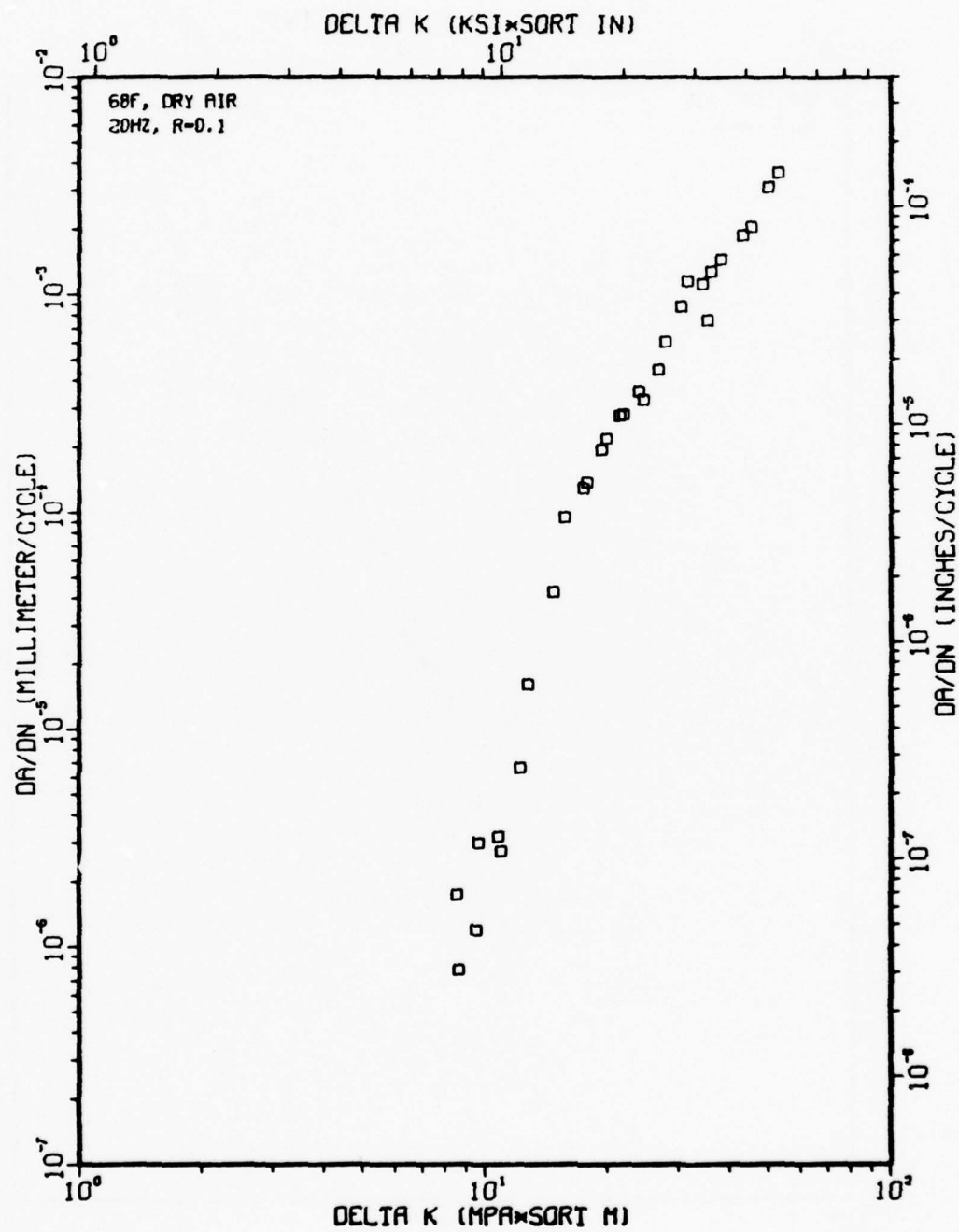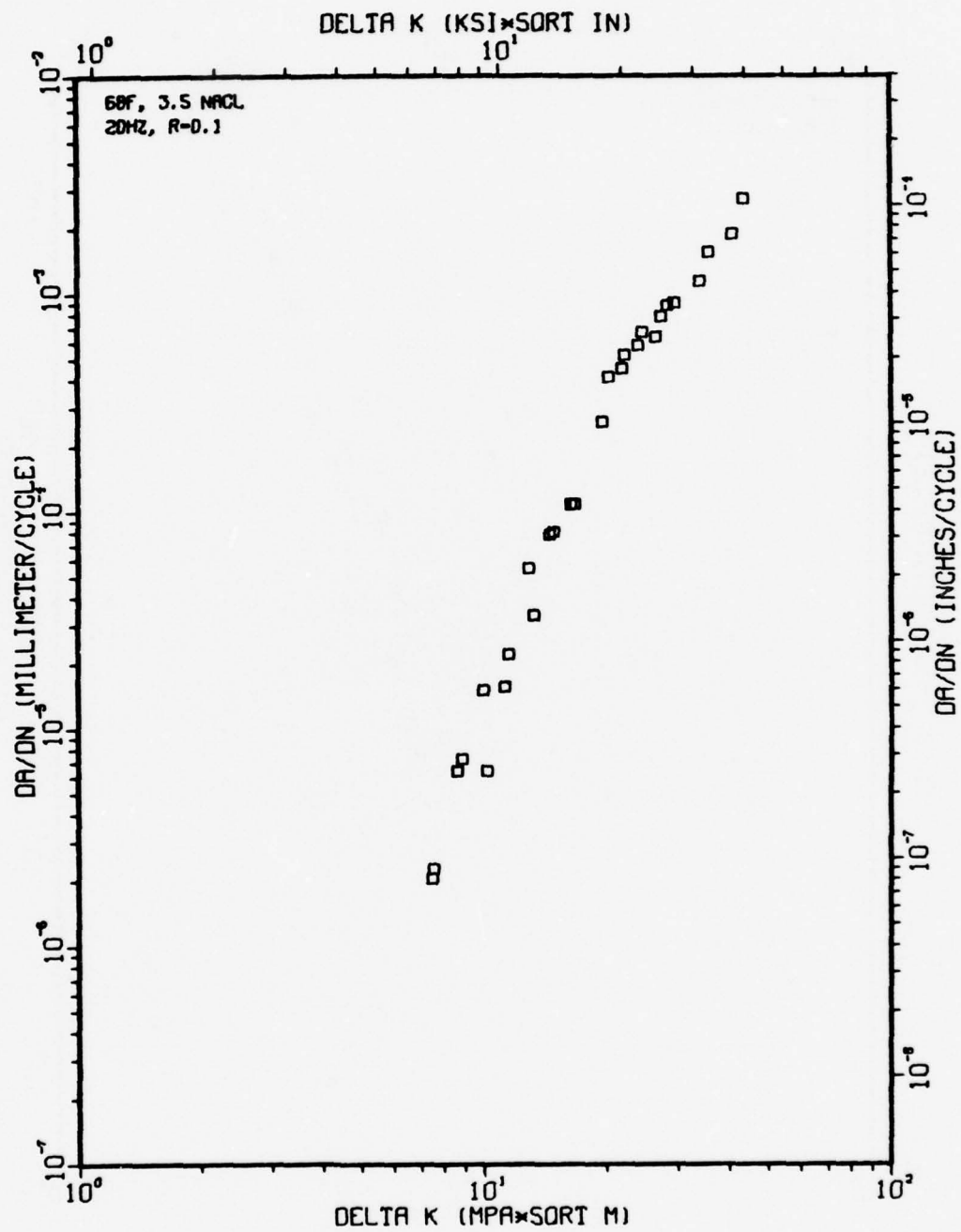
TI-6AL-4V   1-3-8

Figure A33

TI-6AL-4V 1-3-4
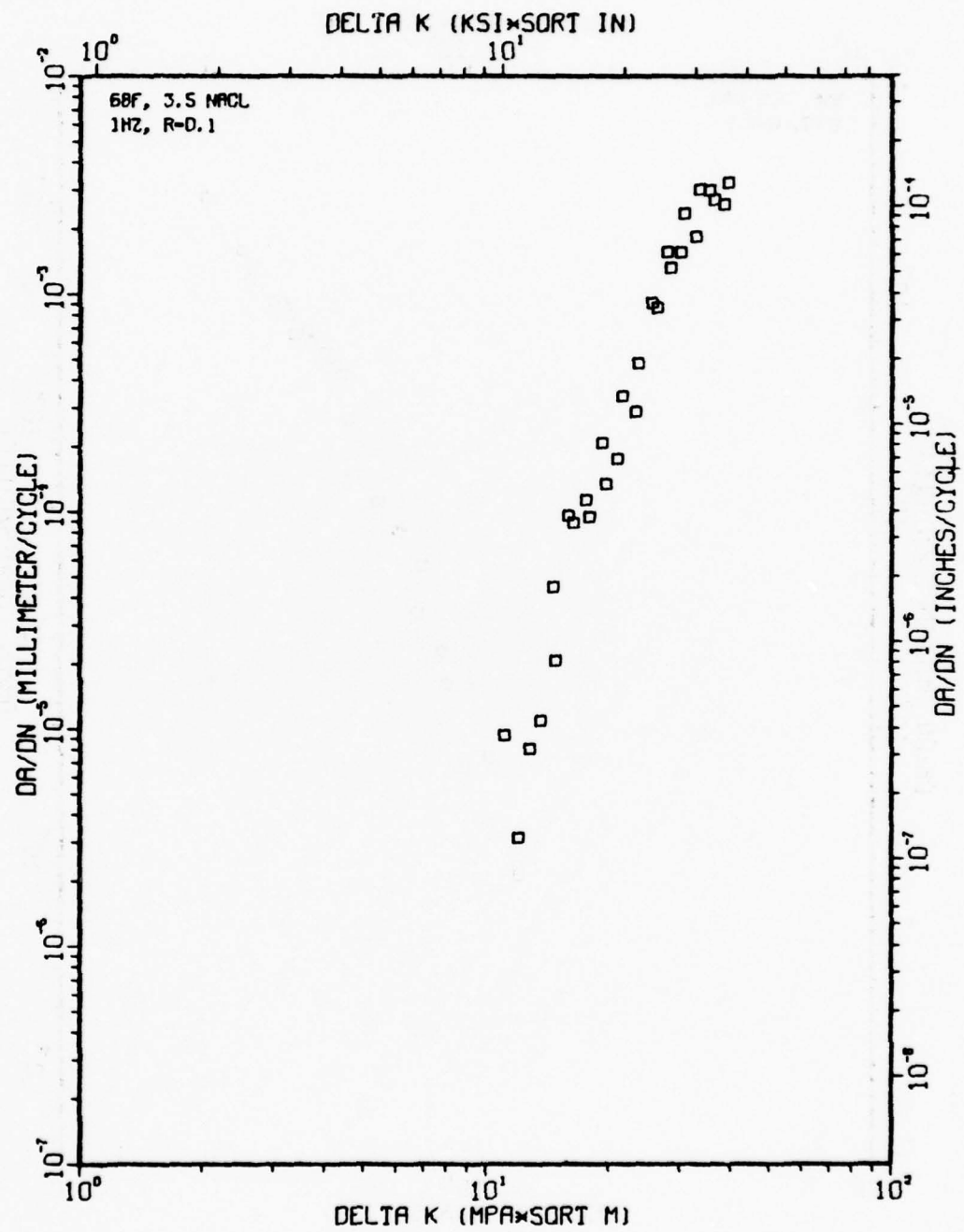
Figure A34

TI-6AL-4V   1-3-7

Figure A35

311
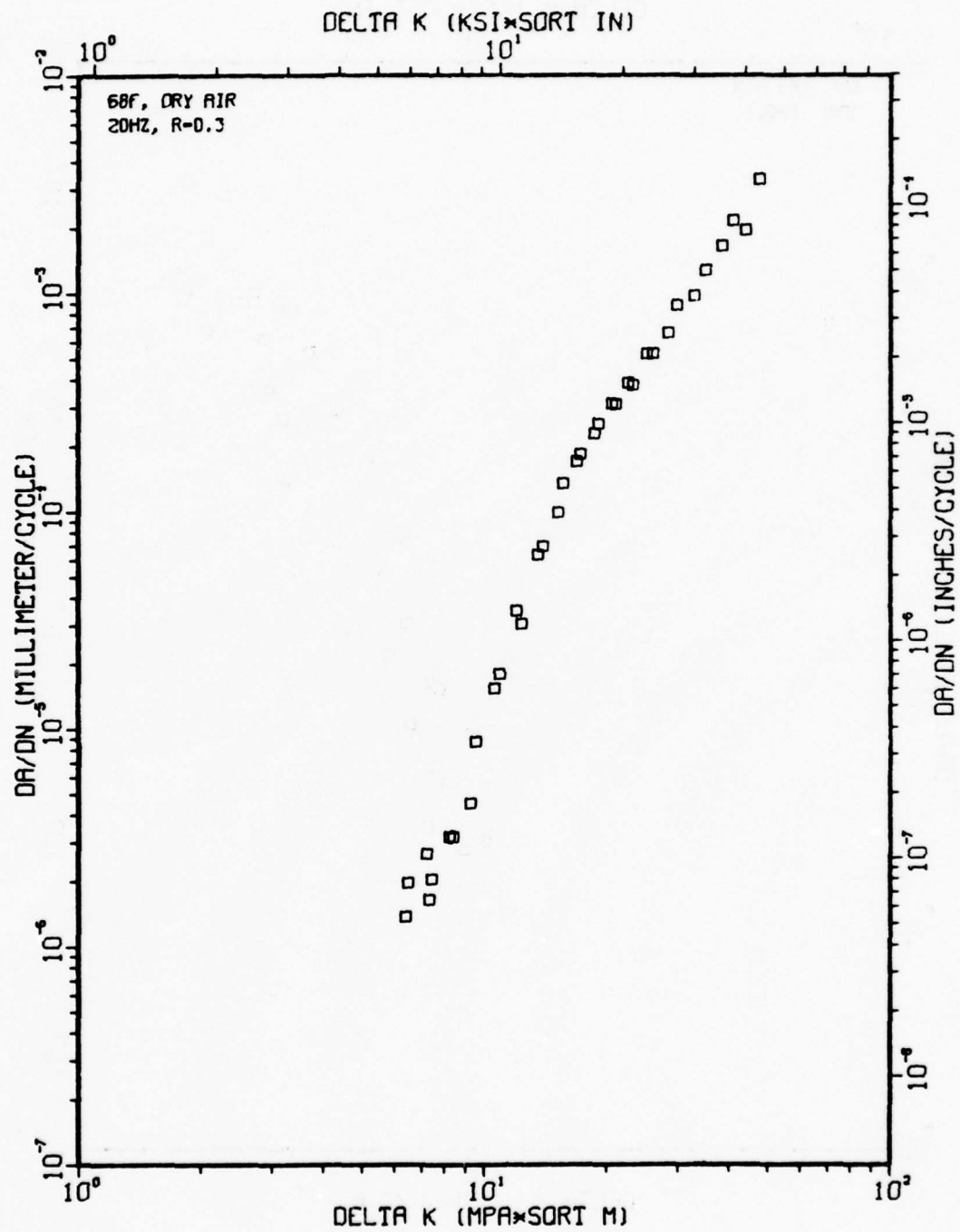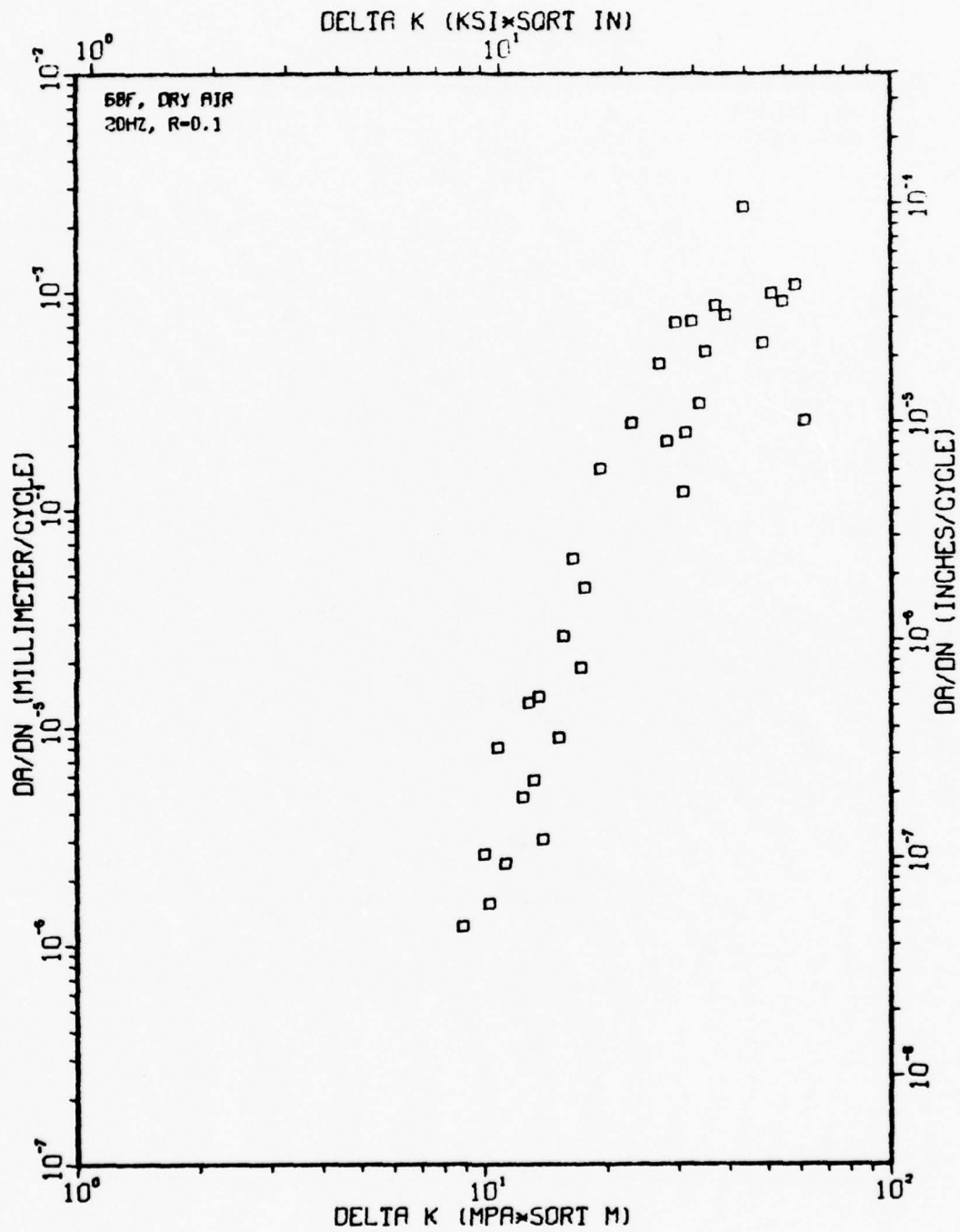
TI-6AL-4V 1-4-1

Figure A36

TI-6AL-4V 1-4-2

Figure A37
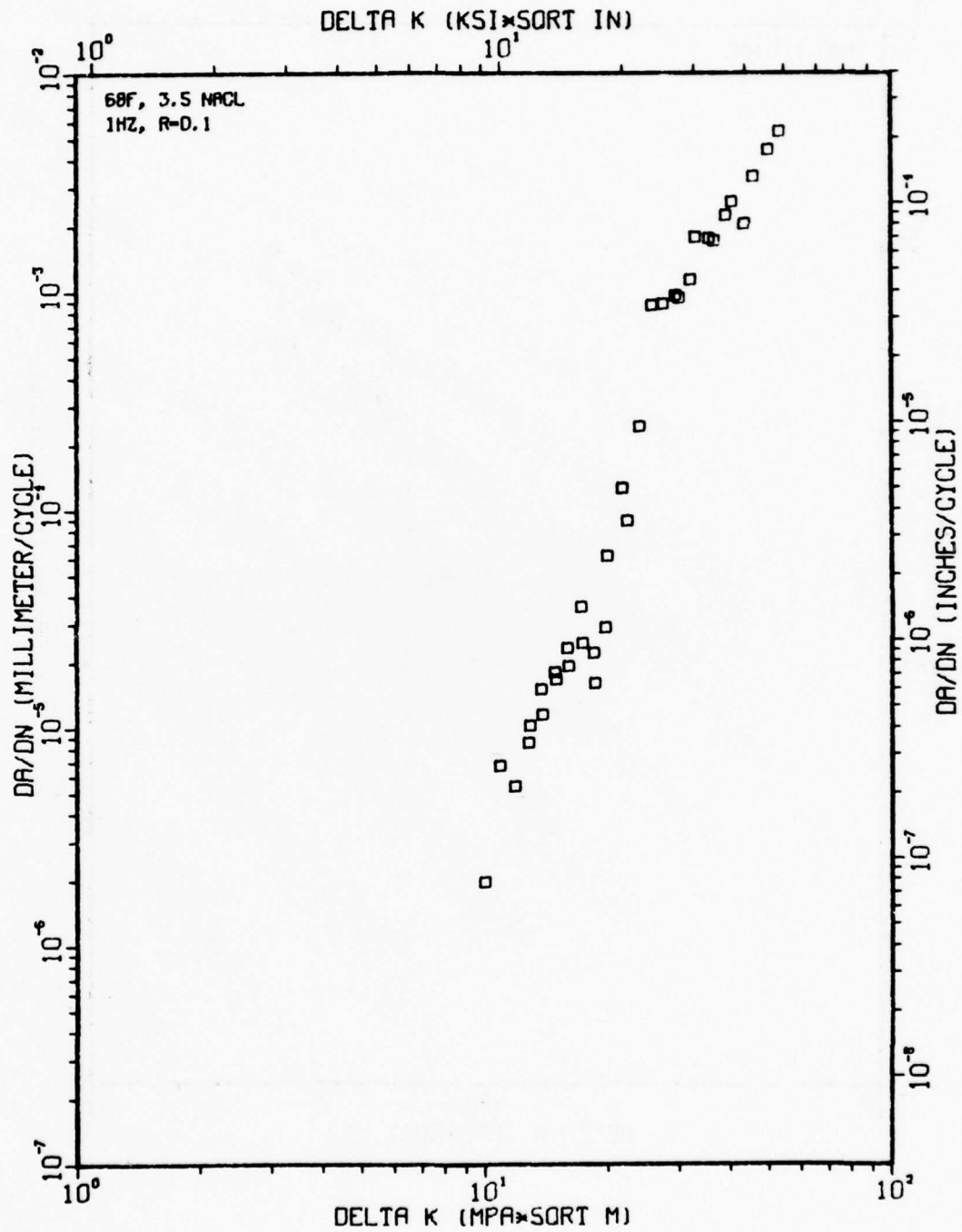
313

TI-6AL-4V   1-4-4

Figure A38

314

TI-6AL-4V (COND. 4), 68F, DRY AIR, R-0.3

Figure A39

TI-6AL-4V 1-4-5

Figure A40

TI-6AL-4V 1-4-6

Figure A41

317

TI-6AL-4V 1-4-9

DELTA K (KSI*SQRT IN)

68F, DRY AIR
20HZ, R=0.5

DA/DN (MILLIMETER/CYCLE)

DA/DN (INCHES/CYCLE)

DELTA K (MPA*SQRT M)

Figure A42

318
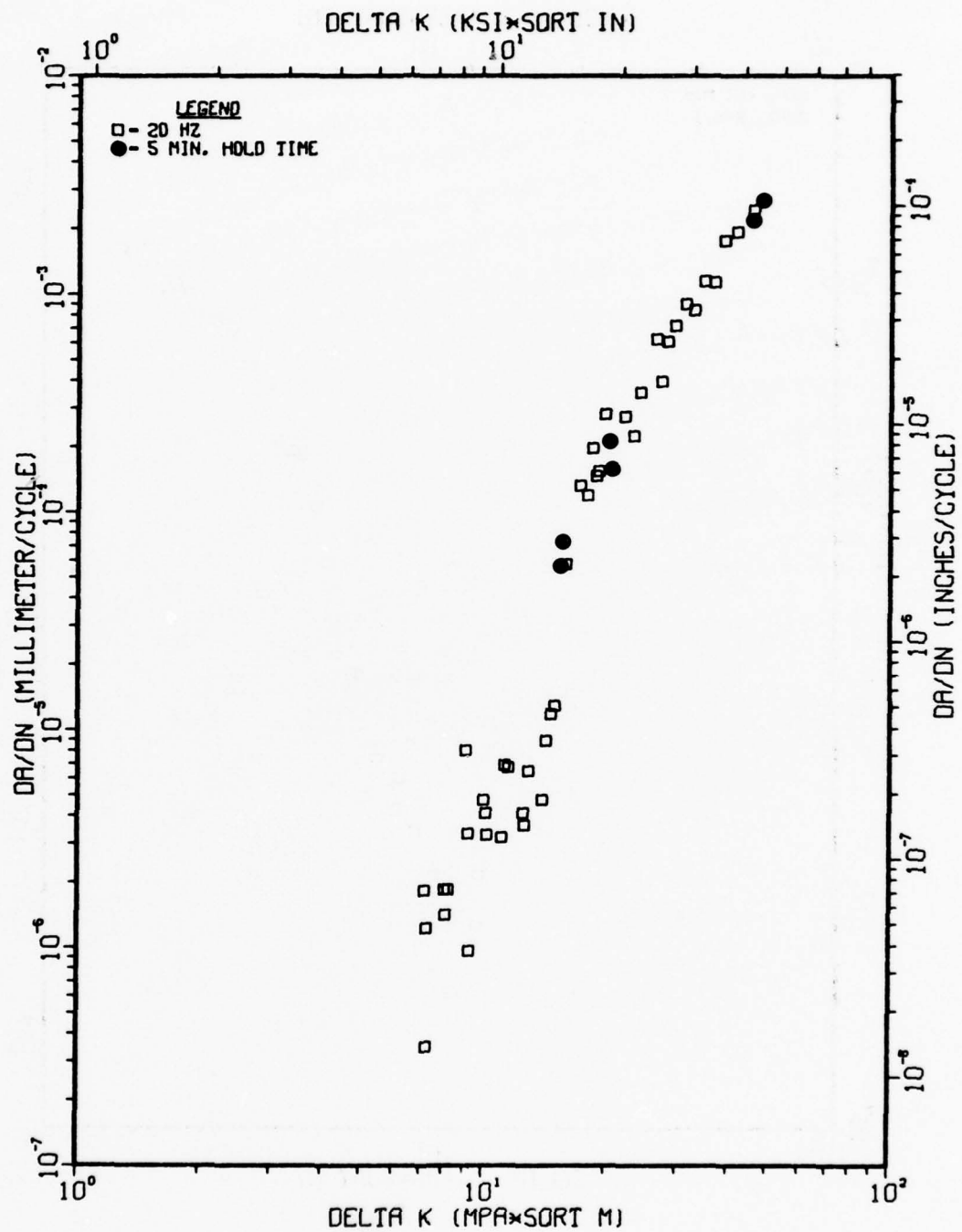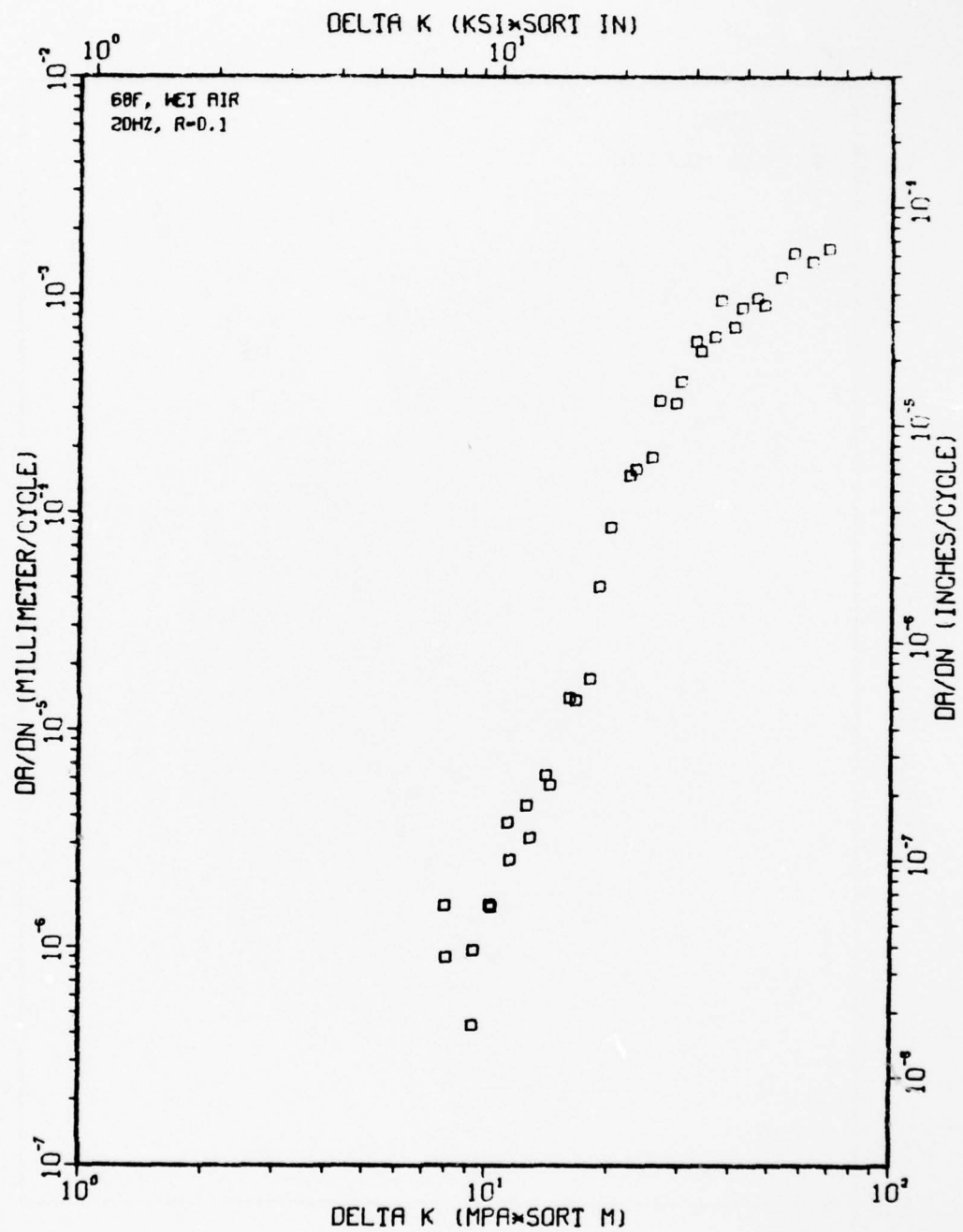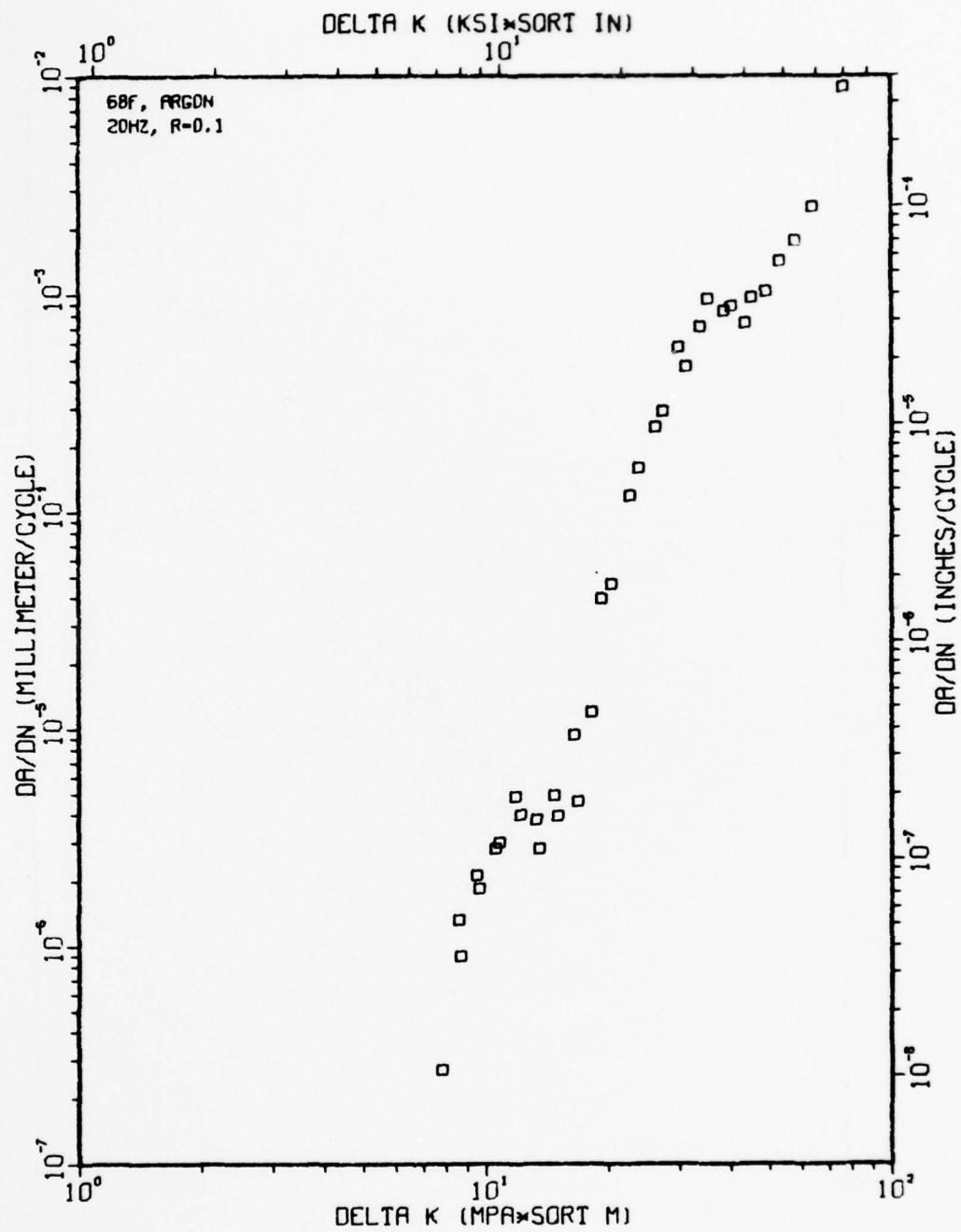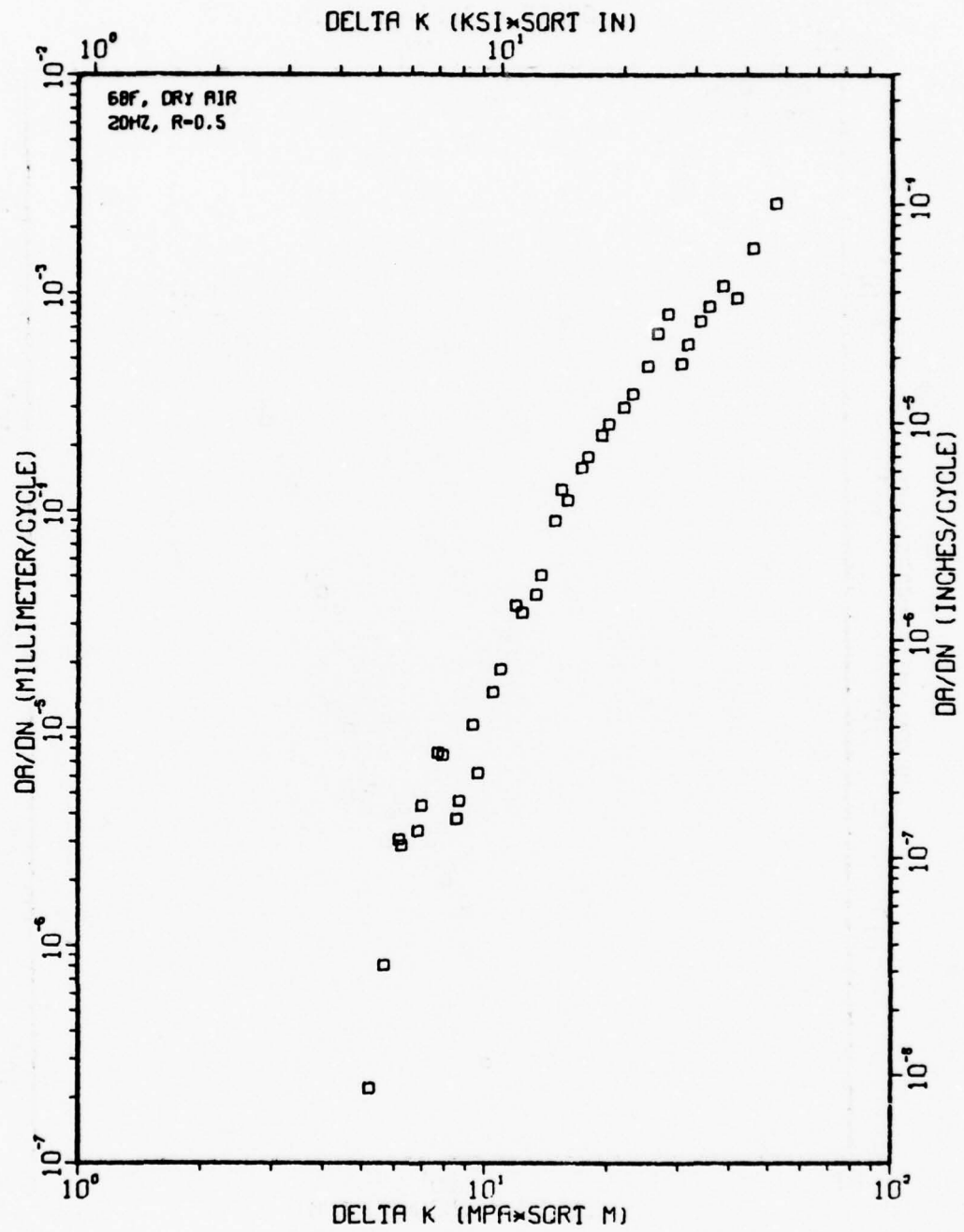
TI-6AL-4V 1-4-21

Figure A43

319
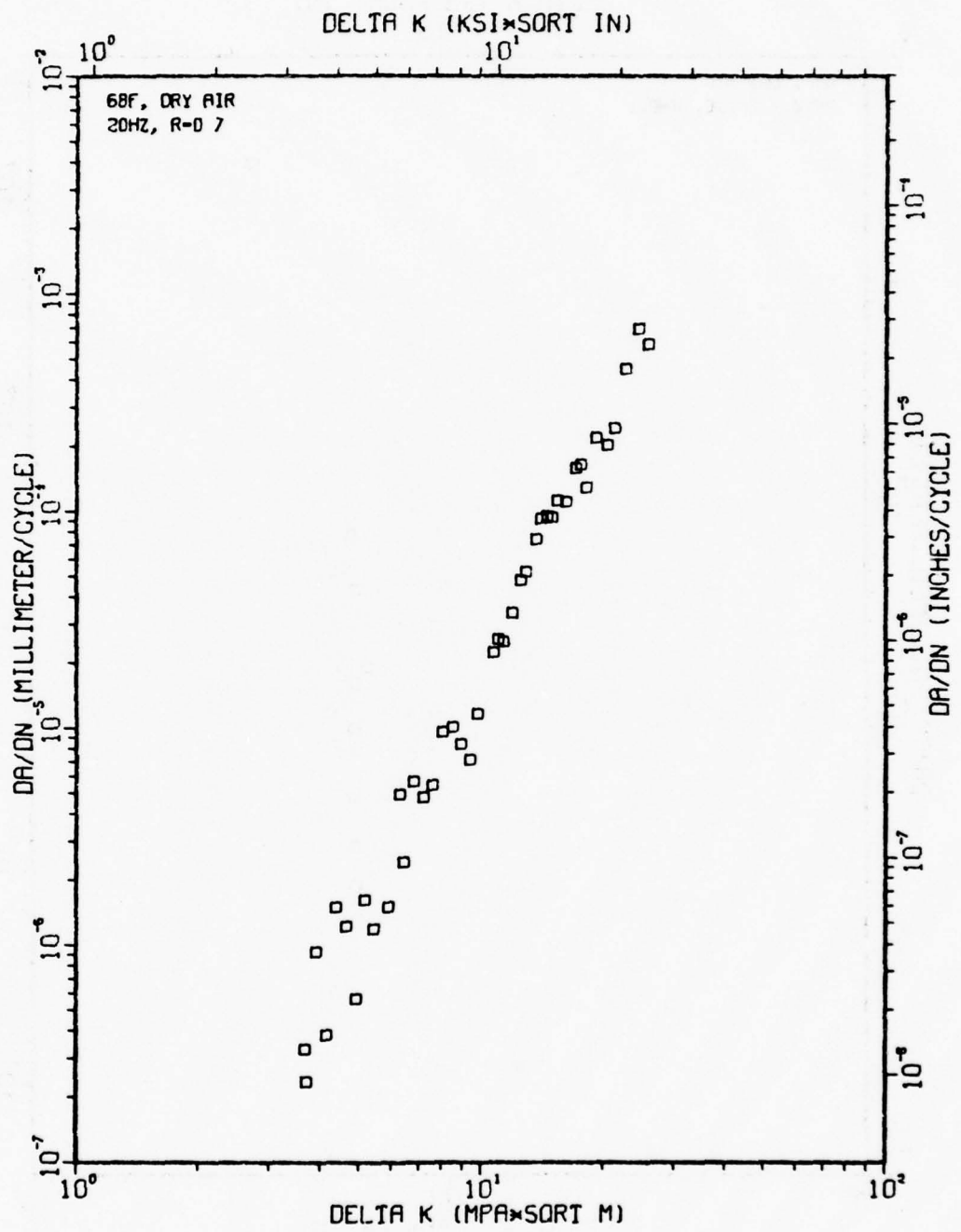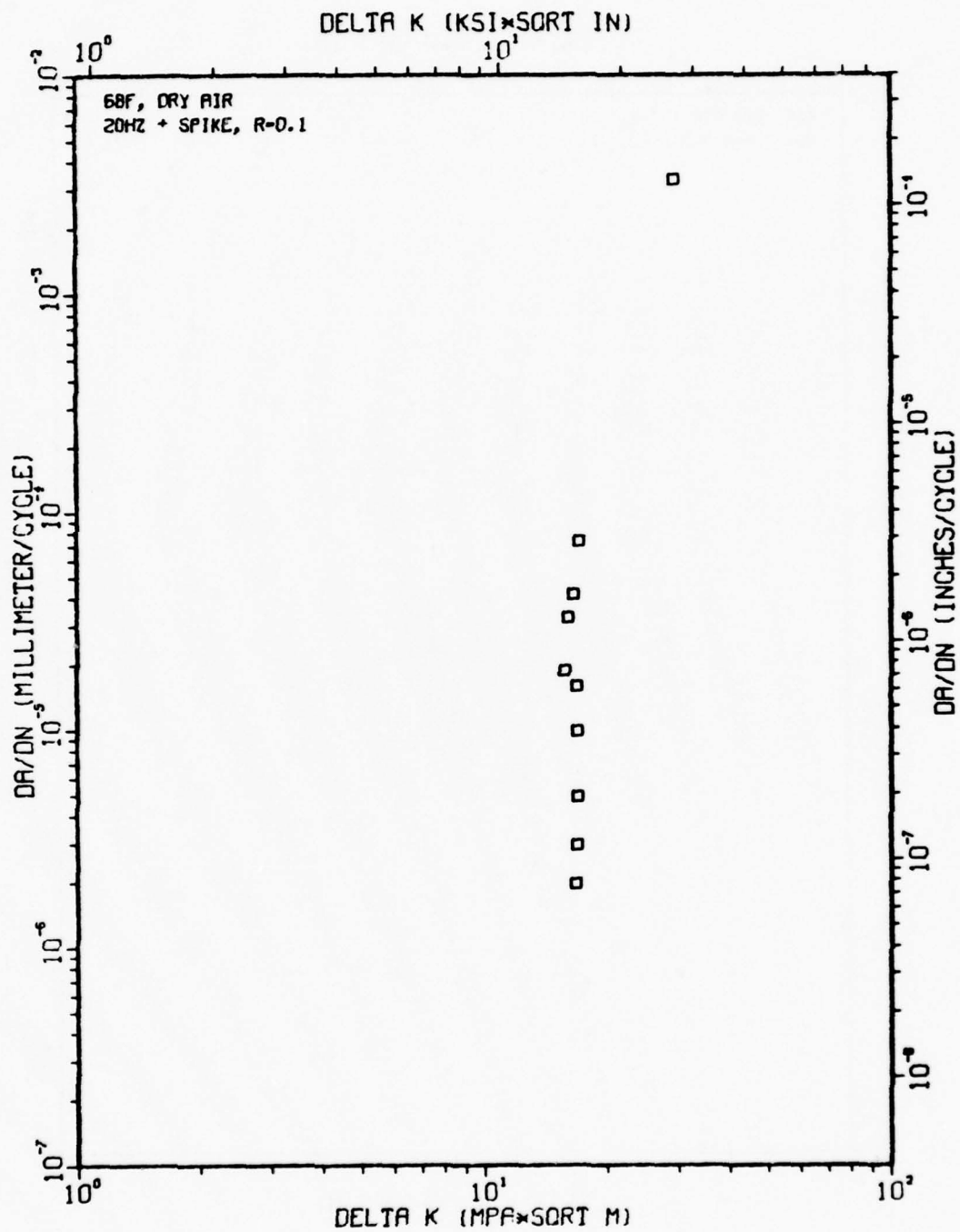
TI-6AL-4V   1-4-7

Figure A44

TI-6AL-4V 1-S-2
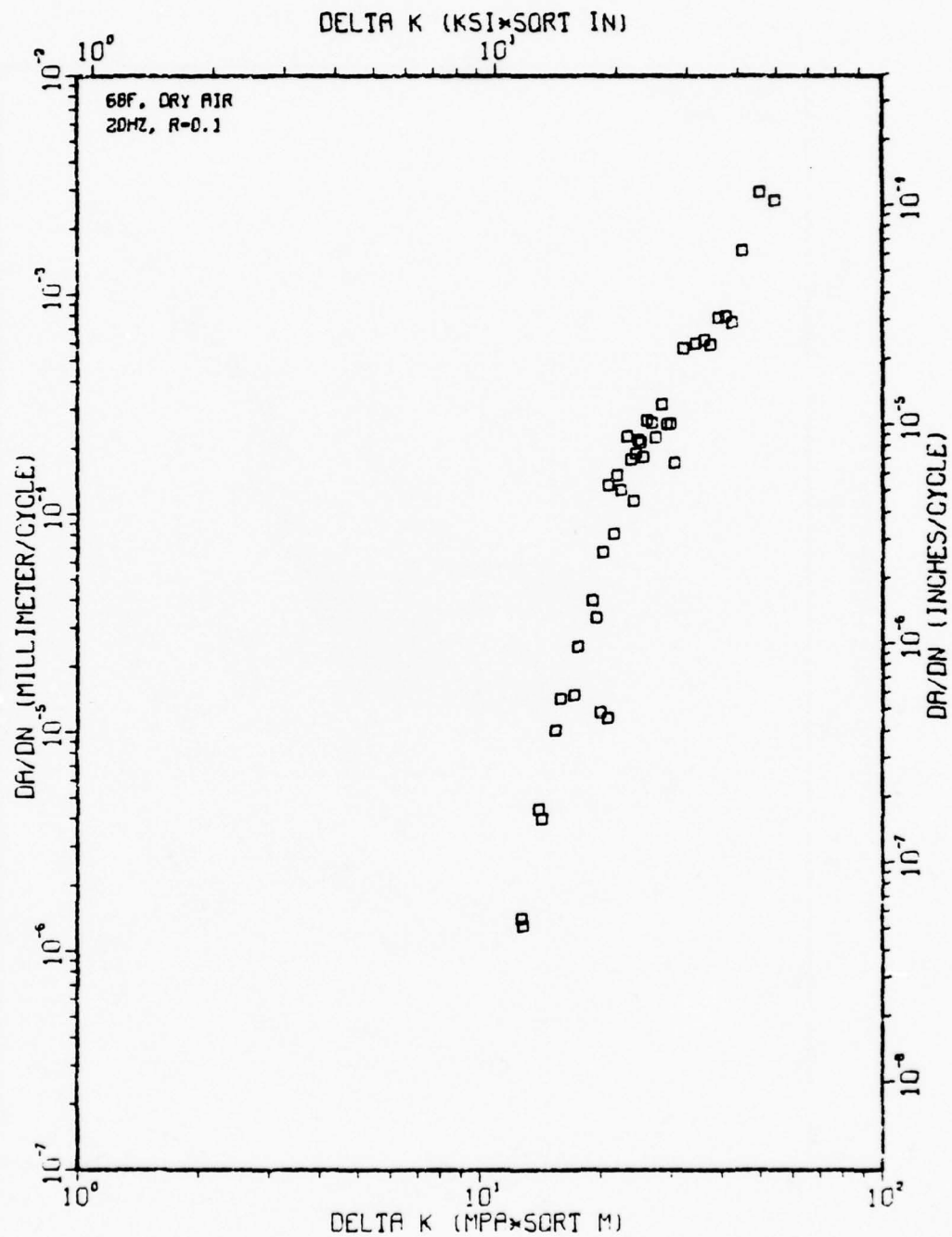
Figure A45

TI-6AL-4V 1-5-5
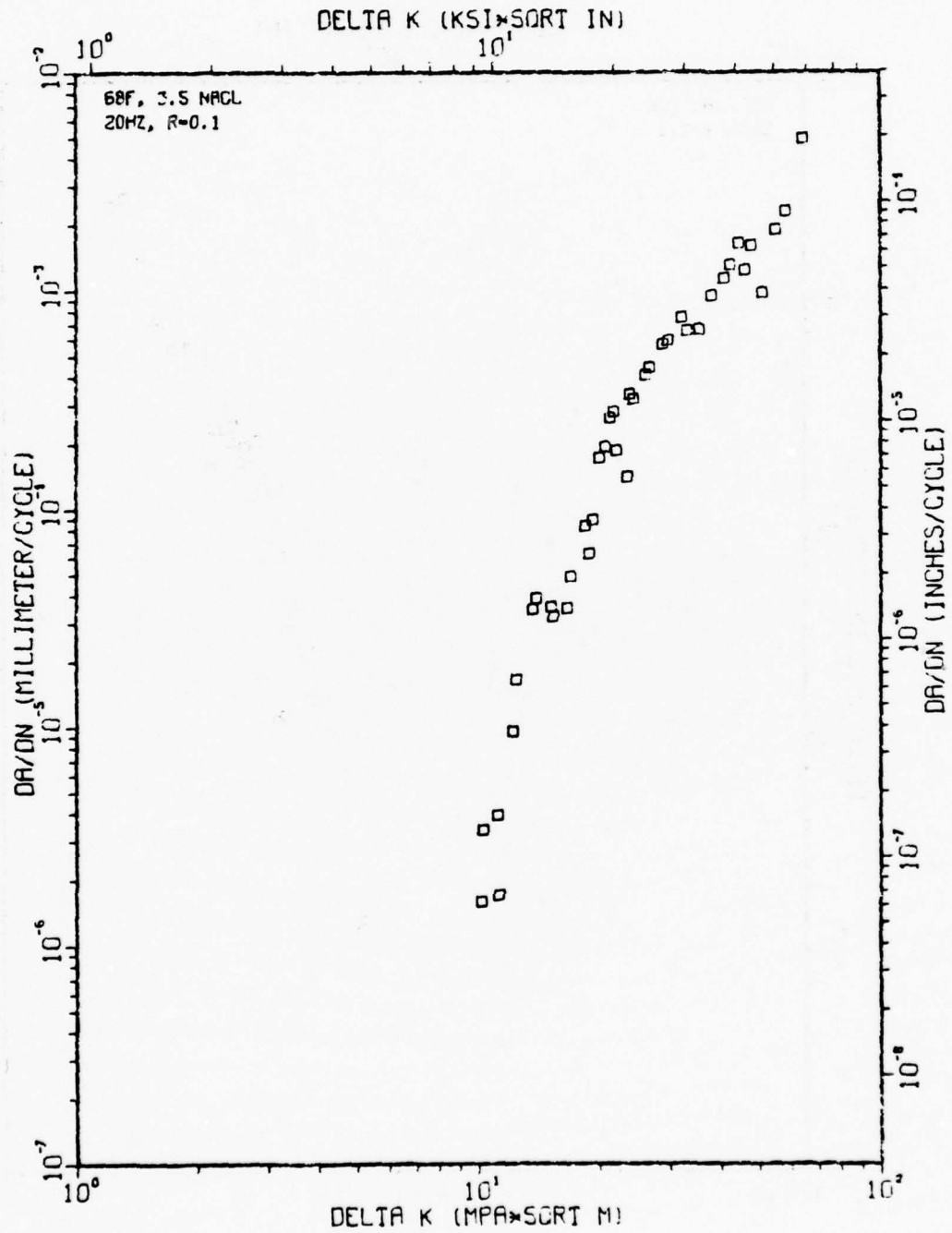
Figure A46

TI-6AL-4V   1-S-3
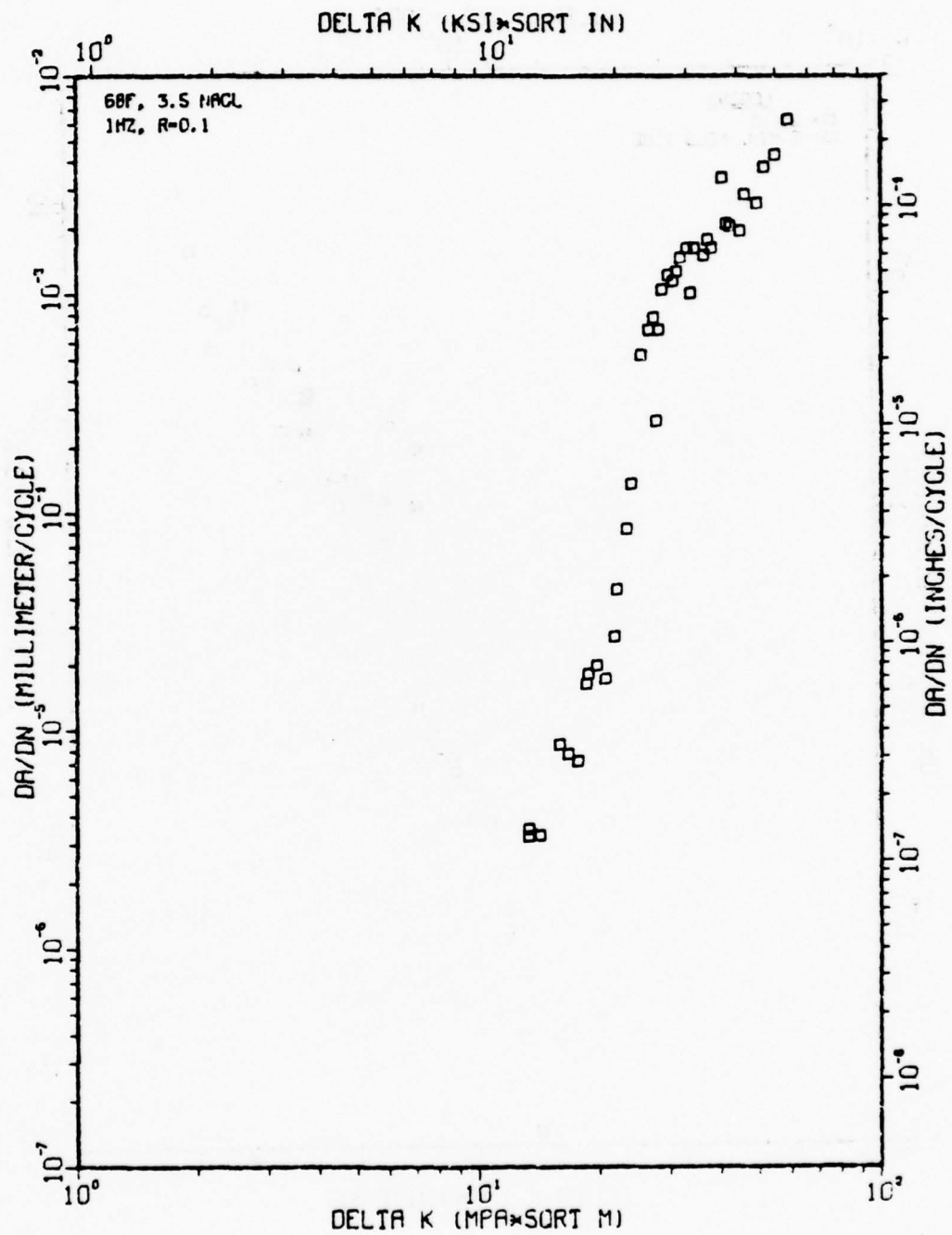
Figure A47

TI-6AL-4V (COND. 5), 68F, DRY AIR, R-0.3

Figure A48

TI-6AL-4V 1-5-6

DELTA K (KSI*SORT IN)
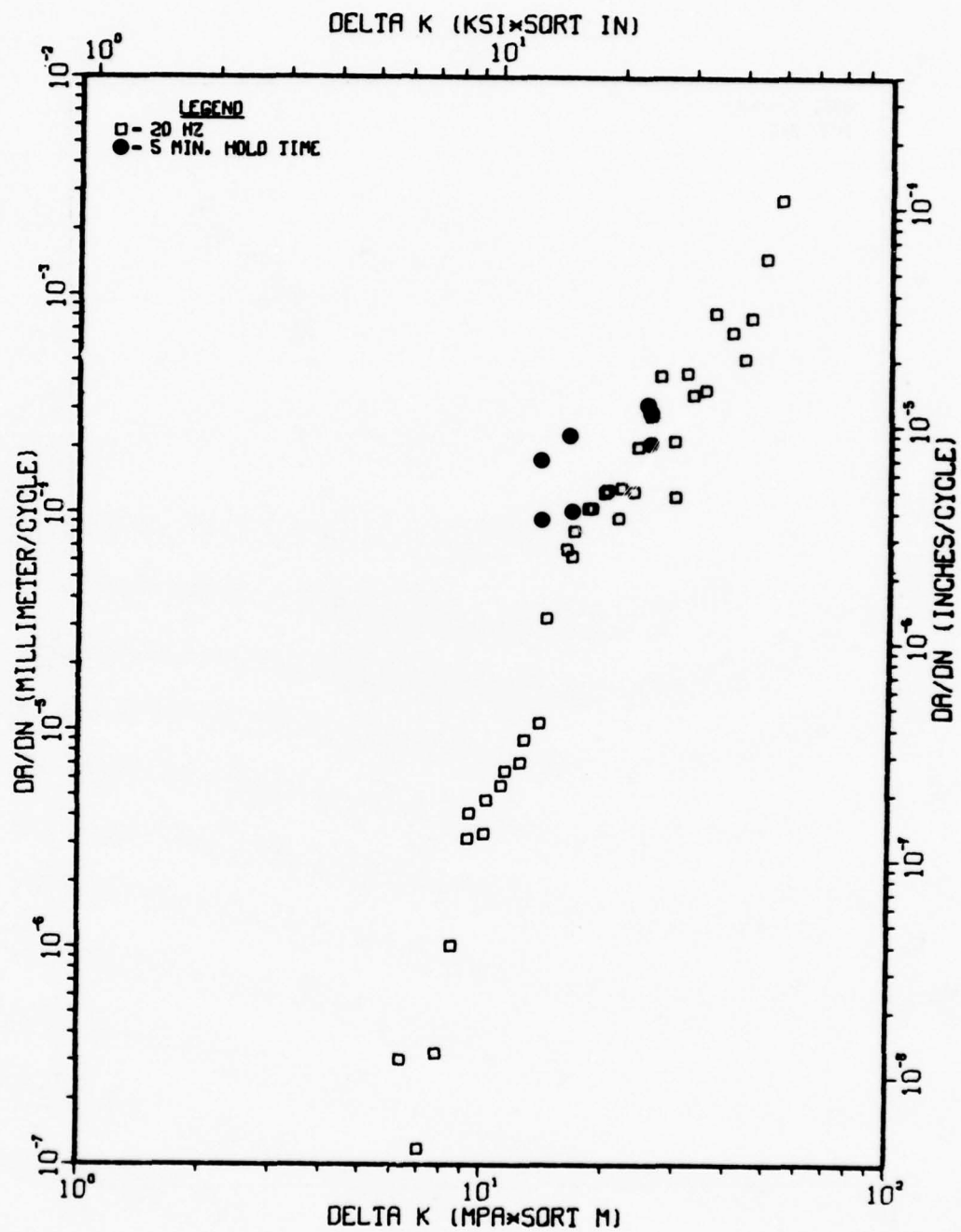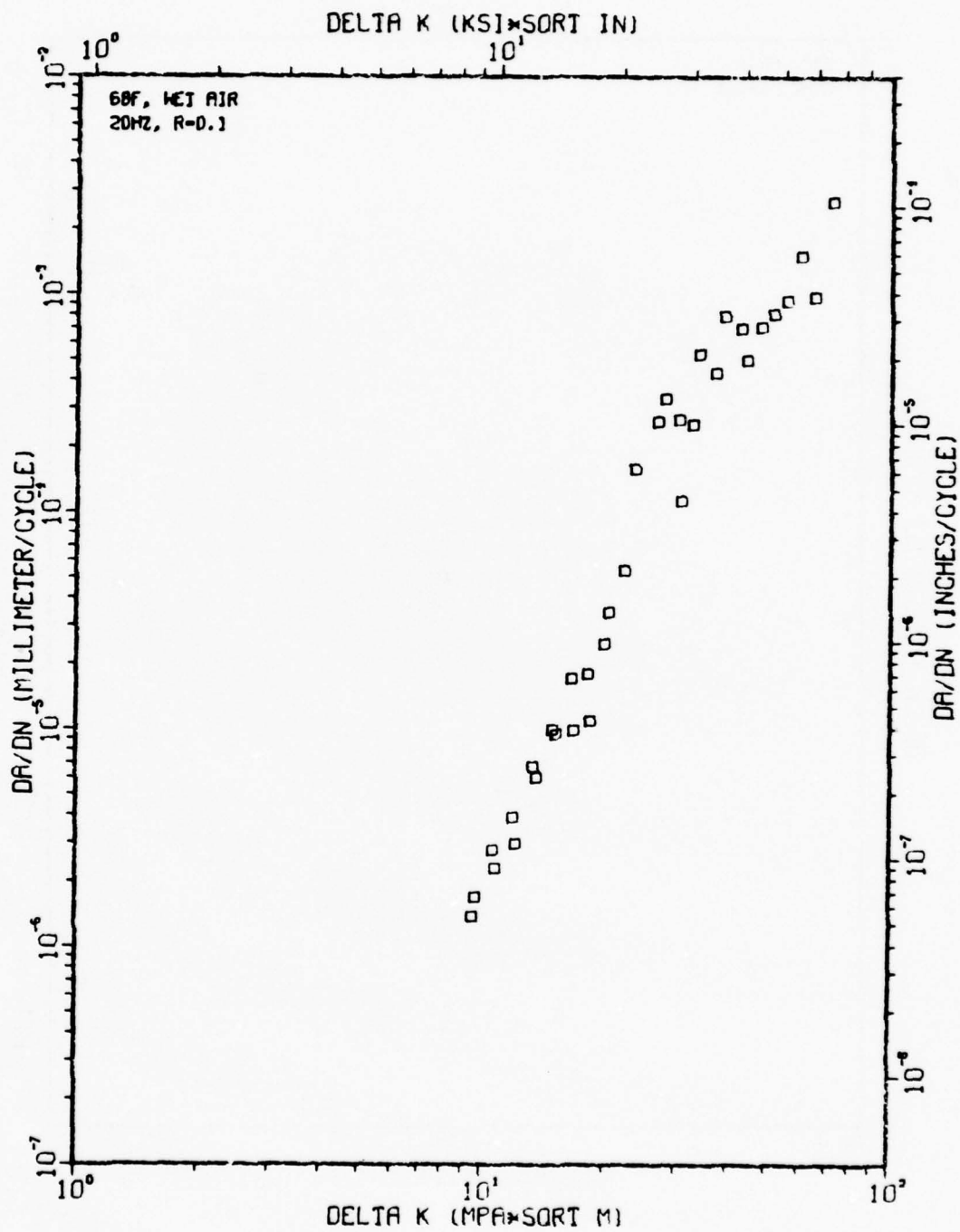
Figure A49
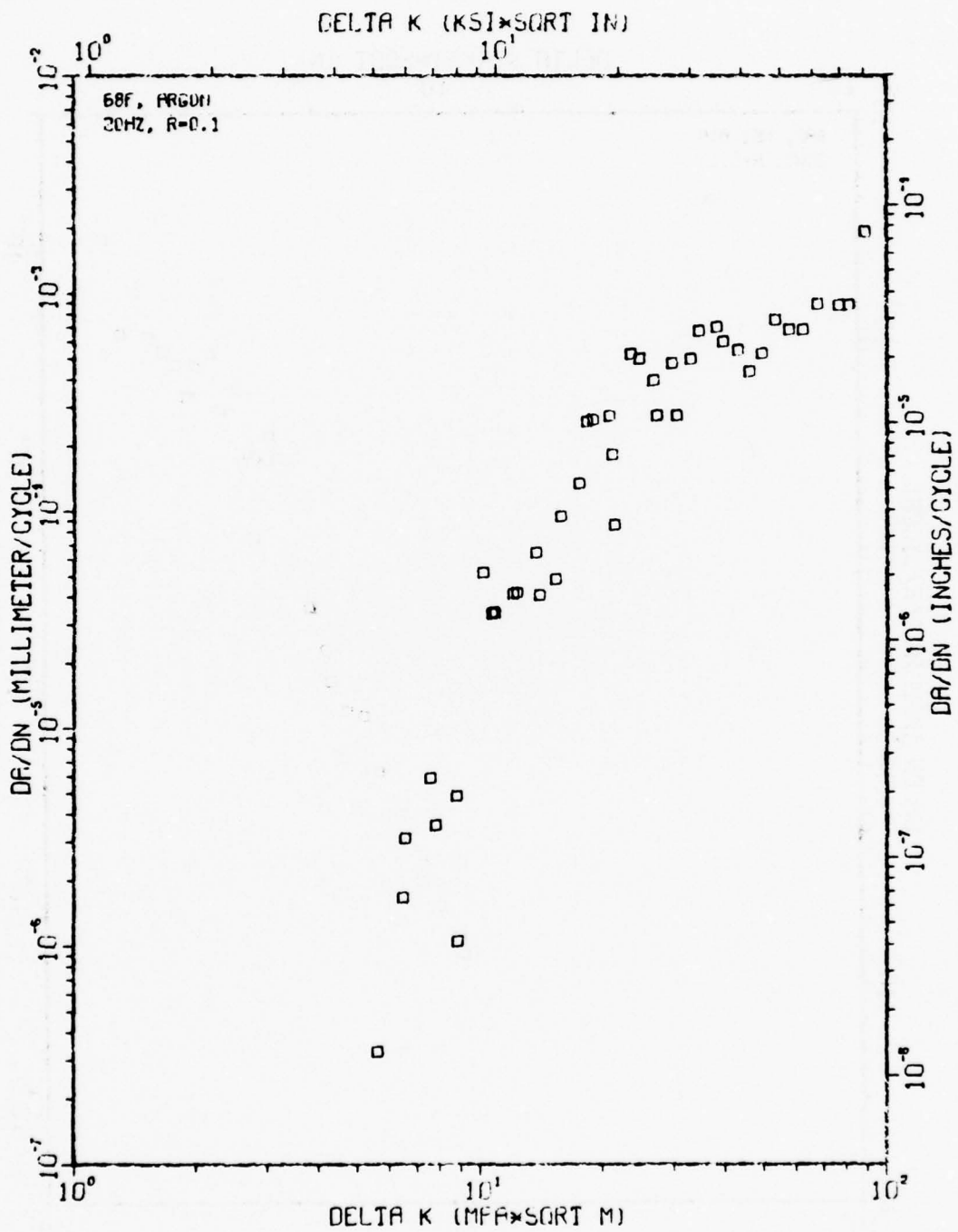
TI-6AL-4V   1-5-9

Figure A50

TI-6AL-4V   1-5-8
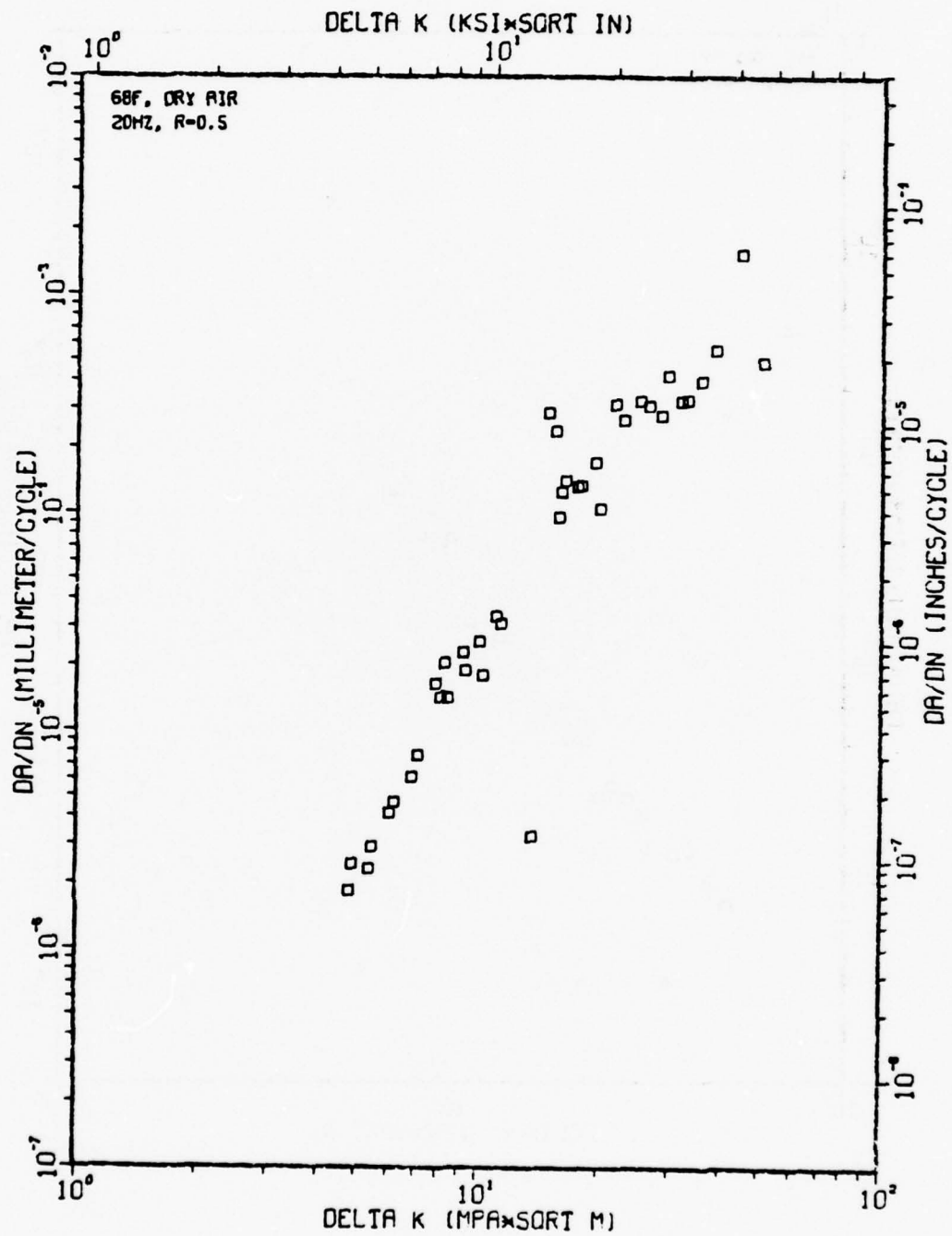
Figure   A51

TI-6AL-4V   1-5-10

Figure A52

328
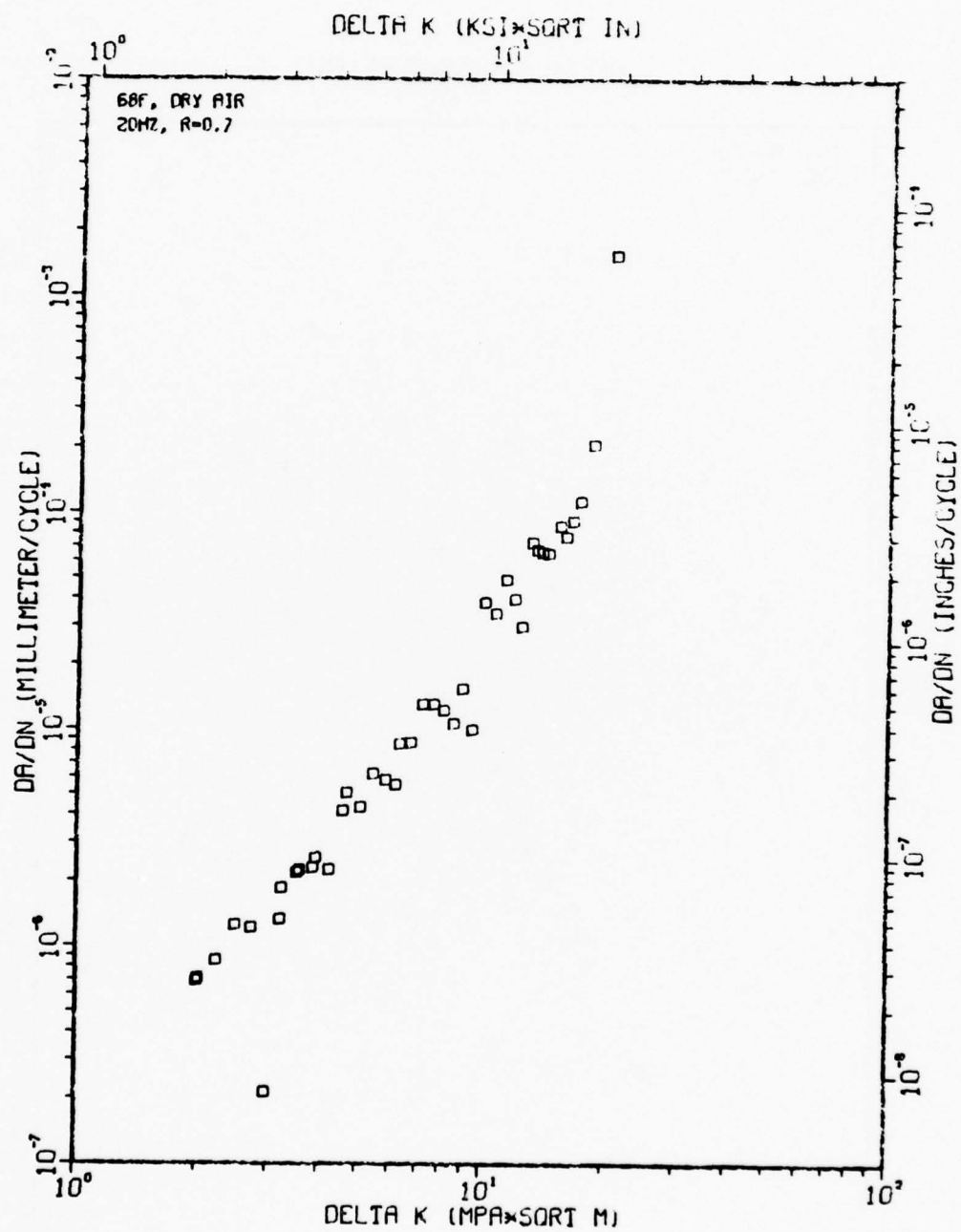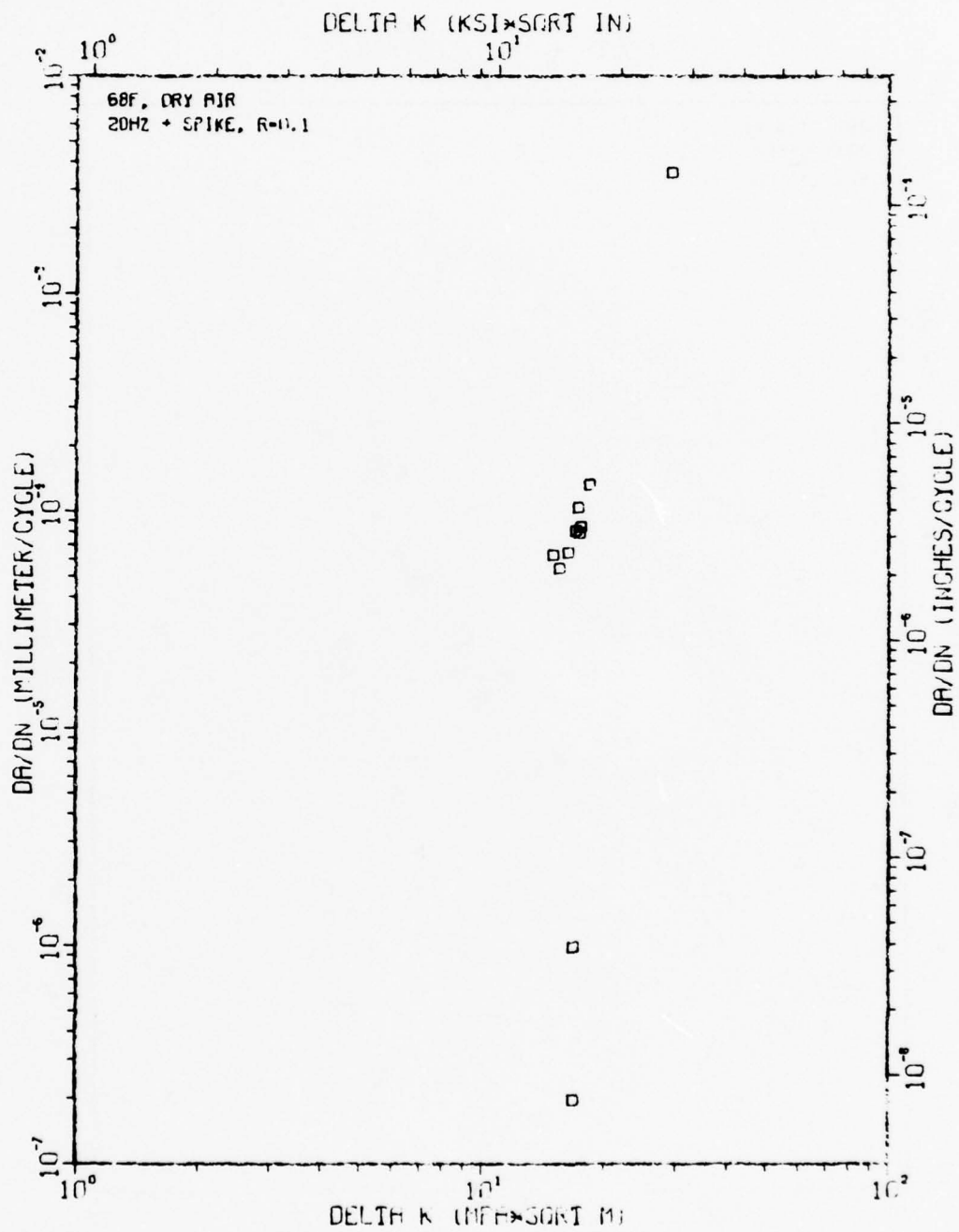
Figure A53

TI-6AL-4V 1-5-31 STD. OX.
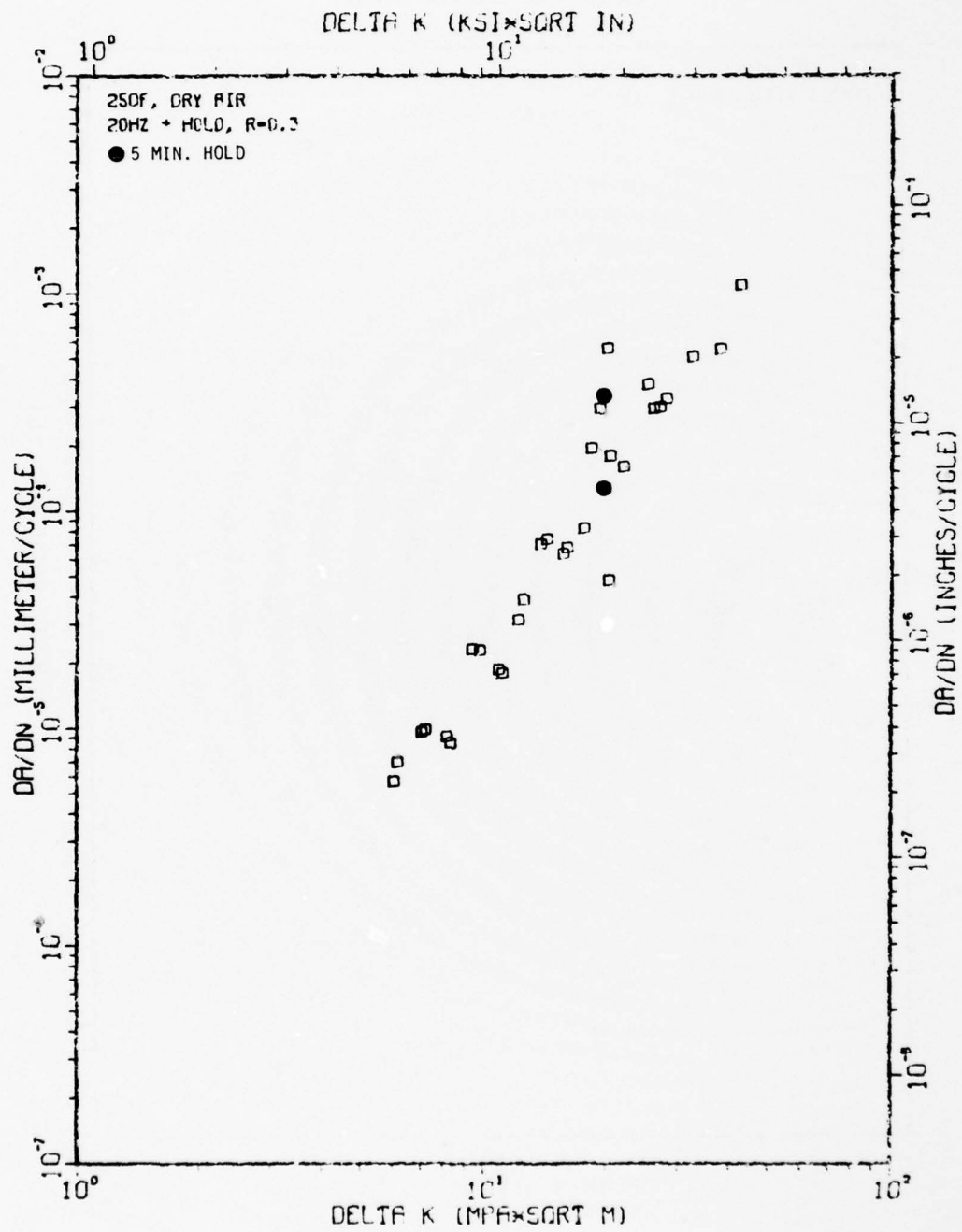
Figure A54

TI-6AL-4V 1-5-32 STD. OX.
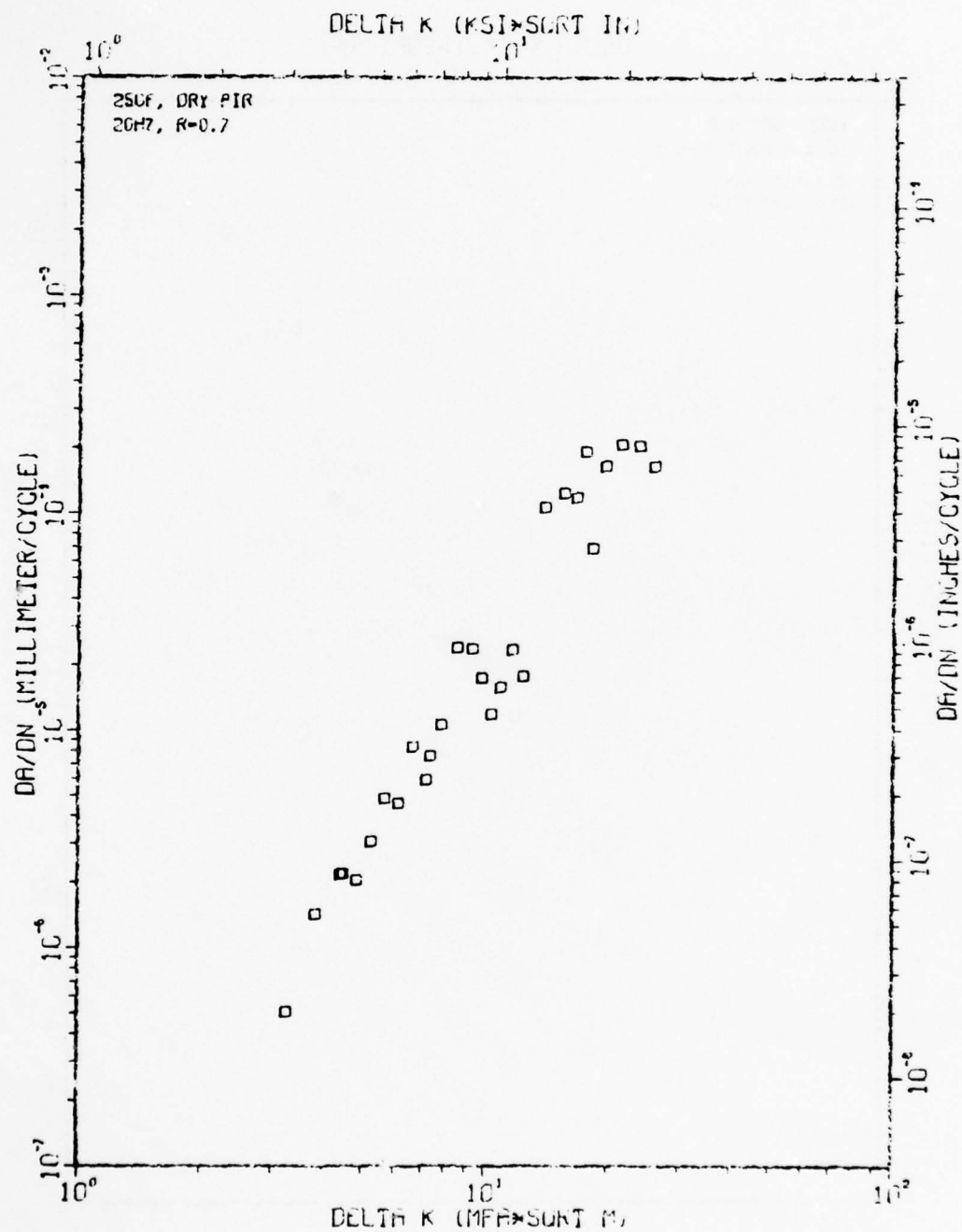
Figure A55

TI-6AL-4V 1-5-33 STD. OX.
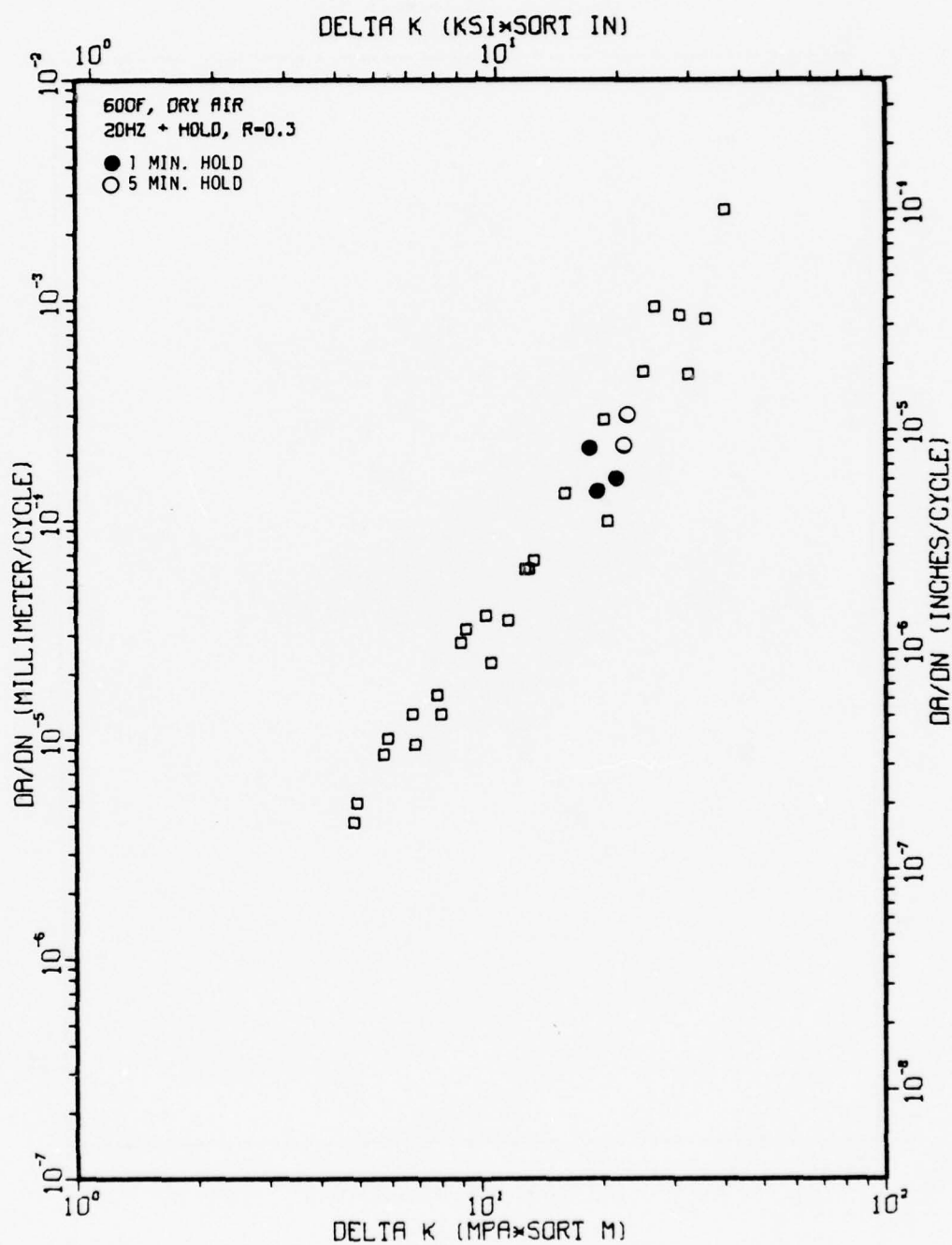
Figure A56

TI-6AL-4V   1-5-38

Figure A57

333

TI-6AL-4V   1-5-48   LO. OX.

Figure A58

334
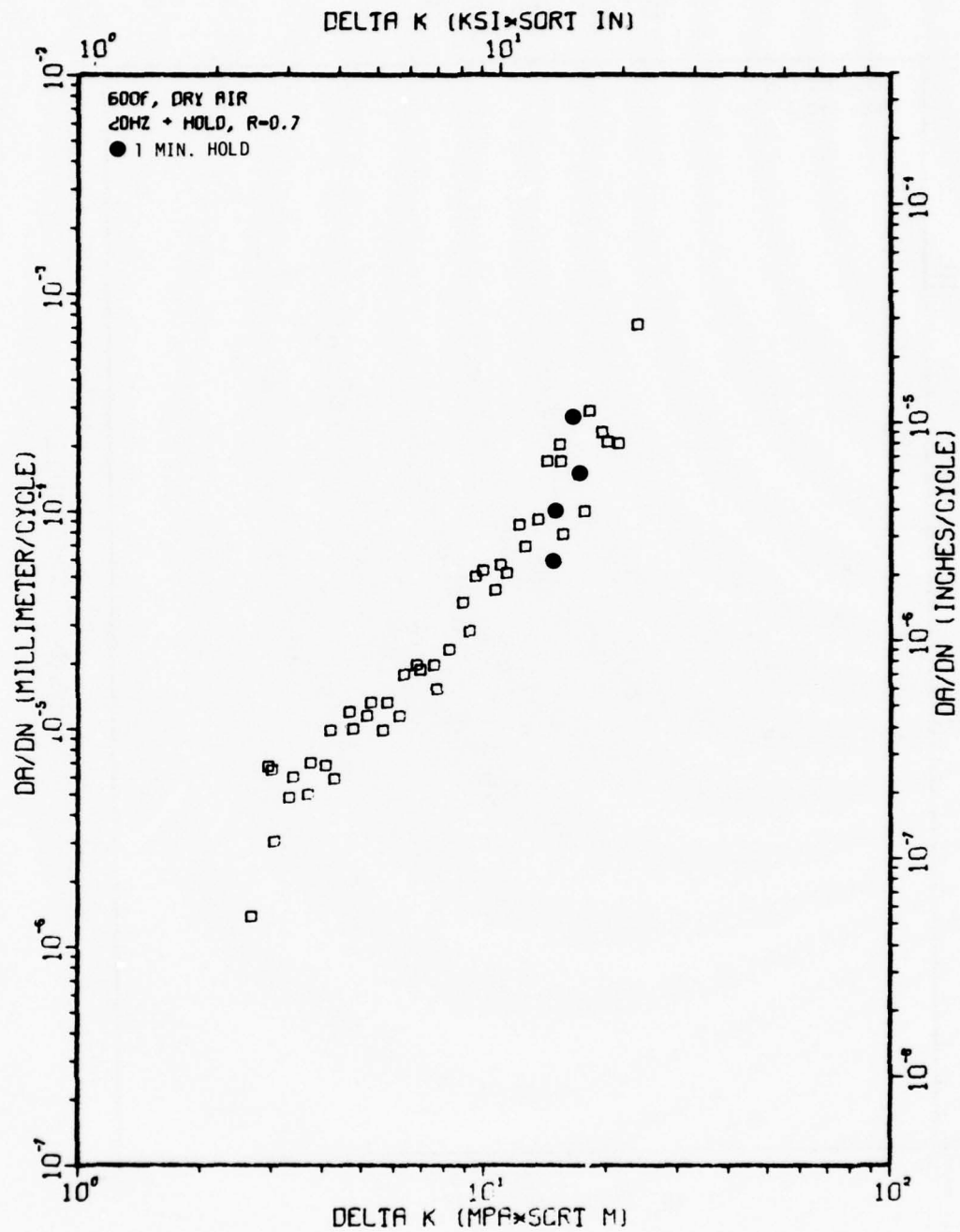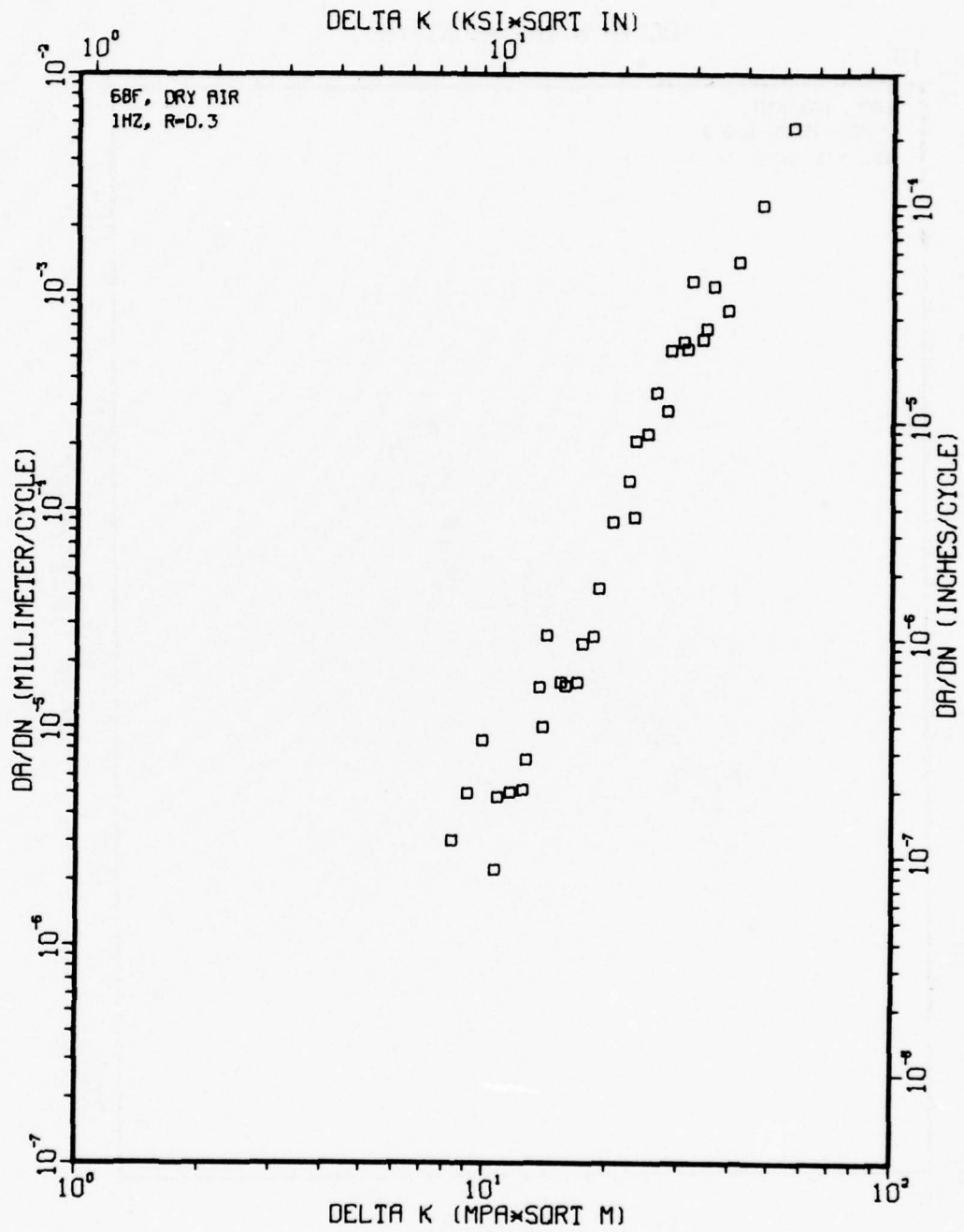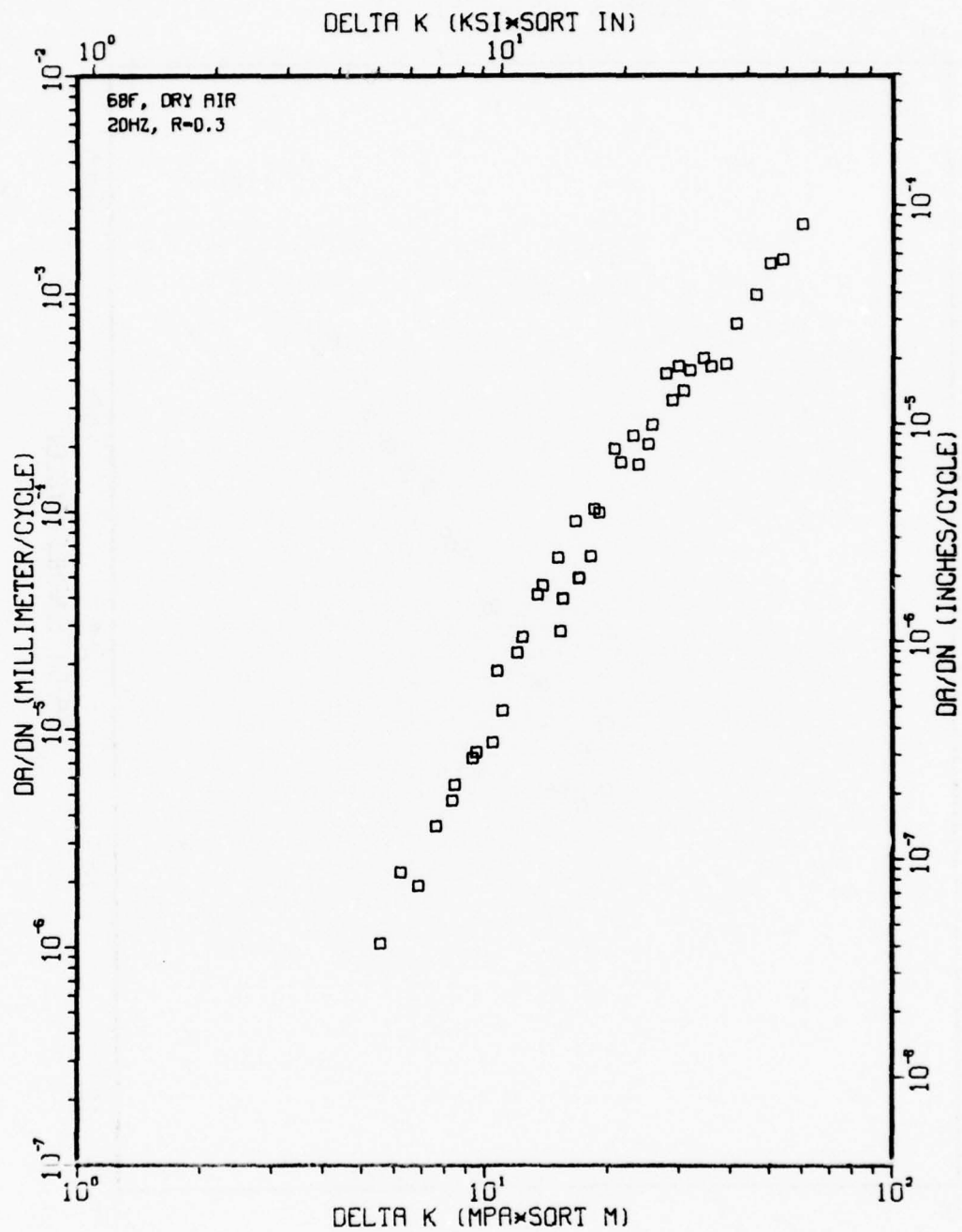
TI-6AL-4V 1-5-47 LO. OX.

Figure A59

TI-6AL-4V 1-5-34 HI. OX.

Figure A60

336
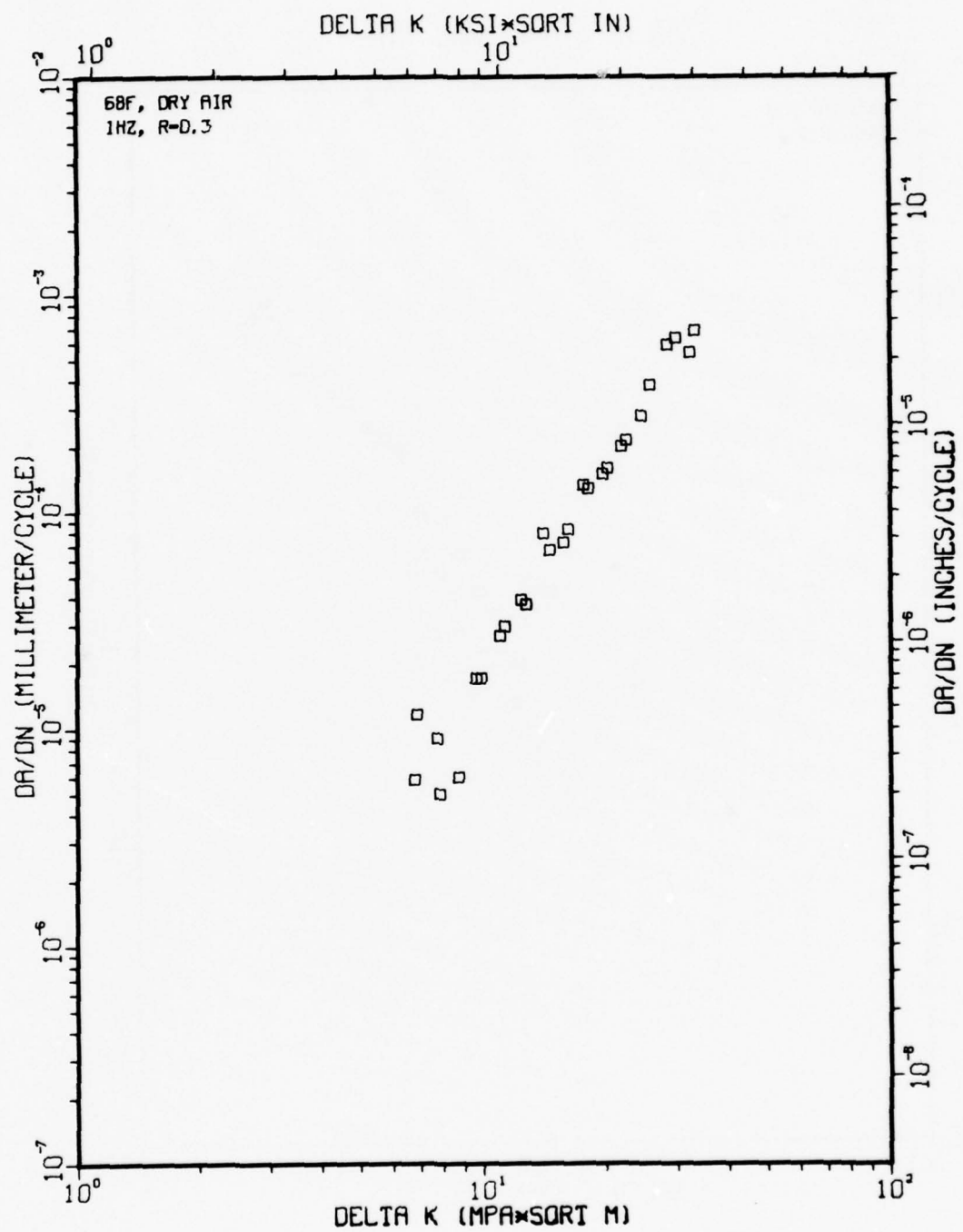
TI-6AL-4V   1-5-37   HI. OX.

Figure A61

337
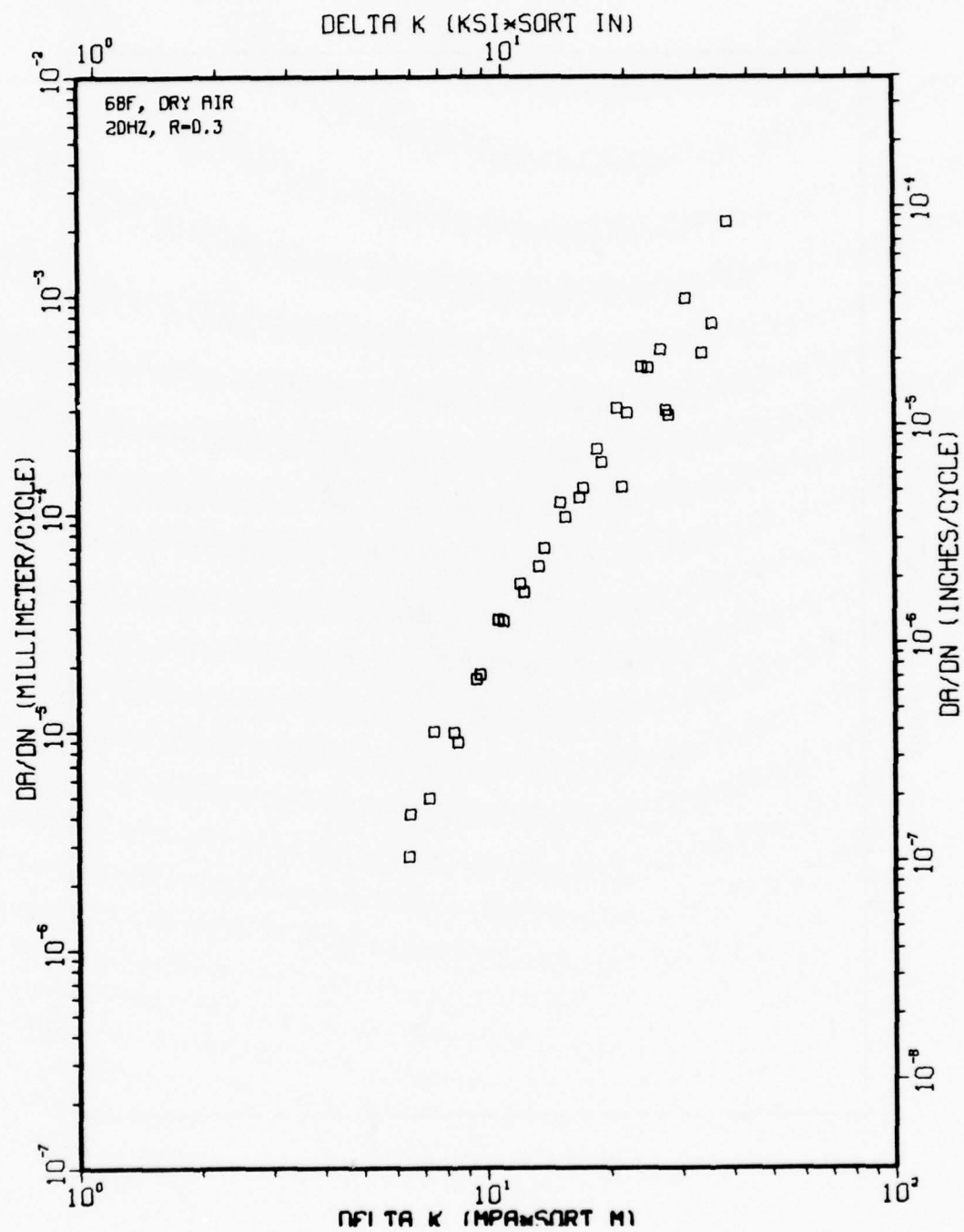
TI-6AL-4V 1-5-46 LO.OX.

Figure A62

338

TI-6AL-4V 1-5-45 LO. OX.

Figure A63

TI-6AL-4V 1-5-36 HI. OX.

Figure A64

340
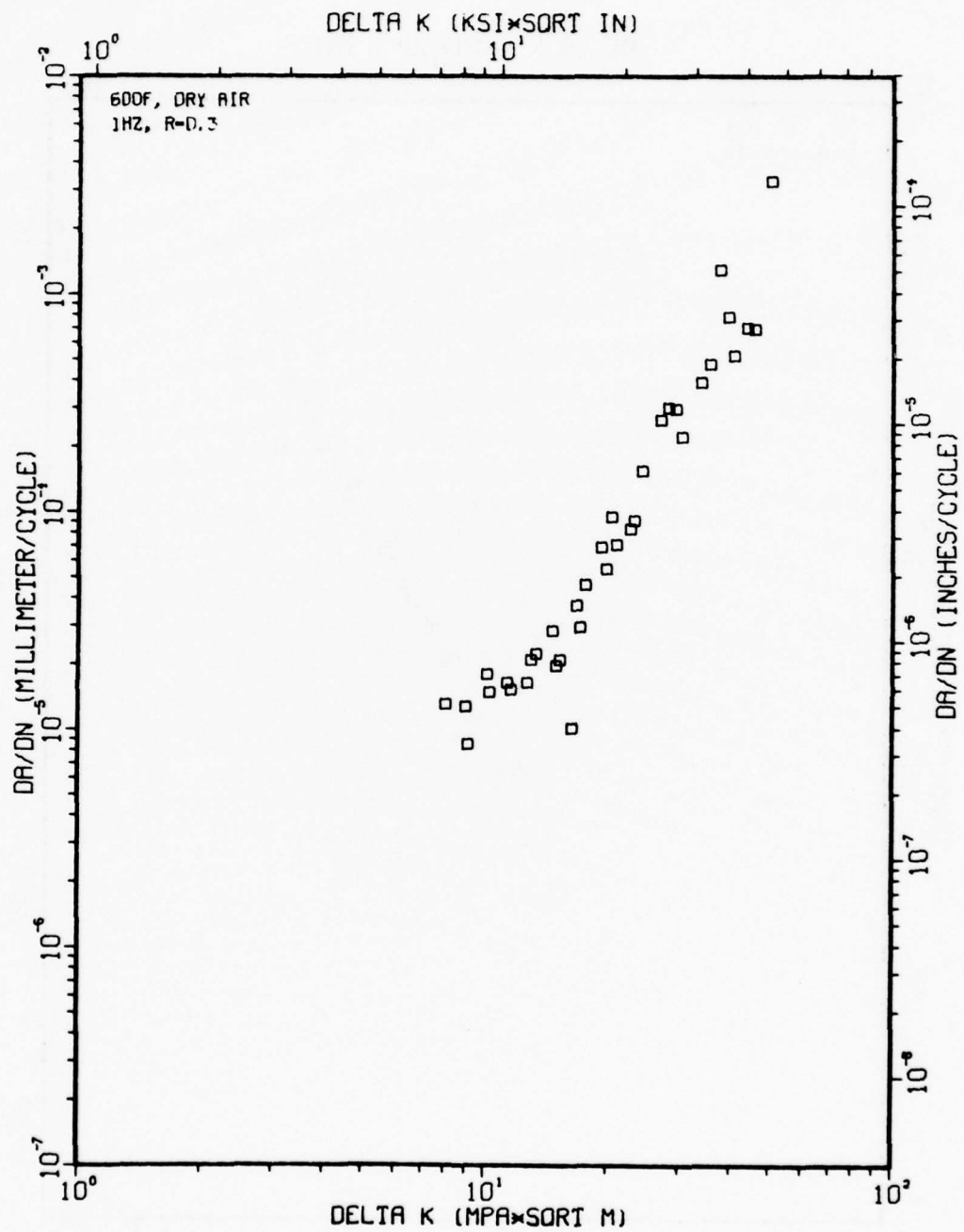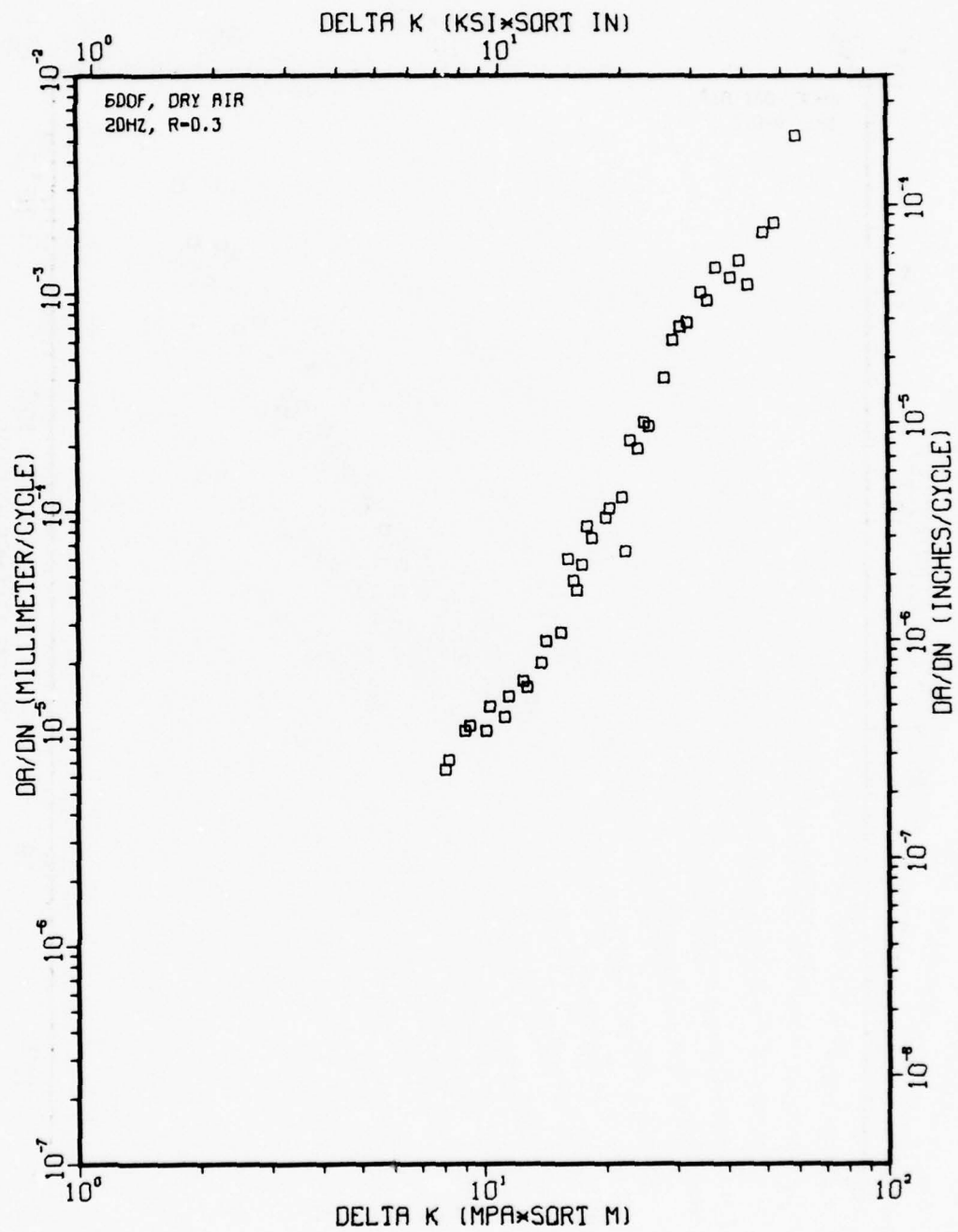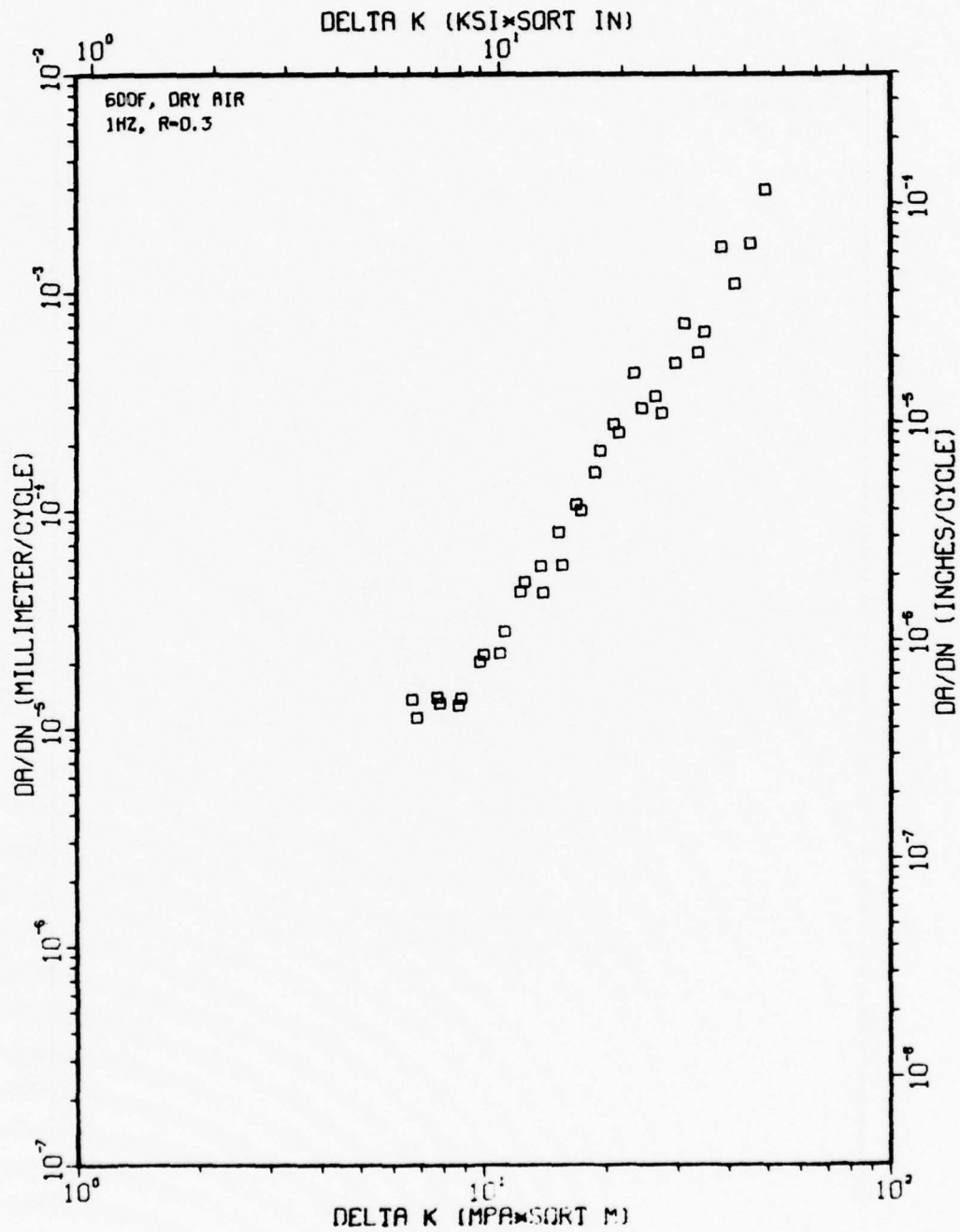
TI-6AL-4V   1-5-35   HI. OX.

Figure A65

341

TI-6AL-4V   1-5-S1   100H

DELTA K (KSI×SQRT IN)

Figure A66

342
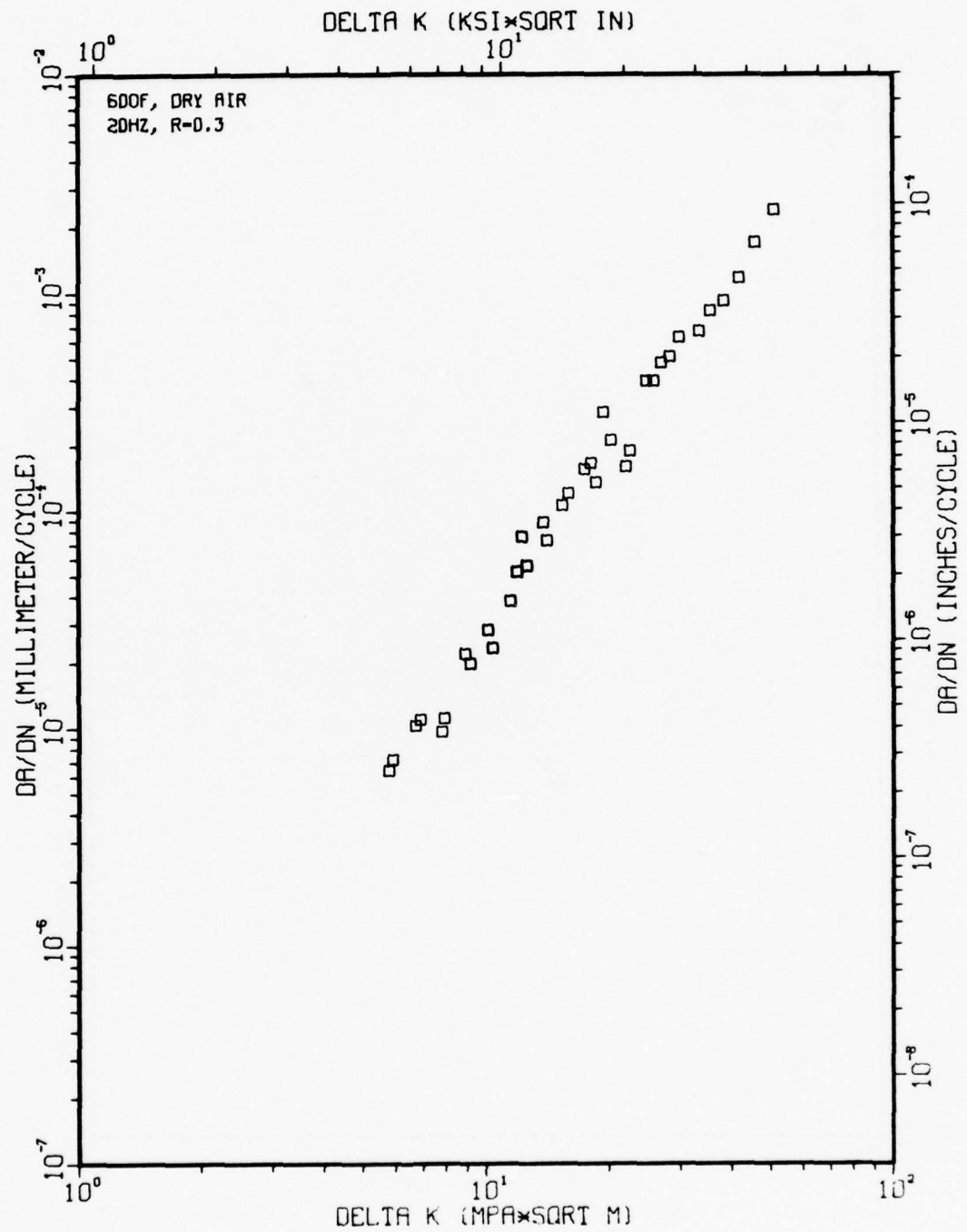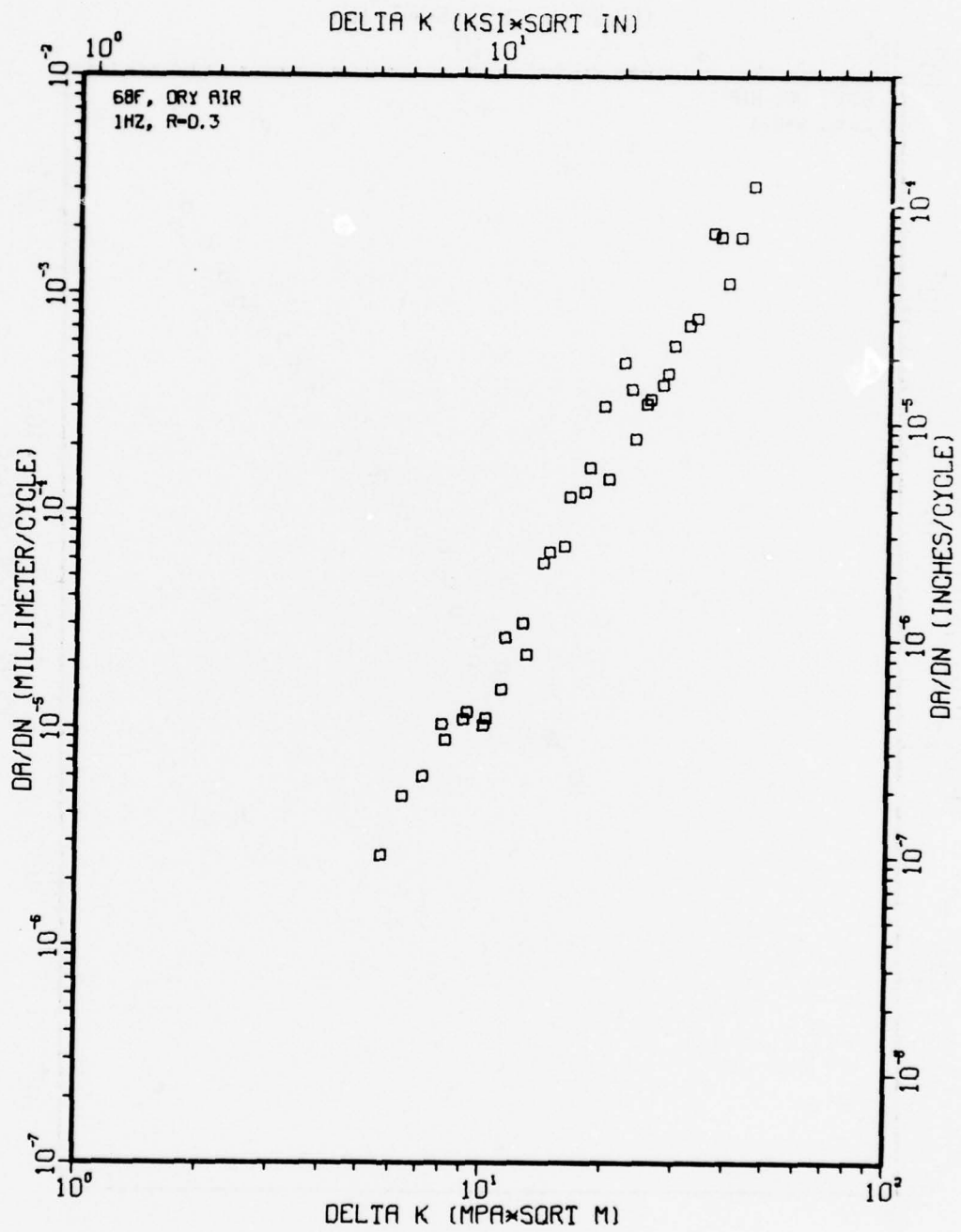
TI-6AL-4V 1-5-50 100H

Figure A67

343

TI-6AL-4V 1-5-61 318H

Figure A68

344

TI-6AL-4V   1-5-60   313H

DELTA K (KSI*SQRT IN)
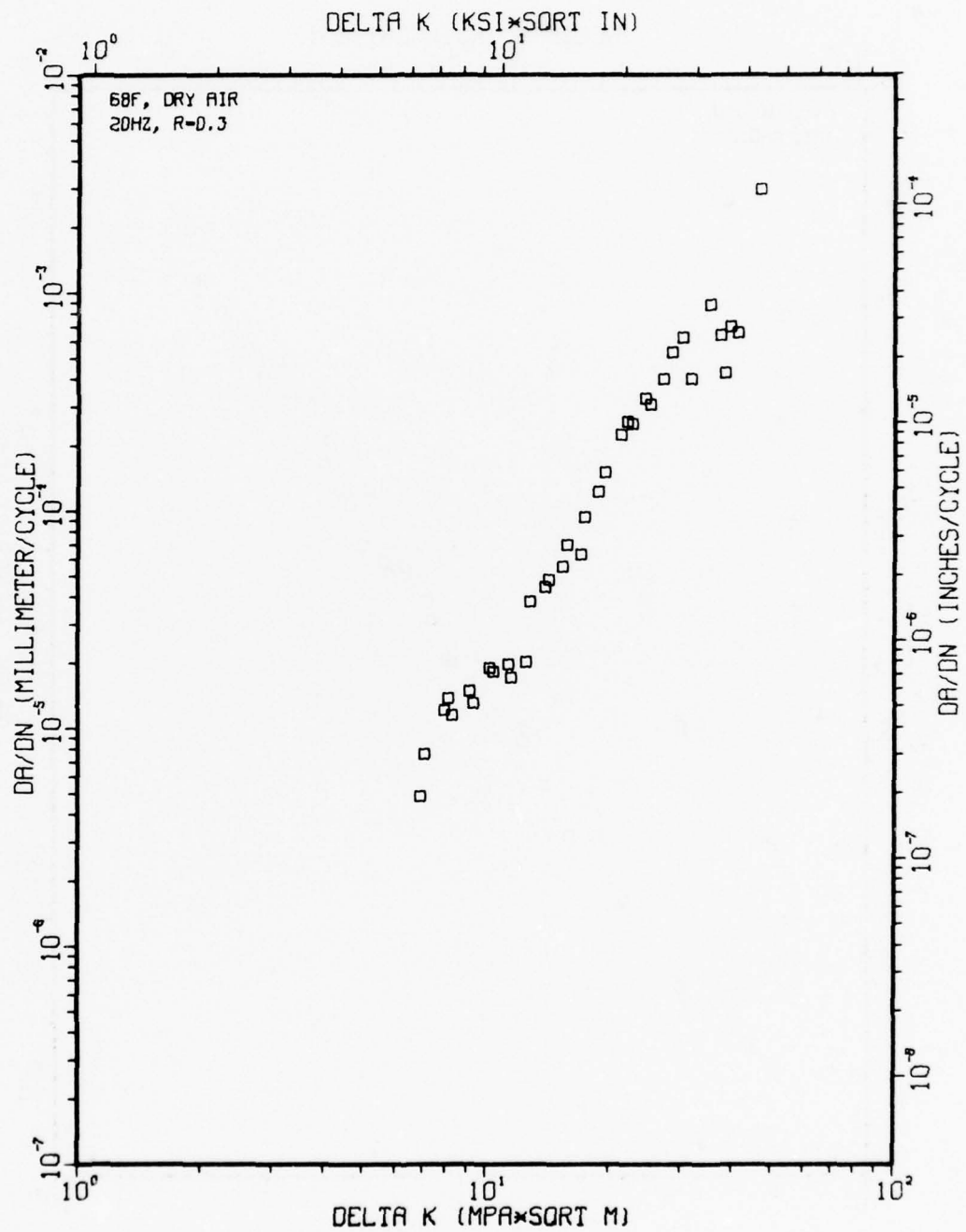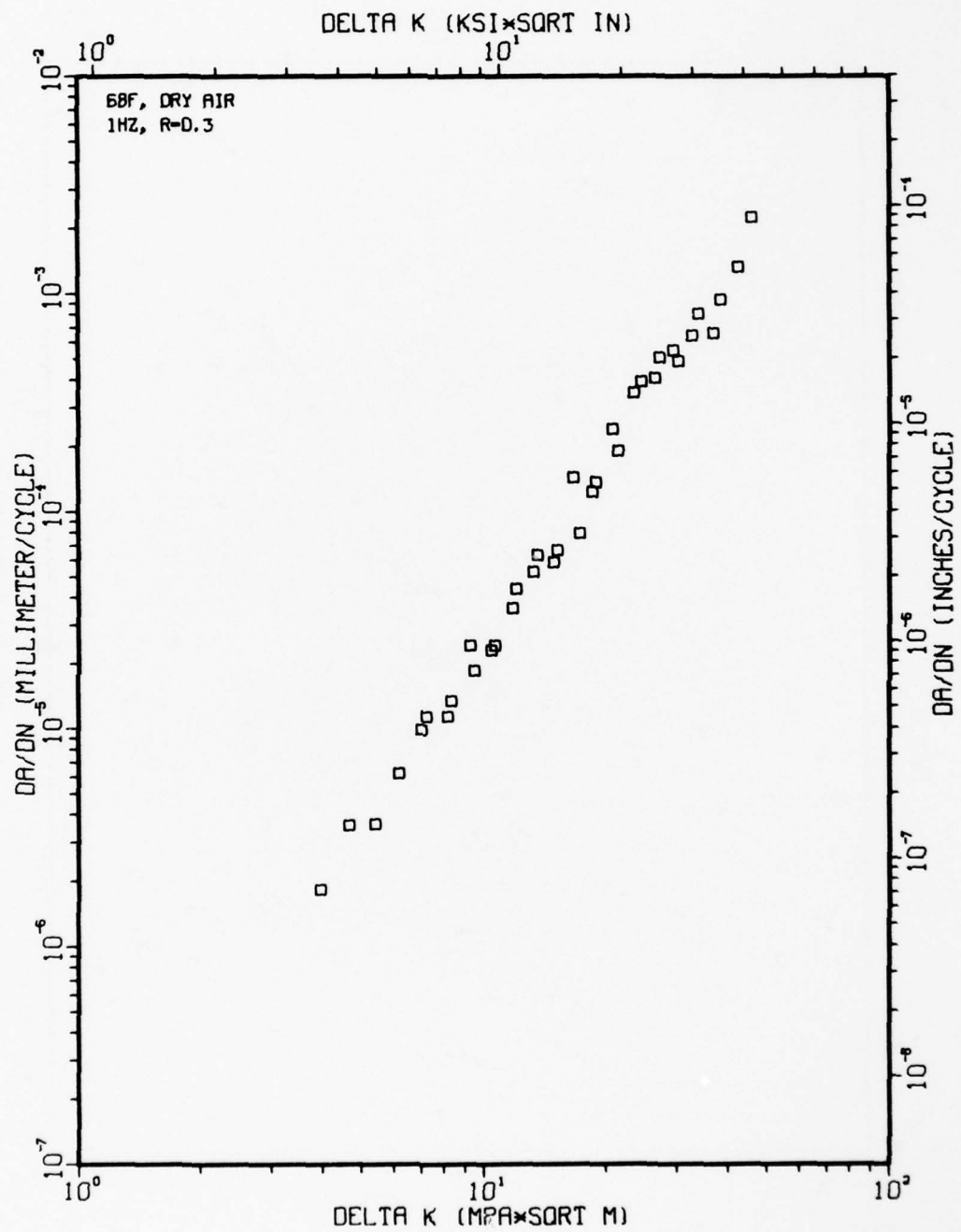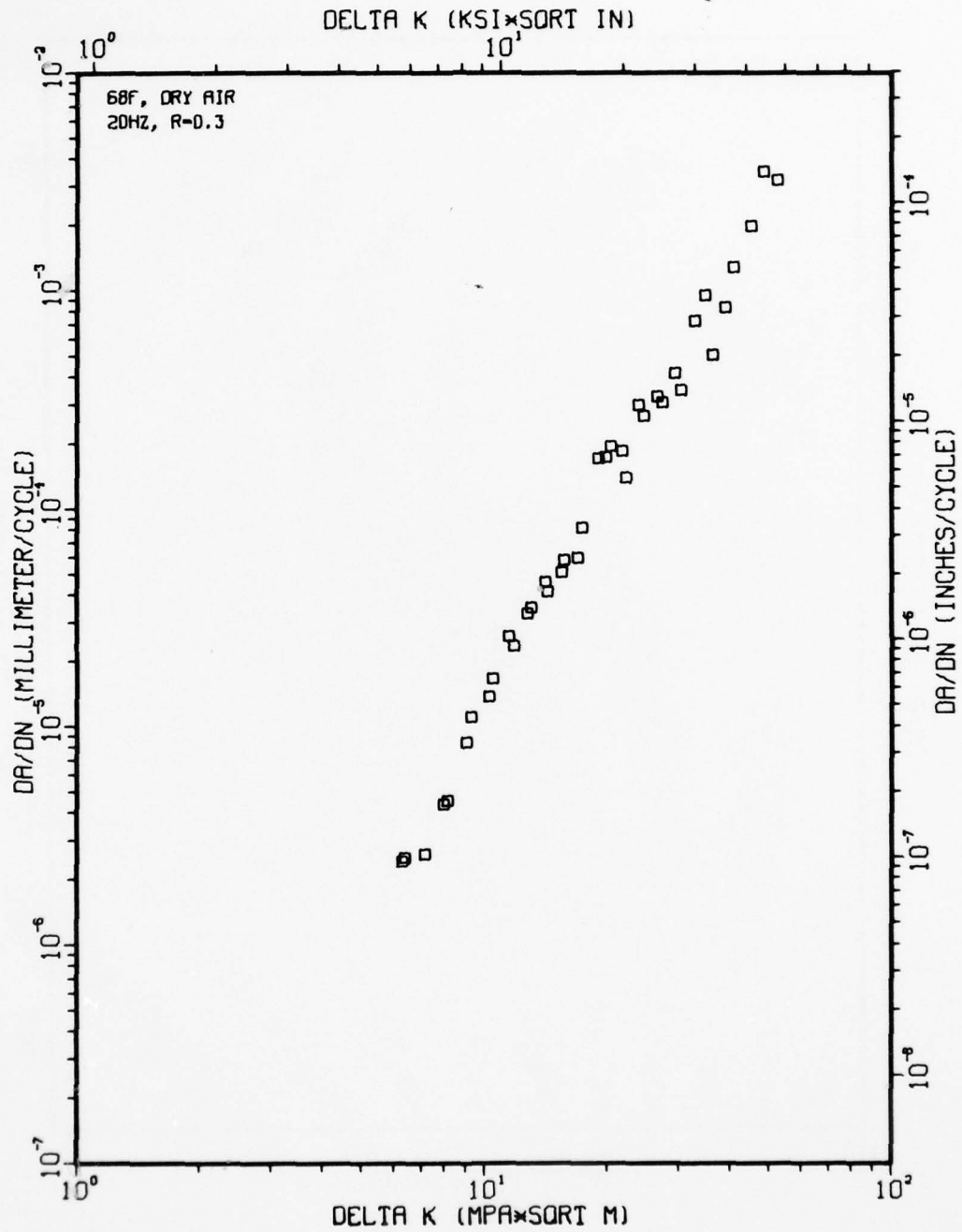
Figure A69

TI-6AL-4V 1-5-53 100H

Figure A70

346

TI-6AL-4V 1-S-63 285H

Figure A71

347
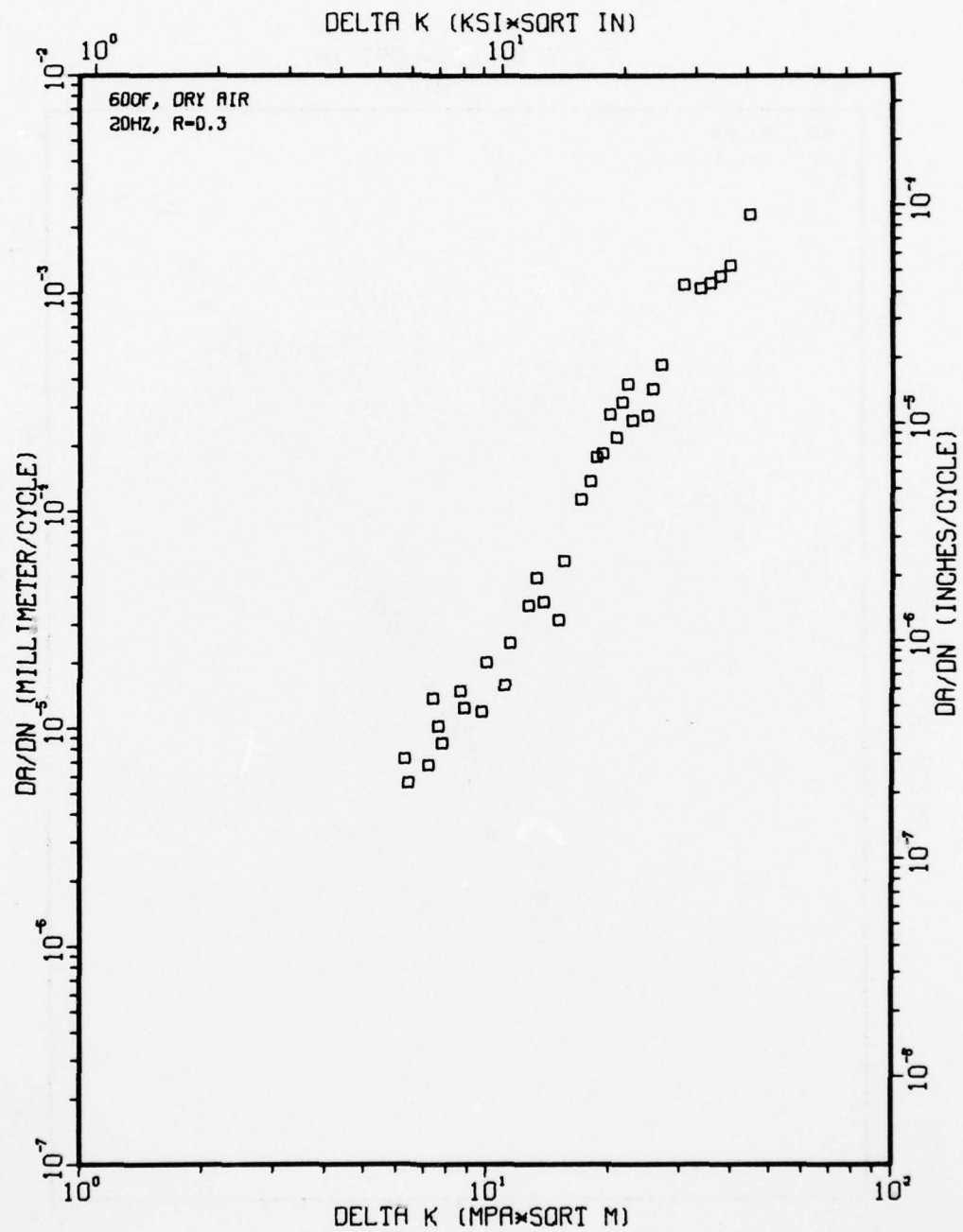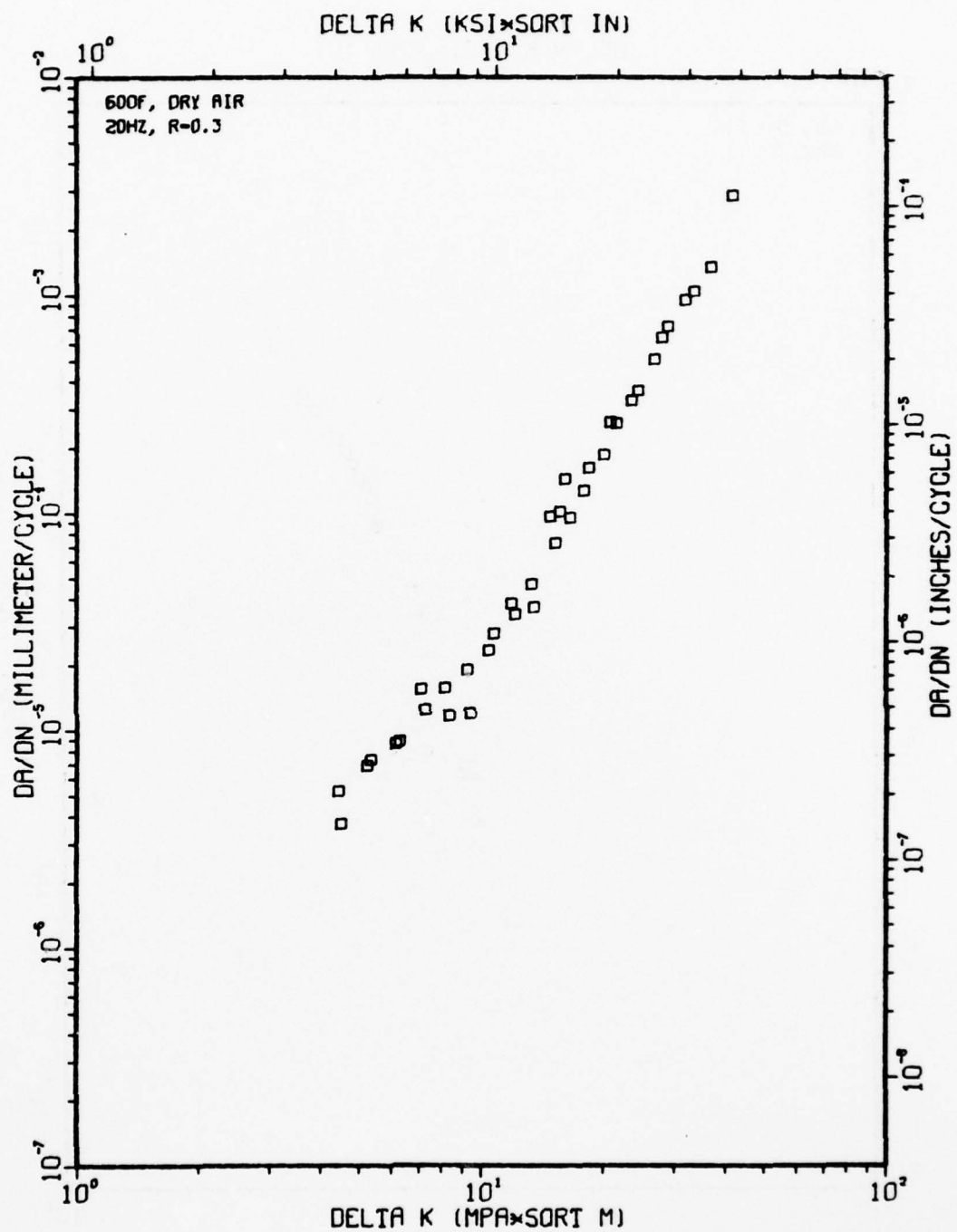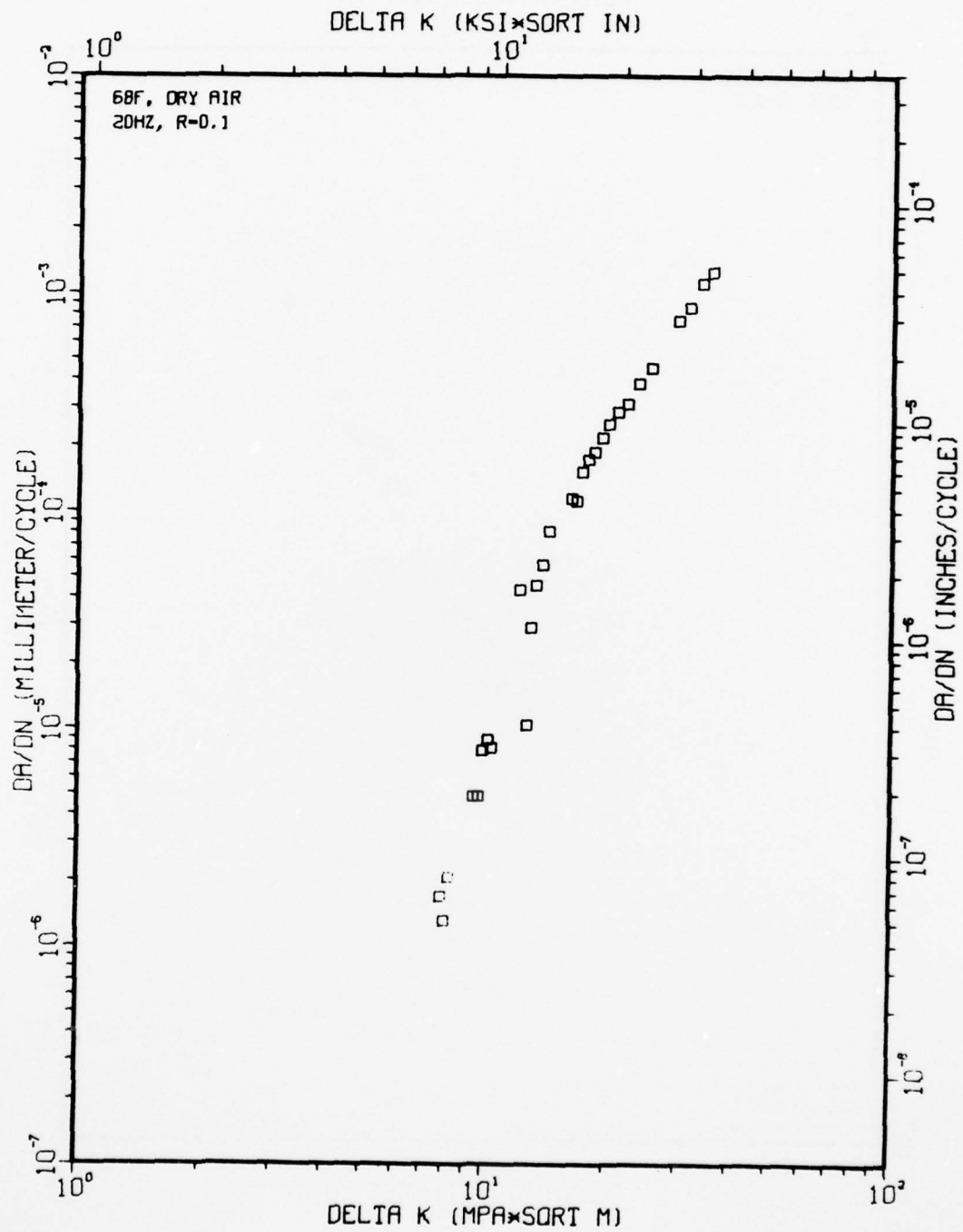
TI-6AL-4V 1-6-1

Figure A72

TI-6AL-4V 1-6-3
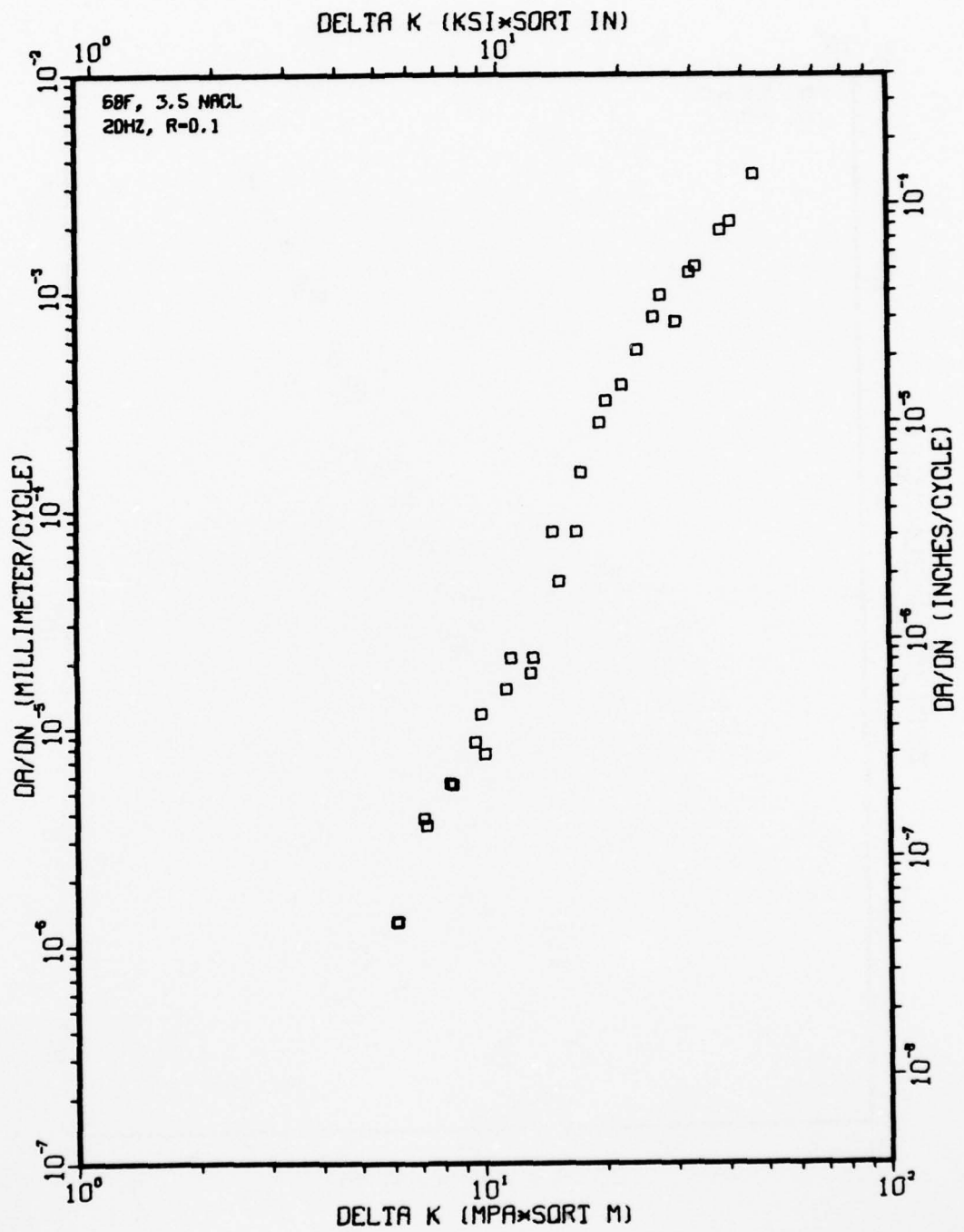
Figure A73
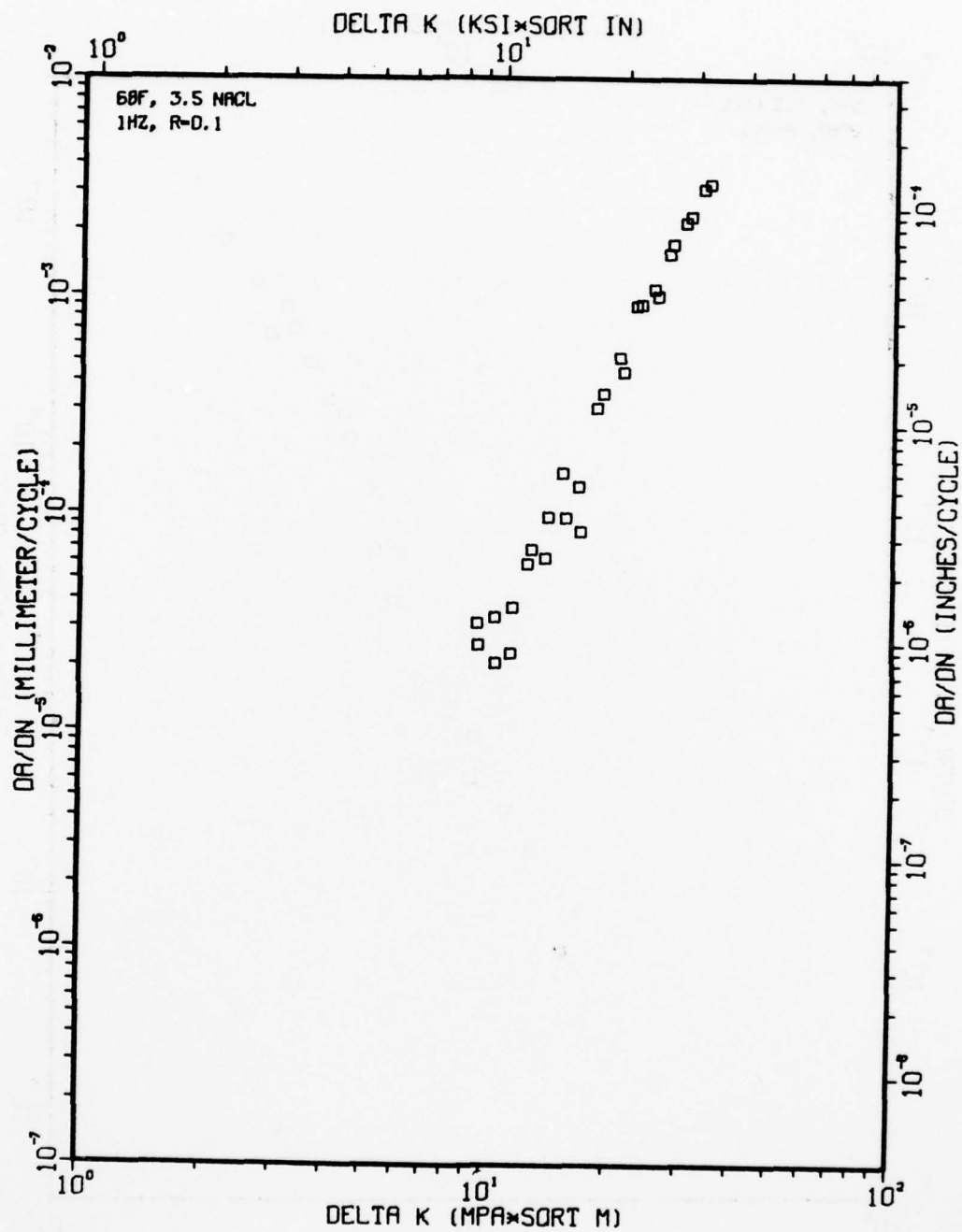
TI-6AL-4V   1-6-4

Figure A74

T1-6AL-4V 1-6-2

Figure A75

TI-6AL-4V   1-7-7

Figure A76

352

TI-6AL-4V   1-7-9

DELTA K (KSI*SORT IN)

Figure A77

353
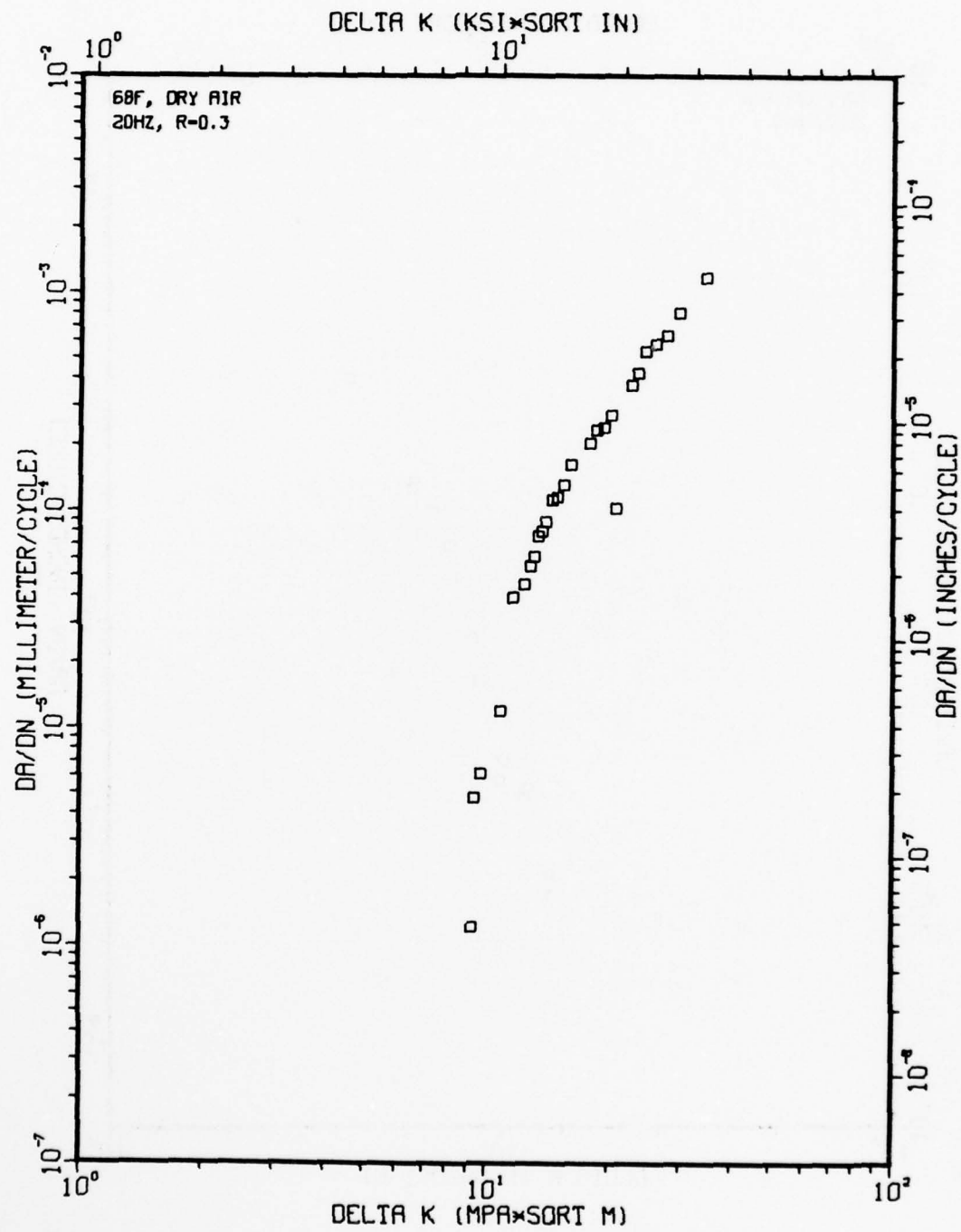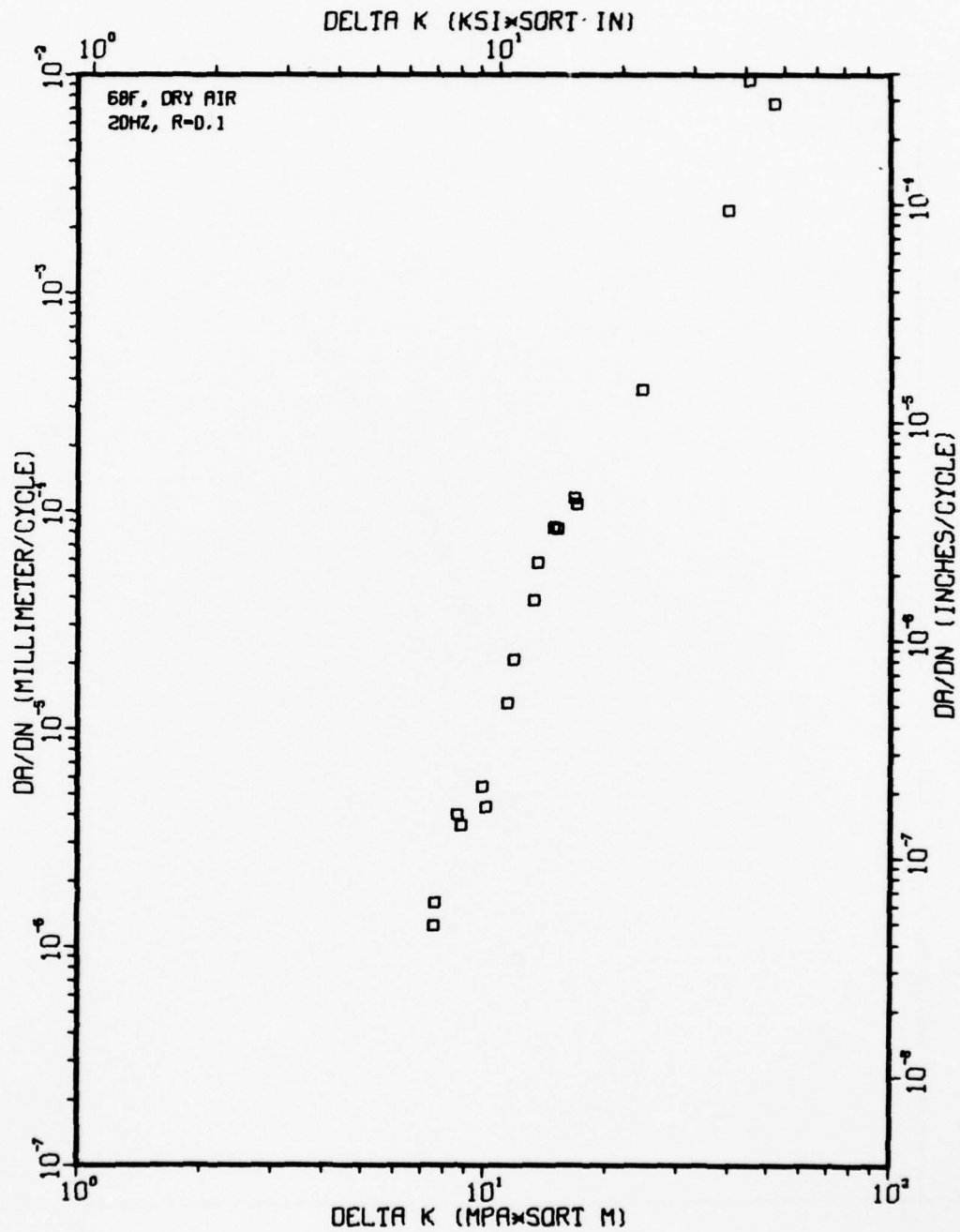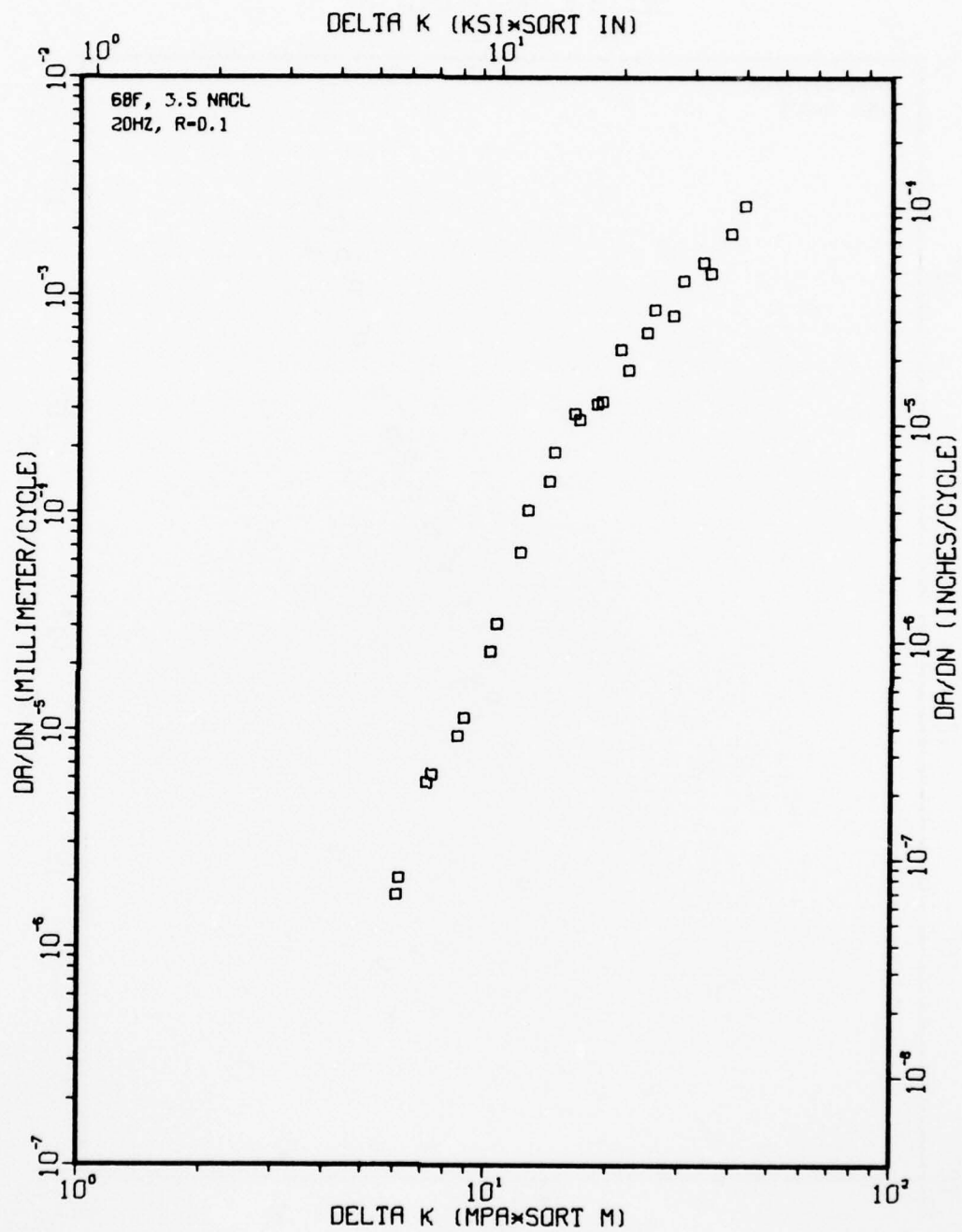
TI-6AL-4V 1-7-8

Figure A78

354

Figure A79

355

TI-6AL-4V 1-7-25

Figure A80

356
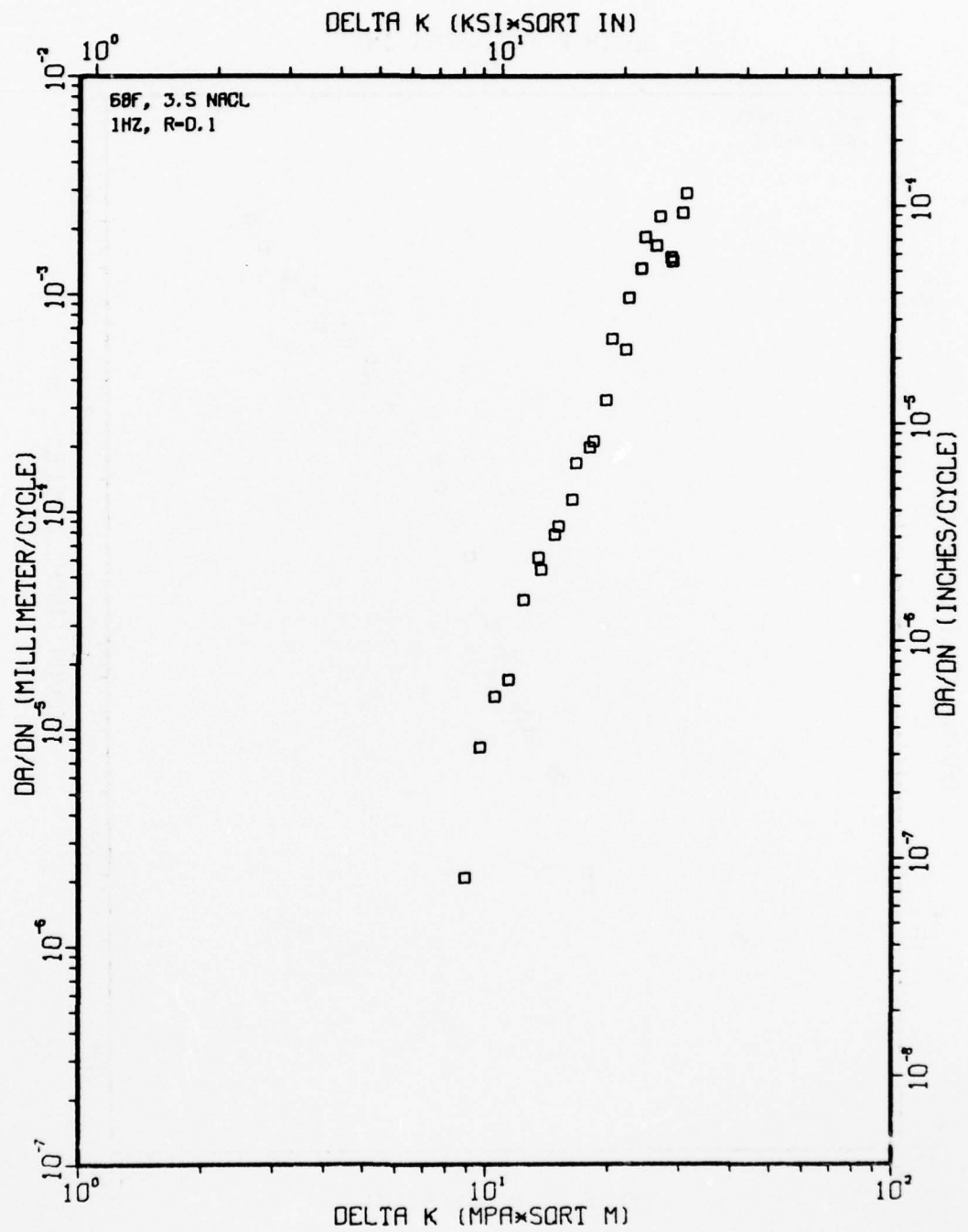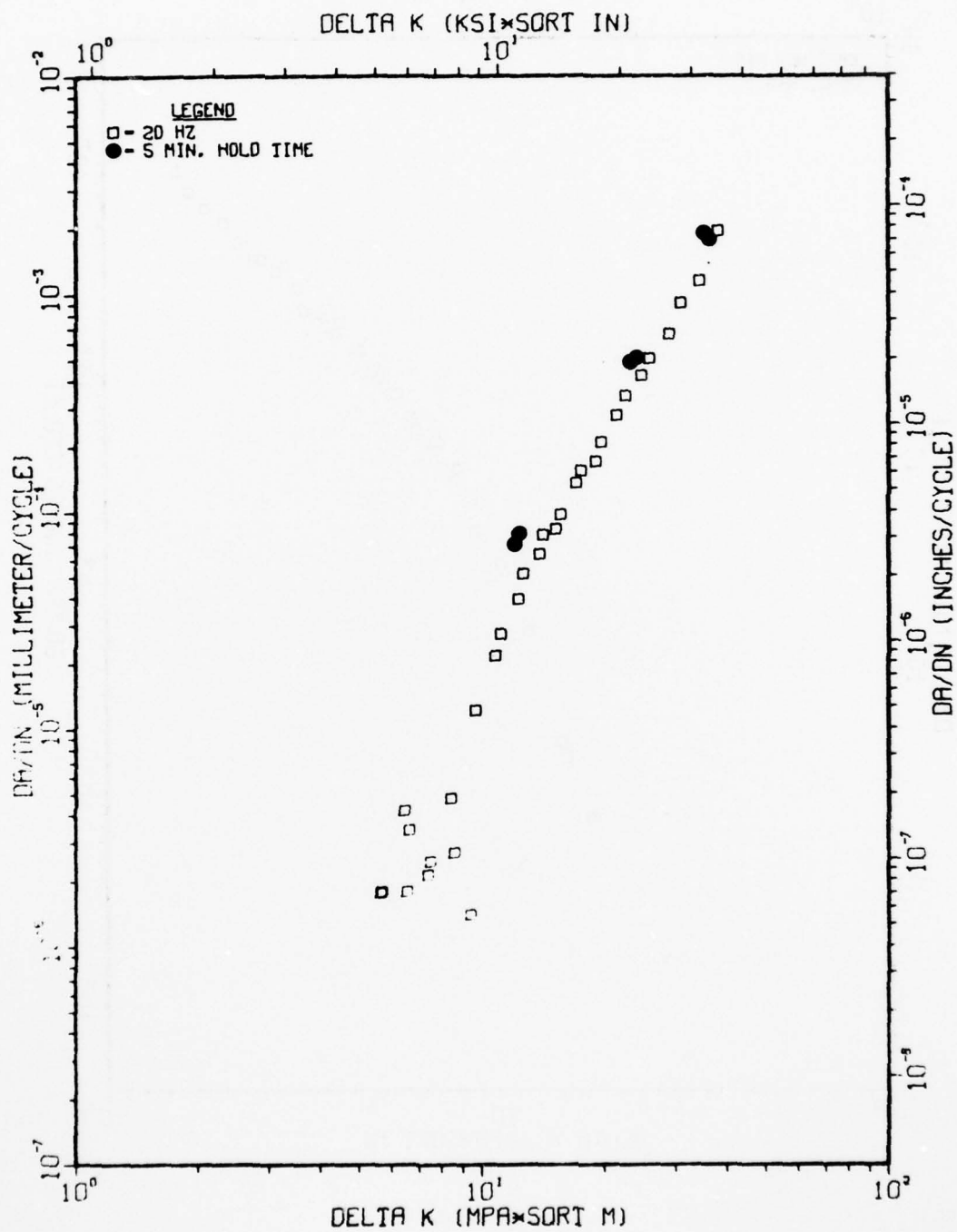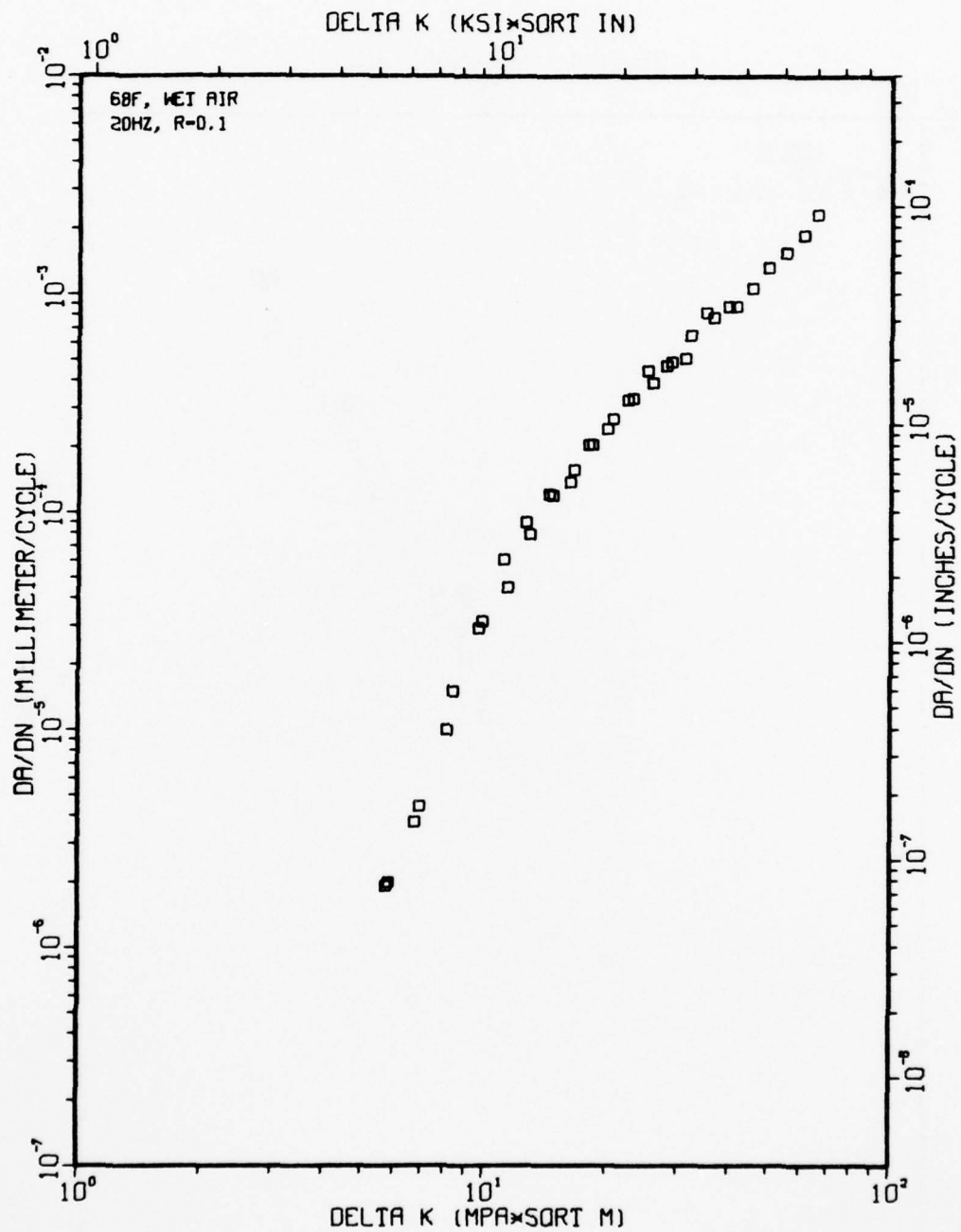
TI-6AL-4V   1-7-21

Figure A81
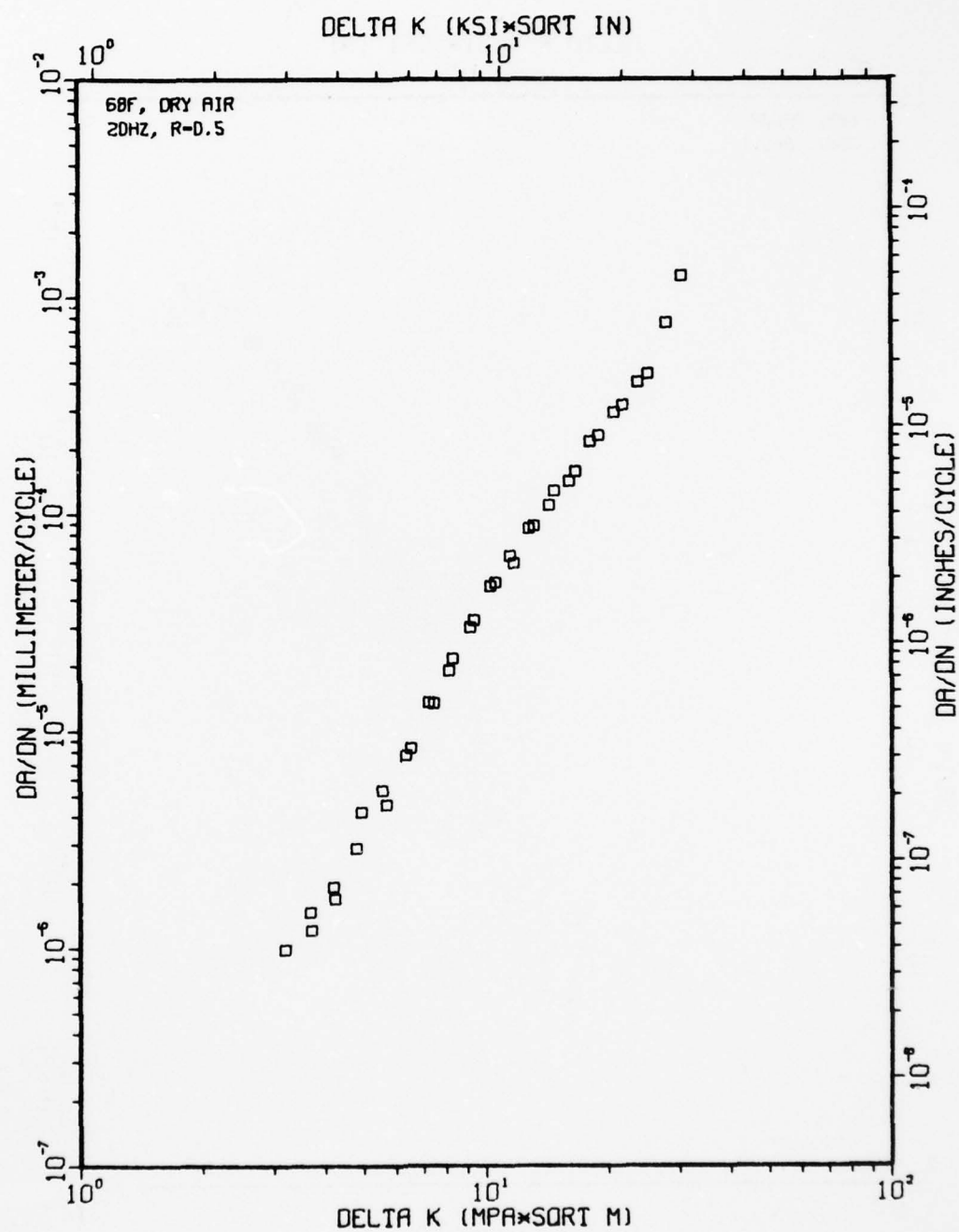
357

TI-6AL-4V   1-7-23

Figure A82

353
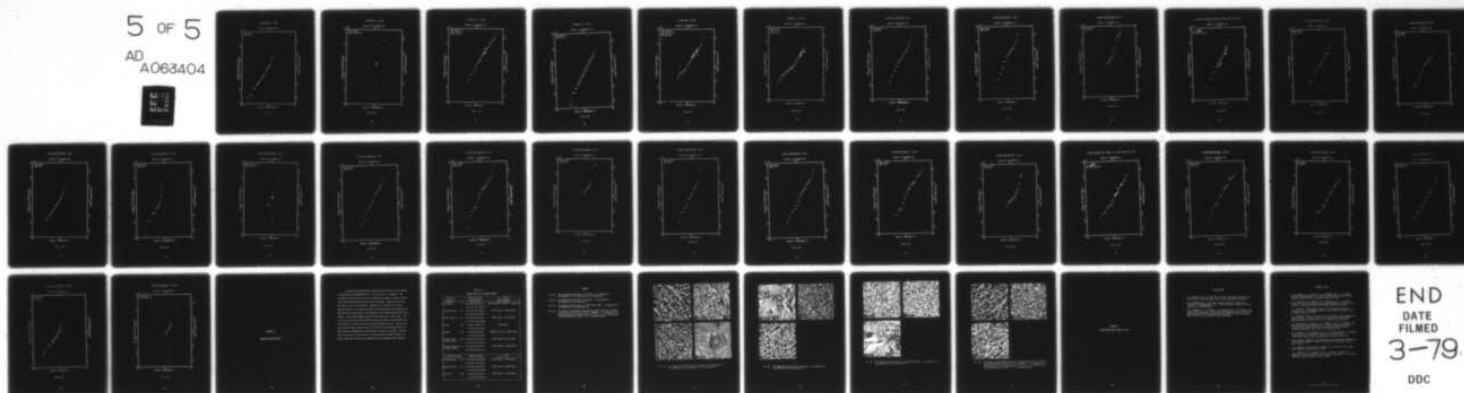
END
DATE
FILMED

3-79

DDC
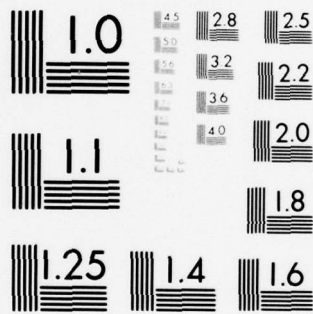
MICROCOPY RESOLUTION TEST CHART

NATIONAL BUREAU OF STANDARDS-1963-A

TI-6AL-4V   1-7-24
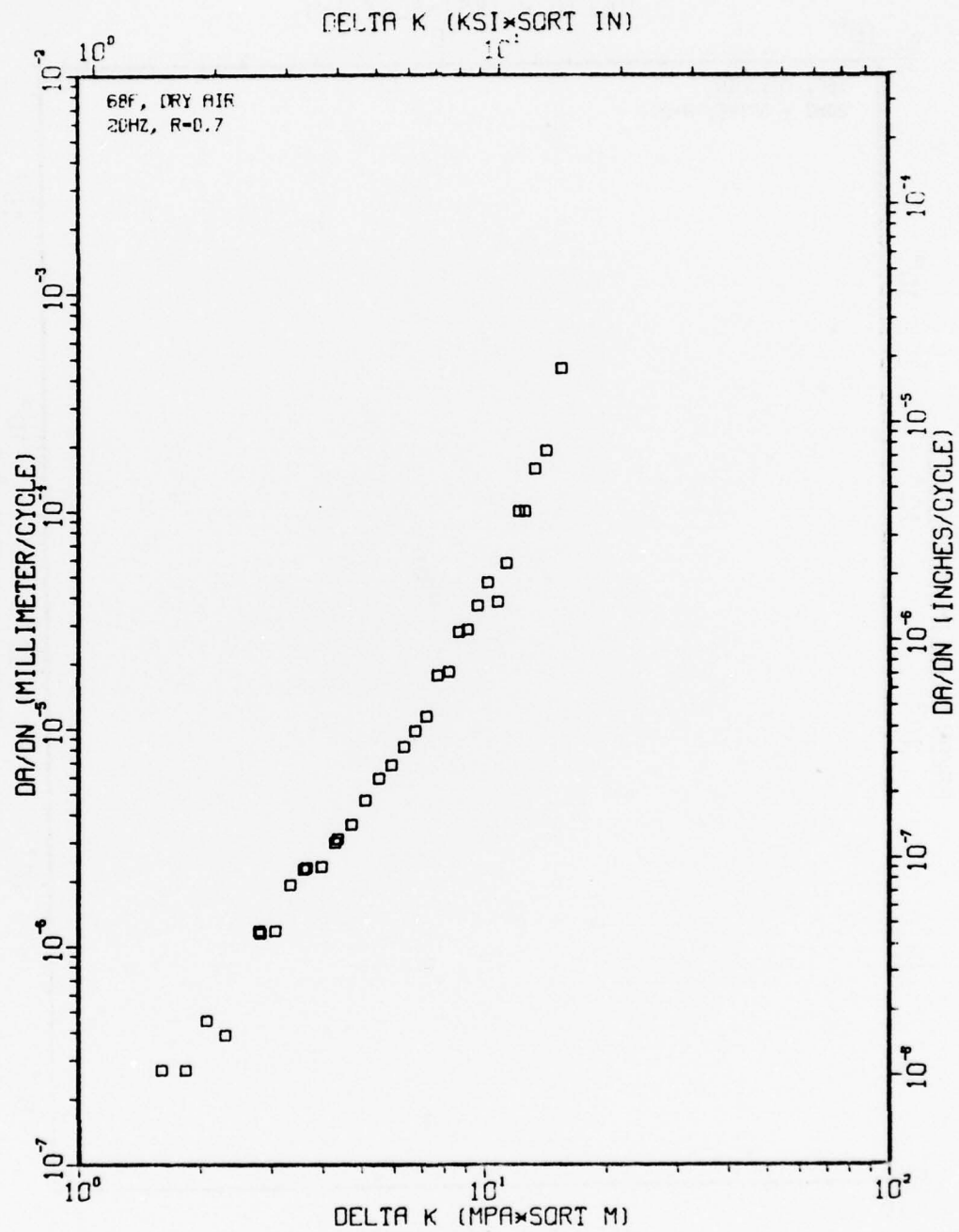
Figure A83

TI-6AL-4V 1-7-28
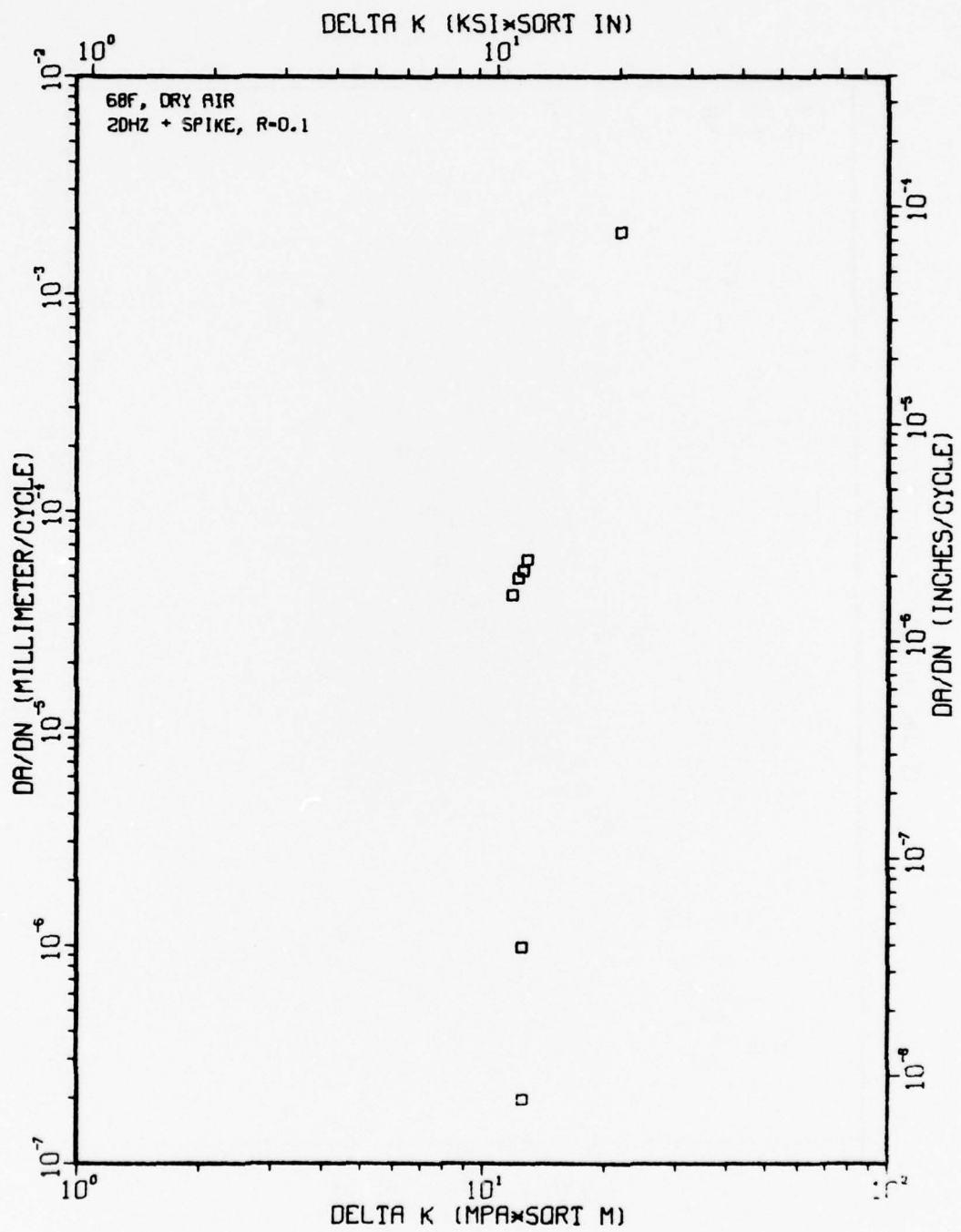
Figure A84

TI-6AL-4V 1-7-29
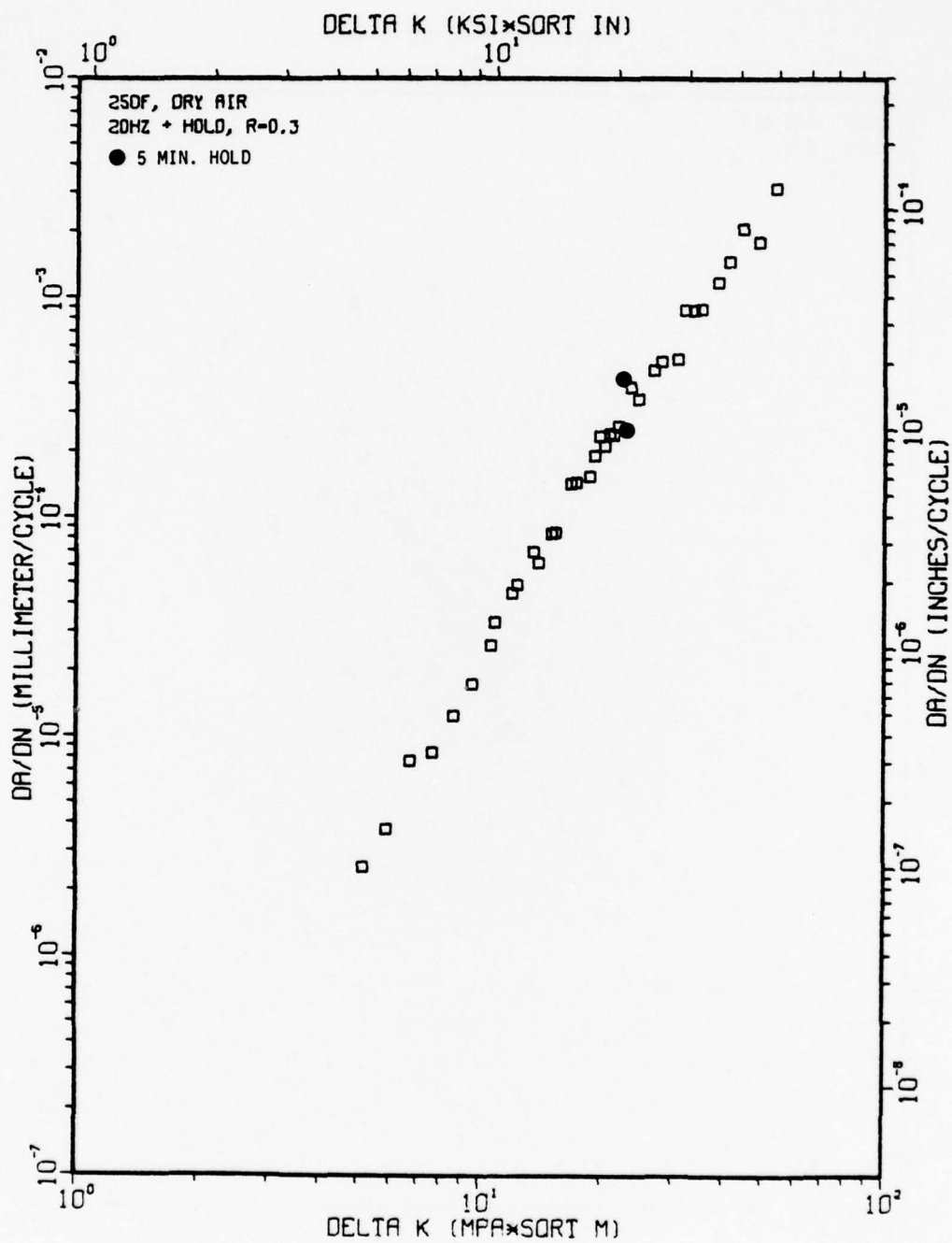
Figure A85

TI-6AL-4V   1-7-30

Figure A86

362

TI-6AL-4V 1-7-31

Figure A87

363
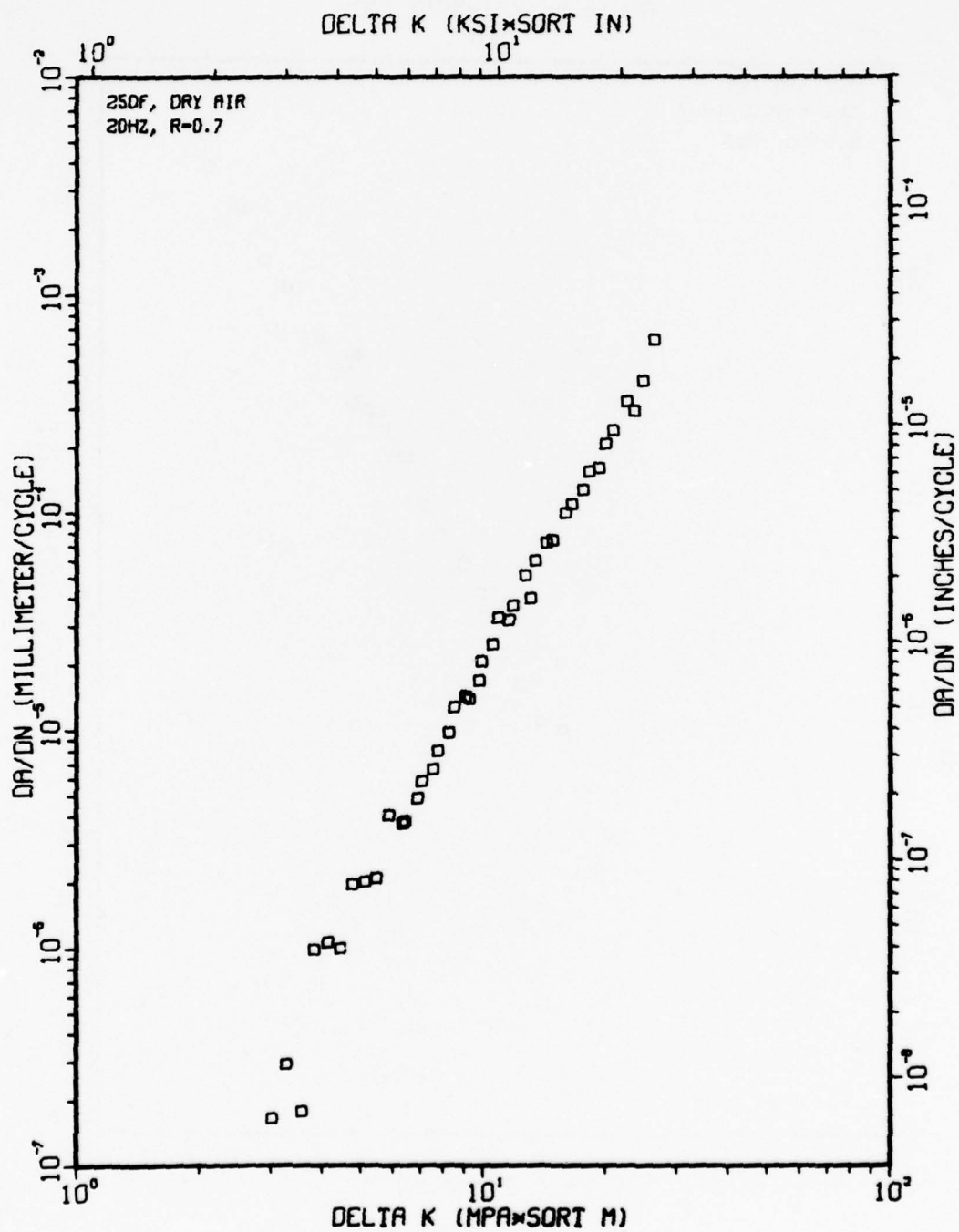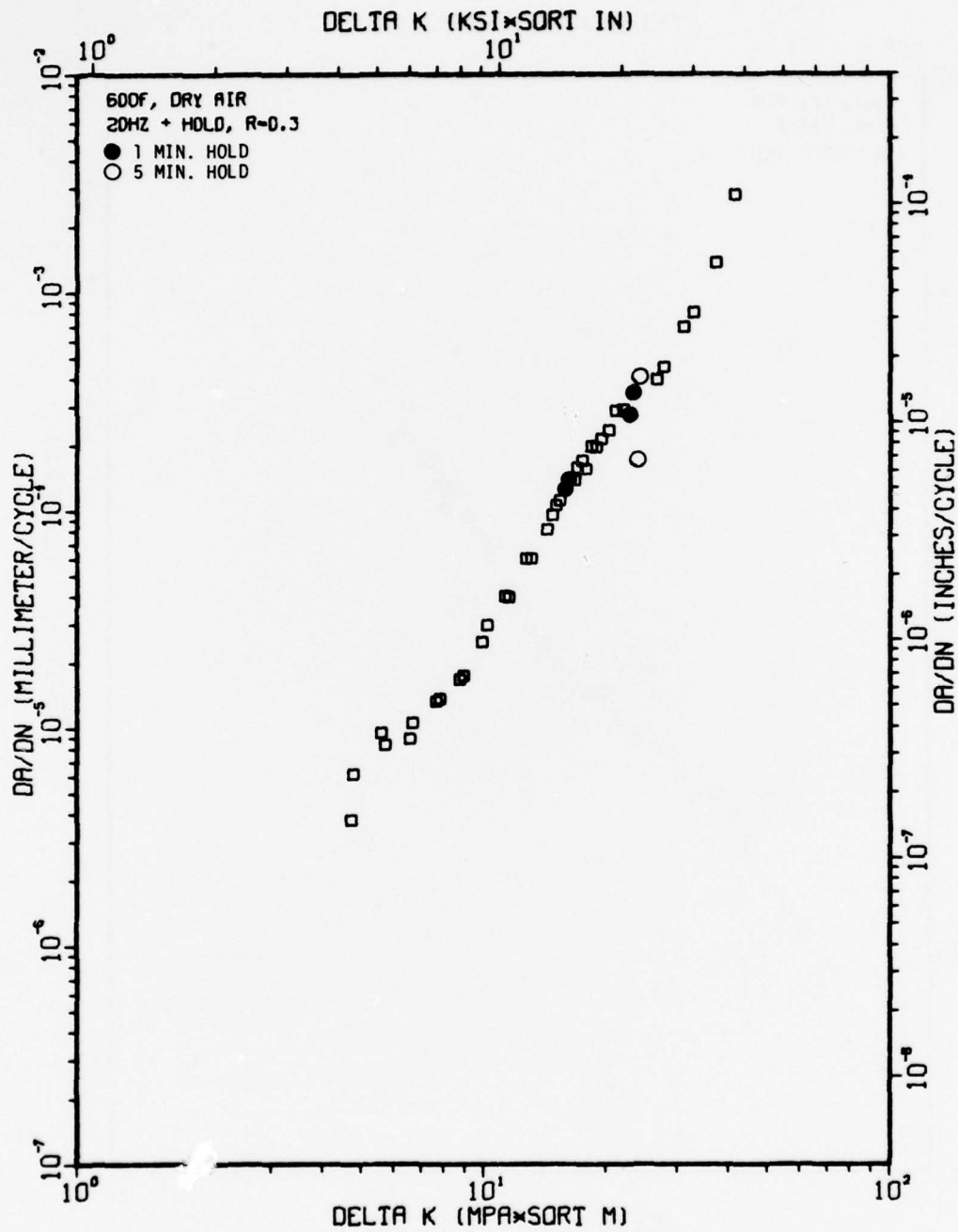
TI-6AL-4V   1-7-32

Figure A88

364
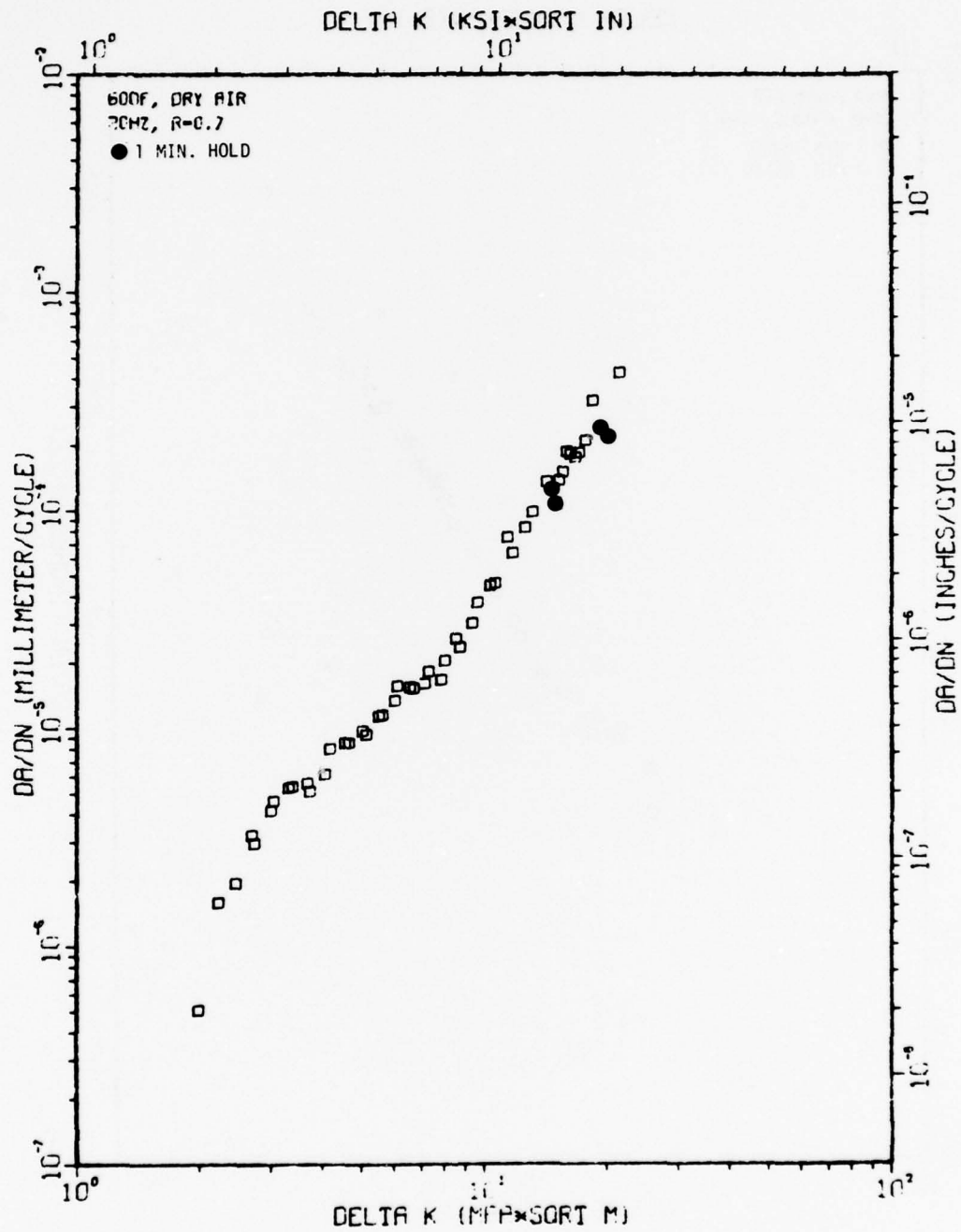
TI-6AL-2SN-4ZR-6MO   2-8-1

Figure A89

365
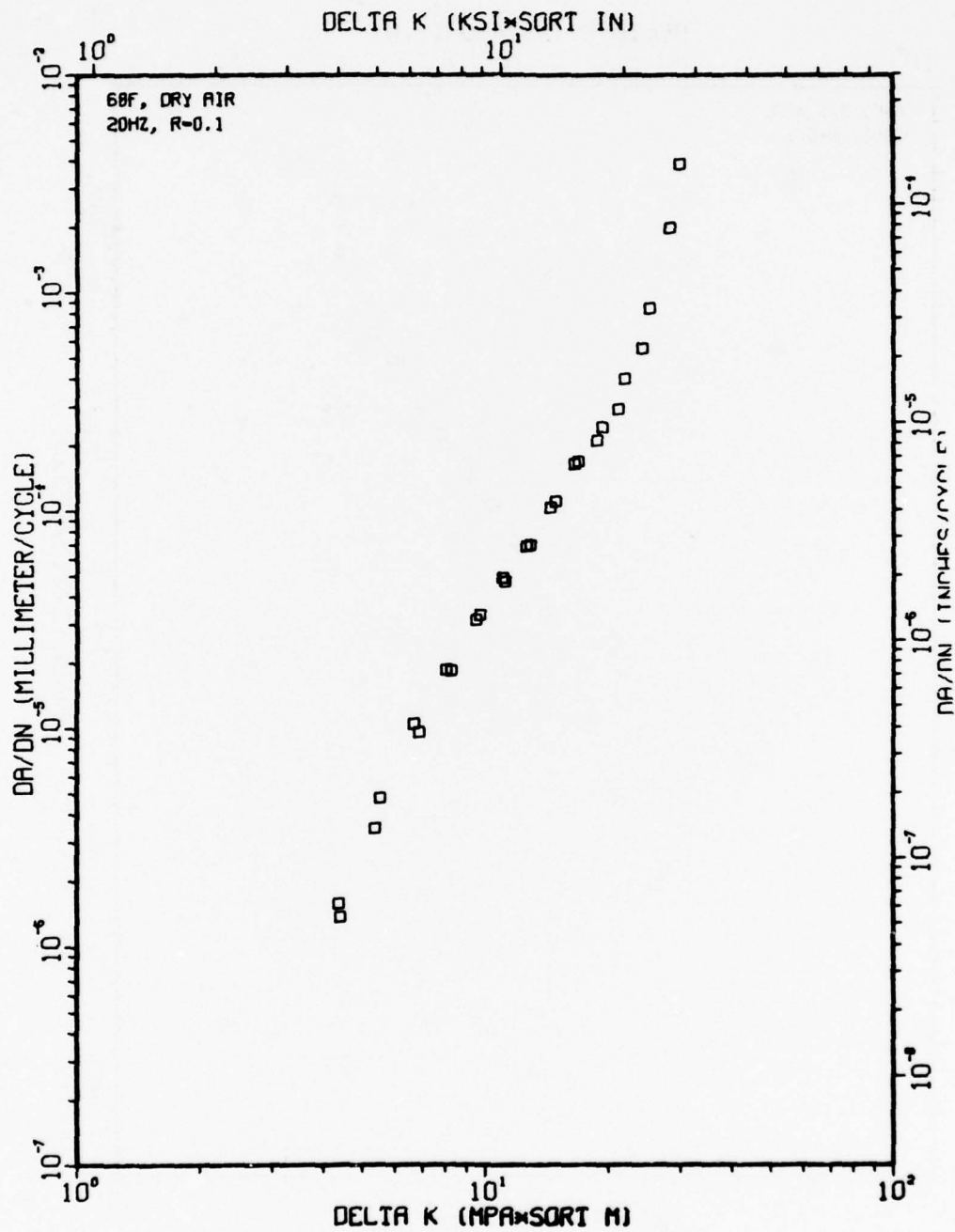
TI-6AL-2SN-4ZR-6MO 2-8-4
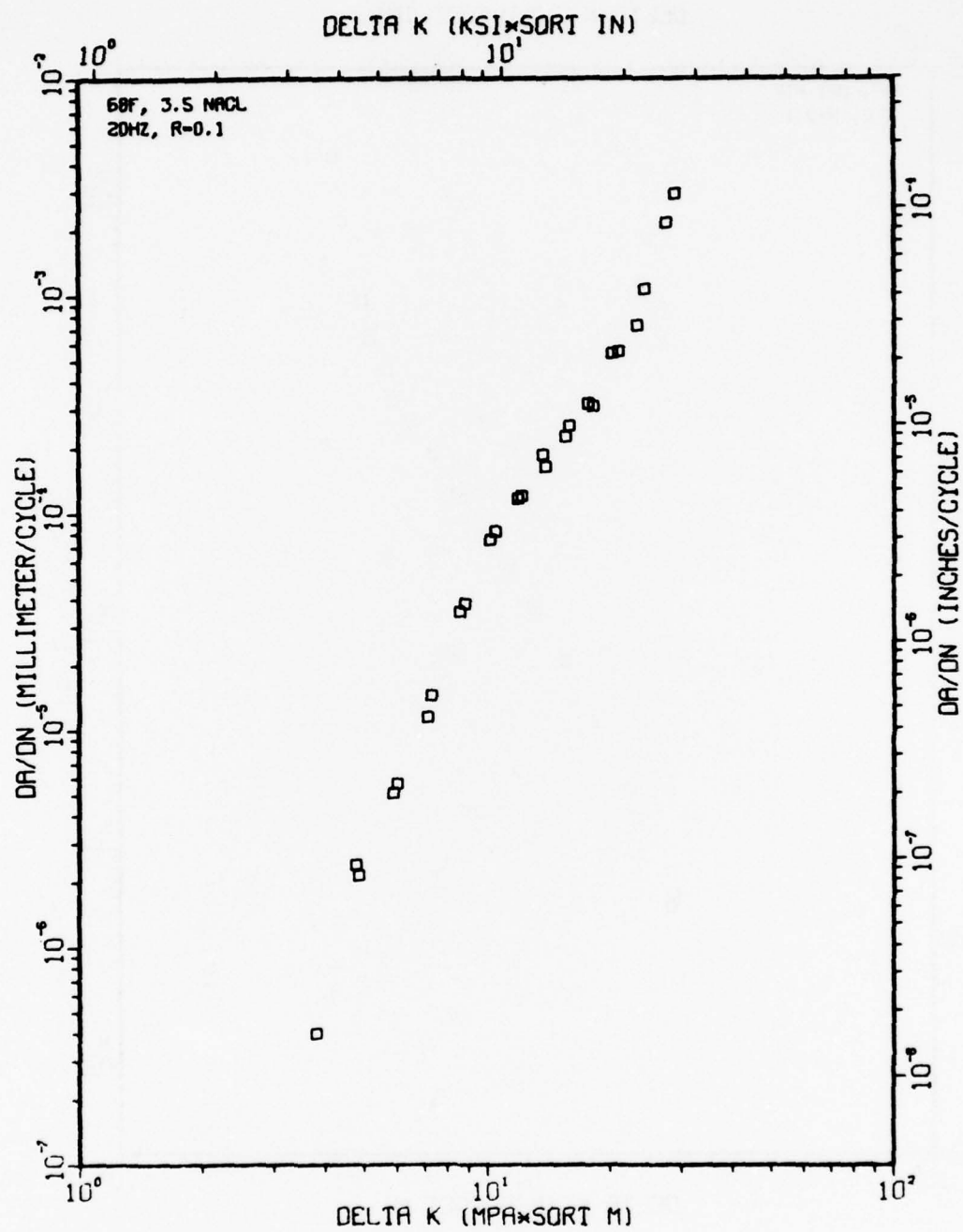
Figure A90

TI-6AL-2SN-4ZR-6MO   2-8-2
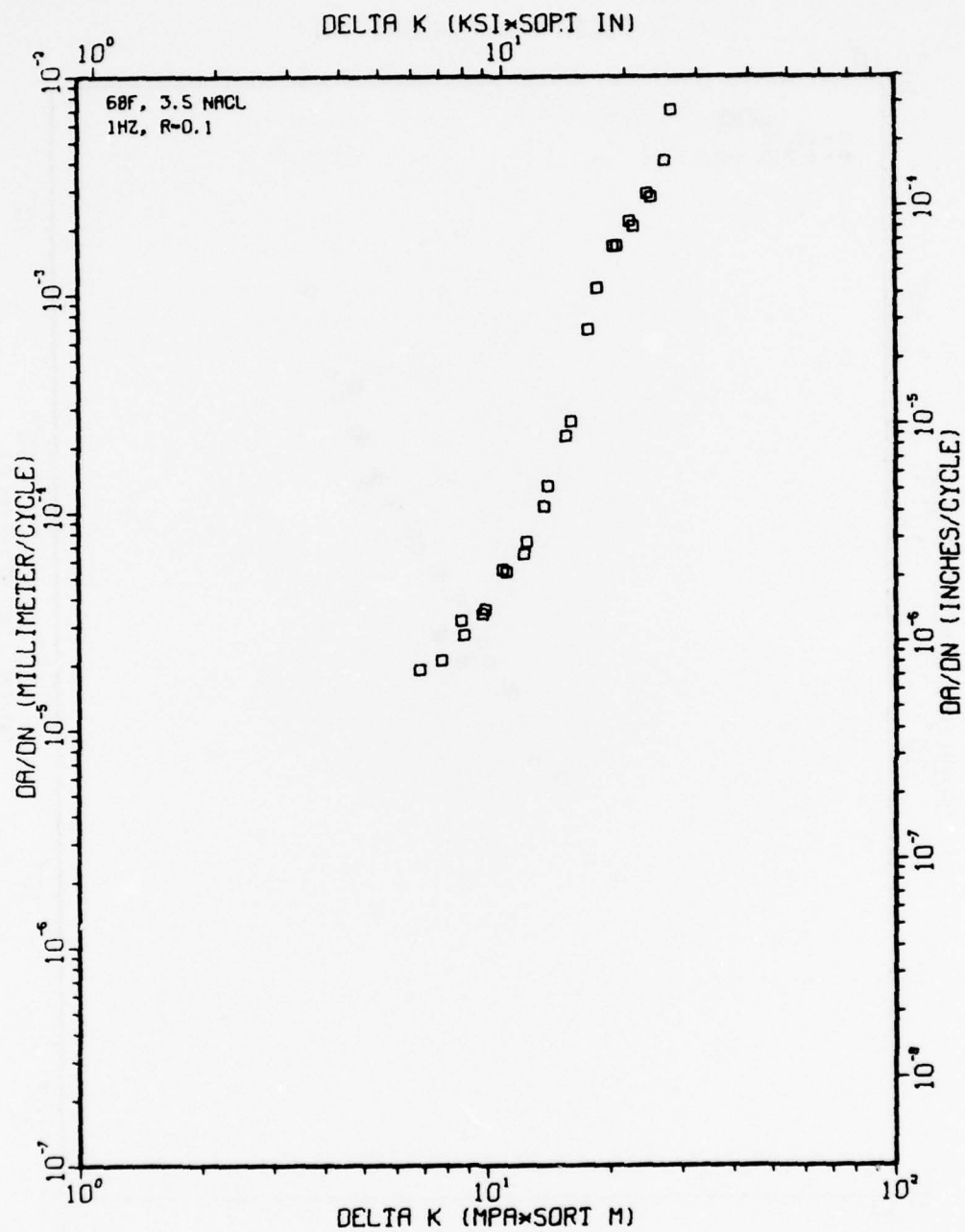
Figure A91

TI-6AL-2SN-4ZR-6MO (COND. 8), 68F, DRY AIR, R-0.3
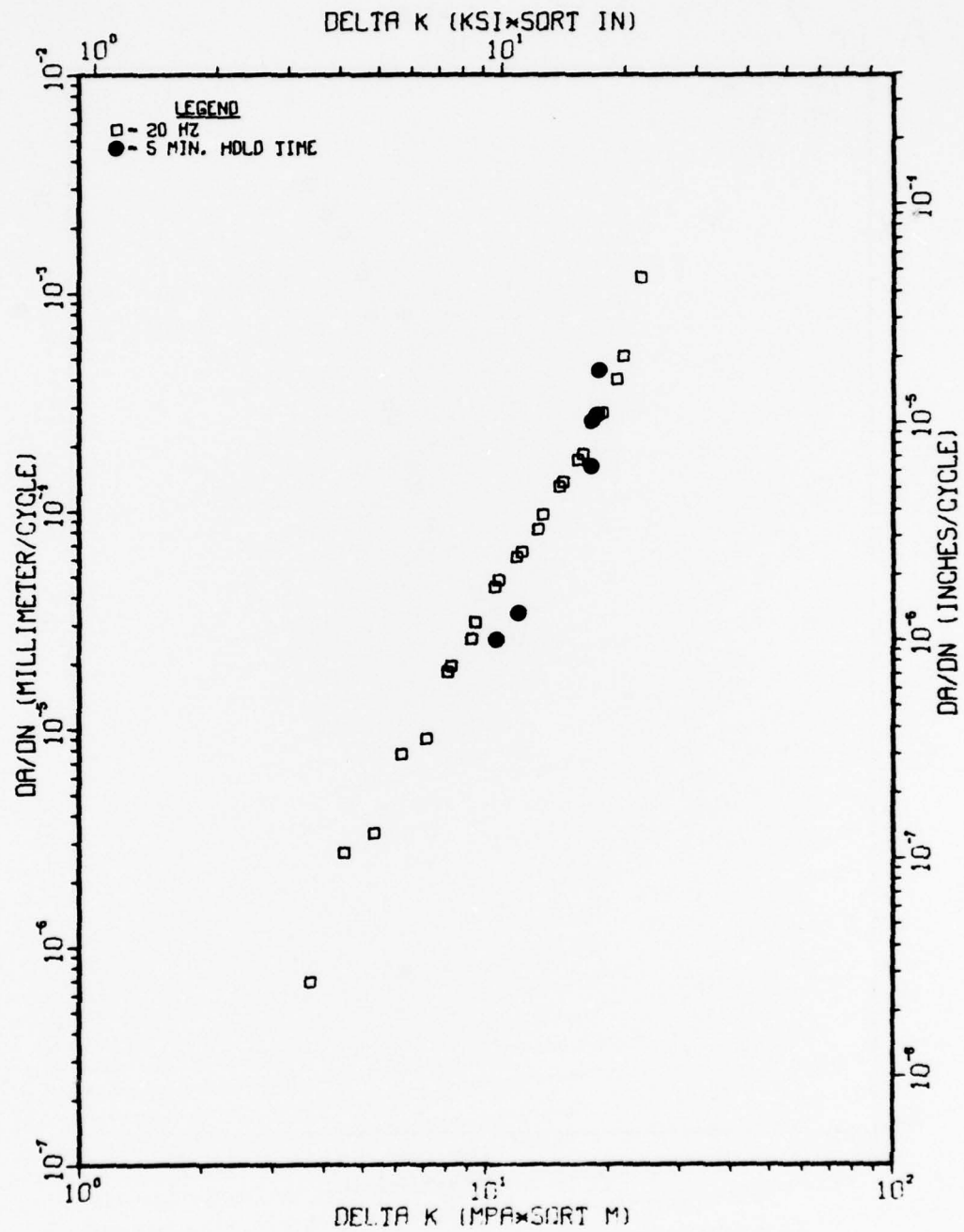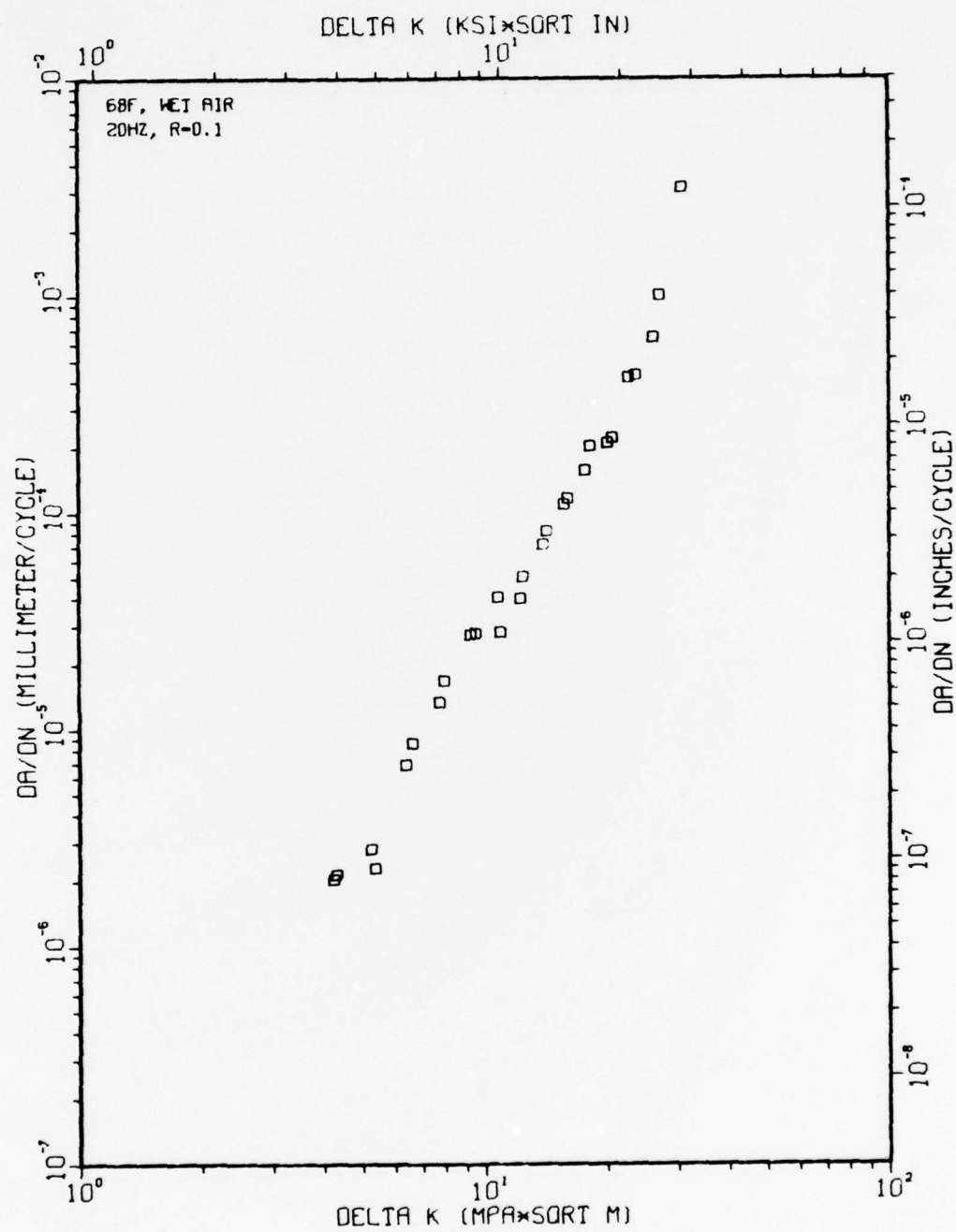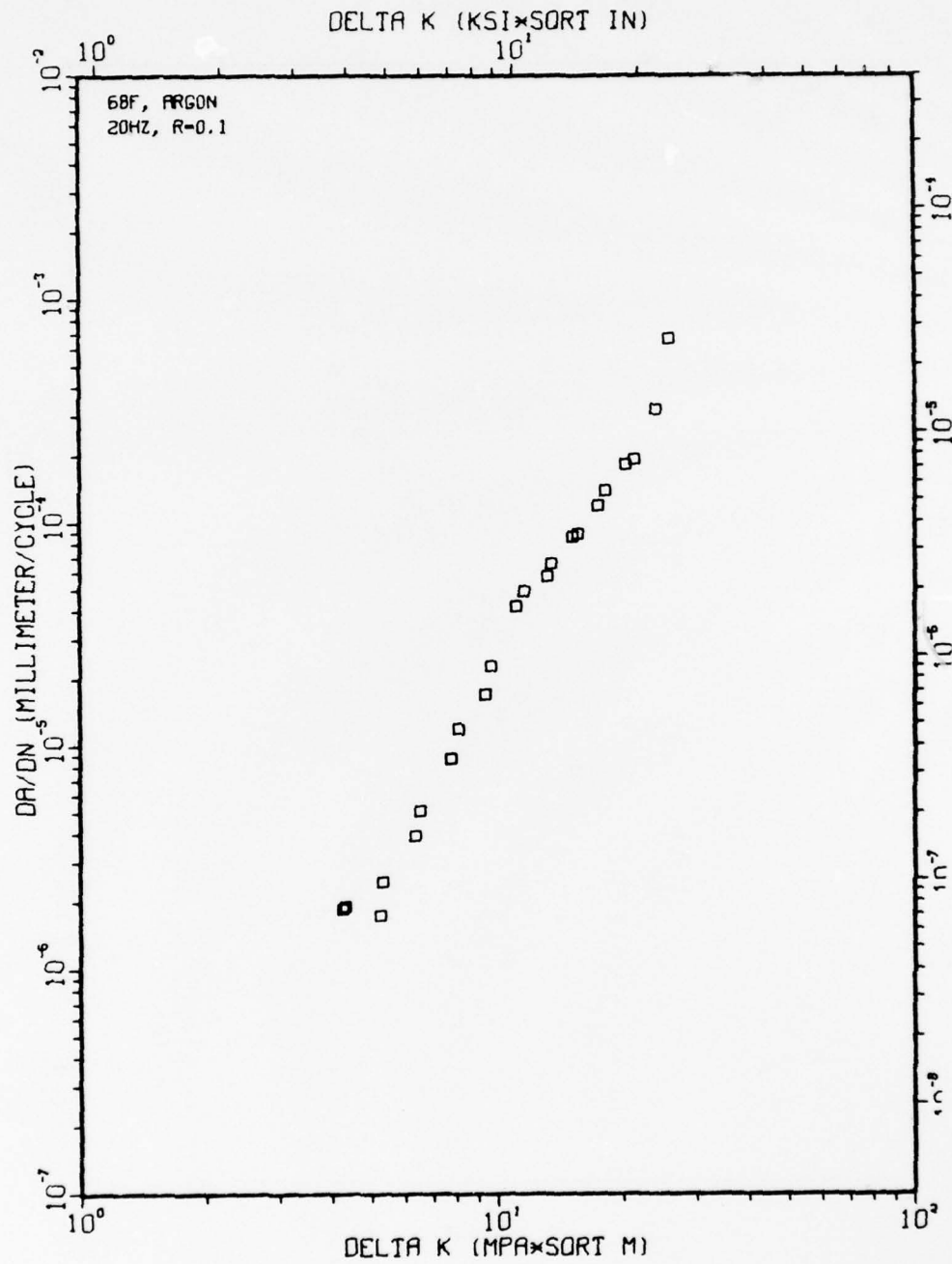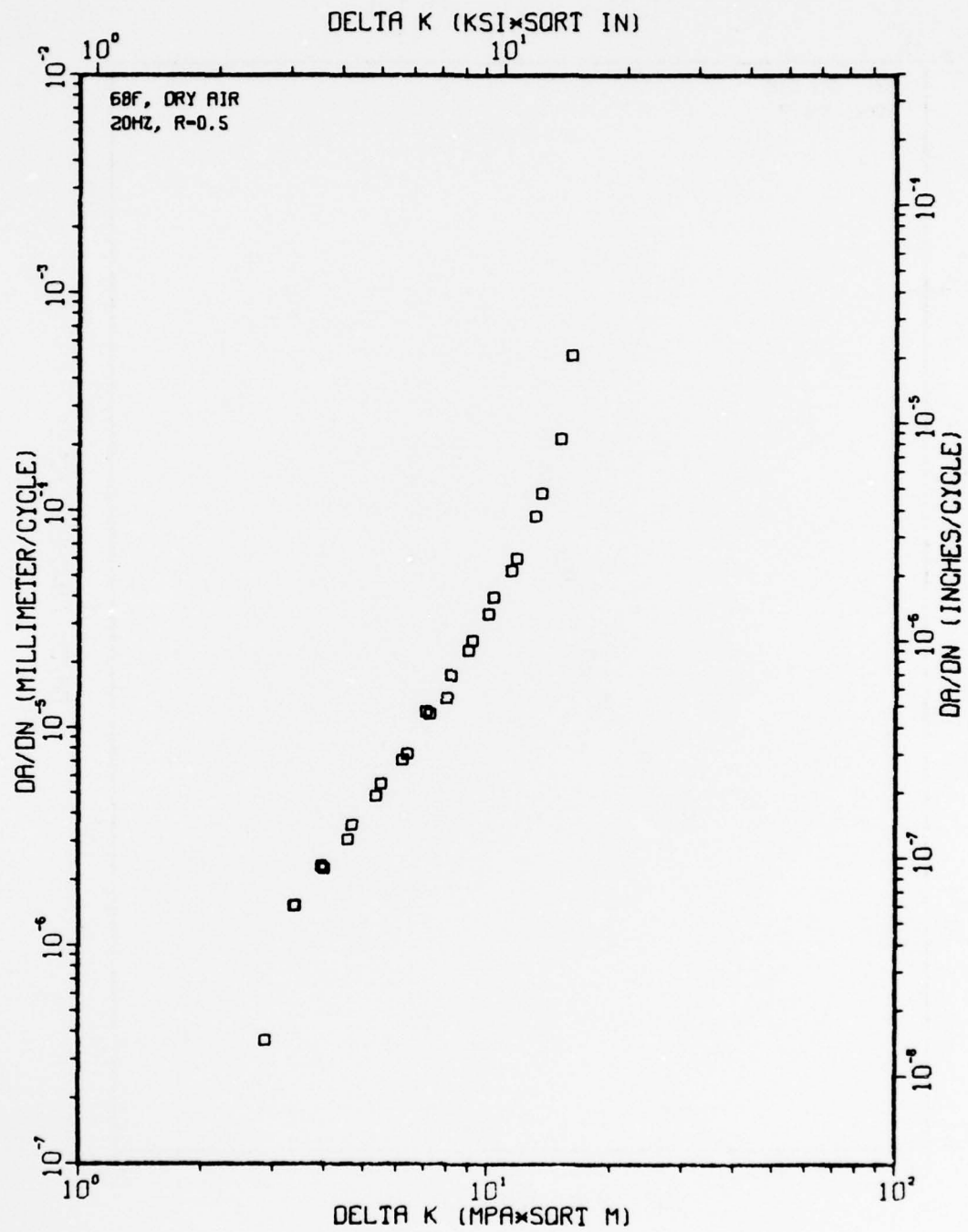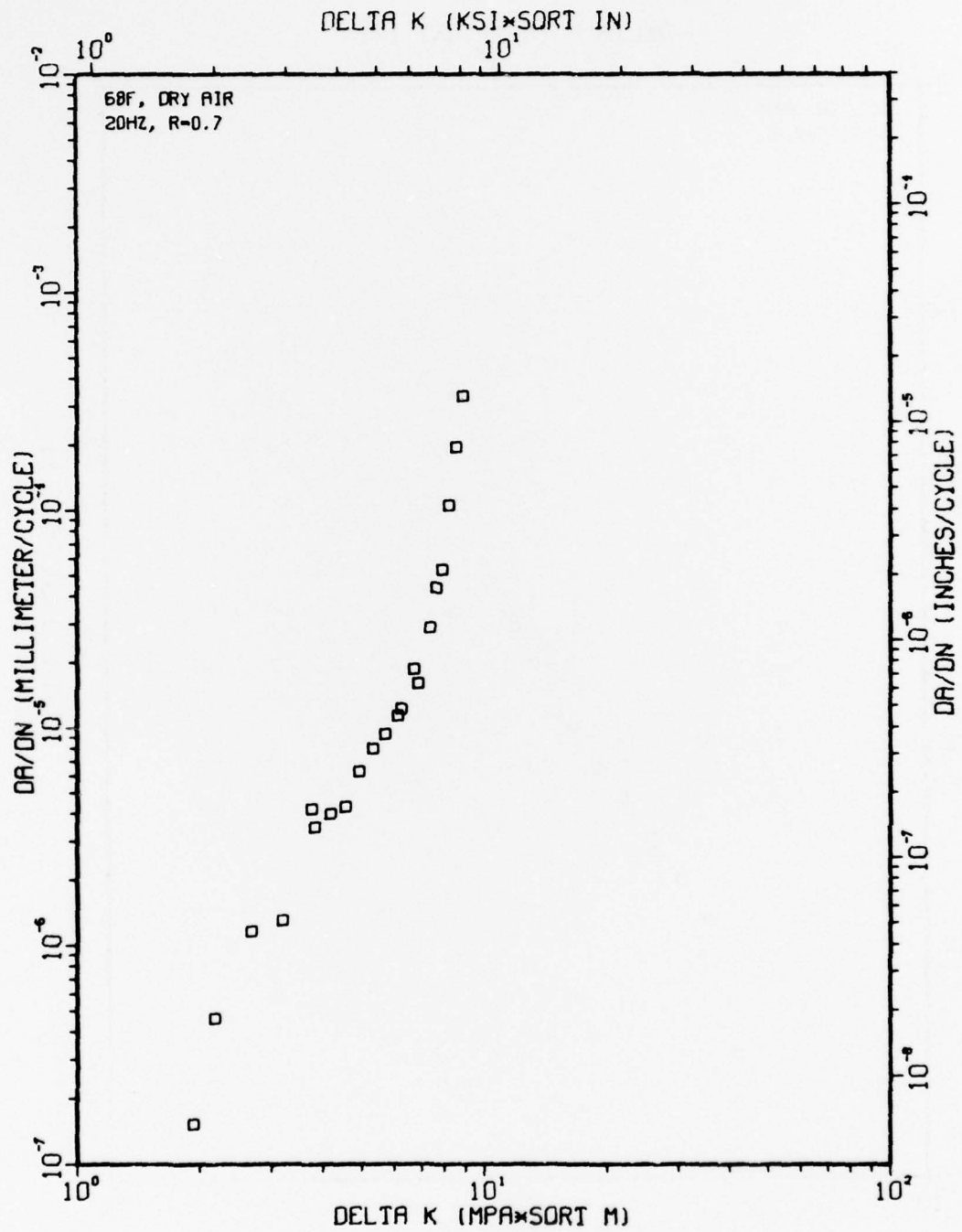

Figure A92

TI-6AL-2SN-4ZR-6MO   2-8-6
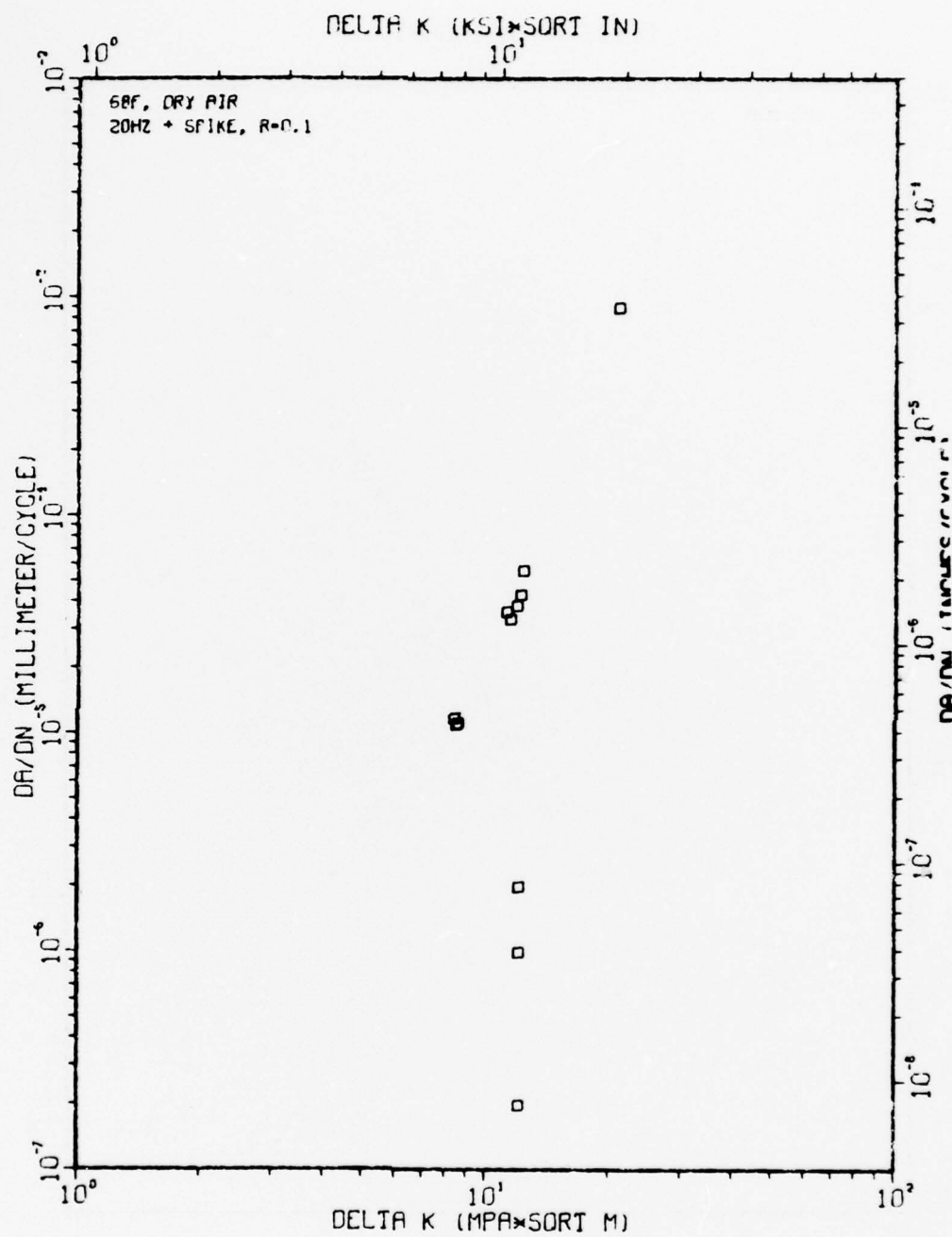

Figure A93

TI-6AL-2SN-4ZR-6MO   2-8-5

Figure A94

TI-6AL-2SN-4ZR-6MO   2-8-7

Figure A95

TI-6AL-2SN-4ZR-6MO   2-8-8

Figure A96

Figure A97

TI-6AL-2SN-4ZR-6MO   2-9-1

Figure A98

Figure A99

TI-6AL-2SN-4ZR-6MO   2-9-3
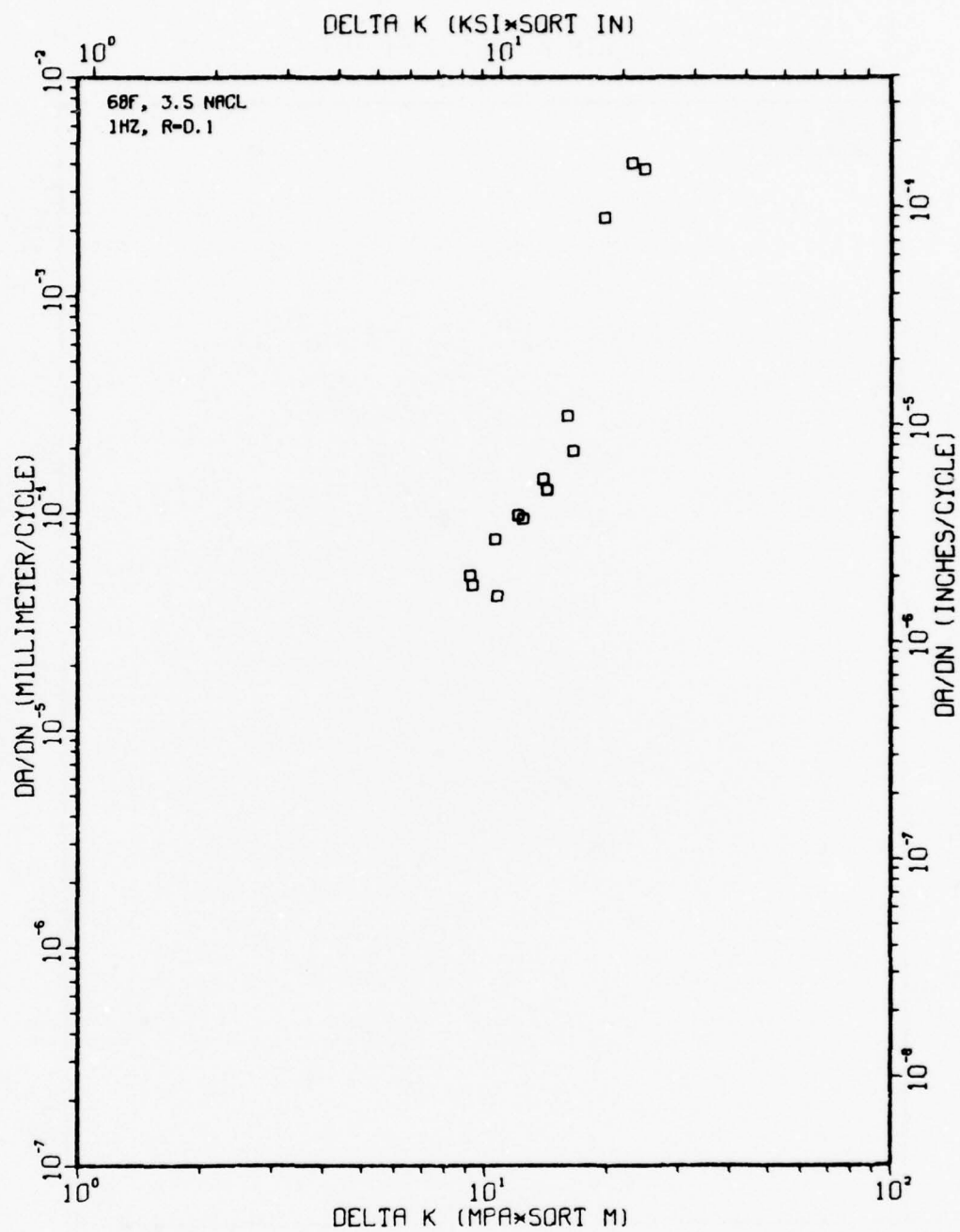
Figure A100

T1-6AL-2SN-4ZR-6MO   2-9-2

Figure A101

377

TI-6AL-2SN-4ZR-6MO   2-10-1

Figure A102

378

Figure A103

TI-6AL-2SN-4ZR-6MO   2-10-3

Figure A104

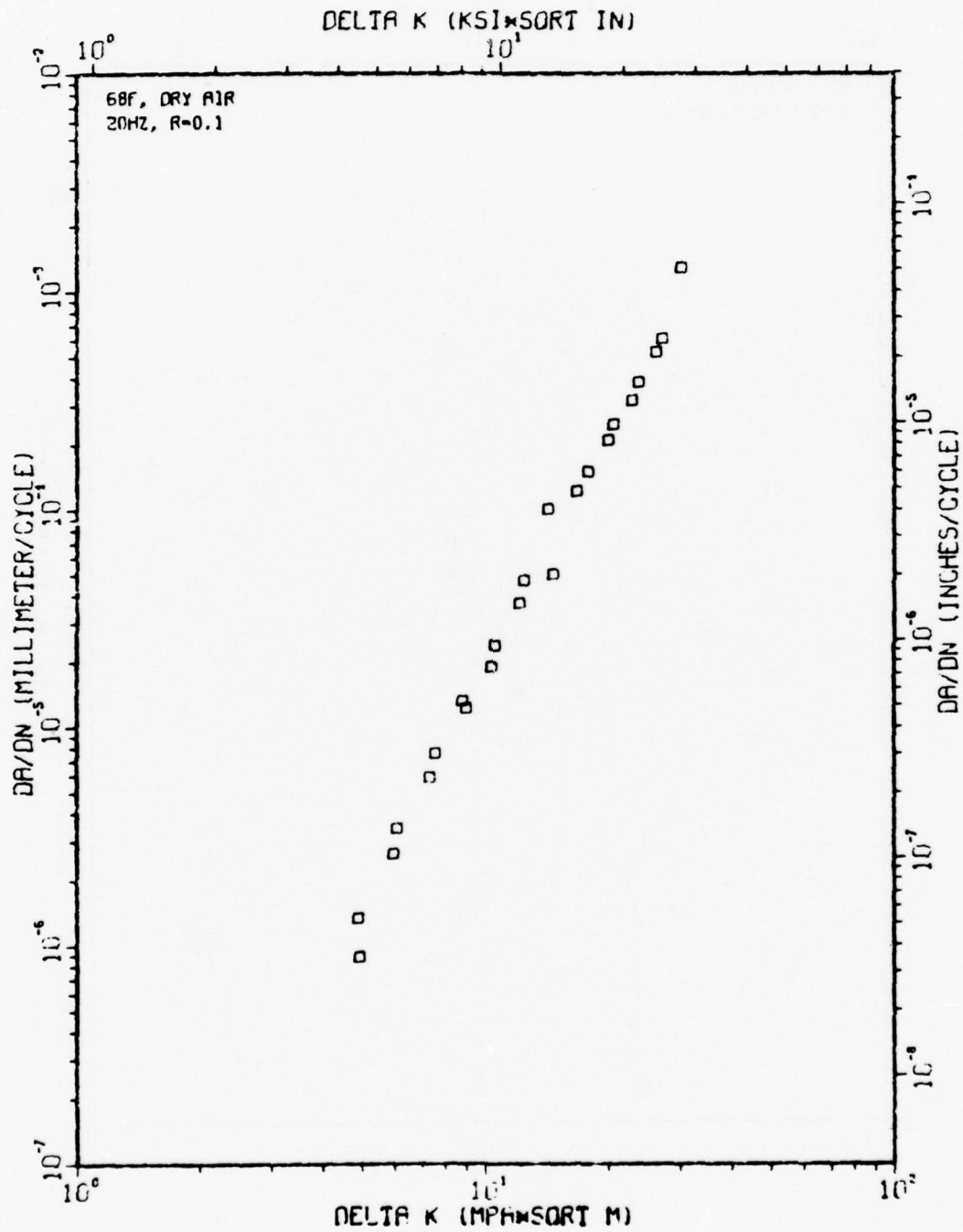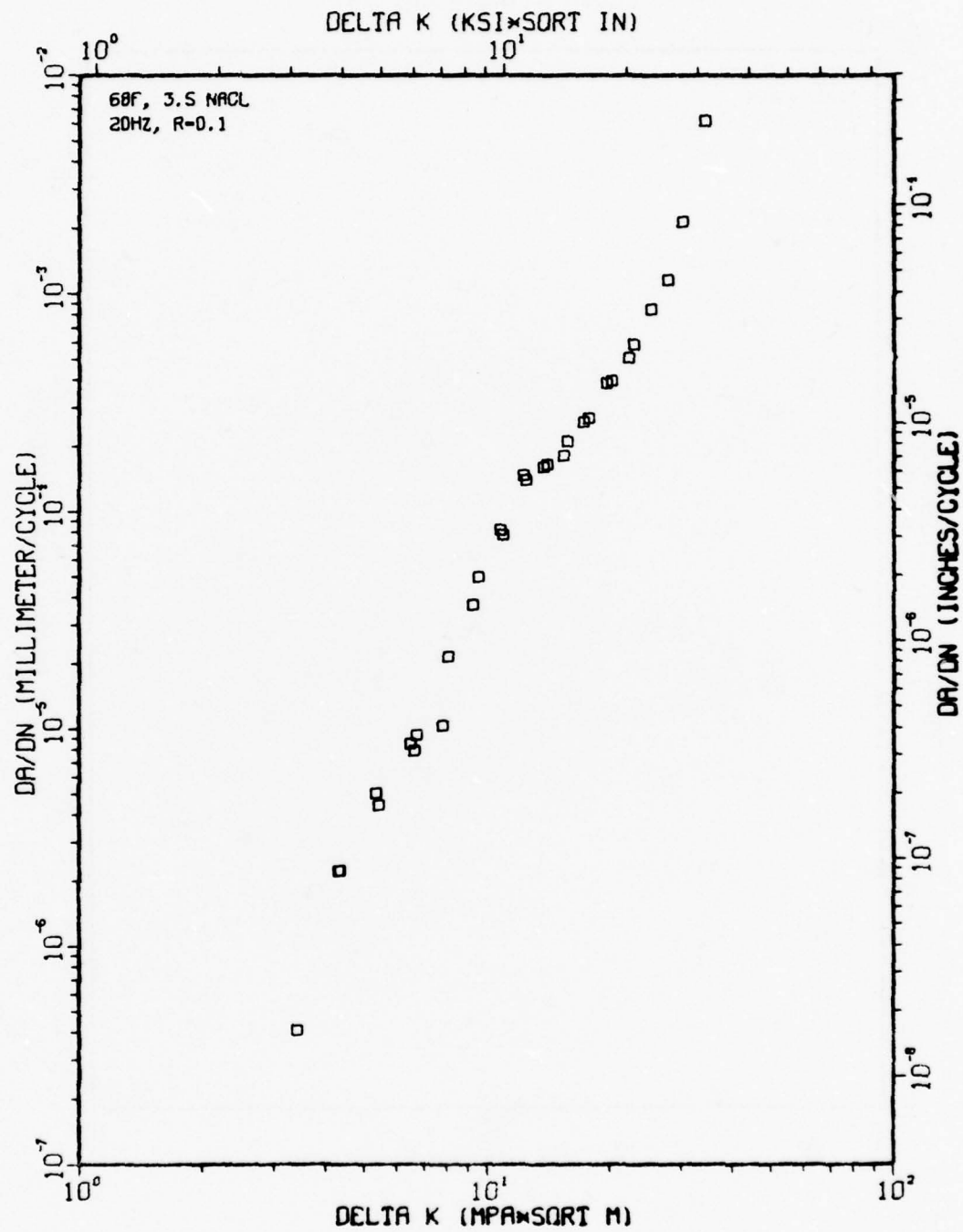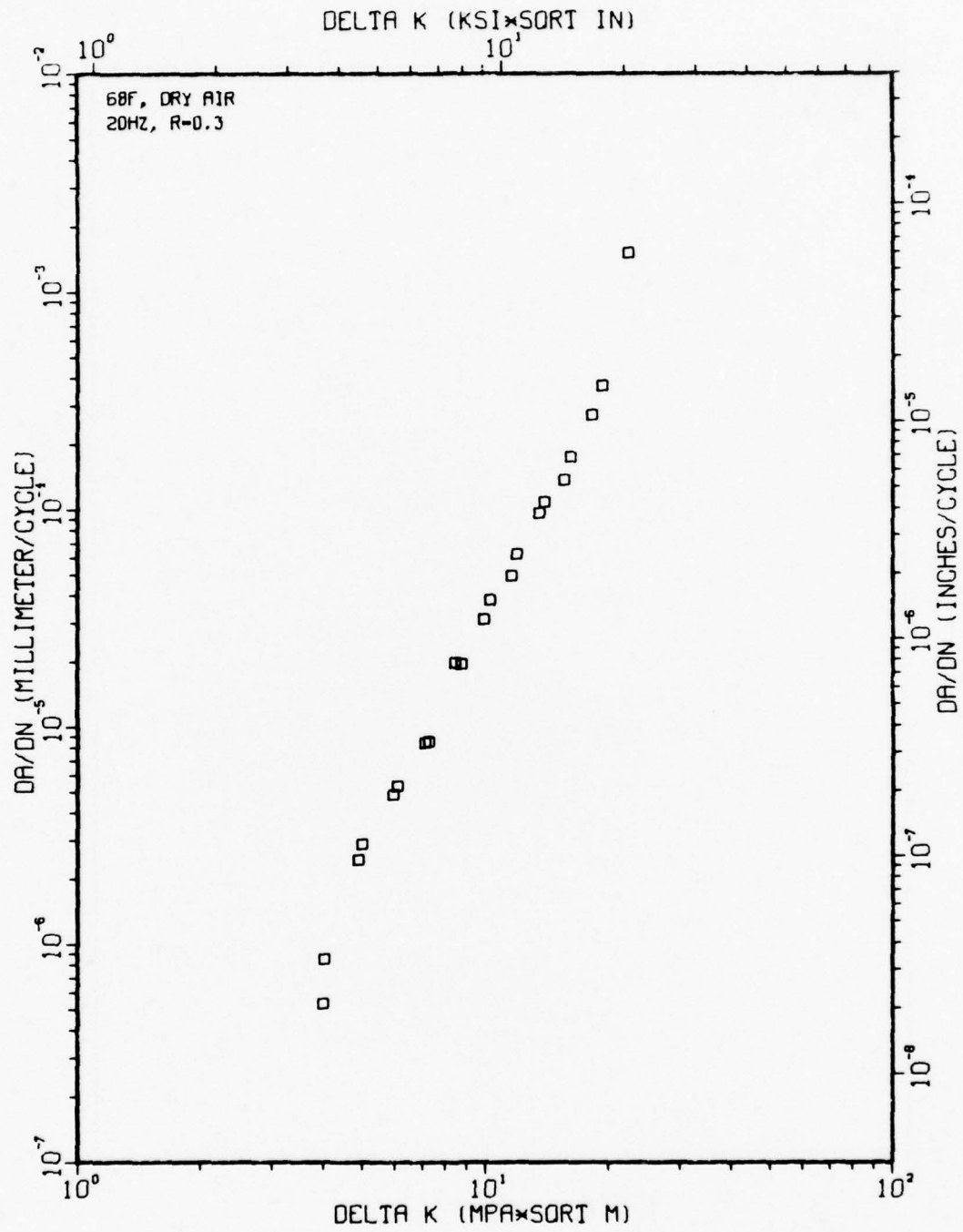TI-6AL-2SN-4ZR-6MO (COND. 10), 68F, DRY AIR, R-0.3

Figure A105

TI-6AL-2SN-4ZR-6MO 2-10-5

Figure A106

TI-6AL-2SN-4ZR-6MO   2-10-7
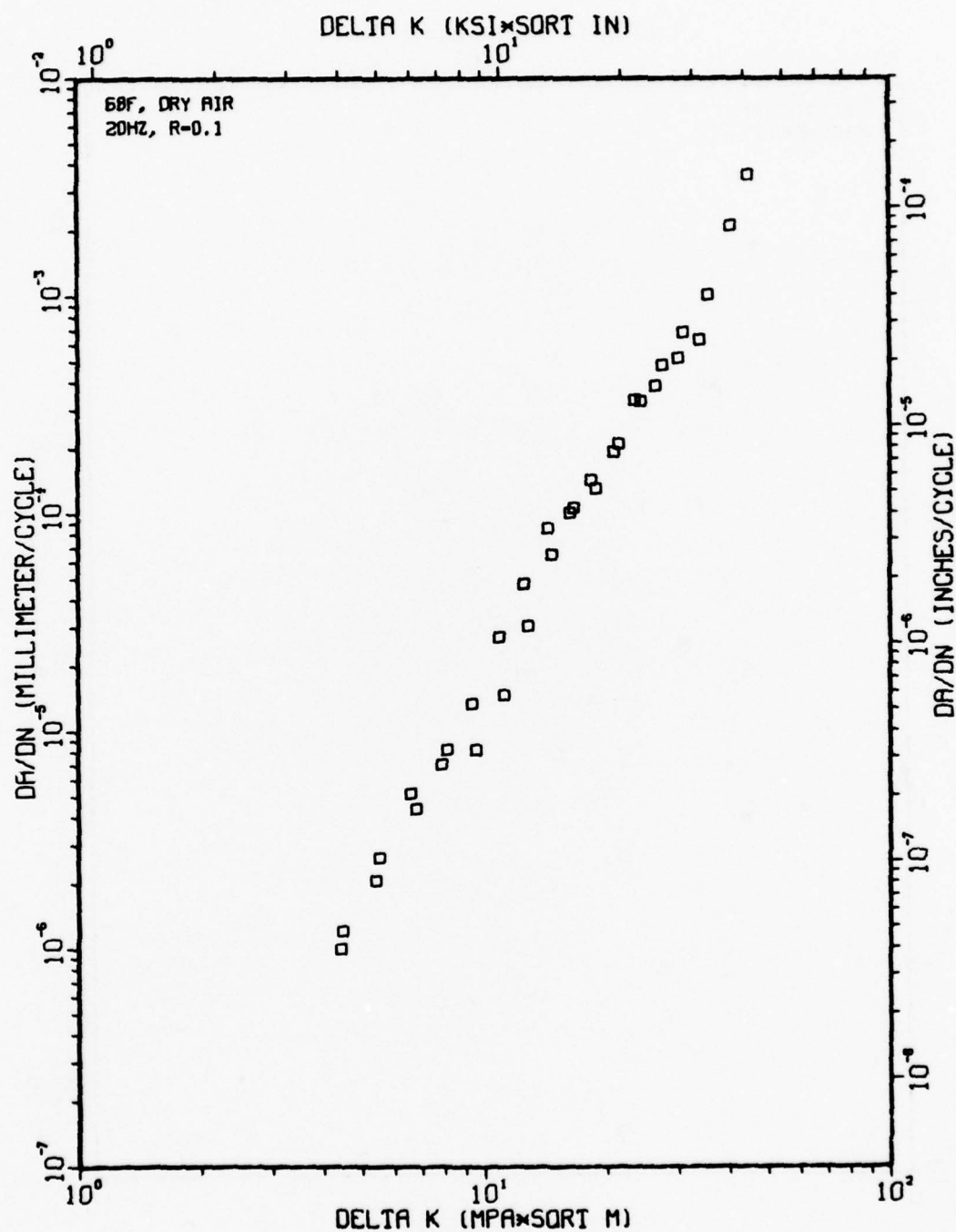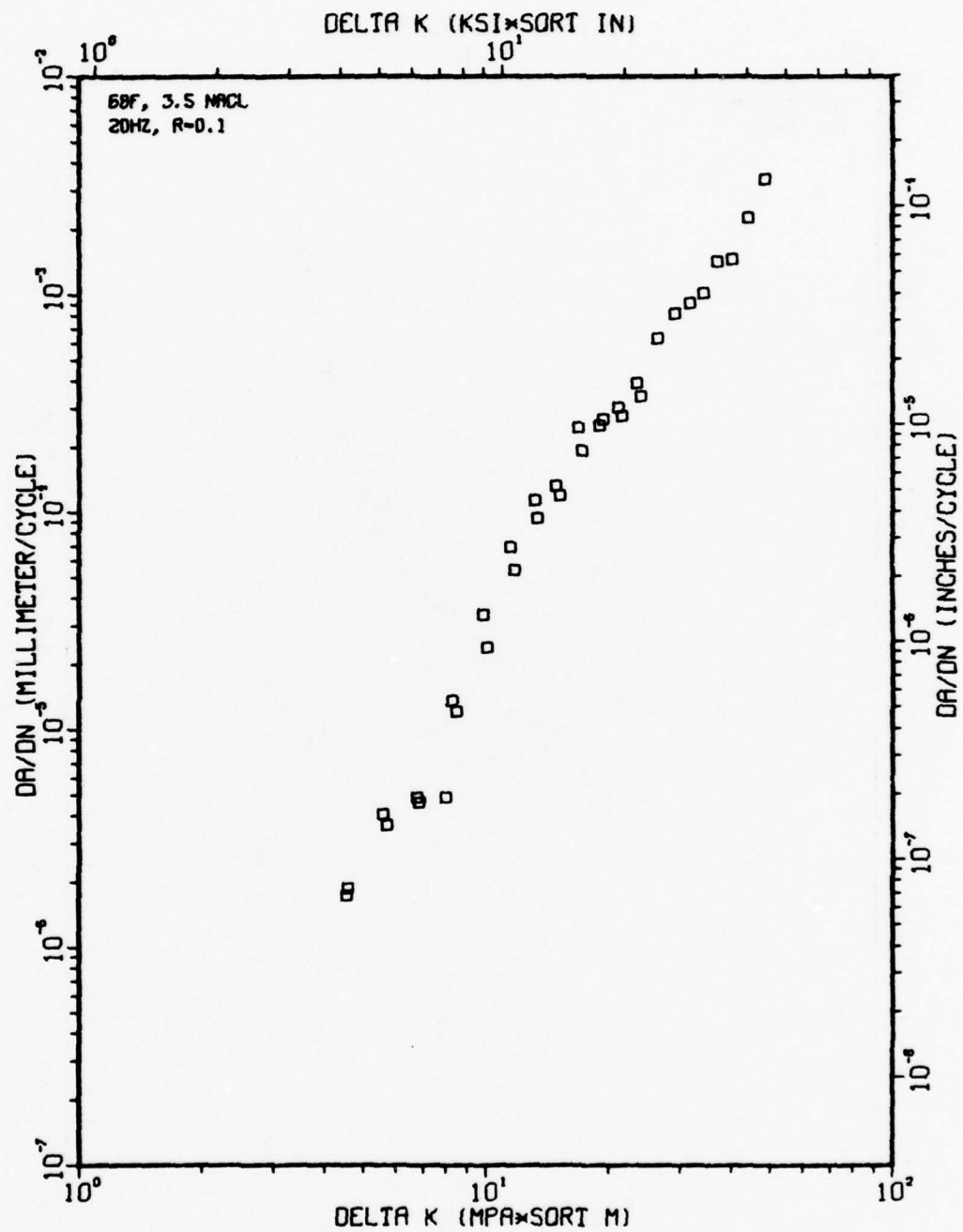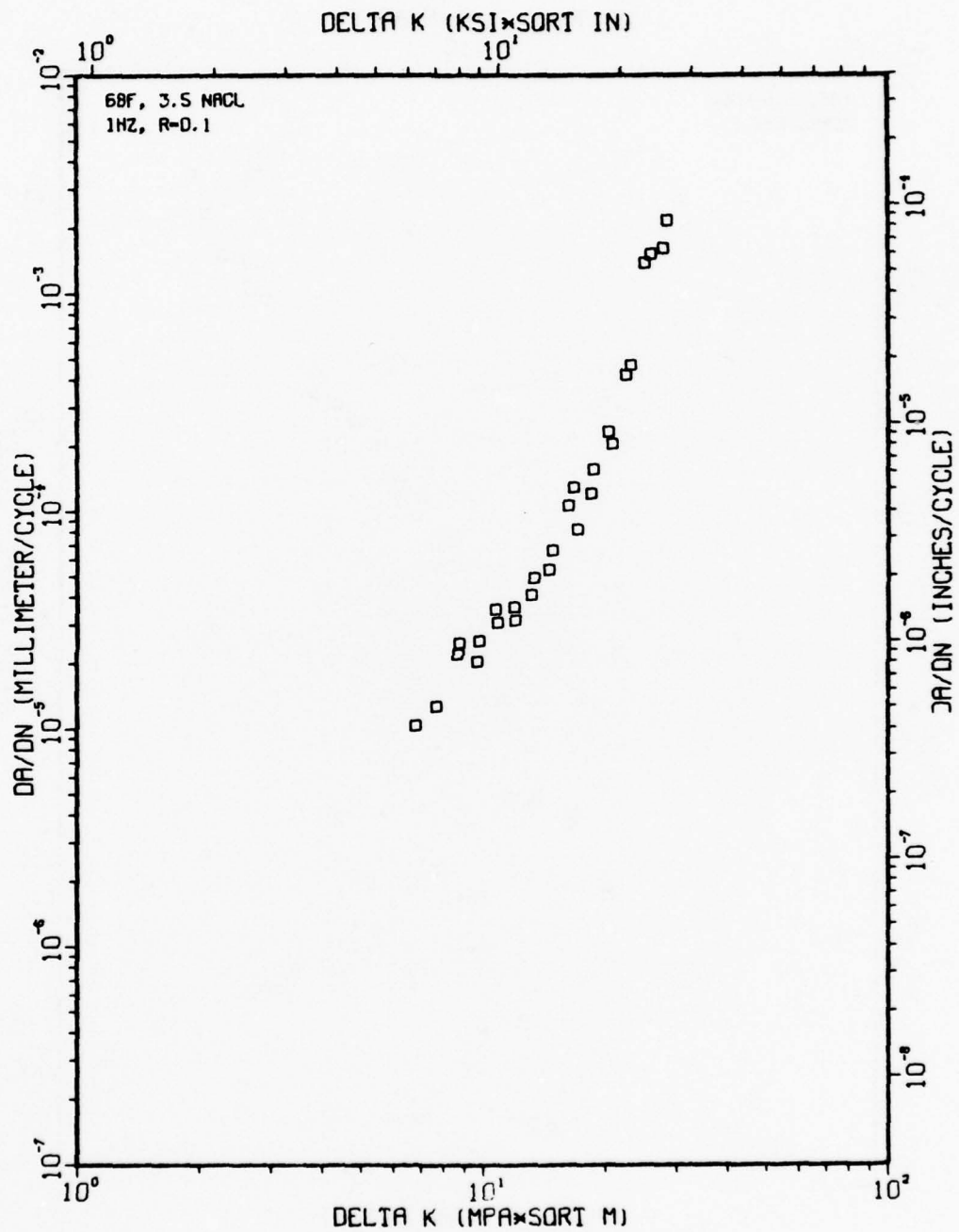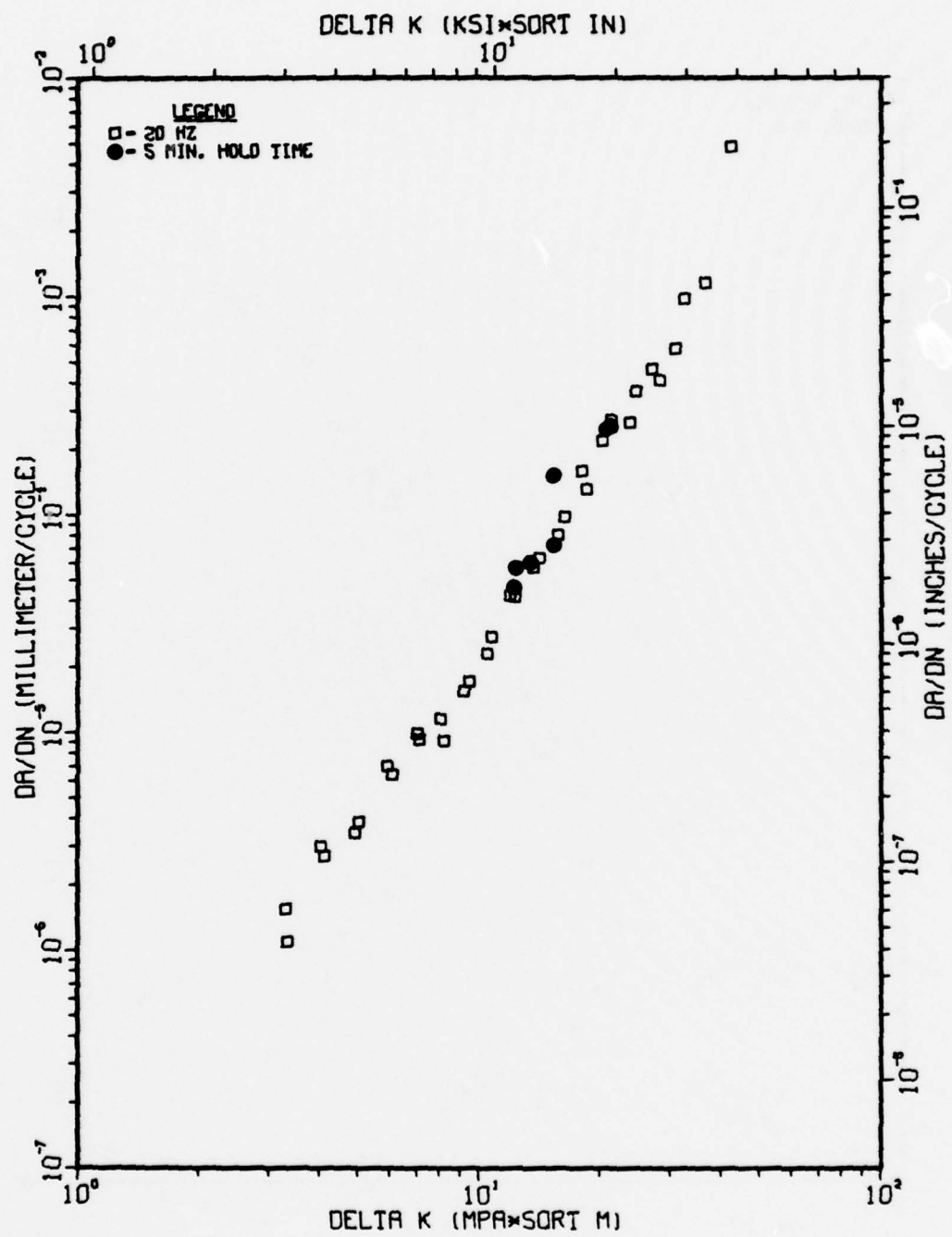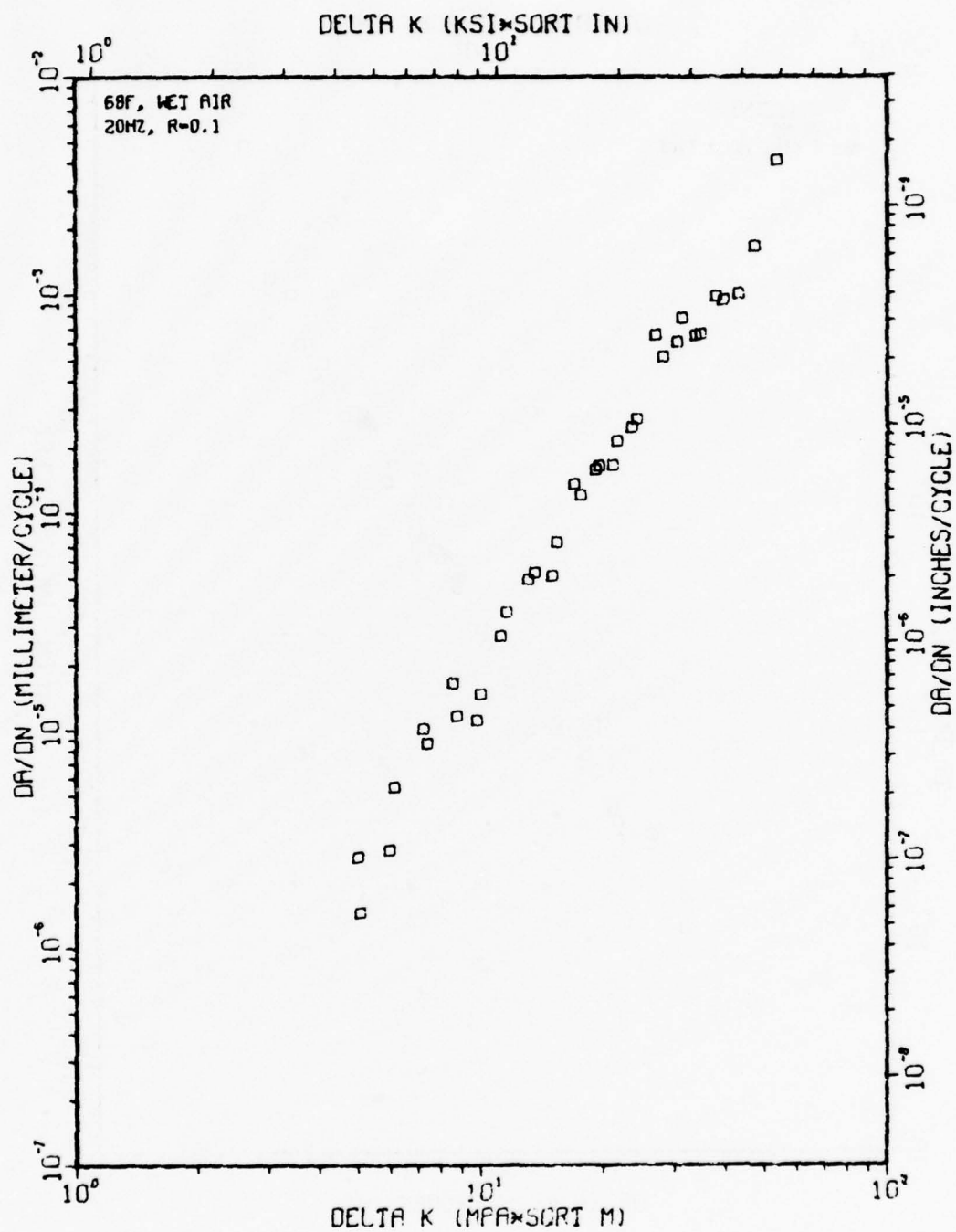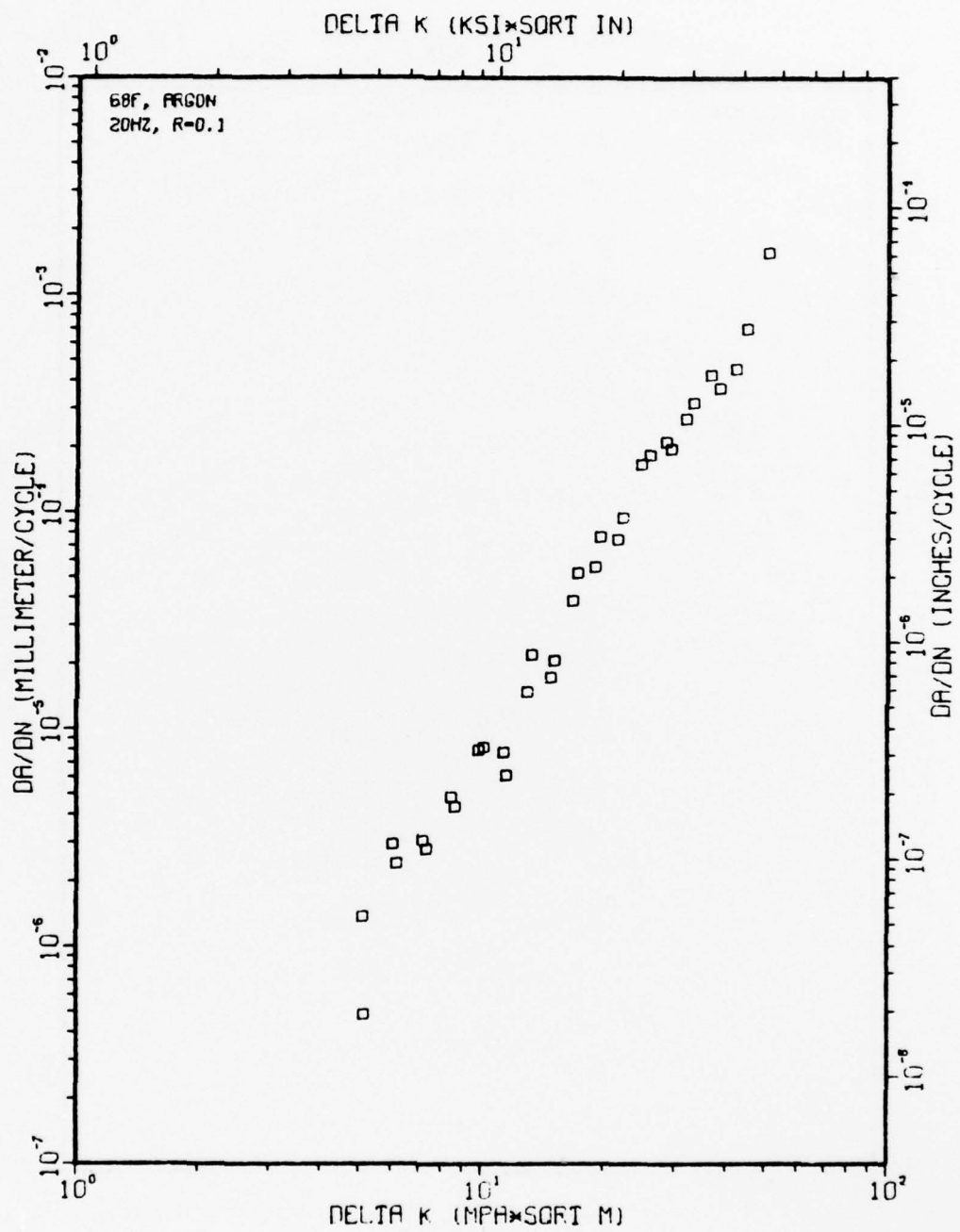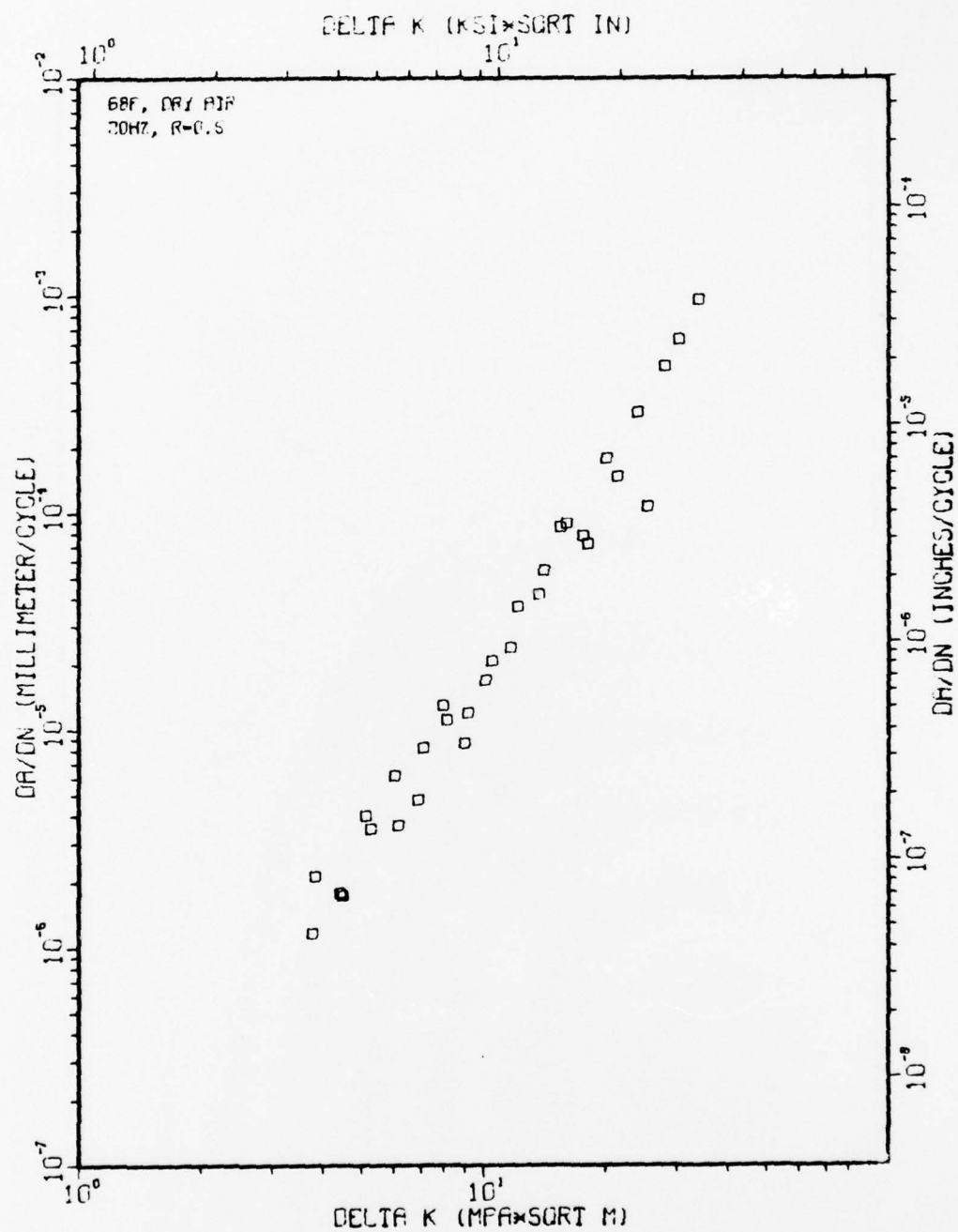

Figure A107

TI-6AL-2SN-4ZR-6MO 2-10-9

DELTA K (KSI*SQRT IN)

Figure A108

TI-6AL-2SN-4ZR-6MO   2-10-8

Figure A109

Figure A110

386
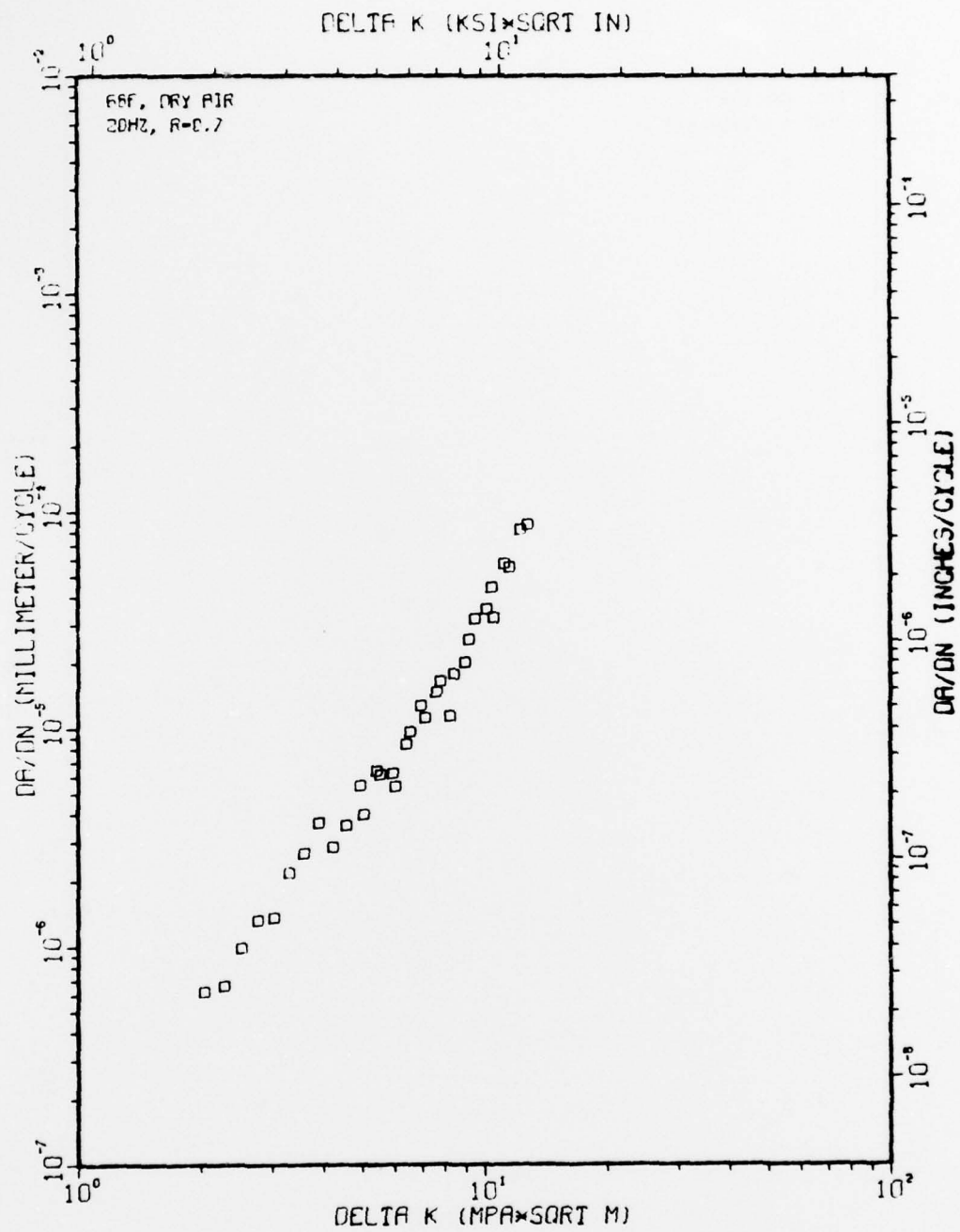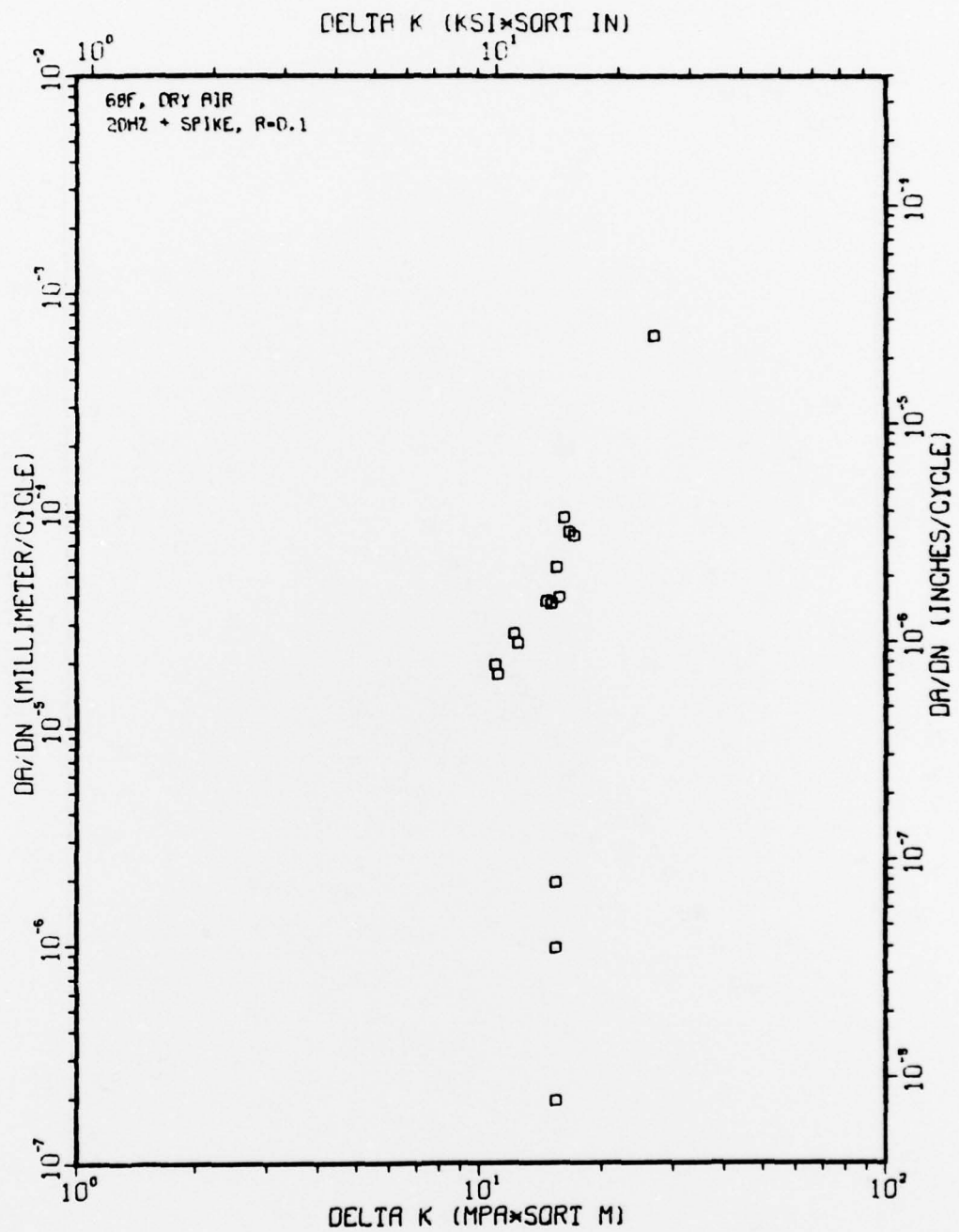
APPENDIX B

FORGING MICROSTRUCTURES

The ten microstructures which were discussed in Part I were produced in forged pancakes approximately 2-in. thick by 14-in. in diameter. The as-forged microstructures of all ten forgings were checked to ensure that the final heat-treated microstructures would be obtained. These ten structures are shown in Figs. B1, B2, and B3. Examination of Table B-I shows that forging schedule is the same for several of the conditions; thus comparison of these microstructures permits the reproducibility of the microstructures to be checked. The evidence suggests that the reproducibility is quite good. The variability of microstructure between surface and center of the pancakes due to variations in cooling rate has also been assessed, Fig. B4. These results show that the higher cooling rate at the surface of the forgings results in some regions of Widmanstätten $\alpha+\beta$ structure as shown in Fig. B4(c). Neither these variations nor the variations in microstructure between forgings are severe enough that they were not remedied by the subsequent heat treatment.

TABLE B-I

FORGING AND HEAT TREATMENT SUMMARY

Ti-6Al-4V		RMI Heat 991174	$(\beta_t \cong 1800^{\mathrm{o}}F)$
Condition		Fabrication	Heat Treatment
Re-X Anneal	(1)	α-β Forge $(\beta_t$-75$)$/AC	1700°F/4h/Cool @ 90°F/h to 1400°F/AC
		α-β Finish $(\beta_t$-100$)$/AC	
10-20% Primary α	(2)	α-β Forge $(\beta_t$-50$)$/AC	1750°F/1h/AC + 1300°F/2h/AC
		α-β Finish $(\beta_t$-25$)$/AC	
40-50% Primary α	(3)	α-β Forge $(\beta_t$-75$)$/AC	1600°F/2h/AC + 1300°F/2h/AC
		α-β Finish $(\beta_t$-100$)$/AC	
β-Forge	(4)	β Forge $(\beta_t$+75$)$/AC	1300°F/2h/AC
		β Finish $(\beta_t$+75$)$/AC	
β-Quench	(5)	β Forge $(\beta_t$+75$)$/AC	1900°F/30 min/WQ + 1300°F/2h/AC
		β Finish $(\beta_t$+75$)$/WQ	
Solution Treat and Age (STA)	(6)	α-β Forge $(\beta_t$-75$)$/AC	1750°F/1h/WQ + 1100°F/4h/AC
		α-β Finish $(\beta_t$-75$)$/AC	
Solution Treat and Overage (STOA)	(7)	α-β Forge $(\beta_t$-75$)$/AC	1750°F/1h/WQ + 1100°F/24h/AC
		α-β Finish $(\beta_t$-75$)$/AC	

Ti-6Al-2Sn-4Zr-6Mo		TMCA Heat N-0241	$(\beta_t \cong 1725^{\mathrm{o}}F)$
10-20% Primary α	(8)	α-β Forge $(\beta_t$-100$)$/AC	1625°F/1h/AC + 1100°F/8h/AC
		α-β Finish $(\beta_t$-25$)$/AC	
40-50% Primary α	(9)	α-β Forge $(\beta_t$-100$)$/AC	1625°F/1h/AC + 1300°F/1h/AC
		α-β Finish $(\beta_t$-100$)$/AC	
β Process	(10)	β Forge $(\beta_t$+75$)$/AC	1625°F/1h/AC + 1100°F/8h/AC
		β Finish $(\beta_t$+75$)$/AC	

FIGURES

Fig. B1   As-forged microstructures of Ti-6Al-4V: (a) Condition 1;
          (b) Condition 2; (c) Condition 3; (d) Condition 4.

Fig. B2   As-forged microstructure of Ti-6Al-4V: (a) Condition 5;
          (b) Condition 6; (c) Condition 7.

Fig. B3   As-forged microstructures of Ti-6Al-2Sn-4Zr-6Mo: (a) Condition 8;
          (b) Condition 9; (c) Condition 10.

Fig. B4   Variations in as-forged microstructure within Condition 1 forging:
          (a) microstructure at D/2, T/2 (D = diameter, T = thickness), i.e.,
          forging center; (b) microstructure at D, T/2, i.e., forging edge;
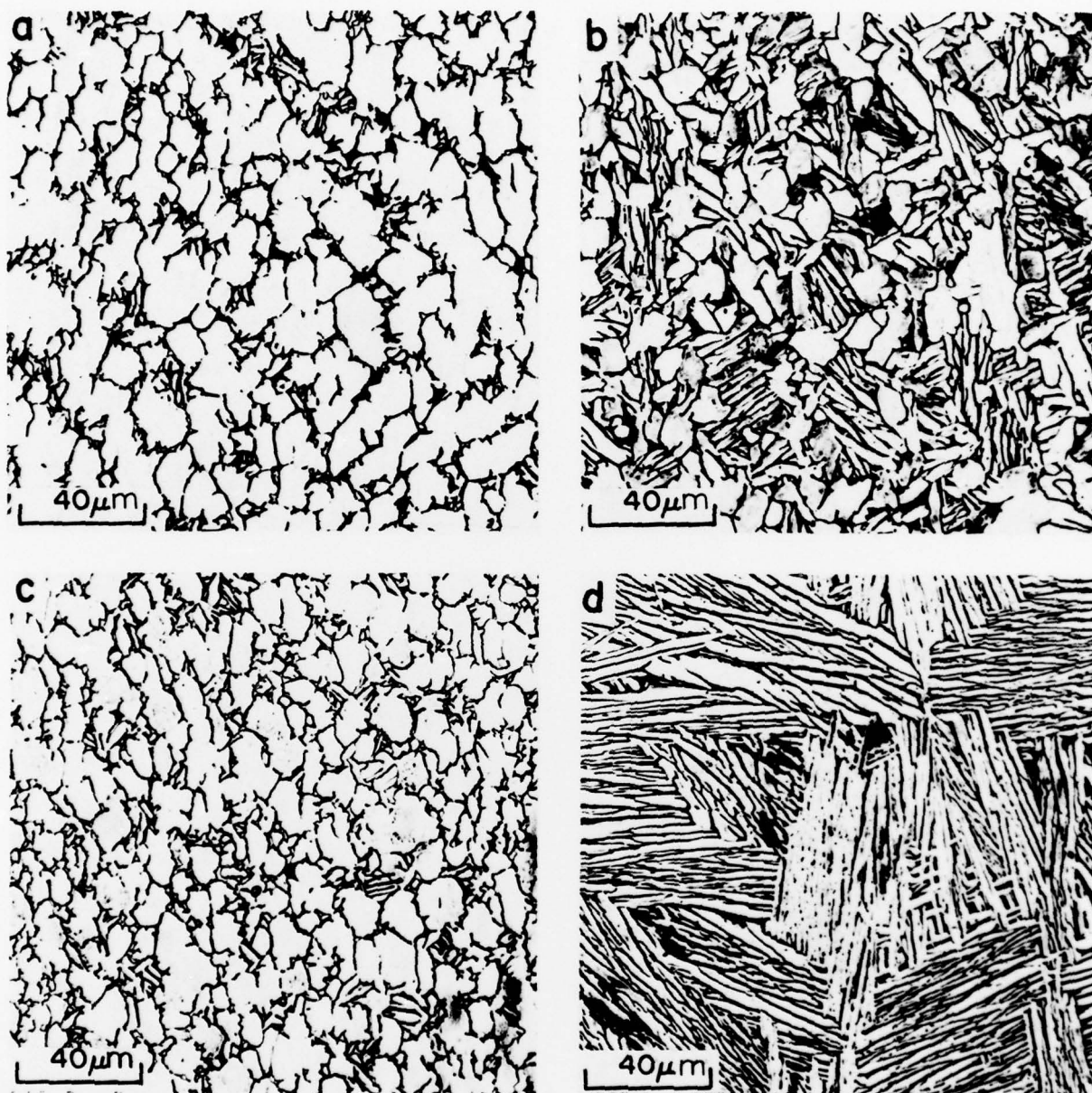   (c) microstructure at D/2, T, i.e., forging surface.

Fig. B1   As-forged microstructures of Ti-6Al-4V: (a) Condition 1;
(b) Condition 2; (c) Condition 3; (d) Condition 4.
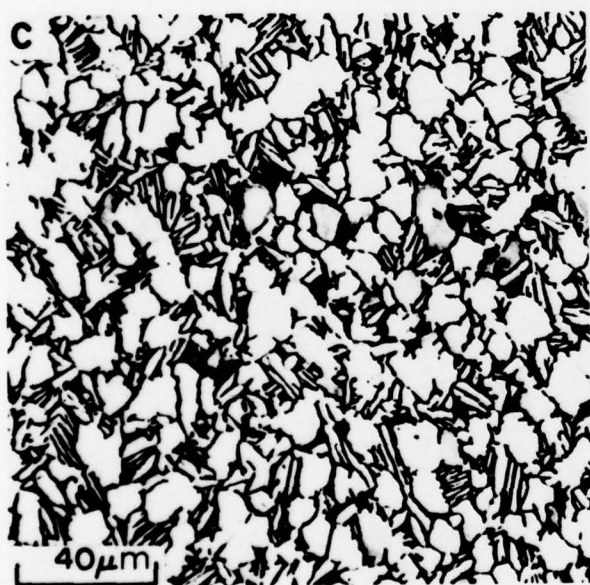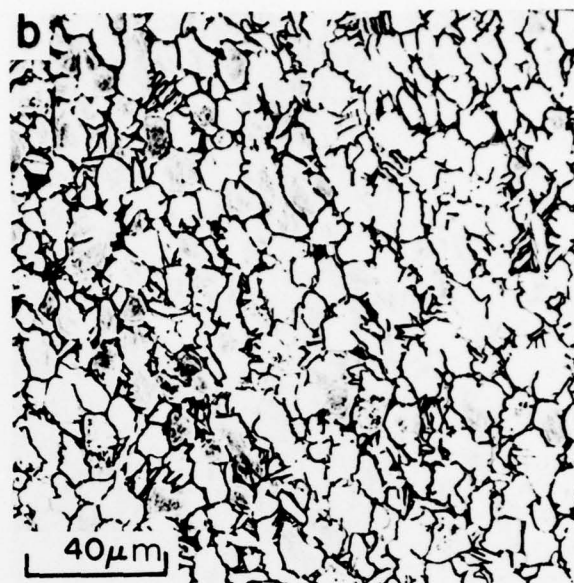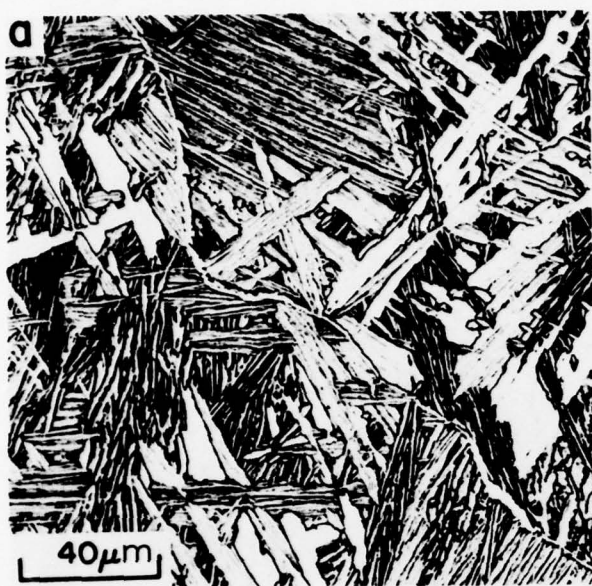
Fig. B2   As-forged microstructure of Ti-6Al-4V: (a) Condition 5;
(b) Condition 6; (c) Condition 7.
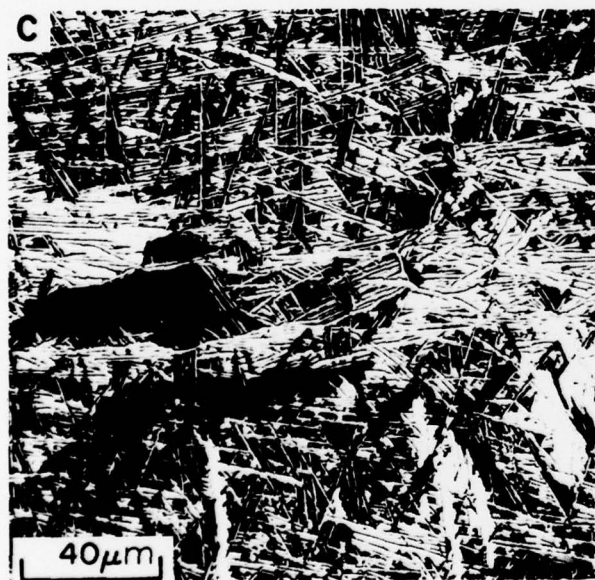
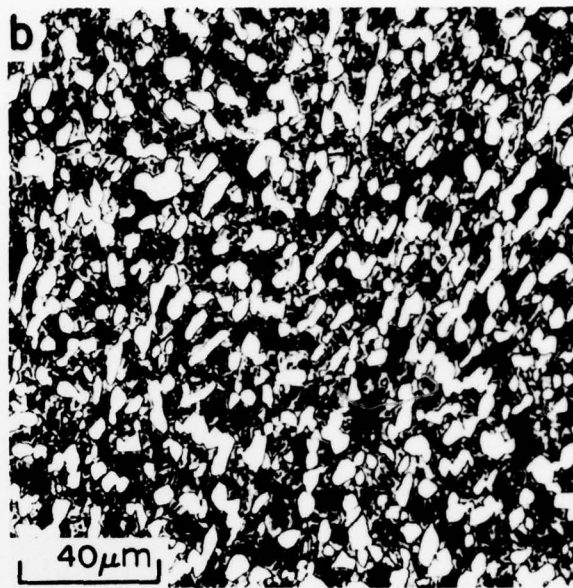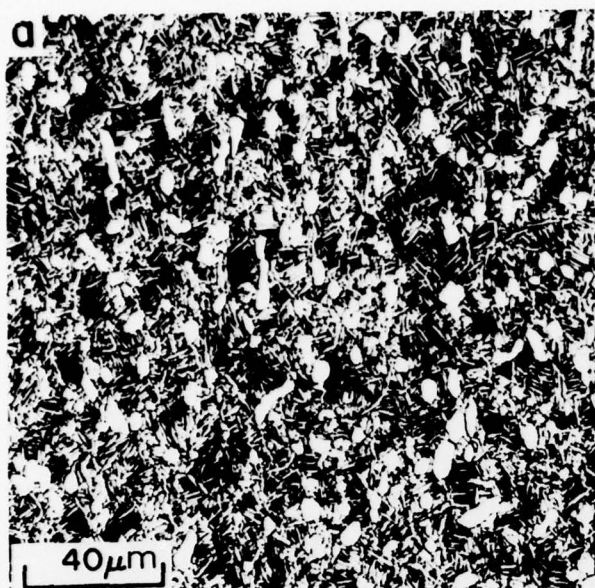Fig. B3   As-forged microstructures of Ti-6Al-2Sn-4Zr-6Mo: (a) Condition 8;
(b) Condition 9; (c) Condition 10.
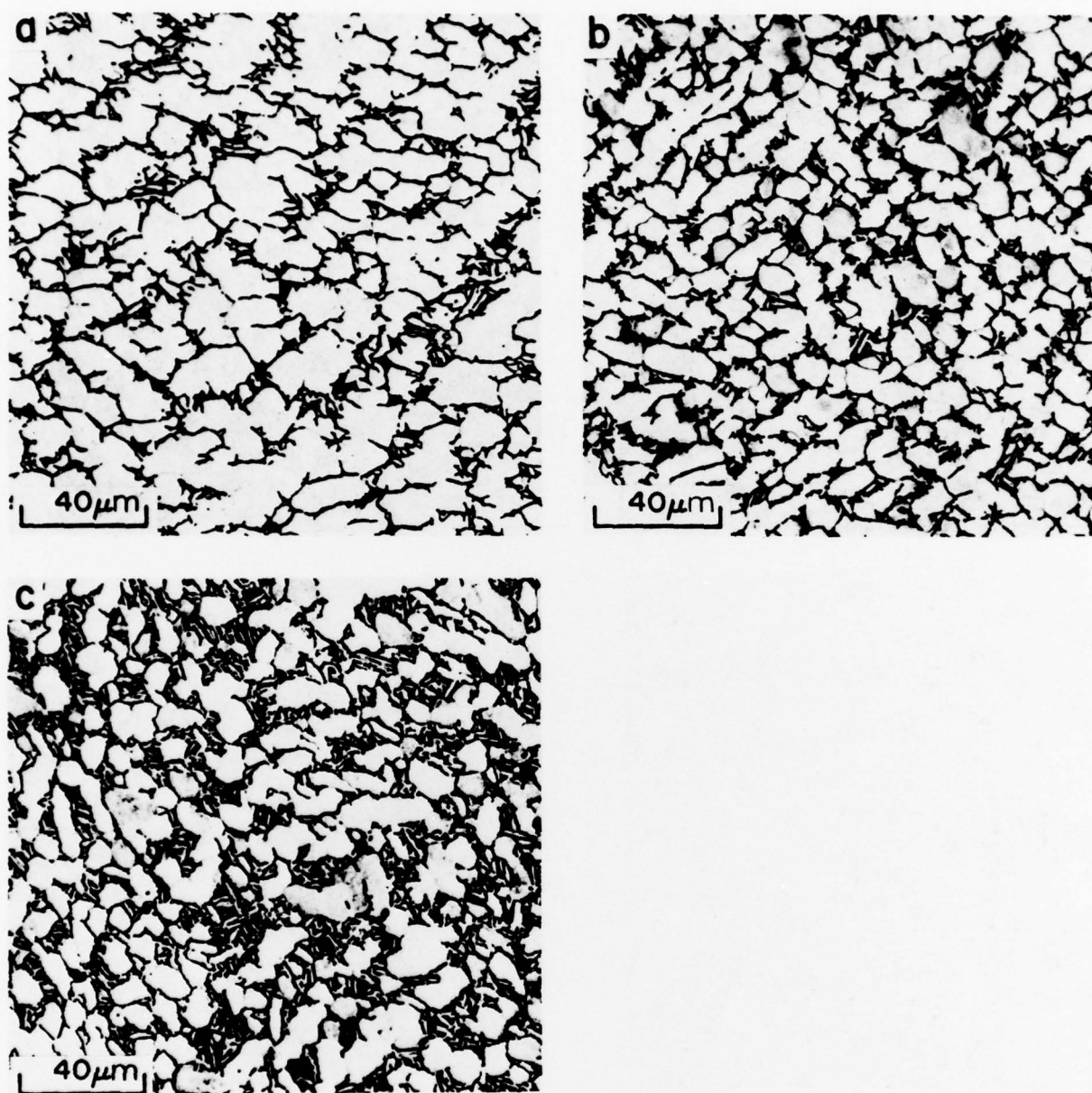
Fig. B4   Variations in as-forged microstructure within Condition 1 forging:
(a) microstructure at D/2, T/2 (D = diameter, T = thickness), i.e.,
forging center; (b) microstructure at D, T/2, i.e., forging edge;
(c) microstructure at D/2, T, i.e., forging surface.

APPENDIX C

PUBLICATIONS AND TECHNICAL TALKS

PUBLICATIONS

1. J. C. Chesnutt and R. A. Spurling, "Fracture Topography-Microstructure Correlations in the SEM," Met. Trans., 1977, Vol. 8A, pp. 216-218

2. A. W. Thompson and J. C. Williams, "Nuclei for Ductile Fracture in Titanium," in Fracture 1977, Vol. 2, ICF4, Waterloo, Canada, 1977 (also presented at the conference)

3. A. W. Thompson, J. C. Williams, J. D. Frandsen, and J. C. Chesnutt, "The Effect of Microstructure on Fatigue Crack Propagation Rate in Ti-6Al-4V," Proceedings of the Third International Conference on Titanium, Moscow, 1976, in press (also presented at the conference)

396

TECHNICAL TALKS

1. J. D. Frandsen, J. C. Chesnutt, A. W. Thompson, and J. C. Williams, "Fatigue Crack Propagation in Ti-6Al-4V," 1975 Western Metal and Tool Exposition (WESTEC 1975), Los Angeles, March 11, 1975

2. J. C. Chesnutt, A. W. Thompson, J. D. Frandsen, and J. C. Williams, "Effect of Microstructure on Toughness and Fatigue Crack Propagation in Ti-6Al-4V," AIME Annual Meeting, Las Vegas, February 25, 1976

3. J. C. Chesnutt, "Fractographic Aspects of Fatigue and Fracture in Titanium Alloys," 1976 Western Metal and Tool Exposition (WESTEC 1976), Los Angeles, March 10, 1976

4. A. W. Thompson, "Effect of Microstructure on Fatigue Crack Propagation in Titanium Alloys" (invited), Meeting on Fatigue Crack Growth, ARPA Materials Research Council, La Jolla, California, July 8, 1976

5. J. C. Chesnutt, L. R. Bidwell, A. W. Thompson, and J. D. Frandsen, "The Relationship Between Microstructure, Texture, Fatigue and Fracture in Ti-6Al-4V and Ti-6Al-2Sn-4Zr-6Mo," Golden Gate Welding and Metal Conference (QUINTECH), San Francisco, January 28, 1977

6. J. C. Chesnutt, A. W. Thompson, and J. D. Frandsen, "Effect of Load Ratio and Hold Time on Fatigue Crack Propagation in Ti-6Al-4V and Ti-6Al-2Sn-4Zr-6Mo," AIME Annual Meeting, Atlanta, March 8, 1977

7. A. W. Thompson, "Advances in Understanding of Fatigue Crack Propagation," Conférence Dévelopments Récents en Mécanique de la Rupture, Paris, June 3, 1977

8. A. W. Thompson, "Fatigue Crack Propagation in Titanium Alloys," AIME Annual Meeting, Denver, March 1, 1978

9. J. C. Chesnutt, A. W. Thompson, and J. C. Williams, "Effect of Temperature and Interstitials on Fatigue Crack Propagation in Ti-6Al-4V," AIME Annual Meeting, Denver, March 1, 1978